Niloy K. Dutta & Qiang Wang

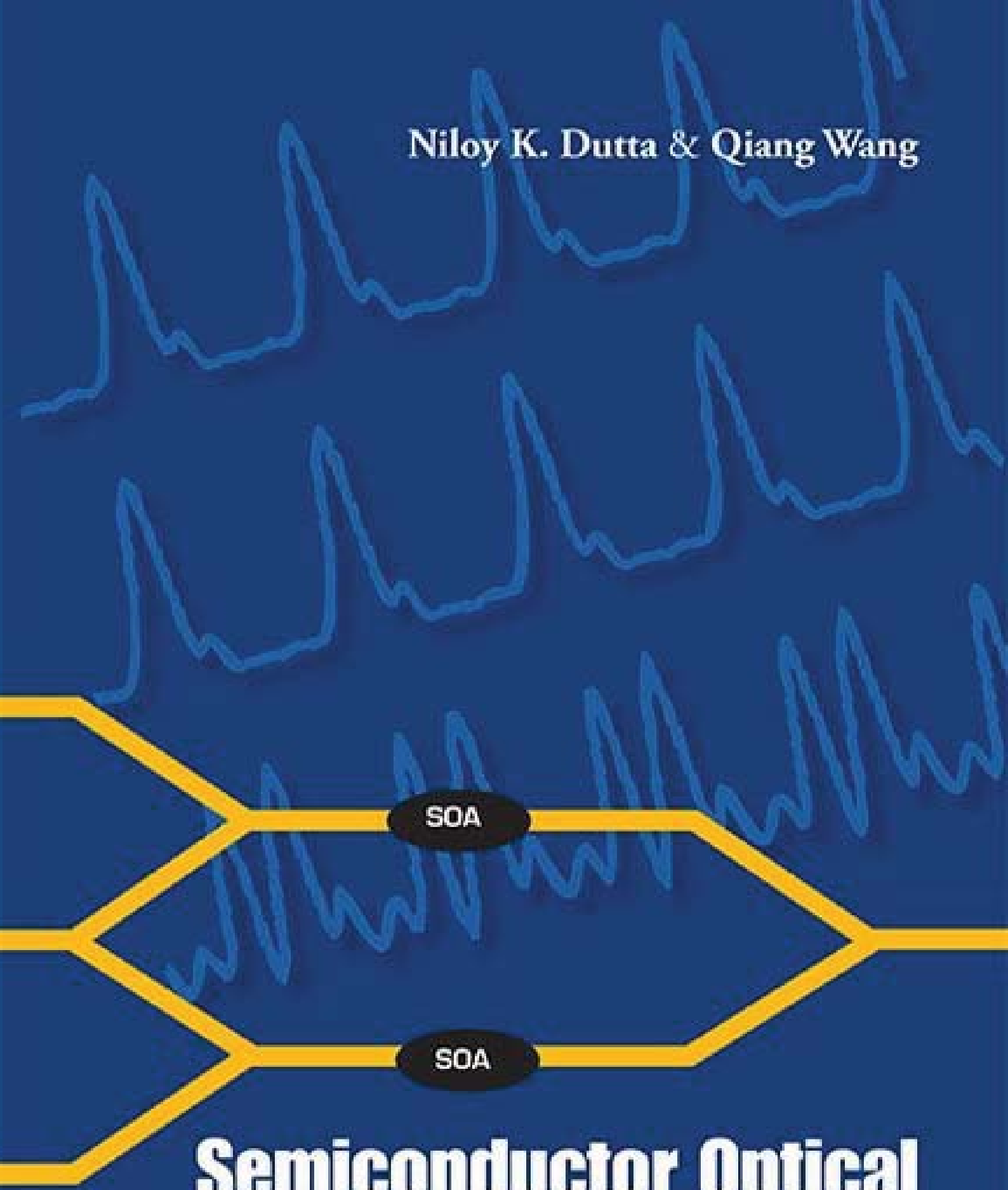

Semiconductor Optical Amplifiers

Second Edition

Semiconductor Optical Amplifiers

Second Edition

This page intentionally left blank

Semiconductor Optical Amplifiers

Second Edition

Niloy K. Dutta & **Qiang Wang**

University of Connecticut, USA

World Scientific

NEW JERSEY • LONDON • SINGAPORE • BEIJING • SHANGHAI • HONG KONG • TAIPEI • CHENNAI

Published by

World Scientific Publishing Co. Pte. Ltd.

5 Toh Tuck Link, Singapore 596224

USA office: 27 Warren Street, Suite 401-402, Hackensack, NJ 07601

UK office: 57 Shelton Street, Covent Garden, London WC2H 9HE

Library of Congress Cataloging-in-Publication Data

Dutta, N. K. (Niloy K.), 1953–

Semiconductor optical amplifiers / Niloy K. Dutta & Qiang Wang. -- 2nd edition.

pages cm

Includes bibliographical references and index.

ISBN 978-9814489034 (hardcover : alkaline paper)

1. Semiconductors. 2. Optical communications. I. Wang, Qiang. II. Title.

TK8320.D87 2013

621.382'7--dc23

2013018607

British Library Cataloguing-in-Publication Data

A catalogue record for this book is available from the British Library.

In-house Editor: Song Yu

Typeset by Stallion Press

Email: enquiries@stallionpress.com

Printed in Singapore

Preface

In the past two decades, optical communications has totally changed the way we communicate. It is a revolution that has fundamentally transformed the core of telecommunications, i.e. its basic science, its enabling technology, and its industry. The optical networking technology represents a revolution inside the optical communication revolution and it allows the latter to continue its exponential growth.

The existence and advance of optical fiber communications are based on the invention of low-loss optical fibers, the invention of the laser, particularly the semiconductor junction laser and related disciplines like photodetectors and integrated optics. From the early pioneering ideas, it took more than 25 years, to the first commercial deployment of optical communications; the Northeast Corridor system linking Washington and New York in 1983. Another important advance is the deployment of the first transatlantic submarine optical fiber transmission system in 1988. Optical fiber communications began to seriously impact the way information is transmitted beginning with these milestone achievements.

The market demand for higher capacity transmission was helped by the fact that computers continued to become more powerful and needed to be interconnected. This is one of the key reasons why the explosive growth of optical fiber transmission technology parallels that of computer processing and other key information technologies. These technologies have combined to meet the explosive global demand for new information services including data, internet, and broadband services — and, most likely, their rapid advances have helped fuel this demand. This demand is continuing its strong growth as internet traffic keeps increasing every year.

Optical networking represents the next advance in optical communications technology. Semiconductor optical amplifier is a key

device for all-optical networks. The advances in research and many technological innovations have led to superior designs of semiconductor amplifiers. Although many optical communication systems use optical fiber amplifiers for signal amplification, semiconductor optical amplifiers are suitable for integration and can also be used as functional devices. These functional properties such as wavelength conversion, optical demultiplexing, and, optical logic elements make them attractive for all-optical network and optical time division multiplexed systems.

The need for higher capacity is continuing to encourage research in wavelength division multiplexed (WDM) based and optical time division multiplexing (OTDM) based transmission, which needs optical demultiplexer and high power tunable lasers. An important research area would continue to be the development of semiconductor optical amplifiers as Mach-Zehnder, Michelsen interferometers and low power amplifiers in integrated devices. Semiconductor optical amplifiers with quantum dot active region are important for high speed optical signal processing systems due to their high saturation power and short gain recovery time. Reflective semiconductor optical amplifiers are important for commercial wavelength division multiplexed based passive optical network (WDM-PON). Two-photon absorption in a semiconductor optical amplifier is a very fast process and may be suitable for Tera-bit/s signal processing. Semiconductor optical amplifiers and superluminescent diodes (SLDs) are high power broadband sources suitable for optical coherence tomography and sensors applications.

All-optical signal processing is expected to become increasingly important in future ultrahigh capacity telecommunication networks. The development of all-optical logic technology is important for a wide range of applications in all-optical networks, including high speed all-optical packet routing, and optical encryption. An important step in the development of this technology is the demonstration of optical logic elements and circuits, which can also operate at high speeds. These logic elements include the traditional Boolean logic functions such as XOR, OR, AND, INVERT etc, and circuits such as parity checker, all-optical adder and shift register. Semiconductor

optical amplifier based devices such as Mach-Zehnder interferometers are being investigated for the development of all-optical logic circuits.

N. K. Dutta
Q. Wang

This page intentionally left blank

Contents

Chapter 1

Introduction

1.1. Historical Developments

The semiconductor optical amplifier (SOA) is very similar to a semiconductor laser. The laser has a gain medium and an optical feedback mechanism. The latter is generally provided by the cleaved facets of the semiconductor itself or by a grating of suitable periodicity etched close to the gain medium. At threshold, the gain equal loss for a laser, and the gain needed for laser action is typically ∼5 to 10 dB. A traveling wave optical amplifier has only a gain medium. However, the gain is generally larger (∼20 to 25 dB) compared to that for a laser. The optical gain is caused by the recombination of electrons and holes (electrons and holes are injected by external current). Thus the semiconductor amplifier operates at a higher current density than a laser at threshold.

The concept of the laser dates back to 1958 [1]. The successful demonstration of a solid state ruby laser and He-Ne gas laser was reported in 1960 [2, 3]. Laser action in semiconductor was considered by many groups during that period [4–6]. The semiconductor injection laser was demonstrated in 1962 [7–10]. CW operation of semiconductor laser was demonstrated in 1970 [11, 12] using the concept of double heterostructure [13]. Since then the semiconductor injection laser has emerged as an important device in many optoelectronic systems such as optical recording, high-speed data transmission through fibers, optical sensors, high-speed printing, and guided wave signal processing. An important impact of semiconductor lasers is in the area of fiber optic transmission systems where the information is sent through encoded light beams propagating in glass fibers.

These lightwave transmission systems, which have been installed throughout the world, offer a much higher transmission capacity at a lower cost than coaxial copper cable transmission systems.

The advantages of semiconductor lasers over other types of lasers, such as gas lasers, dye lasers, and solid-state lasers, lie in their considerably smaller size and lower cost and their unique ability to be modulated at gigahertz speeds simply by modulation of the injection current. These properties make the laser diode an ideal device as a source in several optoelectronic systems, especially optical fiber transmission systems. Semiconductor laser properties are discussed in several books [14–17]

Historically, the research on optical amplifier followed that of the semiconductor laser. Early work was carried out using GaAs/AlGaAs material system [18–21]. A majority of the follow-on work has been using the InGaAsP/InP material system. This material system is suitable for producing amplifiers with optical gain in the 1300 to 1600 nm wavelength range. The fiber optic transmission systems operate in this wavelength range due to the low loss of optical fibers and the commercial application of optical amplifiers are going to be driven by their need in fiber communication systems. This book provides a comprehensive and detailed account of design, fabrication, and performance of SOAs in optical networks. Earlier work is discussed in previous books [22, 23].

1.2. Semiconductor Materials

The choice of materials for semiconductor amplifiers is principally determined by the requirement that the probability of radiative recombination should be sufficiently high that there is enough gain at low current. This is usually satisfied for "direct gap" semiconductors. The various semiconductor material systems along with their range of emission wavelengths are shown in Fig. 1.2.1. Many of these material systems are ternary (three-element) and quaternary (four-element) crystalline alloys that can be grown lattice-matched over a binary substrate.

Many of these materials were first used to make semiconductor lasers [7–10, 14–17]. The lines represent the range of band gaps can

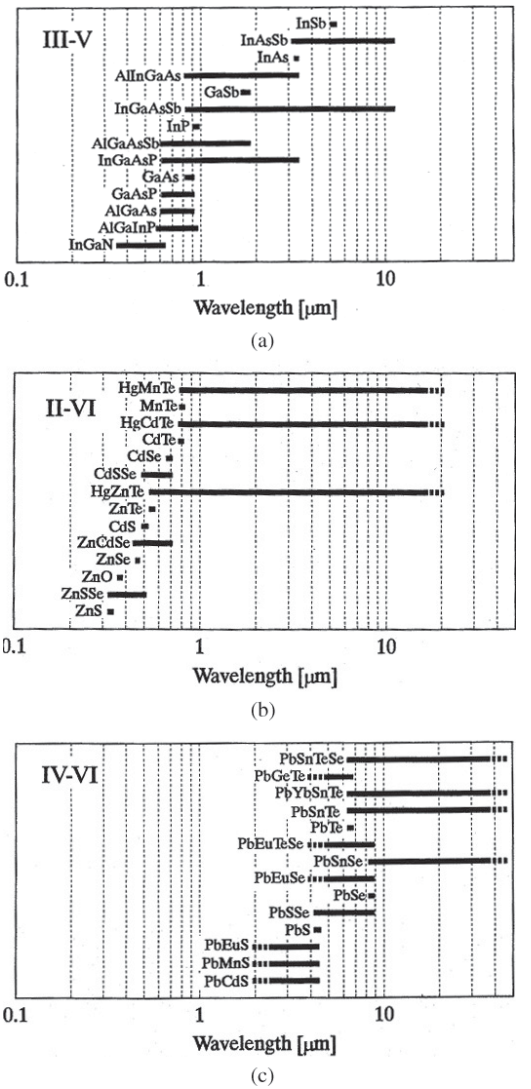

Fig. 1.2.1. Semiconductor materials used in laser fabrication at different regions of the spectrum. The three figures refer to compound semiconductors formed using group III and group V elements (III–V), group II and group VI elements (II–VI) and group IV and group VI elements (IV–VI) of the periodic table [24]. The quantum cascade lasers are fabricated using III–V semiconductors and they operate on intraband transitions in a quantum well.

be obtained by varying the composition (fraction of the constituting elements) of the material. The optical gain in amplifiers occurs at wavelengths close to the band gap. Thus a suitable set of materials must be chosen to get optical gain at the desired wavelength.

Another important criterion in selecting the semiconductor material for a specific heterostructure design is related to lattice matching i.e. the crystalline materials that form the heterostructure must have lattice constants which are equal to within $\sim$0.01 %. The binary substrates that are commonly used are GaAs and InP. They can be grown in a single crystal form from a melt. The ternary or quaternary semiconductors are epitaxially grown over the binary substrate for semiconductor laser or amplifier fabrication. In the epitaxial growth process the single crystal nature is preserved across the interface of the two materials. This leads to near absence of defect sites at the interface.

The development of epitaxial growth techniques has been of major significance for the development of semiconductor photonic devices such as lasers, amplifiers, and, photodetectors. The commonly used techniques for epitaxial growth are liquid phase epitaxy (LPE) [25], vapor-phase epitaxy (VPE) [26], molecular beam epitaxy (MBE) [27], and metal organic chemical vapor deposition (MOCVD) [28]. Early work on lasers and amplifiers were carried out using the LPE growth technique. The MBE technique is very useful for the growth of very thin semiconductor layers and was first used to fabricate quantum well structures [29]. The MOCVD technique and its variants are generally used for commercial production of lasers, amplifier and photodetectors. These growth techniques are described in detail in Ch. 4. In addition to growth, processing techniques of semiconductor materials for laser or amplifier fabrication was developed. The processing techniques include current confinement, low resistance contacts and etching of the semiconductor material to form specific geometries [33–35].

In the absence of lattice match, the quality of the hetero-interface is poor, i.e. there are lattice defects which serve as non-radiative recombination sites. In certain instances it is possible to grow epitaxially thin layers of one semiconductor on top of another in the

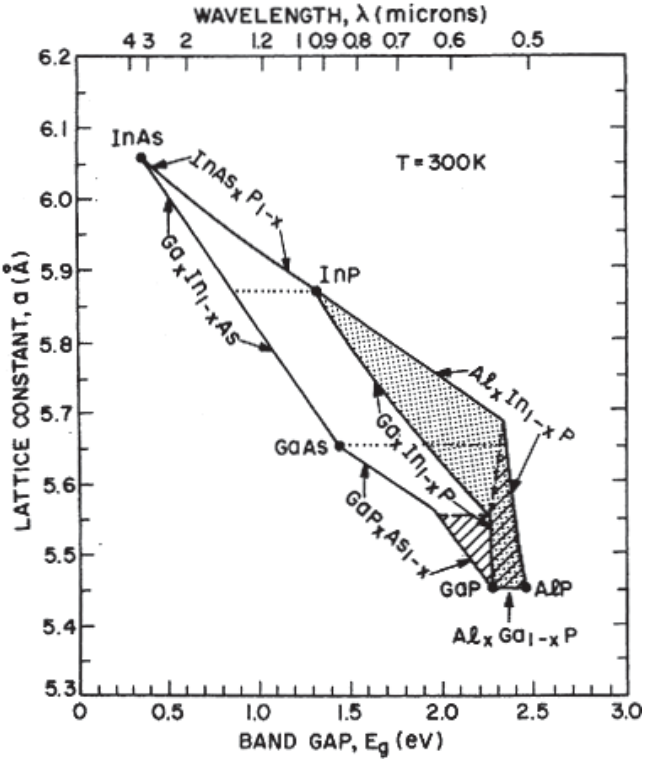

Fig. 1.2.2. Band gap and lattices constants of several ternary and quaternary compounds formed from the binary compounds. For $In_{1-x}Ga_xAs_yP_{1-y}$ quaternary material, the clear region is the region of direct band gap [2].

presence of a lattice mismatch of few percent. Such growth is called strained layer epitaxy, it is discussed in Sec. 4.4. Figure 1.2.2 shows the relationship between band gap E_g and lattices constant a of several ternary compound semiconductors. The dots correspond to the binary compounds and the lines represent the ternary compounds.

The ternary semiconductor $Al_xGa_{1-x}As$ can be grown over a GaAs substrate over the entire range of Al fraction x because GaAs and AlAs have nearly the same lattice constant. However, the $Al_xGa_{1-x}As$ material has a direct band gap for compositions with $x < 0.45$. Semiconductors with direct band gap are needed for efficient light emission. Heterostructures using the AlGaAs/GaAs material

system was the first to be studied extensively. Semiconductor lasers, amplifiers, bipolar transistors, field effect transistors have been made using this material system.

In the 1970's, considerable resources were devoted for lasers and photodetector fabrication using the quaternary $In_{1-x}Ga_xAs_yP_{1-y}$/InP material system. This material system is particularly suitable for lasers in the ∼1.3 to 1.55 μm wavelength range which is the region of low dispersion and low optical loss for silica optical fibers. $In_{1-x}Ga_xAs_yP_{1-y}$ can be grown lattice matched over a InP single crystalline substrate for $In_{1-x}Ga_xAs_yP_{1-y}$ compositions for which $x \sim 0.45\,y$. Lasers and detectors based on this material system are widely used in current fiber optic communication systems. Semiconductor amplifiers are important for all-optical networks which operate near 1.55 μm wavelength range. Thus much of the developments on optical amplifiers in the 1990's and continuing on has been using the $In_{1-x}Ga_xAs_yP_{1-y}$ /InP material system.

1.3. Operating Principles

SOA is very similar to a laser except it has no reflecting facets [36, 37]. A typical amplifier chip is ∼0.6 to 2 mm long. It has a *p*-cladding layer, a *n*-cladding layer and a gain region all of which are epitaxially grown over a binary substrate.

The schematic of a SOA chip is shown in Fig. 1.3.1. The amplifier chips have cleaved facets with anti-reflection coating (and possibly other modifications) which reduce its reflectivity to nearly zero. Just like the laser, the amplifier has a p-n junction which is forward biased

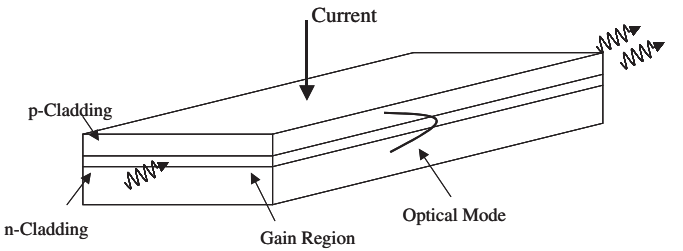

Fig. 1.3.1. Schematic of a SOA with no waveguide in the lateral (along the plane of p-n junction) direction.

during operation. The injected current produces gain in the gain region.

The majority carries are holes in the *p*-cladding layer and they are electrons in the *n*-cladding layers. The electrons and holes are injected into the gain region which is made of a lower band gap semiconductor than the cladding layers. The co-located electrons and holes recombine. This results in spontaneous emission of light and optical gain for light propagating in the gain region. It is a fortunate coincidence that semiconductor with lower band gap also has a higher index than semiconductors with higher band gap. The small index difference produces a waveguide for the propagating signal light. The signal is guided in this waveguide and it experiences amplification (gain) until it emerges from the output facet of the amplifier. Thus the double heterostructure material with *n*-type and *p*-type high band gap semiconductors around a low band gap semiconductor is instrumental in simultaneous confinement of the charge carriers (electrons and holes) and the optical signal. This is illustrated in Fig. 1.3.2

The electrons are located in the conduction band and holes are present in the valence band. In the gain region, the electrons and holes recombine to produce photons through both spontaneous and

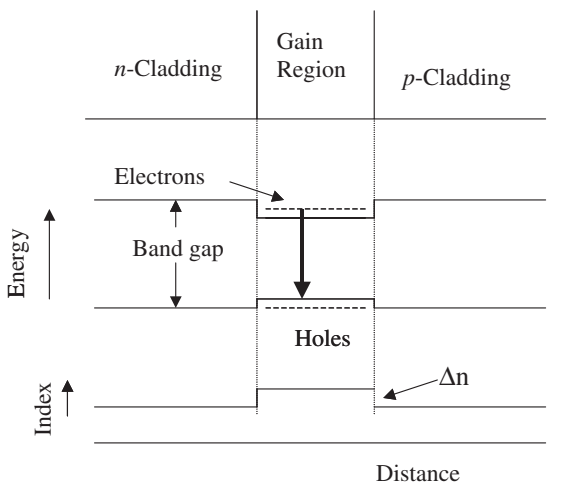

Fig. 1.3.2. Schematic illustration of confinement of the electrons and holes and also simultaneous confinement of optical mode in a double heterostructure.

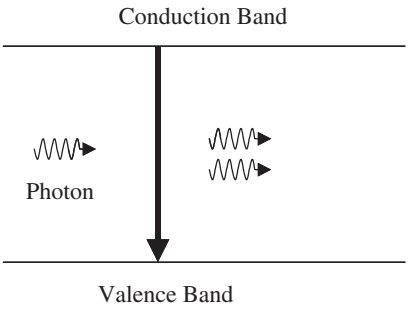

Fig. 1.3.3. Schematic illustration of gain (or amplification). An electron-hole pair recombines to generate a photon. This photon is emitted in the same direction as the incident photon. The process is known as stimulated emission.

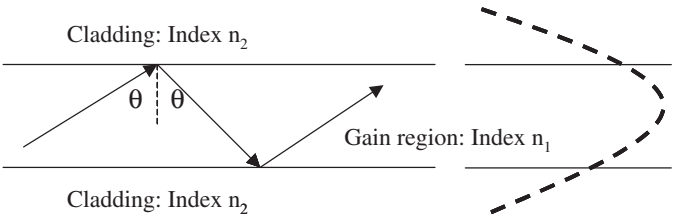

Fig. 1.3.4. Waveguiding in a double heterostructure. The gain region of index n_1 has cladding layers of index n_2 on both sides. The index $n_1 > n_2$. The above figure shows the total internal reflection of a ray incident at an angle θ (with $\sin\theta > (n_2/n_1)$ propagating in the gain region. An alternate view is that a confined optical mode with intensity profile (shown dashed in the figure) propagates in the waveguide.

stimulated emission process (Fig. 1.3.3). The optical gain of the input signal is due to the stimulated emission process. In the absence of current (electrons and holes), the semiconductor would absorb the incident photons. Certain minimum density of electrons and holes are needed to achieve net optical gain or amplification.

Low current operation of an amplifier or laser requires that the optical signal remain confined in the vicinity of the gain region. In the double heterostructure this is accomplished by slightly higher index of the gain material compared to that for the cladding materials. These three layers form a waveguide. The optical mode propagation in a three layer waveguide using the ray approach is shown in Fig. 1.3.4. The rays incident at an angle θ, with $\sin\theta > (n_2/n_1)$,

undergoes total internal reflection at the interface of the cladding and active region. Thus rays with these sets of angle of incidence continue to propagate through the amplifier and gets amplified. Other rays escape from the gain region. An alternative view is an optical mode with a certain profile determined by the thickness of the gain region and the indices can propagate through the amplifier without any diffraction loss. The intensity profile of a propagating mode is also sketched in Fig. 1.3.4. A fraction of the incident optical signal can, in general, be coupled to the propagating mode. The remaining fraction is lost. When an amplifier is viewed as an optical element if a larger optical system, this lost optical signal is viewed as a coupling loss, typically ∼50% per facet (∼3 dB). Various schemes exist to reduce the coupling losses. So, far optical waveguiding normal to the p-n junction has been discussed. Optical waveguding in the lateral direction (along the plane of the p-n junction) is also important for fabrication of high performance (low noise) amplifiers that have high gain at low current. Various schemes for lateral optical guiding and current confinement have been developed. These are described in detail in Ch. 4.

1.4. Applications

As the name of SOA implies, it could be used as an amplifier in a fiber optic communication system or other types of optical amplifier applications. Although many studies on applications of SOA in optical fiber systems have been reported, in these applications a limitation is a relatively low saturation power of the SOA (∼10 to 100 mW).

However, the SOA have found many novel applications in all-optical networks. This includes wavelength conversion where data on a signal at wavelength λ_1 is converted to data at another wavelength λ_2. Optical demultiplexing where a very high speed (>100 Gb/s) optical data is converted to several tributaries of low speed (∼10 to 20 Gb/s) data for information retrieval using conventional electronic means. Optical clock recovery where a clock signal (timing signal which determines the positions of the 1's and 0's) are generated from the high speed optical data signal. SOA is

also suitable for many all optical processing such as label swapping, optical header recognition and optical switching.

All-optical signal processing is expected to become increasingly important in future ultrahigh capacity telecommunication networks. The development of all-optical logic technology is important for a wide range of applications in all-optical networks, including high speed all-optical packet routing, and optical encryption. An important step in the development of this technology is a demonstration of optical logic elements and circuits, which can also operate at high speeds. These logic elements include the traditional Boolean logic functions such as XOR, OR, AND, INVERT etc, and circuits such as parity checker, all-optical adder and shift register. SOA based devices like Mach-Zehnder interferometers are being investigated for the development for all-optical logic circuits.

1.5. Book Overview

This is the second edition of a book on "Semiconductor Optical Amplifiers" first published in 2006 by the same authors. Chapters 11 to 14 are major additions in the second edition. Also, several sections and subsections representing new developments in previous chapters of the first edition have been added. The new chapters cover quantum dot semiconductor optical amplifiers (QD-SOA), reflective semiconductor optical amplifiers (RSOA), two-photon absorption in amplifiers and broadband sources. They represent advances in research, technology and commercial trends in the area of semiconductor optical amplifiers.

The fundamental operating principles of SOAs are described in Ch. 2. The optical gain spectrum, saturation of gain at high powers and the mechanism for gain is discussed. The minimum carrier density needed for amplification is given. The propagation of optical mode through the dielectric waveguide and mode confinement is discussed. The need for p-n junction is discussed. Various amplifier gain region designs such as multiquantum well and design for specific performance is described.

Chapter 3 describes radiative and non-radiative recombination mechanism of electrons and holes in semiconductors. Expressions for

optical gain, spontaneous recombination rate as a function of carrier density for various temperatures is obtained and their dependence on band structure parameters is discussed. Optical gains in quantum well, quantum wire and quantum dot amplifiers are described.

Epitaxial growths of amplifier materials are described in Ch. 4. Various growth processes and amplifier fabrication methods are described. Index guided amplifier structures and their fabrication are described. Strained layer gain region important for polarization independent gain is described. Growth of quantum dot materials is described.

In an ideal traveling wave (TW) amplifier the optical beam should not experience any reflectivity at the facets. However, in practice the facets with antireflection (AR) coating exhibit some residual reflectivity. This residual reflectivity results in the formation of an optical cavity which has resonance at the longitudinal modes. This results in a variation in gain as a function of wavelength of a traveling wave semiconductor amplifier. Various schemes for ultra low reflectivity facets are discussed in Ch. 5.

The rate equations for pulse propagation in semiconductor optical amplifiers are developed in Ch. 6. Effect of multiple pulses on gain and phase changes, multiwavelength operation is discussed. Various factors for optical noise in amplifiers such as spontaneous-spontaneous beat noise, signal-spontaneous beat noise are described.

There have been a significant number of developments in the technology of integration of semiconductor lasers, amplifiers and other related devices on the same chip. These chips allow higher levels of functionality than that achieved using single devices. The name photonic integrated circuits (PIC) is generally used when all the integrated components are photonic devices, e.g. lasers, detectors, amplifiers, modulators, and couplers. The design and performance of several photonic integrated circuits with amplifiers are described in Ch. 7.

The commercial use of SOAs are projected to be in the form of functional devices in all-optical networks. Such functional applications include, wavelength conversion, transparent switch networks, optical demultiplexing, optical clock recovery and others. Many of

these applications utilize gain saturation phenomenon (which results in cross gain/cross phase modulation) or nonlinear four wave mixing in optical amplifiers. Both the mechanisms needed for the functional performance and the viability of the amplifier in such applications is discussed in Ch. 8.

A class of PICs which use amplifiers are being investigated for photonic logic systems. The design and performance of these PICs are described in Chs. 9 and 10. Optical logic circuits are discussed in Ch. 10.

SOAs with quantum dot active region which are suitable for high speed optical signal processing systems due to their high saturation power and short gain recovery time are discussed in Ch. 11.

Reflective semiconductor optical amplifier (RSOA) is being investigated for commercial wavelength division multiplexed based passive optical network (WDM-PON). This is discussed in Ch. 12. These devices simplify the design of optical network unit at the subscriber terminal significantly.

Two-photon absorption in a SOA is a very fast process and may be suitable for Tera-bit/s signal processing speeds. The significance of TPA in various functional application of amplifiers and in optical logic systems are discussed in Ch. 13.

SOAs and superluminescent diodes (SLDs) are high power broadband sources. The fabrication and performance of these sources in various applications such as optical coherence tomography and sensors are discussed in Ch. 14.

1.6. Future Challenges

Tremendous advances in InP based SOA technology have occurred over the last decade. The advances in research and many technological innovations have led to improved designs of semiconductor amplifiers. Although most lightwave systems use optical fiber amplifiers for signal amplification, SOA's are suitable for integration and can also be used as functional devices. These functional properties such as wavelength conversion, optical demultiplexing, and, optical logic elements make them attractive for all-optical network and optical time division multiplexed systems.

The need for higher capacity is continuing to encourage research in wavelength division multiplexed (WDM) based and optical time division multiplexing (OTDM) based transmission, which needs optical demultiplexer and high power tunable lasers. An important research area would continue to be the development of semiconductor amplifiers such as Mach-Zehnder, Michelson interferometers and low power amplifiers in integrated devices.

Improving SOA performance at high temperature is an important area of investigation. The InGaAsN based system is a promising candidate for making gain regions near 1.3 μm with good high temperature performance. Strained quantum well structures provide ways of making polarization independent amplifiers. Amplifiers using quantum dot active region have fast gain and phase recovery times which makes them suitable for fast optical systems.

Finally, much of the advances in the SOA development would not have been possible without the advances in materials and processing technology. The challenges of much of the current SOA research is intimately linked with the challenges in materials growth which include not only the investigation of new material systems but also improvements in existing technologies, i.e. quantum dots, to make them more reproducible and predictable.

References

[1] A. L. Schawlow and C. H. Townes, *Phys. Rev.* **112**, 1940 (1958).
[2] T. H. Maiman, *Nature* **187**, 493 (1960).
[3] A. Javan, W. R. Bennett, Jr. and D. R. Herriot, *Phys. Rev. Lett.* **6**, 106 (1961).
[4] N. G. Basov, O. N. Krokhin and Yu. M. Popov, *Sov. Phys. JETP* **13**, 1320 (1961).
[5] M. G. A. Bernard and G. Duraffourg, *Phys. Status Solidi* **1**, 699 (1961).
[6] W. P. Dumke, *Phys. Rev.* **127**, 1559 (1962).
[7] R. N. Hall, G. E. Fenner, J. D. Kingley, T. J. Soltys and R. O. Carlson, *Phys. Rev. Lett.* **9**, 366 (1962).
[8] M. I. Nathan, W. P. Dumke, G. Burns, F. H. Dill, Jr. and G. Lasher, *Appl. Phys. Lett.* **1**, 63 (1962).
[9] T. M. Quist, R. H. Rediker, R. J. Keyes, W. E. Krag, B. Lax, A. L. McWhorter and H. J. Ziegler, *Appl. Phys. Lett.* **1**, 91 (1962).
[10] N. Holonyak Jr. and S. F. Bevacqua, *Appl. Phys. Lett.* **1**, 82 (1962).

[11] Zh. I. Alferov V. M. Andreev E. L. Portnoi and M. K. Trukan, *Sov. Phys. Semiconductors* **3**, 1107 (1970).
[12] I. Hayashi, M. B. Panish, P W. Foy and S. Sumski, *Appl. Phys. Lett.* **17**, 109 (1970).
[13] H. Kroemer, *Proc. IEEE* **51**, 1782 (1963).
[14] H. Kressel and J. K. Butler, *Semiconductor Lasers and Heterojunction LEDs* (Academic Press, New York, 1977).
[15] H. C. Casey, Jr. and M. B. Panish, *Heterostructure Lasers* (Academic Press, New York, 1978).
[16] G. P. Agrawal and N. K. Dutta, *"Semiconductor Lasers" Van Nostrand Reinhold*, 2nd edn. (NY, 1986, 1992).
[17] L. A. Coldren and S. W. Corzine, *Diode Lasers and Photonic Integrated Circuits* (John Wiley, NY 1995).
[18] M. J. Coupland, K. G. Mambleton and C. Hilsum, *Phys. Lett.* **7**, 231 (1963).
[19] J. W. Crowe and R. M. Craig, Jr., *Appl. Phys. Lett.* **4**, 57 (1964).
[20] W. F. Kosnocky and R. H. Cornely, *IEEE J. Quantum Electron.* **QE-4**, 225 (1968).
[21] M. Nakamura and S. Tsuji, *IEEE J. Quantum Electron.* **QE-17**, 994 (1981).
[22] H. Ghafouri-Shiraz, *Fundamentals of Laser Diode Amplifiers* (John Wiley, NY 1995).
[23] M. J. Connelly, *Semiconductor Optical Amplifiers* (Springer Verlag, 2002).
[24] P. G. Eliseev, Ch. 2, in *Semiconductor Lasers II*, ed. E. Kapon (Academic Press, 1998).
[25] H. Nelson, *RCA Rev.* **24**, 603 (1963).
[26] W. F. Finch and E. W. Mehal, *J. Electrochem Soc.* **111**, 814 (1964).
[27] A. Y. Cho, *J. Vac. Sci. Technol.* **8**, 531 (1971).
[28] R. D. Dupuis, *J. Crystal Growth* **55**, 213 (1981).
[29] R. Dingle, W. Wiegmann and C. H. Henry. *Phys. Rev. Lett.* **33**, 827 (1974).
[30] J. C. Dyment, *Appl. Phys. Lett.* **10**, 84 (1967).
[31] J. J. Hsieh, J. A. Rossi and J. P. Donnelly, *Appl. Phys. Lett.* **28**, 709 (1976).
[32] Y. Suematsu, *Proc. IEEE* **71**, 692 (1983).
[33] I. P. Kaminow, R. E. Nahory, M. A. Pollack, L. W. Stulz and I. C. Dewinter, *Electron. Lett.* **15**, 763 (1979).
[34] Y. Suematsu, K. Iga and K. Kishino, in *GalnAsP Alloy Semiconductors*, ed. T. P. Pearsall (New York: John Wiley & Sons, 1982).
[35] R. J. Nelson and N. K. Dutta, in *Semiconductor and Semimetals*, **22**, Part C, ed. W. T. Tsang (New York: Academic Press, 1985).
[36] T. Saitoh and T. Mukai, *J. Lightwave Technol.* **6**, 1656 (1988).
[37] M. O'Mahony, *J. Lightwave Technol.* **5**, 531 (1988).

Chapter 2

Basic Concepts

2.1. Introduction

Significant advances in research results, development and application of semiconductor lasers, amplifiers and modulators have occurred over the last decade. The fiber optic revolution in telecommunication which has provided several orders of magnitude improvement in transmission capacity at low cost would not have been possible without the development of reliable semiconductor lasers. Semiconductor optical amplifier (SOA) is an important device for next generation all-optical networks.

Optical amplifier, as the name implies, is a device that amplifies an input optical signal. The amplification factor or gain can be higher than 1000 (>30 dB) in some devices. There are two principal types of optical amplifiers. They are the semiconductor optical amplifier and the fiber optical amplifier. In a SOA, amplification of light takes place when it propagates through a semiconductor medium. The amplifier medium is sandwiched between semiconductor layers with higher band gap and lower refractive index. The three layers form a waveguide through which the light travels and undergoes amplification. SOAs are typically less than few mm in length. The operating principals, design, fabrication and performance characteristics of InP based semiconductor amplifiers are described in this Chapter.

SOA [1–7] is a device very similar to a semiconductor laser. Optical amplifiers amplify light through stimulated emission which is responsible for gain. Hence their operating principals, fabrication and design are also similar. The semiconductor amplifier is electrically

pumped (current injection) to produce gain. For details on lasers please see Ref. [8–12].

2.2. Optical Gain

The optical gain depends on the frequency (or wavelength) of the incident signals and also on the local intensity of the signal. For simplicity, the gain medium can be modeled as a homogeneously broadened two-level system (similar to that often done for a two-level laser). The gain coefficient (gain per unit length) of such a medium can be written as

$$g(\omega) = \frac{g_0}{1 + (\omega - \omega_0)^2 T_2^2 + P/P_s}, \tag{2.2.1}$$

where g_0 is the maximum (peak) value of the gain, ω is the optical frequency of the incident signal, ω_0 is the atomic transition frequency and P is the optical power of the signal being amplified. The quantity P_s is known as the saturation power of the gain medium. It depends on the parameters of the gain medium such as radiative recombination time and transition cross section. The parameter T_2 in Eq. (2.2.1) is known as the dipole relaxation time. The typical T_2 value is in the 0.1 to 1 ps range. For radiative transitions there is another characteristic lifetime (T_1). This radiative lifetime is often called the fluorescence lifetime or the population relaxation time. T_1 values can vary from 100 ps to 10 ms depending on the gain medium used to make the amplifier. For semiconductor amplifiers, Eq. (2.2.1) is a useful approximation to the actual gain spectrum which is discussed in detail in Ch. 3. For semiconductors, $T_2 \sim 0.1$ ps and $T_1 \sim 200$ ps to 1 ns. We use Eq. (2.2.1) to discuss important amplifier characteristics such as gain bandwidth, net amplification and output power.

2.2.1. *Gain spectrum and bandwidth*

For low powers, i.e. $P/P_s \ll 1$, the gain coefficient is given by

$$g(\omega) = \frac{g_0}{1 + (\omega - \omega_0)^2 T_2^2}. \tag{2.2.2}$$

The equation shows the gain is maximum when the incident frequency $\omega = \omega_0$. The gain spectrum is given by a Lorentzian profile which is characteristic of a two-level system. As we will see in Ch. 3, the actual spectrum can deviate from this Lorentzian profile. The gain bandwidth is defined as the full width at half maximum (FWHM) of the gain spectrum $g(\omega)$. For the spectrum of Eq. (2.2.2) the gain bandwidth, $\Delta\omega_{\mathrm{g}}$ is the given by $\Delta\omega_{\mathrm{g}} = 2/T_2$ or equivalently by $\Delta\nu_{\mathrm{g}} = \Delta\omega_{\mathrm{g}}/2\pi = 1/\pi T_2$.

For a typical semiconductor amplifier $T_2 \sim 0.1\,\mathrm{ps}$, this results in $\Delta\nu_{\mathrm{g}} \sim 3\,\mathrm{THz}$. Amplifiers with large bandwidth are desirable for multiwavelength amplification such as would be the case for a wavelength division multiplexed (WDM) optical transmission system. $\Delta\nu_{\mathrm{g}}$ is the bandwidth of the gain spectrum. A related concept is the gain bandwidth. The difference between the two becomes clear when the amplifier is considered as a single element with a gain G defined as

$$G = P_{\mathrm{out}}/P_{\mathrm{in}}, \tag{2.2.3}$$

where P_{in} and P_{out} are the optical input and output power of the amplifier. P_{in} and P_{out} are related by the amplifier equation

$$dP/dz = gP, \tag{2.2.4}$$

where P(z) is the optical power at a distance z from the input end ($z = 0$). For a constant g, Eq. (2.2.4) has the solution

$$P(\mathrm{z}) = P_{\mathrm{in}} \exp(gz). \tag{2.2.5}$$

For an amplifier medium of length L, using $P(\mathrm{L}) = P_{\mathrm{out}}$, it follows from the above

$$G(\omega) = \exp[g(\omega)\mathrm{L}]. \tag{2.2.6}$$

The amplifier gain $G(\omega)$ is maximum for $\omega = \omega_0$, i.e. when $g(\omega)$ is maximum and decreases when ω departs from ω_0. However, $G(\omega)$ decreases faster than $g(\omega)$ because of the exponential dependence. Using Eq. (2.2.6) , the FWHM of $G(\omega)$, $\Delta\nu_{\mathrm{a}}$ can be related to $\Delta\nu_{\mathrm{g}}$ by

$$\Delta\nu_a = \Delta\nu_g \left(\frac{\ln 2}{g_0 L - \ln 2} \right). \tag{2.2.7}$$

$\Delta\nu_a$ is known as the amplifier bandwidth. As expected, $\Delta\nu_a$ is smaller than $\Delta\nu_g$, the value of $\Delta\nu_a$ depends on the amplifier gain.

2.2.2. *Gain saturation*

Equation (2.2.1) shows that the material gain depends on the optical power (P). For low optical powers, the gain is higher than that for high optical powers. This is the origin of gain saturation. Since g is reduced when P becomes comparable to P_s, the amplifier gain G also decreases when P becomes large. For simplicity, we consider the case when the frequency of the incident light $\omega = \omega_0$, in this case, by using Eqs. (2.2.1) and (2.2.4) it follows

$$\frac{dP}{dz} = \frac{g_0 P}{1 + P/P_s}. \tag{2.2.8}$$

The above equation can be solved using the boundary conditions $P(0) = P_{in}$ and $P(L) = P_{out}$ where L is the length of the amplifier. The amplifier gain $G = P_{out}/P_{in}$.

The following relation is then obtained for the large signal amplifier gain

$$G = G_0 \exp\left(-\frac{G-1}{G}\frac{P_{out}}{P_s}\right), \tag{2.2.9}$$

where $G_0 = \exp(g_0 L)$ is the unsaturated gain of the amplifier i.e. gain for $P \ll P_s$. Equation (2.2.9) shows that the gain G decreases from G_0 when P_{out} becomes comparable to P_s. Figure 2.2.1 shows the saturation characteristics under two different unsaturated gain G_0 values.

A parameter known as output saturation power P_{sout} is defined as the output power at which the saturated gain decreases to half of its unsaturated value i.e. value of P_{out} for which $G = G_0/2$. Using Eq. (2.2.9) P_{sout} is given by

$$P_{sout} = \frac{G_0 \ln 2}{G_0 - 2} P_s. \tag{2.2.10}$$

P_{sout} is smaller than P_s. For amplifiers with large gain ($G_0 > 100$), P_{sout} is nearly independent of G_0. For a typical amplifier with 30 dB gain ($G_0 = 1000$), $P_{sout} \sim 0.69 P_s$.

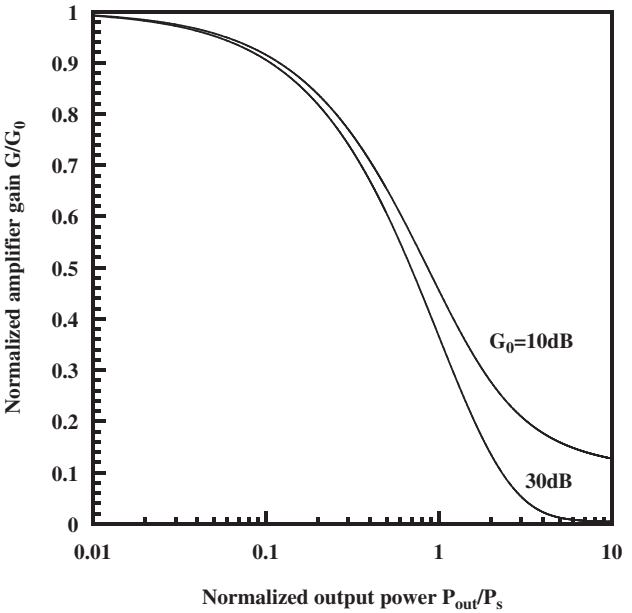

Fig. 2.2.1. Normalized saturated amplifier gain G/G_0 as a function of the normalized output power.

2.3. Dielectric Waveguide

Conceptually, stimulated emission in a semiconductor amplifier arises from electron-hole radiative recombination in the active region, and the light generated is confined and guided by a dielectric waveguide (Fig. 2.3.1). The active region has a slightly higher index than the p- and n-type cladding layers, and the three layers form a dielectric waveguide. The energy distribution of the fundamental mode of the waveguide is also sketched in Fig. 2.3.1. A fraction of the optical mode is confined in the active region. Two types of fundamental transverse modes can propagate in the waveguide: the transverse electric (TE) and the transverse magnetic (TM) modes.

The expression for the confinement factor Γ, the fraction of mode in the active region, has been previously calculated [13, 14]. Figure 2.3.2 shows the calculated Γ as a function of active layer thickness for the TE and TM modes for the $\lambda = 1.3\,\mu$m InGaAsP double heterostructure with p-InP and n-InP cladding layers.

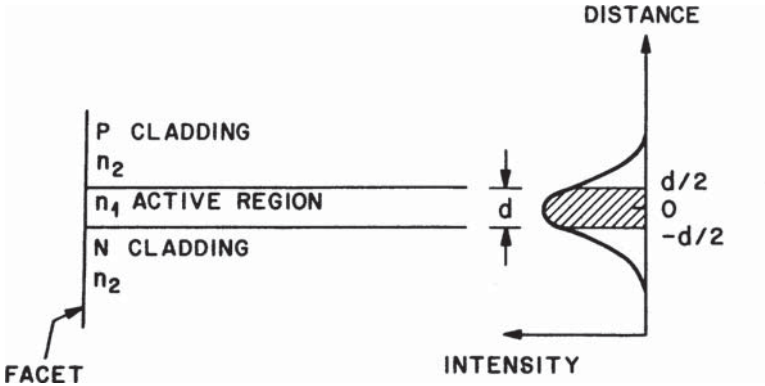

Fig. 2.3.1. The dielectric waveguide of the semiconductor amplifier. n_2 is the refractive index of the cladding layers and n_1 that of the active region. $n_1 > n_2$. The cladding layers are of a higher bandgap material than the active region. The intensity distribution of the fundamental mode is shown. The cross-hatched region represents the fraction of the mode Γ within the active region.

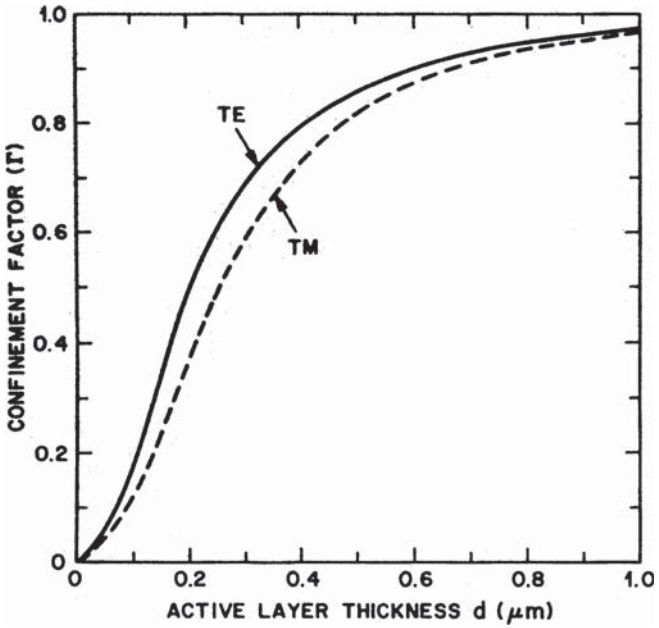

Fig. 2.3.2. Confinement factor of the fundamental TE and TM modes for a waveguide with InGaAsP ($\lambda = 1.3\,\mu$m) active layer and InP cladding layers as a function of the thickness of the active region [13]. The refractive indexes of the active and cladding region are 3.51 and 3.22, respectively.

For a three layer slab waveguide with cladding layer index n_2 and active layer index n_1, the confinement factor of the fundamental mode can be approximated by [14]

$$\Gamma = D^2/(2 + D^2), \tag{2.3.1}$$

with $D = k_0(n_1^2 - n_2^2)^{1/2}d$, where d is the thickness of the active region and $k_0 = 2\pi/\lambda_0$ where λ_0 is the wavelength in free space.

The optical gain of a signal in the fundamental mode traveling through the amplifier is given by

$$g_m = \Gamma g. \tag{2.3.2}$$

The mode gain g_m is proportional to the mode confinement factor Γ. Since the TE and TM modes have different confinement factors the optical gain for the TE and TM modes are different i.e. the semiconductor optical amplifier generally exhibits a polarization dependence of gain. This is generally not desirable. Figure 2.3.2 shows that amplifiers with thick active region will have low polarization dependence of gain.

If P_s is the saturation power of the gain medium, the observed saturation power is given by

$$P_s(\text{observed}) = P_s/\Gamma. \tag{2.3.3}$$

Thus amplifiers with small mode confinement factor (small Γ) such as quantum well amplifiers exhibit high saturation power.

The amplifiers used in lightwave system applications, either as preamplifiers in front of a receiver or as in line amplifiers as a replacement of regenerators, must exhibit nearly equal optical gain for all polarizations of the input light. For thick active regions, the confinement factors of the TE and TM mode are nearly equal (Fig. 2.3.2). Hence the gain difference between the TE and TM modes is smaller for amplifiers with a thick active region [4]. The calculated TE/TM gain difference for an amplifier operating in the 1550 nm wavelength range is shown in Fig. 2.3.3. The active region consists of InGaAsP active layer with *p*-InP and *n*-InP cladding layers.

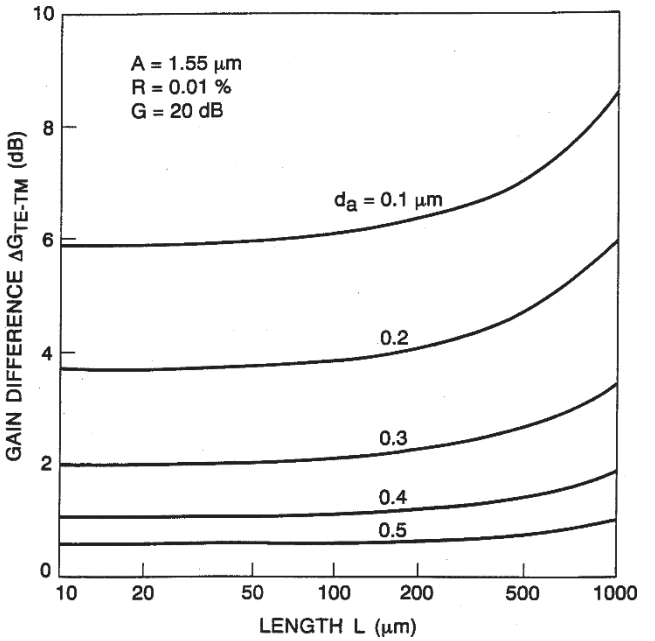

Fig. 2.3.3. The optical gain difference between the TE and TM mode of a semiconductor amplifier is plotted as a function of device length for different active layer thickness [7]. For the plot, the amplifier gain for the TE mode is 20 dB. The reflectivity of each facet is 0.01%.

2.4. Condition for Amplification

Sufficient numbers of electrons and holes must be created in the semiconductor for stimulated emission or net optical gain [15–19]. A semiconductor with no injected carriers would absorb a photon whose energy is larger than the band gap. With increasing carrier injection this absorption decreases until there is no absorption (the material is transparent to the photon). At carrier densities higher than this amount the semiconductor will exhibit net optical gain. The condition for zero net gain or absorption (transparency) at photon energy E is given by [20, Ch. 3, Eq. (3.2.8)]

$$E_{f_c} + E_{f_v} = E - E_g, \tag{2.4.1}$$

where E_{f_c}, E_{f_v} are the quasi-Fermi levels of electrons and holes, respectively, measured from the respective band edges (positive into

the band) and E_g is the band gap of the semiconductor. For zero net gain (transparency), the above condition becomes $E_{f_c} + E_{f_v} = 0$. For undoped material at a temperature T the quasi-Fermi energy E_{f_c} is related to the injected carrier (electron or hole) density n by [8–10]

$$n = N_c \frac{2}{\sqrt{\pi}} \int \frac{d\varepsilon}{1 + \exp(\varepsilon - \varepsilon_{f_c})}, \tag{2.4.2}$$

with $N_c = 2\left(2\pi m_c \frac{kT}{h^2}\right)^{3/2}$ and $\varepsilon_{f_c} = E_{f_c}/kT$, where k is the Boltzmann constant, h is Planck's constant, T is the temperature, and m_c is the effective mass of the electrons in the conduction band. A similar equation holds for holes.

Figure 2.4.1 shows the variation of the injected carrier density for transparency n_t as a function of temperature for undoped $\lambda = 1.3\,\mu$m InGaAsP. The parameter values used in the calculation are $m_c = 0.061\,m_0$, $m_{hh} = 0.45\,m_0$, $m_{lh} = 0.08\,m_0$, where m_0 m_{hh} m_{lh} are the free electrons, heavy hole, and the light hole mass, respectively. Figure 2.4.1 shows that n_t, is considerably smaller at low temperatures. For optical gain the injected carrier density must be higher than n_t.

The high carrier densities needed for gain can be generated in a semiconductor by optical excitation or current injection. The optical gain as a function of carrier density and current density is discussed

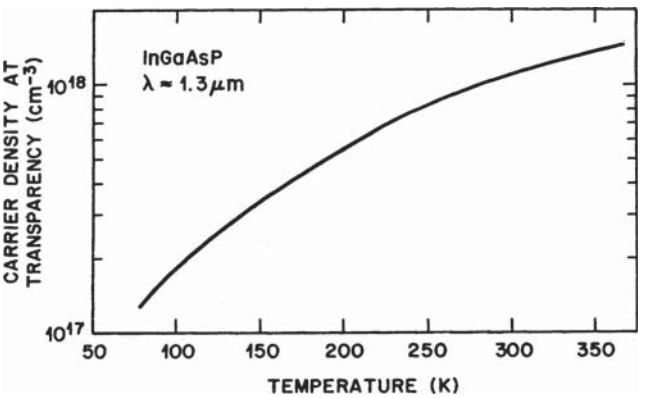

Fig. 2.4.1. The calculated injected carrier density for transparency as a function of temperature for undoped $\lambda = 1.3\,\mu$m InGaAsP.

in detail in Ch. 3. The amplifier gain is higher at low temperature for the same injection current.

2.5. P-N Junction

Under high current injection through a p-n junction a region near the depletion layer can have a high density of electrons and holes. These electrons and holes can recombine radiatively if the interfaces are free of traps. The device will amplify light if the number density of electrons and holes are sufficiently high.

The energy-band diagram of a p-n junction between two similar semiconductors (homojunction) at zero bias is shown in Fig. 2.5.1.

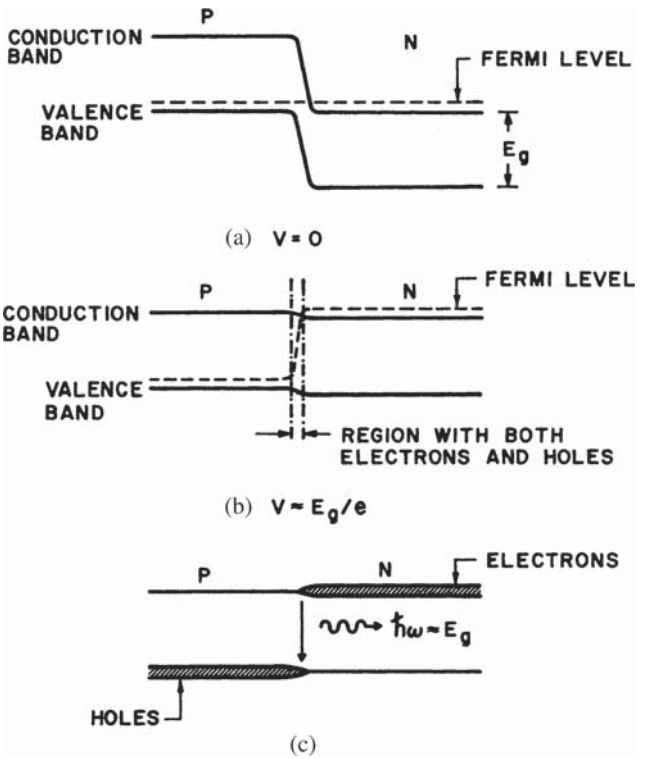

Fig. 2.5.1. Energy band diagram of a p-n junction at (a) zero bias, (b) forward bias $V \approx E_g/e$. (c) Schematic representation of electrons and hole densities under forward bias $V \approx E_g/e$.

The dashed line represents the Fermi level. Under forward bias, both electrons and holes are present near the depletion region. This region can have net gain if the electron and hole densities are sufficiently high. However, the thickness of the gain region is very small ($\sim$100 Å), which makes the confinement factor Γ for an optical mode very small. Hence from Eq. (2.3.1), it follows that the gain is low for homostructures.

The threshold current of an injection laser was historically reduced using a double heterostructure for carrier confinement, which increased the size of the region of optical gain [21–23]. The double heterostructure laser utilizes a p-n heterojunction for carrier injection. The semiconductor optical amplifiers also utilize a double heterostructure for carrier injection and carrier confinement.

A p-n heterojunction is a p-n junction in a single crystal between two dissimilar semiconductors. Thus the fabrication of heterojunctions had to wait until the development of epitaxial growth techniques. The energy-band diagram of a double heterostructure laser at zero bias is shown in Fig. 2.5.2. The device consists of a narrow-gap semiconductor (p-type, n-type, or undoped) sandwiched between higher-gap p-type and n-type semiconductors. The narrow-gap semiconductor is the light-emitting region (active region) of the laser. The dashed line represents the Fermi level. For the purpose of illustration we have chosen the active region to be p-type in Fig. 2.5.2. The band diagram under forward bias is shown in Fig. 2.5.2(b). Electrons and holes are injected at the heterojunction and are confined in the active region. Thus the region of optical gain is determined by the thickness of the active region in double heterostructure lasers. In addition, the refractive index of the lower-gap active region is higher than that for the n-type and p-type higher-gap confining (also known as cladding) layers. These three layers form a waveguide for the propagating optical mode, as discussed previously.

The active region thickness of an optical amplifier is typically in the range of 0.2–0.4 μm. Amplifiers with thick active region are needed for polarization independent gain. In addition, in many cases, thick active region or a separate layer with a band gap intermediate

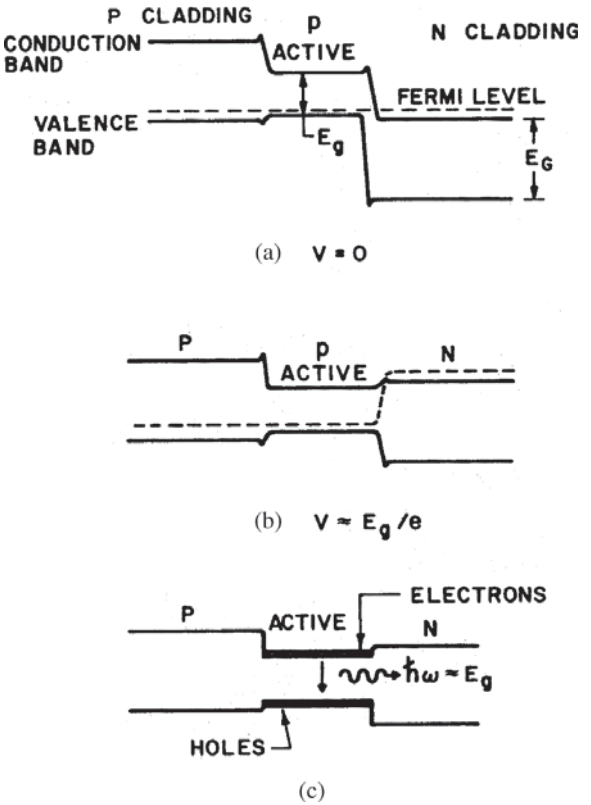

Fig. 2.5.2. Energy band diagram of a double heterostructure laser (a) zero bias, (b) forward bias $V \approx E_g/e$.

between the active region and cladding layer is used for fast gain recovery and hence fast performance of semiconductor amplifiers.

Within the last two decades, with the development of molecular beam epitaxy (MBE) and metal organic chemical vapor deposition (MOCVD) growth techniques, it has been possible to fabricate very thin epitaxial layers (<200 Å) bounded by higher-gap cladding layers. These double heterostructures are called quantum well double heterostructures because the kinetic energy for carrier motion normal to the plane of the active region is quantized, similar to that for a one-dimensional potential well [24, 25]. The modification of the electron-hole recombination characteristics (which is the basis of

amplification) in quantum wells is described in Ch. 3. Optical amplifiers with quantum well active regions have low confinement factor and high saturation power and is therefore suitable for integration with other optical devices on a single chip. Such photonic integrated circuits are discussed in Ch. 7.

2.6. Amplifier Characteristics

Extensive work on optical amplifiers were carried out in the 1960s using the AlGaAs material system [1–3]. Much of the recent experimental work on semiconductor optical amplifiers have been carried out using the InGaAsP material system with the optical gain centered around 1.3 μm or 1.55 μm. This is primarly due to their potential use in all optical networks.

SAO can be classified into two categories, the Fabry Perot (FP) amplifier and the traveling wave (TW) amplifier. A FP amplifier has considerable reflectivity at the input and output ends which results in resonant amplification at Fabry Perot modes. Thus, a FP amplifier exhibits a very large optical gain at wavelengths corresponding to the longitudinal modes of the cavity and the gain is small in between the cavity modes. This modulation in gain is not desirable if the amplifier is used in optical networks. The TW amplifier, by contrast, has negligible reflectivity at each end which results in signal amplification during a single pass. The optical gain spectrum of a TW amplifier is quite broad and corresponds to that of the semiconductor gain medium. Most practical TW amplifiers exhibit some small ripple in the gain spectrum which arises from residual facet reflectivity. TW amplifiers are more suitable for system applications. An example of the gain spectrum of a TW amplifier with antireflection coated cleaved facets is shown in Fig. 2.6.1. The output exhibits modulations at longitudinal modes of the cavity because the optical gain is slightly higher at the modes than in between the modes. Both TE (transverse electric) and TM (transverse magnetic) fundamental modes can propagate in a TW amplifier. These modes have slightly different effective indices due to slightly different confinement factors and hence the precise antireflection coating needed for these modes

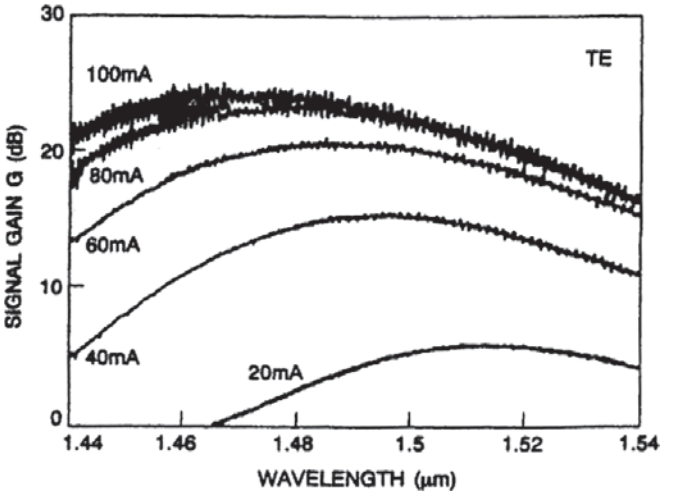

Fig. 2.6.1. Measured gain spectrum of a traveling wave (TW) type semiconductor optical amplifier at several current levels.

are different. Thus the residual modulation in TE and TM mode gain in TW amplifiers due to nonzero facet reflectivity are spectrally displaced. This problem is reduced considerably for amplifiers with thick active region.

For plane waves, a quarter wave thick (thickness $= \lambda_0/4n$ where n is the index of the dielectric layer) single layer dielectric coating with an index $n = n_{\mathrm{m}}^{1/2}$ where n_{m} is the index of the semiconductor material is sufficient to create a perfect (zero reflectivity) antireflection coating. The waves propagating in the amplifier are not plane waves and the above therefore serves only as an approximation. For low gain modulation (also known as gain ripple) the facet reflectivity of a TW amplifier must be $<0.01\%$. Much effort has been devoted to fabricate amplifiers with very low effective facet reflectivity. Such amplifier structures either utilize special low effective reflectivity dielectric coatings, or have tilted or buried facets. Fabrication and performance of these devices are described in Ch. 5.

Another parameter of interest for amplifier characteristics is gain as a function of current. The optical gain is found to increase with increasing current, then it saturates. Typical data for this

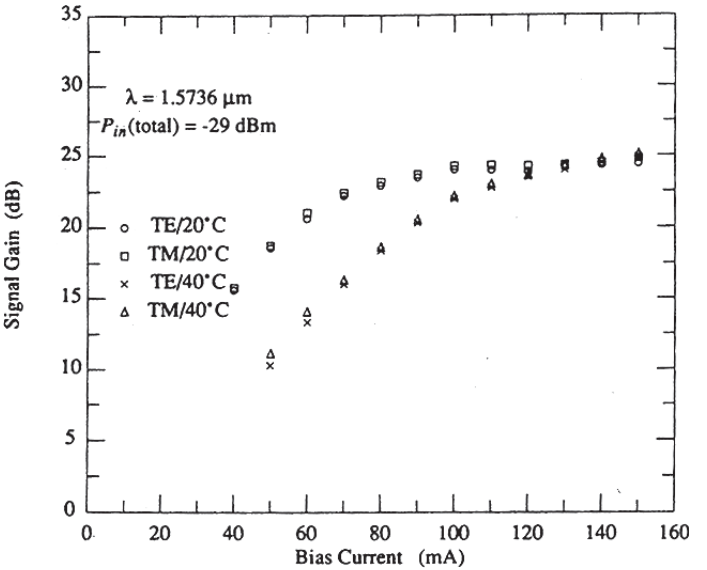

Fig. 2.6.2. Gain as a function of current of a semiconductor amplifier. The input power is -29 dBm ($\sim 1\,\mu$W). The device has a buried heterostructure design.

characteristics is shown in Fig. 2.6.2. The optical gain decreases with increasing temperature at a given current. This is due to several factors. Electrons are distributed over a wider energy range at high temperature and hence the number of electrons available for participating in optical transition (gain) at a given energy is fewer. Nonradiative recombination which increases with increasing temperature for long wavelength materials ($\sim 1.55\,\mu$m) causes a reduction in gain for a given current. In addition, many semiconductor amplifiers are fabricated using buried heterostructure designs (for good mode stability). These designs rely on reverse biased junctions for confinement of the current to the active region and therefore necessarily have higher leakage current (current going around the active region) at high temperatures. This is discussed in Ch. 3.

As discussed earlier, the optical gain decreases with increasing optical input power. This phenomenon also exhibits itself as a saturation in gain as a function of current. With increasing current the gain increases and hence the signal acquires high enough intensity to reduce

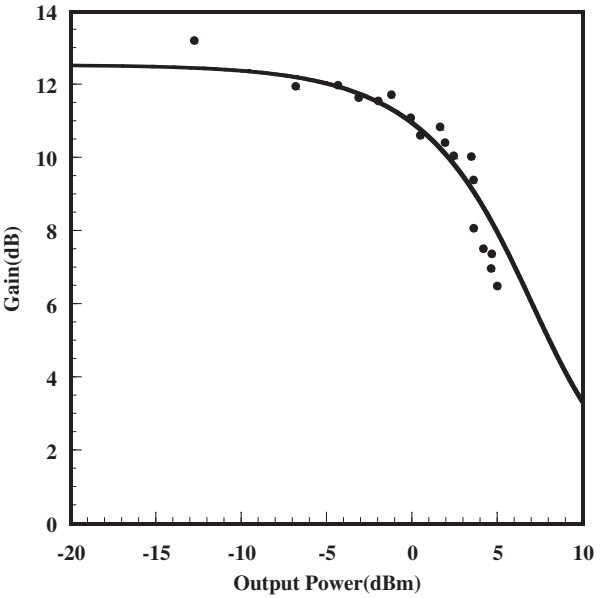

Fig. 2.6.3. Gain as a function of output power. Solid line is plotted using Eq. (2.2.9), with $G_0 = 18$, $P_s = 2.5\,\text{mW}$. Dots are measured gain.

its gain before reaches the output facet. Since the optical power in a TW amplifier increases as the signal propagates through the amplifier, the maximum gain saturation occurs near the output port. The gain saturation characteristics of an amplifier is generally plotted as the measured gain as a function of output power (Fig. 2.6.3). The saturation output power is the power at which the gain is reduced by a factor of 2 (3 dB) from that for small output powers.

When an amplifier is operated in the saturated regime with multiple input signals (for example at different wavelengths) a cross talk (i.e. transfer of modulation from one signal to another) occurs. This crosstalk limits the use of amplifier in multi-channel transmission systems.

2.7. Multiquantum Well Amplifiers

Semiconductor optical amplifiers with multiquantum well (MQW) active region are used in many applications. The active region

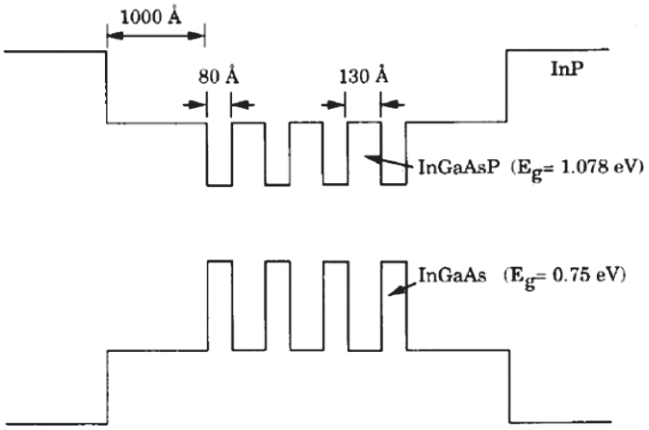

Fig. 2.7.1. Schematic of the band diagram of a MQW active region. The gain region wells are 80 Å thick InGaAsP (band gap 0.75 eV) and the barriers layers are 130 Å thick InGaAsP (band gap 1.08 eV). There are four gain region wells and three barrier layers. The SOA length is 800 μm and the facet reflectivity is 0.3% [28].

consists of many quantum wells (regions less than 10 nm thick) separated by barrier layers and the entire set of these layers are sandwiched between higher gap semiconductor layers. A schematic of the band structure of such an active region is shown in Fig. 2.7.1 [28].

The laser wafer was fabricated using MOCVD epitaxial growth technique (Ch. 4). The TE and TM single pass optical gain and noise figure of this device as a function of wavelength has been measured. The results are shown in Fig. 2.7.2. The injection current is 225 mA. The TM mode gain in lattice matched MQW structures is less than that of the TE mode due to fundamentals of optical transition in quantum well structures (discussed in Ch. 3). The noise figure (discussed in detail in Ch. 6) is given by [28, 29]

$$F_{TWA} = 2\frac{P_{\text{meas}}}{\eta}\frac{\lambda^3}{hc_0^2\Delta\lambda}\frac{1-RG_s}{(1-R)(G_s-1)}, \tag{2.7.1}$$

where P_{meas} is the measured spontaneous emission power for one polarization in a certain optical filter bandwidth $\Delta\lambda$, G_{s} is the single-pass gain, η is the total coupling efficiency from the amplifier into the optical power meter, R the modal reflectivity, λ is the wavelength

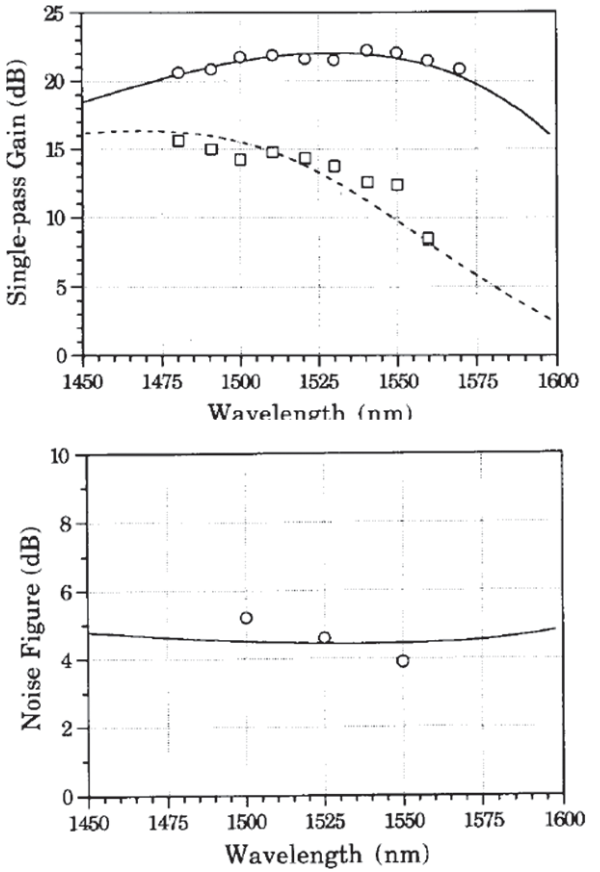

Fig. 2.7.2. Measured gain and noise figure of the MQW SOA of previous Fig. 2.7.1 [28]. The noise figure is defined as the signal to noise ratio of the output (amplified) signal and that of the input signal.

in vacuum, c_o is the speed of light in vacuum, and, h is the Planck's constant, The measured noise figure is $\sim$5 dB.

Semiconductor amplifiers with a multiquantum well (MQW) active region (see Ch. 3 for details) have high gain in TE polarization. The gain in TM polarization is considerably lower. In addition, these amplifiers have high saturation power due to small confinement factor. Typical gain as a function of output power is shown in Fig. 2.7.3.

The saturation power of this amplifier is 28 mW. This amplifier had a four-quantum well active region. Because of high saturation

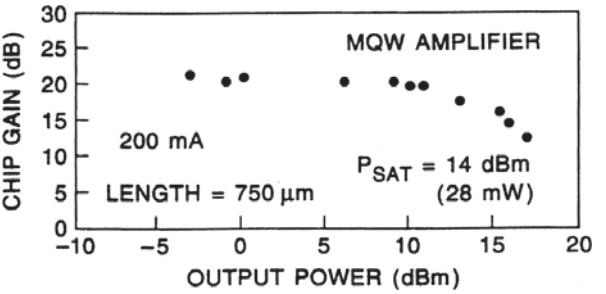

Fig. 2.7.3. Gain as a function of output power for multiquantum well amplifiers.

power and high TE mode gain, MQW amplifiers are attractive candidates for on chip integration with lasers (which also emit in TE mode) as power boosters. An important reason for higher saturation power of MQW amplifiers is low confinement factor of the optical mode (Eq. (2.3.2)).

MQW amplifiers fabricated using lattice matched semiconductors have high gain in the TE mode. The TM mode gain is significantly smaller. This is because TM mode transitions involve light holes and the light hole population is smaller than the heavy hole population. However, polarization independent gain in MQW SOA with tensile strained active region has been reported [26, 27] (see Ch. 4 for strained layer growth). The tensile strain results in nearly degenerate valence band maximum and thus equal transition probability for light and heavy holes. A more versatile design has been reported using both compressive and tensile strained quantum well layers in the MQW structure [30, 31]. In this design, the quantum well layers are tailored (strain, composition or well width) in order to equalize the bandgaps as shown in Fig. 2.7.4. The compressively strained quantum well structure only contribute to TE polarized gain, and the tensile strained quantum wells contribute mainly to TM gain and to TE gain to some extent. The ratio of TE to TM gain (given by ratio of the matrix elements) for electron-light hole recombination (in tensile strained material) is about 1 to 4. The ratio of the number of both types (compressive and tensile) strained layers and their widths are optimized in the structure so as to yield polarization insensitive gain.

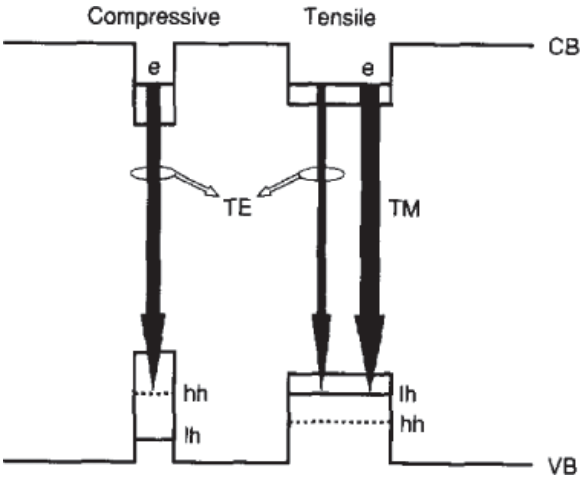

Fig. 2.7.4. Operating principle of polarization insensitive multiquantum well amplifier [30].

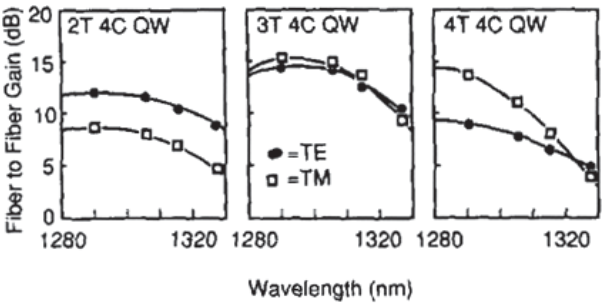

Fig. 2.7.5. TE and TM polarization resolved gain spectrum for four compressively strained (4C) and two, three and four tensile strained (2T, 3T, and 4T) MQW amplifier respectively [30].

Figure 2.7.5 shows the polarization resolved (fiber-to-fiber) gain spectra of a MQW semiconductor optical amplifier with four 1% compressively (4C) strained $In_{0.83}$ $Ga_{0.17}As_{0.67}$ $P_{0.33}$ (width = 4.5 nm) and two, three and four 1% tensile (2T, 3T, 4T) strained $In_{0.5}$ $Ga_{0.5}As_{0.78}$ $P_{0.22}$ (width = 11 nm) wells respectively. The amplifier is driven at 100 mA and the amplifier length is 750 μm. Nearly polarization independent gain is obtained for the 3T/4C design.

Amplifiers using quantum dot active region have also been studied. These amplifiers have a fast gain and phase recovery characteristics which make them suitable for high speed optical processing applications. SOAs based on quantum dot active region are discussed in detail in Ch. 11.

References

[1] M. J. Coupland, K. G. Mambleton and C. Hilsum, *Phys. Lett.* **7**, 231 (1963).
[2] J. W. Crowe and R. M. Craig, Jr., *Appl. Phys. Lett.* **4**, 57 (1964).
[3] W. F. Kosnocky and R. H. Cornely, *IEEE, J. Quantum Eelectron.* **QE-4**, 225 (1968).
[4] T. Saitoh and T. Mukai in Chap. 7, Coherence, *Amplification and Quantum Effects in Semiconductor Lasers*, ed. by Y. Yamamoto (Wiley, New York, 1991).
[5] M. Nakamura and S. Tsuji, *IEEE J. Quantum Electron.* **QE-17**, 994 (1981).
[6] T. Saitoh and T. Mukai, *J. Lightwave Technol.* **6**, 1656 (1988).
[7] M. O'Mahony, *J. Lightwave Technol.* **5**, 531 (1988).
[8] H. Kressel and J. K. Butler, *Semiconductor Lasers and Heterojunction LEDs* (Academic Press, New York, 1977).
[9] H. C. Casey, Jr. and M. B. Panish, *Heterostructure Lasers* (Academic Press, New York, 1978).
[10] G. P. Agrawal and N. K. Dutta, "*Semiconductor Lasers*" Van Nostrand Reinhold, NY, 1986, 2nd edn. (1992).
[11] L. A. Coldren and S. W. Corzine, *Diode Lasers and Photonic Integrated Circuits* (John Wiley, NY, 1995).
[12] G. H. B. Thompson, *Physics of Semiconductor Laser Devices* (John Wiley & Sons, New York, 1980).
[13] G. P. Agrawal and N. K. Dutta, "*Semiconductor Lasers*", Van Nostrand Reinhold, NY, 1992. Sec. 2.5
[14] D. Botez, *IEEE J. Quantum Electron.* **QE-17**, 178 (1981).
[15] G. Lasher and F. Stern, *Phys. Rev.* **133**, A553 (1964).
[16] F. Stern, *Phys. Rev.* **148**, 186 (1966).
[17] C. J. Hwang, *Phys. Rev. B* **2**, 4126 (1970).
[18] F. Stern, *Phys. Rev. B* **3**, 2636 (1971).
[19] N. K. Dutta and R. J. Nelson, *Appl. Phys. Lett.* **38**, 407 (1980); *J. Appl. Phys.* **53**, 74 (1982).
[20] M. G. A. Bernard and G. Duraffourg, *Phys. Status Solidi* **1**, 699 (1961).
[21] H. Kroemer, *Proc. IEEE* **51**, 1782 (1963).
[22] Zh. I. Alferov, V. M. Andreev, E. L. Portnoi and M. K. Trukan, *Sov. Phys. Semiconductors* **3**, 1107 (1970).
[23] I. Hayashi, M. B. Panish, P. W. Foy and S. Sumski, *Appl. Phys. Lett.* **17**, 109 (1970).
[24] R. Dingle, W. Wiegman and C. H. Henry, *Phys. Rev. Lett.* **33**, 827 (1974).

[25] P. Zory (ed.), *Quantum Well Lasers* (John Wiley, New York, 1992).
[26] K. Magari, M. Okamoto and Y. Noguchi, *IEEE Photon Tech. Letts.* **3**, 998 (1991).
[27] M. Joma, H. Horokawa, C. Q. Xu, K. Yamada, Y. Katoh and T. Kamijoh, *Appl. Phys. Lett.* **62**, 121 (1993).
[28] K. S. Jepsen, B. Mikkelsen, J. H. Povlsen, M. Yamaguchi and K. E. Stubkjaer, *IEEE Photonic Tech. Letts.* **4**, 550 (1992).
[29] Y. Yamamoto, *IEEE J. Quantum Electron.* **QE-16**, 107 (1980).
[30] P. J. A. Thijs, L. F. Tiemeijer, J. J. M. Binsma and T. van Dongen, *IEEE JQE* **90**, 477 (1994).
[31] L. F. Tiemeijer, P. J. A. Thijs, T. van Dongen, R. W. M. Slootweg, J. M. M. van der Heijden, J. J. M. Binsma and M. P. C. M. Krijn, *Appl. Phys. Lett.* **62**, 826 (1993).

Chapter 3

Recombination Mechanisms and Gain

3.1. Introduction

Recombination mechanisms in direct gap semiconductors are described in this chapter. Recombination mechanisms can, in general, be divided into two categories: radiative and non-radiative. The radiative recombination of the electrons and holes are responsible for stimulated optical emission or gain. Sufficient numbers of electrons and holes must be excited in the semiconductor for net optical gain.

The optical processes associated with radiative recombination are: optical gain or optical absorption, spontaneous emission and stimulated emission. Calculation of the rates associated with these processes for direct gap semiconductors are described here. Quantum well, quantum wire and quantum dots are semiconductor heterostructures with very small dimensions along one, two or all three directions respectively. In these structures, the optical gain is modified due to the modification of the density of electron and hole states.

Non-radiative recombination of an electron-hole pair, as the name implies, is characterized by the absence of an emitted photon in the recombination process. This recombination can occur at defect in the material or at semiconductor surfaces/interfaces which have dangling bonds. Auger recombination is a particular type of non-radiative recombination process which is expected to be larger for lower band gap semiconductors and at high temperatures. Calculation of these non-radiative recombination processes and their impact is described.

3.2. Radiative Recombination

The basis of light emission in semiconductors is the recombination of an electron in the conduction band with a hole from the valence band; the excess energy is emitted as a photon (light quantum). The process is called radiative recombination. The energy versus wavevector diagram of the electrons and holes in a cubic (zinc blende type) semiconductor is shown in Fig. 3.2.1. For direct gap semiconductors, the bottom of the conduction band and the top of the valence band are at the same point in momentum space or $\vec{k}$ space ($\vec{k} = 0$ in Fig. 3.2.1). This allows both energy and momentum conservation in the process of photon emission by electron-hole recombination.

For indirect gap semiconductors (e.g. silicon), the momentum conservation can be achieved with the assistance of a phonon (lattice vibration), which significantly decreases the probability of radiative recombination.

The valence band in many III-V semiconductors is represented by three major subbands. These are the heavy hole band, the light hole band, and the spin-split off band. The radiative transitions occurring

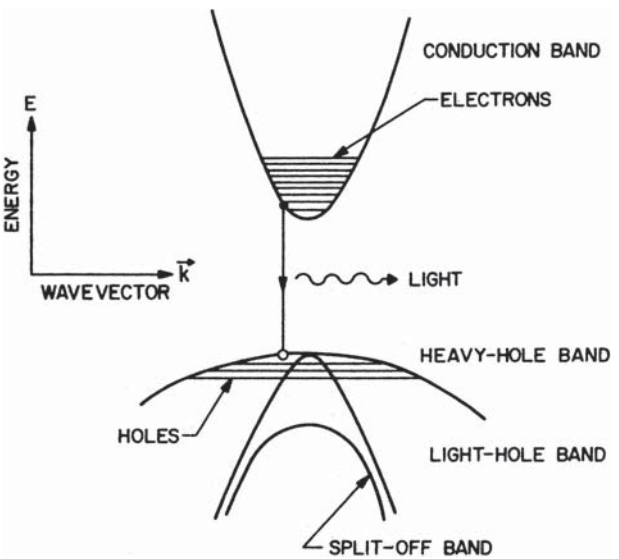

Fig. 3.2.1. Energy versus wavevector of the four major energy bands for a zinc blende type of direct gap semiconductor [1].

near bandgap energies are due to the recombination of electrons with heavy holes and light holes. A heavy hole, as the name implies, has larger effective mass than a light hole, which makes the density of states (and also the available number of heavy holes for a given Fermi level) larger than that for the light holes.

3.2.1. *Condition for gain*

Consider the transition shown in Fig. 3.2.1 for a photon whose energy $h\nu = E = E_g + E_c + E_v$, where E_g is the band gap, E_c, E_v are energies of the electron and hole respectively. The photon can be absorbed creating an electron of energy E_c and hole of energy E_v. The stimulated emission rate is given by

$$R_e = Bf_c f_v \rho(E), \tag{3.2.1}$$

where B is the transition probability, $\rho(E)$ is the density of states of photons of energy E, $f_c(E_c)$ and $f_v(E_v)$ are the Fermi factors which is the probability that electron and hole states of energy E_c and E_v are occupied. The quantities $f_c(E_c)$ and $f_v(E_v)$ are given by

$$f_c(E_c) = \frac{1}{1 + \exp[(E_c - E_{fc})/kT]}, \tag{3.2.2}$$

$$f_v(E_v) = \frac{1}{1 + \exp[(E_v - E_{fv})/kT]}, \tag{3.2.3}$$

where E_{fc}, E_{fv} are the quasi Fermi levels of the electrons and holes respectively. The stimulated emission process involves the recombination of an electron and hole pair and the absorption process creates an electron and hole pair. The absorption rate for photons of energy E is given by

$$R_a = B(1 - f_c)(1 - f_v)\rho(E). \tag{3.2.4}$$

The condition for net stimulated emission or gain is

$$R_e > R_a. \tag{3.2.5}$$

Using Eqs. (3.2.1) and (3.2.4) this becomes

$$f_c + f_v > 1. \tag{3.2.6}$$

Using equations (3.2.2) and (3.2.3) for f_c and f_v the condition for gain at photon energy E becomes

$$E_{fc} + E_{fv} > E - E_g. \tag{3.2.7}$$

This condition was first derived in Ref. [2]. The condition for zero net gain or zero absorption at photon energy is

$$E_{fc} + E_{fv} = E - E_g. \tag{3.2.8}$$

Since the minimum value of E is Eg, the condition for gain at any energy is $E_{fc} + E_{fv} = 0$. This is often known as the condition for transparency.

3.2.2. *Gain calculation*

The quantities associated with a radiative recombination are the absorption spectrum, emission spectrum, gain spectrum, and total radiative emission rate. The optical absorption or gain for a transition between the valence band and the conduction band at an energy E is given by [3,4]

$$\alpha(E) = \frac{e^2 h}{2\varepsilon_0 m_0^2 cnE} \int_{-\infty}^{+\infty} \rho_c(E')\rho_v(E'')|M(E', E'')|^2 \times [f(E'' = E' - E) - f(E')]dE', \tag{3.2.9}$$

where m_0 is the free electron mass, h is the Planck's constant, e is the electron charge, ε_0 is the permittivity of free space, E is the photon energy, n is the refractive index at energy E, and ρ_c and ρ_v are the densities of state for unit volume per unit energy in the conduction and valence band, respectively. $f(E')$ is the probability that a state of energy E' is occupied by an electron and M is the effective matrix clement between the conduction band state of energy E' and the valence band state of energy E''. Hwang [5] has shown that the contribution of the band-tail impurity states can be significant for photon energies near the band edges. Several models for the density of states and matrix element for transition between band-tail states exist [3,4]. The latest of such models that take into account the contributions of the parabolic bands and impurities is a Gaussian

fit of the Kane form to the Halperin-Lax model of band tails. This was first proposed by Stern [6] and used to calculate the gain and recombination rate in GaAs.

The matrix element M may be expressed as a product of two terms: $M = M_b\, M_{env}$ The quantity M_b arises from the band-edge Bloch functions and M_{env} arises from the envelope wave functions. For III-V semiconductors using the Kane model [1],

$$|M_b|^2 = \frac{m_c^2 E_g}{12 m_o} \frac{E_g + \Delta}{E_g + \frac{2}{3}\Delta}, \tag{3.2.10}$$

where m_c is the conduction-band effective mass, E_g is the energy gap, and Δ is the spin-orbit coupling. The envelop matrix element for the band-tail states have been calculated by Stern [6].

The calculated spectral dependence of absorption or gain at various injected carrier densities is shown in Fig. 3.2.2 for InGaAsP ($\lambda \sim 1.3\,\mu$m) with acceptor and donor concentrations of $2\times10^{17}\,\mathrm{cm}^{-3}$. The calculation was done using Gaussian Halperin-lax band tails and Stern's matrix element [4]. The material parameters used in the calculation are $m_c = 0.061\, m_0$, $m_{hh} = 0.45\, m_0$, $m_{lh} = 0.08\, m_0$, $\Delta = 0.26\,\mathrm{eV}$, $E_g = 0.96\,\mathrm{eV}$, and $\varepsilon = 11.5$. Figure 3.2.2 shows that the gain peak shifts to higher energies with increasing injection. This is observed in semiconductor amplifiers.

Figure 3.2.3 shows the maximum gain as a function of injected carrier density at different temperatures. Figure 3.2.4 shows the maximum gain as a function of nominal current density for InGaAsP ($\lambda = 1.3\,\mu$m) at different temperatures. Figure 3.2.5 and 3.2.6 shows similar results for InGaAsP ($\lambda \sim 1.55\,\mu$m). The differences between the two sets of results for the two materials is primarily due to differences in the band structure parameters such as effective masses of the conduction band electrons and valence band holes. Note that considerably lower injected carrier density is needed at a lower temperature to achieve the same optical gain. This is the origin of the lower threshold current at low temperature. It is often convenient to use a linear relationship between the gain g and the injected carrier density n of the form

$$g = a(n - n_0), \tag{3.2.11}$$

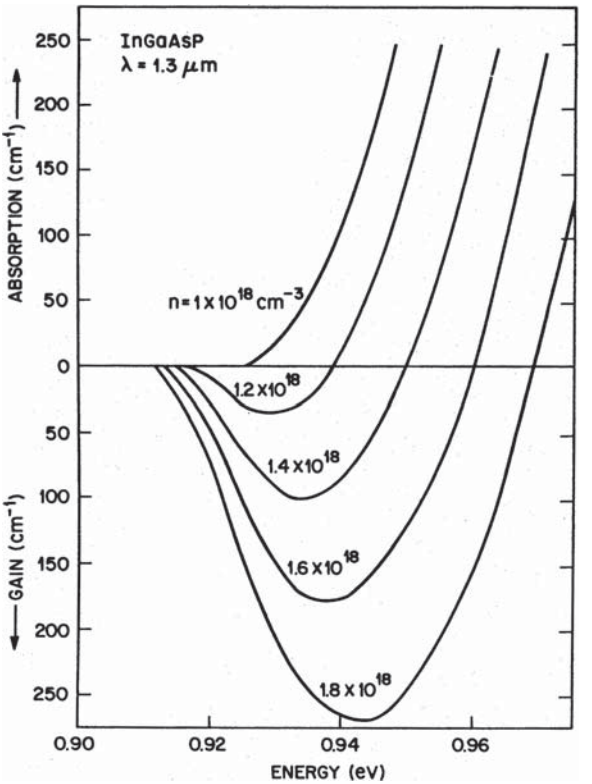

Fig. 3.2.2. Calculated gain or absorption as function of photon energy for $\lambda = 1.3\,\mu$m ($E_g = 0.96\,$eV) InGaAsP at various injected carrier densities [7]

where a is the gain coefficient and n_0 is the injected carrier density at transparency.

3.2.3. *Spontaneous emission rate*

At unity quantum efficiency, the total spontaneous radiative recombination rate R equals the excitation rate. The latter is usually expressed in terms of the nominal current density J_n [3,4]:

$$J_n[A/(\mathrm{cm}^2\mu\mathrm{m})] = eR, \tag{3.2.12}$$

with $R = \int r_{\mathrm{spon}}(E)dE$ where e is the electron charge and the thickness of the active region is assumed to be $1\,\mu$m. $r_{\mathrm{spon}}(E)$ is

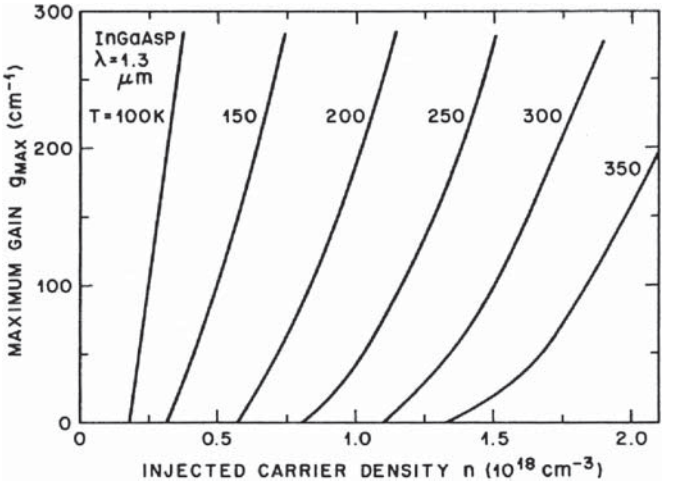

Fig. 3.2.3. The maximum gain as a function of injected carrier density for undoped InGaAsP ($\lambda = 1.3\,\mu$m) at different temperatures [8].

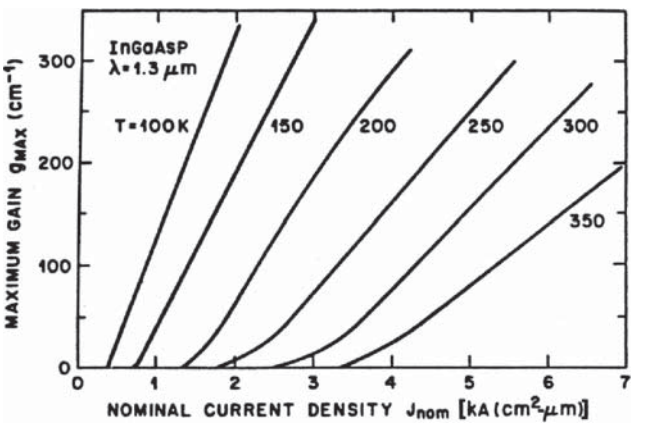

Fig. 3.2.4. The maximum gain as a function of nominal current density for InGaAsP ($\lambda = 1.3\,\mu$m) at different temperatures [8].

the spontaneous emission rate at a photon energy E. It is given by [3,4].

$$r_{\text{spon}}(E) = \frac{4\pi n e^2 E}{m_o^2 \varepsilon_0 h^2 c^3} \int_{-\infty}^{+\infty} \rho_c(E')\rho_v(E'')|M(E', E'')|^2 f(E') \times [1 - f(E'')]dE'. \tag{3.2.13}$$

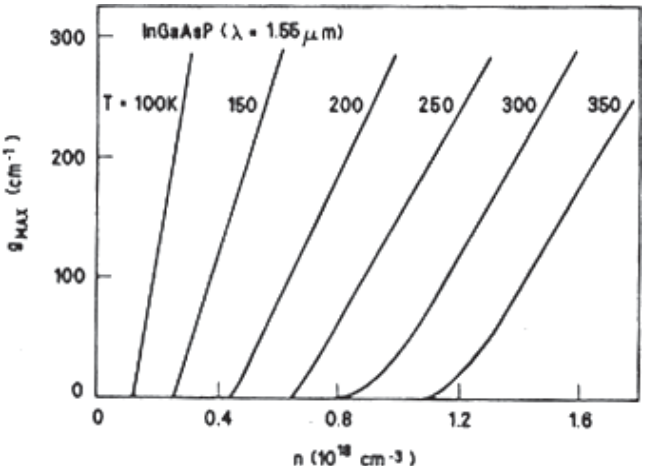

Fig. 3.2.5. The maximum gain as a function of injected carrier density for undoped InGaAsP ($\lambda \sim 1.55\,\mu$m) at different temperatures [8].

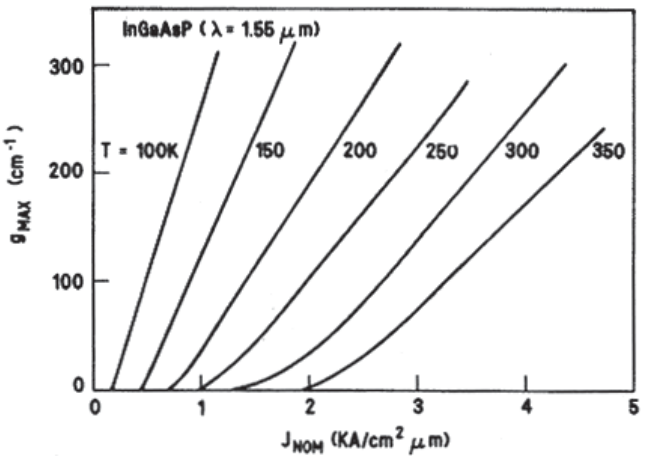

Fig. 3.2.6. The maximum gain as a function of nominal current density for undoped InGaAsP ($\lambda \sim 1.55\,\mu$m) at different temperatures [8].

The calculated maximum optical gain g as a function of the nominal current density at various temperatures is shown in Fig. 3.2.4 for InGaAsP ($\lambda \sim 1.3\,\mu$m). The calculation is for an undoped lightly compensated material with $10^{17}\,\mathrm{cm}^{-3}$ of acceptors and donors, respectively. Note that gain varies linearly with J_n above a certain

gain. From the above figure, the relationship between gain and nominal current density for InGaAsP ($\lambda \sim 1.3\,\mu$m) at 300 K is approximately given by

$$g = 0.08(J_n - 3100)\ \text{cm}^{-1}, \tag{3.2.14}$$

where J_n is expressed in amperes per square centimeter per micron. The total spontaneous radiative recombination rate R can be approximated by

$$R = Bnp, \tag{3.2.15}$$

where B is the radiative recombination coefficient and n, p are the electron and hole densities, respectively. For undoped semiconductors, Eq. (3.2.15) becomes $R = Bn^2$. For GaAs, the measured $B = 1 \times 10^{-10}\,\text{cm}^3/\text{s}$. Calculation of the radiative recombination rate shows that B decreases with increasing carrier density [4]. This has been confirmed by carrier lifetime measurements [9].

In double heterostructure materials, the injected carriers can recombine by both radiative and non-radiative recombination. The injected current density J is simply the sum of the radiative R and non-radiative R_{nr} recombination rates in the absence of carrier leakage:

$$J = e(R + R_{nr})d = J_r + J_{nr} \quad (J_r = J_n d), \tag{3.2.16}$$

where e is the electron charge, d is the active layer thickness, and J_r, J_{nr} are the radiative and non-radiative components of the current density, respectively.

For a GaAs double heterostructure material where the quantum efficiency is believed to be close to unity, that is, most of the injected carriers recombine radiatively, $J \sim J_r$. The relation between the optical gain and the nominal current density for GaAs material system has been calculated by Stern [6]. It is given by

$$g = 0.045(J_n - 4200)\ \text{cm}^{-1}, \tag{3.2.17}$$

where J_n is expressed in amperes per square centimeter per micron.

It is useful to make connection with the operation of a GaAs laser for which the non-radiative recombination is believed to be

very small. For a laser the optical gain provided by current injection must equal optical loss. The latter includes mirror losses. This is expressed as

$$\Gamma g_{\text{th}} = \alpha_a \Gamma + (1 - \Gamma)\alpha_c + \frac{1}{L} \ln \frac{1}{R}, \tag{3.2.18}$$

where g_{th} is the threshold gain in the active region; α_a, α_c are the absorption losses in the active and cladding regions, respectively; L is the cavity length; and R is the mirror facet reflectivity. Typically, $\text{L} \sim 300\,\mu\text{m}$ and $\text{R} \sim 0.3$. For a 0.2-μm-thick active layer, Γ(TE) is ∼0.6, and using $\alpha_a = \alpha_c = 20\,\text{cm}^{-1}$, $\alpha_a \approx 30\,\text{cm}^{-1}$, the calculated $g_{\text{th}} \sim 110\,\text{cm}^{-1}$

The threshold current of a 250-μm-long GaAs-A1GaAs double heterostructure laser with $2\,\mu\text{m} \times 0.2\,\mu\text{m}$ active region can now be calculated using Eq. (3.2.17). The calculated $J_{\text{th}} = 1.35\,\text{kA/cm}^2$, and the threshold current is 6.7 mA. This compares well with the experimentally observed threshold currents in the range 5-10 mA for GaAs-A1GaAs double heterostructure lasers with good current confinement.

Figure 3.2.4 shows that the current density needed to achieve a certain optical gain increases with temperature. The same figure also illustrates that the threshold current density of a laser is expected to increase with increasing temperature. For InGaAsP lasers, a significant amount of non-radiative recombination is believed to be present at high carrier densities needed for gain. The nonradiative recombination can increase the current needed for gain (as shown in Eq. (3.2.16)) and also its temperature dependence.

3.3. Non-radiative Recombination

An electron-hole pair can recombine non-radiatively, meaning that the recombination can occur through any process that does not emit a photon. In many semiconductors, for example pure germanium or silicon, the non-radiative recombination dominates radiative recombination. The measurable quantities associated with nonradiative recombination are internal quantum efficiency and carrier lifetime. The variation of these quantities with parameters such as temperature,

pressure, and carrier concentration are by and large the only way to identify a particular non-radiative recombination process.

The effect of non-radiative recombination on the performance of amplifiers is to increase the current needed for a certain optical gain. If τ_{nr} is the carrier lifetime associated with the non-radiative process, the increase in current density is given approximately by

$$J_{nr} = \frac{en_d}{\tau_{nr}}, \tag{3.3.1}$$

where n is the carrier density, d is the active layer thickness, and e is the electron charge. The non-radiative recombination processes described in this section are the Auger effect, surface recombination, and recombination at defects or traps.

3.3.1. *Auger effect*

Since the pioneering work by Beattie and Landsberg [10] it is generally accepted that Auger recombination can be a major non-radiative recombination mechanism in narrow-gap semiconductors. Recent attention to the Auger effect has been in connection with the observed greater higher temperature of threshold current of long-wavelength InGaAsP laser compared to short-wavelength A1GaAs lasers [11-15]. It is generally believed that the Auger effect plays a significant role in determining the observed high-temperature sensitivity of threshold current of InGaAsP lasers and amplifiers operating near 1.3 and 1.55 μm. There are several types of Auger recombination processes. The three major types are band-to-band process, phonon-assisted Auger process, and trap-assisted Auger processes.

The band-to-band Auger processes in direct gap semiconductors are shown in Fig. 3.3.1. The three processes are labeled CCCH, CHHS, and CHHL, where C stands for the conduction band and H, L, S stand for heavy-hole, light-hole, and split-off valence band hole, respectively. The CCCH mechanism involves three electrons and a heavy hole and is dominant in n-type material. The process was first considered by Beattie and Landsberg [10].

The CHHS process involves one electron, two heavy holes, and a split-off band hole. The CHHL process is similar to the CHHS

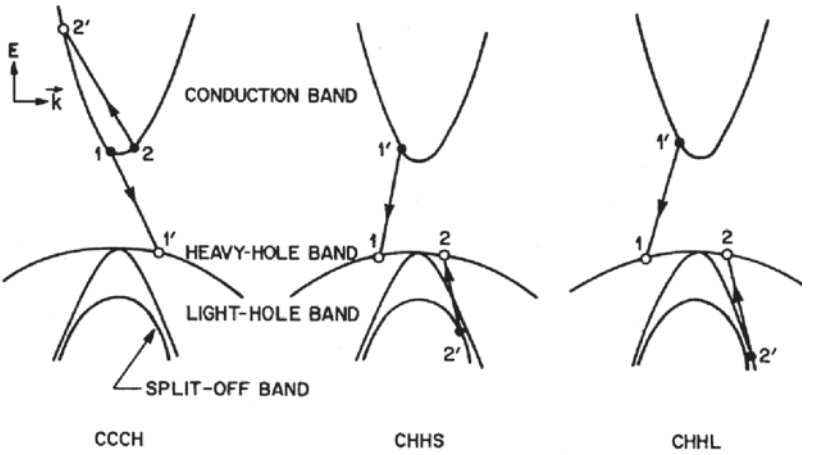

Fig. 3.3.1. Band-to-band Auger recombination processes in a direct gap semiconductor [8].

process except that it involves a light hole. The CHHS and CHHL mechanisms are dominant in p-type material. Under the high injection conditions present in lasers and amplifiers, all these mechanisms must be considered.

Band-to-band Auger processes are characterized by a strong temperature dependence and band gap dependence, the Auger rate decreasing rapidly either for low temperature or for high band-gap materials. These dependencies arise from the energy and momentum conservation that the four free particle states involved (1, 2, 1', 2' in Fig. 3.3.1) must satisfy. The momentum and energy conservation laws give rise to a threshold energy E_T for each of the processes. For the CCCH process, if we assume $E_1 \sim E_2 = 0$, only holes with energies greater than $\sim (E_T - E_g) = \delta E_g$ can participate (δ is a constant that depends on effective masses). The number of such holes varies approximately as exp $(-\delta E_g/kT)$ for nondegenerate statistics and thus the Auger rate varies approximately as exp $(-\delta E_g/kT)$ in the nondegenerate case.

The Auger rate calculations [8] can be applied to any direct-gap semiconductor for which the Kane model of the band structure is valid. The various band-to-band Auger processes are characterized by a strong dependence on both the band gap E_g and the temperature T.

In the nondegenerate approximation, the proportional dependence of the Auger rate R_A on E_g and T may be approximately written as

$$R_A \propto \exp(-\Delta E/kT), \tag{3.3.2}$$

where for the CCCH process

$$\Delta E = \frac{m_c}{2m_{c0} + m_v - m_c} E_g,$$

for the CHHS process

$$\Delta E = \frac{m_s}{2m_v + m_{c0} - m_s}(E_g - \Delta),$$

and for the CHHL process

$$\Delta E = \frac{m_l}{2m_v + m_{c0} - m_l} E_g,$$

where m_{c0}, m_v are the conduction-band and the valence-band (heavy-hole) mass at the band edge and m_c, m_s, and m_l are the effective masses of an electron, split-off band hole and the light hole at the energy $E_T = E_g + \Delta E$ where ΔE is given by the above equations for the respective processes and E_g is the band gap. Thus the non-parabolicity of the band structure plays a significant role in determining the Auger recombination rate. The calculated Auger recombination lifetime for the three processes CCCH, CHHS and CHHL at a carrier density of $10^{18}\,\mathrm{cm}^{-3}$ as a function of y (the arsenic composition) for InGaAsP lattice matched to InP is shown in Fig. 3.3.2.

The bandgap of InGaAsP decreases with increasing y as

$$E_g(y) = 1.35 - 0.75\,y + 0.12\,y^2, \tag{3.3.3}$$

for compositions that is lattice matched to InP ($x \sim 0.45\,y$). The Auger lifetime decreases i.e. Auger recombination rate increases with decreasing band gap.

First consider n-type materials where the CCCH process is dominant. In the nondegenerate approximation with parabolic bands

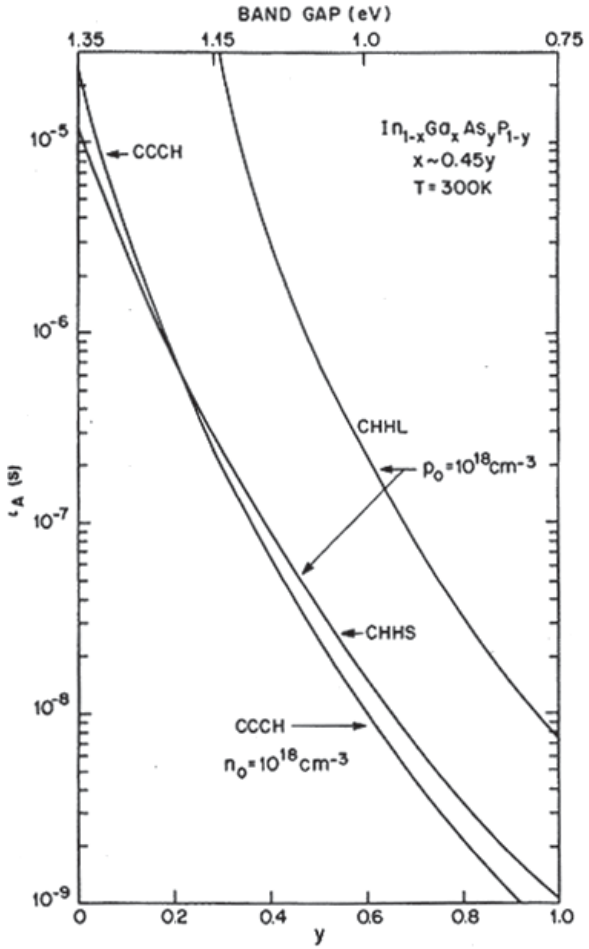

Fig. 3.3.2. The calculated Auger recombination lifetime for the three processes CCCH, CHHS and CHHL at a carrier density of 10^{18} cm^{-3} as a function of y (the arsenic composition) for InGaAsP lattice matched to InP [8].

($m_c = m_{c0}$), Eq. (3.3.2) can be further simplified to yield

$$R_A \propto \exp\left|-\frac{\mu}{1+\mu}\frac{E_g}{kT}\right|, \tag{3.3.4}$$

where $\mu = m_{c0}/m_v$. Since, in general, the conduction-band effective mass decreases with decreasing band gap, it follows that the lower band-gap materials will have a larger band-to-band Auger rate.

A similar results holds for p-type materials for the CHHL Auger process. However, an interesting case may arise for the CHHS process (in p-type materials) when $E_g - \Delta$ is small. Since both E_g and Δ depend on temperature, if at some temperature $E_g \cong \Delta$, the Auger rate is strongly peaked at that temperature. Such a situation may arise in GaSb ($E_g = 0.7\,\text{eV}$), where at 77 K very large Auger coefficients ($\sim 10^{-25}\,\text{cm}^6\,\text{sec}^{-1}$) have been measured. [8]. The calculated Auger lifetime at a carrier density of $10^{18}\,\text{cm}^{-3}$ as a function of temperature for the three Auger processes for InGaAsP which emits near $1.3\,\mu$m is shown in Fig. 3.3.3. The Auger lifetime

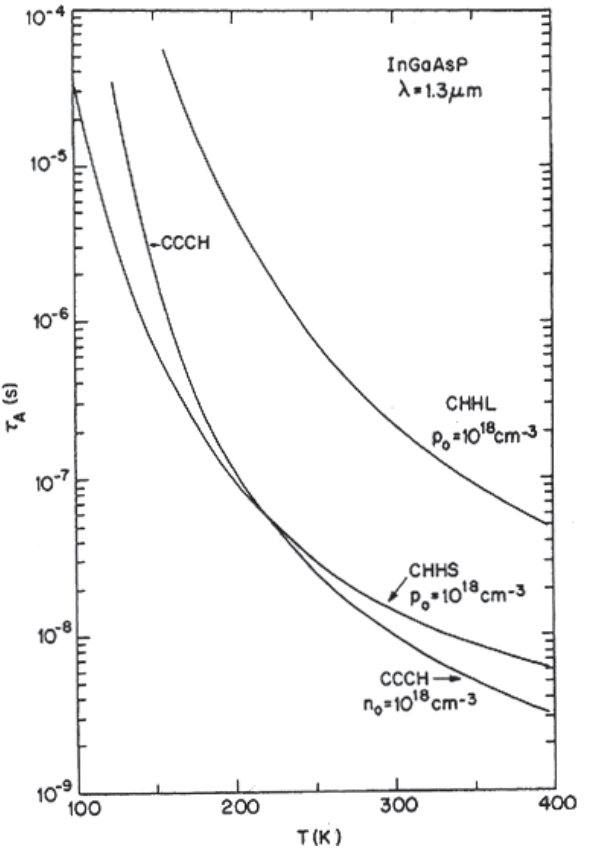

Fig. 3.3.3. The calculated Auger lifetime at a carrier density of $10^{18}\,\text{cm}^{-3}$ as a function of temperature for the three Auger processes for InGaAsP which emits near $1.3\,\mu$m [8].

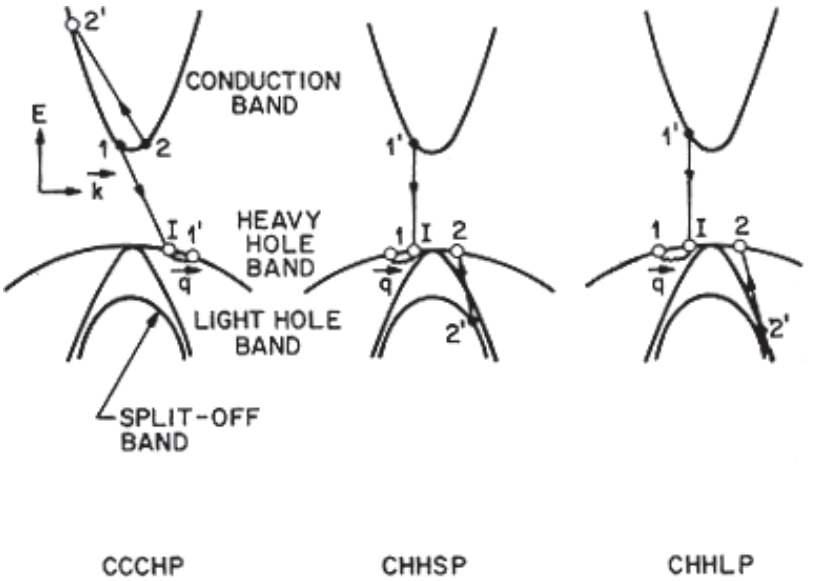

Fig. 3.3.4. Phonon assisted Auger recombination processes in a direct gap semiconductor [8].

decreases i.e. the Auger recombination rate increases with increasing temperature.

In the absence of momentum conservation, there is no threshold energy E_T [8,16-24] Thus the strong temperature dependence does not appear if the individual particle states are not states of definite momentum, for example, if they are trap states, or if momentum conservation is satisfied through phonon assistance. The energy vs. wave vector diagram of phonons illustrate that they can carry considerable amount of momentum for a very small energy. Examples of various types phonon-assisted processes are shown in Fig. 3.3.4.

The CCCH process involves two electrons, a heavy hole and a phonon. The CHHS process involves one electron, two heavy holes, a split-off band hole and a phonon. The CHHL process is similar to the CHHS process except that it involves a light hole. The CHHS and CHHL mechanisms are dominant in p-type material. Under the high injection conditions present in lasers, all these mechanisms

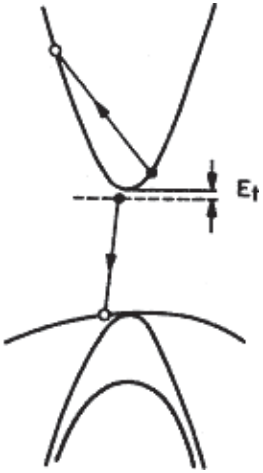

Fig. 3.3.5. Auger recombination process using a donor trap [8].

must be considered. Since the phonons can participate in momentum conservation, the four particle states in the conduction and valence band alone does not need to conserve momentum. This means a minimum kinetic energy for the process to occur is no longer needed here. This implies for the CCCHP process the electron states 1 and 2 does not need to have a minimum energy. Hence all electrons can participate in phonon assisted Auger recombination.

Thus the phonon assisted Auger recombination processes has a larger rate than band-to-band processes at low temperatures and they do not exhibit strong temperature and band gap dependence.

Figure 3.3.5 shows the Auger recombination process involving a donor trap. Since the trap state is not a state of definite momentum, the Auger recombination rate in this case is not a strong function of temperature or band gap. The rate varies linearly with the concentration of the trap. The Auger rate R_a in n-type semiconductors with a carrier concentration n_0 varies as [8, 10]

$$R_a = Cn_0^2\delta p, \tag{3.3.5}$$

where $\delta p \ll n_0$ is the injected minority carrier (hole) density and C is the Auger coefficient. Thus the minority carrier lifetime is

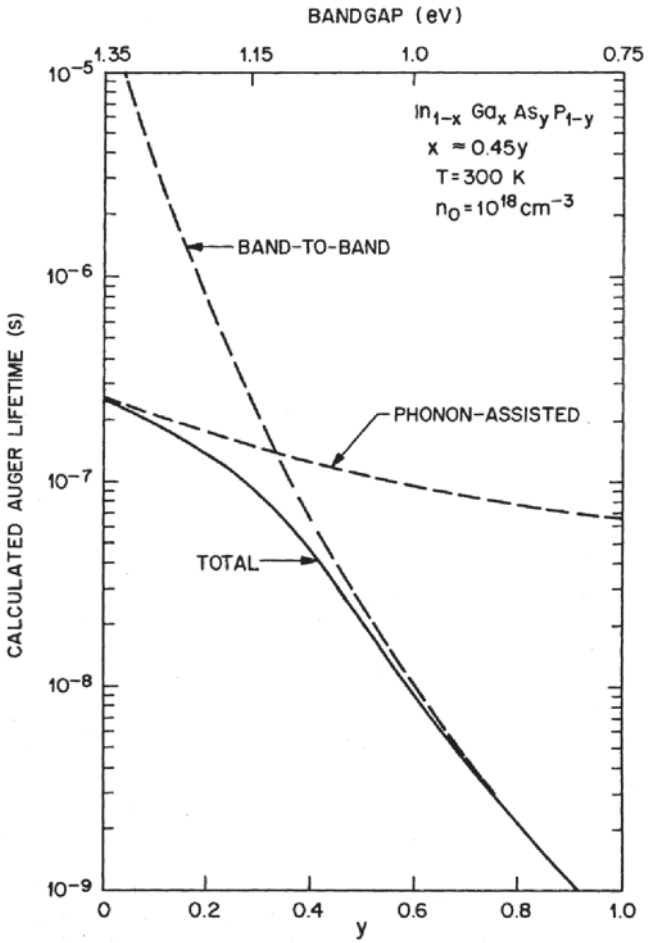

Fig. 3.3.6. The calculated Auger lifetime for n-InGaAsP with a carrier concentration of $10^{18}\,\mathrm{cm}^{-3}$ [8].

given by

$$\tau_A = \frac{R_a}{\delta p} = \frac{1}{Cn_0^2}. \tag{3.3.6}$$

The calculated τ_A for n-InGaAsP with a carrier concentration $10^{18}\,\mathrm{cm}^{-3}$ is shown in Fig. 3.3.6. The phonon-assisted process dominates at high bandgap, and the band-to-band processes dominate for low bandgap semiconductors. The active region of an InGaAsP laser

is nominally undoped. Under high injection the Auger rate R_a varies approximately as

$$R_a = Cn^3, \tag{3.3.7}$$

where n is the injected carrier density. Calculations of the Auger coefficient using the Kane band model [1] yield a value of $10^{-28}\,\mathrm{cm}^6/\mathrm{s}$ for $\lambda \approx 1.3\,\mu\mathrm{m}$ InGaAsP. A value of $\sim 2.5\times10^{-29}\,\mathrm{cm}^6/\mathrm{s}$ for $\lambda \approx 1.3\,\mu\mathrm{m}$ InGaAsP using a different model for the band structure has been calculated [15]. The experimental values of the Auger coefficient for this material are in the range $2\times10^{-29} \sim 7\times10^{-29}\,\mathrm{cm}^6/\mathrm{s}$ [4]. For GaAs, $C \approx 10^{-31}\,\mathrm{cm}^6/\mathrm{s}$. From Eqs. (3.2.16) and (3.3.7), the current lost to Auger recombination at threshold is given by

$$J_A = edCn^3. \tag{3.3.8}$$

The effect of Auger recombination on the threshold current of GaAs amplifiers is small compared to that for InGaAsP amplifiers because the Auger coefficient in GaAs is smaller by two orders of magnitude. Since the carrier density needed for a certain optical gain increases with increasing temperature, the carrier loss to the nonradiative Auger process increases with increasing temperature, which results in a more rapid increase of the current with increasing temperature for long-wavelength InGaAsP amplifiers compared to that for GaAs amplifiers. In addition, Auger recombination produces hot carriers and when they relax they lose their energy to the lattice raising the lattice temperature and equilibrium carrier temperature. This increase in temperature results in a reduction in gain for the same carrier density. Carrier temperatures as high as 400 K has been reported for 300 K lattice temperature for 1nGaAsP/InP double heterostructure under high injection [25,26]. High carrier temperature increases carrier leakage over the heterobarrier. This is discussed in a detail in later section. Thus all of these processes can result in a sublinearity of gain vs. carrier density curve.

It is useful to make a comparison with lasers now. The measured variation of threshold current density as a function of temperature for InGaAsP lasers can be expressed by the relation $J_{\mathrm{th}} = J_0 \exp(T/T_0)$ with $T_0 = 50 - 70\,\mathrm{K}$ in the temperature range 300–350 K.

Auger recombination plays a significant role in determining the smaller T_0 values of InGaAsP ($\lambda \approx 1.3\,\mu$m and $1.55\,\mu$m) lasers compared to shorter wavelength ($\lambda \approx 0.85\,\mu$m) GaAs lasers[4]. Auger recombination also increases the current needed for a certain optical gain in InGaAsP amplifiers.

3.3.2. *Surface recombination*

In an amplifier, the facets are surfaces exposed to the ambient. In addition, in many index-guided amplifier structures, the edges of the active region can be in contact with curved surfaces, which may not be a perfect lattice. A surface, in general, is a strong perturbation of the lattice, creating many dangling bonds that can absorb impurities from the ambient. Hence a high concentration of defects can occur that can act as non-radiative recombination centers. Such localized non-radiative centers, in addition to increasing the threshold current, can cause other performance problems (e.g. low operating lifetime) for amplifiers.

The recombination rate of carriers at the surface is expressed in terms of a surface recombination velocity S. If A is the surface area and n the carrier density, then the increase in threshold current, ΔI, due to surface recombination is given by

$$\Delta I = en_S A, \tag{3.3.9}$$

where e is the electron charge. The surface recombination velocity for InP surface exposed to air is about two orders of magnitude smaller than that for GaAs.

3.3.3. *Recombination at defects*

Defects in the active region of an amplifier can be formed in several ways. In many cases, they are grown in during the epitaxial growth process. They can also be generated, multiply, or propagate during a stress aging test [27]. Defects can propagate along a specific crystal axis in a strained lattice. The well-known dark line defect (DLD; dark region of linear aspect) is generally believed to be responsible for the high degradation rate (short life span) of early A1GaAs lasers.

Defects in general produce a continuum of states in a localized region. Electrons or holes that are within a diffusion length from the edge of the defect may recombine non-radiatively via the continuum of states. The rate of recombination at a defect or trap is usually written as

$$R = \delta \cdot \nu \cdot N_t, \tag{3.3.10}$$

where δ is the capture cross section of the trap, N_t is the density of traps, and v is the velocity of the electrons or holes. A trap can preferentially capture electrons or holes. The study of recombination at defects in semiconductors is a vast subject. A detailed discussion of which is beyond the scope of this chapter.

3.3.4. *Carrier leakage over the heterobarrier*

The carrier leakage over the heterobarrier is not a non-radiative recombination mechanism. But it can result in a significant loss of carriers (and hence current) at high temperatures or for low heterojunction barrier heights [28-35]. Heterojunction carrier leakage is caused by diffusion and drift of electrons and holes from the edges of the active region to the cladding layers. It is schematically shown in Fig. 3.3.7(a). The heterojunction leakage in both AlGaAs/GaAs and InGaAsP/InP double heterostructure has been studied. In thermal equilibrium, at the boundary between the active and cladding layers, a certain number of electrons and holes are present. Figure 3.3.7(b) shows an energy-level diagram for the heterojunction of active and cladding layers; the electron and hole quasi-Fermi levels E_{fc} and E_{fv} are assumed to be continuous at the boundary [35]. The number of electrons n_b at the boundary of the p-cladding layer is given by

$$n_b = N_{cc}\frac{2}{\pi^{1/2}}\int_{\varepsilon_c}^{\infty}\frac{\varepsilon^{1/2}d\varepsilon}{1+\exp(\varepsilon-\varepsilon_{fc})}, \tag{3.3.11}$$

where

$$N_{cc} = 2\left(\frac{2\pi m_c kT}{h^2}\right)^{3/2}, \quad \varepsilon_c = \Delta E_c/kT$$

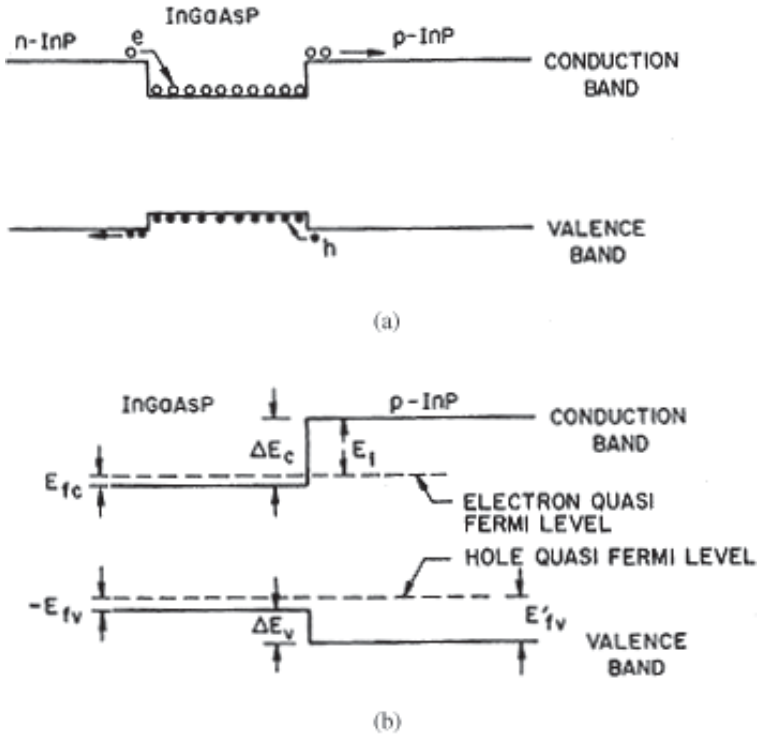

Fig. 3.3.7. Schematic representation of the conduction and valence band in the semiconductor heterostructure. The various energy band offsets are shown in (b) [4].

and m_c is the conduction-band mass of the p-cladding layer. Note that n_b is the number of electrons with energy greater than the conduction-band barrier height ΔE_c. Using the Boltzmann approximation, Eq. (3.3.11) may be simplified to yield

$$n_b = N_{cc}\frac{2}{\pi^{1/2}}\int_{\varepsilon_c}^{\infty}\varepsilon^{1/2}d\varepsilon\exp(-\varepsilon+\varepsilon_{fc}) = N_{cc}\exp\left(-\frac{E_1}{kT}\right). \tag{3.3.12}$$

The quantity $E_1 = \Delta E_c - E_{fc}$ is shown in Fig. 3.3.7. In deriving the above, we have used the relation $\varepsilon_{fc} = E_{fc}/kT$. We now show that E_1 is related to the band-gap-difference ΔE_g between the active and cladding layers. From Fig. 3.3.7 we note that

$$E_1 = \Delta E_c - E_{fc} = \Delta E_g - \Delta E_v - E_{fc}. \tag{3.3.13}$$

Further, ΔE_v is given by

$$\Delta E_v = E'_{fv} + E_{fv}, \tag{3.3.14}$$

where E'_{fv} and E_{fv} are the hole quasi-Fermi levels in the p-cladding layer and active layer respectively. From Eqs. (3.3.11), to (3.3.14) it follows that

$$n_b = \frac{N_{cc}N_{vc}}{P} \exp\left(-\frac{\Delta E_g + E_{fc} + E_{fv}}{kT}\right), \tag{3.3.15}$$

where

$$P = N_{vc} \exp\left(-\frac{E'_{fv}}{kT}\right), \tag{3.3.16}$$

and

$$N_{vc} = 2\left(\frac{2\pi kT}{h^2}\right)^{3/2} (m_{hh}^{3/2} + m_{lh}^{3/2}), \tag{3.3.17}$$

is the valence-band density of states for the p-cladding layer. P is the majority (hole) carrier density. The quantities E_{fc} and E_{fv} can be calculated from the known carrier density in the active region. Note that m_c, m_{hh}, and m_{lh} are the effective masses for the p-cladding layer. An equation similar to (3.3.15) can be derived for the density of holes (p_b) at the boundary between the n-cladding layer and the active layer. Equation (3.3.15) shows that n_b increases rapidly with increasing temperature and suggests that the carrier leakage can be a major carrier-loss mechanism at high temperatures, especially for low heterojunction-barrier heights. The electron leakage current density j_n at the p-cladding layer is given by [35]

$$j_n = -eD_n \frac{dn}{dx} + en\mu_n E, \tag{3.3.18}$$

where the first term represents diffusive leakage and the second term represents drift leakage in the presence of an electric field E. D_n is the electron diffusivity, μ_n is the minority carrier mobility, e is the charge of the electron, and $n(x)$ is the density of electrons at

a distance x from the boundary between the active region and the p-cladding layer. The current j_n also satisfies the continuity equation

$$\frac{1}{e}\frac{dj_n}{dx} + \frac{n}{\tau_n} = 0, \tag{3.3.19}$$

where τ_n is the minority carrier lifetime. Equation (3.3.19) can be solved using the boundary condition $n(x = 0) = n_b$ and $n(x = h) = 0$. The second condition assumes that the minority carrier density at the contact, which is at a distance h from the boundary, is 0. The result for the electron leakage current at $x = 0$ is

$$j_n = eD_n n_b \frac{(Z - Z_1)\exp(Z_2 h) + (Z_2 - Z)\exp(Z_1 h)}{\exp(Z_2 h) - \exp(Z_1 h)}, \tag{3.3.20}$$

where

$$Z = eE/kT, \tag{3.3.21}$$

$$Z_{2,1} = \frac{1}{2}Z \pm \left(\frac{1}{L_n^2} + \frac{1}{4}Z^2\right)^{1/2}, \tag{3.3.22}$$

$$L_n = (D_n \tau_n)^{1/2}. \tag{3.3.23}$$

L_n is the electron diffusion length. In the above, the relation $D_n = \mu_n kT/e$ has been used. In the limit $E = 0$, Eq. (3.3.20) reduces to the case of pure diffusive leakage, and for $L_n \gg h$, it reduces to $i_n = en_b\mu_n E$, which holds if only drift leakage is present.

A similar equation can be derived for the hole leakage current j_p in the n-cladding layer. However, since the diffusion length and mobility of electrons are large compared to those of holes, the electron leakage is considerably larger than the hole leakage. The total leakage is given by the sum

$$J_L = j_n + j_p. \tag{3.3.24}$$

Figure 3.3.8 shows the calculated leakage current (J_L) for the diffusive heterojunction leakage in an InGaAsP-InP double heterostructure [4]. At higher temperatures, the leakage current is considerably higher. The leakage current increases rapidly when the barrier height decreases.

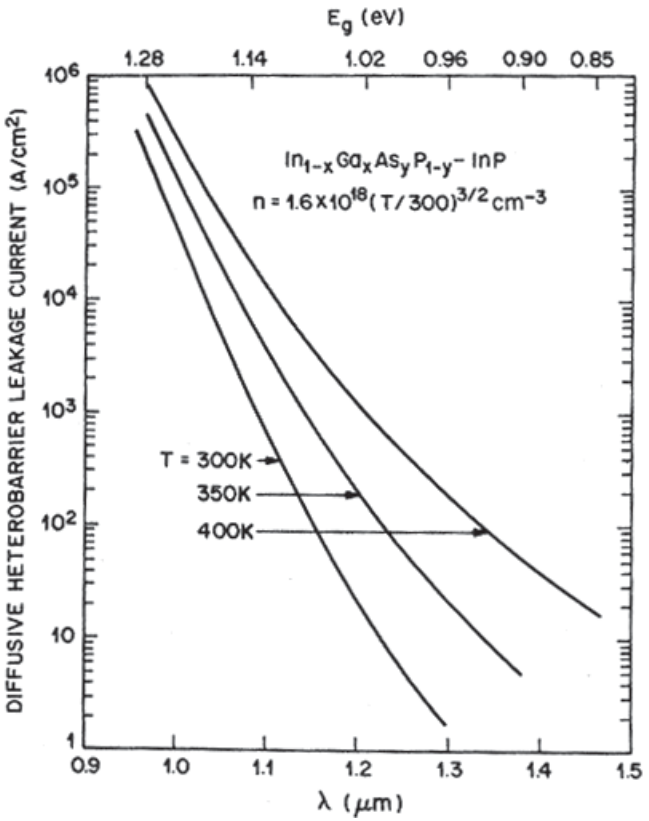

Fig. 3.3.8. Calculated carrier leakage current density for a InGaAsP-InP heterojunction as a function of the band gap of the InGaAsP material. The leakage current increases with increasing temperature and with lower energy band difference between the active region and cladding layers [4].

3.4. Quantum Well Amplifiers

A regular double heterostructure amplifier consists of an active layer sandwiched between higher-gap cladding layers. The active layer thickness is typically 0.1-0.5 μm. Double heterostructure lasers and amplifiers have been fabricated with an active layer thickness $\sim$100Å or less. The carrier (electron or hole) motion normal to the active layer in these structures is restricted. This may be viewed as carrier confinement in a one-dimensional potential well, and hence these lasers are called quantum well lasers and amplifiers [36–44].

3.4.1. *Energy levels*

When the thickness L_z of a narrow-gap semiconductor layer confined between two wide-gap semiconductors becomes comparable to the de Broglie wavelength ($\lambda \sim h/p \sim L_z$), quantum-mechanical effects are expected to occur.

The energy levels of the carriers confined in the narrow-gap semiconductor can be determined by separating the Hamiltonian into a component normal to the layer (z component) and into the usual (unconfined) Bloch function components (x, y) in the plane of the layer. The resulting energy eigenvalues are:

$$E(n, k_x, k_y) = E_n + \frac{\hbar^2}{2m_n^*}(k_x^2 + k_y^2), \tag{3.4.1}$$

where E_n is the n_{th} confined-particle energy level for carrier motion normal to the well. m_n^* is the effective mass of the nth level, $\hbar$ is Planck's constant divided by 2π, and k_x, k_y are the usual Bloch function wave-vectors in the x and y directions. Figure 3.4.1 shows schematically the energy levels E_n of the electrons and holes confined in a quantum well. The confined particle energy levels E_n are denoted by E_{1c}, E_{2c}, E_{3c} for electrons; E_{1hh}, E_{2hh} for heavy holes; and E_{1lh}, E_{2lh}, for light holes. The calculation of these quantities is a standard problem in quantum mechanics for a given potential barrier (ΔE_c, ΔE_v). For an infinite potential well, the following simple result is obtained:

$$E_n = \frac{h^2 n^2}{8L_z^2 m_n^*}. \tag{3.4.2}$$

Since the separation between the lowest conduction band level and the highest valence band level is given by

$$E_q = E_g + E_{1c} + E_{1hh} \approx E_g + \frac{h^2}{8L_z^2}\left(\frac{1}{m_c} + \frac{1}{m_h}\right). \tag{3.4.3}$$

It follows that in a quantum well structure the energy of the emitted photons can be varied simply by varying the well width L_z. This has been observed experimentally for InGaAs active region sandwiched between InP layers [42].

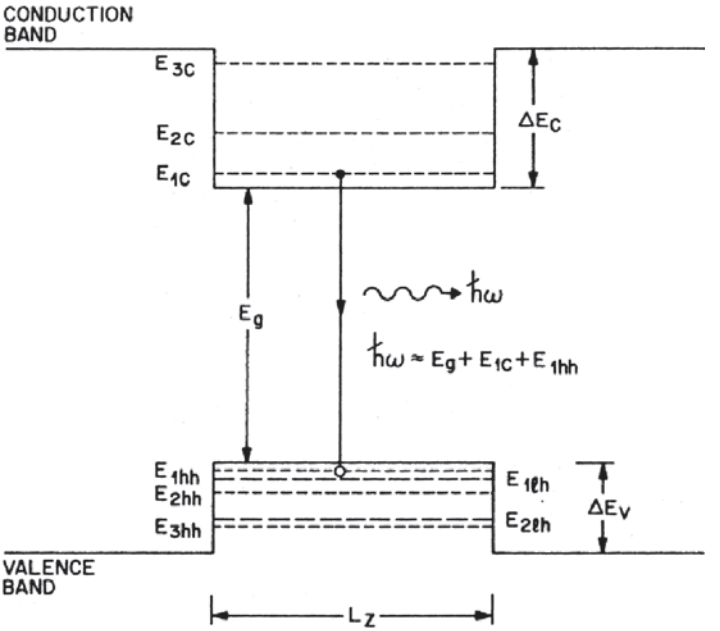

Fig. 3.4.1. Energy levels in a quantum well structure [38].

The discrete energy levels results in a modification of the density of states in a quantum well to a "two dimensional-like" density of states. This modification of the density of states results in several improvements in laser characteristics such as lower threshold current, higher efficiency, higher modulation bandwidth and lower CW and dynamic spectral width. Many of these improvements were first predicted theoretically and then demonstrated experimentally [40–44]. Various types of quantum well laser and also amplifier active region designs have been reported. The conduction and valence band diagram of these designs along with their names are shown in Fig. 3.4.2.

Since one of the advantages of QW amplifiers is high saturation power which arises in part due to low confinement factor, we now discuss the mode confinement factor of single and multiquantum well amplifiers. For a SQW amplifier of active layer thickness d, the confinement factor is

$$\Gamma \cong 2\pi^2(n_a^2 - n_c^2)d^2/\lambda_0^2, \tag{3.4.4}$$

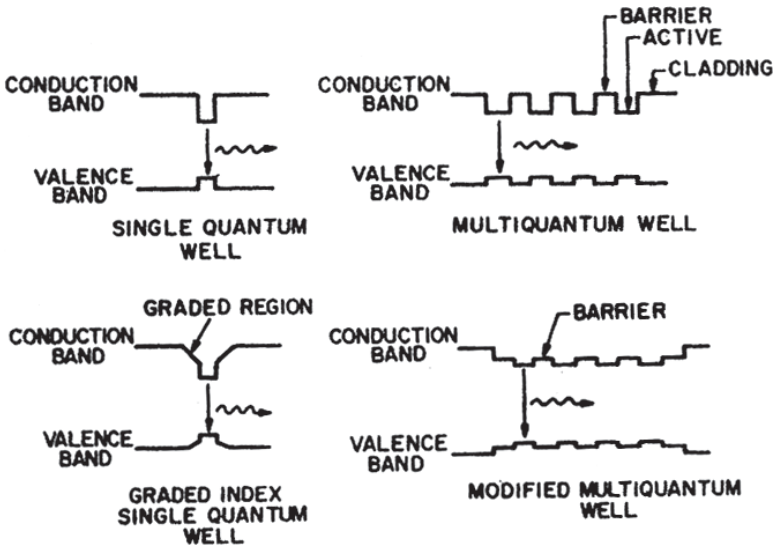

Fig. 3.4.2. Various types of quantum well amplifier active region design.

where n_a, n_c are indices of the cladding and active region, λ_0 is the free space wavelength and d is the thickness of the single quantum well.

For a MQW active region, the confinement factor can be calculated by solving the wave equation in a multi-layer waveguide consisting of the active, the barrier and the cladding layers. The procedure is quite complicated due to the large number of layers involved. The following formula gives reasonably accurate results

$$\Gamma(MQW) = \gamma \frac{N_a d_a}{N_a d_a + N_b d_b}, \tag{3.4.5}$$

with

$$\gamma = 2\pi^2 (N_a d_a + N_b d_b) \frac{\bar{n}^2 - n_c^2}{\lambda_0^2}, \tag{3.4.6}$$

$$\bar{n} = \frac{N_a d_a n_a + N_b d_b n_b}{N_a d_a + N_b d_b}, \tag{3.4.7}$$

where N_a, N_b are the number of active and barrier layers in the MQW structure and d_a, d_b are the thickness of the active and barrier layers, n_a, n_b, n_c are the refractive indices of the active, barrier, and,

cladding layer respectively. The quantity $\bar{n}$ can be interpreted as the effective index of the MQW region (consisting of all the active layers and barrier layers) and γ is the confinement factor in this layer of index $\bar{n}$. The confinement factor Γ of the active region is obtained by multiplying γ by the ratio of the active region thickness to the total thickness of the MQW region.

3.4.2. *Optical gain and auger recombination*

In a quantum well structure the kinetic energy of the electrons and holes for motion normal to the well (z-direction) is quantized into discrete energy levels. Each of these discrete levels form a set of two-dimensional subbands. This modifies the density of states from the regular three dimensional case. Using the principle of box quantization for kinetic energies in the x and y direction, the number of electrons per unit area in the x-y plane for the ith subband within an energy interval dE is given by

$$D_i(E)dE = 2\frac{d^2\vec{k}}{(2\pi)^2}, \tag{3.4.8}$$

where the factor 2 arises from two spin states and $\vec{k} = (k_x, k_y)$ is the momentum vector. Using the parabolic approximation, namely $E = \frac{\hbar^2 k^2}{2m_{ci}}$ and the relation $d^2\vec{k}k = 2\pi k dk$,

$$D_i = \frac{m_{ci}}{\pi\hbar^2}, \tag{3.4.9}$$

where m_{ci} is the effective mass of the electron in the i^{th} subband of the conduction band. Thus the density of states per unit volume g_{ci} is given by

$$g_{ci} = \frac{D_i}{L_z} = \frac{m_{ci}}{\pi\hbar^2 L_z}. \tag{3.4.10}$$

A similar equation holds for the valence band. The density of states for regular three dimensional case can be similarly obtained. It is given by $\rho_c(E)$ where

$$\rho_c(E) = 4\pi\left(\frac{2m_c}{\hbar^2}\right)^{3/2} E^{1/2}. \tag{3.4.11}$$

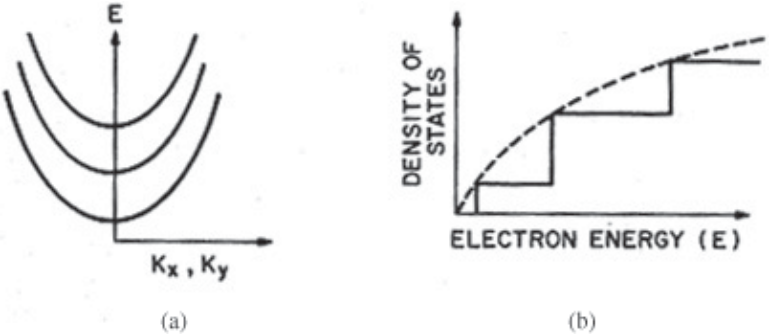

Fig. 3.4.3. (a) Schematic representation of two-dimensional parabolic subbands (b) The density of states in QW (solid line) and that for thick double heterostructures (dashed line).

The main difference between the optical gain of a quantum well structure and regular double heterostructure structures arises from the difference between the density of states in the two cases. For a QW structure the density of states in a subband does not depend on energy of the electron and that for a regular double heterostructure (thick active region) it varies with energy E of the electron as $E^{1/2}$. This is sketched in Fig. 3.4.3. This modification in the density of states can significantly alter the recombination rates in a QW structure compared to that for regular double heterostructure (DH) with thick active regions.

The expression for optical absorption or gain is given by Eq. (3.2.9). For gain, the simplistic view is that the number of electrons in the conduction band at a certain energy must be sufficiently high. The number of electrons at a given energy is the product of the density of states and Fermi factor. The latter represents the occupancy probability of an electron of a certain energy. The Fermi factor at room temperature approximately has the dependence on energy E of the electron as exp $(-E/kT)$. The density of states for both QW and regular DH, the Fermi factors and the product of the two are sketched in Fig. 3.4.4.

For a regular DH, the density of states is small for energies where the Fermi factor is large whereas for QW the density of states is large where the Fermi factor is large. This results in high gain at the

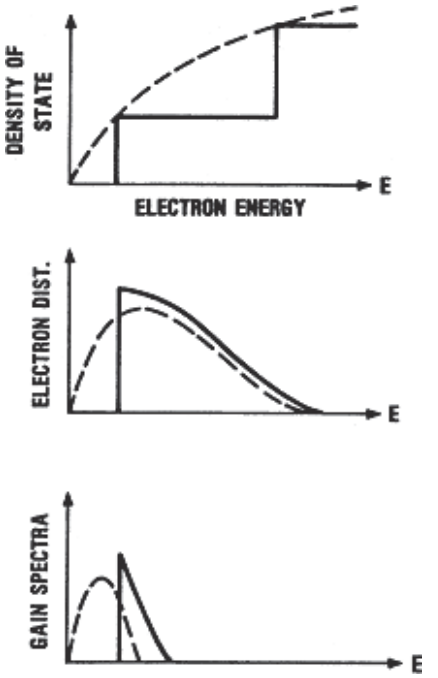

Fig. 3.4.4. The density of states, the electron distribution (product of density of states and Fermi Factor), and gain spectrum are plotted for both QW (solid lines) and regular DH (dashed lines) structure.

bottom of the band for a QW whereas for a DH the conduction band must be filled with electrons up to a certain energy level for sufficient optical gain.

The QW structure as a result has high gain at low currents compared to a regular DH.

In the simplified gain model just discussed, the spectral broadening effects and effects resulting from the anisotropy of quantum well have been ignored. The gain spectrum and the spontaneous emission spectrum exhibit unrealistic sharp edges as a result of the step like density of states a quantum well (Fig. 3.4.5).

The spectral broadening results mostly from intraband carrier relaxation due to scattering [45,46]. These include carrier-carrier, carrier-phonon and carrier-impurity scattering. The energy broadening due to intraband scattering δE is much larger than that due

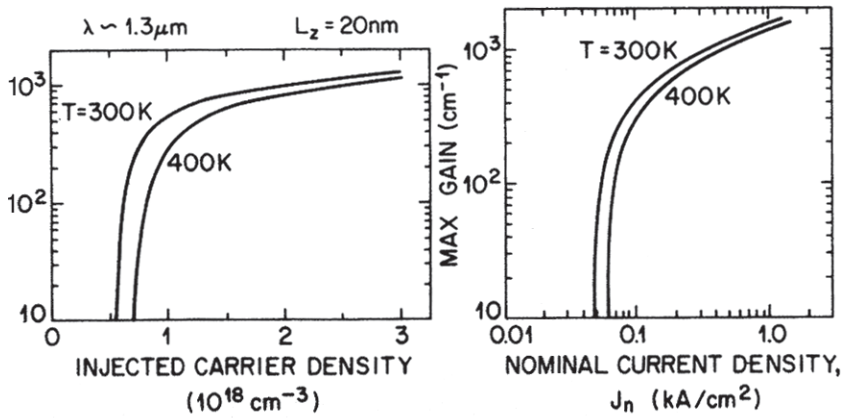

(a) (b)

Fig. 3.4.5. The calculated maximum gain as a function of injected carrier density and nominal current density at two temperatures for a 1.3 μm InGaAsP/InP quantum well structure.

to radiative transitions. This is due to vastly different lifetimes. The radiative recombination lifetime $\tau_r \sim$ 1-2 ns and the intraband scattering time is $\tau_{\text{in}} \sim 0.1$ to 1 ps. The quantity δE is related to the lifetime by the uncertainty principle

$$\delta E = \hbar/\tau_{in}. \tag{3.4.12}$$

Without broadening, the number of electrons per unit energy and per unit volume ($n(E)$) with energies between E and $E + dE$ is

$$n(E) = \rho(E) f_c(E) \tag{3.4.13}$$

where $\rho(E)$ is the density of states and $f_c(E)$ is the Fermi factor. With broadening the above equation changes to

$$n(E) = \rho(E) f_c(E) L\,(E - E1), \tag{3.4.14}$$

where

$$L(E - E_1) = \frac{\delta E}{2\pi} \frac{1}{(E - E_1)^2 + \left(\frac{\delta E}{2}\right)^2}, \tag{3.4.15}$$

is the normalized Lorentzian function which is valid for $\delta E \ll E$ and $\delta E = \hbar/\tau_{in}$

For the broad energy distribution of carriers, the unbroadened gain function ($g_u(E)$) and the spontaneous emission function ($R_{sp,u}(E)$) is integrated with the Lorentzian broadening factor to obtain the gain spectrum and the spontaneous emission spectrum.

$$g(E) = \int_{-\infty}^{\infty} g_u(E')\, L(E - E')dE', \tag{3.4.16}$$

$$R_{sp}(E) = \int_{-\infty}^{\infty} R_{sp,u} L(E - E')dE'. \tag{3.4.17}$$

The planar symmetry of the electronic wavefunction in a QW structure results in a polarization dependence of the optical transitions. A modification of the transition matrix elements takes place resulting in a difference for the dipole transition matrix elements for the e-lh (electron-light hole) and e-hh (electron-heavy hole) transitions. The e-lh transition is shifted to higher energy from that of the e-hh transition due to the lower effective mass of the light holes. Light polarized in the plane of the QW (TE mode in a waveguide) experiences higher gain than that for the light polarized perpendicular to the plane of the well (TM mode).

A TE mode gain spectrum calculated using the more complete model is compared with the spectrum calculated using the simple model in Fig. 3.4.6 under the same injection. The peak of the gain spectrum is reduced by broadening. However, the enhancement of the TE mode transition matrix element compensates for the decrease in gain due to broadening. The maximum TE gain as a function of injected carrier density is plotted in Fig. 3.4.7 for the simplified model and for the more accurate model.

Similar calculations have been reported for the InGaAsP material system. The radiative recombination rate in a QW structure taking into account transition between all subbands (in the Γ valley) as well as the filling of the L valleys has been calculated [47]. Figure 3.4.8 shows the dependence of gain on well thickness for different injected carrier densities. The modulation in the maximum gain is due to the recombination of electrons in the various subbands in the conduction band and heavy and light holes in the valence band. The steep decrease in gain for small well thickness is due to the distribution of

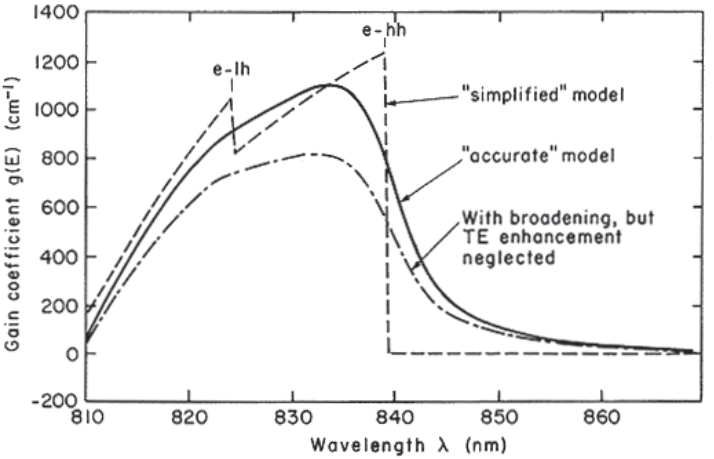

Fig. 3.4.6. Quantum well gain spectrum at $N = 3.04 \times 10^{18} cm^{-3}$ injected carrier density. The intraband scattering time is 0.1 ps. The material is GaAs QW between AlGaAs barrier layers [46].

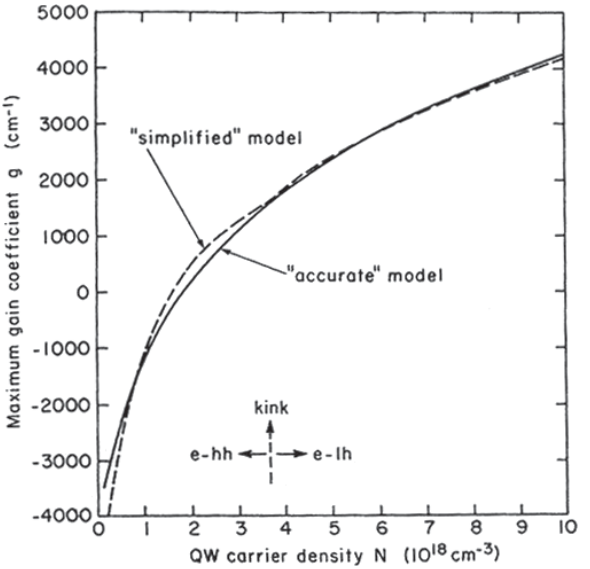

Fig. 3.4.7. The calculated maximum gain as a function of injected carrier density for the simplified model and the accurate model for the $n = 1$ quantum well transition i.e. transition from the lowest conduction band level. The intraband scattering time is 0.1 ps. The material is GaAs QW between AlGaAs barrier layers [46].

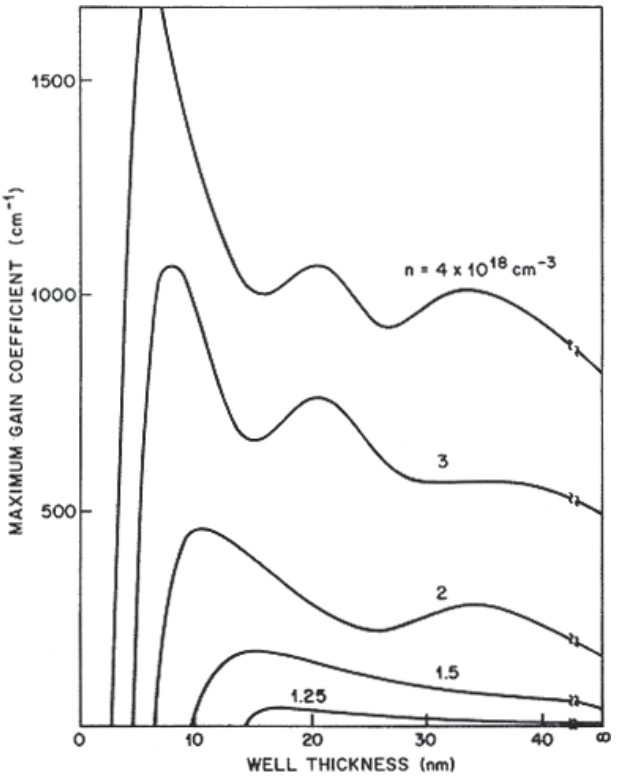

Fig. 3.4.8. Maximum gain for a undoped InGaAs/InP ($\lambda \sim 1.07\,\mu$m) quantum well as a function of well thickness for several carrier densities [47].

carriers in the L valley which reduces the number of carriers in the Γ valley.

Nonradiative Auger recombination of an electron-hole pair, as the name implies, is characterized by the absence of an emitted photon in the recombination process. As in the case of bulk semiconductors, there are several types of Auger recombination processes. The three major types are band-to-band Auger process, phonon-assisted Auger process, and trap-assisted Auger processes. The band-to-band Auger processes in direct gap quantum well semiconductors are shown in Fig. 3.4.9. The three processes are labeled CCCH, CHHS, and CHHL, where C stands for the conduction band and H, L, S stand for heavy-hole, light-hole, and split-off valence band hole, respectively.

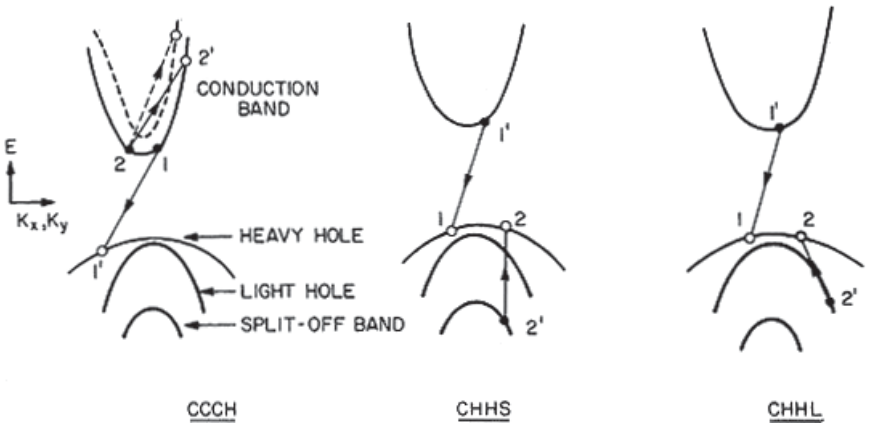

Fig. 3.4.9. Band-to-band Auger processes in a quantum well semiconductor.

The CCCH mechanism involves three electrons and a heavy hole and is dominant in n-type material. The CHHS process is dominant in p-type material. Under high injection conditions present in lasers and amplifiers all three processes must the considered.

Similar to the case for regular double heterostructure (3-dimensional density of states) the Auger rate in QW structures is also expected to increase with increasing temperature and for low band gap materials. However, the Auger rate itself is different. In the absence of momentum conservation, there is no threshold energy (Sec. 3.3.1). Thus the strong temperature dependence does not appear if the individual particle states are not states of definite momentum, for example, if they are trap states, or if momentum conservation is satisfied through phonon assistance. The energy vs. wave vector diagram of phonons illustrate that they can carry considerable amount of momentum for a very small energy.

The Auger recombination rate for quantum well structures have been calculated [47–50]. The calculated Auger lifetime τ_A for a InGaAsP QW material as a function of well thickness for several injected carrier densities is shown in Fig. 3.4.10. The undulations in the vicinity of well thickness of $\sim$10 nm is due to the filling of the higher order subbands with increasing n. The value of the Auger

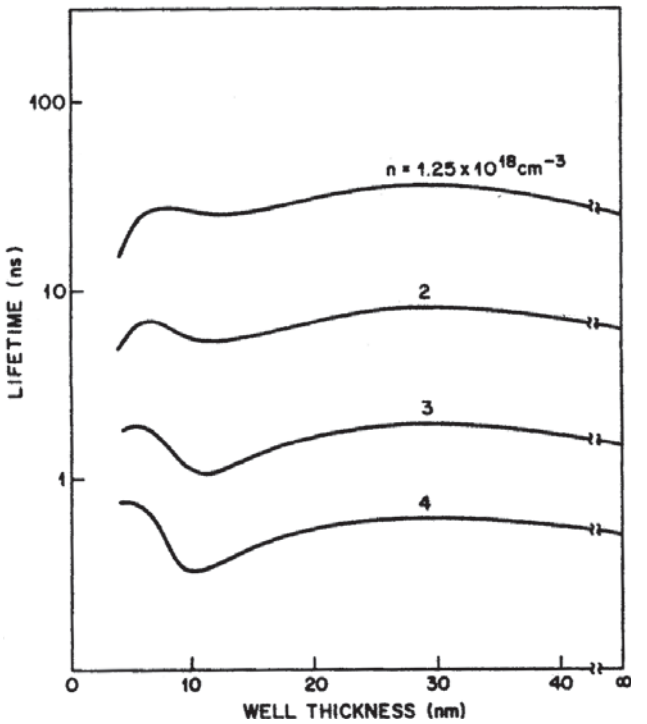

Fig. 3.4.10. Nonradiative Auger lifetime as as a function of well thickness for several carrier density values for $\lambda \sim 1.07\,\mu$m InGaAsP [47].

coefficient, C, can be estimated from Fig. 3.4.10 using the equation

$$R_A = n/\tau_A \tag{3.4.18}$$

For a well thickness of 30 nm, $\mathrm{n} = 2 \times 10^{18}\,\mathrm{cm}^{-3}$ (typical values), $\mathrm{C} \sim\ 2.5 \times 10^{-29}\,\mathrm{cm}^{-6}\mathrm{s}^{-1}$ from Fig. 3.4.9. It should be noted that due to various uncertainties in the matrix elements and effective masses only order of magnitude estimates of the Auger rate is feasible. Phonon assisted Auger recombination rates for quantum well structures has also been investigated. The Auger processes can be represented by transitions described previously for regular double heterostructures. As expected, the phonon assisted Auger rates dominate at low temperatures and band-to-band Auger rates are larger at high temperatures. Trap assisted Auger processes are also feasible for QW structures.

3.4.3. *Strained quantum well amplifiers*

Quantum-well amplifiers have also been fabricated using an active layer whose lattice constant differs slightly from that of the substrate and cladding layers. Such materials are known as strained quantum-wells. Over the last few years, strained quantum-well materials have been extensively investigated [51–63]. For lasers, they show many desirable properties such as: (i) a very low threshold current density and (ii) a lower linewidth than regular quantum well lasers both under CW operation and under modulation. Amplifiers using strained quantum well materials also show high gain (Fig. 3.4.11). The origin of the improved device performance lies in the band-structure changes induced by the mismatch-induced strain [60–63]. Strain splits the heavy-hole and the light-hole valence bands at the Γ point of the Brillouin zone where the band gap is minimum in direct band gap semiconductors.

Superlattice structures of InGaAs/InGaAsP with tensile and compressive stress have been grown by both MOCVD and CBE growth techniques over an n-type InP substrate. The broad-area threshold current density for the compressively strained MQW structure is found to be lower than that for the lattice-matched MQW structure.

Buried-heterostructure (BH) lasers have been fabricated using compressive and tensile strained MQW lasers. Lasers with compressive strain have a lower threshold current than that for lasers with tensile strain. This can be explained by splitting of the light hole and heavy hole bands under stress [60–63]. Detailed discussion on quantum well band structure under stress can be found in Ref. [64].

3.5. Gain in Quantum Wire (QWR) and Quantum Dot (QD) Structures

The electron motion is restricted further in quantum wire and quantum dot structures compared to that for a quantum well [65–69]. For QWR structures the electron motion is restricted in two directions and in QD structures the electron motion is restricted in all directions. Using the similar procedure the density of states of QWR and

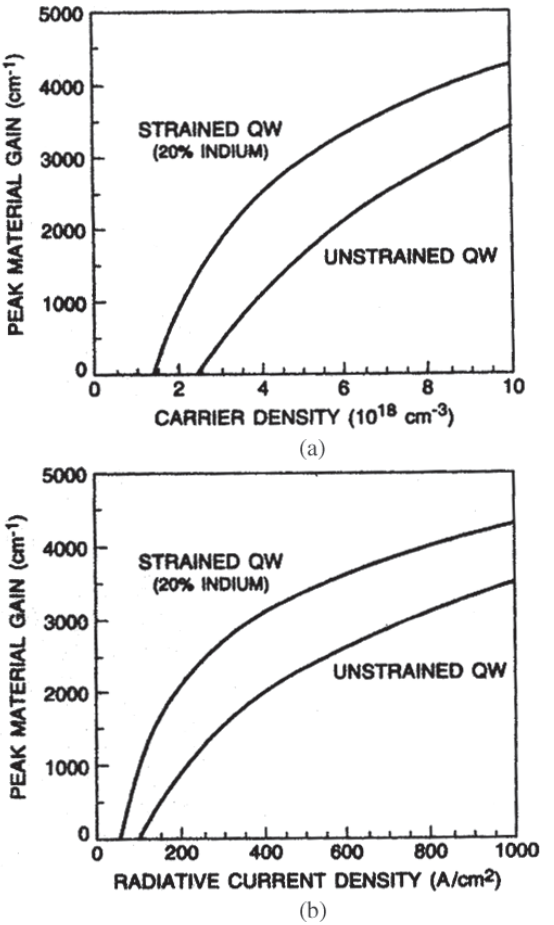

Fig. 3.4.11. Optical gain calculated as a function of injected carrier density (top) and radiative current density (bottom) for strained and unstrained quantum well laser [61].

QD structures are given by [65]

$$\rho_{QWR} = \sum_n \sum_m \frac{1}{2\pi} \left(\frac{2m}{\hbar^2} \right)^{1/2} n_{QWR} (E - E_{n,m})^{1/2}, \qquad (3.5.1)$$

$$\rho_{QD} = \sum_n \sum_m \sum_l 2 n_{QD} \delta (E - E_{n,m,l}), \qquad (3.5.2)$$

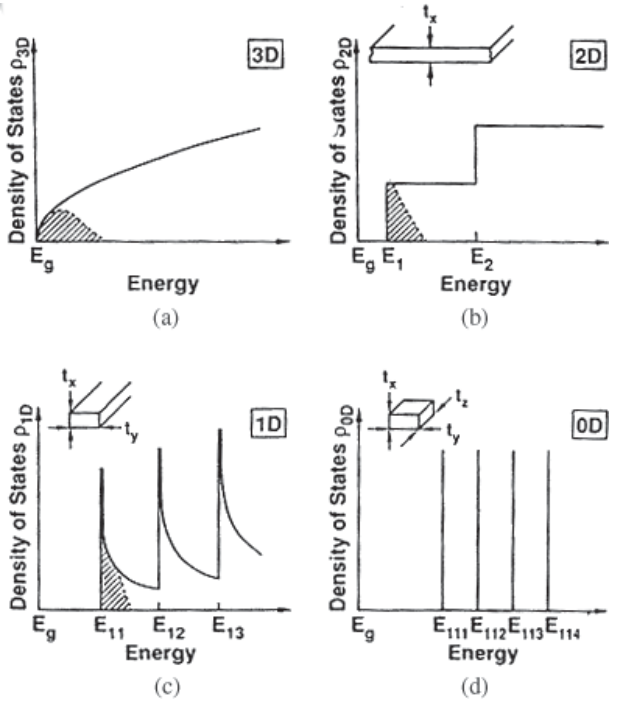

Fig. 3.5.1. Schematic description of the density of states for regular bulk semiconductor, quantum well (QW), quantum wire (QWR) and quantum dot (QD) structures. The dimensionalities of each of these types are: Bulk (3D), QW (2D), QWR (1D), QD (0D) [65].

where n_{QWR} (cm^{-1}) and n_{QD} (cm^{-2}) are the density of quantum wires and quantum dot respectively and the summation is over the discrete energy levels. The density of states for regular bulk materials, QW, QWR and QD material are sketched in Fig. 3.5.1. For QWR the density of states has sharp maximum at the position of the each of the discrete energy states and for QD the density of states is large at only the discrete energy states.

As discussed previously for QW structures, the density of states for QWR and QD structures are not sharp in practice, they get broadened by the interband carrier relaxation time for QWR structures and for distribution of dot sizes and interaction with surrounding material for QD structures. The broadening for QWR structures

is given by a term similar to Eq. (3.4.15) i.e.

$$L(E - E_{n,m,l}) = \frac{\hbar}{2\pi\tau_{\text{in}}} \frac{1}{(E - E_{n,m,l})^2 + \left(\frac{\hbar}{2\tau_{\text{in}}}\right)^2}, \tag{3.5.3}$$

where τ_{in} the intraband relaxation time. The gain spectrum for QWR structures have been calculated. The calculated gain spectrum is shown in Fig. 3.5.2. The dimensions of the wire is $12\,\text{nm} \times 20\,\text{nm}$. In the QWR structure the discrete energy levels are labeled by (n,m) where the integers n,m correspond to discrete energy levels corresponding to energy quantization in the two orthogonal direction. The lowest energy state is labeled (0,0); (0,1) and (1,0) for the next two levels and so on. The quantity τ_{in}, the intraband relaxation time, is assumed to be 0.1 ps. Size fluctuations in QWR structure (i.e. fluctuation in QWR cross section) can significantly reduce the peak gain. In addition anisotropy of the dipole moment may play a role in the QWR observed gain. Gain anisotropy of $\sim$2 has been predicted for QWR of equal width and height i.e. gain for light polarized along the wire is larger by a factor of $\sim$2 [70].

Semiconductor optical amplifier with quantum dot active region is described in detail in Ch. 11. A few important features are discussed here. QDs fabricated by self assembly (described in Ch. 4) generally show a fluctuation in size which results in an energy distribution of the discrete energy states in an array of QDs. This, in effect, results in a broadening of the density of states in an array of QDs. The QDs are formed from a wetting layer by the self assembly process and the entire assembly is immersed in a cladding layer matrix. Additional broadening of the discrete energy states takes place due to its interaction with the states in the wetting layer and in the surrounding matrix.

The density of states in a QD array is characterized by a set of subbands that result from the inhomogeneously broadened quantum levels of the ground and excited states of each QD. These subbands can overlap depending on the size distribution of the dots. The density of states of a self assembled QD array is schematically shown in

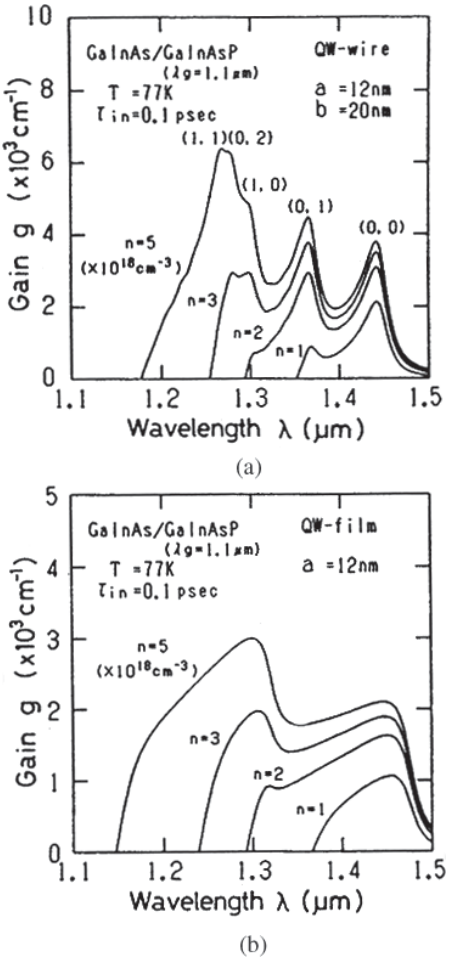

Fig. 3.5.2. Calculated gain spectrum at 77 K for InGaAsP/InGaAs quantum wires for various values of carrier density n. For comparison, the calculated gain spectrum of a InGaAsP/InGaAs quantum well is also shown. The same value of intraband relaxation time (0.1 ps) is used in both calculations [65,71].

Fig. 3.5.3. Both the ground state and the first subbands are broadened and at high energy they merge with the bands in the wetting layer.

For an ideal QD array, the energy width of the density of states is given by homogeneous broadening (Δ) which is $\sim$0.1 meV. This

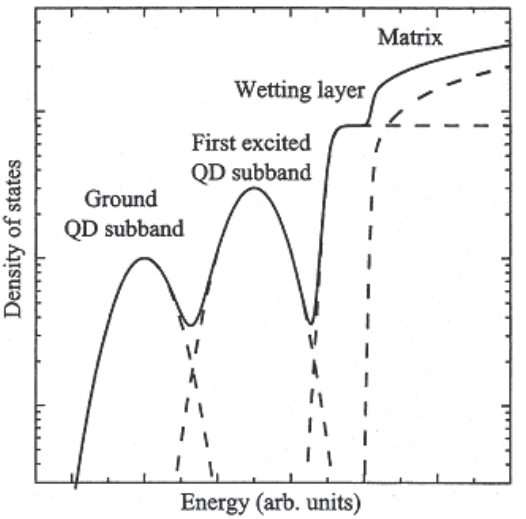

Fig. 3.5.3. Density of states of a self assembled QD array. The dashed lines represent the states of the ground and excited subbands, the wetting layer and the matrix [72].

homogeneous broadening is due to the interaction of the dot with the surrounding material. The saturated gain (G_s) of a QD array is proportional to

$$G_s \sim g n_{\mathrm{QD}}/\Delta, \tag{3.5.4}$$

where n_{QD} is the density of QDs and g is the degeneracy of the level. The current density needed for zero net gain (transparency) is proportional to $\mathrm{n_{QD}}$. Thus for high saturated gain, the current density needed for transparency is also high. In addition to the ground state level one or more excited state levels can be thermally populated. Since the excited states have a higher degeneracy, the saturated gain of the excited states is higher i.e. with increasing current the gain of the QD array would increase and its spectrum will shift to higher energies. A schematic representation of the gain for ideal and self assembled QD array is shown in Fig. 3.5.4. For self assembled array (non-ideal), the broadening factor (Δ) is higher and hence the transparency current density is higher and the saturated gain is lower.

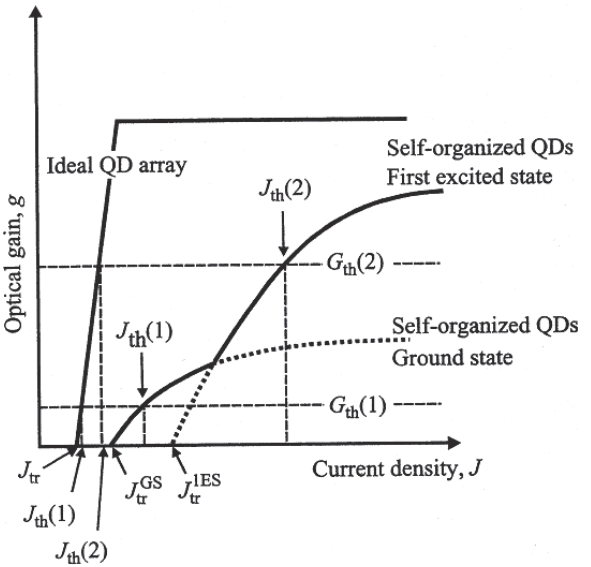

Fig. 3.5.4. Schematic representation of gain as a function of current density for an ideal QD array and for a non ideal (self assembled) QD array. The two $J_{\rm th}$ (1) shows the current needed for the same optical gain for the ideal and non-ideal case for the ground state transition. The $J_{\rm th}$ (2) shows the current needed for a certain optical gain for the non-ideal case for the first excited state transition [72].

The experimental results for InGaAs QD array in a AlGaAs matrix is shown in Fig. 3.5.5. The ground state lasing is observed at low current density when the lasers had low optical loss and excited state lasing is observed at high current densities when the lasers have high optical loss. The optical loss for a laser can be varied using facet coating.

The dependence of optical gain on modal G can be empirically fitted [73] to the following expression

$$G = G_s\{1 - \exp(-\gamma(J/J_{\rm tr} - 1)\},$$

which simplifies for low current density to

$$G = \gamma G_s(J/J_{\rm tr} - 1) \tag{3.5.5}$$

where G_s, $J_{\rm tr}$, J are the saturated gain, the transparency current density, and the injected current density respectively. The quantity

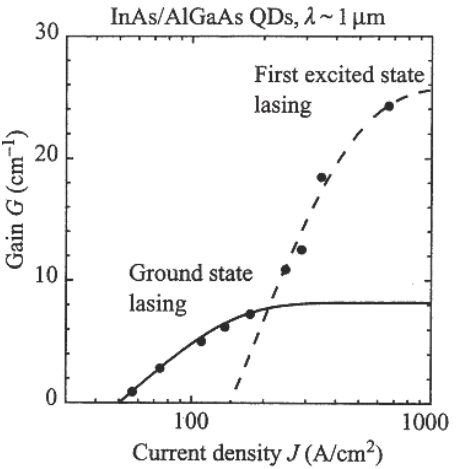

Fig. 3.5.5. Experimental relation between modal gain G and current density J [72].

γ is a parameter. The values of G_s, $J_{\rm tr}$, γ for the data shown in Fig. 3.5.5 are $8.2\,{\rm cm}^{-1}$, $50\,{\rm A/cm}^2$ and 0.9 respectively for the ground state and $25.8\,{\rm cm}^{-1}$, $145\,{\rm A/cm}^2$ and 0.8 respectively for the first excited state.

Theory of the signal amplification in a QD SOA has been developed [74–76]. The carriers are injected into the wetting layers from which it makes a fast transfer to the quantum dot. QD SOA has a fast gain and phase recovery which makes them suitable for high speed system applications. The primary reason for the faster response of QD SOA compared to that for SOA with regular active region is due to the presence of the wetting layer. The wetting layer serves as a carrier reservoir layer. Carriers depleted by the injected optical pulse in the QD ground state are replaced by fast carrier transfer from the wetting layer. The fabrication, design and performance of QD SOA are discussed in detail in Ch. 11.

References

[1] E. O. Kane, *J. Phys. Chem. Solids* **1**, 249 (1957).
[2] M. G. A. Bernard and G. Duraffourg, *Phys. Stat. Solidi.* **1**, 699 (1961).
[3] H. C. Casey, Jr. and M. B. Panish, *Heterostructure Lasers*, Part A, Chapter 3 (Academic, New York, 1978).

[4] G. P. Agrawal and N. K. Dutta, "*Semiconductor Lasers*" Van Nostrard Reinhold, NY, Chapter 3, 2nd edn. (1992).
[5] C. J. Hwang, *Phys. Rev. B*, **2**, 4117 (1970).
[6] F. Stern, *J. Appl. Phys.* **47**, 5382 (1976); *IEEE J. Quantum Electron.* **QE-9**, 290 (1973).
[7] N. K. Dutta, *J. Appl. Phys.* **51**, 6095 (1980); **52**, 55 (1981).
[8] N. K. Dutta and R. J. Nelson, *J. Appl. Phys.* **53**, 74 (1982).
[9] R. Olshansky, C. B. Su, J. Manning and W. Powaznik, *IEEE J. Quantum Electron.* **QE-20**, 838 (1984).
[10] A. R. Beattie and P. T. Landsberg, *Proc. R. Soc. London* **249**, 16 (1959); *Ser. A* **258**, 486 (1960).
[11] Y. Horikoshi and Y. Furukawa, *Jap. J. Appl. Phys.* **18**, 809 (1979).
[12] G. H. B. Thomson and G. D. Henshall, *Electron. Lett.* **16**, 42 (1980).
[13] N. K. Dutta and R. J. Nelson, (a) *Appl. Phys. Lett.* **38**, 407 (1981) (b) *J. Appl. Phys.* **53**, 74 (1982) and references therein.
[14] A. Sugimura, *IEEE J. Quantum Electron.* **QE-17**, 627 (1981).
[15] A. Haug, *Appl. Phys. Lett.* **42**, 512 (1983).
[16] A. R. Beattie and G. Smith, *Phys. Status Solidi.* **19**, 577 (1967).
[17] M. Takashima, *J. Appl. Phys.* **43**, 4114 (1972).
[18] M. Takashima, *J. Appl. Phys.* **44**, 4717 (1973).
[19] A. Sugimura, *J. Appl. Phys.* **51**, 4405 (1980).
[20] S. Brand and R. A. Abram, *J. Phys. C. Solid State Phys.* **17**, L201 (1984).
[21] M. G. Burt and C. Smith, *J. Phys. C. Solid State Phys.* **17**, L47 (1984).
[22] D. M. Eagles, *Proc. Phys. Soc. London* **78**, 204 (1961).
[23] W. Lochmann, *Phys. Status Solidi. A* **40**, 285 (1977).
[24] W. Lochmann, *Phys. Status Solidi. A* **42**, 181 (1977).
[25] J. Shah, R. F. Leheny, R. E. Nahory and H. Temkin, *Appl. Phys. Lett.* **39**, 618 (1981).
[26] B. Etienne, J. Shah, R. F. Leheny and R. E. Nahory, *Appl. Phys. Lett.* **41**, 1018 (1982).
[27] B. C. DeLoach, Jr., B. W. Hakki, R. L. Hartman and L. A-. D'Asaro, *Proc. IEEE* **61**, 1042 (1973).
[28] D. L. Rode, *J. Appl. Phys.* **45**, 3887 (1974).
[29] A. R. Goodwin, J. R. Peters, M. Pion, G. H. B. Thompson and J. E. A. Whiteaway, *J. Appl. Phys.* **46**, 3126 (1975).
[30] H. C. Casey, Jr., *J. Appl. Phys.* **46**, 49 (1978).
[31] P. J. Anthony and N. E. Schumaker, *IEEE Electron. Device Lett.* **EDL-1**, 58 (1980); *J. Appl. Phys.* **51**, 5038 (1980).
[32] M. Yano, H. Imai, K. I. Hori and M. Takusagawa, *IEEE J. Quantum Electron.* **QE-17**, 619 (1981).
[33] M. Yano, H. Imai and M. Takusagawa, *J. Appl. Phys.* **52**, 3172 (1981); *IEEE J. Quantum Electron.* **QE-17**, 1954 (1981).
[34] M. Yano, Y. Nishitani, K.-I. Hori and M. Takusagawa, *IEEE J. Quantum Electron.* **QE-19**, 1319 (1983).
[35] N. K. Dutta, *J. Appl. Phys.* **52**, 70 (1981).

[36] R. Dingle, W. Wiegman and C. H. Henry, *Phys. Rev. Lett.* **33**, 827 (1974).
[37] R. Dingle, *Festkorperprobleme* **XV**, 21 (1975).
[38] N. Holonyak Jr., R. M. Kolbas, R. D. Dupuis and P. D. Dapkus, *IEEE J. Quantum Electron.* **QE-16**, 170 (1980).
[39] K. Hess, B. A. Vojak, N. Holonyak, Jr., R. Chin and P. D. Dapkus, *Solid State Electron.* **23**, 585 (1980).
[40] N. K. Dutta, (a) *Electron. Lett.* **18**, 451 (1982) (b) *J. Appl. Phys.* **53**, 7211 (1982).
[41] Y. Arakawa and A. Yariv, *IEEE J. Quantum Electron.* **QE-21**, 1666 (1985).
[42] H. Temkin, N. K. Dutta, T. Tanbun-Ek, R. A. Logan and A. M. Sergent, *Appl. Phys. Lett.* **57**, 1610 (1990).
[43] C. Kazmierski, A. Ougazzaden, M. Blez, D. Robien, J. Landreau, B. Sermage, J. C. Bouley and A. Mirca, *IEEE J. Quantum Electron.* **27**, 1794 (1991).
[44] P. Morton, R. A. Logan, T. Tanbun-Ek, P. F. Sciortino, Jr., A. M. Sergent, R. K. Montgomery and B. T. Lee, *Electronic Lett.* **29**, 1429 (1993).
[45] M. Asada and Y. Suematsu, *IEEE, J. Quantum Electron.* **QE-21**, 434 (1985); M. Asada, *IEEE J. Quantum Electron.* **QE-25**, 2019 (1989).
[46] R. W. H. Engelmann, C. L. Shieh and C. Shu, Chapter 3, in *Quantum Well Lasers*, ed. by P. Zory (Academic Press, NY, 1993).
[47] A. Sugimura, *IEEE J. Quantum Electron.* **QE-19**, 932 (1983).
[48] N. K. Dutta, *J. Appl. Phys.* **54**, 1236 (1983).
[49] L. C. Chiu and A. Yariv, *IEEE J. Quantum Electron.* **QE-18**, 1406 (1982).
[50] C. Smith, R. A. Abram and M. G. Burt, *J. Phys. C,* **16**, L171 (1983).
[51] P. J. A. Thijs, L. F. Tiemeijer, P. I. Kuindersma, J. J. M. Binsma and T. van Dongen, *IEEE J. Quantum Electron.* **QE-27**, 1426 (1991).
[52] P. J. A. Thijs , L. F. Tiemeijer, J. J. M. Binsma and T. van Dongen, *IEEE, J. Quantum Electron.* **QE-30**, 477 (1994).
[53] H. Temkin, T. Tanbun-Ek and R. A. Logan, *Appl. Phys Lett.* **56**, 1210 (1990).
[54] W. T. Tsang, L. Yang, M. C. Wu, Y. K. Chen and A. M. Sergent, *Electron. Lett.* **26**, 2035 (1990).
[55] W. D. Laidig, Y. F. Lin and P. J. Caldwell, *J. Appl. Phys.* **57**, 33 (1985).
[56] S. E. Fischer, D. Fekete, G. B. Feak and J. M. Ballantyne, *Appl. Phys. Lett.* **50**, 714 (1987).
[57] N. Yokouchi, N. Yamanaka, N. Iwai, Y. Nakahira and A. Kasukawa, *IEEE J. Quantum Electron.* **QE-32**, 2148 (1996).
[58] K. J. Beernik, P. K. York and J. J. Coleman, *Appl. Phys. Lett.* **25**, 2582 (1989).
[59] H. Temkin, T. Tanbun-Ek, R. A. Logan, D. A. Coblentz and A. M. Sergent, *IEEE Photon. Technol. Lett.* **3**, 100 (1991).
[60] J. P. Loehr and J. Singh, *IEEE J. Quantum Electron.* **27**, 708 (1991).
[61] S. W. Corzine, R. Yan and L. A. Coldren, Chapter 1, in *Quantum Well Lasers*, ed. by P. Zory (Academic Press, NY, 1993).
[62] A. R. Adams, *Electron. Lett.* **22**, 249 (1986).
[63] E. Yablonovitch and E. O. Kane, *J. Lightwave Technol.* **LT-4**, 50 (1986).
[64] J. Loehr, *Physics of Strained Quantum Well Lasers* (Springer Verlag, 1997).

[65] E. Kapon, Chapter 10, in *Quantum Well Lasers*, ed. by P. Zory (Academic Press, NY, 1993).
[66] Y. Arakawa and H. Sasaki, *Appl. Phys. Lett.* **40**, 939 (1982).
[67] M. Asada, Y. Miyamoto and Y. Suematsu, *IEEE J. Quantum Electron.* **QE-22**, 1915 (1986).
[68] A. Yariv, *Appl. Phys. Lett.* **53**, 1033 (1988).
[69] Y. Miyamoto, Y. Miyake, M. Asada and Y. Suematsu, *IEEE J. Quantum Electron.* **QE-25**, 2001 (1989).
[70] M. Asada, Y. Miyamoto and Y. Suematsu, Japan *J. Appl. Phys.* **L95**, 24 (1985).
[71] M. Cao, Y. Miyake, S. Tamura, H. Hirayama, S. Arai, Y. Suematsu and Y. Miyamoto, *Trans. IEICE* **E73**, 63 (1990).
[72] V. M. Ustinov, A. E. Zhukov, A. Yu. Egorov and N. A. Maleev, *Quantum Dot Lasers* (Oxford University Press, 2003).
[73] A. E. Zhukov, A. R. Kovsh, A. Yu. Egorov, N. A. Maleev, V. M. Ustinov, B. V. Volovik and M. V. Maximov, *Semiconductors* **33**, 153 (1999).
[74] M. Sugawara, T. Akiyama, N. Hatori, Y. Nakata, H. Ebe and H. Ishikawa, *Meas. Sci. Technol.* **13**, 1683 (2002).
[75] M. Sugawara, H. Ebe, N. Hatori, M. Ishida, Y. Arakawa, T. Akiyama, K. Otsubo and Y. Nakata, *Phys. Rev. B.* **69**, Art No. 235332 (2004).
[76] H. Sun, Q. Wang, H. Dong and N. K. Dutta, *Optics Express* **13**, 1892 (2005).

Chapter 4

Epitaxial Growth and Amplifier Designs

4.1. Introduction

The lattice matched crystalline growth of one semiconductor over another is called epitaxy. The development of epitaxial growth techniques has been of major significance for the development of semiconductor photonic devices such as lasers, amplifiers, and, photodetectors. The commonly used techniques for epitaxial growth are liquid phase epitaxy (LPE) [1], vapor-phase epitaxy (VPE) [2], molecular beam epitaxy (MBE) [3], and metal organic chemical vapor deposition (MOCVD) [4].

In LPE, the epitaxial layer is grown by cooling a saturated solution of the composition of the layer to be grown while that solution is in contact with substrate. In VPE, the epitaxial layer is grown by the reaction of gaseous elements or compounds at the surface of a heated substrate. The VPE technique has also been called chemical vapor deposition (CVD) depending on the constituents of the reactants. A variant of the technique is metal-organic chemical vapor deposition (MOCVD) [4], which has been very successful for lasers in which metal alkyls are used as the compound source. In MBE, the epitaxial layer growth is achieved by the reaction of atomic or molecular beams of the constituent elements (of the layer to be grown) with a crystalline substrate held at high temperature in ultrahigh vacuum.

In this chapter, the epitaxial growth techniques used for the fabrication of amplifiers is described. Transverse optical confinement of the guided light is also important for high performance amplifiers. Various current confinement and optical confinement schemes as it

relates to semiconductor optical amplifier design are discussed. For further details please also see Ref. [5–7].

4.2. Material Systems

Extensive work on optical amplifiers were carried out in the 1980s using the AlGaAs material system. These amplifiers had GaAs active region surrounded by p-$Al_{1-x}Ga_xAs$ and n-$Al_{1-x}Ga_xAs$ cladding layers. Much of the recent experimental work on semiconductor optical amplifiers have been carried out using the $In_{1-x}Ga_xAs_yP_{1-y}$ material system with the optical gain centered around 1.3 μm or 1.55 μm. The 1.3 μm and 1.55 μm wavelength region are of interest for fiber optic communication. The discussion in this chapter is for the InGaAsP material system. Liquid phase epitaxy growth of AlGaAs/GaAs and InGaAsP/InP heterostructures were studied by several researchers in the 1960s and 1970s [8–30]. Much of this work enabled determination of material parameters.

The InGaAsP material can be grown lattice matched to InP for a range of compositions. The composition of the quaternary solid is determined by X-ray analysis. Figure 4.2.1 shows the measured

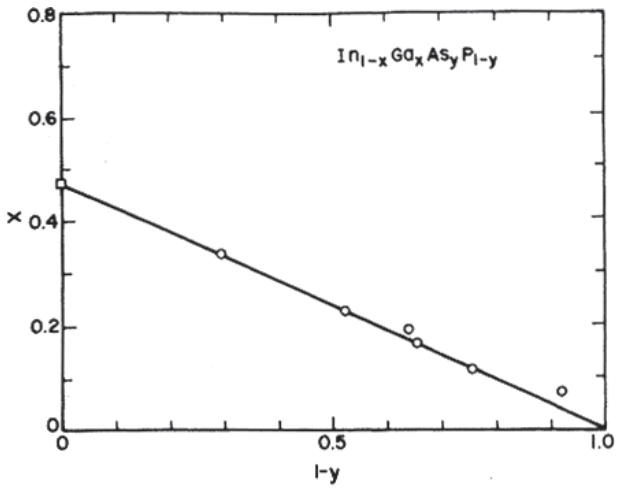

Fig. 4.2.1. Relationship between the mole fractions x and y of the quaternary material $In_{1-x}Ga_xAs_yP_{1-y}$ that is lattice matched to InP. The circles are experimental data and the line illustrates Vegard's law [29].

composition (open circles) of the quaternary solid lattice matched to InP. The solid line is the calculated result using Vegard's law according to which the lattice constant $a(x, y)$ of $In_{1-x}Ga_xAs_yP_{1-y}$ is given by

$$a(x,y) = xy\ a(\mathrm{GaAs}) + x(1-\mathrm{y})a(\mathrm{GaP}) + (1-\mathrm{x})y\ a(\mathrm{InAs}) + (1-x)(1-y)a(\mathrm{InP}), \tag{4.2.1}$$

where a(GaAs), a(GaP), a(InAs), a(InP) are the lattice constants of the binary semiconductors GaAs, GaP, InAs, InP respectively. Using $a(x, y) = \mathrm{a(InP)}$, Eq. (4.2.1) gives the following relationship between x and y for $In_{1-x}Ga_xAs_yP_{1-y}$ compositions lattice matched to InP.

$$x = 0.4526y/(1 - 0.031y) \quad \text{or} \quad x \sim 0.45\,y. \tag{4.2.2}$$

The direct band gap of $In_{1-x}Ga_xAs_yP_{1-y}$ grown lattice matched over InP has been measured using photoluminescence. In this technique, electrons and holes are created by photoexcitation in the conduction and valence bands respectively and when they recombine, light at energy corresponding to the band gap is emitted. Figure 4.2.2 shows the measured band gap as a function of arsenic mole fraction y. From the data the band gap (at 300 K) of $In_{1-x}Ga_xAs_yP_{1-y}$ lattice matched to InP can be represented by the following expression [30]

$$E_g\,(\text{in eV}) = 1.35 - 0.72y + 0.12y^2. \tag{4.2.3}$$

A knowledge of the refractive index as a function of composition of $In_{1-x}Ga_xAs_yP_{1-y}$ is important for understanding the waveguiding properties of InGaAsP/InP semiconductor heterostructures. The following analytic form is often used for the refractive index $n(y)$ of $In_{1-x}Ga_xAs_yP_{1-y}$ lattice matched to InP (for which $x \sim 0.45\,y$) at an wavelength corresponding to the band gap

$$n(y) = 3.4 + 0.256y - 0.095y^2. \tag{4.2.4}$$

Measurements of refractive index of $In_{1-x}Ga_xAs_yP_{1-y}$ lattice matched to InP has also been carried out. The results (shown in Fig. 4.2.3) show the refractive index for all compositions decreases with increasing wavelength.

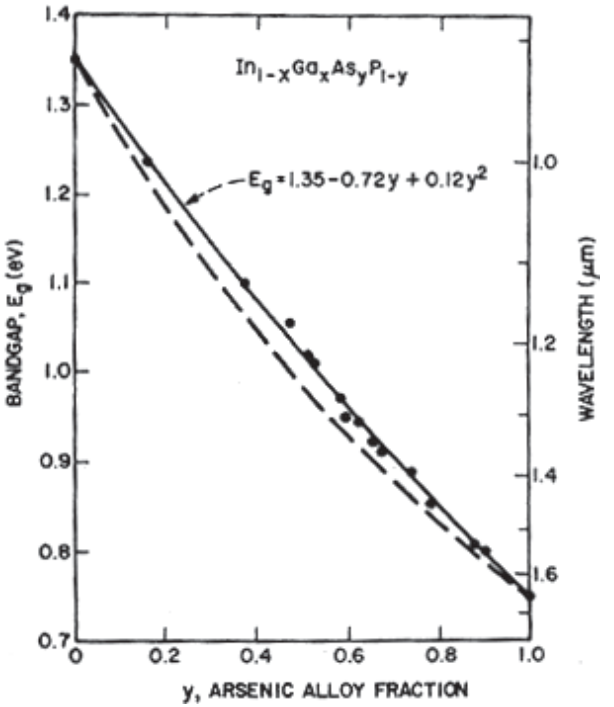

Fig. 4.2.2. Band gap of $In_{1-x}Ga_xAs_yP_{1-y}$ lattice matched to InP obtained from photoluminescence measurements. The solid line is a fit to the data points (solid circles) [30].

4.3. Epitaxial Growth Methods

This section describes briefly the various epitaxial growth techniques used to fabricate InGaAsP material. The most commonly used technique for growing a variety of semiconductors today is the metal organic chemical vapor deposition (MOCVD) growth technique.

4.3.1. *Liquid phase epitaxy*

The liquid phase epitaxy (LPE) technique has been used successfully to fabricate lasers, amplifiers, photodetectors, bipolar transistors, and field-effect transistors. It was first demonstrated in 1963 [1]. In LPE a supersaturated solution of the material to be grown is brought into contact with a single crystalline substrate for a short

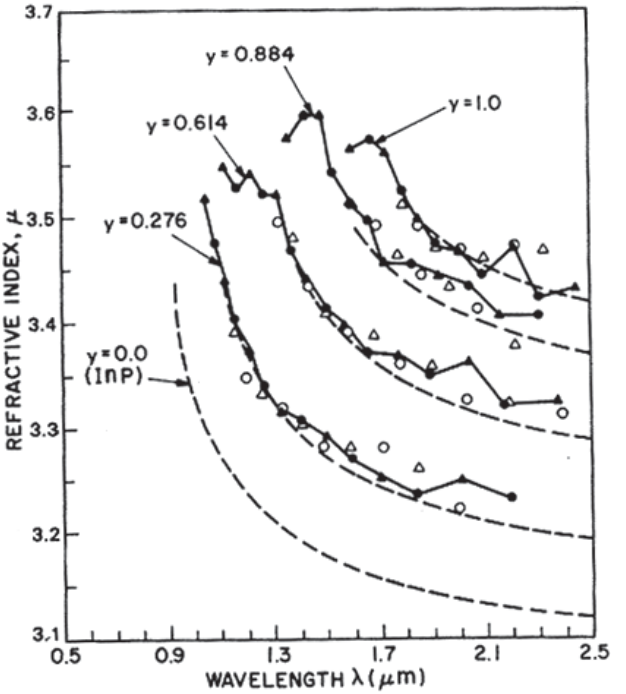

Fig. 4.2.3. Refractive index of $In_{1-x}Ga_xAs_yP_{1-y}$ as a function of wavelength for several As fractions y. Different symbols are for measurement on different samples [31].

duration [8–29]. If the material to be grown has the same lattice constant as the substrate, then some of this material precipitates on the substrate while maintaining the crystalline structure across the interface. The deposited material forms a lattice-matched epitaxial layer on the substrate.

LPE apparatus used for growing heterostructures must have the ability to perform successive growth of several epitaxial layers. A multi-bin apparatus used for growing double heterostructures is shown in Fig. 4.3.1. It consists of a furnace, a graphite "boat", a slider and several thermopcouples etc. The graphite boat has a number of reservoirs each of which contains a saturated solution of the corresponding epitaxial layer to be grown. The graphite boat is inside the furnace which is heated to the melting point ($\sim$650°C) of the material

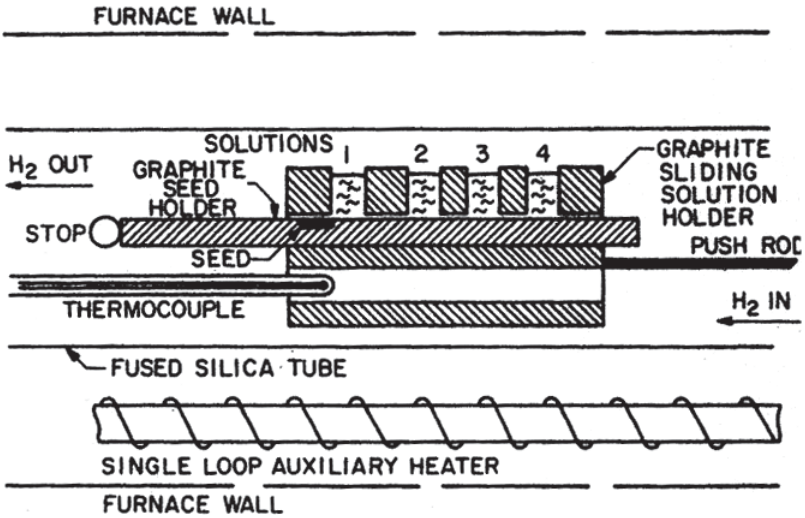

Fig. 4.3.1. Schematic diagram of a multi-bin LPE apparatus used for growing double heterostructures [32].

to be grown. The substrate (seed) is placed in a graphite slider that has a groove to hold the substrate. The slider is attached to a long rod that allows an operator to position the substrate under different reservoirs from outside the furnace. This allows growth of successive layers of desired thickness and composition on the substrate. Hydrogen or helium is generally used as an ambient gas during the growth process.

4.3.2. *Vapor phase epitaxy*

In vapor phase epitaxy (VPE) the source chemicals from which the layers are grown are gaseous. The technique has been used for the growth of several III–V compound semiconductors [33–41]. Chlorides or hydrides of the elements are often used as sources for the growth of the semiconductor. In the chloride method, $AsCl_3$ or PCl_3 is passed over elemental Ga or In to form chlorides. These metal chlorides then react with AsH_3 and PH_3 near the InP substrate to form epitaxial layers of InGaAsP on InP. The metal chlorides can also be formed by using GaAs or InP sources instead of elemental Ga or In.

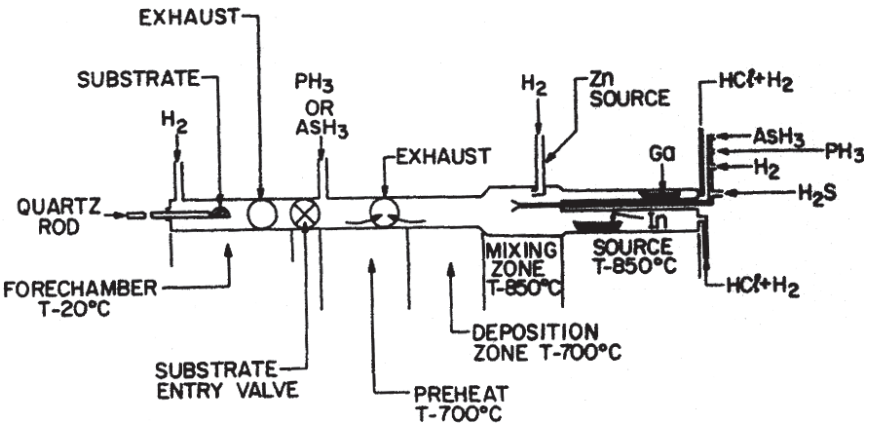

Fig. 4.3.2. Schematic illustration of a vapor phase epitaxy (VPE) reactor [33].

Figure 4.3.2 shows the schematic of a VPE reactor. The composition of the layers to be grown is changed by altering the flow rates of the reactants. *P*-type doping (Zn doped) is carried out by flowing H_2 over hot Zn metal which carries Zn into the reaction chamber and *n*-type doping (S doped) is done by flowing H_2S into the reaction chamber.

4.3.3. *Metal organic chemical vapor deposition*

Metal organic chemical vapor deposition (MOCVD), also known as metal organic vapor phase epitaxy (MOVPE) is a variant of the VPE technique that uses metal alkyls as sources from which epitaxial layers are formed [42–54]. The low pressure MOCVD technique where the gas pressure is ∼0.1 atm has been used for the growth of InGaAsP. MOCVD is a very versatile technique, it has been used to grow a wide variety of II–VI and III–V compound semiconductors.

Figure 4.3.3 shows the schematic of a low pressure MOCVD system. The quartz reaction chamber contains the InP substrate placed on a radio frequency (RF) heated (∼600°C) carbon susceptor. Group III alkyls ($Ga(C_2H_5)_3$ and $In(C_2H_5)_3$) and group V hydrides (AsH_3 and PH_3) are introduced into the reaction chamber. The gas flow near the substrate is laminar with velocities in the range of 1–15 cm/s for a pressure of ∼0.1 atm. At the hot substrate surface, the

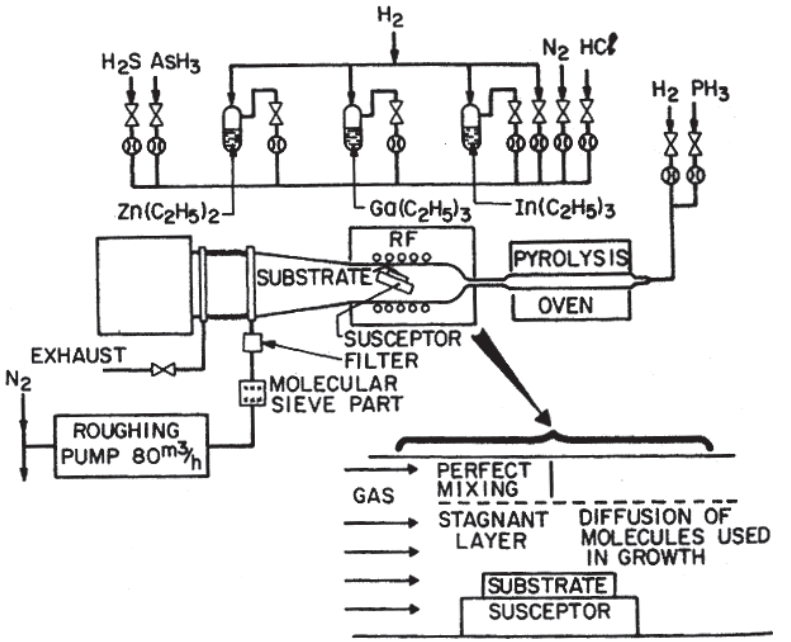

Fig. 4.3.3. Schematic illustration of a metal organic chemical vapor deposition (MOCVD) growth system [50].

metal alkyls and hydrides decompose, producing elemental In, Ga, As and P. The elemental species deposit on the surface forming an epitaxial layer. The gas flow rates are controlled to produce InGaAsP layers of different compositions. $Zn(C_2H_5)_3$ and H_2S are used as sources for p-type (Zn doped) and n-type (S doped) doping respectively.

4.3.4. *Molecular beam epitaxy*

In the molecular beam epitaxy (MBE) technique, epitaxial layers are grown by impinging atomic or molecular beams on a heated substrate kept in ultra high vacuum [55–60]. The constituents of the beam "stick" to the substrate resulting in a lattice matched layer. Since different elements have different sticking coefficients, the beam intensities are separately controlled to take into account the differences.

MBE technique was first used to make AlGaAs heterostructures (Fig. 4.3.4). The substrate is attached to a Mo (molebdenum) block

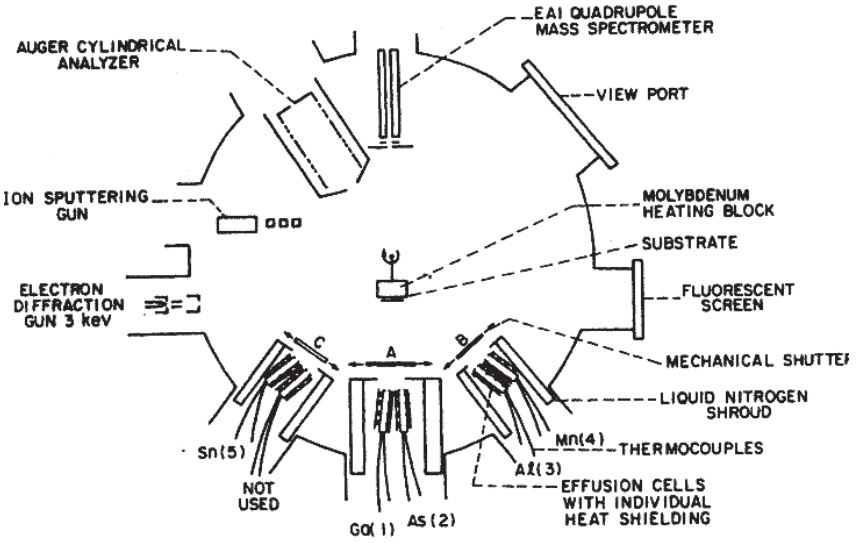

Fig. 4.3.4. Schematic illustration of a molecular beam epitaxy (MBE) growth chamber used for epitaxial growth of AlGaAs [58].

which is RF heated inside a vacuum chamber at a pressure of 10^{-7} to 10^{-10} torr. The electro-diffraction gun, the Auger analyzer, and the mass spectrometer can be used to study the layer characteristics during growth.

The sources Ga, Al, As etc. are kept in independently heated effusion cells enclosed in shrouds containing liquid nitrogen. The dopants also have separate effusion cells. The effusion cells are heated to high enough temperature to have adequate beam flux rate of the elements on the substrate. For the growth of GaAs on AlGaAs, the Ga flux is in the range of 10^{12} to 10^{14} atoms/(cm^2 s). The flux needed depends on the sticking coefficient. For many group III elements e.g. Al, Ga the sticking coefficient is near unity. However, the sticking coefficients differ significantly for group V elements.

Growth of high quality InGaAsP layer on InP by MBE has been demonstrated using gas sources for As_2 and P_2 beams. The As_2 and P_2 beams are generated by decomposing AsH_3 and PH_3 in a heated chamber and then allowing them to leak out to the MBE growth chamber. The decomposition chambers are operated at 900–1200°C and are filled to a pressure of ∼0.3 to 2 atm.

4.3.5. *Chemical beam epitaxy*

Chemical beam epitaxy (CBE) is a variant of MBE. In this technique all sources are gaseous and are derived from group III and group V alkyls. Schematic of a CBE system is shown in Fig. 4.3.5. The growth chamber is similar to a conventional MBE system.

It is kept at high vacuum ($<5\times10^{-4}$ torr). In and Ga are obtained by pyrolysis of either trimethylindium (TMIn) or troethylindium (TEIn) and trimethylgallium (TMGa) or troethylgallium (TEGa) at the heated surface of the substrate. The As_2 and P_2 beams are obtained by thermal decomposition of trimethylarsine (TMAs) and triethylphosphine (TEP) passing through a heated alumina tube at a temperature of 950–1200°C. The metal alkyls decompose on the heated surface leaving the metal to form epitaxial layer. The growth rate for MOCVD technique is diffusion limited (pressure ∼0.1 atm)

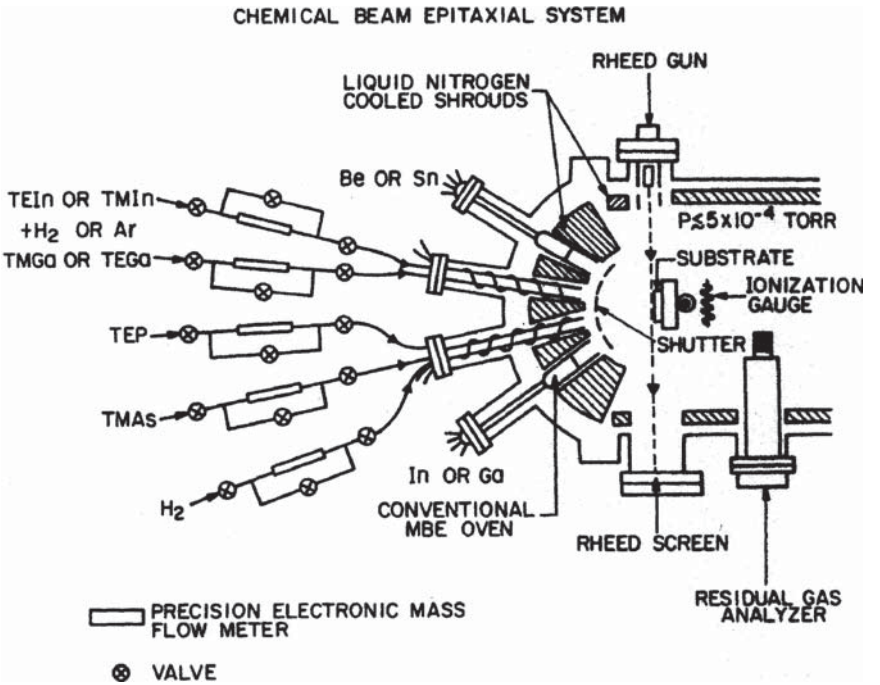

Fig. 4.3.5. Schematic illustration of a chemical beam epitaxy (CBE) growth chamber. It is similar to the MBE apparatus [61].

and that of the CBE technique is limited by the flow rate of metal alkyls (pressure $<5 \times 10^{-4}$ torr).

4.4. Strained Layer Epitaxy

Although lattice matching is important for growth of high quality epitaxial layers, it is possible to make high quality semiconductor heterostructures with a small degree of lattice mismatch among them [62–68]. This lattice mismatch introduces strain in the material, hence these are called strained layer heterostructures. The strain alters the band structure in a favorable way so as to produce higher gain than in the absence of strain. Typical values of tolerable strain ($\Delta a/a$ where a is the lattice constant of the substrate and Δa is the difference in lattice constant between the epitaxial layer and that of the substrate) are less than 1.5%. The larger the amount of strain, the thinner is the layer that can be grown free of dislocations on the substrate. Beyond a certain thickness, known as critical thickness, very large number of dislocations are generated. These dislocations reduce the luminescence property of the grown material.

InGaAsP layers have been grown on InP with both compressive and tensile strain. Generally, the grown heterostructures have very thin active region, they are often called strained quantum well (QW) active region. The light emission wavelength is in 1.2 μm to 1.6 μm range. The strained QW layers are grown by the MOCVD growth process. For the growth of $In_{1-x}Ga_x$ As layer on InP, the strain in the grown $In_{1-x}Ga_x$ As layer is achieved by simply changing the flow rate of the In source trimethylindium (TMIn). InGaAs composition of $In_{0.53}Ga_{0.47}As$ is lattice matched to InP. Figure 4.4.1 shows the In content (percent) in the solid InGaAs epitaxial layer grown over InP as a function of TMIn flow rate. The figure shows that by varying the flow rate of TMIn, InGaAs layers with In fraction less than 0.53 (tensile strain) and InGaAs layers with In fraction greater than 0.53 (compressive strain) can be grown.

Another well studied material system for strained layer epitaxial growth is $In_{1-x}Ga_x$ As grown over GaAs. This system is used to make lasers emitting near 980 nm and for quantum dot structures.

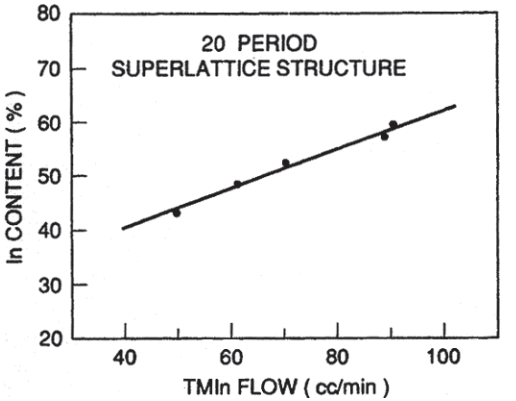

Fig. 4.4.1. In concentration in $In_{1-x}Ga_x$ As epitaxial layer grown over InP as a function of TMIn flow rate [62].

4.5. Selective Area Growth

The low pressure MOCVD based selective area growth (SAG) process [69–71] is very important for building low loss interconnection between active/active and active/passive regions. Such interconnections are needed for integrated chips consisting of many optical devices such as lasers, amplifiers, and, photodetectors. Many of these photonic integrated devices are discussed in Ch. 7. The key reason for using the SAG process is that it produces a smooth transition between materials of different composition. The SAG process development has been carried out for the InGaAsP/InP material system.

The fundamental concept in SAG is the following. Consider an InP substrate with prefabricated oxide (SiO_2) based masks deposited on it (Fig. 4.5.1). When such a substrate is put inside a MOCVD growth chamber, the growth precursors trimethylindium (TMIn), trimethylgallium (TMGa), arsenic (As) and phosphorus (P) are incident on the wafer.

However, they do not react to form the compounds on the oxide and hence must diffuse to the exposed regions for growth. Thus the exposed regions in between the oxide masks have more materials compared to regions further away from the oxide masks. This results in variation in composition and thickness of the material deposited near the oxide masks relative to that far from the masks. By a suitable

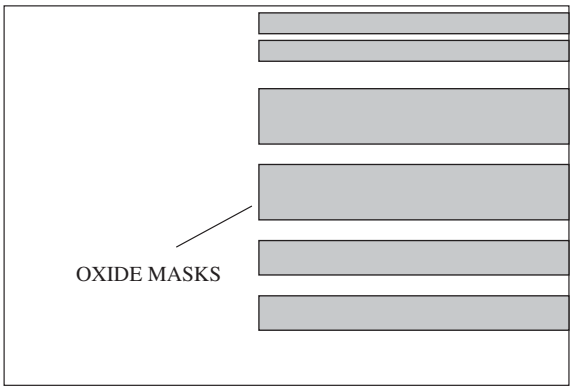

Fig. 4.5.1. Schematic of a wafer with oxide masks. The shaded regions represent masks of different widths.

design of the oxide masks it is then possible to deposit films of desired thickness, composition and strain selectively on different parts of the wafer. These films could then be active regions of different devices (e.g. laser, amplifiers and modulator) or they could form waveguides for interconnection. For laser-amplifier integrated device, the active region of the laser and the amplifier are grown in the same epitaxial growth but with the amplifier region grown between oxide masks so that the composition of the amplifier active region has lower band gap compared to that of the laser region. This is important since the amplifier gain shifts to shorter wavelength with increasing current. In addition, the laser area can be grown over a grating so that it emits at a specific wavelength determined by the periodicity of the grating. Similar SAG process is important for laser-modulator (electroabsorption) integrated device. The advantage of the SAG process is that both the amplifier and laser active regions are vertically self aligned. A set of SAG based devices and corresponding masks are shown schematically in Fig. 4.5.2. Figure 4.5.2(a) shows a laser-amplifier integrated device. Figure 4.5.2(d) shows a type of mask needed for the fabrication of an integrated laser and amplifier. Figure 4.5.2(b) shows the case of an expanded beam amplifier for low coupling losses to fibers. In this case, a waveguide is integrated with the amplifier output and input so that the mode at the facet is expanded for better coupling to optical fibers. For this adiabatic spot

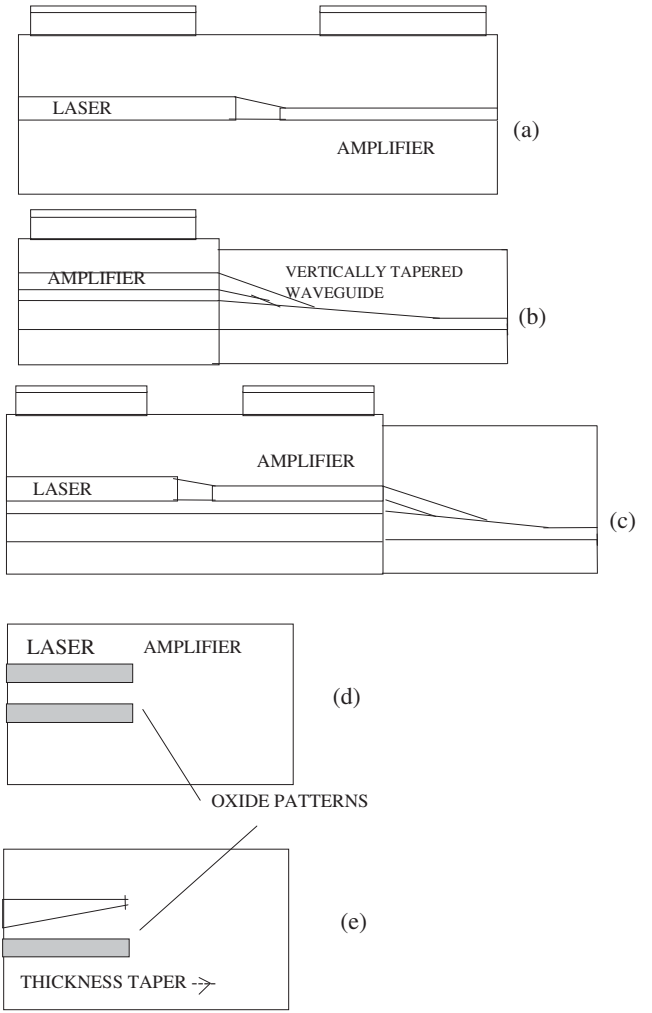

Fig. 4.5.2. (a) Laser-Amplifier integrated chip (b) Expanded beam amplifier for low coupling losses (c) Expanded beam laser-amplifier (d) Oxide mask for laser-amplifier, laser active region is fabricated between masks (e) Oxide mask for expanded beam amplifier.

size conversion (expansion) to take place the waveguide must change its thickness. Such a vertically tapered waveguide could be formed using a set of oxide masks whose separation varies with the distance. Figure 4.5.2(e) shows such a mask. The tapering in the lateral

direction could be carried by standard photolithography and etching techniques. Figure 4.5.2(c) shows the case of an expanded beam laser-amplifier integrated device with an expanded beam region.

4.5.1. *Model of SAG*

High performance integrated devices require precise control of composition and layer thickness. A model of the SAG process would be very useful in the design of oxide masks needed for selective growth in various parts of the wafer. Such a model should be able to predict the composition, thickness and strain of the grown layers for different oxide pattern configurations.

A modeling of the selective area growth process by solving the diffusion equation in conjunction with the reaction rate equation for various reacting species (TMIn, TMGa, As, P) has been developed [70, 71]. An iterative procedure using both analysis and experimental results is employed to determine the optimum conditions for materials growth that are applicable to various devices. The modeling is important for the design of masks for specific device fabrication. Figure 4.5.3 shows an example of the modeling results.

4.5.2. *Materials growth using SAG*

Semiconductor layer growth using the SAG process in a MOCVD reactor has been carried out for various types of integrated device fabrication. The various integrated devices are discussed in Ch. 7. For growth studies, a series of MQW layers with fixed lattice constant is grown over InP substrates with different SiO_2 mask patterns. The electroluminescence (EL) wavelength of the material grown between the masks is measured. Figure 4.5.4 shows the measured electroluminescence peak wavelength as a function of the width of the dielectric SiO_2 mask. By simply varying the width, the electroluminescence wavelength can be changed considerably. For the data shown in Fig. 4.5.4, the epitaxial growth was carried out at 650°C and at a reactor pressure of 80 mbar. TMIn, TMGa, AsH_3 and PH_3 were used as precursors.

Although the SAG process was initially developed for laser-electroabsorption modulator device fabrication, it is very important

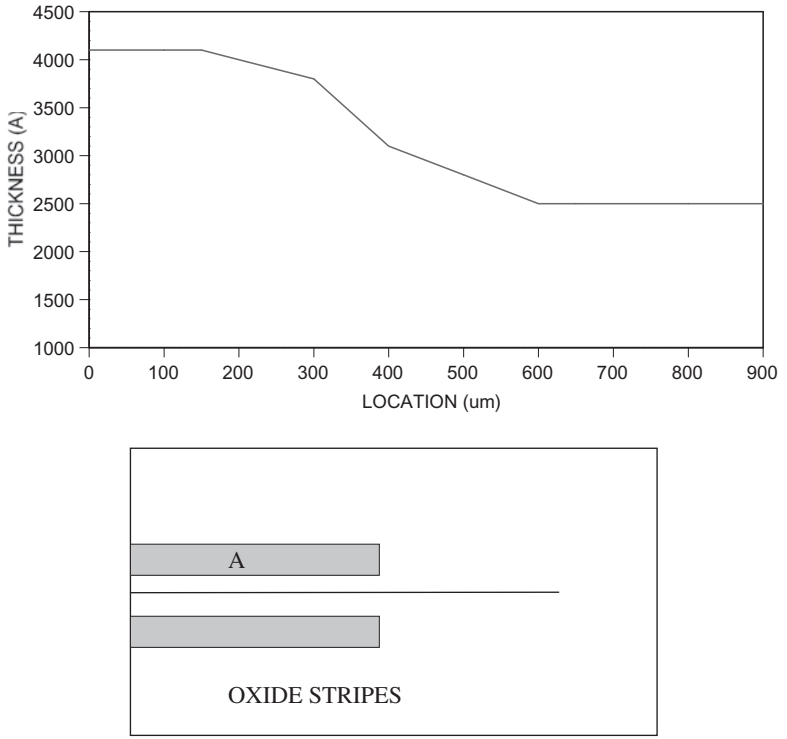

Fig. 4.5.3. Calculated variation in thickness of the grown layer as a function of distance from the pattern . The lower figure shows the geometry used in the calculation. The location refers to position along the line A. A location of $\sim$400 μm corresponds to the place where the masks end. The oxide masks are separated by 10 μm and have width of 10 μm.

for amplifiers with low coupling loss or in general for other amplifier based devices such as Mach-Zehnder modultors that also need to have low coupling losses. A major importance of SAG process for SOA based devices is for the fabrication of mode matched beam modifiers.

4.6. Amplifier Designs

It is important to design amplifiers that operate at low currents in a single transverse mode. Traveling wave amplifiers must have very low facet reflectivity. Amplifier designs for low reflectivity are discussed

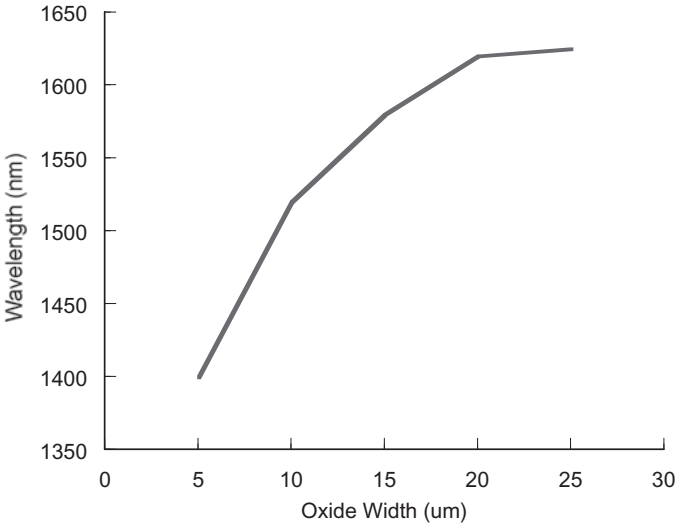

Fig. 4.5.4. Variation of electroluminescence peak wavelength as a function of the width of the oxide masks. The separation between the masks is 10 μm.

in Ch. 5. In this chapter, amplifier designs as it relates to current confinement (to the gain region) and single transverse mode operation are discussed.

Since semiconductor optical amplifier is very similar to a laser, the amplifier design development followed the development of the semiconductor lasers. Early amplifier work based on the GaAs/AlGaAs or InGaAsP/InP material system used a dielectric stripe for single transverse mode operation and current confinement. The amplifier chip has ∼4 to 6 μm opening in a dielectric layer through which the current flows. Similar laser structures have been extensively studied [72–76]. An alternative to dielectric deposition is ion implantation (e.g. proton implantation with ∼300 keV proton) through a mask, which creates a high resistance in the implanted regions. This confines the current injection to a small stripe. Figure 4.6.1 shows the transverse cross section of these amplifier structures.

The transverse guiding of the input optical signal in these structures is primarily due to small gain/index guiding due to the injected

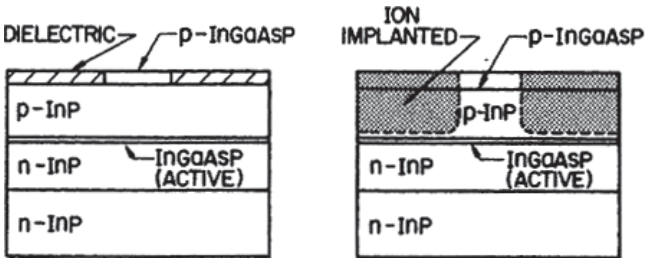

Fig. 4.6.1. Schematic cross section of dielectric stripe and ion implanted amplifier structures.

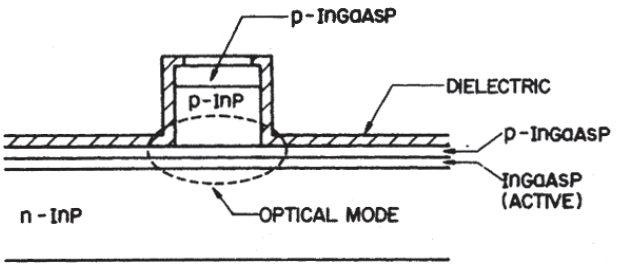

Fig. 4.6.2. Schematic cross section of a ride waveguide type amplifier.

carriers in the stripe region. This gain guiding has been studied in detail in connection with stripe geometry semiconductor lasers [7].

Good transverse guiding is important for good amplifier performance. This is due to an improved overlap of the propagating optical mode and gain. A ridge waveguide type structure (Fig. 4.6.2) provides such an improvement. For a ridge waveguide amplifier, the propagating fundamental mode is weakly index guided. This guiding arises because of the overlap of the optical mode profile (shown dashed in Fig. 4.6.2) with the dielectric layer on the sides of the ridge. The ridge width is typically $\sim$3 to 4 μm and the dielectric layer is SiO_2 or Si_3N_4. The index of these materials ($\sim$1.5 or 1.8) is considerably smaller than that of the semiconductor ($\sim$3.2 to 3.5). Thus a small overlap is sufficient to provide weak index guiding.

Ridge waveguide devices [77–79] are relatively simple to fabricate. It involves one epitaxial growth (growth of the active gain region, cladding layers and the contact layer), followed by ridge

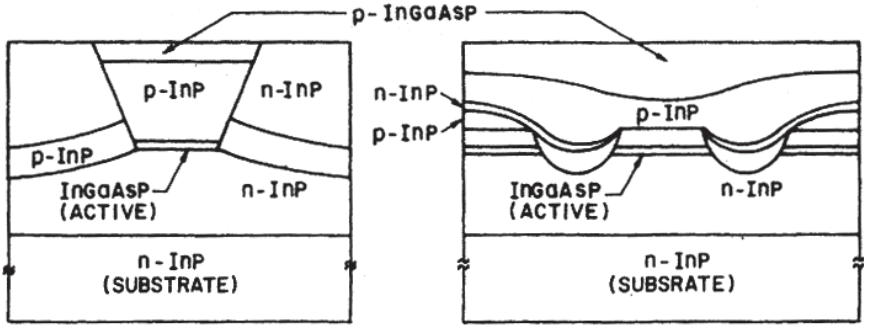

Fig. 4.6.3. Schematic of two index guided buried heterostructure designs. (a) [81] (b) [82].

etching followed by metal contact depositions, cleaving and coating. However, better performance (such as low amplified spontaneous emission and noise) is achieved using strongly index guided designs. Figure 4.6.3 shows the schematic cross section of two strongly index guided designs. These designs were originally developed for lasers but they are also suitable for amplifiers. The gain region (InGaAsP-Active) in these structures are surrounded (or buried) on all sides by InP layers. As a result, they are also known as buried heterostructure designs. The index of InP is ∼3.22 and that of the active region is ∼3.5. The effective transverse index difference for these structures is ∼0.3, compared to ∼0.03 for ridge waveguide structures (Fig. 4.6.2) and ∼0.005 for gain guided structures (Fig. 4.6.1).

Variations of the above designs have been reported in the literature [80–89]. A buried heterostructure design that is currently used for amplifier fabrication is the capped mesa buried heterostructure (CMBH) design. Scanning electron micrograph of a capped mesa (CMBH) buried heterostructure design along with the cross section is shown in Fig. 4.6.4. The current blocking layers in this structure consist of *i*-InP (Fe doped InP), *n*-InP, *i*-InP and *n*-InP layers. These sets of blocking provide good current confinement i.e. most of the current injected at the top contact goes through the active region instead of around it. An optimization of the thickness of these layers is needed for high gain performance.

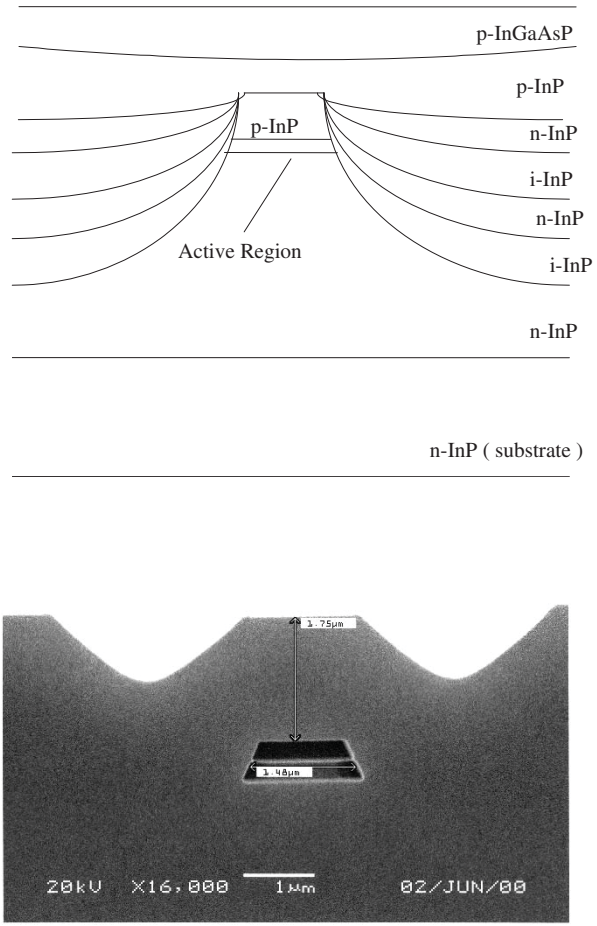

Fig. 4.6.4. Schematic and scanning electron photomicrograph of a buried heterostructure (BH) amplifier.

The fabrication involves the following steps. A n-InP layer, a InGaAsP gain layer (active region), a p-InP layer, and a p-InGaAs layer are grown over a (100) oriented n-InP substrate using MOCVD growth technique. The p-InGaAs layer is etched away. Then $\sim 1\,\mu$m wide mesas are etched on the wafer using a SiO_2 mask and wet chemical etching. The current blocking layers consisting of i-InP, n-InP i-InP and n-InP layers are grown on the wafer using a second MOCVD growth with the SiO_2 (oxide) layer on top of the mesa in place.

The oxide layer is then removed and a third growth of p-InP cladding layer and p-InGaAs contact layer is carried out. The wafer is then processed using standard lithography, metal deposition and cleaving techniques to produce the chips. The chips are then antireflection (AR) coated to produce amplifiers. For some amplifiers (buried facet — see Ch. 5) designs, the current blocking layers are also grown near the facet regions. These layers then serve as a beam expanding region which reduces the effective residual facet reflectivity.

4.6.1. *Leakage current*

For buried heterostructure devices the confinement of the injected current to the active region is achieved through reverse biased heterojunctions or forward biased InP homojunctions (which turn on at a voltage higher than that needed for light amplification). The difference between the total current I injected into the lasers and the current going through the active region I_a is the leakage current I_l i.e.

$$I_l = I - I_a. \tag{4.6.1}$$

The magnitude of I_a and its variation with I depends on the carrier concentration of the current blocking layers, their thickness and also on the presence of any defects in the current confining junctions or in any of the layers. A large leakage current would lead to low optical gain at high injected currents and is therefore not desirable. The amount of amplified spontaneous is also significantly reduced.

For the analysis of leakage currents, a buried heterostructure design is represented by its electrical equivalent circuit. This circuit has several paths for the flow of current from p-contact to the n-contact; one of which is the active region, represented by a diode. For the purpose of illustration, one of the buried heterostructure designs of Fig. 4.6.3 along with its various electrical paths is shown in Fig. 4.6.5. The values of the resistors and the gain of the transistors determine the amount of leakage. These quantities are determined by the carrier concentration in the layers and their thickness.

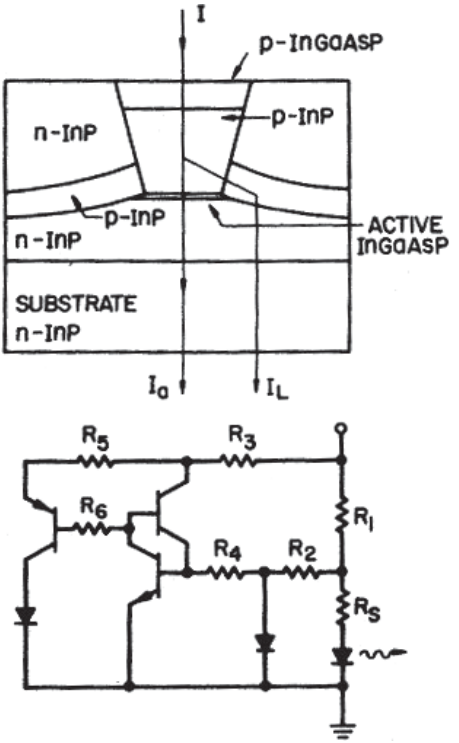

Fig. 4.6.5. Schematic cross section of a buried heterostructure design and its electrical equivalent circuit [90].

A detailed analysis of leakage in buried heterostructure designs is given in Ref. [90]. The leakage effect is more severe for amplifiers because unlike a laser, the voltage across the active junction does not saturate at threshold.

The leakage path marked by I_l in the schematic of Fig. 4.6.6 shows the leakage path consisting of a resistor and a InP homojunction diode. The electrical equivalent circuit of the active junction and this leakage path is shown in Fig. 4.6.6.

The low current turn-on voltage of the InP homojunction is higher than that of the amplifier active junction. However, at high current depending on the value of the resistors in each path the I-V curves associated with these two paths would cross and the homojunction leakage may exceed the current going through the active

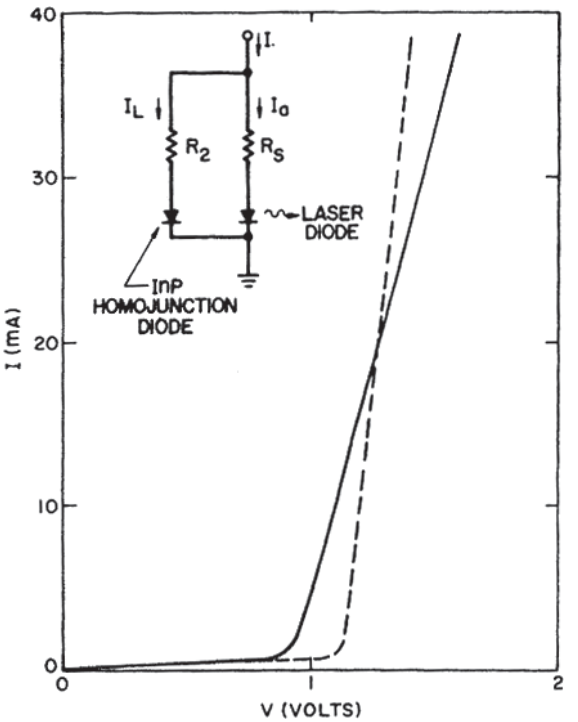

Fig. 4.6.6. Electrical equivalent circuit of an active heterojunction diode in parallel with a InP homojunction diode is shown in the inset. Representative I–V characteristics of the heterojunction diode path (solid curve) and that of the homojunction diode path (dashed curve) [90].

junction. This is also illustrated in Fig. 4.6.6. Thus the design of the current confinement layers is important for the fabrication of amplifiers that operate at high current and hence high gain.

4.7. Growth of QWR and QD Materials

For the quantum well structures, the continuous set of energies is related to carrier motion in two dimensions in the plane of the well. For quantum wire (QWR) structures, the carrier motion is allowed only in one dimension i.e. along the length of the wire. The carrier confinement in the other two directions result in a discrete set of levels. For quantum dot (QD) structures, the carriers are confined in

all three directions. Over the last decade, low dimensional quantum well structures have found application in optoelectronic devices such as lasers, amplifiers and FETs. Lasers with quantum structure are expected to have improved performance characteristics such as low threshold operation, low temperature sensitivity and low spectral width [91–98]. Many of these improved performances have been realized in quantum well structures. The advantages of QWR's are enhanced with respect to quantum wells because of their confinement in one dimension. In addition, theory predicts that QD's being confined in all three dimensions should have even superior properties for laser applications. The superior property of QD's as it relates to semiconductor optical amplifiers are high speed of response since the gain and phase recovery times are short compared to other structures [99].

For the growth of quantum well structures, thin layers (few nm thick) need to be grown on a planar substrate. This is accomplished by growth techniques such as MOCVD or MBE discussed earlier. Growth times are adjusted so that the desired thickness is achieved. The typical growth rates in MBE process is $\sim 1\,\mu$m/hour and that for MOCVD process is $\sim 0.1\,\mu$m/min. The growth rate for LPE process is generally too large, $\sim 1\,\mu$m/min, to allow suitable reproducible growth of the thin layers needed for quantum well structures.

Many efforts have been devoted to the realization of QWR structures [91, 92]. These include self organized growth, growth on a ridge structure, growth on step structures, and, growth in V-grooves [100–104]. Quantum wire lasers using InAsP/InP and InGaAs/InP material system has been fabricated using growth in V-grooves. Fabrication of QWR structure by mass transport is sketched is shown in Fig. 4.7.1. V-grooves are etched on a InP substrate by wet chemical etching. The substrate is then heated in a MOCVD reactor to a temperature of $\sim 600\,$C in the presence of As and P. No group III sources are present. Mass transport is believed to take place as follows. InP on the top edges of the ridge release P to form metallic In which then migrates to the bottom to recapture the P. If there is As present in the ambient, it captures As at a certain rate. Thus InAsP is formed at the bottom of the V-groove under certain partial pressure of As and P.

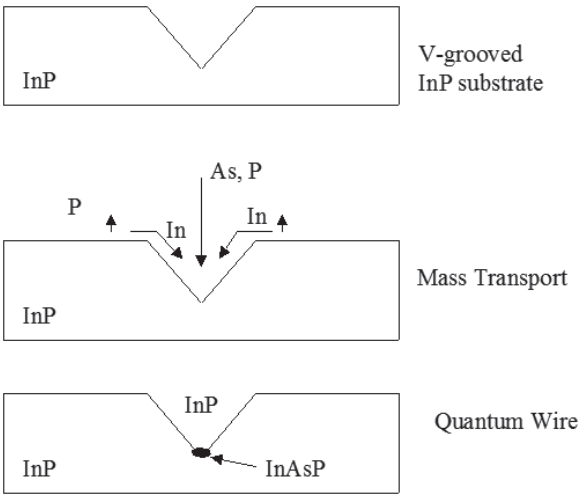

Fig. 4.7.1. Schematic of the mass transport process for the formation of InAs/InP quantum wires.

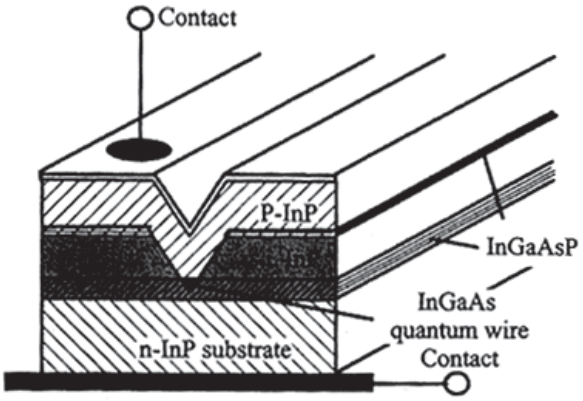

Fig. 4.7.2. Structure of a QWR laser on a V-groove substrate [92, 105].

Quantum wire lasers need very good current confinement i.e. a large fraction of the injected current must flow through the active region and not around it. Quantum wire lasers with semi-insulating Fe doped InP current confining layer has been reported [105].

The schematic of the device fabricated using the InGaAsP/InP material system is shown in Fig. 4.7.2. First, a n-InGaAsP layer

followed by a Fe:InP layer is grown on a (100) oriented n-InP substrate by MOCVD growth technique [105]. V-grooves are then etched on the wafer using a SiO_2 mask and wet chemical etching. Then the undoped InGaAs QWR active region is grown in the tip of the V-groove. Thus is followed by the growth of a thin undoped InGaAsP layer, p-InP layer and a p-InGaAs layer. The last layer serves as a contact layer for current injection. Modifications of the structure which includes ion implantation to create a high resistance in the p-InP layer (for better current confinement) has been reported [104].

In addition to V-grooves, QWR structures have been grown in ridges or side walls. Growth of InGaAs and InAlAs on the (100) oriented mesa has been reported. The growth experiments showed the exact shape (flat topped or pyramid shape) is important in determining the growth conditions for the growth of a particular material.

Optical amplifiers using QWR active region generally have low gain due to difficulty in current confinement at high currents. In addition, the optical mode confinement factor is small. However, for the same reason they are likely to have high saturation powers.

Although the advantages of low dimensional structures (such as QD and Q-wire) were determined early on [93–95], the experimental challenge has been to fabricate QDs ($\sim$10 nm in dimension) of uniform size in a reproducible way. There has been considerable work on fabrication of semiconductor nanostructures using the phenomenon of island formation during strained layer epitaxy, a process called Stranski-Krastanow growth mode. A formation of clusters is observed during epitaxial growth of a semiconductor layer (e.g. InGaAs) on top of another (e.g. GaAs) that has a lattice constant several (3 to 5) percent smaller. For the first few layers the atoms arrange themselves in a planar layer called the wetting layer. As the epitaxial growth proceeds, the atoms bunch up to form clusters. The cluster growth is energetically favorable since it relaxes the strain and thus reduces the strain energy. Since the QD's appear spontaneously, the process is often called a self assembly process. Although this process generally produces dots of different sizes, lasers and amplifiers with QD active region has been fabricated [92]. The self assembly process is

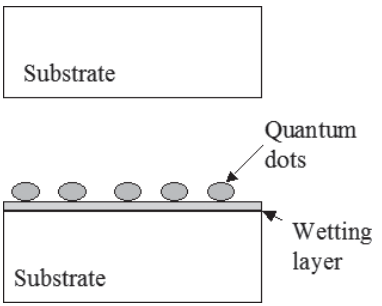

Fig. 4.7.3. Schematic of quantum dot formation. The top figure shows the planar substrate. The lower figure shows quantum dots on the wetting layer. The dots are covered in a high band gap material for laser or amplifier devices.

observed in several material systems. For example GaAs and InAs to form InGaAs quantum dots, InP and GaP to form InGaP quantum dots and Ge and Si which form GeSi dots.

The advantages of self assembly are: a large number of quantum dots can be formed in a single step without lithography and they can covered epitaxially by the host material without any interface defects. The size of the dots can be controlled within in a certain range by controlling the amount of deposited material. The schematic of QD formation is shown in Fig. 4.7.3.

The emission wavelength depends on the size of the dot and thus the emission wavelength can be controlled to a certain extent for the same material system. All techniques of doping and energy band modifications from planar layer growth can, in principle, be adapted to quantum dot growth by self assembly.

References

[1] H. Nelson, *RCA Rev.* **24**, 603 (1963).
[2] W. F. Finch and E. W. Mehal, *J. Electrochem Soc.* **111**, 814 (1964).
[3] A. Y. Cho, *J. Vac. Sci. Technol.* **8**, 531 (1971).
[4] R. D. Dupuis, *J. Crystal Growth* **55**, 213 (1981).
[5] H. Kressel and J. K. Butler, *Semiconductor Lasers and Heterojunction LEDs* (Academic Press, New York, 1977).
[6] H. C. Casey, Jr. and M. B. Panish, *Heterostructure Lasers* (Academic Press, New York, 1978).
[7] G. P. Agrawal and N. K. Dutta, *"Semiconductor Lasers"* Van Nostrand Reinhold, NY, 1986, 2nd edn. (1992).

[8] J. M. Woodall, H. Rupprecht and W. Reuter, *J. Electrochem. Soc.* **116**, 899 (1969).
[9] H. Nelson, U.S. Patent 3,565,702 (1971).
[10] I. Hayashi, M. B. Panish, P. W. Foy and S. Sumski, *Appl. Phys. Lett.* **17**, 109 (1970).
[11] M. Feng, L. W. Cook, M. M. Tashima and G. E. Stillman, *J. Electron. Mater.* **9**, 241 (1980).
[12] I. Ladany and F. Z. Hawrylo, *J. Cryst. Growth* **54**, 69 (1981).
[13] J. J. Hsieh, *Appl. Phys. Lett.* **28**, 283 (1976).
[14] R. J. Nelson, *Appl. Phys. Lett.* **35**, 654 (1979).
[15] J. J. Hsieh, *J. Cryst. Growth* **27**, 49 (1974).
[16] D. L. Rode, *J. Cryst. Growth* **20**, 13 (1973).
[17] W. A. Tiller, *J. Cryst. Growth* **2**, 69 (1968).
[18] M. B. Small and I. Crossley, *J. Cryst. Growth* **27**, 35 (1974).
[19] R. L. Moon, *J. Cryst. Growth* **27**, 62 (1974).
[20] P. Besomi, J. Degami, N. K. Dutta, W. R. Wagner and R. J. Nelson, *J. Appl. Phys.* **56**, 2879 (1984).
[21] A. Doi, N. Chin one, A. Aiki and R. Ito, *Appl. Phys. Lett.* **34**, 393 (1979).
[22] M. A. DiGuiseppe, H. Temkin and W. A. Bonner, *J. Cryst. Growth* **58**, 279 (1982).
[23] A. R. Clawson, W. Y. Lum and G. W. McWilliams, *J. Cryst. Growth* **46**, 300 (1979).
[24] G. A. Antypas, *Appl. Phys. Lett.* **37**, 64 (1980).
[25] P. Besomi, R. B. Wilson, W. R. Wagner and R. J. Nelson, *J. Appl. Phys.* **54**, 535 (1983).
[26] G. A. Antypas and R. L. Moon, *J. Electrochem. Soc.* **120**, 1574 (1973).
[27] G. A. Antypas and J. Edgecumbe, *J. Cryst. Growth* **34**, 132 (1976).
[28] K. Nakajima, T. Tanahashi, K. Akita and T. Yamaoka, *J. Appl. Phys.* **50**, 4975 (1979).
[29] K. Nakajima, T. Kusunoki, K. Akita and T. Kotani. *J. Electrochem. Soc.* **125**, 123 (1978).
[30] R. E. Nahory, M. A. Pollack, W. D. Johnston Jr. and R. L. Barns, *Appl. Phys. Lett.* **33**, 659 (1978).
[31] P. Chandra, L. A. Coldren and K. E. Strege, *Electron Lett.* **17**, 6 (1981).
[32] I. Hayashi, M. B. Panish, P. W. Foy and S. Sumski, *Appl. Phys. Lett.* **17**, 109, (1970).
[33] G. H. Olsen, Chap. 1, in *GainAsP Alloy Semiconductors*, ed. T. P. Pearsall (John Wiley & Sons, New York, 1982).
[34] J. J. Tietjen and I. A. Amick, *J. Electrochem. Soc.* **113**, 724 (1966).
[35] G. H. Olsen and T. J. Zamerowski, *IEEE J. Quantum Electron.* **QE-17**, 128 (1981).
[36] H. Enda, *Jpn. J. Appl. Phys. Part 1* **18**, 2167 (1979).
[37] R. E. Enstrom, C. J. Nuese, J. R. Appert and N. J. DiGuiseppe, *Electrochem. Soc. Ext. Abstr.* **78-1**, 504 (1978).
[38] S. S. Hyder, R. R. Saxena and C. B. Cooper, *Appl. Phys. Lett.* **34**, 584 (1979).

[39] H. A. Seki, Konkitu and M. Matsumura, *J. Cryst. Growth* **54**, 615 (1981).
[40] W. D. Johnston Jr. and K. E. Strege, *38th Annual IEEE Device Research ConI Abstr.*, Vol. IVB-3 (Cornell University, Ithaca, N.Y. 1980).
[41] T. Mizutani, M. Yoshida, A. Usai, H. Watanabe, T. Yuasa and I. Hayashi, *Jpn. J. Appl. Phys. Part 2* **L113**, 19 (1980).
[42] H. M. Manasevit and W. I. Simpson, *J. Electrochem. Sac.* **116**, 1725 (1969).
[43] Y. Seki, K. Tanno, K. Iida and E. Ichiki, *J. Electrachem. Soc.* **122**, 1108 (1975).
[44] R. D. Dupuis, P. D. Dapkus, R. D. Yingling and L. A. Moudy. *Appl. Phys. Lett.* **31**, 201 (1978).
[45] R. D. Dupuis, *J. Cryst. Growth* **55**, 213 (1981).
[46] P. D. Dapkus, *Annu. Rev. Mater. Sci.* **12**, 243 (1982).
[47] J. P. Hirtz, M. Razeghi, M. Bonnet and J. P. Duchemin, Ch. 3, in *GalnAsP Alloy Semiconductors*, ed. T. P. Pearsall (New York: John Wiley & Sons, 1982); S. Hersee and J. P. Duchemin, *Annu. Rev. Mater. Sci.* **12**, 65 (1982).
[48] J. P. Hirtz, J. P. Larivain, J. P. Duchemin, T. P. Pearsall and M. Bonnet, *Electron. Lett.* **16**, 415 (1980).
[49] J. P. Hirtz, J. P. Larivain, D. Leguen, M. Razeghi and J. P. Duchemin, pp. 29–35 in *Gallium Arsenide and Related Compounds 1980, Conf. Series 56* (Institute of Phys. Bristol, 1981).
[50] J. P. Hirtz, M. Razeghi, J. P. Larivain, S. Hersee and J. P. Duchemin, *Electron. Lett.* **17**, 113 (1981).
[51] M. Razeghi, S. Hersee, J. P. Hirtz, R. Blondeau, B. de Cremoux and I. P. Duchemin, *Electron. Lett.* **19**, 336 (1983).
[52] T. Fukui and Y. Horikoshi, *Jpn. J. Appl. Phys. Part 1* **19**, 395 (1980).
[53] C. B. Cooper, R. R. Saxena and M. J. Ludowise, *Electron. Lett.* **16**, 892 (1980).
[54] J. Yoshino, T. lawnot and H. Kukimoto, *J. Cryst. Growth* **55**, 74 (1981).
[55] J. R. Arthur, *J. Appl. Phys.* **39**, 4032 (1968).
[56] J. R. Arthur and J. J. LePore, *J. Vac. Sci. Technol.* **6**, 545 (1969).
[57] A. Y. Cho, *J. Vac. Sci. Technol.* **8**, S31 (1971).
[58] A. Y. Cho, *J. Appl. Phys.* **41**, 2780 (1970).
[59] A. Y. Cho, *J. Appl. Phys.* **42**, 2074 (1971).
[60] A. Y. Cho and J. R. Arthur, in *Progress in Solid State Chemistry*, ed. J. O. McCladin and G. Somorjai, Vol. 10 (New York: Pergamon Press, 1975), p. 157.
[61] W. T. Rsang, *Appl. Phys. Lett.* **45**, 1234 (1984).
[62] T. Tanbun-Ek, R. A. Logan, H. Temkin, S. N. G. Chu, N. A. Olsson, A. M. Sergent and K. W. Wecht, *IEEE J. Quantum Electron.* **QE-26**, 1323 (1990).
[63] G. C. Osbourne, *J. Vac. Sci. Technol.* **B1**, 379 (1983).
[64] W. T. Massalink, T. Henderson, J. Klem, R. Fischer, P. Pearah, H. Morkoc, M. Hafich, P. D. Wang and G. Y. Robinson, *Appl. Phys. Lett.* **45**, 1309 (1984).
[65] S. E. Fischer, D. Fekete, G. B. Feak and J. A. Ballantyne, *Appl. Phys. Lett.* **50**, 714 (1984).

[66] J. W. Matthews and A. E. Blakeslee, *J. Cryst. Growth* **27**, 118 (1974).
[67] T. Tanbun-Ek, R. A. Logan, H. Temkin, S. N. G. Chu, N. A. Olsson, A. M. Sergent and K. W. Wecht, *IEEE J. Quantum Electron.* **QE-26**, 1323 (1990).
[68] P. R. Berger, K. Chang, P. Bhattacharya, J. Singh and K. K. Bajaj, *Appl. Phys. Lett.* **53**, 684 (1988).
[69] R. Bhat, *J. Crystal Growth* **120**, 362 (1992).
[70] R. P. Gale, R. W. McClelland, J. C. C. Fan and C. O. Bozler, *Appl. Phys. Lett.* **41**, 545 (1982).
[71] C. Joyner, Chapter 5, in *Optical Fiber Communications*, eds. I. P. Kaminow and T. L. Koch, III B (Academic Press, 1997).
[72] K. Oe and K. Sugiyama, *Jpn. J. Appl. Phys.* **15**, 2003 (1976).
[73] J. C. Dyment, *Appl. Phys. Lett.* **10**, 84 (1967).
[74] J. C. Dyment, L. A. D'Asaro, J. C North, B. I. Miller and J. E. Ripper, *Proc. IEEE* **60**, 726 (1972).
[75] G. D. Henshall, G. H. B. Thompson, J. E. A. Whiteway, P. R. Selway and M. Broomfield, *IEE Proc.* **I 3**, 1 (1979).
[76] B. Schwartz, M. W. Focht, N. K. Dutta, R. J. Nelson and P. Besomi, *IEEE Trans. Electron Devices* **ED-31**, 841 (1984).
[77] I. P. Kaminow, L. W. Stulz, J. S. Ko, A. G. Dentai, R. E. Nahory, I. C. DeWinter and R. L. Hartman, *IEEE J. Quantum Electron.* **QE-19**, 1312 (1983).
[78] W. T. Tsang and R. A. Logan, *Appl. Phys. Lett.* **45**, 1025 (1984).
[79] H. Temkin, R. A. Logan, M. B. Panish and J. P. Van der Ziel, *Appl. Phys. Lett.* **45**, 330 (1984).
[80] T. Tsukada, *J. Appl. Phys.* **45**, 4899 (1974).
[81] M. Hirao, S. Tsuji, K. Mizuishi, A. Doi and M. Nakamura, *J. Opt. Commun.* **1**, 10 (1980).
[82] I. Mito, M. Kitamura, K. Kobayashi, S. Murata, M. Seki, Y. Odagiri, H. Nishimoto, M. Yamaguchi and K. Kobayashi, *J. Lightwave Technol.* **LT-1**, 195 (1983).
[83] I. Mito, M. Kitamura, K. Kaede, Y. Odagiri, M. Seki, M. Sugimoto and K. Kobayashi, *Electron. Lett.* **18**, 2 (1982).
[84] R. J. Nelson, P. D. Wright, P. A. Barnes, R. L. Brown, T. Cella and R. G. Sobers, *Appl. Phys. Lett.* **36**, 358 (1980).
[85] H. Ishikawa, H. Imai, T. Tanahashi, Y. Nishitani, M. Takusagawa and K. Takahei, *Electron. Lett.* **17**, 465 (1981).
[86] N. K. Dutta, D. P. Wilt, P. Besomi, W. C. Dautremont-Smith, P. D. Wright and R. J. Nelson, *Appl. Phvs. Lett.* **44**, 483 (1984).
[87] R. A. Logan, J. P. Van der Ziel and H. Tamkin, *Proc. SPIE Int. Soc. Opt. Eng.* **280**, 181 (1981).
[88] M. Oron, N. Tamari, H. Shtrikman and C. A. Burrus, *Appl. Phys. Lett.* **41**, 609 (1982).
[89] T. Murotani, E. Oomura, H. Higuchi, H. Namizaki and W. Susaki, *Electron. Lett.* **16**, 566 (1980).

[90] N. K. Dutta, D. P. Wilt and R. J. Nelson, *J. Lightwave Technol.* **LT-2**, 201 (1984).
[91] E. Kapon, Chapter 10, in *Quantum Well Lasers*, ed. P. Zory (Academic Press, NY, 1993).
[92] V. M. Ustinov, A. E. Zhukov, A. Yu. Egorov and N. A. Maleev, *Quantum Dot Lasers* (Oxford University Press, 2003).
[93] Y. Arakawa, H. Sasaki, *Appl. Phys. Lett.* **40**, 939 (1982).
[94] M. Asada, Y. Miyamoto and Y. Suematsu, *IEEE J. Quantum Electron* **QE-22**, 1915 (1986).
[95] A. Yariv, *Appl. Phys. Lett.* **53**, 1033 (1988).
[96] Y. Miyamoto, Y. Miyake, M. asada and Y. Suematsu, *IEEE J. Quantum Electron* **QE-25**, 2001 (1989).
[97] M. Asada, Y. Miyamoto and Y. suematsu, *Japan J. Appl. Phys.* **24**, L95 (1985).
[98] M. Cao, Y. Miyake, S. Tamura, H. Hirayama, S. Arai ,Y. Suematsu and Y. Miyamoto, *Trans. IEICE* **E73**, 63 (1990).
[99] M. Sugawara, T. Akiyama, N. Hatori, Y. Nakata, H. Ebe and H. Ishikawa, *Meas. Sci. Technol.* **13**, 1683 (2002); M. Sugawara, H. Ebe, N. Hatori, M. Ishida, Y. Arakawa, T. Akiyama, K. Otsubo and Y. Nakata, *Phys. Rev. B* **69**, Art. No. 235332 (2004).
[100] M. Ishikawa, W. Pan, Y. Kaneko, H. Yaguchi, K. Onabe, R. Ito and Y. Shiraki, *Jpn. J. Appl. Phys.* **37**, 1556 (1998).
[101] T. Toda and Y. Nakano, in *Proc. of 11th Int. Conf. on InP and Related Materials* (Davos, Switzerland, May 16–20, 1999), pp. 17.
[102] S. Tiwari and G. D. Petiti, *Appl. Phys. Lett.* **64**, 3536 (1994).
[103] E. Kapon, D. M. Hwang and R. Bhat, *Phys. Rev. Lett.* **63**, 430 (1989).
[104] E. Kapon, S. Simhony, R. Bhat and D. M. Hwang, *Appl. Phys. Lett.* **55**, 2715 (1989).
[105] D. Piester, P. Bonsch, T. Schrimpf, H. Wehmann and A. Schlachetzki, *IEEE J. Select. Topics Quantum Electron.* **6**, 511 (2000).

Chapter 5

Low Reflectivity Facet Designs

5.1. Introduction

Semiconductor optical amplifiers can be classified into two categories, the Fabry Perot (FP) amplifier [1, 2] and the traveling wave (TW) amplifier [3–8]. A FP amplifier has considerable reflectivity at the input and output ends which results in resonant amplification between the end mirrors. Thus, a FP amplifier exhibits larger optical gain at wavelengths corresponding to the longitudinal modes of the cavity and the gain is small in between the cavity modes. This modulation in gain is not desirable if the amplifier is used in optical networks. The TW amplifier, by contrast, has negligible reflectivity at each end which results in wavelength independent (no modulation in gain) signal amplification during a single pass. The optical gain spectrum of a TW amplifier is quite broad and corresponds to that of the semiconductor gain medium. Most practical TW amplifiers exhibit some small ripple in the gain spectrum which arises from residual facet reflectivity. TW amplifiers are more suitable for system applications. An example of the gain spectrum of a TW amplifier with antireflection coated cleaved facets is shown in Fig. 5.1.1. The output exhibits some modulations at longitudinal modes of the cavity because the optical gain is slightly higher at the modes than in between the modes. Both TE (transverse electric) and TM (transverse magnetic) fundamental modes can propagate in a TW amplifier. These modes have slightly different effective indices due to slightly different confinement factors and hence the precise antireflection coating needed for these modes are different. Thus the residual modulation in TE and TM mode gain in TW amplifiers

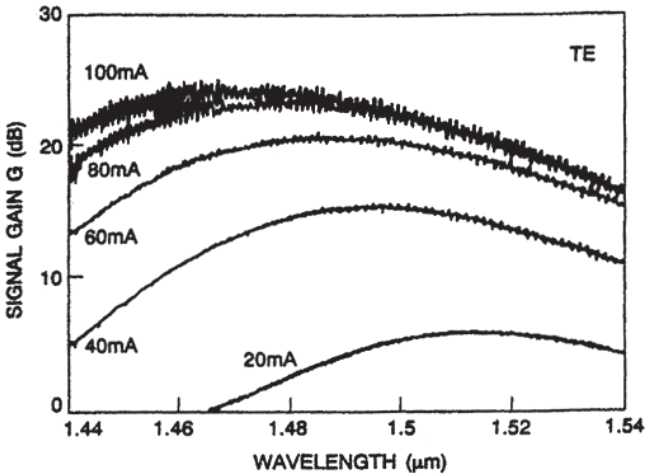

Fig. 5.1.1. Optical gain spectrum of a traveling wave SOA at several injection currents [4].

due to nonzero facet reflectivity results are spectrally displaced. This problem is reduced considerably for amplifiers with nearly equal confinement factor for TE and TM modes.

For plane waves, a quarter wave thick (thickness $= \lambda_0/4n$ where n is the index of the dielectric layer) single layer dielectric coating with an index $n = n_m^{1/2}$ where n_m is the index of the semiconductor material is sufficient to create a perfect (zero reflectivity) antireflection coating. The waves propagating in the amplifier are not plane waves and the above therefore serves only as an approximation. For very low gain modulation (also known as gain ripple) the facet reflectivity of a TW amplifier must be $<0.01\%$. Much effort has been devoted to fabricate amplifiers with very low effective facet reflectivity. Such amplifier structures either utilize special low effective reflectivity dielectric coatings, or have tilted or buried facets. Fabrication and performance of these devices are described in this chapter.

In an ideal TW amplifier the optical beam should not experience any reflectivity at the facets. However, in practice the facets with anti-reflection (AR) coating exhibit some residual reflectivity. This residual reflectivity results in the formation of an optical cavity which has resonance at the longitudinal modes. This results in

a variation in gain as a function of wavelength of a traveling wave semiconductor amplifier. This variation in gain appears in the form of a ripple (periodic variation in gain at the cavity mode spacing). Figure 5.1.1 shows the gain spectrum of a typical TW amplifier with a good AR coating at the facets. Note the gain ripple increases with increasing current i.e. gain ripple increases with the gain of the amplifier. The peak of the gain spectrum also shifts to short wavelength with increasing current.

The gain of an amplifier in the presence of residual reflectivity has been calculated. The optical beam propagating through the amplifier undergoes both a change in intensity (amplitude) and phase. The gain G of the intensity is given by [8]

$$G = \frac{(1-R_1)(1-R_2)G_s}{(1+\sqrt{R_1R_2}G_s)^2 + 4\sqrt{R_1R_2}G_s \sin^2\phi}, \tag{5.1.1}$$

where G_s is the single pass gain and R_1, R_2 are the residual reflectivity of the two facets. The quantity ϕ is the phase shift through the amplifier given by

$$\phi = \phi_0 + \frac{g_0 L\alpha}{2}\left(\frac{P}{P+P_s}\right), \tag{5.1.2}$$

where $\phi_0 = 2\pi L\overline{n}/\lambda$ is the nominal phase shift , $\overline{n}$ is the effective refractive index of the amplifier, α is the linewidth enhancement factor, g_0 is the unsaturated gain and the quantities P and P_s are the internal optical power and saturation power respectively. The $\sin^2\phi$ term in Eq. (5.1.1) is responsible for the modulation in output signal intensity. The case of practical interest is for R_1, $R_2 < 10^{-3}$. In this case, the residual facet reflectivity appears as small ripples on the overall gain spectrum.

The peak to valley ratio V of the gain modulation obtain from Eq. (5.1.1) is given by

$$V = \left[\frac{1+\sqrt{R_1R_2}G_s}{1-\sqrt{R_1R_2}G_s}\right]. \tag{5.1.3}$$

For an ideal TW amplifier both R_1, $R_2 = 0$; in this case $V = 1$, i.e. no ripple occurs at the cavity mode frequencies. The quantity V is

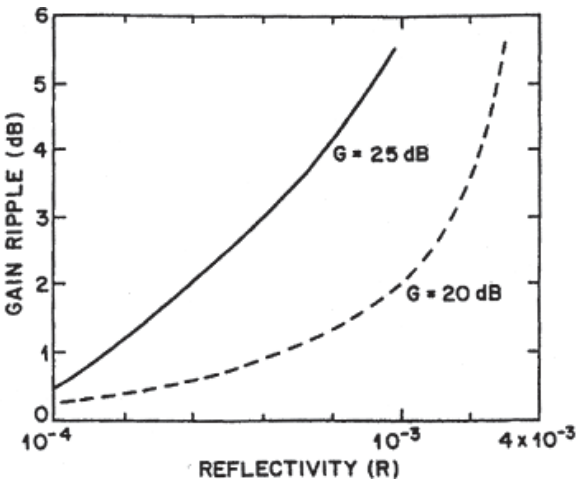

Fig. 5.1.2. The calculated gain ripple as a function of residual reflectivity, $(R = (R_1 R_2)^{1/2})$ for two values of internal gain [4].

plotted in Fig. 5.1.2 as a function of $(R_1 R_2)^{1/2}$ (reflectivity) for two different values of gain. The figure shows the gain ripple increases with increasing gain and increasing facet reflectivity.

5.2. Low Reflectivity Coatings

A key factor for good performance characteristics (low gain ripple and low polarization selectivity) for TW amplifiers is very low facet reflectivity [3–9]. The reflectivity of cleaved facets can be reduced by dielectric coating.

For plane waves incident on an air interface from a medium of refractive index n, the reflectivity can be reduced to zero by coating the interface with a dielectric whose refractive index equals $n^{1/2}$ and whose thickness equals $\lambda/4$.

However, the fundamental mode propagating in a waveguide is not a plane wave and therefore the above $n^{1/2}$ law only provides a guideline for achieving very low ($\sim 10^{-4}$) facet reflectivity by dielectric coatings. In practice, very low facet reflectivities are obtained by monitoring the amplifier performance during the coating process. The effective reflectivity can then be estimated from the ripple at

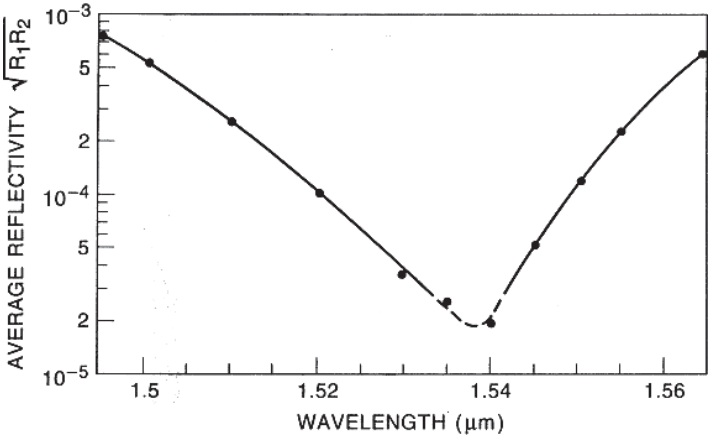

Fig. 5.2.1. The measured reflectivity is plotted as a function of wavelength [10].

the Fabry Perot mode spacings, caused by residual reflectivity, in the spontaneous emission spectrum. The result of such an experiment is shown in Fig. 5.2.1 [9, 10]. The reflectivity is very low ($<10^{-4}$) only in a small range of wavelengths. Although laboratory experiments have been carried out using amplifiers that rely only on low reflectivity coatings for good performance, the critical nature of the thickness requirement and a limited wavelength range of good AR coating led to the investigation of alternate schemes as discussed below.

5.3. Buried Facet Amplifiers

The principal feature of the buried facet (also known as the window structure) optical amplifiers relative to AR-coated cleaved facet devices is a polarization independent reduction in mode reflectivity due to the buried facet, resulting in better control in achieving polarization independent gain.

Schematic cross section of a buried-facet optical amplifier is shown in Fig. 5.3.1. Current confinement in this structure is provided by semi-insulating Fe-doped InP layers grown by the MOCVD growth technique. Fabrication of this device involves a procedure similar to that used for lasers. The first four layers are grown on a (100)-oriented n-InP substrate by MOCVD. These layers are (i) an

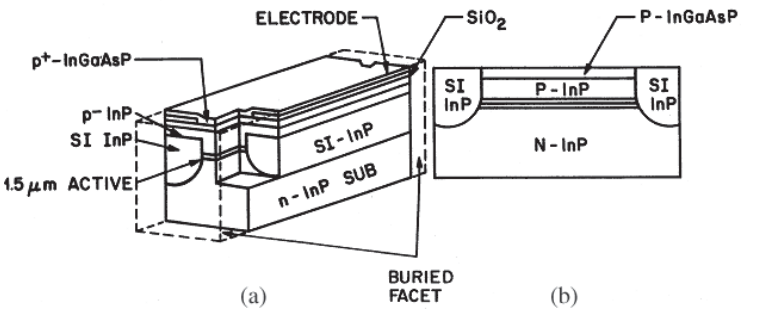

Fig. 5.3.1. Schematic of a buried facet optical amplifier [11].

n-InP buffer layer, (ii) an undoped InGaAsP ($\lambda \sim 1.55\,\mu$m) active layer, (iii) a p-InP cladding layer, and (iv) a p-InGaAs ($\lambda \sim 1.65\,\mu$m) layer. Mesas are then etched on the wafer along the [110] direction with 15 μm wide channels normal to the mesa direction using a SiO_2 mask. The latter is needed for buried-facet formation. Semi-insulating Fe-doped InP layers are then grown around the mesas by MOCVD growth process with the oxide mask in place. The oxide mask and the p-InGaAs layer is removed and a p-InP cladding layer and p-InGaAs ($\lambda \sim 1.65\,\mu$m) contact layer are then grown over the entire wafer by the MOCVD growth technique. The wafer is processed using standard lithography methods, metal depositions and cleaved to produce 0.5 mm to 3 mm-long buried-facet chips with ∼7 μm long buried facets at each end. The facets of the chips are then AR-coated using a single-layer film of ZrO_2. Fabrication of cleaved-facet devices follows the same procedure as described above, except that the mesas are continuous with no channels separating them. The latter is needed for defining the buried-facet regions. The semi-insulating layer, in both types of devices, provides current confinement and lateral index guiding. For buried-facet devices it also provides the buried-facet region where beam expansion takes place.

The effective reflectivity of a buried facet decreases with increasing separation between the facet and the end of the active region. The effective reflectivity (R_{eff}) of such a facet can be calculated by using a Gaussian beam approximation for the propagating optical

mode. It is given by [11]

$$R_{\text{eff}} = R/(1 + (2S/k\omega^2)^2), \tag{5.3.1}$$

where R is the reflectivity of the cleaved facet, S is the length of the buried-facet region, $k = 2\pi/\lambda$, where λ is the optical wavelength in the medium, and ω is the spot size at the facet. The calculated reflectivity using $\omega = 0.7\,\mu\text{m}$ and $R = 0.3$ for an amplifier operating near $1.55\,\mu\text{m}$ is less than 10^{-2} for buried-facet lengths larger than $\sim 15\,\mu\text{m}$ (Fig. 5.3.2).

Although increasing the length of the buried-facet region decreases the reflectivity, if the length is too long the beam emerging from the active region will strike the top metallized surface, producing multiple peaks in the far-field pattern, a feature not desirable for coupling into a single-mode fiber. The beam waist w of a Gaussian beam after traveling a distance z is given by the equation [12]

$$\omega^2(z) = \omega_0^2(1 + (\lambda z/\pi\omega_0^2)^2), \tag{5.3.2}$$

where ω_0 is the spot size at the beam waist and λ is the wavelength in the medium. Since the active region is about $4\,\mu\text{m}$ from the top

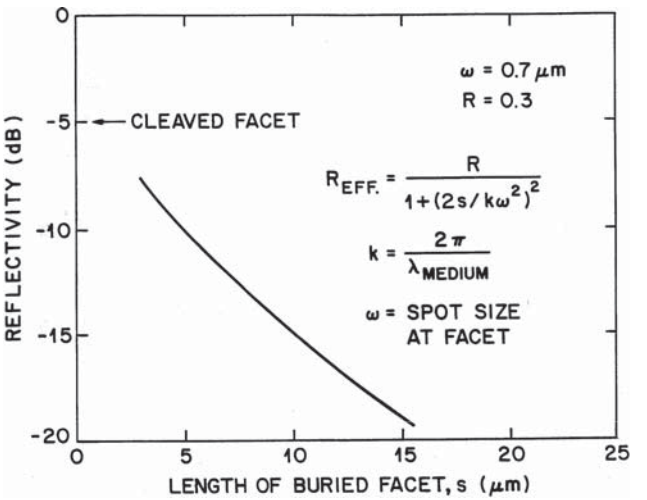

Fig. 5.3.2. Effective reflectivity of a buried facet configuration plotted as a function of the length of the buried facet [11].

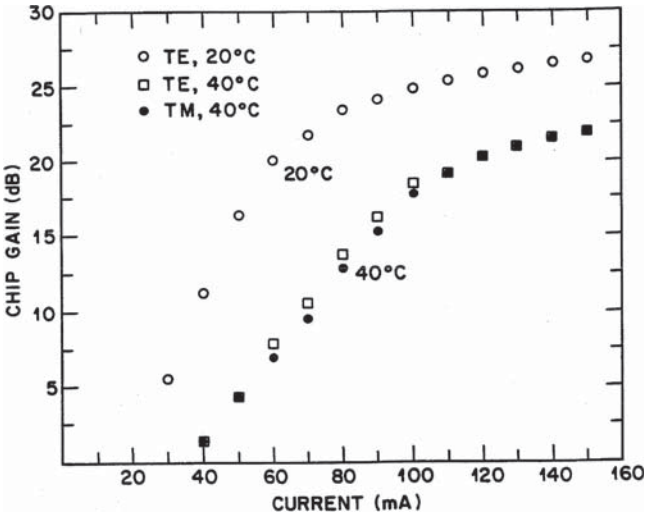

Fig. 5.3.3. Measured chip gain as a function of amplifier current [13].

surface of the chip, it follows from the above equations that the length of the buried-facet region must be less than 12 μm for single lobed far-field operation.

The optical gain is determined by injecting light into the amplifier and measuring the output beam characteristics. The internal gain of an amplifier chip as a function of current at two different temperatures is shown in Fig. 5.3.3 [13]. Open circles and squares represent the gain for a linearly polarized incident light with the electric field parallel to the p-n junction in the amplifier chip (TE mode). Solid circles represent the measured gain for the TM mode at 40°C. Measurements were done for low input power (−40 dBm), so that the observed saturation is not due to gain saturation in the amplifier, but rather to due to carrier loss caused by Auger recombination. Note that the optical gain for the TE and TM input polarizations are nearly equal.

Figure 5.3.4 shows the measured gain as a function of input wavelength for TE-polarized incident light. The modulation in the gain (gain ripple) with a periodicity of 0.7 nm is due to residual facet reflectivity. The measured gain ripple for this device is less than 1 dB. The estimated facet reflectivity from the measured gain ripple

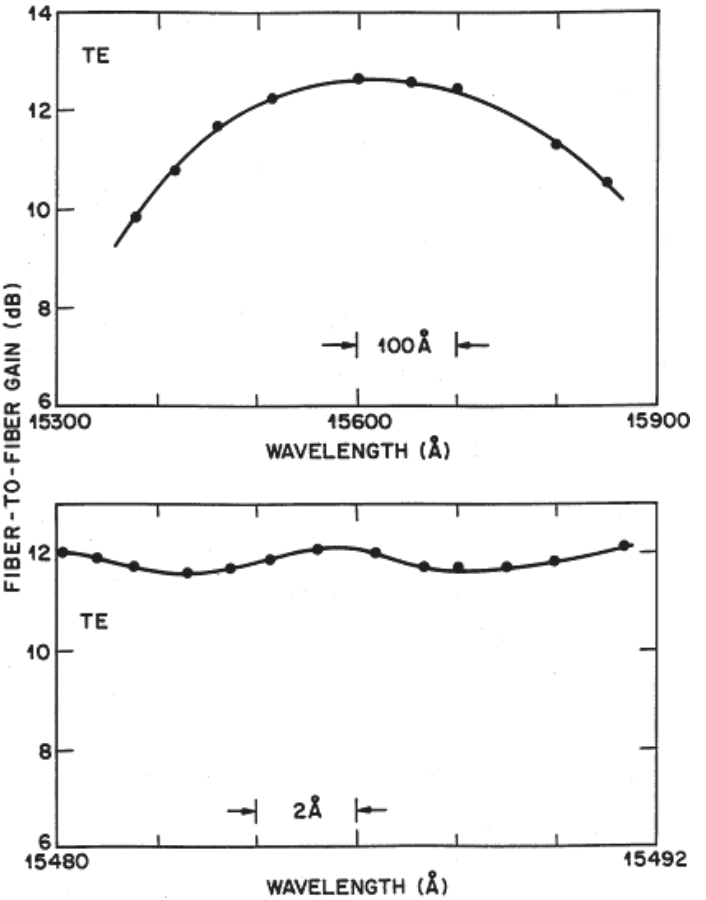

Fig. 5.3.4. Measured gain as a function of wavelength for the TE mode.

of 0.6 dB at 26 dB internal gain is 9×10^{-5}. The 3-dB bandwidth of the optical gain spectrum is 45 nm for this device.

It has been shown that the gain ripple and polarization dependence of gain correlate well with the ripple and polarization dependence of the amplified spontaneous emission spectrum. Measurements of amplified spontaneous emission are much simpler to make than gain measurements, and provide a good estimate of the amplifier performance [11, 13]. This is discussed in detail in Sec. 5.5. Buried facet and cleaved facet traveling wave amplifiers have

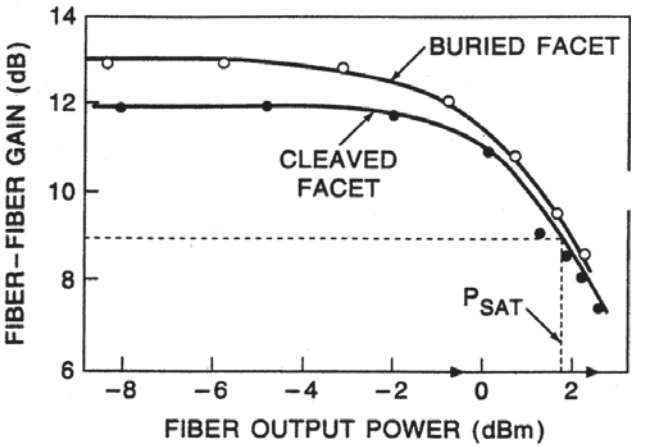

Fig. 5.3.5. A comparison of gain vs. saturation power of buried facet and cleaved facet traveling wave amplifiers [11].

been well studied. Figure 5.3.5 shows the typical output saturation characteristics of these amplifiers.

5.4. Tilted Facet Amplifiers

Another way to suppress the resonant modes of the Fabry-Perot cavity is to slant the waveguide (gain region) from the cleaved facet so that the light incident on it internally does not couple back into the waveguide [14]. The process essentially decreases the effective reflectivity of the tilted facet relative to a normally cleaved facet. The reduction in reflectivity as a function of the tilt angle is shown in Fig. 5.4.1 for the fundamental mode of the waveguide.

Schematic of a tilted facet optical amplifier is shown in Fig. 5.4.2 [14]. Waveguiding along the junction plane is weaker in this device than that for the strongly index guided buried heterostructure device. Weak index guiding for the structure of Fig. 5.4.2 is provided by a dielectric defined ridge. The fabrication of the device follows a procedure similar to that described previously.

The measured gain as a function of injection current for TM and TE polarized light for a tilted facet amplifier is shown in

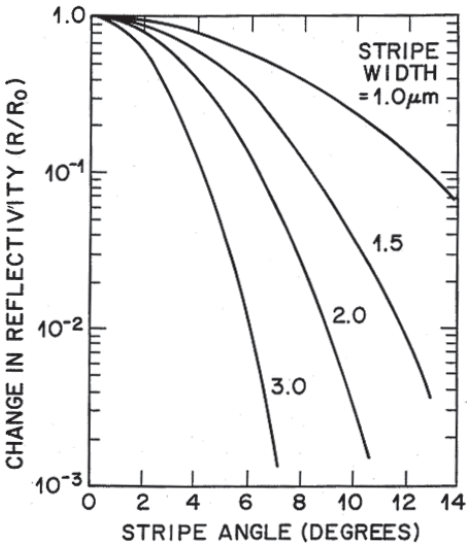

Fig. 5.4.1. Calculated change in reflectivity as a function of tilt angle of the facet.

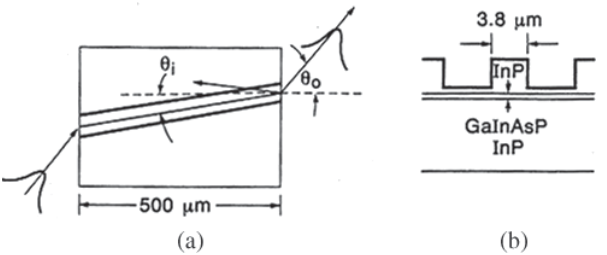

Fig. 5.4.2. Schematic of a tilted facet amplifier [14].

Fig. 5.4.3 [14]. Optical gains as high as 30 dB have been obtained using titled facet amplifiers. Although the effective reflectivity of the fundamental mode decreases with increasing tilt of the waveguide, the effective reflectivity of the higher order modes increases. This may cause appearance of higher order modes at the output (which may reduce fiber-coupled power significantly), especially for large ridge widths.

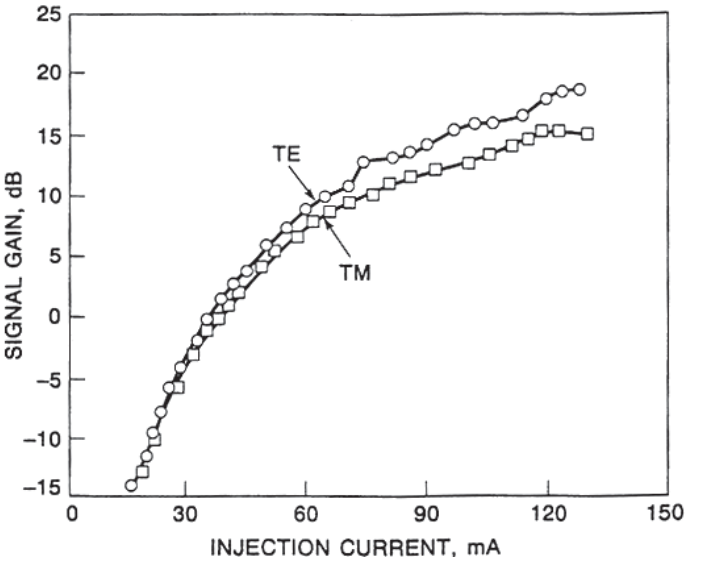

Fig. 5.4.3. Measured gain is plotted as a function of injection current [14].

5.5. Amplified Spontaneous Emission and Optical Gain

The optical gain measurements require an elaborate set up and thus it is time consuming, which can make it unsuitable to perform in a manufacturing setting. In this section, it is shown that a significant portion of the relevant information may be derived from amplified spontaneous measurements.

The light vs. current (L-I) characteristics and the amplified spontaneous emission spectrum of a buried facet amplifier is shown in Fig. 5.5.1. The L-I curve exhibits a soft turn on (I_a in Fig. 5.5.1(a)). The turn on is a result of amplification of the spontaneous emission. For high gain, the amplifier should be operated at currents larger than I_a. Figure 5.5.1(b) of he amplified spontaneous emission spectrum shows that the spectrum shifts to shorter wavelength with increasing current. This is primarily due to filling of the band with injected electrons and holes. This is discussed in Ch. 3. The high resolution spectrum of Fig. 5.5.1(c) shows the modulation of the intensity

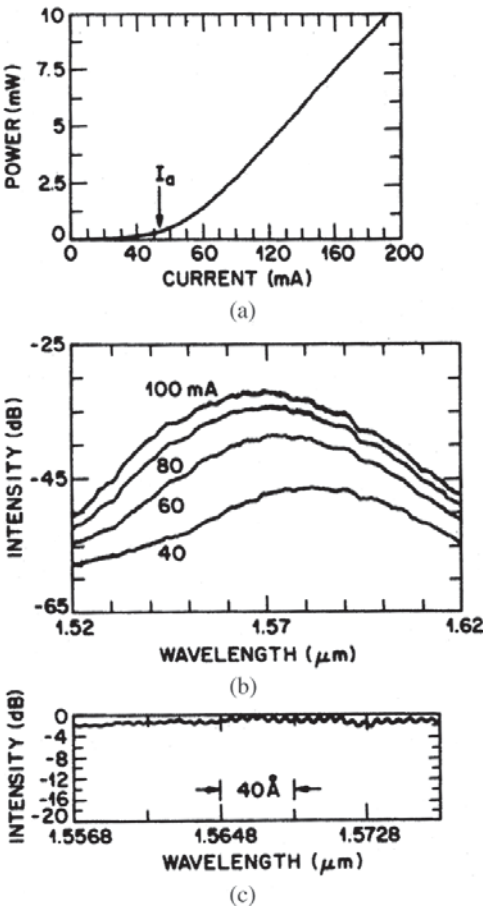

Fig. 5.5.1. (a) Light vs. current characteristics of an optical amplifier (b) Amplified spontaneous emission spectrum at three currents (c) Amplified spontaneous emission spectrum under high resolution showing the longitudinal modes.

at the longitudinal mode spacing caused by residual reflectivity of the facets.

The relationship between the optical gain, current and amplified spontaneous emission is calculated as follows. The material gain at an injection current density n is approximately given by

$$g = a(n - n_0), \tag{5.5.1}$$

where a is the gain constant and n_0 is the injected carrier density needed for transparency.

The signal gain G, the amplified spontaneous emission power P, and the injection current I are given by [8,15]

$$G = \exp[(\Gamma g - \alpha)L], \tag{5.5.2}$$

$$P = h\nu f W d B n^2 (G-1)/(\Gamma g - \alpha), \tag{5.5.3}$$

$$I = eWdL(Bn^2 + Cn^3), \tag{5.5.4}$$

where B and C are radiative and Auger recombination constants respectively, W, D, L are the width, thickness and length of the gain medium respectively, Γ is the confinement factor, α is the optical absorption, $h\nu$ is the photon energy, e is the charge of the electron and f is the fraction of spontaneous emission that gets amplified.

As an example, the calculated signal gain and amplified spontaneous emission power as a function of injection current is shown in Fig. 5.5.2 [11]. The parameters used are $L = 500\,\mu\text{m}$, $d = 0.4\,\mu\text{m}$, $W = 1.5\,\mu\text{m}$, $C = 10^{-28}\,\text{cm}^6\,\text{s}^{-1}$, $B = 1.2 \times 10^{10}\,\text{cm}^3\,\text{s}^{-1}$. At an amplified spontaneous emission (ASE) of few mW optical gain of ~25–30 dB is feasible. The calculated ASE shows a turn on similar to that observed. The actual values will depend on the value of the parameters used in the calculation.

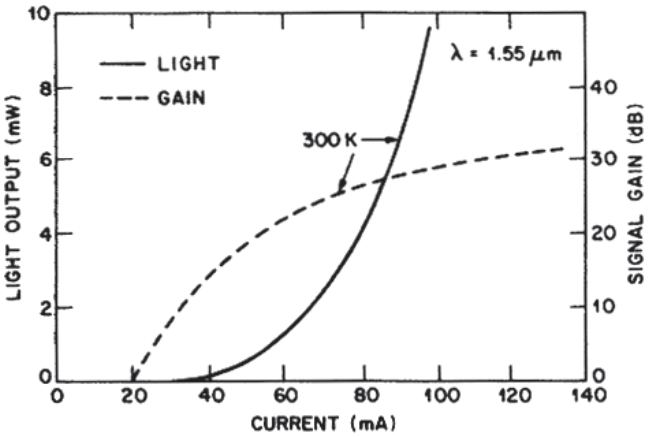

Fig. 5.5.2. Calculated signal gain and amplified spontaneous emission power as a function of current.

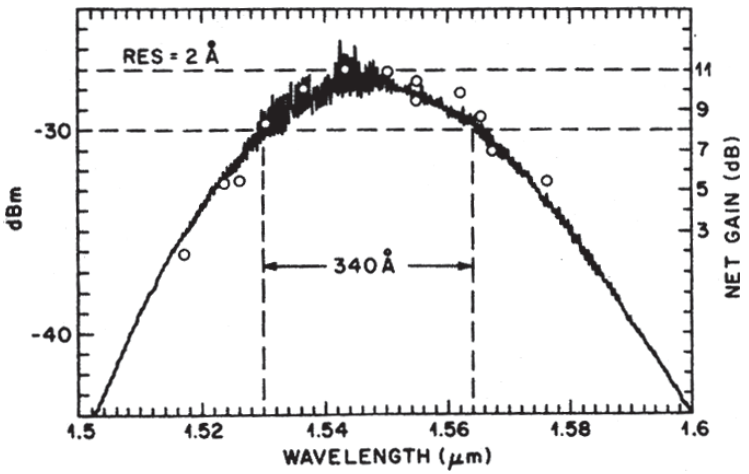

Fig. 5.5.3. ASE spectrum and the amplifier gain (open circles) as a function of wavelength [11].

The ASE spectrum is also a good measure of the position of the gain peak, full width at half maximum of the gain curve and the gain ripple. This is expected from Eq. (5.5.3) since the ASE is proportional to the amplifier gain G. Figure 5.5.3 shows the measured gain and the ASE as a function of wavelength. The correlation between the gain roll-off and the ASE intensity is good.

The gain ripple i.e. the small variation in gain at longitudinal mode spacing is caused by the residual facet reflectivity. The gain ripple also appears on the ASE spectrum. Figure 5.5.5 shows the gain ripple plotted as a function of the ASE ripple. The good correlation shows that the ASE ripple can provide a good indication of gain ripple. The ASE ripple is obtained from the amplified spontaneous emission spectrum. The gain ripple is obtained by measuring the gain as a function of wavelength. A tunable external cavity laser is used as the source of tunable wavelength for the measurement of gain ripple. The light from the laser was coupled into the amplifier using a single mode optical fiber.

Another factor of importance for amplifiers used in fiber systems is low polarization dependence of gain. The ASE has been measured along the TE and TM directions using a polarizer at the output.

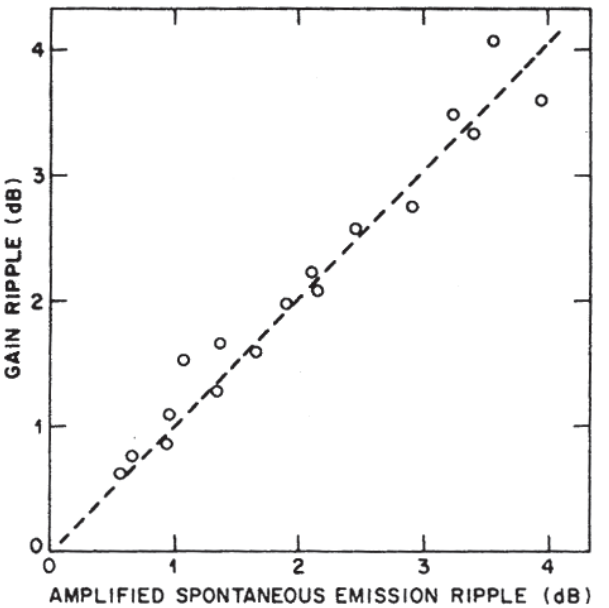

Fig. 5.5.4. Gain ripple plotted as a function of ASE ripple [11]. The dashed represents an ideal correlation with a unity slope.

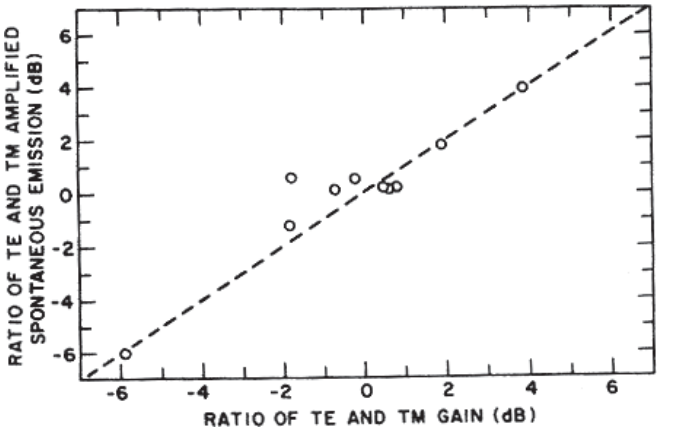

Fig. 5.5.5. Polarization dependence of ASE (ratio of TE polarized ASE power to TM polarized ASE power) is plotted as a function of polarization dependence of gain (ratio of TE polarized gain to TM polarized gain) [11].

Figure 5.5.5 shows a plot of the ratio of the TE-TM polarized gain versus the ratio of the TE to TM polarized ASE. The dashed line is for ideal correlation. The departure from ideal behavior may be due to gain ripple since the gain measurements are carried out at specific wavelengths and the ASE represents an average over a wavelength window.

Much of the discussions in this chapter have been using the InGaAsP/InP material system which is used to fabricate amplifiers for operation in the 1.3 μm and 1.55 μm spectral regions. These concepts related to low reflectivity are applicable also for other material systems. The importance of reflectivity was recognized in the early work on semiconductor optical amplifiers [17–20].

References

[1] Y. Yamamoto, *J. Lightwave Technol.* **LT-16**, 1047 (1980).
[2] T. Mukai, Y. Yamamoto and T. Kimura, *IEEE Trans. Microwave Theory Tech. MIT* **30**, 1548 (1982).
[3] T. Saitoh and T. Mukai, *IEEE J. Quantum Electron.* **QE-32**, 1010 (1987).
[4] T. Saitoh and T. Mukai, *J. Lightwave Technol.* **LT-6**, 1656 (1988).
[5] G. Eisentein and R. M. Jopson, *Int. J. Electron.* **60**, 113 (1986).
[6] J. C. Simon, *J. Lightwave Tech.* **LT-5**, 1286 (1987).
[7] M. G. Oberg and N. A. Olsson, *Electron. Lett.* **23**, 1114 (1986).
[8] M. O'Mahony, *J. Lightwave Technol.* **5**, 531 (1988).
[9] G. P. Agrawal and N. K. Dutta, "Semiconductor Lasers" Van Nostrand Reinhold, NY, Chapter 11, 1992.
[10] N. A. Olsson, *J. Lightwave Technol.* **LT-7**, 1071 (1989).
[11] N. K. Dutta, M. S. Lin, A. B. Piccirilli and R. L. Brown, *J. Appl. Phys.* **67**, 3943 (1990).
[12] H. Kogelnik and T. Li, *Proc. IEEE* **54**, 1312 (1966).
[13] M. S. Lin, A. B. Piccirilli, Y. Twu and N. K. Dutta, *Electron Lett.* **25**, 1378 (1989).
[14] C. E. Zah, J. S. Osinski, C. Caneau, S. G. Menocal, L. A. Reith, J. Salzman, F. K. Shokoohi and T. P. Lee, *Electron. Lett.* **23**, 1990 (1987).
[15] N. K. Dutta and R. J. Nelson, *J. Appl. Phys.* **53**, 74 (1982).
[16] M. J. Coupland, K. G. Mambleton and C. Hilsum, *Phys. Lett.* **7**, 231 (1963).
[17] J. W. Crowe and R. M. Craig, Jr. *Appl. Phys. Lett.* **4**, 57 (1964).
[18] W. F. Kosnocky and R. H. Comely, *IEEE J. Quantum Electron.* **QE-4**, 225 (1968).
[19] T. Saitoh and T. Mukai, Ch. 7 in Coherence, Amplification and Quantum Effects in Semiconductor Lasers, Ed. by Y. Yamamoto. New York: Wiley, 1991.
[20] M. Nakamura and S. Tsuji, *IEEE J. Quantum Electron.* **QE-17**, 994 (1981).

Chapter 6

Amplifier Rate Equations and Operating Characteristics

6.1. Introduction

The dynamics of semiconductor optical amplifier performance and application in optical communication systems is discussed in this Chapter. A traveling wave amplifier with very low facet reflectivity ($\sim$0.01%) is a promising candidate for amplifier applications. The amplifier has a large bandwidth ($\sim$5 THz), this allows amplification of pulses as short as few ps. If the amplifier is operated in the linear regime, the amplified pulse is a replica of the input pulse, However, in most cases the amplifier operates near saturation particularly near the peak of the pulse, this results in time dependent optical gain. Thus the amplified pulse undergoes a change in shape. The leading edge of the pulse saturates the amplifier which results in a lower gain for the trailing edge. The gain nonlinearity is accompanied by nonlinearities in the refractive index. This may be viewed as follows. The gain saturation leads to a change in carrier density which results in a change in refractive index. The amount of index change is a nonlinear function of the instantaneous intensity of the pulse. This nonlinear refractive index induces a time dependent phase shift and hence a time dependent frequency shift (chirp) on the pulse. The spectrum generally shifts to the long wavelength side (red shift).

Optical amplifiers have been used in several optical transmission experiments with good performance. The application areas are in-line amplification and pre-amplification. As an in-line amplifier, the amplifier is used to compensate for the optical losses during transmission. This allows longer distance transmission without

regeneration of the optical signal through an optical to electrical conversion, signal retiming and back to optical conversion process. Error-free transmission over more than 300 km has been demonstrated. For pre-amplification, the amplifier is used in front of the photodiode in the receiver to increase the receiver sensitivity.

Amplifiers degrade the signal to noise ratio (SNR) of the amplified signal primarily because of amplified spontaneous emission which adds to the signal. The effect of spontaneous emission is to add fluctuations in the signal which adds noise to the detected photocurrent. The SNR degradation is generally characterized by a quantity called noise figure, F which is defined as the ratio of the SNR value at the input of the amplifier to the SNR value at the output of the amplifier. The smallest noise figure possible is 3 dB. However, in real systems values of ∼6 to 8 dB range is common. This is due to signal-spontaneous beat noise and spontaneous-spontaneous beat noise that fall within the receiver bandwidth. Various amplifier noise issues are discussed in this chapter. Amplifier characteristics have been studied by several authors [1–19].

6.2. Amplifier Rate Equations for Pulse Propagation

In this section, the basic rate equations for pulse propagation in semiconductor optical amplifiers is developed [20–27]. The amplitude and the phase change of an optical signal propagating through the SOA is a result of gain saturation. The propagation of an electromagnetic field inside the amplifier is governed by the wave equation

$$\nabla^2 \overrightarrow{E} - \frac{\varepsilon}{c^2} \frac{\partial^2 \overrightarrow{E}}{\partial t^2} = 0, \tag{6.2.1}$$

where $\overrightarrow{E}(x, y, z, t)$ is the electric field vector of the wave, c is the velocity light and ε is the dielectric constant of the amplifier medium. The dielectric constant is given by

$$\varepsilon = n_b^2 + \chi, \tag{6.2.2}$$

where n_b is the background refractive index which takes into dielectric waveguiding in the semiconductor medium. It is, in general, a

function of x, y which represent the transverse coordinates of the waveguide medium. The susceptibility χ represents the effect of injected carriers on the dielectric constant. It depends on the injected carrier density n. The exact dependence of χ on n is quite complicated. However, a phenomenological model is found to be quite effective. In this model χ is given by [23]

$$\chi(n) = -\frac{\bar{n}c}{\omega_0}(\alpha + i)g(n), \tag{6.2.3}$$

where $\bar{n}$ is the effective mode index. As discussed in Ch. 3, the optical gain g approximately varies as

$$g = a(n - n_0), \tag{6.2.4}$$

where a is the gain constant, n is the injected carrier density and n_0 is the carrier density needed for transparency. The carrier induced change in index is accounted for using the linewidth enhancement factor, α, which is the ratio of the change in real part of the index to the imaginary part of the index. The latter represents optical gain. The typical values of α are in the range of 3 to 8. It is useful to make some simplifying approximation of the wave equation. Assume a traveling wave amplifier with a single propagating optical mode whose electric field distribution is $\phi(x, y)$. Assume the light is linearly polarized and it remains linearly polarized in the amplifier. The electric field $\overrightarrow{E}(x, y, z, t)$ can then be written as

$$\overrightarrow{E}(x, y, z, t) = \hat{\varepsilon}\frac{1}{2}\{\phi(x, y)A(z, t)\exp[i(k_0 z - \omega_0 t)] + \text{c.c.}\}, \tag{6.2.5}$$

where $\hat{\varepsilon}$ is the polarization unit vector, $k_0 = \bar{n}\omega_0/c$, ω_0 is the photon angular frequency, and, $A(z, t)$ is the slowly varying amplitude of the propagating wave. Using Eqs. (6.2.1) and (6.2.5) and neglecting second derivatives of $A(z, t)$ with respect to t, and z and integrating over the transverse dimensions x, y, we obtain

$$\frac{\partial^2\phi}{\partial x^2} + \frac{\partial^2\phi}{\partial y^2} + (n_b^2 - \bar{n}^2)\frac{\omega_0^2}{c^2}\phi = 0, \tag{6.2.6}$$

$$\frac{\partial A}{\partial z} + \frac{1}{v_g}\frac{\partial A}{\partial t} = \frac{i\omega_0\Gamma}{2\bar{n}c}\chi A - \frac{1}{2}\alpha_{\text{int}}A, \tag{6.2.7}$$

where the group velocity $v_g = c/n_g$, the group index n_g is given by

$$n_g = \bar{n} + \omega_0 \left(\frac{\partial \bar{n}}{\partial \omega} \right)$$

The confinement factor, Γ is given by

$$\Gamma = \frac{\int_0^w \int_0^d |\phi(x,y)|^2 dxdy}{\int_{-\infty}^{\infty} \int_{-\infty}^{\infty} |\phi(x,y)|^2 dxdy}. \tag{6.2.8}$$

The solution of Eq. (6.2.6) with appropriate boundary conditions provides the mode index n and the transverse field distribution $\phi(x, y)$. The last term in Eq. (6.2.7) represents the optical loss of the mode. The quantities w and d are the width and thickness of the amplifier active region. The loss coefficient is α_{int}. The confinement factor Γ in Eq. (6.2.7) takes into account the effect of the transverse mode. The group velocity dispersion has been neglected in the above Eq. (6.2.7) since the amplifier lengths are typically small ($\sim$1 mm).

The evolution of carrier density n can be described by the following Eq. (6.2.9) [23]. The equation assumes that the carrier density is nearly uniform in the transverse direction and hence an average value can be used. Also, carrier diffusion has been neglected since the amplifier length is much larger than the diffusion length and the width, thickness are much smaller than the diffusion length. In Eq. (6.2.9) V is the volume of the active region, I is the injected current, e is the charge of the electron, τ_c is the carrier lifetime, and σ_{m} is the cross section of the active region.

$$\frac{\partial n}{\partial t} = \frac{I}{eV} - \frac{n}{\tau_c} - \frac{\Gamma g(n)}{\hbar \omega_0 \sigma_m} |A|^2. \tag{6.2.9}$$

For pulse propagation, Eqs. (6.2.7) and (6.2.9) can be further simplified by using the retarded time frame:

$$\tau = t - z/v_g. \tag{6.2.10}$$

Then, we obtain

$$\frac{\partial n}{\partial \tau} = \frac{I}{eV} - \frac{n}{\tau_c} - \frac{\Gamma g(n)}{\hbar\omega_0 \sigma_m}|A|^2, \tag{6.2.11}$$

$$\frac{\partial A}{\partial z} = \frac{i\omega_0 \Gamma}{2\bar{n}c}\chi A - \frac{1}{2}\alpha_{\text{int}} A. \tag{6.2.12}$$

We assume

$$A = \sqrt{P}\exp(i\phi), \tag{6.2.13}$$

where $P(z, \tau)$ and $\phi(z, \tau)$ are the instantaneous power and the phase of the propagating pulse, respectively. Using Eqs. (6.2.3) to (6.2.13), we obtain the following equations [23]:

$$\frac{\partial A}{\partial z} = \frac{g}{2}(1 + i\alpha)A, \tag{6.2.14}$$

$$\frac{\partial g}{\partial \tau} = -\frac{g - g_0}{\tau_c} - \frac{gP}{E_s}, \tag{6.2.15}$$

$$\frac{\partial P}{\partial z} = (g - \alpha_{\text{int}})P, \tag{6.2.16}$$

$$\frac{\partial \phi}{\partial z} = -\frac{1}{2}\alpha_{\text{g}}. \tag{6.2.17}$$

Equation (6.2.14) is the equation for the complex amplitude A. The quantity $E_s = \tau_c P_s \cdot P_s$ is the saturation power of the amplifier which is given by

$$Ps = h\omega_0\, \sigma_{\text{m}}/(a\Gamma\tau_{\text{c}}), \tag{6.2.18}$$

g_0 is the small signal gain, which is given by

$$g_0 = \Gamma a(I\tau_c/eV - n_0), \tag{6.2.19}$$

and $\sigma_m \cong wd$ (w and d are the width and thickness of the active layer).

6.3. Pulse Amplification

For many applications, a series of intensity modulated signals are injected into the amplifier. Such intensity modulated pulses are short

in duration for high speed communication systems. Amplification of pulses of light is considered in this section. Using the formulation of the previous section, a net gain $g(z,\tau)$ can be defined as

$$g(z,\tau) = g - \alpha_{\text{int}}. \tag{6.3.1}$$

Equation (6.2.16) can be integrated over the amplifier length to provide the following expression for output power P_{out} (τ)

$$P_{\text{out}}(\tau) = P_{\text{in}}(\tau)\exp[h(\tau)], \tag{6.3.2}$$

where P_{in} (τ) is the input power and $h(\tau)$ is the total integrated net gain defined as

$$h(\tau) = \int_0^L g(z,\tau)dz. \tag{6.3.3}$$

Under the assumption that the pulse width $\tau_0 \ll \tau_c$, the first term in Eq. (6.2.15) can be neglected. Then Eq. (6.2.15) can be integrated over the amplifier length L to provide the following equation for h(t).

$$\frac{dh}{d\tau} = -\frac{P_{\text{in}}(\tau)}{E_s}(e^h - 1). \tag{6.3.4}$$

Equation (6.3.4) can be integrated to obtain h(τ) for different input pulse shapes $P_{\text{in}}(\tau)$. The parameter of interest is the evolution of total gain $G(t)$ as a function of time. From Eq. (6.3.4) it is given by [23]

$$G(\tau) = \exp(h(\tau)) = \frac{G_0}{G_0 - (G_0 - 1)\exp[-E_0(\tau)/E_s]}, \tag{6.3.5}$$

where G_0 is the unsaturated gain of the amplifier and the quantity $E_0(\tau)$ is given by

$$E_0(\tau) = \int_{-\infty}^{\tau} P_{\text{in}}(\tau)d\tau \tag{6.3.6}$$

Equation (6.3.5) shows the gain is time dependent i.e. different portion of the pulse experience different amounts of gain. This leads to a modification of the pulse shape after transmission through the

amplifier. For the purpose of a general discussion, a super-Gaussian pulse is used as the input.

$$P_{\text{in}}(\tau) = P_0 \exp[-(\tau/\tau_p)^{2m}], \tag{6.3.7}$$

where m is the shape parameter. For $m = 1$, the pulses are Gaussian and it becomes flat topped as m increases. Figure 6.3.1 shows the output pulse shape for a Gaussian input pulse for several values of unsaturated gain G_0. The pulse is given by

$$P_{\text{in}}(\tau) = P_0 \exp[-(\tau/\tau_0)^2]. \tag{6.3.8}$$

Figure 6.3.1 is obtained by solving the above equations. The calculated pulse shape for several values of gain is shown. For higher gain, the output pulse is asymmetric, i.e. the leading edge of the pulse has a faster rise time than the trailing edge.

The optical gain is accompanied by a change in phase. The gain changes the carrier density in the material. The phase of the propagating pulses change because the real index varies with the carrier density. The total phase change for the pulse propagating through

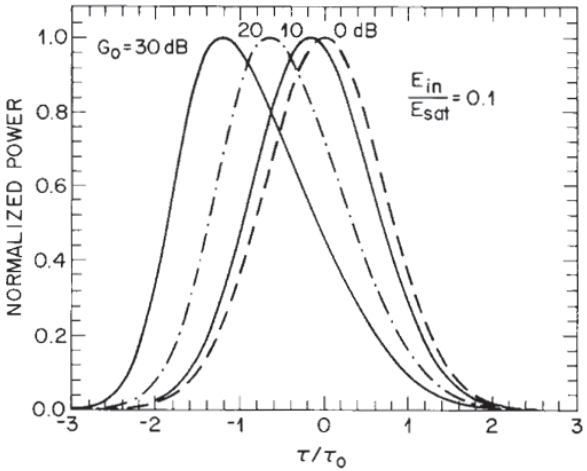

Fig. 6.3.1. Output amplified pulse shape for several values of τ/τ_0 when a Gaussian pulse of width τ_0 is amplified by an amplifier. The output pulse is shown for several values of small signal gain [23].

the amplifier is given by integrating Eq. (6.2.17) [23]

$$\phi(\tau) = -\frac{1}{2}\alpha \int_0^L g(z,\tau)d\tau = -\frac{1}{2}\alpha h(\tau), \tag{6.3.9}$$

where α is the linewidth enhancement factor. The value of α depends on the wavelength of the input light. It is typically in the 3 to 8 range for regular double heterostructure gain region and is smaller (∼2 to 5) for multiquantum well gain region.

A time dependent phase change leads to a variation in optical frequency of the pulse. The instantaneous variation in frequency, known as the frequency chirp $\Delta\nu(\tau)$ is given by

$$\Delta\nu(\tau) = -\frac{1}{2\pi}\frac{d\phi}{d\tau} = \frac{\alpha}{4\pi}\frac{dh}{d\tau}. \tag{6.3.10}$$

The chirp of the output pulse $\Delta\nu_{\text{out}}(\tau)$ is given by $\Delta\nu_{\text{out}}(\tau) = \Delta\nu_{\text{in}}(\tau) + \Delta\nu(\tau)$ where $\Delta\nu_{\text{in}}(\tau)$ is the chirp of the input pulse. Figure 6.3.2 shows the pulse spectrum during the evolution of a Gaussian pulse for various amplifier gains. The linewidth enhancement factor, $\alpha = 5$ is used in the calculation. For high gain the spectrum has multiple peaks. With increasing gain, the main peak in the spectrum shifts

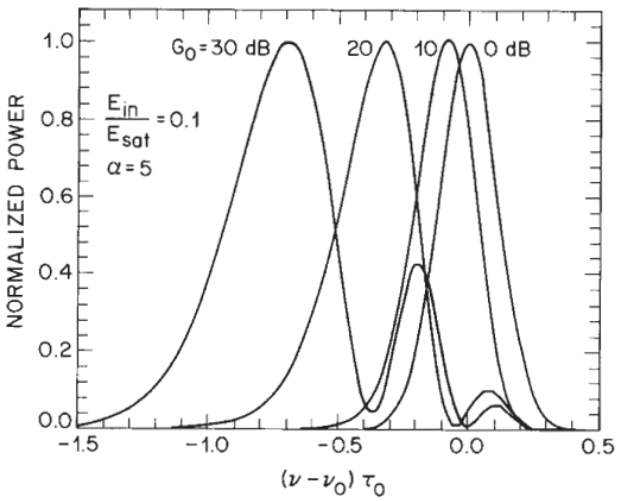

Fig. 6.3.2. Output pulse spectrum for an input Gaussian pulse [23].

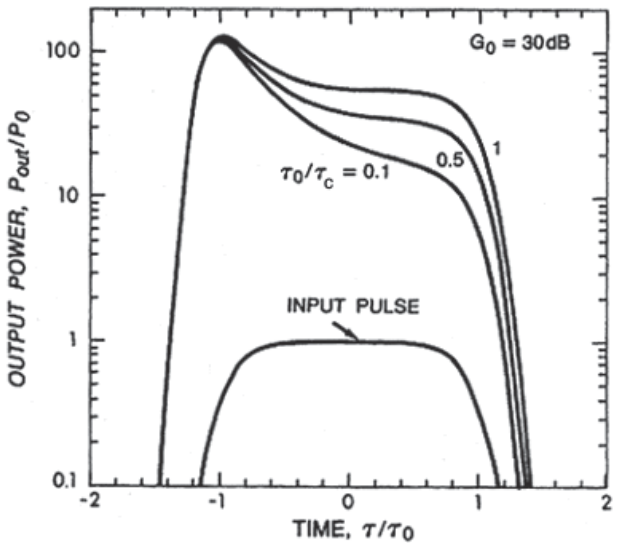

Fig. 6.3.3. Amplified pulse shape for several values of τ_0/τ_c when a super-Gaussian pulse of with τ_0 is amplified by an amplifier with a small signal gain of 30 dB [28].

to the low frequency side (red shift) The shift is larger than the spectral width of the pulse. For 10 ps wide pulses, the shift can exceed 100 GHz.

The phenomenon of multiple peaks in the output spectrum and the associated change in output phase is called self phase modulation (SPM). Such SPM induced broadening has been observed in the amplifier output spectrum.

Figure 6.3.3 shows the shape of the output pulse for a super-Gaussian input pulse of width τ_0. The complete Eq. (6.2.15) for the temporal evolution of gain is used in this calculation [23]. The pulse shape is calculated for various values of τ_0/τ_c. The x-axis is in units of τ_0. The pulse energy is chosen so that $E_{\rm in}/E_{\rm s} = 0.1$. The amplifier has a 30 dB small signal gain. The calculated pulse distortion is larger for short pulses (small τ_0/τ_c).

As before, a numerical solution of Eq. (6.3.10) gives $\Delta\upsilon(\tau)$ as a function of time for super Gaussian pulses. Figure 6.3.4 shows the frequency chirp of an amplified pulse for various values of pulse energies.

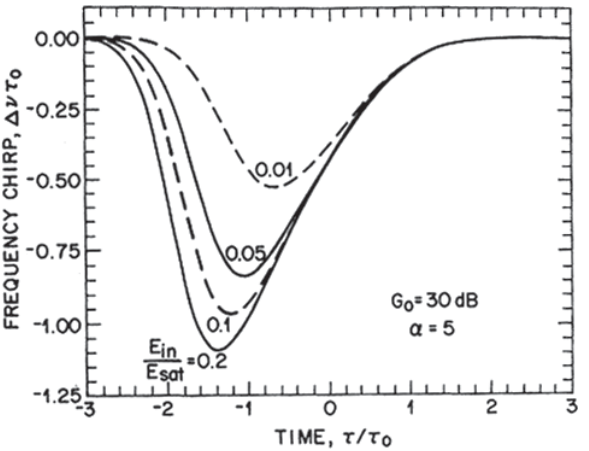

Fig. 6.3.4. Frequency chirp as a function of time during the pulse duration for various pulse energies [28].

The frequency chirp is larger for higher energy pulses because the gain saturation occur earlier for such pulses. A value of 5 for α is used in the calculation.

In addition to the above frequency chirp pulses propagating through a SOA also exhibit self phase modulation. This happens for high enough energies for which the index varies with the intensity of the pulse.

6.4. Multichannel Amplification

An early motivation behind the development of SOA has been simultaneous amplification of many signals at different wavelengths such as that used in a wavelength division multiplexed (WDM) communication system. An error free amplification is possible if there is no cross talk between light at different wavelengths. Cross talk can arise from two mechanisms viz. gain saturation and carrier density modulation. Gain saturation results in cross talk because presence of one signal saturates the gain of the other. This is similar to cross gain modulation discussed previously. If the amplifier is operated in the unsaturated regime the gain saturation induced cross talk can be made small. Experimental and theoretical studies of multichannel amplification have been published [29–37].

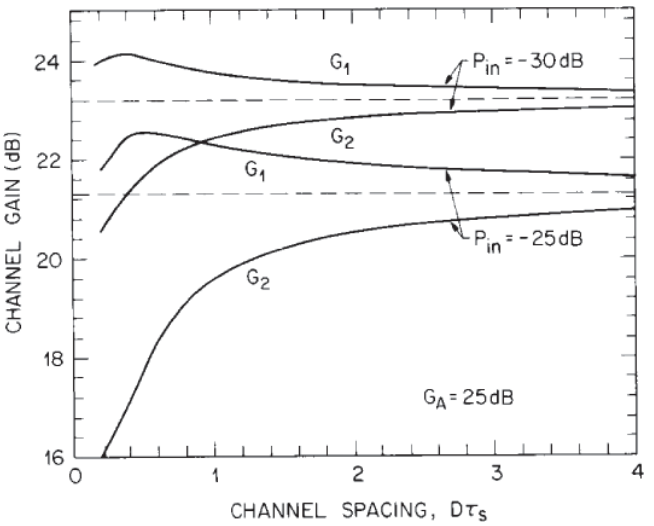

Fig. 6.4.1. The optical gain is plotted as a function of $D\tau_s$ where τ_s is the carrier lifetime in the amplifier and D is the frequency separation between the two input signals [37].

In the presence of two optical signals at two different frequencies the carrier density in the SOA is modulated at the difference frequency. The carriers modulating at this difference frequency in turn can interact with the optical signals to produce sidebands on the input optical frequencies. The process is similar to four-wave mixing. The sidebands act as noise sources for the other channels when SOA is used in a multichannel system. The cross gain effect as a function of frequency spacing between the two input signals and the sideband powers for a SOA has been calculated [37].

Figure 6.4.1 shows the calculated variation of gain of the input signals as a function of the frequency separation $D\tau_s$ where τ_s is the carrier lifetime in the amplifier and D is the frequency separation between the two input signals. The input powers P_1 and P_2 of the two signals are assumed to be the same. The two cases shown in Fig. 6.4.1 are for equal input powers of -30 dBm and -25 dBm respectively. The unsaturated gain of the amplifier is 25 dB. The quantities G_1 and G_2 are the optical gains of the two signals. They are defined as the ratio of the output power and the input power for the amplifier.

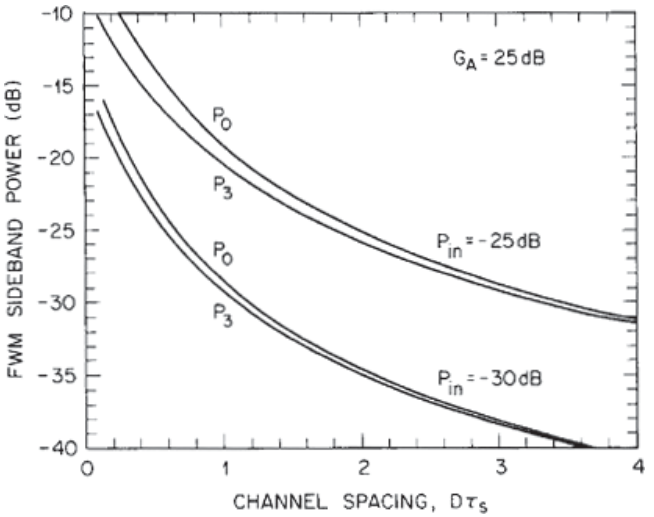

Fig. 6.4.2. Calculated low frequency P_0 and high frequency P_3 side band powers as a function of $D\tau_s$ [37].

For large channel spacing, the optical gains of the two signals are close. The effect of four wave mixing is to decrease the gain for the low frequency signal and increase it for the high frequency signal. The gain difference is much larger for the high power input case (-25 dBm) compared to that for the low power input (-30 dBm). The saturation power is assumed to be 0 dBm (1 mW) in the calculation. The intensity of the sidebands relative to the saturation power is shown in Fig. 6.4.2. P_0 and P_3 refers to the power in the low frequency and high frequency sidebands. The side band powers are large for low $D\tau_s$. The typical value of τ_s is $\sim$0.2 to 0.5 ns. The large crosstalk limits SOA use in WDM systems.

6.5. Amplifier Application in Optical Transmission Systems

In an optical transmission system, as the optical signal travels through the fiber, it weakens and gets distorted. Regenerators are used to restore the optical pulses to their original form. Figure 6.5.1(a) shows the block diagram of a typical lightwave regenerator. Its main components are an optical receiver, an optical

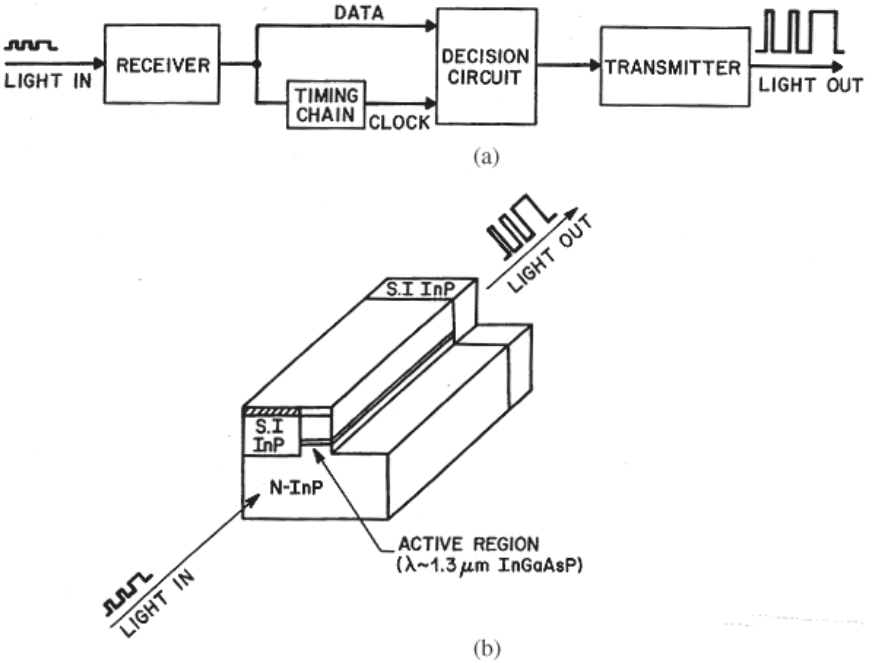

Fig. 6.5.1. (a) Block diagram of a lightwave regenerator, (b) Schematic of a semiconductor optical amplifier used as an amplifier.

transmitter, and electronic timing and decision circuits. Optical amplifiers can nearly restore the original optical pulses and thereby increase the transmission distance without using conventional regenerators. An example of SOA that functions as a regenerator is shown schematically in functions Fig. 6.5.1(b). The semiconductor amplifiers need external current to produce gain and fiber amplifiers need pump lasers for the same purpose. Because of its simplicity, an optical amplifier is an attractive alternative to regenerators.

In current optical transmission systems, fiber amplifiers are used for amplification. The properties of fiber amplifiers are discussed in several articles [38–44]. The fiber amplifiers used in communication systems consists of a doped silica fiber (Er doping produces gain near 1.55 μm) which is pumped by a semiconductor laser (pump laser) operating near 0.98 μm or 1.48 μm. The pump laser excites the Er atoms to a higher energy level and when it makes a transition to a

lower energy level the stimulated photons (gain) are emitted in the presence of a signal photon. Thus the signal propagating in the fiber is amplified by the fiber amplifier. The advantages of fiber amplifiers over SOA are polarization independent gain and high saturation power. Although SOA's can be made with polarization independent gain and low facet reflectivities, these SOA's generally have low saturation powers. SOA's with high saturation power have quantum well active region which also have a significantly higher gain in the TE polarization than that for the TM polarization. SOA has the advantage of much lower power consumption than a fiber amplifier and it can be monolithically integrated with other devices such as lasers, couplers etc. Thus it is useful to discuss the potential uses of SOA as an amplifier in a fiber transmission system [14–18, 45–53]

The fabrication and design of SOA that can serve as amplifiers are discussed in previous chapters. The main areas where the SOA can be used are as in-line amplifiers, as receiver pre-amplifiers and as power amplifiers. For in-line amplifier applications, the amplifier simply provides gain to compensate for the transmission losses between the transmitter and the receiver. For a receiver pre-amplifier, the amplifier provides gain to increase the signal level in front of the photodetector in the receiver thus increasing receiver sensitivity. For a power amplifier, the amplifier increases the output power of the transmitter. The optimum amplifier design depends on the application.

6.5.1. *In-line amplifiers*

In-line amplifiers can be used to compensate for optical losses in a fiber optic transmission system. Experiments have been carried out using both direct detection (on-off keying technique) and coherent detection. An in-line amplifier configuration used in a direct detection experiment is shown in Fig. 6.5.2. The signal source is a laser which emits in a single wavelength. In this experiment the laser is made to emit in a single frequency using an intracavity Bragg reflector fabricated using silicon waveguide technology (SCBR Laser in Fig. 6.5.2). In principle, any good single wavelength laser with

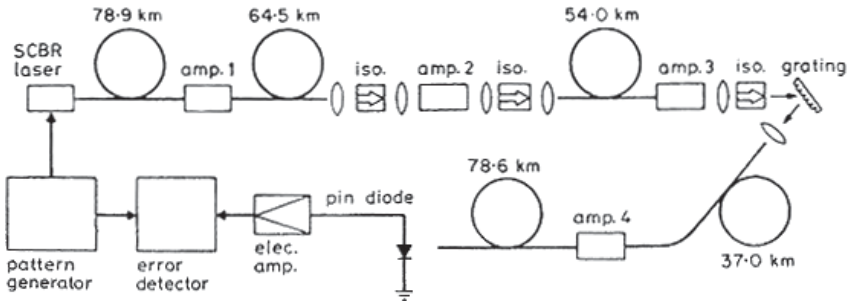

Fig. 6.5.2. Experimental set up for an in-line optical amplifier transmission experiment [52].

low spectral width under direct modulation should be usable. The laser output is modulated by modulating the laser current at 1 Gb/s. A total of 313 km of fiber representing a total optical loss of −69.9 dB is used between the transmitter (laser) and receiver. Three in-line amplifiers are used with the separations between them as stated in the figure. A fourth amplifier is used as a pre-amplifier in front of the receiver to amplify the signal so as to produce enough photocurrent. Optical isolators are used to reduce reflection effects. The total fiber–to–fiber coupling loss for each amplifier is estimated to be ∼10 dB.

An optical band pass filter (grating) is used at the output of amplifier #3 to reduce the amount of spontaneous emission. Figure 6.5.3 shows the measured bit-error-rate (BER) as a function of received power. The line with solid circles is for the 313 km transmission with amplifiers and the line with open circles is for back-to-back measurements. With four amplifiers and 313 km of fiber the receiver sensitivity (power needed for 10^{-9} bit error rate) increases by only 1.4 dB. This power penalty is due to a number of factors such as signal-spontaneous beat noise, pattern effects due to gain saturation and fiber dispersion.

An in-line amplifier configuration used in an experiment which utilizes coherent detection is shown in Fig. 6.5.4 [17]. The system has four amplifiers approximately 55 to 65 km apart. The total transmission distance is ∼372 km. The total internal gain of the amplifiers is ∼87 dB. However, due to coupling losses the net gain was ∼47 dB (50,000). The gain is sufficient to compensate for the coupling

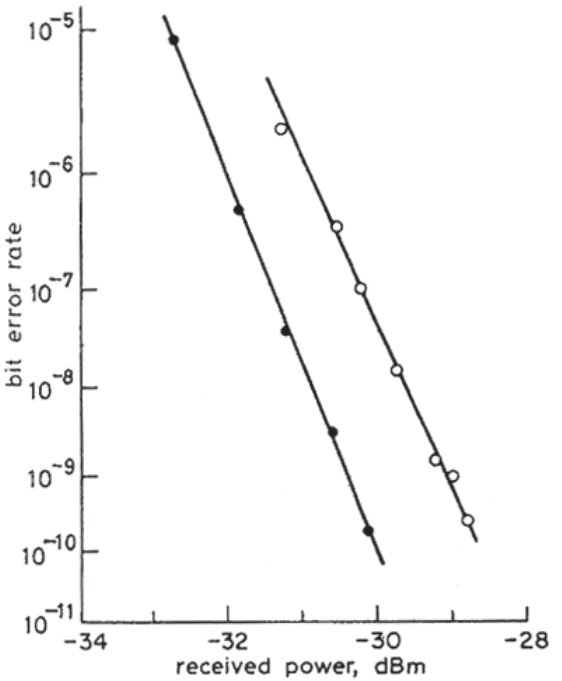

Fig. 6.5.3. Measured bit-error-rate (BER) as a function of received power. The line with solid circles is for the 313 km transmission with amplifiers and the line with open circles is for back-to-back (short fiber and no SOA) measurements [52].

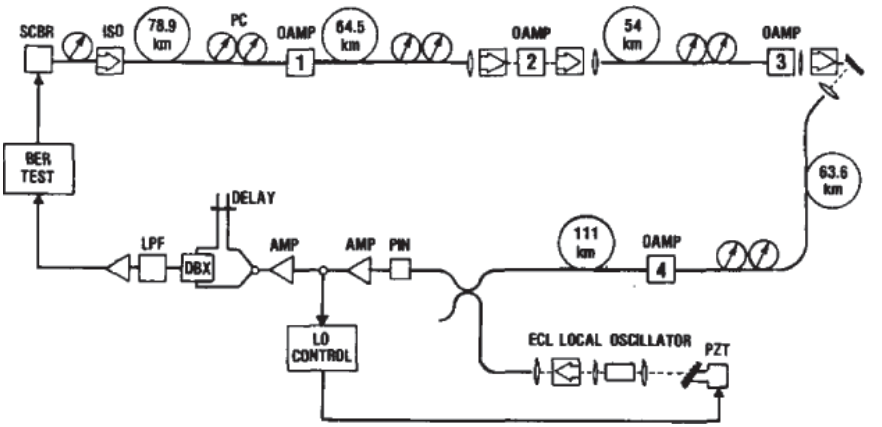

Fig. 6.5.4. Experimental set up for a long distance transmission experiment using semiconductor optical amplifiers [17].

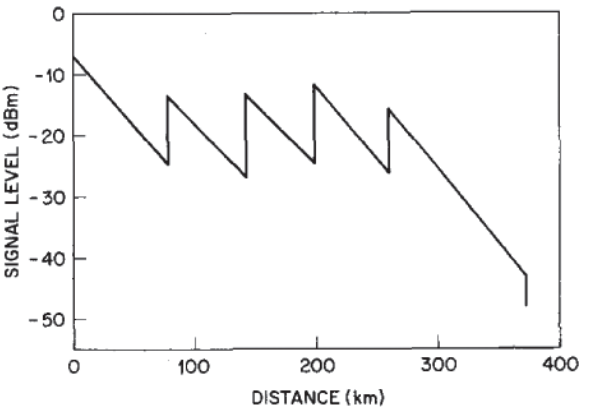

Fig. 6.5.5. Optical signal level along the transmission path [17].

losses. The system operated at 400 Mb/s with coherent detection and frequency shift keying (FSK) modulation format. The polarization controllers and isolators are inserted between amplifiers. The polarization controller is necessary for controlling the input polarization because both the isolators and amplifiers are sensitive to the polarization of input light.

Figure 6.5.5 shows the variation of optical power along the transmission path. In between the amplifiers the signal drops exponentially with distance (linear in the log scale) with the exponent given by fiber loss. The optical power is increased at each amplifier site by an amount equal to the amplifier net gain.

Figure 6.5.6 shows the bit-error-rate curves for the transmission experiment. Since the optical power is generally low ($\sim$1 mW) for in-line amplifier applications with a single wavelength transmission, the major amplifier requirements in addition to suitable gain are the polarization independent gain and absence of gain ripple due to non-zero facet reflectivity. Many fiber optic transmission systems use data at multiple wavelengths of light which propagate through the same fiber (Also known as Wavelength Division Multiplexed or WDM transmission). For these systems light at each wavelength needs to be amplified to about the same power level i.e. for a N-wavelength WDM system, the saturation power of the amplifier needs to be N

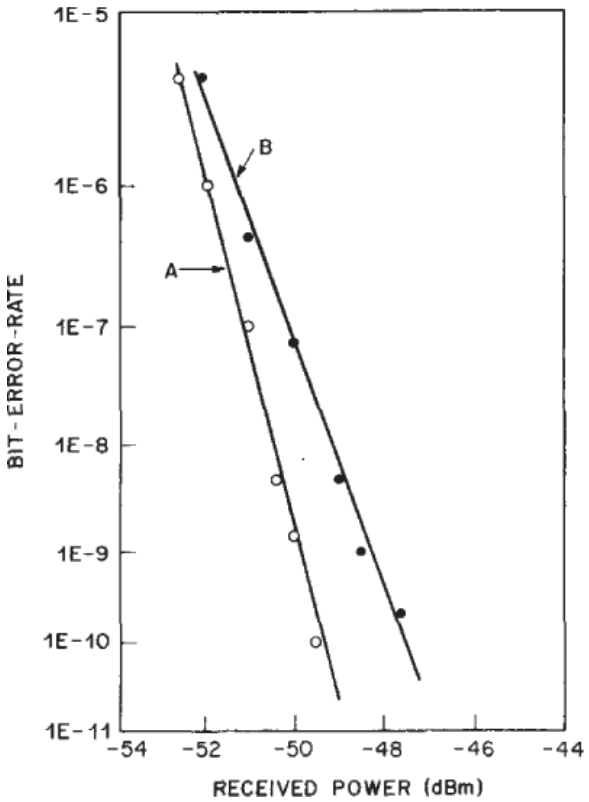

Fig. 6.5.6. Bit-error-rate characteristics for a 372 km, in-line amplifier experiment. The line labeled A is the baseline for receiver i.e. without amplifiers and with a short fibers and the line labeled B is after 372 km transmission with amplifiers [17].

times larger. Since N is typically $\sim$16 or 32 or 64, polarization independent SOA with $\sim$100 mW saturation power is needed. This is difficult to achieve in practice and fiber amplifiers can easily provide polarization independent gain with high ($\sim$100 mW to 1 W) saturation power.

6.5.2. *Optical pre-amplifier*

When a SOA is used as an optical pre-amplifier it is located in front of the photodetector in the receiver. This, in effect, provides

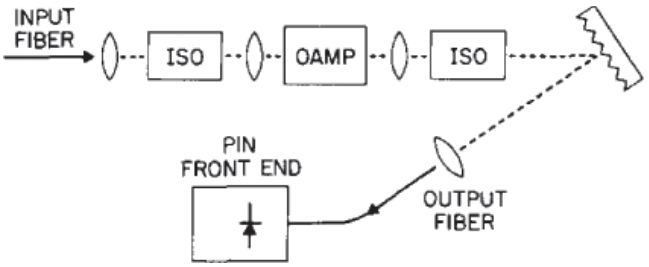

Fig. 6.5.7. Experimental set up for a SOA based pre-amplifier receiver [17].

a photodetector with gain (similar to an avalanche photodiode [53, 54]). Thus optical pre-amplifier application are important for cases where the gain of the avalanche photodiode is not high enough for the receiver bandwidth needed i.e. at high data rate. Optical pre-amplification using SOA has been reported by several authors [45–50].

An experimental set up for optical pre-amplification is shown in Fig. 6.5.7. The SOA has isolators at both the input and the output and lenses are used to couple light between the input and output fibers and the amplifier. A filter (grating) is inserted between the amplifier and the photodiode. This filter is important for reducing noise from the amplified spontaneous emission impinging on the photodiode. The filter bandwidth is $\sim$1 nm. The input light is from a distributed feedback laser emitting near 1.55 μm wavelength and modulated at 4 Gb/s. The output of the photodiode (p-i-n type) is connected to the receiver electronics which has a high impedance ($\sim$5 kohm) front end. Received power in the system is the optical power at the input fiber. The bit-error-rate (BER) as a function of received power for 4 Gb/s data is shown in Fig. 6.5.8. The receiver sensitivity (power needed for an error rate of 10^{-9}) is -34.3 dBm. The sensitivity with optical pre-amplifier for the same receiver is -25 dBm at 4 Gb/s. Thus the pre-amplifier provides an improvement of $\sim$9 dB. The BER decreases with increasing power linearly in the above plot without an error floor. This shows that a configuration of the above form which utilizes filters can make the amplifier noise for the pre-amplifier system sufficiently low.

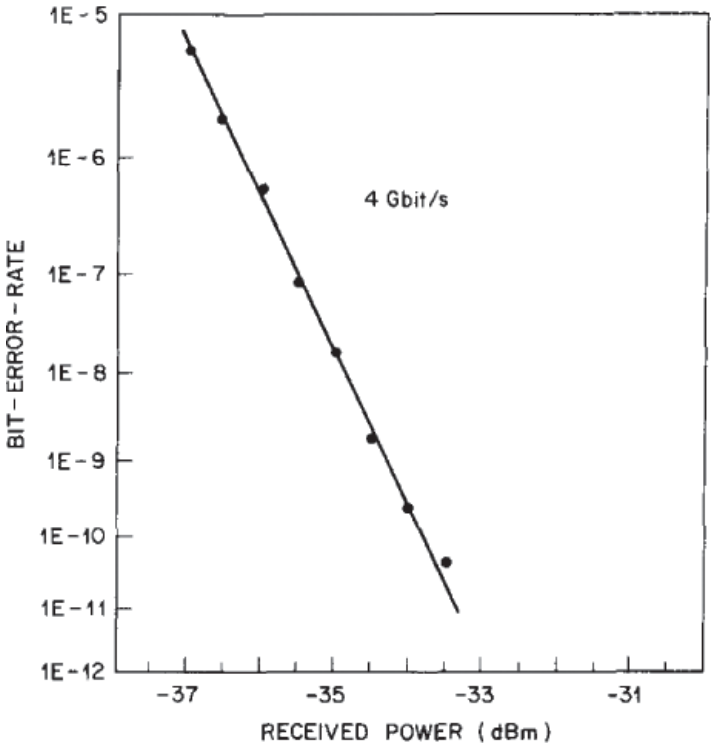

Fig. 6.5.8. Bit-error-rate (BER) for a receiver with optical preamplifier at 4 Gb/s [17].

6.5.3. *Power amplifier*

When SOA is used as a power amplifier, a key requirement is high saturation power. As discussed in previous chapters, SOA with MQW active region can have high saturation powers. Such SOA has a strong polarization dependent gain i.e. TE mode gain is considerable higher than TM mode gain. Since the laser light is TE polarized, this is not a major concern. An example of integrated chips where the SOA is used as a power amplifier is shown in Fig. 6.5.9.

In both cases, the amplifier is used to compensate the losses from the coupler. Such integrated chips are suitable as transmitters for WDM systems. Various integrated laser–amplifier structures have been fabricated. These are discussed in detail in Ch. 7.

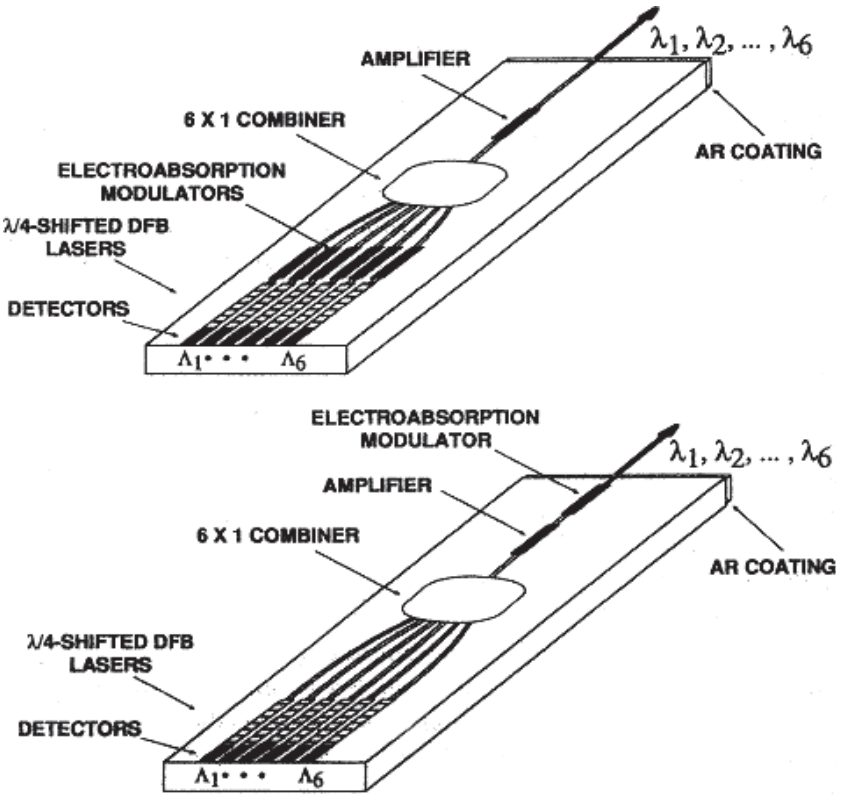

Fig. 6.5.9. The figure shows two configurations of distributed feedback laser array as sources for transmission in WDM systems. (a) Each laser can be separately modulated at high speed for simultaneous multiwavelength transmission (b) The lasers output is combined for single wavelength, wavelength selectable transmission [55].

6.6. Amplifier Noise

Amplifiers degrade the signal to noise ratio (SNR) of the amplified signal primarily because of amplified spontaneous emission which adds to the signal [56]. The effect of spontaneous emission is to add fluctuations in the signal which adds noise to the detected photocurrent. The SNR degradation is generally characterized by a quantity called noise figure, F which is defined as

$$F = \frac{(SNR)_{\text{in}}}{(SNR)_{\text{out}}}, \tag{6.6.1}$$

where SNR refers to the signal to noise ratio of the electrical power generated when the signal is converted to current by a photodetector. The SNR of the photodetector is determined by both the thermal noise and the shot noise. For an ideal detector, considered below, shot noise is the only noise. In this case simple expressions can be obtained.

Consider an amplifier with an input optical power P_{in}, amplifier gain G, a detector with a responsivity R with an electrical bandwidth B. The responsivity R is the ratio of the photocurrent (Amp) per unit power (W). For an ideal detector $R = (e/h\nu)$ where e is the charge of the electron and ν is the frequency of the incident optical signal. The photocurrent generated is given by

$$I_i = RP_{\text{in}}, \tag{6.6.2}$$

and the r.m.s (root mean square value of the photocurrent) due to shot noise is

$$\sigma^2 = 2e(RP_{\text{in}})B$$

Thus the input SNR is given by

$$(SNR)_{\text{in}} = \frac{\langle I_i \rangle^2}{\sigma^2} = \frac{P_{\text{in}}}{2h\nu B}. \tag{6.6.3}$$

In order to determine the output SNR, the spontaneous emission must be added. The spectral density of spontaneous emission induced noise (white noise) is given by

$$S(\nu) = (G-1)N_{\text{sp}}h\nu, \tag{6.6.4}$$

where N_{sp} is the spontaneous emission factor or the population inversion factor. For a two level atom, it is given by

$$N_{\text{sp}} = \frac{N_2}{N_2 - N_1}, \tag{6.6.5}$$

where N_2 and N_1 are the number of atoms in the upper and lower state respectively. Thus for high population inversion $N_2 \gg N_1$, $N_{\text{sp}} \sim 1$. However, for low population inversion, N_{sp} could be much larger. Various sources of noise in an optical amplifier are discussed later. For the discussion here only the dominant contribution is

considered i.e. the variance of the photocurrent arises mainly from the beating of the spontaneous emission with the signal. The spontaneous emission mixes coherently with the signal at the photodetector and produces a fluctuating photocurrent within the bandwidth B. The signal and the variance of the photocurrent after amplification is given by

$$I = RGP_{\text{in}}, \tag{6.6.6}$$

$$\sigma^2 = 2qIB + 4IRSB. \tag{6.6.7}$$

The variance in Eq. (6.6.7) is the sum of the shot noise and spontaneous-signal beat noise. All other noise contributions (discussed later) has been neglected. Thus the SNR at the output is given by

$$(SNR)_{\text{out}} = \frac{\langle I \rangle^2}{\sigma^2} \approx \frac{GP_{\text{in}}}{4SB}, \tag{6.6.8}$$

where the last relation is obtained by neglecting shot noise and assuming G $\gg$ 1. The amplifier excess noise figure can then be written as

$$\begin{aligned} F &= 2N_{\text{sp}}(G-1)/G \\ &\approx 2N_{\text{sp}}. \end{aligned} \tag{6.6.9}$$

The equation shows that for the SNR of the amplifier is degraded by a factor of 2 (3 dB) for the ideal case of $N_{\text{sp}} = 1$. For most practical amplifiers the SNR degradation is in the range of 5 to 7 dB.

6.6.1. *Noise analysis for optical transmission*

The following analysis follows the procedure of Ref. [17]. Assume an optical amplifier with unity coupling efficiency, uniform gain G, over an optical bandwidth B_o, and an input power of P_{in} at optical frequency ω_0 centered in the optical pass band B_o.

The spontaneous emission power in the optical bandwidth B_0 is given by (using Eq. 6.6.4):

$$P_{\text{sp}} = N_{\text{sp}}(G-1)h\nu B_o. \tag{6.6.10}$$

Writing the electric field $E_{\rm sp}$, representing the spontaneous emission as sum of cosine terms:

$$E_{\rm sp} = \sum_{k=(-B_0/2\delta\nu)}^{B_0/2\delta\nu} \sqrt{2N_{\rm sp}(G-1)h\nu\delta\nu} \cdot \cos((\omega_0 + 2\pi k\delta\nu)t + \Phi_k), \tag{6.6.11}$$

where Φ_k is a random phase for each component of spontaneous emission. Using

$$N_{\rm sp}(G-1)h\nu = N_0 \quad \text{and} \quad \frac{B_o}{2\delta\nu} = M \tag{6.6.12}$$

the total electric field at the output of the amplifier is

$$E(t) = \sqrt{2GP_{\rm in}}\cos(\omega_0 t) + \sum_{k=-M}^{M} \sqrt{2N_0\delta\nu} \cdot \cos((\omega_0 + 2\pi k\delta\nu)t + \Phi_k). \tag{6.6.13}$$

The photocurrent $i(t)$ generated by a unity quantum efficiency photodetector is proportional to the intensity. It is given by

$$i(t) = \overline{E^2(t)}\frac{e}{h\nu}, \tag{6.6.14}$$

where the bar indicates time averaging over optical frequencies. Hence

$$i(t) = GP_{\rm in}\frac{e}{h\nu} + \frac{4e}{h\nu}\sum_{k=-M}^{M} \sqrt{GP_{\rm in}N_0\delta\nu} \cdot \cos(\omega_0 t)\cos((\omega_0 + 2\pi k\delta\nu)t + \Phi_k) + \frac{2eN_0\delta\nu}{h\nu} \cdot \left[\sum_{k=-M}^{M} \cos((\omega_0 + 2\pi k\delta\nu)t + \Phi_k)\right]^2. \tag{6.6.15}$$

The three terms in Eq. (6.6.15) represent, signal, signal-spontaneous beat noise, and spontaneous-spontaneous beat noise, respectively. Note that the noise within the electrical bandwidth is important.

The signal-spontaneous beat noise term from Eq. (6.6.15) is given by

$$i_{s-\mathrm{sp}}(t) = \frac{4e}{h\nu}\sum_{k=-M}^{M}\sqrt{GP_{\mathrm{in}}N_0\delta\nu}\cdot\cos(\omega_0 t)\cos((\omega_0+2\pi k\delta\nu)t+\Phi_k)$$

$$= \frac{2e}{h\nu}\sqrt{GP_{\mathrm{in}}N_0\delta\nu}\sum_{k=-M}^{M}\cos(2\pi k\delta\nu t+\Phi_k), \tag{6.6.16}$$

where terms $\sim\cos(2\omega_0 t)$, which average to zero, have been neglected. For each frequency, $2\pi k\delta\nu$, in Eq. (6.6.16), the sum has two components but with a random phase. Hence, the power spectrum of $i_{s-\mathrm{sp}}(t)$ is uniform in the frequency interval $0\sim B_0/2$ with a density of

$$N_{s-\mathrm{sp}} = \frac{4e^2}{(h\nu)^2}GP_{\mathrm{in}}N_0\cdot\frac{1}{2}\cdot 2$$

$$= \frac{4e^2}{h\nu}P_{\mathrm{in}}N_{\mathrm{sp}}(G-1)G \tag{6.6.17}$$

The spontaneous-spontaneous beat noise term from Eq. (6.6.15) is

$$i_{s-\mathrm{sp}}(t) = 2N_0\frac{\delta\nu e}{h\nu}\left[\sum_{k=-M}^{M}\cos((\omega_0+2\pi k\delta\nu)t+\Phi_k)\right]^2$$

$$= 2N_0\frac{\delta\nu e}{h\nu}\left[\sum_{k=-M}^{M}\cos(\beta_k)\sum_{j=-M}^{M}\cos(\beta_j)\right], \tag{6.6.18}$$

where

$$\beta_k = (\omega_0+2\pi k\delta\nu)t+\Phi_k \quad\text{and}\quad \beta_j = (\omega_0+2\pi j\delta\nu)t+\Phi_j. \tag{6.6.19}$$

Equation (6.6.18) can be written as

$$i_{\mathrm{sp}-\mathrm{sp}}(t) = 2N_0\frac{\delta\nu e}{h\nu}\sum_{k=-M}^{M}\sum_{j=-M}^{M}\frac{1}{2}\cos(\beta_k-\beta_j)+\frac{1}{2}\cos(\beta_k+\beta_j). \tag{6.6.20}$$

The terms $\sim\cos(\beta_k+\beta)$ have frequencies $\sim 2\omega_0$ and average to zero. Rewriting Eq. (6.6.20) gives:

$$i_{\text{sp-sp}}(t)=\frac{N_0\delta\nu e}{h\nu}\sum_{k=-0}^{2M}\sum_{j=0}^{2M}\cos((k-j)2\pi\delta\nu\cdot t+\Phi_k-\Phi_j). \tag{6.6.21}$$

The dc term is obtained for k = j and there are 2M such terms:

$$I_{\text{sp}}^{dc}=\frac{e}{h\nu}N_0\delta\nu 2M=N_{\text{sp}}(G-1)eB_o. \tag{6.6.22}$$

A list of the various terms according to their frequencies is shown below:

frequency	# terms
$-(2M-1)\delta\nu$	1
$\vdots$	$\vdots$
$-l\delta\nu$	$2M-l$
$\vdots$	$\vdots$
$-1\delta\nu$	$2M-1$
$1\delta\nu$	$2M-1$
$\vdots$	$\vdots$
$-l\delta\nu$	$2M-l$
$\vdots$	$\vdots$
$(2M-1)\delta\nu$	1

The terms with same absolute frequency but of opposite sign add in phase. Therefore, the power spectrum of the spontaneous-spontaneous beat noise extends from 0 to B_0, with a triangular shape and a power density near dc of

$$N_{\text{sp-sp}}=\frac{4N_0^2\delta\nu e^2}{h\nu^2}\left(\frac{B_o}{\delta\nu}-1\right)\cdot\frac{1}{2}=2N_{\text{sp}}^2(G-1)^2e^2B_o. \tag{6.6.23}$$

Using Eq. (6.6.10) the photo current equivalent of the spontaneous emission power is:

$$I_{\text{sp}}=P_{\text{sp}}e/h\nu=N_{\text{sp}}(G-1)eB_o. \tag{6.6.24}$$

I_{sp} may be called the photocurrent equivalent of the spontaneous emission power. In the following, many of the parameters are defined as photocurrent equivalents. According to square law detection in the receiver, the received signal power is given by:

$$S = (GI_s\eta_{\text{in}}\eta_{\text{out}}L)^2 \tag{6.6.25}$$

where G is the optical gain of the amplifier, L is optical loss between the amplifier and receiver, I_s is the photocurrent equivalent of the amplifier input power defined in the same way as Eq. (6.6.24). The quantities η_{in} and η_{out} are amplifier input and output coupling efficiencies.

The noise terms are:

$$N_{\text{shot}} = 2B_e e\eta_{\text{out}}L(GI_s\eta_{\text{in}} + I_{\text{sp}}), \tag{6.6.26}$$

$$N_{\text{s-sp}} = 4GI_s\eta_{\text{in}}\eta_{\text{out}}^2 I_{\text{sp}}L^2B_e/B_o, \tag{6.6.27}$$

$$N_{\text{sp-sp}} = (I_{\text{sp}}\eta_{\text{out}}L)^2B_e(2B_o - B_e)/B_o^2, \tag{6.6.28}$$

$$N_{\text{th}} = I_{\text{th}}^2. \tag{6.6.29}$$

The total noise is given by

$$N_{\text{tot}} = N_{\text{shot}} + N_{\text{s-sp}} + N_{\text{sp-sp}} + N_{\text{th}}, \tag{6.6.30}$$

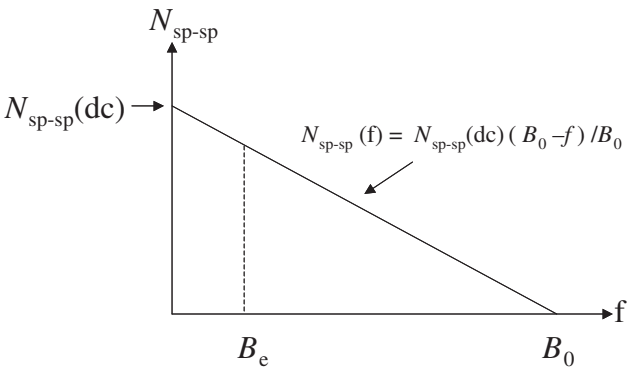

Fig. 6.6.1. Schematic of the spontaneous-spontaneous beat noise spectrum. F is the frequency. The dc value $N_{\text{sp-sp}}$ is given by Eq. (6.6.23). The equation for the line is written above [17].

where N_{shot}, $N_{\text{s-sp}}$, $N_{\text{sp-sp}}$ and N_{th} are the shot noise, signal-spontaneous beat noise, spontaneous-spontaneous beat noise and thermal noise respectively. N_{tot} is the total noise. The quantity I_{th} is the equivalent thermal noise induced photocurrent and B_{e} is the electrical bandwidth. The quantity $N_{\text{sp-sp}}$ in Eq. (6.6.28) is obtained by integrating $N_{\text{sp-sp}}(f)$ from 0 to B_e and taking the average (per unit bandwidth) of the result as follows:

$$N_{\text{sp-sp}} = \frac{1}{B_e}\int_0^{B_e} N_{\text{sp-sp}}(f)df. \tag{6.6.31}$$

For an amplitude modulated signal of average power P_{in}, with a 50-percent duty cycle and an extinction ratio of $r(= I_s(1)/I_s(0))$, the photo current equivalents of the input powers for a mark ($I_s(1)$) and a space ($I_s(0)$) are:

$$I_s(1) = eP_{\text{in}}2r/(h\nu(r+1)), \tag{6.6.32}$$

$$I_s(0) = eP_{\text{in}}2/(h\nu(r+1)), \tag{6.6.33}$$

using $r = I_{\text{s}}(1)/I_{\text{s}}(0)$ and $(I_{\text{s}}(1) + I_{\text{s}}(0))/2 = eP_{\text{in}}/h\nu$ is the average photocurrent. The bit-error-rate (BER) is given by [57]

$$BER = \frac{1}{\sqrt{2\pi}}\frac{\exp(-Q^2/2)}{Q}, \tag{6.6.34}$$

where Q is given by

$$Q = \frac{\sqrt{S(1)} - \sqrt{S(0)}}{\sqrt{N_{\text{tot}}(1)} + \sqrt{N_{\text{tot}}(0)}}. \tag{6.6.35}$$

$S(1), S(0)$ and $N_{\text{tot}}(1)$, $N_{\text{tot}}(0)$ are the signal and total noise for a mark and space, respectively. A BER of 10^{-9} requires $Q = 6$.

Some results of the amplifier noise on receiver sensitivity calculations are now presented. The amplifier parameters are gain G, noise figure N_{sp} and optical bandwidth B_0. Figure 6.6.2 shows the receiver sensitivity of a receiver with a semiconductor optical amplifier (as a preamplifier). The data rate is 5 Gb/s. The value of the thermal noise chosen corresponds to a base receiver sensitivity of −25 dBm. At low

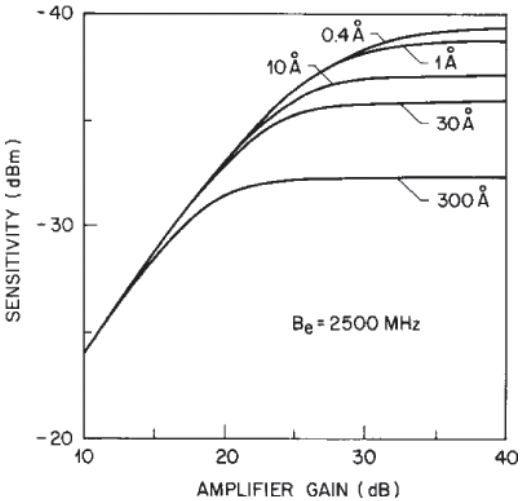

Fig. 6.6.2. Optical preamplifier receiver sensitivity as a function of amplifier gain. The parameter values used in the calculation are $B_e = 2.5\,\text{GHz}$, $N_{\text{sp}} = 1.4$, $\eta_{\text{in}} = 0.31$, $\eta_{\text{out}} = 0.26$ and $\lambda = 1.55\,\mu\text{m}$. The data rate is 5 Gb/s [17].

receiver sensitivity, the receiver performance is limited by thermal noise (not by amplifier noise). Hence the receiver sensitivity increases linearly with amplifier gain. For high gain, the amplifier noise terms (signal-spontaneous beat noise and spontaneous-spontaneous beat noise becomes dominant and the receiver sensitivity depend on the optical bandwidth of the amplifier.

Optical preamplifier sensitivity as a function of the spontaneous emission factor is shown Fig. 6.6.3 for various amplifier gains. The optical bandwidth is 10 A. For low amplifier gains, the dominant effect is from thermal noise, the spontaneous emission power is low and hence the sensitivity on spontaneous emission factor is low. The reverse is true at high gain, hence a strong dependence on spontaneous emission factor is observed.

For in-line amplifier applications, the important parameter is power penalty introduced by the amplifier chain. Power penalty is the amount of extra input power needed to compensate for the accumulated noise. The results of a power penalty calculation are shown in Fig. 6.6.4. The electrical bandwidth $B_{\text{e}} = 2.5\,\text{GHz}$.

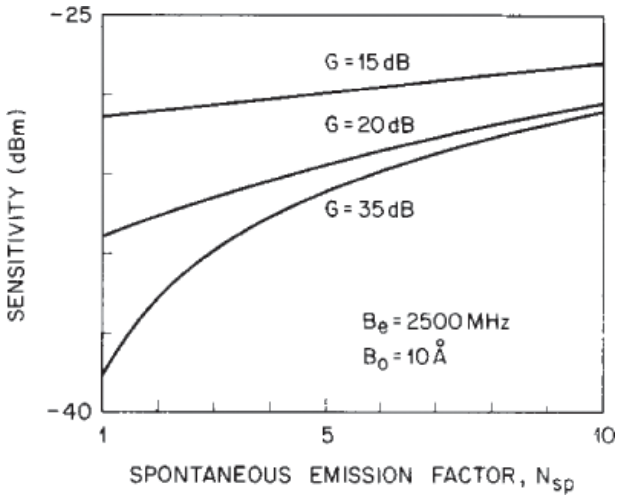

Fig. 6.6.3. Optical preamplifier sensitivity as a function of spontaneous emission factor. The parameter values used in the calculation are $B_e = 2.5$ GHz, $\eta_{in} = 0.31$, $\eta_{out} = 0.26$ and $\lambda = 1.55\,\mu$m [17].

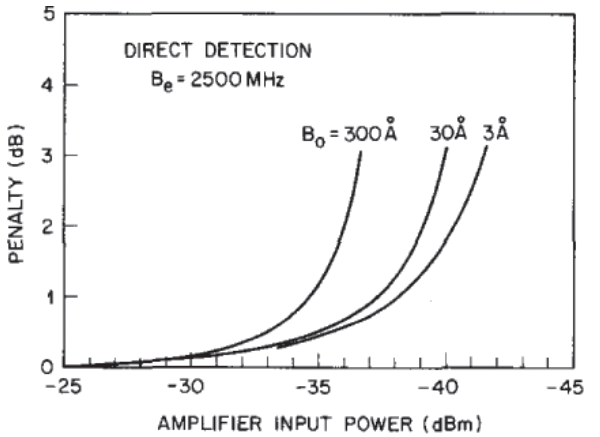

Fig. 6.6.4. Power penalty for an in-line amplifier system versus amplifier input power. The curves are for different optical bandwidths. The parameter values used in the calculation are $B_e = 2.5$ GHz, $\eta_{in} = 1.0$, $N_{sp} = 1.4$, and $\lambda = 1.55\,\mu$m [17].

6.7. Gain Dynamics

The gain and phase dynamics in a SOA is important for many SOA applications [58–79]. For example, SOA based Mach-Zehnder

inter-ferometers where two SOA's are used in a Mach-Zehnder configuration (one in each arm) is used for optical demultiplexing, optical clock recovery and for photonic logic systems. The interferometer works on the principle of gain and phase change imposed on a probe signal in the presence of a series of pulsed signals. For simplicity, the gain and phase change of a CW probe signal in the presence of a pulsed signal is considered first. The schematic of an experiment is shown in Fig. 6.7.1 where the wavelength of both the CW probe beam and that of the pulsed beam are within the gain bandwidth of the amplifier.

The high power pulsed signal saturates the gain of the amplifier. This results in a decrease in gain (decrease in transmission) for the CW signal following which the gain recovers due to redistribution

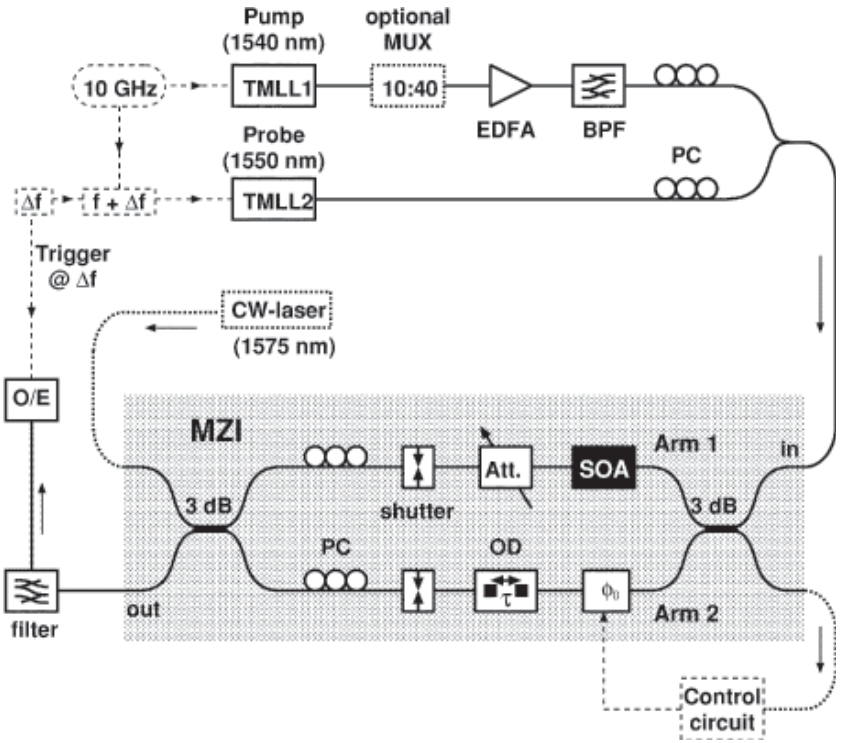

Fig. 6.7.1. Schematic of a gain recovery (top) and phase recovery (bottom) measurement [68].

of carriers and injection current. Thus the gain dynamics is inferred from the measured transmission of the probe as a function of time. The phase change of the probe beam as a function of time can be obtained if the SOA is used in a Mach-Zehnder configuration. Then the output of the Mach-Zehnder is determined by the phase change in the arm which has the SOA.

For SOAs with bulk or multiquantum well active region, the mechanism for gain recovery is current injection, carrier heating and spectral hole burning. The amplifier is biased with a certain CW current which provides carriers. Thus the carriers depleted by the pulse are continuously being replaced by the current carrying carriers. The time scale of this process is given by the carrier life time τ_c. The quantity τ_c decreases with increasing injected current density. For high current densities it is in the 100 to 200 ps range. The carrier heating results from a thermalization of carriers in the entire energy band following the pulse. This is fast process occurring is time scale of $\sim$1 ps to $\sim$0.7 ps.

The injected pulse reduces the gain at the photon energy of this pulse i.e. in the gain spectrum it burns a hole. The process is known as spectral hole burning. Following the pulse, the gain spectrum returns to its original shape through redistribution of carriers. The process is fast occurring in a time scale of $\sim$0.6 ps to $\sim$0.3 ps. The phase recovery is related to the gain recovery by the α-factor (Eq. (6.3.9)). Separate measurements of gain and phase recovery have shown different α-factor values are associated with the three processes. For carrier injection the value of α depends on the wavelength and it is typically in the range of $\alpha \sim 4$ to 7. For carrier heating $\alpha \sim 1$ and for spectral hole burning $\alpha \sim 0$. The small α-factor for fast processes suggests that phase recovery is slower than the gain recovery. In addition, in order to observe the fast gain recovery, sufficiently short ($\sim$1 ps wide) pulses must be used.

The measured gain and phase dynamics of a CW probe signal following a series of pulses at 10 GHz and 40 GHz is shown in Fig. 6.7.2. The phase dynamics is obtained using an interferometer set up. The fast recovery observed for gain recovery is not present in the phase recovery data. Also, for higher repetition rate (40 GHz), the gain

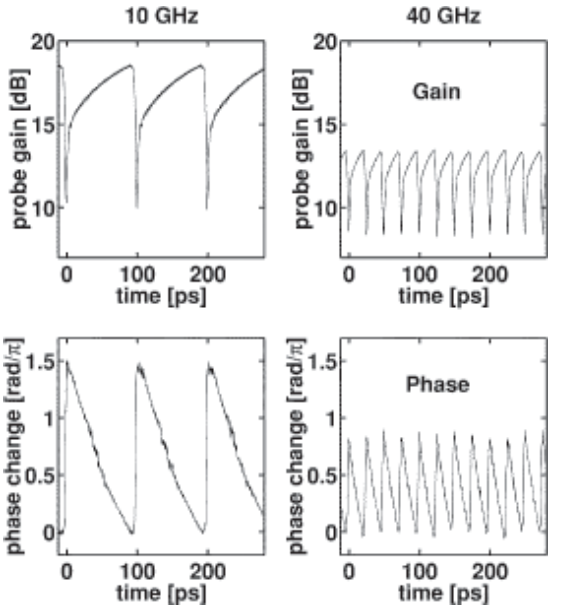

Fig. 6.7.2. Measured gain and phase dynamics for 10 GHz and 40 GHz repetition rate. The amplifier length is 0.75 mm. The pump pulses are 1.6 ps wide with an average power of 8.4 dBm [68].

modulation and phase modulation produced by the pulses is smaller than that for low repetition rate (10 GHz) due to shorter recovery time between pulses.

The data of Fig. 6.7.2 illustrates the presence of different response times for gain and phase recovery. The gain recovery following a short pulse takes place due to several processes. They are: current injection, carrier heating and spectral hole burning. It also may include carrier relaxation from a higher energy states in a semiconductor layer next to active region. Since such relaxation times are fast ($\sim$1 to 3 ps), this layer serves as a carrier reservoir. The carrier reservoir allows a fast replacement of carriers depleted by the short pulse [79]. The gain saturation energies for different pulse widths have been measured. The result is shown in Fig. 6.7.3. In the experiment the optical pulses were obtained from a Ti-sapphire laser. The pulse repetition rate is 250 KHz. The gain saturation (decrease of gain with increasing optical power) takes place at lower energy for short pulses.

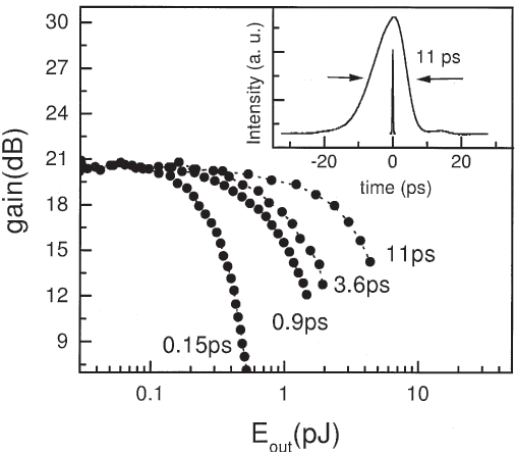

Fig. 6.7.3. Measured gain as a function of output energy for different input pulse widths. The SOA is 0.55 mm long and the bias current is 200 mA. The inset shows the autocorrelation traces of the longest (11 ps) and the shortest (0.15 ps) pulses [70].

Fast gain recovery is important for high speed applications of SOA's. This is generally achieved by increasing the injection current or by increasing the input optical power. Increasing injection current leads to heating effects which may not be desirable. Another technique for decreasing the gain recovery is by injection of an optical signal into the SOA [71–74]. This optical signal generally has a wavelength shorter than the system operating wavelength (e.g. 1480 nm wavelength light is injected into a 1550 nm wavelength band SOA). The absorbed optical signal creates carriers in the conduction and valence band. These carriers relax to the bottom of the band to replace the carriers depleted by the input pulse. The experiment set up used for the measurement is shown in Fig. 6.7.4. The CW laser light on which the gain recovery is measured has a wavelength of 1555 nm.

The wavelength of the CW pump light used for gain recovery is 1480 nm and the mode locked fiber ring laser (MLFRL) which depletes the carriers operates at a wavelength of 1544 nm. The laser produced 3 ps wide pulses at 2.5 GHz repetition rate. An optical filter is used prior to streak camera to detect the 1555 nm signal.

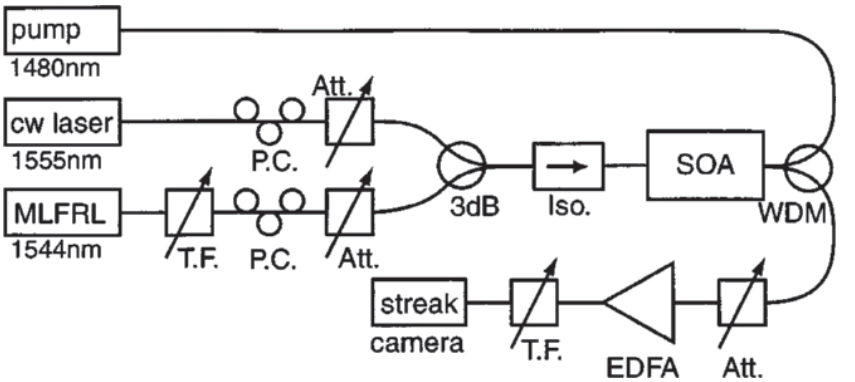

Fig. 6.7.4. Experimental set up used for gain recovery measurements [71].

The streak measurements of the 1555 nm light as a function of time is shown in Fig. 6.7.5 (Top traces). The bottom part of Fig. 6.7.5 shows the 3-dB gain recovery times plotted as a function of the power of the 1480 nm wavelength light. Gain recovery times ∼27 ps is obtained with 80 mW input power. This method of decreasing the gain recovery time using a holding beam has been used in several transmission system demonstrations (see Ch. 8).

The long gain recovery times causes pattern effects when a SOA is used in an optical system for wavelength conversion i.e. response of a single pulse "1", is different from that of a long string of 1's or 0's. One way to examine this is by plotting the eye pattern. Experiments have been carried out where a 80 Gb/s pulse train is amplified using a SOA with or without holding beam (also known assist light). The amplified output of 80 Gb/s pattern @ 1555 nm wavelength is found to be much clearer with the holding beam (10 mW @ 1480 nm) than in its absence.

6.7.1. *Model of gain recovery*

The temporal response of the optical gain in a SOA has been previously derived (Sec. 6.3). It is rewritten as follows for convenience

$$\frac{dh}{dt} = -\frac{h - h_0}{\tau_c} - [\exp(h) - 1]P(t, 0), \tag{6.7.1}$$

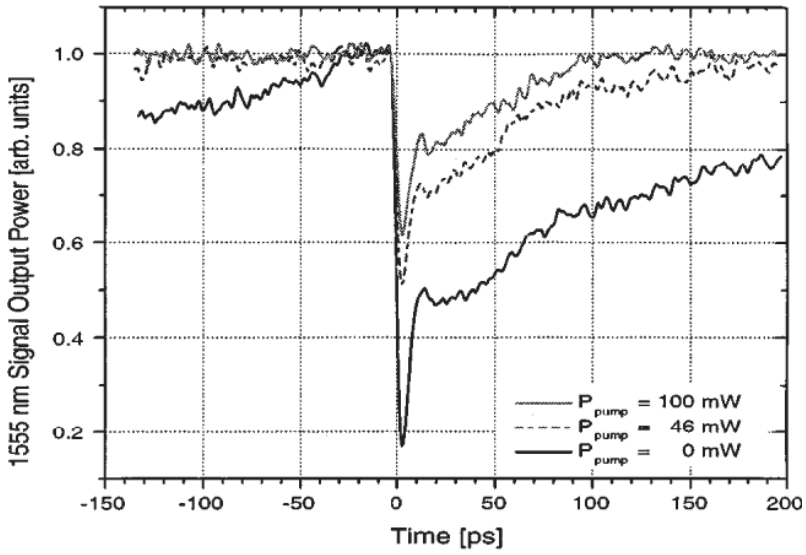

(a)

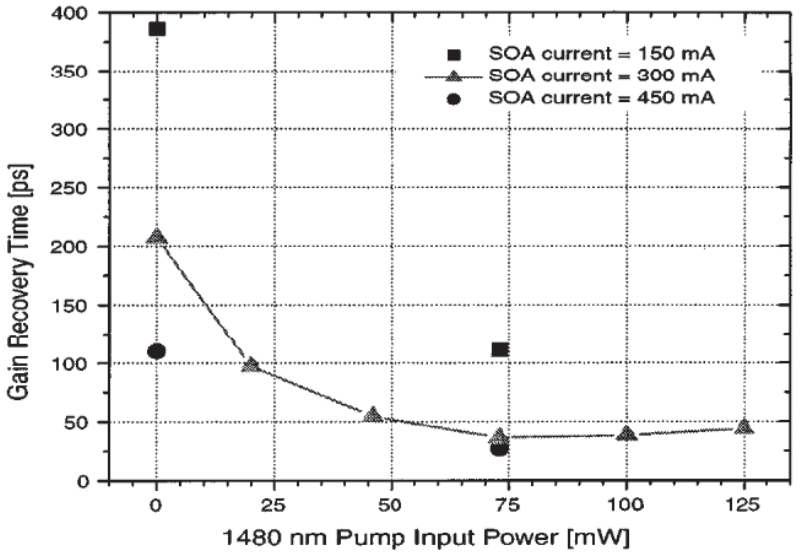

(b)

Fig. 6.7.5. (a) Transmitted intensity of 1555 nm signal as a function of time for various levels of 1480 nm pump. (b) 3-dB gain recovery time plotted as a function of power of 1480 nm pump [71].

where

$$h(t) = \int_0^L g(t,z)dz. \tag{6.7.2}$$

The quantity h(t) is the integrated gain defined earlier, $g(z,t)$ is the optical gain at a distance z from the input facet, h_0 is the value of integrated gain h at $t = 0$, and $P(t,0)$ is the input optical power normalized to the saturation power. The above equation takes into account only the carrier lifetime associated with transition from conduction band to valence band. However, there are other processes such as spectral hole burning and carrier heating which causes a redistribution of carriers in the conduction band and hence contribute to the gain recovery process [75–77]. For example, carriers at higher energy can reach thermal equilibrium fast and in the process replace the depleted carriers by a fast pulse which results in faster gain recovery. Two additional gain dynamic equations are introduced to take into account carrier heating and spectral hole burning effects [76]:

$$\frac{\partial g_{\mathrm{SHB}}}{\partial t} = -\frac{g_{\mathrm{SHB}}}{\tau_{\mathrm{SHB}}} - \frac{\varepsilon_{\mathrm{SHB}}}{\tau_{\mathrm{SHB}}} g_{\mathrm{total}} P(t,z) - \left(\frac{\partial g_{\mathrm{CH}}}{\partial t} + \frac{\partial g_a}{\partial t}\right), \tag{6.7.3}$$

$$\frac{\partial g_{\mathrm{CH}}}{\partial t} = -\frac{g_{\mathrm{CH}}}{\tau_{\mathrm{CH}}} - \frac{\varepsilon_{\mathrm{CH}}}{\tau_{\mathrm{CH}}} g_{\mathrm{total}} P(t,z). \tag{6.7.4}$$

τ_{SHB}^{-1} is the spectral hole burning or carrier-carrier scattering rate, while τ_{CH}^{-1} is the carrier temperature relaxation rate. ε_{SHB} and ε_{CH} are the nonlinear gain suppression factors due to spectral hole burning and carrier heating. $P(t,z)$ is the optical power at time t at position z. Using g_a as the gain in Eq. (6.7.2), the corresponding equation for integrated gain h_a is given by Eq. (6.7.1). The total gain is given by:

$$g_{\mathrm{total}} = g_a + g_{\mathrm{SHB}} + g_{\mathrm{CH}} \tag{6.7.5}$$

The h-function for the spectral hole burning (SHB) and carrier heating (CH) can be defined as the integral over the amplifier length of the corresponding gain functions. Then the following equations are

obtained for the h-functions [76].

$$\frac{dh_a}{dt} = -\frac{h_a - h_0}{\tau_c} - [\exp(h_a + h_{\mathrm{SHB}} + h_{\mathrm{CH}}) - 1]P(t,0), \tag{6.7.6}$$

$$\frac{dh_{\mathrm{SHB}}}{dt} = -\frac{h_{\mathrm{SHB}}}{\tau_{\mathrm{SHB}}} - \frac{\varepsilon_{\mathrm{SHB}}}{\tau_{\mathrm{SHB}}}[\exp(h_a + h_{\mathrm{SHB}} + h_{\mathrm{CH}}) - 1]P(t,0) - \frac{dh_a}{dt} - \frac{dh_{\mathrm{CH}}}{dt}, \tag{6.7.7}$$

$$\frac{dh_{\mathrm{CH}}}{dt} = -\frac{h_{\mathrm{CH}}}{\tau_{\mathrm{CH}}} - \frac{\varepsilon_{\mathrm{CH}}}{\tau_{\mathrm{CH}}}[\exp(h_a + h_{\mathrm{SHB}} + h_{\mathrm{CH}}) - 1]P(t,0). \tag{6.7.8}$$

The optical gain as a function of time can be numerically solved from Eqs. (6.7.6)–(6.7.8). The calculated gain recovery curves for a SOA are plotted in Fig. 6.7.6. The input optical signal was set as a Gaussian pulse train at 10 GHz repetition rate. The full width at half maximum of the pulse width is 1 ps.

Rest of the parameters used here are [76]: $\tau_c = 150$ ps, $\tau_{\mathrm{SHB}} = 100$ fs, $\tau_{\mathrm{CH}} = 300$ fs, $\varepsilon_{\mathrm{SHB}} = \varepsilon_{\mathrm{CH}} = 0.2$/Watt [78]. The initial gain at $t = 0$ is given by $h_0 = \ln(200)$ i.e. total gain =200 or 23 dB. The calculated gain (value of h) and phase recovery as a function of time following the pulse is shown in Fig. 6.7.6. Note the fast rise time for the gain due to spectral hole burning and carrier heating are not present in the phase recovery curves. The phase recovery is proportional to the gain recovery. The proportionality constant is the α-factor. The α value for spectral hole burning (SHB) process has been estimated to be ∼0, and, for the carrier heating process (CH), α ∼ 1 [76–78]. For the normal band to band transitions α ∼ 5 to 8. The calculation in Fig. 6.7.6 uses α = 7 for this process. Thus although the gain change due to SHB and CH process can be fast, the associated phase change to an input light is small. Thus, the phase recovery times are longer than gain recovery times. This is consistent with the experimental data of Fig. 6.7.2.

The calculated response of the gain and phase recovery for 100 GHz pulses are shown in Fig. 6.7.7. The parameters used in the calculation are the same as that for Fig. 6.7.6.

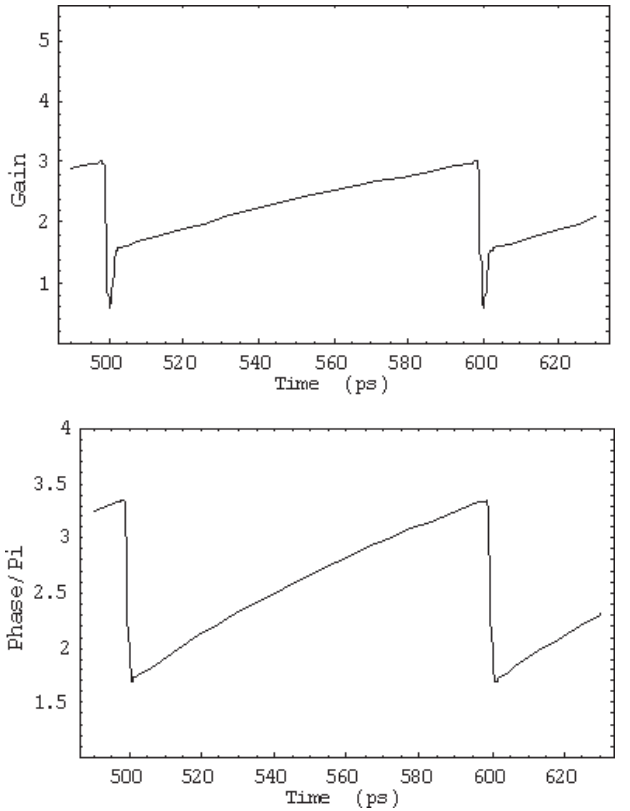

Fig. 6.7.6. (Top) Gain recovery for a 10 GHz, 1 ps wide pulse stream, (Bottom) Phase recovery for a 10 GHz, 1 ps wide pulse stream, pulse energy = 2.5 pJ for both cases. The gain plotted above is the value of h.

Initially the gain is high because there is no pulse. As the number of pulses increase with time the average gain decreases and it recovers between pulses. Note the gain modulation by successive pulses is small at high speeds. It follows that for a pseudo random input bit stream the optical gain experienced by a pulse would depend on the history of prior input pulses i.e. number of sequential 1's and 0's. This would lead to pattern dependence of the output when the amplifier is used in cross gain modulation or cross phase modulation applications. It has been suggested that a carry reservoir (higher band gap layer next to active region) can be used

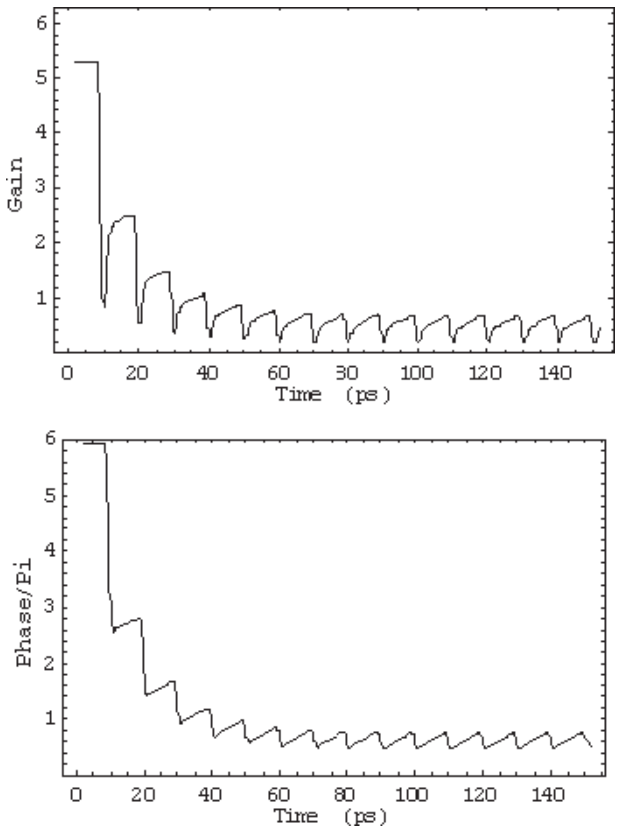

Fig. 6.7.7. (Top) Gain recovery for a 100 GHz, 1 ps wide pulse stream, (Bottom) Phase recovery for a 10 GHz, 1 ps wide pulse stream, pulse energy = 2.5 pJ for both cases. The gain plotted above is the value of h.

to enhance the gain recovery rate in semiconductor amplifiers [79]. So far the discussion has been for SOAs with regular or quantum well active region, over the last few years, SOAs with quantum dot (QD) active region have been fabricated and studied. These types of SOAs are discussed in detail in Ch. 11. QD SOA has a fast gain and phase recovery which makes them suitable for high speed system applications. The primary reason for the faster response of QD SOA compared to that for SOA with regular active region is due to the presence of the wetting layer. The wetting layer serves as a carrier reservoir layer. Carriers depleted by the injected optical pulse in the

QD ground state are replaced by fast carrier transfer from the wetting layer.

6.8. SOA with Carrier Reservoir

Similar to that for QD-SOA, it has been suggested that SOA with a carrier reservoir can have a short gain recovery time [80–83]. A calculation of gain and phase recovery times of a SOA with a carrier reservoir layer is carried out in this section. The faster response of SOA with carrier reservoir (CR-SOA) is based on a similar principle as that for QD-SOA. In CR-SOA, the CR region is grown in the vicinity of the active region. Under certain condition CR is significantly populated, and it supplies the active region with carriers with nearly the same transition time as that for QD-SOA, i.e 0.5–10 ps [81]. This ultra-fast transition dominates the gain dynamics, thus CR-SOA is expected to have fast temporal gain and phase response. For the SOA design considered here, a carrier reservoir region is placed close to the active region (Fig. 6.8.1). The band-gap of the CR layer is larger than that of the active region (AR). When a current is injected into the SOA, carriers start to fill the available states in AR and CR. At low injection level, quasi-Fermi level is close to the band edge of AR, carrier density in the AR is larger than in CR.

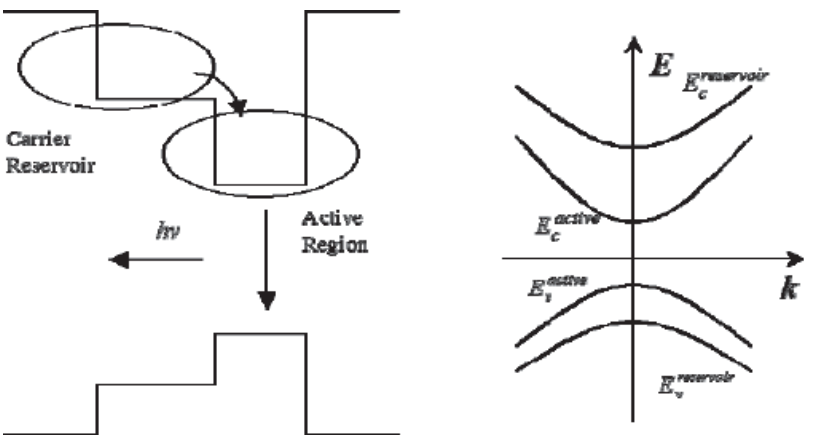

Fig. 6.8.1. Schematic of the band diagram of SOA with a CR.

With the increase of injection current, quasi-Fermi level moves up over the band edge of CR. Consequently, CR accumulates sufficient carriers to function as a reservoir of carriers. Carrier density in CR and AR can be derived from:

$$N_i = \int 2 \times \rho_i(E) \left[1 + \exp \frac{(E - E_f)}{kT}\right]^{-1} dE. \tag{6.8.1}$$

The electron densities in the AR and CR are determined by the quasi-Fermi level E_f in the conduction band and effective masses. In the presence of an input optical signal, the carriers in the active region are depleted. The depletion-induced unoccupied-states are rapidly filled by carriers from the CR. The carrier relaxation time from CR to AR is primarily determined by electron-phonon interaction time, this time has been indirectly measured to be in the ∼0.5 to 5 ps range in GaAs [83]. A shorter transition time would result in faster recovery. The carrier relaxation time for holes is shorter than that for electrons [84]. Hence, we assume that electron relaxation time determines the SOA gain or phase response. The dynamic model of CR-SOA can be described by the following non-linear coupled equations:

$$\frac{\partial N_{\text{active}}}{\partial t} = \frac{I_1}{eV_{\text{active}}} - \frac{N_{\text{active}}}{\tau_c} - gP(t,z) + \frac{N_{\text{reservior}} - N_{\text{active}}}{\tau_t(1+\eta)}, \tag{6.8.2}$$

$$\frac{\partial N_{\text{reservior}}}{\partial t} = \frac{I_2}{eV_{\text{reservior}}} - \frac{N_{\text{reservior}}}{\tau_c} - \frac{\eta(N_{\text{reservior}} - N_{\text{active}})}{\tau_t(1+\eta)}, \tag{6.8.3}$$

where N is the carrier density in each region, V is the volume, I is the injected current, τ_c is the recombination lifetime in both active region and reservoir region, τ_t is the transition time from CR level to AR level. τ_t is assumed to be 5 ps in the numerical calculation reported here. The total injected current is the sum of I_1 and I_2. The quantity $P(t,z)$ denotes the power in the optical pulse at a distance z from the input facet of SOA. The quantity η is the population inversion factor defined as the ratio of steady-state carrier densities in AR and CR (i.e. $\eta = N_{ar}/N_{cr}$). The last terms in Eqs. (6.8.2) and

(6.8.3) represent the transition process between CR level to AR level. Optical gain in SOA can be linearly scaled to the carrier density in active region as:

$$g_l = a(N_d - N_{tr}), \tag{6.8.4}$$

where g_l is the optical gain arising from carrier density in AR at the input optical wavelength and $\mathrm{N_d}$ is the carrier density in the AR. The quantity a is differential gain (i.e. $a = 1 \times 10^{-16}\,\mathrm{cm}^2$) and N_{tr} is the transparency carrier density. The time dependent gain equation (similar to Eq. (6.8.2)) is as follows:

$$\frac{\partial g_{ar}}{\partial t} = \frac{g_0^{ar} - g_{ar}}{\tau_c} - g_{ar}P(t,z) + \frac{g_{cr} - g_{ar}}{\tau_t(1+\eta)}, \tag{6.8.5}$$

$$g_0^{ar} = \Gamma a N_{\mathrm{tr}}(I_1\tau_c/qV_1N_{\mathrm{tr}} - 1). \tag{6.8.6}$$

Carrier heating and spectral hole burning effects on the gain g are introduced using the procedure of a previous analysis [85]:

$$\frac{\partial g_{\mathrm{SHB}}}{\partial t} = -\frac{g_{\mathrm{SHB}}}{\tau_{\mathrm{SHB}}} - \frac{\varepsilon_{\mathrm{SHB}}}{\tau_{\mathrm{SHB}}} g_{\mathrm{total}} P(t,z) - \left(\frac{\partial g_{\mathrm{CH}}}{\partial t} + \frac{\partial g_l}{\partial t}\right), \tag{6.8.7}$$

$$\frac{\partial g_{\mathrm{CH}}}{\partial t} = -\frac{g_{\mathrm{CH}}}{\tau_{\mathrm{CH}}} - \frac{\varepsilon_{\mathrm{CH}}}{\tau_{\mathrm{CH}}} g_{\mathrm{total}} P(t,z). \tag{6.8.8}$$

g_{SHB} and g_{CH} are additional gains at the input optical wavelength due to spectral hole burning and carrier heating processes. $1/\tau_{\mathrm{SHB}}$ is the carrier-carrier scattering rate while $1/\tau_{\mathrm{CH}}$ is the carrier temperature relaxation rate. $\varepsilon_{\mathrm{SHB}}$ and $\varepsilon_{\mathrm{CH}}$ are the nonlinear gain suppression factors due to carrier heating and spectral hole burning. The total gain is given by:

$$g_{\mathrm{total}} = g_l + g_{\mathrm{SHB}} + g_{\mathrm{CH}}. \tag{6.8.9}$$

The optical gain as a function of time can be numerically solved from rate equations in temporal gain forms [85]. For a regular SOA (no CR),

$$\frac{dh_{\mathrm{active}}}{dt} = -[\exp(h_{\mathrm{active}} + h_{\mathrm{SHB}} + h_{\mathrm{CH}}) - 1]P(t,0) + \frac{h_0}{\tau_c} - \frac{h_{\mathrm{active}}}{\tau_c} \tag{6.8.10}$$

$$\frac{dh_{\mathrm{SHB}}}{dt} = -\frac{\varepsilon_{\mathrm{SHB}}}{\tau_{\mathrm{SHB}}}[\exp(h_{\mathrm{active}} + h_{\mathrm{SHB}} + h_{\mathrm{CH}}) - 1]P(t,0) - \frac{dh_{\mathrm{active}}}{dt} - \frac{dh_{\mathrm{CH}}}{dt} - \frac{h_{\mathrm{SHB}}}{\tau_{\mathrm{SHB}}} \tag{6.8.11}$$

$$\frac{dh_{\mathrm{CH}}}{dt} = -\frac{h_{\mathrm{CH}}}{\tau_{\mathrm{CH}}} - \frac{\varepsilon_{\mathrm{CH}}}{\tau_{\mathrm{CH}}}[\exp(h_{\mathrm{active}} + h_{\mathrm{SHB}} + h_{\mathrm{CH}}) - 1]P(t,0) \tag{6.8.12}$$

where the quantities h are defined as the total integrated gain as follows:

$$h_0 = \int g_0 dz' = \int_0^z \frac{\alpha I \tau_c}{eV} dz. \tag{6.8.13}$$

The expression for phase change is given by:

$$\phi(t) = -\frac{1}{2}[\alpha h_d(t) + \alpha_{\mathrm{CH}} h_{\mathrm{CH}}(t)], \tag{6.8.14}$$

where α is the usual linewidth enhancement factor associated with the interband transitions and α_{CH} is the linewidth enhancement factor for carrier heating. The linewidth enhancement factor for spectral hole burning (SHB) process, $\alpha_{\mathrm{SHB}} \sim 0$ [86].

Typical α values are in the 4 to 7 range and $\alpha_{\mathrm{CH}} \sim 1$ [86]. As a result, gain recovery in SOA can be faster than the phase change as is shown in Fig. 6.8.2. The input optical signal is a 10 Gb/s Gaussian pulse train (FWHM = 1 ps).

For a CR-SOA, (i.e. SOA with a carrier reservoir) temporal gain rate equations are derived from Eqs. (6.8.2)–(6.8.5). They are

$$\frac{dh_{\mathrm{active}}}{dt} = \frac{h_{\mathrm{reservior}} - h_{\mathrm{active}}}{\tau_t(1+\eta)} + \frac{\eta h_0}{\tau_c(1+\eta)} - \frac{h_{\mathrm{active}}}{\tau_c} - [\exp(h_{\mathrm{active}} + h_{\mathrm{SHB}} + h_{\mathrm{CH}}) - 1]P(t,0), \tag{6.8.15}$$

$$\frac{dh_{\mathrm{reservior}}}{dt} = -\frac{\eta(h_{\mathrm{reservior}} - h_{\mathrm{active}})}{\tau_t(1+\eta)} + \frac{h_0 - h_{\mathrm{reservior}}}{\tau_c(1+\eta)} - \frac{h_{\mathrm{reservior}}}{\tau_c}, \tag{6.8.16}$$

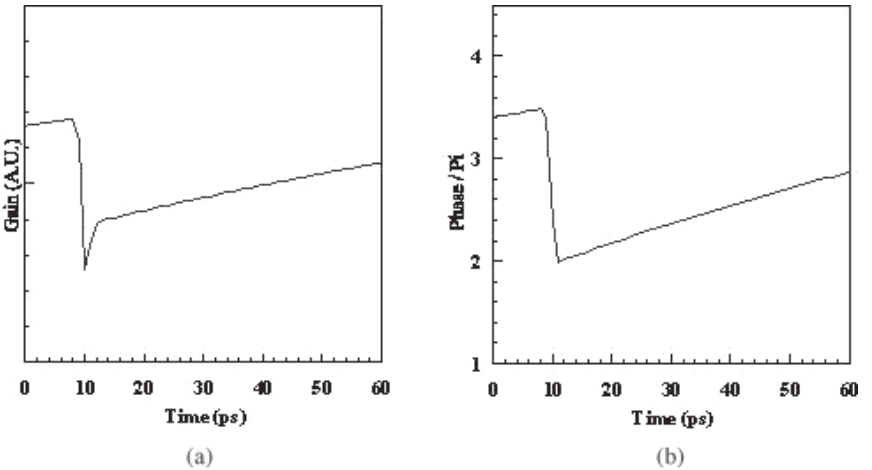

Fig. 6.8.2. Calculated (a) gain, and (b) phase recovery for normal SOA Input 10 Gb/s Gaussian pulse train [89].

$$\frac{dh_{\mathrm{SHB}}}{dt} = -\frac{\varepsilon_{\mathrm{SHB}}}{\tau_{\mathrm{SHB}}}[\exp(h_{\mathrm{active}} + h_{\mathrm{SHB}} + h_{\mathrm{CH}}) - 1]P(t,0) - \frac{dh_d}{dt} - \frac{dh_{\mathrm{CH}}}{dt} - \frac{h_{\mathrm{SHB}}}{\tau_{\mathrm{SHB}}}, \tag{6.8.17}$$

$$\frac{dh_{\mathrm{CH}}}{dt} = -\frac{h_{\mathrm{CH}}}{\tau_{\mathrm{CH}}} - \frac{\varepsilon_{\mathrm{CH}}}{\tau_{\mathrm{CH}}}[\exp(h_{\mathrm{active}} + h_{\mathrm{SHB}} + h_{\mathrm{CH}}) - 1]P(t,0). \tag{6.8.18}$$

The calculated gain and phase recovery following an optical pulse are plotted in Fig. 6.8.3. The parameters used above are [85–87]: $\tau_c = 200$ ps, $\tau_t = 5$ ps, $\tau_{\mathrm{SHB}} = 100$ fs, $\tau_{\mathrm{CH}} = 300$ fs, $\varepsilon_{\mathrm{SHB}} = \varepsilon_{\mathrm{CH}} = 0.1$, $\eta = 0.3$.

Due to fast gain and phase recovery, CR-SOA is more suitable than regular SOAs for high speed operation. Figure 6.8.4 shows the comparison of gain recovery for these two types of SOAs for 100 Gb/s input optical signals. Figure 6.8.4(b) shows that although the short term recovery is considerably improved the gain takes a long time to recover completely. We believe the SOA with CR will improve the performance in Manchester coded systems where long sequences of 1's and 0's are not present.

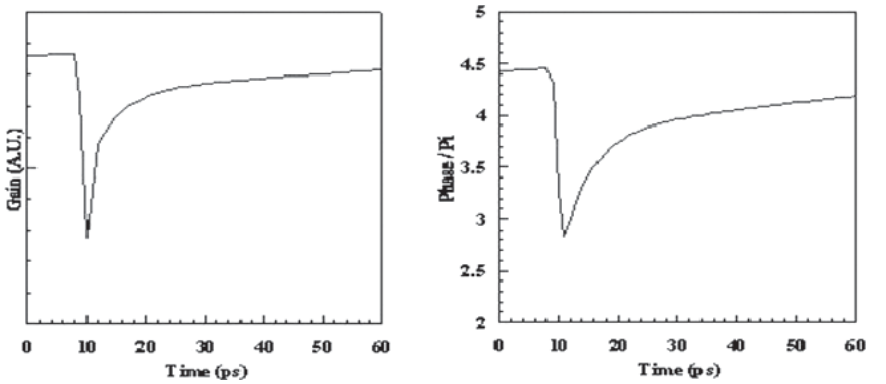

Fig. 6.8.3. Calculated gain (left) and phase (right) recovery for CR-SOA for an input 10 Gb/s Gaussian pulse train.

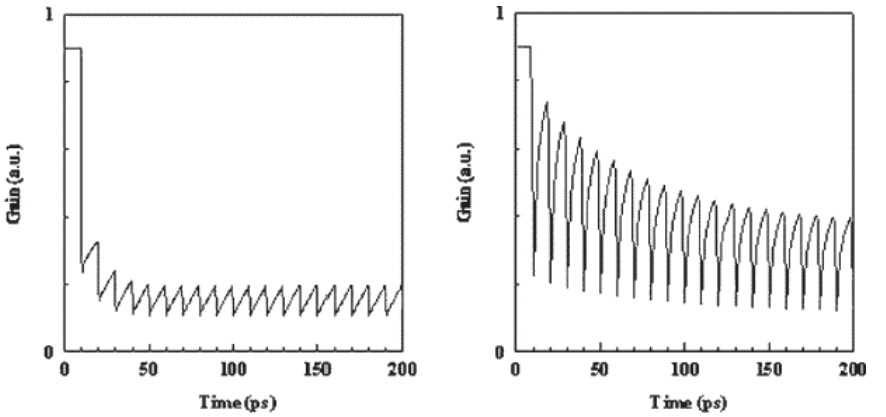

Fig. 6.8.4. Calculated gain recovery for SOA without CR (a) and CR-SOA (b) for an input 100 Gb/s Gaussian pulse train [89].

The population inversion factor η plays a key role in the gain recovery in CR-SOA. It represents the ratio of carriers in the active region and carrier reservoir and hence it is a measure of the amount of carriers available for fast gain recovery. The gain recovery is faster if the carrier reservoir population is high, i.e. if η is small. As expected η is smaller at high temperature and decreases with increasing current [88, 89].

Carriers in the CR and AR are initially both furnished by injection current. In steady state, inversion factor η can be calculated as

a function of injection current and temperature from (6.8.1). For a given carrier density n, the Fermi level E_{fc} is approximately given by [88]

$$E_{fc} = kT\left[\ln\left(\frac{N_{\text{total}}}{N_c}\right) + \sum_{i}^{\infty} A_i \left(\frac{N_{\text{total}}}{N_c}\right)^i\right]. \tag{6.8.19}$$

N_{total} is the total number of carriers injected in AR and CR, N_i is described in (6.8.1). From (6.8.2) and (6.8.3), we can obtain a steady state equation which links injection current to the carrier density as follows:

$$I_1/eV_{\text{active}} + I_2/eV_{\text{reservoir}} = N_{\text{total}}/\tau_c. \tag{6.8.20}$$

By solving (6.8.1), (6.8.19) and (6.8.20) numerically, the inversion factor η as function of injection current is obtained. In the integration of (6.8.1), the band edge difference of AR and CR is set to 70 meV. Figure 6.8.5 shows η decreases with increase of injection current i.e. carriers are more likely to be present at higher energy levels at high

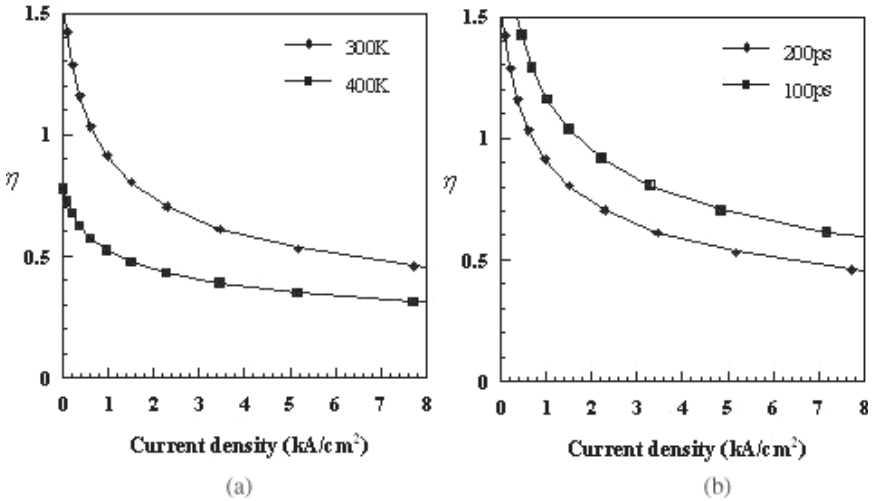

Fig. 6.8.5. Population inversion relation (η - ratio of active region to carrier reservoir carrier density) plotted as a function of injection current density for (a) different temperature (b) different τ_c [89].

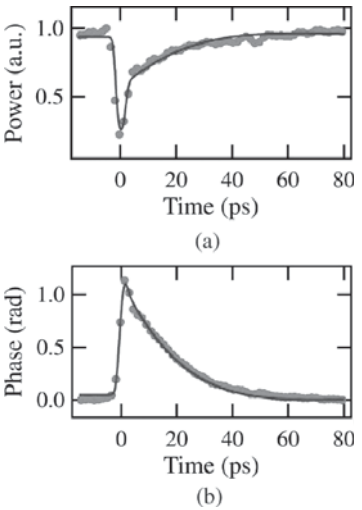

Fig. 6.8.6. (a) The measured (circles) and calculated (curves) power of a CW signal modulated by a 2.5-ps injected pulse in a SOA with a carrier reservoir. (b) Measured (circles) and calculated (curves) phases of the CW signal [90].

current density, and, also at high temperature. η is also plotted for different τ_c values in Fig. 6.8.5.

In order not to affect the gain of the SOA the CR region should be undoped (to reduce optical loss) and should not be too thick so as not to reduce the confinement. Thus a trade-off between optical gain and speed may exist. SCH and GRIN-SCH designs may also serve as CR regions.

The gain and phase response of a SOA with a CR layer has been measured using a pump-probe method [90]. The measured data is shown in Fig. 6.8.6. Note the gain recovery time is ~ 11 ps with a carrier reservoir layer.

References

[1] T. Saitoh and T. Mukai, Chap. 7 in, *Coherence, Amplification and Quantum Effects in Semiconductor Lasers*, ed. by Y. Yamamoto (New York, Wiley, 1991).
[2] M. Nakamura and S. Tsuji, *IEEE J. Quantum Electron.* **QE-17**, 994 (1981).
[3] T. Saitoh and T. Mukai, *J. Lightwave Technol.* **LT-6**, 1656 (1988).
[4] M. J. O'Mahony, *J. Lightwave Technol.* **LT-6**, 531 (1988).

[5] M. S. Lin, A. B. Piccirilli, Y. Twu and N. K. Dutta, *Electron. Lett.* **25**, 1378 (1989).
[6] N. K. Dutta, M. S. Lin, A. B. Piccirilli, R. L. Brown and U. K. Chakrabarti, *J. Appl. Phys.* **67**, 3943 (1990).
[7] C. E. Zah, J. S. Osinski, C. Caneau, S. G. Menoca1, L. A. Reith, J. Salzman, F. K. Shokoohi and T. P. Lee, *Electron. Lett.* **23**, 990 (1987).
[8] Y. Yamamoto, *Y. IEEE J. Quantum Electron.* **QE-16**, 1047 (1980).
[9] V. N. Luk'yanov, A. T. Semenov and S. D. Yakubovich, *Sov. J. Quantum Electron.* **10**, 1432 (1980).
[10] F. Favre, L. Jeunhomme, I. Joindot, M. Monerie and J. C. Simon, *IEEE J. Quantum Electron.* **QE-17**, 897 (1981).
[11] J. C. Simon, *Electron. Lett.* **18**, 438 (1982).
[12] T. Mukai, Y. Yamamoto and T. Kimura, *IEEE J. Quantum Electron.* **QE-18**, 1560 (1982).
[13] T. Saitoh, and T. Mukai, *IEEE J. Quantum Electron.* **QE-23**, 1010 (1987).
[14] J. C. Simon, *J. Lightwave Technol.* **LT-5**, 1286 (1987).
[15] G. Eisenstein, B. C. Johnson and G. Raybon, *Electron. Lett.* **23**, 1020 (1987).
[16] M. G. Oberg and N. A. Olsson, *Electron. Lett.* **24**, 99 (1988).
[17] N. A. Olsson, *J. Lightwave Technol.* **LT-7**, 1071 (1989).
[18] M. Fujiwara, H. Nishimoto, T. Kajitami, M. Hoh and S. Suzuki, *J. Lightwave Technol.* **LT-9**, 155 (1991).
[19] G. P. Agrawal, Ch. 8 in, *Fiber-Optic Communication Systems* (New York, Wiley, 1992).
[20] G. P. Agrawal and N. A. Olsson, *Opt. Lett.* **14**, 500 (1989).
[21] N. A. Olsson and G. P. Agrawal. *Appl. Phys. Lett.* **55**, 13 (1989).
[22] N. A. Olsson, G. P. Agrawal and K. W. Wecht, *Electron. Lett.* **25**, 603 (1989).
[23] G. P. Agrawal and N. A. Olsson, *IEEE J. Quantum Electron.* **QE-25**, 2297 (1989).
[24] I. W. Marshall, D. M. Spirit and M. J. O'Mahony, *Electron. Lett.* **23**, 818 (1987).
[25] J. M. Wiesenfeld, G. Eisenstein, R. S. Tucker, G. Raybon and P. B. Hansen, *Appl. Phys. Lett.* **53**, 1239 (1988).
[26] T. Saitoh, H. Itoh, Y. Noguchi, S. Sudo and T. Mukai, *IEEE Photon. Technol. Lett.* **1**, 297(1989).
[27] G. P. Agrawal, *Electron. Lett.* **27**, 620 (1991); *IEEE J. Quantum Electron.* **QE-27**, 1843 (1991).
[28] G. P. Agrawal and N. K. Dutta, Chapter 11, *Semiconductor Lasers* (van Nostrand Reinhold, 1992).
[29] G. Grosskopf, R. Ludwig and H. G. Weber. *Electron. Lett.* **22**, 900 (1986).
[30] T. Mukai, K. Inoue and T. Saitoh. *Electron. Lett.* **23**, 396 (1987).
[31] R. M. Jopson, K. L. Hall, G. Eisenstein, G. Raybon and M. S. Whalen. *EIectron. Lett.* **25**, 510 (1987).
[32] G. P. Agrawal, *Electron. Lett.* **23**, 1175 (1987).
[33] K. Inoue, *Electron. Lett.* **23**, 1293 (1987).

[34] R. M. Jopson, T. E. Darcie, K. T. Gayliard, R. T. Ku, R. E. Tench, T. C. Rice and N. A. Olsson, *Electron. Lett.* **23**, 1394 (1987).
[35] I. M. I. Habbab and G. P. Agrawal, *J. Lightwave Technol.* **LT-7**, 1351 (1989).
[36] S. Ryu, K. Mochizuki and H. Wakabayashi. *J. Lightwave Technol.* **LT-7**, 1525 (1989).
[37] G. P. Agrawal and I. M. I. Habbab. *IEEE J. Quantum Electron.* **QE-26**, 501 (1990).
[38] C. J. Koester and E. Snitzer, *Appl. Opt.* **3**, 1182 (1964).
[39] R. J. Mears, L. Reekie, S. B. Poole and D. N. Payne. *Electron. Lett.* **22**, 159 (1986).
[40] E. Desurvire, J. R. Simpson and P. C. Becker, *Opt. Lett.* **12**, 11 (1987).
[41] C. R. Giles and D. J. Di Giovanni, *IEEE Photon. Technol. Lett.* **2**, 866 (1990).
[42] W. I. Way, A. C. Von Lehman, M. J. Andrejco, M. A. Saifi and C. Lin, *Opt. Amp. Mtg., Monteray, CA* (Aug. paper TuB3, 1990).
[43] Y. Kimura, K. Suzuki and M. Nakagawa, *Electron. Lett.* **27**, 147 (1991).
[44] S. F. Carter, D. Szebesta, S. T. Davey, R. Wyatt, M. C. Brierley and P. W. France, *Electron. Lett.* **27**, 628 (1991).
[45] M. J. O'Mahony, I. W. Marshall, H. J. Westlake and W. G. Stallard, *Electron Lett.* **23**, 1238 (1986).
[46] N. A. Olsson and P. A. Garbinski, *Electron Lett.* **23**, 1114 (1986).
[47] I. W. Marshall, M. J. O'Mahony, *Electron. Lett.* **24**, 1052 (1987).
[48] I. W. Marshall, M. J. O'Mahony and P. Constantine, *Electron Lett.* **22**, 253 (1986).
[49] M. J. O'Mahony, I. W. Marshall, H. J. Westlake, W. J. Devlin and J. C. Regnault, presented at OFC '86 (Atlanta, Ga 1986).
[50] N. A. Olsson, *Electron Lett.* **21**, 1086 (1985).
[51] N. A. Olsson, M. G. Oberg, L. A. Koszi and G. J. Prezybylek, *Electron Lett.* **24**, 36 (1988).
[52] M. G. Oberg, N. A. Olsson, L. A. Koszi and G. J. Prezybylek, *Electron Lett.* **23**, 38 (1988).
[53] P. S. Henry, *IEEE J. Quantum Electron.* **QE-21**, 1862 (1985).
[54] M. Kobayashi and T. Mikawa, Chapter 9, in "WDM Technologies- Active Components" Ed. A. K. Dutta, N. K. Dutta and M. Fujiwara (Elsevier Science, 2002).
[55] T. L. Koch, Chapter 4, in *Optical Fiber Communications III B* eds. I. P. Kaminow and T. L. Koch (Academic Press, 1997).
[56] G. P. Agrawal and N. K. Dutta, Chapter 11, *Semiconductor Lasers* (van Nostrand Reinhold, 1992).
[57] G. P. Agrawal, Chapter 4, *Fiber Optic Communication Systems* (John Wiley, 1997).
[58] K. L. Hall and K. A. Rauschenbach, *Electron. Lett.* **32**, 1214 (1996).
[59] A. J. Poustie, K. J. Blow, R. J. Manning and A. E. Kelly, *Opt. Commun.* **159**, 208, (1999).
[60] T. Fjelde, A. Kloch, D. Wolfson, B. Dagens, A. Coquelin, I. Guillemot, F. Gaborit, F. Poingt and M. Renaud, *IEEE Photon. Technol. Lett.* **13**, 750 (2001).

[61] N. S. Patel, K. L. Hall and K. A. Rauschenbach, *Applied Optics* **37**, 2831 (1998).
[62] M. Jinno and T. Matsumoto, *Opt. Lett.* **16**, 220 (1991).
[63] T. Houbavlis, K. Zoiros, A. Hatziefremidis, H. Avramopoulos, L. Occhi, G. Guekos, S. Hansmann, H. Burkhard and R. Dall'Ara, *Electron. Lett.* **35**, 1650 (1999).
[64] C. Bintjas, M. Kalyvas, G. Theophilopoulos, T. Stathopoulos, H. Avramopoulos, L. Occhi, L. Schares, G. Guekos, S. Hansmann and R. Dall'Ara, *IEEE Photon. Technol. Lett.* **12**, 834 (2000).
[65] T. Fjelde, D. Wolfson, A. Kloch, B. Dagens, A. Coquelin, I. Guillemot, F. Gaborit, F. Poingt and M. Renaud, *Electron. Lett.* **36**, 1863 (2000).
[66] Q. Wang, G. Zhu, H. Chen, J. Jaques, J. Leuthold, A. B. Piccirilli and N. K. Dutta, *IEEE J. Quantum Electron.* **40**, 703 (2004).
[67] H. Chen, G. Zhu, J. Jaques, J. Leuthold, A. B. Piccirilli and N. K. Dutta, *Electron. Lett.* **38**, 1271 (2002).
[68] L. Schares, C. Shubert, C. Schmidt, H. G. Weber, L. Occhi and G. Guekos, *IEEE J. Quantum Electron.* **39**, 1394 (2003).
[69] R. Gutierrez-Castrejon, L. Occhi, L. Schares and G. Guekos, *Opt. Commun.* **195**, 167 (2001).
[70] P. Borri, S. Scaffetti, J. Mork, W. Langbein, J. M. Hvam, A. Mecozzi and F. Martelli, *Opt. Comm.* **164**, 51 (1999).
[71] J. Pleumeekers, M. Kauer, K. Dreyer, C. Burrus, A. G. Dentai, S. Shunk, J. Leuthold and C. H. Joyner, *IEEE Photon. Tech. Lett.* **14**, 12 (2002).
[72] M. Usami, T. Tsurusawa and Y. Matsushima, *Appl. Phys. Lett.* **72**, 2657 (1998).
[73] M. A. Dupertuis, J. L. Pleumeekers, T. P. Hessler, P. E. Selbmann, B. Deveaud, B. Dagens and J. Y. Emery, *IEEE Photon. Tech. Lett.* **12**, 1453 (2000).
[74] R. J. Manning and D. A. O. Davies, *Opt. Lett.* **19**, 889 (1994).
[75] J. Mark and J. Mørk, *Appl. Phys. Lett.* **61**, 2281 (1992).
[76] A. Mecozzi and J. Mørk, *IEEE J. Sel. Top. Quant. Electron.* **3**, 1190 (1997).
[77] A. Mecozzi and J. Mork, *J. Opt. Soc. Am. B.* **14**, 761 (1997).
[78] J. M. Tang and K. A. Shore, *IEEE, J. Quantum Electron.* **35**, 1704 (1999).
[79] G. Eisenstein, J. M. Wiesenfeld, M. Wegener, G. Sucha, D. S. Chemla, S. Weiss, G. Raybon and U. Koren, *Appl. Phys. Lett.* **58**, 158 (1991).
[80] M. A. Dupertuis, J. Lpleumeekers, T. P. Hessler, P. E. Selbmann, B. Deveaud, B. Dagens and J. Y. Emery, *IEEE Photon. Technol. Lett.* **12**, 1453 (2000).
[81] M. Sugawara, T. Akiyama, N. Hatori, Y. Nakata, H. Ebe and H. Ishikawa, *Meas. Sci. Technol.* **13**, 1683 (2002).
[82] G. Eisenstein, R. S. Tucker, J. M. Wiesenfeld, P. B. Hansen, G. Raybon, B. C. Johnson, T. J. Bridges, F. G. Storz and A. Burrus, *Appl. Phys. Lett.* **54**, 454(1991)
[83] T. Furata, in *Semiconductors and Semimetals* Vol. 39, Ch. 3 (New York, Academic, 1993).
[84] T. W. Berg and J. Mørk, *IEEE J. Quantum Electron.* **40**, 1527 (2004)

[85] A. Mecozzi and J.Møork, *IEEE J. Sel. Topics Quantum Electron.*
[86] J. M. Tang and K. A. Shore, *IEEE J. Quantum Electron.* **35**, 1040 (1999).
[87] M. Sugawara, H. Ebe, N. Hatori, M. Ishida, Y. Arakawa, T. Akiyama, K. Otsubo and Y. Nakata, *Phys. Rev. B. Condens. Matter* **69**, 235 (2004).
[88] G. P. Agrawal and N. K. Dutta, *Semiconductor Lasers*, Ch. 3 (New York: Van Nostrand Reinhold, 1993).
[89] H. Sun, Q. Wang, H. Dong, G. Zhu, N. K. Dutta and J. Jaques, *Photonic Tech. Lett.* **18**, 196 (2006).
[90] I. Kang, C. Dorrer, L. Zhang, M. Dinu, M. Rasras, L. L. Buhl, S. Cabot, A. Bhardwaj, X. Liu, M. A. Cappuzzo, L. Gomez, A. Wong-Foy, Y. F. Chen, N. K. Dutta, S. S. Patel, D. T. Neilson, C. R. Giles, A. Piccirilli and J. Jaques, *IEEE J. of Setected Area of Quantum Electron.* **14**, 258 (2008).

Chapter 7

Photonic Integrated Circuit Using Amplifiers

7.1. Introduction

There have been a significant number of developments in the technology of integration of semiconductor lasers, amplifiers, modulators and other related devices on the same chip. These chips allow higher levels of functionality than that achieved using single devices. The name photonic integrated circuits (PIC) are generally used when all the integrated components are photonic devices, e.g. lasers, detectors, amplifiers, modulators, and couplers. Several review articles and books have been published on PICs [1–6]. A class PICs which use amplifiers are being investigated for photonic logic systems. The design and performance of these PICs are described in Chs. 9 and 10.

For amplifier applications where the amplifier is integrated with another photonic device such as a laser it is not necessary to have polarization independent gain. Since the light from the laser is TE polarized, the parameter of importance in this application is high TE gain and high saturation power. Since multiquantum well (MQW) materials generally have high TE gain than that for regular double heterostructure material, MQW active regions are generally used for amplifiers which are integrated in a photonic circuit. The saturation output power i.e. the power at which the gain decreases by 3 dB from its value at low power is higher for MQW amplifiers. Saturation power as high as 100 mW has been reported for MQW amplifiers.

7.2. Integrated Laser and Amplifier

Since MQW amplifier is ideally suited for amplifying the output power of a semiconductor laser, it is useful to combine the amplifier and laser on a single chip and thereby produce a compact device with low coupling losses. MQW amplifiers have been integrated with both distributed feedback (DFB) and distributed Bragg reflector (DBR) lasers. The schematic of such an integrated device with a MQW amplifier integrated with a DBR laser is shown in Fig. 7.2.1. The integrated device has, a laser whose active region has a band gap of 1.3 μm, a waveguide layer which is present through out the length of the chip with a band gap of ∼1.1 μm, and an amplifier active region with a band gap of 1.3 μm. The waveguide layer couples the laser and the amplifier devices. The grating with a periodicity of 205 nm provides frequency selective feedback so that the laser emits in a single frequency. For the structure shown both the laser and the amplifier have a MQW active region.

The fabrication of a typical similar device involves the following steps. First a n-InGaAsP waveguide layer ($\lambda \sim 1.1\,\mu$m InGaAsP, ∼0.5 μm thick), n-InP layer (∼0.05 μm thick) , a InGaAsP MQW region and a p-InP layer (∼1 μm thick), and a p-InGaAs layer (∼0.5 μm thick) are successively grown over a n-InP substrate using MOCVD growth technique. The InGaAsP MQW region has four InGaAsP active regions (∼8 nm thick) and InP barrier layers (∼10 nm thick). The thin InP layer serves as a stop etch layer for wet

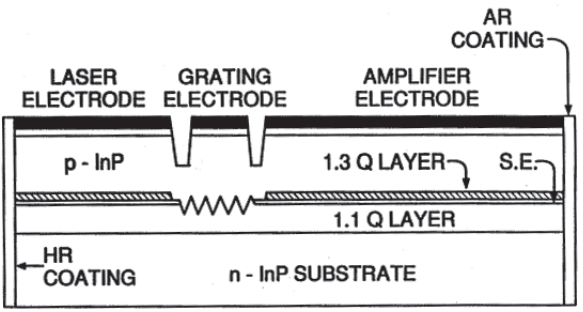

Fig. 7.2.1. Schematic of a photonic integrated circuit with a DBR (distributed Bragg reflector) laser and amplifier [7].

chemical etching. The active region and the InP stop etch layers are removed using selective etching using a dielectric mask. The grating is produced in these regions using wet chemical etching and a phase mask. The wafer is then fabricated into buried heterostructure devices using an active stripe definition by etching followed by second MOCVD growth of current confining layers as described in Ch. 4. This is followed by metal deposition and cleaving. The cleaved facets are antireflection (AR) and high reflection (HR) coated using deposition of dielectrics of suitable thickness. The light vs. current characteristics of the laser with the amplifier driven at 170 mA is shown in Fig. 7.2.2.

Integrated distributed feedback (DFB) laser and amplifier structures are important because they have low spectral width under modulation [8, 9]. The schematic of such a structure is shown in Fig. 7.2.3. The DFB laser and the amplifier have a MQW active region. Semi-insulating Fe doped InP layers are used for both current confinement and for isolation of DFB laser and the amplifier. The DFB laser region has a grating etched under the active region which provides frequency selective feedback.

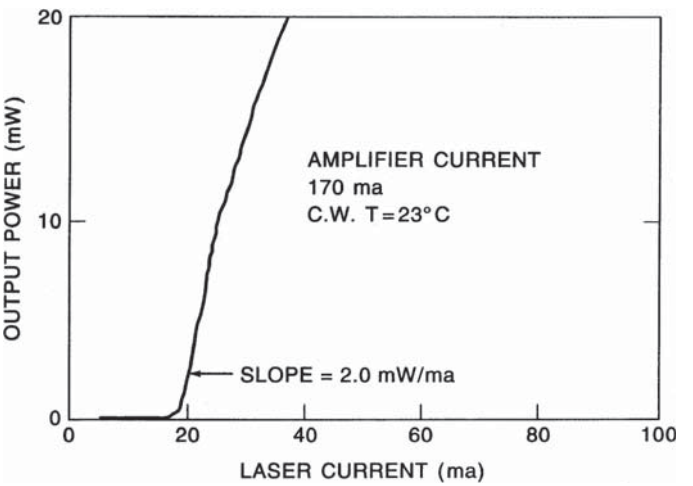

Fig. 7.2.2. Power output as a function of laser current of the device shown in Fig. 7.2.1 [7].

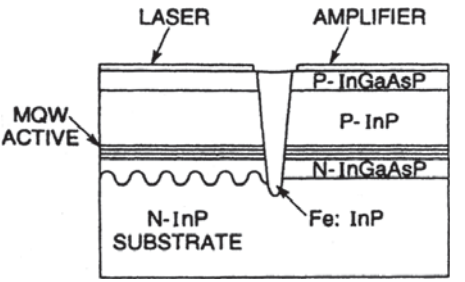

Fig. 7.2.3. Schematic of a distributed feedback (DFB) laser and amplifier structure [8].

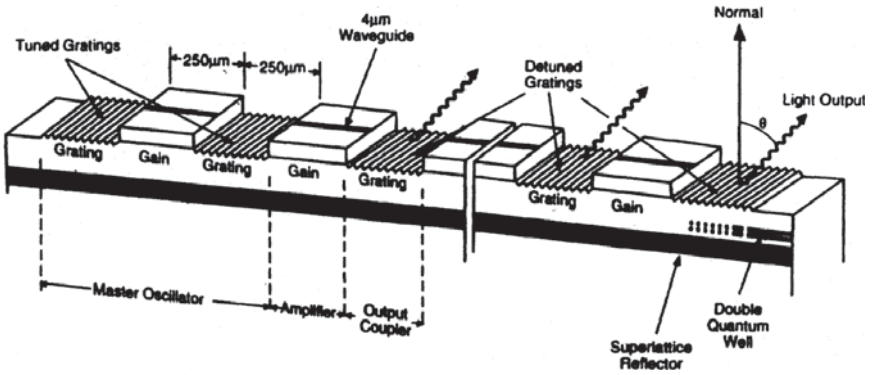

Fig. 7.2.4. A number of amplifiers and a DBR laser connected in series [10].

For low chirp operation, the laser is modulated with low current (∼5 mA) which produces small chirp and the amplifier is used to amplify the output to the required power levels (∼10 mW to 30 mW).

Another interesting laser-amplifier integrated device has a series of amplifiers connected in tandem with a laser (Fig. 7.2.4) [10]. The light is emitted normal to the chip in this device. The first active region-grating combination acts as a laser oscillator. A fraction of the output of this laser propagates along the waveguide and is amplified by the next active region (amplifier). This propagation continues throughout the chip. The device emits in a series of beams normal to the grating. The emission is in a single wavelength and all the emitters emit in phase.

7.3. Multichannel WDM Sources with Amplifiers

An alternative to single channel very high speed (>20 Gb/s) data transmission for increasing the transmission capacity is multichannel transmission using wavelength division multiplexing (WDM) technology. In WDM system many (4, 8, 16 or 32) wavelengths carrying data are optically multiplexed and simultaneously transmitted through a single fiber. The received signal with many wavelengths is optically demultiplexed into separate channels which are then processed electronically in a conventional form. Such a WDM system needs transmitters with many lasers at specific wavelengths. It is desirable to have all of these laser sources on a single chip for compactness and ease of fabrication like electronic integrated circuits.

Figure 7.3.1 shows the schematic of a photonic integrated circuit with multiple lasers for a WDM source [9]. This chip has 4 individually addressable DFB lasers, the output of which are combined using

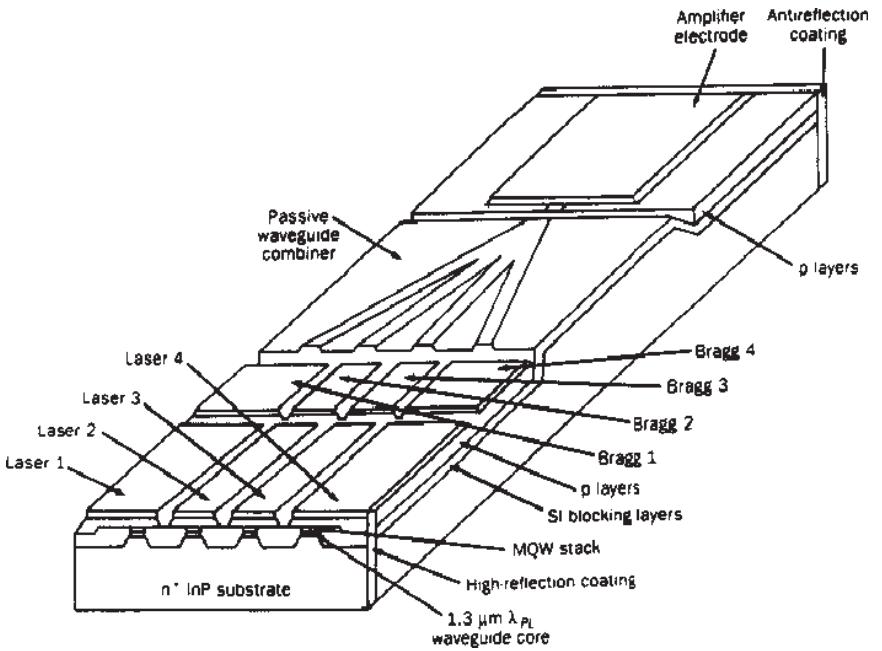

Fig. 7.3.1. Schematic of a photonic integrated circuit with multiple lasers for a WDM source [9].

a waveguide based multiplexer. Since the waveguide multiplexer has an optical loss of ∼8 dB, the output of the chip is further amplified using a semiconductor amplifier. The laser output in the waveguide is TE polarized and hence an amplifier with a multiquantum well gain region which has a high saturation power is integrated in this chip. Many similar devices which use SOA for output amplification have been fabricated [4, 5].

7.4. Spot Size Conversion (SSC)

A typical amplifier diode has too wide (∼30° × 40°) beam pattern for good mode matching to a single mode fiber, which results in a loss of power coupled to the fiber. Thus an amplifier whose output spot size is converted (SSC) to match an optical fiber is an attractive device for low loss coupling to the fiber without a lens and for wide alignment tolerances. Several researchers have reported such devices using lasers [11, 12]. Generally they involve producing a vertically and laterally tapered waveguide near the output facet of the laser. The tapering needs to be done in an adiabatic fashion so as to reduce the scattering losses. The schematic of a spot size converted laser is shown in Fig. 7.4.1.

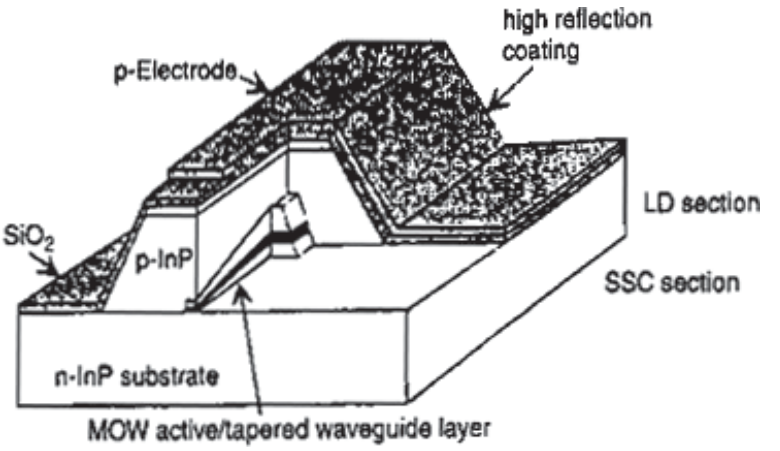

Fig. 7.4.1. Schematic of a Spot Size Converter (SSC) laser [12].

The amplifier designs are similar. The laser is fabricated using two MOCVD growth steps. The SSC section is about 200 μm long. The waveguide thickness is narrowed along the cavity from 300 nm in the active region to ∼100 nm in the region over the length of the SSC section. The laser emits near 1.3 μm, has a multiquantum well active region and a laser section length of 300 μm. Beam divergences of 9° and 10° in the horizontal and vertical direction have been reported for SSC devices [12].

7.5. Mach-Zehnder Interferometer

Semiconductor optical amplifiers incorporated into Mach-Zehnder interferometer (MZI) or Michelson interferometer configurations have been used for wavelength conversion and to demultiplex high-speed time division multiplexed optical signals [13, 14]. The schematic of the device is shown in Fig. 7.5.1.

The input signal beam is split into two beams by an input y-junction, which propagates through semiconductor amplifiers positioned in the upper and lower arms of the interferometer. These beams then merge and interfere at an output y-junction. The phase of the interference is altered by injecting another signal in one of the other ports.

The ratio of the output P_o to the input signal P_i is given by

$$\frac{P_o}{P_i} = \frac{1}{8}\Big\{G_1 + G_2 - 2\sqrt{G_1 G_2}\cos(\phi_1 - \phi_2)\Big\},$$

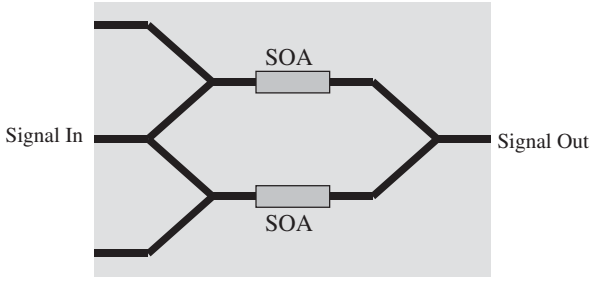

Fig. 7.5.1. Schematic of a Mach-Zehnder interferometer with integrated SOA's.

where G_1, G_2 are the gains of the amplifiers and ϕ_1, ϕ_2 are phase changes induced by nonlinear effects in the two amplifiers. The phase difference, $\Delta\phi = \phi_1 - \phi_2$, at the output is given by:

$$\Delta\phi = \frac{\alpha}{2P_s}\left\{-\frac{h\nu}{e}(I_1 - I_2) + \frac{P_c}{2}(G_1 - 1)\right\},$$

where $\alpha = \delta n_R/\delta n_{\mathrm{Im}}$ is the ratio of the carrier induced change in the real and imaginary part of the index, also known as the linewidth enhancement factor. P_c is the injected power in one of the amplifiers, P_s is the saturation power in the amplifier and I_1, I_2 are the currents through the two amplifiers. For $I_1 \cong I_2$ and $G_1 \cong G_2$, the above reduces to

$$\frac{P_o}{P_i} = \frac{G}{2}\sin^2\left(\frac{\Delta\phi}{2}\right),$$

where $\Delta\phi = \frac{\alpha}{4}\frac{P_c}{P_s}(G-1)$.

Using typical values; $\alpha = 3$, $P_s = 10\,\mathrm{mW}$ and experimental saturated gains $G \cong 40$, we get $Pc \cong 1\,\mathrm{mW}$ for $\Delta\phi = \pi$. Thus, the optical power that need to be injected in one of the other ports for π phase shift can be easily achieved. There may be some thermally induced refractive index changes, but these are considerably smaller than the carrier induced changes considered above and can be ignored. Thus MZI devices operate on the principle of optically induced phase shift on a carrier signal. The Michelson interferometer (MI) operates on a similar principle. Both MZI and MI devices have been used in wavelength conversion, optical demultiplexing and photonic logic systems. They are described in detail in Chs. 8 and 9.

The schematic of a MZI device and bonded version of a similar device used in operation are shown in Fig. 7.5.2. The MZI device is fabricated with tilted waveguides (to reduce residual reflections) at the facets and beam expanders at input and output for high coupling efficiency to single mode fibers which are used to couple light to the semiconductor waveguides. The devices have long amplifiers ($\sim$2 mm long) for high gain/phase change.

The schematic of a MI used as an optical demultiplexer along with a photograph of an actual device is shown in Fig. 7.5.3. The

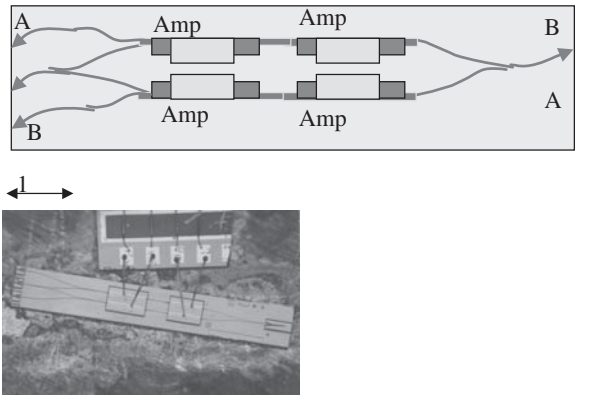

Fig. 7.5.2. Photograph of MZI chip and a schematic of as fabricated device.

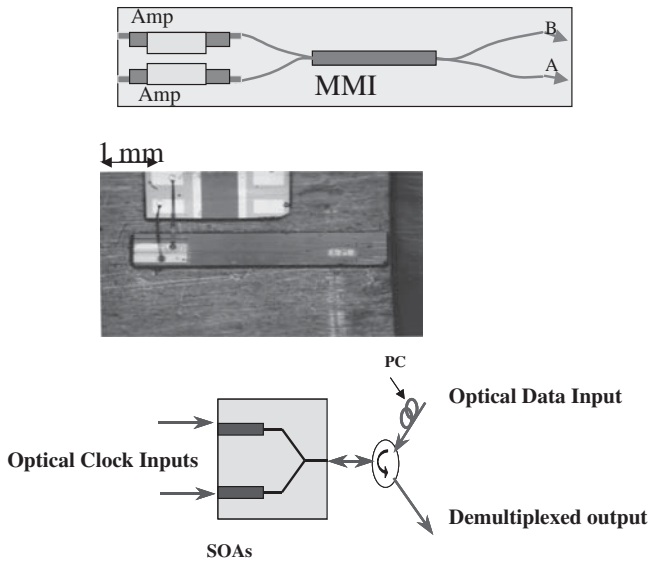

Fig. 7.5.3. Schematic and photograph of a MI device. The bottom figure shows the configuration for an optical demultiplexer. PC is the polarization controller and a circulator is used to get the demultiplexed output.

principle of operation of this device is similar to that for a MZI. The optical signal is reflected back into the amplifiers in this device which results in double pass and hence possibly higher speed compared to MZI devices. This device is also fabricated with tilted waveguides

to reduce the effect of residual reflections. The applications of the semiconductor optical amplifier based interferometer devices, such as Mach-Zehnder and MIs are discussed in Chs. 8–10.

7.6. Photoreceiver

As mentioned in Ch. 6, SOA has been used as a preamplifier for photodiodes for lightwave system applications. A photonic integrated circuit with a SOA and photodiode has been reported [15]. The device uses a traveling wave type photodiode. The input light is injected into a dual section SOA. The front section has high optical confinement for high gain and the back section is offset to produce low confinement and hence high saturation power. The structure is shown in Fig. 7.6.1. The front section is labeled c-MQW (c-centered) and the back section is labeled o-MQW (o-offset). The SOAs are followed by the photodiode which has a InGaAs active region. The wafer is fabricated using the InP/InGaAsP material system using multiple MOCVD growth steps and is processed into ridge waveguide type devices for lateral confinement. The maximum chip gain of the SOA region is 28 dB. The saturation output power of SOA is 18 dB. The internal quantum efficiency of the photodiodes are determined to be 28% and 32% for 30 μm long and 40 μm long photodiodes respectively [15]. These measurements were carried out at an input light wavelength of 1550 nm.

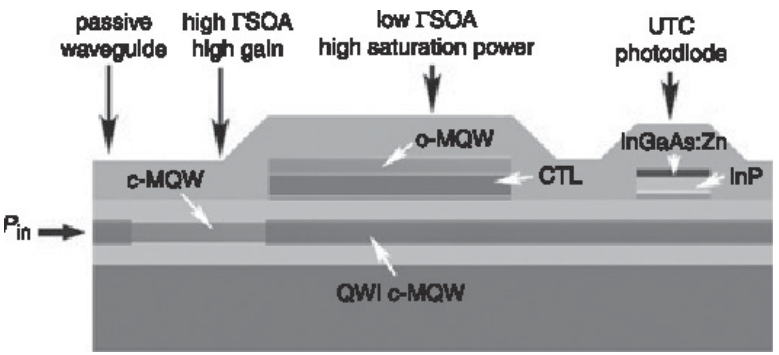

Fig. 7.6.1. Integrated photodiode and SOA preamplifier structure [15].

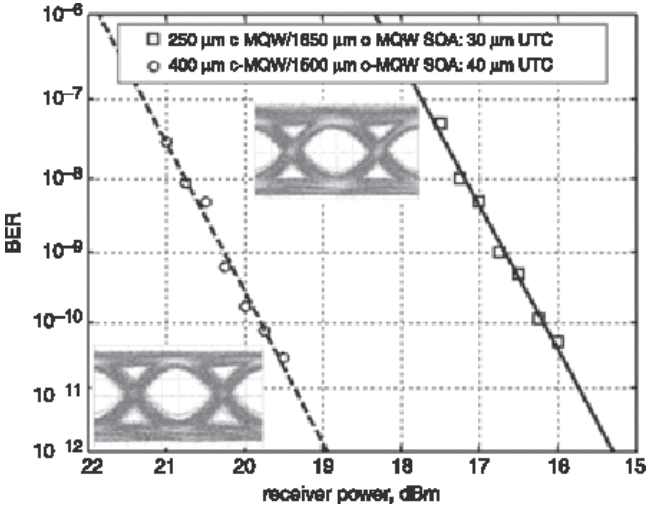

Fig. 7.6.2. Bit-error-rate (BER) as a function of received power [15].

The device was used as a photoreceiver in a 40 Gb/s transmission experiment. The bit-error-rate as a function of received power for two designs with different SOA lengths is shown in Fig. 7.6.2. The measured receiver sensitivity (received power for 10^{-9} BER) for the two designs are -17 dBm and -20 dBm respectively.

Semiconductor optical amplifiers continue to be used as power amplifier and preamplifier in various photonic integrated circuits. The power amplifier applications are primarily in wavelength division multiplexing circuits to compensate for the optical loss of the multiplexer. The preamplifier applications are for a photo-receiver in conjunction with a photodiode. The latter is suitable as an alternative to avalanche photodiode based receiver which requires high voltage ($\sim$50 to 100 V) for operation.

References

[1] K. Kobayashi, Chap. 15, in *Optical Fiber Telecommunications II*, eds. by S. E. Miller and I. P. Kaminow (San Diego: Academic Press, 1988).
[2] T. L. Koch and U. Koren. *IEEE J. Quantum Electron.* **QE-27**, 641 (1991).
[3] O. Wada, T. Sakurai, and T. Nakagami. *IEEE J. Quantum Electron.* **QE-22**, 850 (1986).
[4] S. R. Forrest, *J. Lightwave Technol.* **LT-3**, 1248 (1985).

[5] M. Dagenais (ed.), *Integrated Optoelectronics* (John Wiley, 1995).
[6] O. Wada (ed.), *Optoelectronic Integration: Physics Technology and Applications* (Kluwar Academic, 1994).
[7] T. L. Koch, U. Koren, R. P. Gnall, F. S. Choa, F. Hernandez-Gil, C. A. Burrus, M. G. Young, M. Oron and B. I. Miller, *Electron. Lett.* **25**, 1621 (1989).
[8] N. K. Dutta, J. Lopata, R. Logan and T. Tanbun-Ek, *Appl. Phys. Lett.* **51**, 1676 (1991).
[9] U. Koren, B. I. Miller, G. raybon, M. Oron, M. G. Young and T. L. Koch, *Appl. Phys. Lett.* **57**, 1375 (1990).
[10] D. F. Welch, D. Mehuys, R. Parke, R. Waarts, D. Scifres and W. Streifer, *Electron. Lett.* **17**, 1327 (1990).
[11] R. Y. Fang, D. Bertone, M. Meliga, I. Montrosset, G. Oliveti and R. Paoletti, *IEEE Photon. Technol. Lett.* **9**, 1084 (1997).
[12] H. Yamazaki, K. Kudo, T. Sasaki and M. Yamaguchi, *Proc. OECC '97 Seoul*, Korea, pp. 440–441, paper 10C1-3.
[13] B. Mikklesen, S. L. Danielsen, C. Jorgensen and K. E. Stubkjaer, *IEEE, J. Quantum Electron.* **16**, 2095 (1998).
[14] T. Durhuus, B. Mikkelsen, C. Joergensen and K. E. Stubkjaer, *J. Lightwave Technol.* **14**, 942 (1996).
[15] J. W. Raring, L. A. Johansson, E. J. Skogen, M. N. Sysak, H. N. Poulsen, S. P. DenBaars and L. A. Coldren, *Electronic Lett.* **42**, 16 (2006)

Chapter 8

Functional Properties and Applications

8.1. Introduction

Significant advances in research results, development and application of semiconductor lasers, amplifiers and modulators have occurred over the last two decades. The fiber optic revolution in telecommunications which has provided several orders of magnitude improvement in transmission capacity at low cost would not have been possible without the development of reliable semiconductor lasers. Since semiconductor optical amplifier is similar to a semiconductor laser, much of the initial work on optical amplification using semiconductor amplifiers also has a long history [1–9].

The properties of semiconductor optical amplifiers as it relates to amplification have been discussed in previous chapters. This chapter will focus on functional device characteristics of semiconductor amplifiers. The devices are based on four-wave mixing characteristics or gain/phase modulation characteristics in semiconductor amplifier. Applications include wavelength conversion for all-optical networks, optical demultiplexing, and other applications e.g. clock recovery for optical time division multiplexed (OTDM) transmission [10–14].

8.2. Four-Wave Mixing

Semiconductor amplifiers are known to exhibit optical nonlinear effects, such as four-wave mixing. Four-wave mixing (FWM) in SOA's has been used as a technique for performing wavelength conversion due to its good conversion efficiency and high speed response for

wavelength division multiplexing (WDM) networks [15–21]. FWM is a process by which optical signals at different (but closely spaced) wavelengths can mix to produce new signals at other wavelengths, but with lower power. In the FWM process, light at two frequencies, ω_0 and ω_1, are injected into the amplifier. These injected signals are generally referred to as pump and probe beams. The pump and probe beams can be obtained from two single wavelength distributed feedback (DFB) lasers. The pump signal is of higher power than the probe signal. Consider the case when both the pump and the probe signals are CW. Propagation through the SOA results in the generation of two additional FWM signals with frequencies $2\omega_0 - \omega_1$ and $2\omega_1 - \omega_0$. The intensity of light at these wavelengths is measured using a spectrometer. The FWM signal at frequency $2\omega_0 - \omega_1$ has higher power if the pump signal strength (at frequency ω_0) is higher than that of the probe signal. If I_0 and I_1 are the intensities of the signals at frequencies ω_0 and ω_1, the intensities of the signals at frequencies $2\omega_0 - \omega_1$ and $2\omega_1 - \omega_0$ are proportional to $I_0^2 I_1$ and $I_0 I_1^2$ respectively.

8.2.1. *CW FWM results*

An example of the output spectrum from a SOA with a continuous wave (CW) co-propagating pump and probe signal is shown in Fig. 8.2.1. The pump and probe signals have high intensity. The

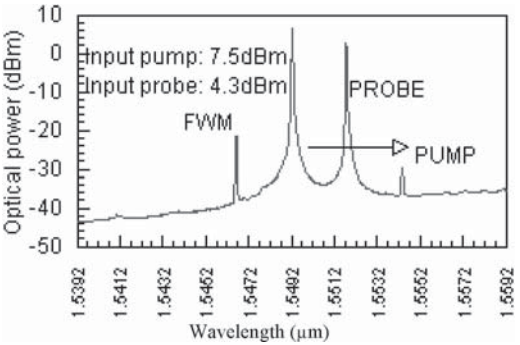

Fig. 8.2.1. Spectra of FWM. The wavelength separation λ_d between the pump and probe signal is 2.5 nm.

additional low intensity signals on the spectrum are due to FWM process. The experiment was carried out using optical fibers for coupling the pump and probe light into the SOA waveguide.

The measured FWM signal power as a function of the applied current in the SOA for two incident signals is shown in Fig. 8.2.2. Also plotted is the measured gain (fiber-to-fiber) as a function of current for the same amplifier. The data are shown for the FWM signal at a frequency of $2\omega_0 - \omega_1$ where ω_0 and ω_1 are the frequencies of the pump and probe respectively.

Another parameter that affects the FWM power is the wavelength separation between the pump and the probe signal. The measured FWM power as a function of this wavelength separation is shown in Fig. 8.2.3.

Also, shown (solid line) is the calculated curve (described later) using typical material parameter values. Both the experimental

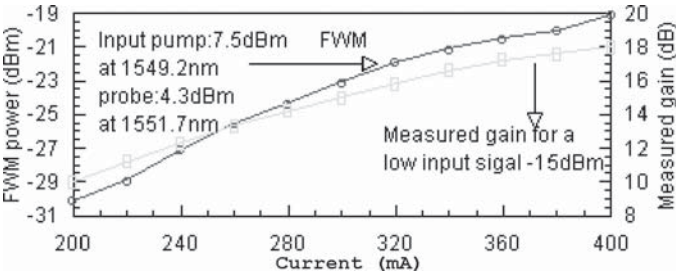

Fig. 8.2.2. Measured FWM signal as a function of current in the SOA. Also shown is the measured gain of the same SOA for a low input signal.

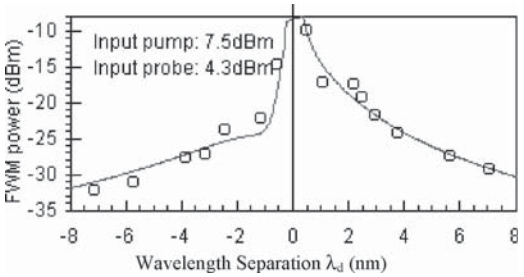

Fig. 8.2.3. Measured FWM power (circles) as a function of the wavelength separation. The solid line is the calculated result using typical parameter values.

results and calculation show that the FWM power is high if the wavelength separation is small. It also shows that the curve is asymmetric viz. for a given $\lambda_d = \lambda_1 - \lambda_0$ FWM signal power is higher for $\lambda_d > 0$ than for $\lambda_d < 0$.

The mechanisms responsible for FWM in an SOA are carrier density modulation and nonlinear gain [15]. The former has a time constant in the range of 0.1 to 0.5 ns and the latter can occur on a much faster time scale (∼500 fs) [15]. Generally $I_{FWM} \ll I_0$, I_1 where I_0 and I_1 are the pump and the probe power respectively.

8.2.1.1. *FWM analysis*

In this section the FWM within a SOA is analyzed in detail. The susceptibility χ of the semiconductor is a tensor. χ also depends on the optical field intensity in the case of high input power. This could be described by expanding the susceptibility as a power series in the optical field E

$$\chi = \chi^{(1)} + \chi^{(2)}E + \chi^{(3)}EE + \ldots, \tag{8.2.1}$$

where $\chi^{(1)}$ is the small signal or linear susceptibility and $\chi^{(2)}$ and $\chi^{(3)}$ are the higher order nonlinear susceptibilities. The third-order susceptibility $\chi^{(3)}$ gives rise to all the nonlinear effects in a SOA such as four-wave mixing (FWM) and self-phase modulation. The induced nonlinear polarization due to $\chi^{(3)}$ is expressed as

$$P = \varepsilon_0 \chi^{(3)} EE \cdot E. \tag{8.2.2}$$

For the FWM case, the third order susceptibility comes from the carrier density modulation due to the beating between the pump and the probe, so Eq. (8.2.2) is written as [19]

$$P = \varepsilon_0 \frac{\partial \chi(n)}{\partial n} n_1 \cdot E, \tag{8.2.3}$$

where n_1 is the modulated carrier density and $n \gg n_1$. It has also been deduced that the susceptibility $\chi(n)$ is related to the carrier

density n by [19] (see also Eq. (6.2.3))

$$\chi(n) = -\frac{\bar{n}c}{\omega_0}(\alpha + i)g(n), \tag{8.2.4}$$

where $g(n) = a(n - n_0)$ is the gain and $\bar{n}$ is the effective mode index. The quantity α is the linewidth enhancement factor, which is defined as

$$\alpha = \frac{\delta n_R}{\delta n_I}, \tag{8.2.5}$$

where n_R and n_I are the real and the imaginary parts of the refractive index.

In FWM, the beat frequency between the pump and probe is

$$\omega_d = \omega_0 - \omega_1. \tag{8.2.6}$$

It is relatively small compared to ω_0 and ω_1. The pump beam is generally more intense than the probe beam, i.e. $E_1 \ll E_0$. (E_0, E_1 correspond to the electrical field of the pump and probe). The carrier density n is described by the following rate equation in the semiconductor optical amplifier when a current I is applied,

$$\frac{dn}{dt} = \frac{I}{eV} - \frac{n}{\tau_c} - \frac{\Gamma g(n)}{\hbar\omega_0 A}|E|^2, \tag{8.2.7}$$

where τ_c is the carrier lifetime and A is the cross section of the waveguide mode. Since typically the length of SOA is less than 5 mm, nearly phase matching condition is satisfied for the pump and probe beams, then the total optical field is:

$$E = E_0 \exp(-i\omega_0 t) + E_1 \exp(-i\omega_1 t), \tag{8.2.8}$$

so

$$|E|^2 = |E_0|^2 + |E_1|^2 + \{E_0^* E_1 \exp[i(\omega_0 - \omega_1)t] + \text{c.c}\}, \tag{8.2.9}$$

where c.c. denotes complex conjugate. It is expected that the carrier density will be modulated by the beat frequency ω_d, then we have

$$n(t) = n_s + n_1 \exp(-i\omega_d t). \tag{8.2.10}$$

Since $E_1 \ll E_0$, and $\bar{n}_s \gg \mathrm{n}_1$. Substitute (8.2.9) and (8.2.10) into (8.2.7), the following is obtained,

$$n_s = \frac{\frac{I}{eV}\tau_c + \frac{|E_0|^2}{P_s} n_0}{1 + \frac{|E_0|^2}{P_s}}, \tag{8.2.11}$$

$$n_1 = \frac{-(n_s - n_0)\frac{E_0^* E_1}{P_s}}{1 + \frac{|E_0|^2}{P_s} - i\omega_d \tau_c}, \tag{8.2.12}$$

where P_s is the saturation power defined as

$$P_s = \frac{Ahv}{\Gamma a \tau_c}, \tag{8.2.13}$$

where A is the cross-sectional area of the waveguide mode, Γ is the confinement factor, $h\nu$ is the photon energy of the signal.

By substituting Eqs. (8.2.4) and (8.2.12) into the Eq. (8.2.3), the induced nonlinear polarization due to the beating signal between the pump and the probe in the SOA is obtained. The optical fields in the SOA satisfy the Maxwell's equation

$$\nabla^2 E - \frac{n^2}{c^2}\frac{\partial^2 E}{\partial t^2} = \frac{1}{\varepsilon_0 c^2}\frac{\partial^2 P}{\partial t^2}. \tag{8.2.14}$$

For the FWM process, generally $I_{FWM} \ll I_1 \ll I_0$ where I_{FWM}, I_0, I_1 are the FWM, the pump and the probe power respectively. Substituting Eq. (8.2.3) into (8.2.14) and following procedures similar to those used in [15], a set of coupled equations are obtained for the electric fields of the pump, the probe and the FWM beams [16]

$$\begin{aligned} \frac{dE_0}{dz} &= \frac{1}{2} g(1 - i\alpha) E_0, \\ \frac{dE_1}{dz} &= \frac{1}{2} g(1 - i\alpha) E_1, \\ \frac{dE_{FWM}}{dz} &= \frac{1}{2} g(1 - i\alpha) E_{FWM} - \frac{1}{2} g\sigma E_1^* E_0^2, \end{aligned} \tag{8.2.15}$$

where

$$\sigma = \frac{1 - i\alpha}{1 + \frac{|E_0|^2}{I_s} - i2\pi \cdot f_d \tau_c} \cdot \frac{1}{I_s} + \frac{1 - i\beta}{1 - i2\pi \cdot f_d \tau_n} \cdot \frac{1}{I_n},$$

where E_0, E_1 are the electric fields of the pump and probe signals, z is the distance traveled in the amplifier, $f_d = f_0 - f_1$ is frequency separation between the pump and the probe. The signals enter the amplifier at $z = 0$ and the amplification length is L. The quantities I_s, I_n, τ_c, and τ_n are the saturation powers and the relaxation time constants for carrier density modulation and nonlinear gain respectively. The quantity g is the material gain multiplied by the optical confinement factor, which is given by:

$$g(z) = \frac{g_0}{1 + \frac{|E_0(z)|^2}{I_s}},$$

where g_0 is the unsaturated gain. The quantity α is the linewidth enhancement factor and β is the ratio of the real and imaginary parts of the refractive index change induced by gain nonlinearity. If $I_0(0) < I_s$, the E_0^2/I_s term in the denominator of σ can be neglected. Also, for $g \cong g_0$, the equations for E_0 and E_1 are easily solved and substituting the solution into the equation for E_{FWM}, the following results:

$$\frac{dE_{\mathrm{FWM}}}{dz} = AE_{\mathrm{FWM}} - Be^{Cz}, \tag{8.2.16}$$

where $A = \frac{1}{2}g(1 - i\alpha)$,

$$B = \frac{1}{2}g \cdot \left[\frac{1 - i\alpha}{1 - i2\pi \cdot f_d\tau_c} \cdot \frac{1}{I_s} + \frac{1 - i\beta}{1 - i2\pi \cdot f_d\tau_n} \cdot \frac{1}{I_n}\right] \cdot I_0(0) \cdot E_1(0), \tag{8.2.17}$$

$$C = \frac{1}{2}g(3 - i\alpha).$$

$I_0(0)$ and $E_1(0)$ are, respectively, the pump intensity and the field of the probe at $z = 0$. Using the boundary condition, $E_{\mathrm{FWM}}(z = 0) = 0$, the solution of the above is

$$E_{\mathrm{FWM}}(z) = \frac{B}{A - C}(e^{Cz} - e^{Az}). \tag{8.2.18}$$

The FWM power at $z = L$ is

$$I_{\mathrm{FWM}} = E_{\mathrm{FWM}}(L) \cdot E^*_{\mathrm{FWM}}(L),$$
$$I_{\mathrm{FWM}} = \frac{|B|^2}{g^2} \cdot f(G),$$

where $G = e^{gL}$ is the total gain of the SOA.

$$f(G) = G^3 - G.$$

In the above calculation, the absorption and reflection losses have been neglected. Although there are other simplifying assumptions, the above equation is a good approximation. Figure 8.2.3 shows the calculated intensity of FWM signal (I_{FWM} -solid curve) using the typical parameter values: $\tau_c = 200\,\mathrm{ps}$, $\tau_n = 650\,\mathrm{fs}$, $I_s = 20\,\mathrm{mW}$, $I_n = 52I_s$, $\alpha = 5$, $\beta = -2.2$ [16], $I_0(0) = 7.5\,\mathrm{dBm}$, $I_1(0) = 4.3\,\mathrm{dBm}$ and $\mathrm{G} = 8.0\,\mathrm{dB}$. The FWM power is proportional to the $f(G)$. For $G > 5\,\mathrm{dB}$, $f(G)$ varies G^3. The FWM power is higher for SOA with high gain, which is consistent with the result shown in Fig. 8.2.2.

8.2.2. *Pulsed FWM results*

For certain transmission networks signal add/drop capability is important. This can be carried out using FWM in a semiconductor amplifier. FWM can also used for all-optical clock recovery and optical demultiplexing in high speed transmission systems [17, 18]. For these systems both the pump and probe signals are pulsed. FWM experiments using pulsed pump and probe beams derived from gain switched DFB lasers have been reported [19–21].

The propagation of an electromagnetic wave along a traveling wave semiconductor optical amplifier is described by [19,20] (also Eq. (6.2.14) to (6.2.17))

$$\frac{\partial g}{\partial t} = \frac{g_0 - g}{\tau_c} - \frac{g}{\tau_c}|E|^2, \tag{8.2.19}$$

$$\frac{\partial E}{\partial z} = \frac{g}{2}(1 + i\alpha)E, \tag{8.2.20}$$

where $g(z,t)$ is the amplifier gain under saturation conditions and g_0 is the small signal unsaturated gain. The optical field, normalized to the saturation field i.e. field corresponding to the saturation intensity, is $E(z,t)$. τ_c is the carrier lifetime, α is the linewidth enhancement factor, and t is the time coordinate in the reference frame of the optical field.

The injected pulsed signals (assuming transform-limited Gaussian pulses) are represented by,

$$E_0(t) = A_0 \exp\left[-\frac{1}{2}\left(\frac{t}{t_0}\right)^2\right], \tag{8.2.21}$$

$$E_1(t) = A_1 \exp\left[-\frac{1}{2}\left(\frac{(t+\phi)}{t_1}\right)^2\right], \tag{8.2.22}$$

where E_0 is the pump signal at ω_0, E_1 is the probe signal at ω_1, and ϕ is the delay time between the two pulses. For pump and probe pulses with 33 ps FWHM, the quantities t_o and t_1 are 20 ps. The optical field at the input facet ($z = 0$) is

$$E_{\text{in}}(z=0,t) = E_0 + E_1 \exp(i\Omega t), \quad \Omega = \omega_1 - \omega_0.$$

Define an integrated gain $h(t) = \int_0^L g(z,t)dz$, (as in Ch. 6) then the above equations can be integrated to yield

$$\frac{dh}{dt} = \frac{h_0 - h}{\tau_c} - (e^h - 1)\frac{|E_{\text{in}}(0,t)|^2}{\tau_c}, \tag{8.2.23}$$

$$E_{\text{out}}(L,t) = E_{\text{in}}(0,t)\exp\left[\frac{h}{2(1-i\alpha)}\right], \tag{8.2.24}$$

where $h_0 = g_0 L$ with L being the length of the SOA. If the probe signal E_1 is much smaller than the pump E_0, then

$$|E_{\text{in}}(0,t)|^2 \cong |E_0|^2 + E_0^* E_1 e^{i\Omega t} \quad \text{and} \quad |E_0|^2 \gg |E_0^* E_1|,$$

so expressing $h(t)$ as follows:

$$h(t) = \bar{h}(t) + \delta h(t) e^{i\Omega t} \quad \text{with } |\bar{h}(t)| \gg |\delta h(t)|,$$

where $\bar{h}(t) = -\ln[1-(1-e^{-h_0})e^{-U_{\rm in}(t)}]$ and $U_{\rm in}(t) = \frac{1}{\tau_c}\int_{-\infty}^{t}|E_0(x)|^2dx$, then the output optical field of SOA is

$$E_{\rm out}(L,t) = E_0(L,t) + E_1(L,t)e^{i\Omega t} + E_2(L,t)e^{-i\Omega t}, \tag{8.2.25}$$

where

$$E_0(L,t) = \exp\left[\frac{\bar{h}}{2(1-i\alpha)}\right](1+F_-(\Omega)|E_1|^2)E_0, \tag{8.2.26}$$

$$E_1(L,t) = \exp\left[\frac{\bar{h}}{2(1-i\alpha)}\right](1+F_+(\Omega)|E_0|^2)E_1, \tag{8.2.27}$$

$$E_2(L,t) = \exp\left[\frac{\bar{h}}{2(1-i\alpha)}\right]F_-(\Omega)E_0^2E_1^*, \tag{8.2.28}$$

$$F_\pm(\Omega) = -\frac{e^{\bar{h}}-1}{2}\left[\frac{1-i\alpha}{1+e^{\bar{h}}|E_0|^2 \pm i\Omega\tau_c} + \frac{1-i\beta_n}{1\pm i\Omega\tau_n}K_n\right]. \tag{8.2.29}$$

The above equations describe the FWM frequency product, E_2, with frequency $\omega_2 = \omega_0 - \Omega = 2\omega_0 - \omega_1$. Other products are also created but they are all much smaller in intensity than E_2 and are therefore neglected. The first term describes FWM due to carrier density pulsations and represents an exact small signal solution. The second term accounts for the nonlinear gain effect of an SOA, where K_n is the nonlinear gain coefficient.

The calculated FWM pulse amplitude is plotted in Fig. 8.2.4 using the following typical parameter values from references [16, 19–21] — $G_0 = 18\,\text{dB}$, $t_0 = t_1 = 21\,\text{ps}$, $\tau_c = 200\,\text{ps}$, $\tau_n = 0.65\,\text{ps}$, $\lambda_0 = 1548\,\text{nm}$, $\lambda_1 = 1551\,\text{nm}$, $\alpha = 5$, $\beta_n = -2.2$, $K_n = 2\times10^{-3}$. Figure 8.2.4 shows the result of the calculation is consistent with the experimental data. The wavelengths used in the calculation correspond to wavelengths used in the measurements in Fig. 8.2.4. Results are reported here for an experiment in which the widths of both pump and probe pulses are 33 ps and their repetition rate is 5 GHz. The gain saturation of the SOA takes place only when there is temporal overlap of the pump and probe pulses in the amplifier. In the experiment the temporal position of the probe pulse was varied by an

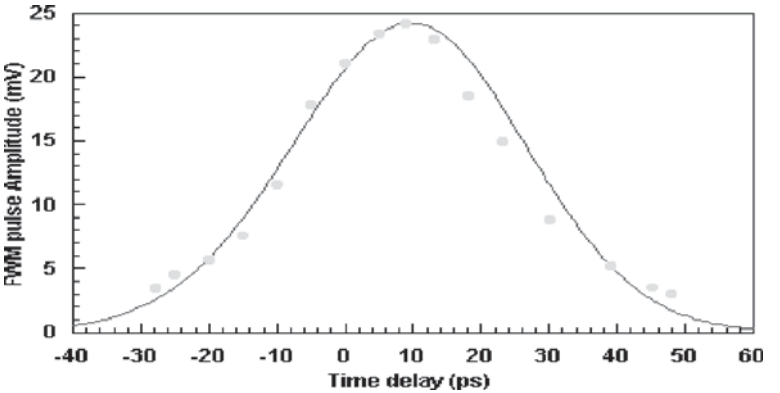

Fig. 8.2.4. The measured (circles) and calculated (solid line) FWM pulse amplitude as a function of the temporal position of the probe beam. The peak intensities of the pump and probe beams in the amplifier are 9 mW and 2 mW respectively.

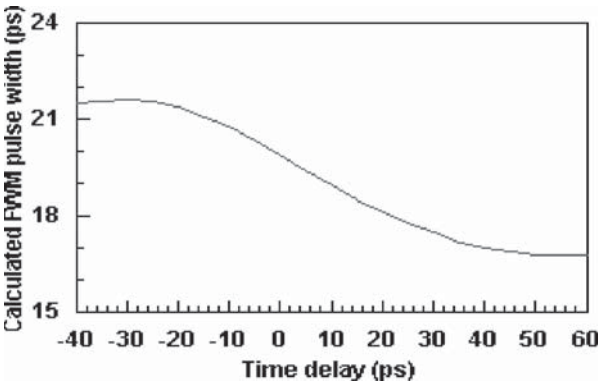

Fig. 8.2.5. Calculated FWM pulse width as a function of the temporal position of the pump pulse. The input pulse width (FWHM) is 33 ps for both the probe and the pump.

optical delay line. The amplitude of the FWM beam (as measured using a sampling oscilloscope) as a function of the temporal position of the probe beam (relative to the pump beam) is shown in Fig. 8.2.4. The solid line is the calculated result using an analysis of FWM using pulsed light input as described.

The calculated FWM pulse width is shown in Fig. 8.2.5. Its value is nearly equal to $1/\sqrt{3}$ of the input pulse width (expected for a

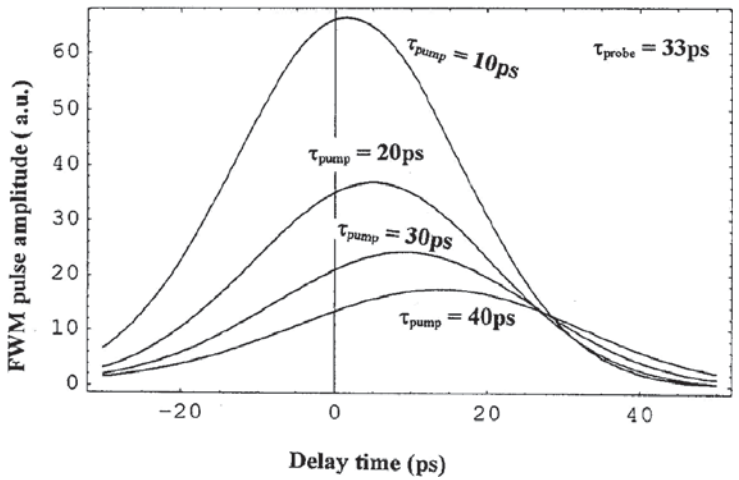

Fig. 8.2.6. Calculated FWM pulse amplitude as a function of time for different input pump pulse widths.

simple Gaussian model) with a slight modulation by the temporal mismatch of the input pulses. The measured FWM pulse was also found to be independent of the temporal mismatch with a value of 19 ± 3 ps. The dependence of the FWM pulse amplitude on the input pump pulse width has been studied. Figure 8.2.6 shows the calculated FWM pulse as a function of time for an input probe pulse width of 33 ps. The temporal profile of the FWM signal is shown as a function of delay between the pump and probe. The figure shows the FWM conversion efficiency increases when the input pump pulse width is reduced from 40 ps to 10 ps. So in the FWM experiments, shorter optical pulses are preferred in order to increase conversion efficiency.

The above analysis has neglected the contribution of ultrafast intraband dynamics on pulse gain saturation, so it is considered valid for optical pulses longer than 10 ps. For shorter pulsewidths, a model of pulsed FWM based on perturbation theory has been developed where the nonlinear gain effects including carrier heating and spectral-hole burning processes on the gain saturation are included [22, 23].

8.2.3. *FWM bandwidth*

Carrier density modulation and nonlinear gain effects (including dynamic carrier heating and spectral hole burning) in the semiconductor optical amplifier contribute to the generation of the FWM signal. When the wavelength separation λ_{d} between the pump and the probe beams is larger than 1 nm, nonlinear gain effects dominate in the generation of FWM. Since the effective time constant of the nonlinear gain effects is ∼0.6 ps [19], which is significantly faster than the time constant for carrier density modulation, it has been shown that the bandwidth of the FWM could reach as high as ∼1 THz [24].

Consider a small modulation signal with angular frequency ω_{m} applied to the probe beam, the corresponding optical field can be expressed as

$$E_1'(z) = [E_1(z) + q_1(z)\exp(-i\omega_m t)]\exp(-i\omega_1 t), \tag{8.2.30}$$

where E_1 is the CW component and q_1 is the modulation component of the electric field. This modulation signal will be transferred to the pump and the FWM beams in the semiconductor optical amplifier through nonlinear interaction. The electric fields of the pump E_0 and the FWM signal E_4 can be similarly expressed as

$$E_0'(z) = [E_0(z) + q_0(z)\exp(-i\omega_m t)]\exp(-i\omega_0 t), \tag{8.2.31}$$

$$E_4'(z) = [E_4(z) + q_4(z)\exp(-i\omega_m t)]\exp(-i\omega_4 t). \tag{8.2.32}$$

The subscripts 0,1,4 denote to the pump, the probe and the FWM beam respectively. The beat frequency ω_d has the relationship

$$\omega_d = \omega_0 - \omega_1 = \omega_4 - \omega_0. \tag{8.2.33}$$

Assuming the phase matching condition is satisfied, the total optical field is:

$$E(z) = E_0'(z) + E_1'(z) + E_4'(z). \tag{8.2.34}$$

In four wave mixing, generally $E_0 \gg E_1 \gg E_4$. Since small modulation signal is applied to the probe wavelength, we also have $E_1 \gg q_1$, $E_0 \gg q_0$, $E_4 \gg q_4$, and $q_1 \gg q_0 \sim q_4$. The total optical intensity is

given by Eq. (8.2.35). In the right side of Eq. (8.2.35), the first term is averaged optical power in the SOA, which mainly comes from the pump. The second term, the beat frequency term between the pump and the probe, which, as discussed previously, is responsible for the generation of the CW FWM.

$$|E|^2 = \{|E_0(z)|^2 + \ldots\} + \{2\mathrm{Re}[E_0^*(z)E_1(z)\exp(-i\omega_d t)] + \ldots\} + \{2\mathrm{Re}[E_0^*(z)q_1(z)\exp(-i(\omega_d+\omega_m)t)] + \ldots\}. \quad (8.2.35)$$

The third term comes from the small modulation applied to the probe, which is responsible for the modulation signal in the FWM and the pump beams. All other smaller terms are neglected. The carrier density equation can be similarly written as

$$N(t) = n_s + n_1\exp(-i\omega_d t) + n_2\exp[-i(\omega_d+\omega_m)t], \quad (8.2.36)$$

where $\bar{n}_s \gg n_1 \gg n_2$. $\bar{n}_s$ and n_1 are expressed in Eqs. (8.2.10) and (8.2.12). Substitute (8.2.35) and (8.2.36) into the carrier density rate Eq. (8.2.7), the following equation for n_2 is obtained

$$n_2 = \frac{-(n_s - n_0)\frac{E_0 \cdot q_1}{P_s}}{1 + \frac{|E_0|^2}{P_s} - i(\omega_d+\omega_m)\tau_c}, \quad (8.2.37)$$

where P_s is the gain saturation power. The term n_2 in (8.2.37) is responsible for the generation of the small modulation signal q_4 and q_0 at the FWM and the pump beams respectively. But Eq. (8.2.37) only includes the mechanism of carrier density modulation. The nonlinear gain effects in the generation of the FWM, would add a similar term in Eq. (8.2.37). The equation for n_2 is then given by (8.2.38)

$$n_2 = \frac{-(n_s - n_0)\frac{E_0^* q_1}{P_s}}{1 + \frac{|E_0|^2}{P_s} - i(\omega_d+\omega_m)\tau_c} + \frac{-(n_s - n_0)\frac{E_0^* q_1}{P_n}}{1 + \frac{|E_0|^2}{P_n} - i(\omega_d+\omega_m)\tau_n}, \quad (8.2.38)$$

where the second term of the right side attributes to the effects of nonlinear gain including both spectral hole burning and dynamic carrier heating. For small signal modulation we have $\mathrm{E}_1 \gg \mathrm{q}_1$,

$E_0 \gg q_0$, $E_4 \gg q_4$, then from the CW FWM coupled Eq. (8.2.15), the following set of coupled equations for q_1 and q_4 is obtained,

$$\frac{dq_1}{dz} = \frac{1}{2}g(1 - i\alpha)q_1 + \frac{1}{2}an_2(1 - i\alpha)E_1, \tag{8.2.39}$$

$$\frac{dq_4}{dz} = \frac{1}{2}g(1 - i\alpha)q_4 + \frac{1}{2}an_2(1 - i\alpha)E_4 - \frac{1}{2}g\sigma E_0^2 q_1^* - \frac{1}{2}an_2\sigma E_0^2 E_1^*, \tag{8.2.40}$$

where σ has the same definition as in (8.2.15). Since $q_1 \gg q_0 \sim q_4$, the effect of q_0 on q_4 is ignored in Eq. (8.2.40). The numerical solution of $q_4(z, \omega_m)$ could be obtained from the coupled Eqs. (8.2.15) and (8.2.39), (8.2.40).

The modulation depth at the input probe signal is defined as

$$m_1(0) = \frac{2E_1^*(0)q_1(0)}{E_1(0)E_1^*(0)}. \tag{8.2.41}$$

The modulation depth at the output FWM beam is defined as

$$m_4(L, \omega_m) = \frac{2E_4^*(L)q_4(L, \omega_m)}{E_4^*(L)E_4(L)}. \tag{8.2.42}$$

So the conversion efficiency of small modulation signal from the probe to the FWM through the SOA is given by

$$\eta(\omega_m) = \frac{m_4(L, \omega_m)}{m_1(0)} = \left|\frac{E_1(0)q_4(L, \omega_m)}{E_4(L)q_1(0)}\right|. \tag{8.2.43}$$

The calculated FWM efficiency for small signal modulation $\eta(\omega_m)$ as a function of the modulation frequency is plotted in Figs. 8.2.7 and 8.2.8. The parameter values used are $\tau_c = 200\,\text{ps}$, $\tau_n = 650\,\text{fs}$, $P_s = 20\,\text{mW}$, $P_n = 50\,P_\text{s}$, $\alpha = 5$, $\beta = -2.2$ [23, 26–28]. Figure 8.2.7 shows the bandwidth of FWM increases from 320 GHz to about 1.5 THz when the wavelength separation between the pump and the probe increases from 0.5 nm to 10 nm. This is because when the wavelength separation $\lambda_d = 0.5\,\text{nm}$, both carrier density modulation and nonlinear gain effects contribute to the signal conversion from the probe to the FWM beam, while when $\lambda_d = 10\,\text{nm}$, only the nonlinear gain effects contribute to the signal conversion.

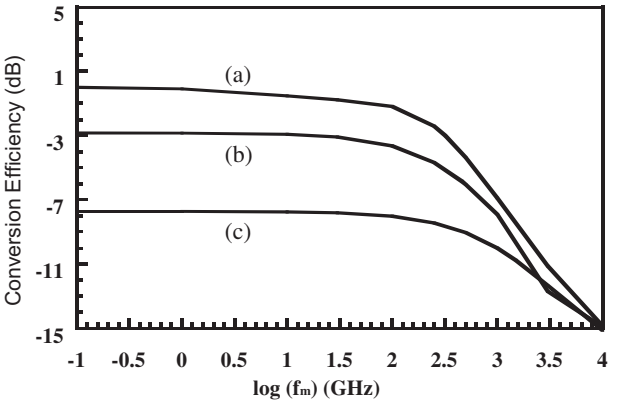

Fig. 8.2.7. Calculated frequency response of FWM conversion efficiency when $g_0L = 7$. (a) wavelength difference between the pump and the probe $\lambda_d = 0.5\,\text{nm}$, FWM bandwidth = 320 GHz, (b) $\lambda_d = 2.5\,\text{nm}$, FWM bandwidth = 460 GHz, (c) $\lambda_d = 10\,\text{nm}$, FWM bandwidth = 1500 GHz. The x-axis is log(base 10) of the modulation frequency f_m in GHz.

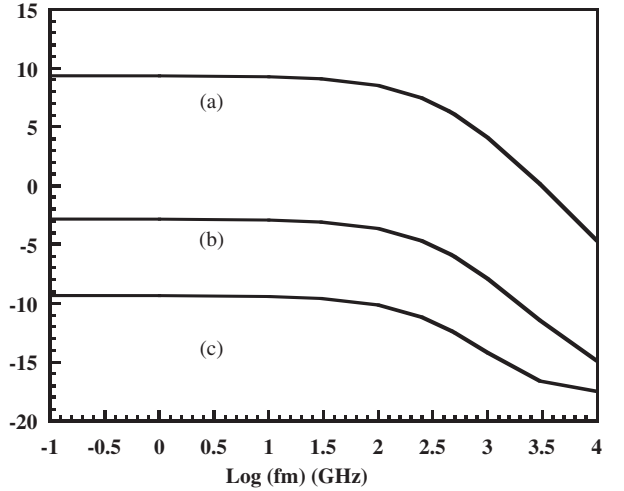

Fig. 8.2.8. Calculated frequency response of FWM conversion efficiency when $\lambda_d = 2.5\,\text{nm}$ (a) $g_0L = 10$, FWM bandwidth = 440 GHz, (b) $g_0L = 7$, FWM bandwidth = 460 GHz, (c) $g_0L = 5$, FWM bandwidth = 470 GHz. The x-axis is log(base 10) of the modulation frequency f_m in GHz.

Figure 8.2.8 shows the frequency response of the FWM conversion efficiency for different g_0L values, corresponding to different gain of the SOA. It shows that, although the absolute value of the FWM conversion efficiency depends strongly on the gain of the SOA, the bandwidth of FWM conversion efficiency decreases slightly when the g_0L value is doubled. However, since the FWM conversion efficiency increases with increasing gain (approximately as g^3) a high gain is necessary for applications, such as for optical demultiplexing and optical wavelength conversion. Thus for large wavelength separation between the pump and the probe, where the nonlinear gain effects dominate the generation of the FWM, the bandwidth of the FWM could exceed 1 THz.

8.3. Cross Gain Modulation

Cross gain modulation is a result of gain saturation in SOA. It occurs when light at two different wavelengths, a pump and a probe, are injected into the semiconductor optical amplifier [12, 15, 25–31]. When operated under gain saturation conditions, the available optical gain is distributed between the two wavelengths depending on their relative photon densities. The changes in the power level of the pump wavelength have an inverse effect on the gain available to the probe wavelength and results in data transfer.

The mechanism of cross gain saturation or data transfer is shown in Fig. 8.8. When the pump ($\lambda_2 = 1550.68$ nm) is not present, the gain to the probe wavelength ($\lambda_1 = 1552.24$ nm) is high so that the output power of the probe is very high (dashed line in Fig. 8.8). When the pump λ_2 and probe λ_1 are injected into the SOA at the same time, the pump power is so high that it saturates the gain of the SOA. The available gain to the probe λ_1 will be reduced. So the output power of the probe is much lower (solid line in Fig. 8.3.1). From Fig. 8.3.1 it follows, the compression efficiency is high, more than 50%.

When the power of the pump is modulated with data, the gain of the probe is also modulated. Thus the output power of the probe is modulated. This results in transfer of data from pump to probe. Thus wavelength conversion is achieved.

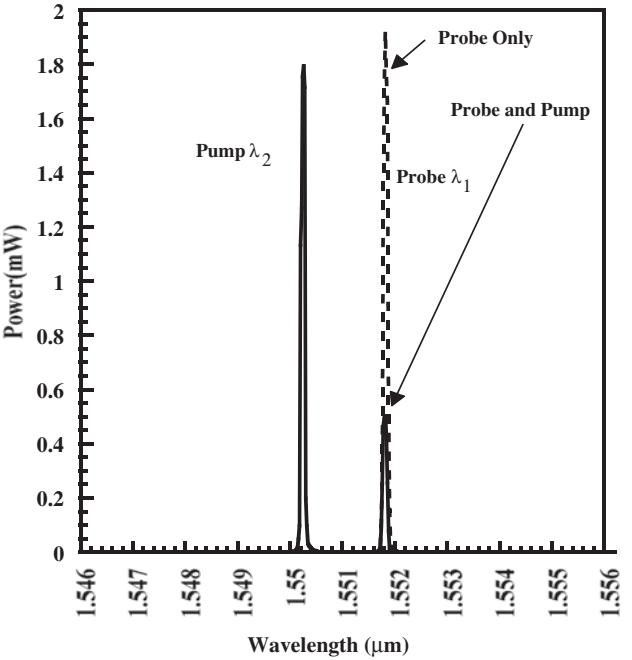

Fig. 8.3.1. Cross gain saturation between two wavelengths in SOA.

8.3.1. *Rate equations for multiple pulse propagation*

The rate equations for the propagation of a single pulse have been derived previously in Ch. 6. Eq. (6.2.14) to Eq. (6.2.17). They are rewritten here as follows:

$$\frac{\partial P}{\partial z} = (g - \alpha_{\text{int}})P, \tag{8.3.1}$$

$$\frac{\partial \phi}{\partial z} = -\frac{1}{2}\alpha g, \tag{8.3.2}$$

$$\frac{\partial g}{\partial \tau} = -\frac{g - g_0}{\tau_c} - \frac{gP}{E_s}. \tag{8.3.3}$$

The quantity $E_s = \tau_c P_s$, where $\mathrm{P_s}$ is the saturation power of the amplifier, g_0 is the small signal mode gain, α is the linewidth enhancement factor. The quantity g_0 is given by

$$g_0 = \Gamma a(I\tau_c/qV - n_0). \tag{8.3.4}$$

If there are two optical fields at wavelengths, λ_1 and λ_2, injected into a SOA, the Eqs. (8.3.1)–(8.3.3) can be expanded to yield the following set of equations:

$$\frac{\partial P_i}{\partial z} = (g_i - \alpha_{\text{int}})P_i, \quad i = 1, 2, \tag{8.3.5}$$

$$\frac{\partial \phi_i}{\partial z} = -\frac{1}{2}\alpha g_i, \tag{8.3.6}$$

$$\frac{\partial g_i}{\partial \tau} = -\frac{g_i - g_{0,i}}{\tau_c} - \frac{g_1 P_1}{E_{s,1}} - \frac{g_2 P_2}{E_{s,2}}, \tag{8.3.7}$$

$$g_i = \Gamma_i a_i (n - n_{0,i}). \tag{8.3.8}$$

The phase of each optical beam depends on the initial phase $\phi_i(0,\tau)$ and the gain g. After going through the amplifier, the spectrum of each beam is given by the Fourier transform of the optical field E (Eq. (6.2.5)),

$$\begin{aligned} S_i(\omega) &= \left| \int E e^{i\omega\tau} d\tau \right|^2 \\ &= \left| A\sqrt{P} e^{i\phi} e^{-i\omega_0} e^{i\omega\tau} d\tau \right|^2 \\ &= \left| \int [P_i(L,\tau)]^{1/2} \cdot \exp[i\phi_i(L,\tau) + i(\omega - \omega_i)\tau] d\tau \right|^2, \quad i = 1, 2. \end{aligned} \tag{8.3.9}$$

8.3.2. *Bandwidth of cross gain modulation*

Wavelength conversion at high bit rate needs high bandwidth for the cross gain modulation phenomenon. A small signal analysis of the above equations is carried out as follows [30, 31].

Assume that there are only two wavelengths injected into the SOA. In order to make the following derivations clearer, Eqs. (8.3.7) and (8.3.5) are rewritten using carrier density n instead of gain g noting $g = a\,(n - n_0)$ where a, n_0 are the gain coefficient and carrier density at transparency. The carrier density, $n(z,\tau)$, and optical

power, $P(z,\tau)$, in the amplifier, evolve with time as

$$\frac{\partial n}{\partial \tau} = \frac{I}{eV} - \frac{n}{\tau_c} - \frac{(n-n_{0,1})P_1}{E_{s,1}} - \frac{(n-n_{0,2})P_2}{E_{s,2}}, \quad (8.3.10)$$

$$\frac{\partial P_i}{\partial z} = [\Gamma a_i(n-n_{0,i}) - \alpha_{\text{int}}]P_i, \quad i=1,2, \quad (8.3.11)$$

where I is the injected current density, V is the volume of the gain region of SOA, $n_{0,i}$ is transparency carrier density, a_i is differential gain coefficient (i = 1,2), P_2 is the pump power, and P_1 is the probe power, α_{int} is the internal loss. $E_{s,i}$ is the saturation field given by

$$E_{s,i} = \frac{\sigma_m \hbar \omega_i}{a_i \Gamma}, \quad (8.3.12)$$

where σ_{m} is the active region area and Γ is the mode confinement factor. The quantity Γ is assumed to be the same for these two beams. Because of the small signal modulation, the optical powers may be written as $P_i = \bar{P}_i + \tilde{p}_i$ and the carrier density as $n = \bar{n} + \tilde{n}$ denoting the steady-state and perturbing signals. The following equations for $\bar{P}_i$, $\bar{n}$, $\tilde{p}_i$ and $\tilde{n}$ are then obtained:

$$0 = \frac{J}{ed} - \frac{\bar{n}}{\tau_c} - (\bar{n}-n_{0,1})\frac{\bar{P}_1}{E_{s,1}} - (\bar{n}-n_{0,2})\frac{\bar{P}_2}{E_{s,2}}, \quad (8.3.13)$$

$$\frac{\partial \tilde{n}}{\partial t} = -\frac{\tilde{n}}{\tau_c} - \frac{[(\bar{n}-n_{0,1})\tilde{p}_1 + \tilde{n}P_1]}{E_{s,1}} - \frac{[(\bar{n}-n_{0,2})\tilde{p}_2 + \tilde{n}P_2]}{E_{s,2}}, \quad (8.3.14)$$

$$\frac{\partial P_i}{\partial z} = [\Gamma a_i(\bar{n}-n_{0,i}) - \alpha_{\text{int}}]P_i, \quad (8.3.15)$$

$$\frac{\partial \tilde{p}_i}{\partial z} = [\Gamma a_i(\bar{n}-n_{0,i}) - \alpha_{\text{int}}]\tilde{p}_i + \Gamma a_i \tilde{n}\bar{P}_i. \quad (8.3.16)$$

For the case of sinusoidal modulation at angular frequency ω:

$$\tilde{n} = -\frac{(\bar{n}-n_{0,1})\frac{\tilde{p}_1}{E_{s,1}} + (\tilde{n}-n_{0,2})\frac{\tilde{p}_2}{E_{s,2}}}{1/\tau_c + 1/\tau_{s,1} + 1/\tau_{s,2} + j\omega}. \quad (8.3.17)$$

At incident facet $z = 0$, $\tilde{p}_1(z = 0) = 0$. Assuming $g = g_1 = g_2 = \Gamma a (\bar{n} - n_0)$ and $E_{s1} = E_{s2} = E_s$. We also assume that the CW intensity of the probe at wavelength λ_1 is smaller than the CW portion of the pump at wavelength λ_2, then the conversion efficiency from pump (λ_2) to probe (λ_1) at position z is given by [30]

$$\eta = \left| \frac{\tilde{p}_1(z, \omega)}{\tilde{p}_2(z, \omega)} \right| = \left| \exp\left(\frac{-gz}{\tau_{s,1}/\tau_e + 1 + j\omega\tau_{s,1}} \right) - 1 \right|, \tag{8.3.18}$$

where $\tau_{s,i}$ is the carrier lifetime due to stimulated emission, which is defined as

$$1/\tau_{s,i} = \bar{P}_i/E_s. \tag{8.3.19}$$

Figure 8.3.2 is a schematic setup for XGM bandwidth measurement. Two DFB lasers are used to provide probe beam at wavelength λ_1, and pump beam at wavelength λ_2. An external $LiNbO_3$ modulator is used to create a modulated optical signal. The modulation power was ~ 5 dBm. Laser 1 produces only CW power. The two beams are coupled by a 3 dB coupler, and injected into a SOA after amplification in an erbium doped fiber amplifier. A polarization controller (PC) is used to increase the coupling efficiency. An optical filter is used after the SOA, and only wavelength λ_1 is selected.

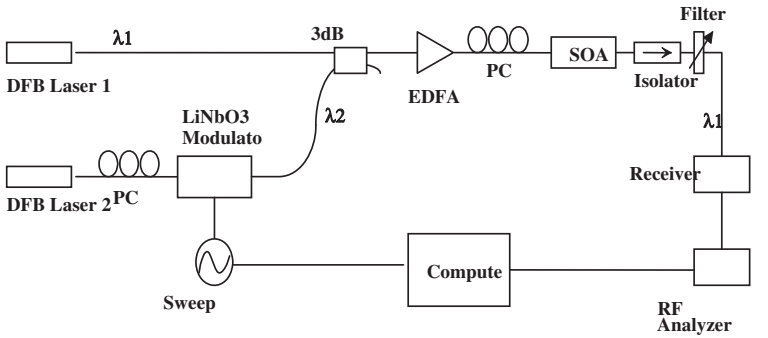

Fig. 8.3.2. Experimental setup for cross gain modulation (XGM) bandwidth measurement. PC is polarization controller. SOA is semiconductor Optical Amplifier.

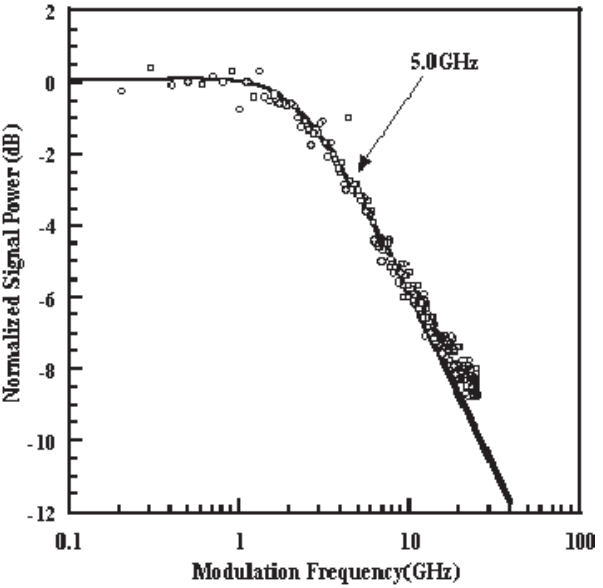

Fig. 8.3.3. Measured frequency response of XGM in SOA. The circles are experimental data, the solid line is theoretical calculation according to Eq. (8.3.18).

The 3dB-bandwidth of the filter is 1 nm. The output optical power at wavelength λ_1 is converted to an electrical signal by a high-speed photodiode. The spectrum analyzer is used to measure the frequency response.

Figure 8.3.3 is the measured frequency response of output probe beam against modulation frequency of the input pump beam. The SOA bias current is ∼200 mA. The dots are the experimental results. From CW gain measurements on the same amplifier the measured saturation power $P_s = 2.5\,\text{mW}$. Using a spontaneous carrier lifetime τ_c of ∼300 ps, the saturation energy $E_s = P_s^* \tau_c = 5.3 \times 10^{-13}\,\text{J}$. The optical power of the probe P_1 was ∼5-6 dBm, then the carrier life due to stimulated emission $\tau_{s,1}$ is ∼210 ps according to Eq. (8.3.19). The small signal gain was ∼18, then gz∼2.89. Substituting these numbers into Eq. (8.3.18), the solid line in Fig. 8.3.3 is obtained. The theory matches the experimental results very well. From the figure, the bandwidth of XGM is about 5 GHz.

8.4. Cross Phase Modulation

A cross-phase modulation (XPM) accompanies the cross gain modulation when two optical signals are simultaneously present in the SOA. An interferometer configuration can be used to convert the phase modulation to an intensity modulation. XPM in a semiconductor optical amplifier (SOA) used in an interferometric configuration has been used for all-optical wavelength conversion, optical demultiplexing and for optical clock recovery. The scheme has conversion efficiency and high signal to noise ratio.

Generally a Mach-Zehnder or Michelsen interferometer configuration integrated on a single chip is used to convert phase modulation to intensity modulation.

8.4.1. *Mach-Zehnder interferometer*

Semiconductor optical amplifiers incorporated into Mach-Zehnder interferometer (MZI) or Michelson interferometer configurations have been used for wavelength conversion and to demultiplex high-speed time division multiplexed optical signals [10–12, 25–43]. The schematic of the device is shown in Fig. 8.4.1. The input signal beam is split into two beams by a y-junction at the input. The two beams propagate through semiconductor amplifiers located in the two arms of the interferometer. These beams then merge and interfere at an output y-junction.

The phase of the interference is altered by injecting another signal in one of the other ports. This phenomenon can be used for functional applications. The ratio of the output signal P_o to the input signal P_i

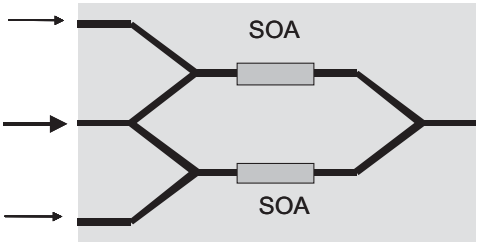

Fig. 8.4.1. Schematic of a MZI with SOA's integrated with waveguides. The device is based on InGaAsP/InP material system.

is given by

$$\frac{P_o}{P_i} = \frac{1}{8}\{G_1 + G_2 - 2\sqrt{G_1 G_2}\cos(\phi_1 - \phi_2)\}, \tag{8.4.1}$$

where G_1, G_2 are the gains of the amplifiers and ϕ_1, ϕ_2 are phase changes induced by nonlinear effects in the two amplifiers. The phase difference, $\Delta\phi = \phi_1 - \phi_2$, at the output is given by:

$$\Delta\phi = \frac{\alpha}{2P_s}\left\{-\frac{h\nu}{e}(I_1 - I_2) + \frac{P_c}{2}(G_1 - 1)\right\}, \tag{8.4.2}$$

where α is the linewidth enhancement factor. P_c is the injected power in one of the amplifiers, P_s is the saturation power in the amplifier and I_1, I_2 are the currents through the two amplifiers. For $I_1 \cong I_2$ and $G_1 \cong G_2 = G$ the above reduces to

$$\frac{P_o}{P_i} = \frac{G}{2}\sin^2\left(\frac{\Delta\phi}{2}\right), \tag{8.4.3}$$

where $\Delta\phi = \frac{\alpha}{4}\frac{P_c}{P_s}(G - 1)$.

Using typical values; $\alpha = 3$, $P_s = 10\,\text{mW}$ and experimental saturated gains $G \cong 40$, we get $P_c \cong 1\,\text{mW}$ for $\Delta\phi = \pi$. Thus, the optical power that need to be injected in one of the other ports for π phase shift can be easily achieved. There may be some thermally induced refractive index changes, but these are considerably smaller than the carrier induced changes considered above and can be ignored.

For a stable MZI, the waveguides and SOAs must be integrated on a single substrate of InP. The starting point for MZI device fabrication is a standard MOVPE-grown n-doped InP base wafer consisting of multi quantum well (MQW) active (amplifying) layers on top of a passive InGaAsP waveguide core. The quantum wells consist of an optimized compressively/tensile strained stack to provide polarization independent gain. The quantum wells are etched away in the passive sections before waveguide formation. For obtaining low-loss transitions between the active and passive sections, low confinement to the active region is good. After etching the waveguide pattern, blocking layers consisting of reversed p-n junctions are grown, in which slots are etched running on top of the active waveguide sections. This is done to confine current injection to the

active regions only. After growth of the p-doped top cladding layer and contact layer, and metal contact formation, the wafer is cleaved into bars of devices. The facets are then coated with a dielectric layer of suitable thickness to suppress reflections.

8.5. Wavelength Conversion

Semiconductor Optical Amplifiers have many potential applications in future all-optical transmission systems. Four-wave mixing (FWM) and cross phase/cross gain modulation in SOA's has been proposed and demonstrated as a technique for performing wavelength conversion for wavelength division multiplexing (WDM) systems [10–14, 25–43].

Wavelength conversion is defined as a process by which data at one wavelength can be converted to data at another wavelength. Such processes are important in all-optical networks where a subscriber node is designed to receive and transmit at one wavelength. The mechanism for wavelength conversion using SOA includes cross gain modulation and cross phase modulation of two simultaneously propagating signals. For cross phase modulation a Mach-Zehnder modulator fabricated using two SOA's in each arm is often used. For wavelength conversion using MZI, a CW signal is injected into the central port. This signal splits and travels through the two SOAs. The two signals undergo a differential phase shift of π, as a result there is no output. The modulated signal is injected into one of the SOAs. This changes the phase of the CW signal propagating through this SOA due to the phenomenon of cross phase modulation, as a result the phase difference between the CW signals traveling through the two SOAs is no longer π and an output is observed. The speed of wavelength conversion is determining the phase recovery dynamics in the SOA. For long pulses, for all practical purposes, the phase recovery is limited by carrier recovery time. For short pulses (<2 ps), carrier heating, and spectral hole burning play a role and the response is faster than the carrier recovery time as discussed in Ch. 6. Careful adjustment of peak power of the modulated signal and SOA bias currents is necessary to get error free performance at high data rates.

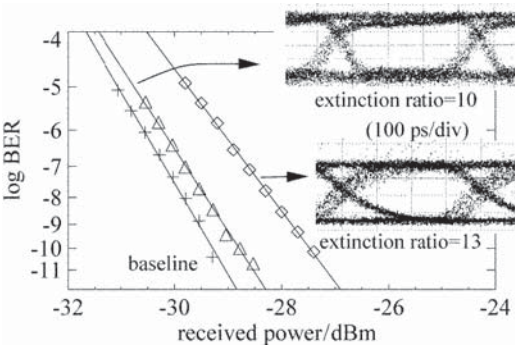

Fig. 8.5.1. BER curves for conversion from 1559 to 1568 nm, optimized for output extinction ratio (diamonds, lower eye diagram), and optimized for speed (triangles, upper eye diagram).

Bit error rate curves for conversion of a pseudo random data from 1559 nm to 1568 nm at 10 Gb/s are shown in Fig. 8.5.1. When the MZI is optimized for maximum output extinction ratio (11 dB), a wavelength conversion penalty of 1.6 dB is measured at a BER of 10^{-9}. The eye diagram in the lower inset of Fig. 8.5.1 shows that this penalty is mainly caused by inter-symbol interference (ISI) due to rather slow gain/phase dynamics in the SOA, which is driven with a moderate bias of 100 mA. The speed increases by adjusting the bias point of the MZI. This reduces the extinction ratio to 10 dB, but significantly enhances the switching speed, as shown by the eye in the upper inset of Fig. 8.5.1. The wavelength conversion penalty is reduced to 0.5 dB.

SOA based MZI devices can be operated in a differential mode (see Sec. 8.6.2) for higher speed wavelength conversion results. The carrier lifetime in a SOA is an important parameter for high speed operation of MZI devices. The measured lifetimes for various types of SOA devices are shown in Fig. 8.5.2. the times plotted are for 10% to 90% gain recovery. The data shows that longer amplifiers are good for high data rates. Additional reduction in gain recovery times can be obtained using a holding beam as discussed in Ch. 6.

Wavelength conversion of high speed signals has been demonstrated using a semiconductor optical amplifier-delayed interferometer (SOA-DI) combination [44–46]. The delayed interferometer can

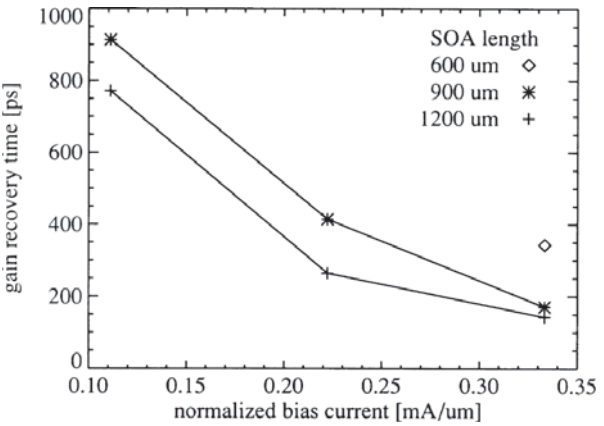

Fig. 8.5.2. Gain recovery times for cross-gain modulation in 600, 900, and 1200 μm long SOAs, for bias currents up to 200, 300, and 400 mA, respectively. Bias currents are normalized with respect to the length of the devices in the x-axis of the above figure.

be formed using birefringent crystals (e.g. calcite), delay loop in waveguides, or a polarization maintaining fiber.

The experimental set up for a 168 Gb/s wavelength conversion experiment is shown in Fig. 8.5.3. The modulated signal and the CW light (to which the data will be converted) are both injected into the SOA. In the SOA, the data pulses deplete the carriers which give to cross phase modulation of the CW light. The phase modulated CW light enters the delayed interferometer in which it splits into two paths (or two polarizations) and propagates in these two paths (or two polarizations) at different speeds. Thus at the output the two temporally displaced components of the phase modulated signal interfere producing an output pulse. The duration of the pulse is determined duration of the phase gate produced by the differential temporal delay between the two paths.

The 168 Gb/s signal is generated by multiplexing 16 times pulses at 10.5 GHz repetition rate from a mode locked fiber laser. The pulse width is 1.0 ps. The pulsed signal wavelength is 1564 nm and the CW signal wavelength is 1547 nm. The output 168 Gb/s pulses (viewed using a streak camera) is shown in Fig. 8.5.4.

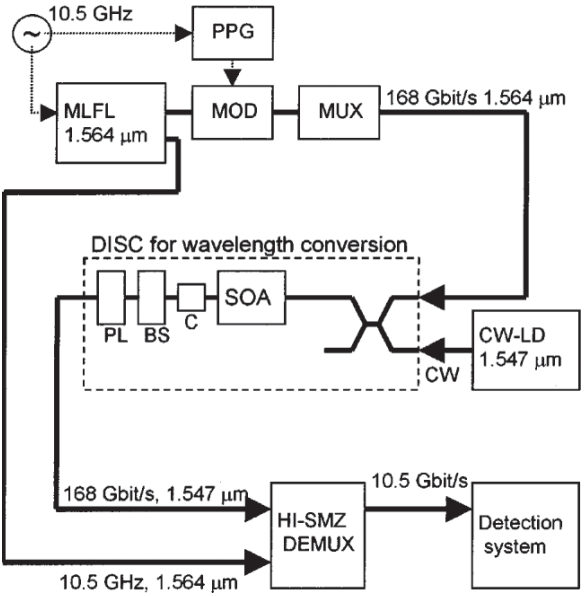

Fig. 8.5.3. Schematic of a wavelength conversion experiment using SOA-delayed interferometer [44].

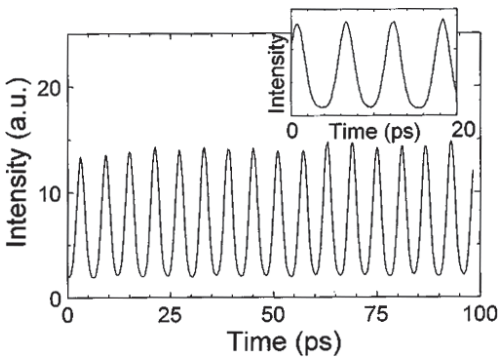

Fig. 8.5.4. Streak camera trace of 1547 nm wavelength converted pulse train [46].

Wavelength conversion has been demonstrated using differential phase shift keyed (DPSK) signals. The schematic of the set up is shown in Fig. 8.5.5 [47].

The wavelength converter has a delayed interferometer (DI) built using silica waveguide at the front end. The front end converts the input DPSK signal into OOK binary data D and its complement $\overline{D}$, followed by a SOA–MZI differentially driven by the D and $\overline{D}$ in a

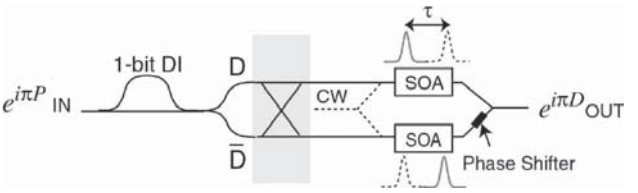

Fig. 8.5.5. Schematic of a DPSK wavelength converter [47].

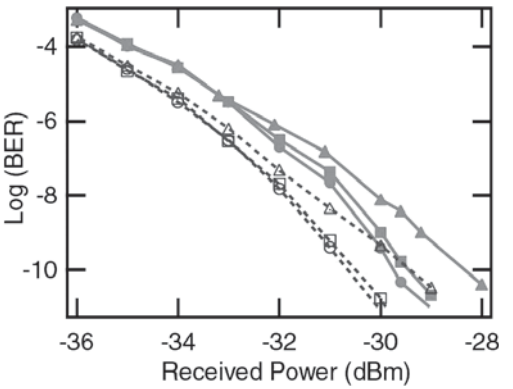

Fig. 8.5.6. BER of back-to-back (hollow symbols with dashed curves) and wavelength-converted signals (solid symbols and curves) [47].

"push–pull" mode. The SOA–MZI is a hybrid device fabricated by butt-coupling a bar of 2-mm long bulk InGaAsP/InP SOA arrays with an input and an output silica planar lightguide circuit (PLC) waveguides. The proposed DPSK wavelength converter has an all-optical OOK-to-PSK data conversion system as shown in Fig. 8.5.5. For the experiment, an electro-absorption modulator is used to modulate the output of a CW laser ($\lambda = 1554$ nm) for generating ∼6-ps optical pulses at 40-GHz repetition rate. These optical pulses are modulated by a lithium niobate Mach–Zehnder modulator biased at the null position to encode the DPSK signals at 40 Gb/s. The wavelength converted signal at 1549 nm is separated from the input data using an optical filter with 1 nm bandwidth. The filtered wavelength converter output is demodulated using a one-bit delay DI prior to input to a erbium doped fiber based preamplifier. The results of the bit-error-rate (BER) measurement using a photoreceiver with 40 GHz bandwidth is shown in Fig. 8.5.6.

8.6. Optical Demultiplexing

Several reports have been published on optical demultiplexing as applications of FWM [47–64] and cross gain/cross phase modulation [32–43]. FWM occurs both in semiconductor optical amplifiers, and in optical fibers. FWM in fibers need long fiber lengths. It does not lead to compact devices and it will not be discussed here.

8.6.1. *FWM based scheme*

A schematic of optical demultiplexing using FWM is shown Fig. 8.6.1. This technique allows any regularly spaced set of bits to be simultaneously extracted from the incoming data stream using a semiconductor optical amplifier (SOA) [32, 47]. Consider the high-speed data (at a data rate B) at wavelength λ_1 and an optical clock (at a clock rate B/N) at wavelength λ_2 injected into an optical amplifier. The output of the amplifier will include FWM signals at wavelengths $2\lambda_1$-λ_2 and $2\lambda_2$-λ_1. Typically, one of the FWM signals is filtered out using an optical filter at the exit port of the nonlinear element and represents the data signal before further processing. Thus, a signal representing the data every N^{th} bit time slot (where the mixing occurs with the clock signal) is generated by the FWM process (Fig. 8.6.1). The clock signal can then be delayed by 1 additional bit each time to retrieve the original data in successive time slots as described below or a bit-delayed parallel system (similar to Fig. 8.6.1)

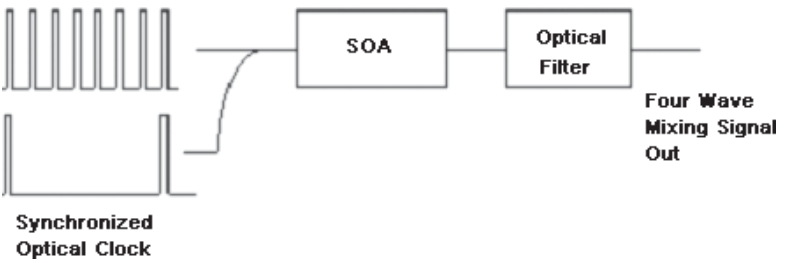

Fig. 8.6.1. Schematic of a FWM based demultiplexer. The FWM takes place in the SOA only when there is a temporal overlap between the signal and the clock pulse.

could be set up for simultaneous extraction of N data streams each at B/N data rate.

A complete system would need N SOA elements in order to extract N data bits simultaneously. The FWM process can have modulation bandwidths as high as 1.5 Tb/s (Sec. 8.2). Thus in principle demultiplexing from Tb/s optical data is feasible using the FWM process. Optical transmission experiments using FWM is described in Sec. 8.7.

8.6.2. *Cross phase modulation based scheme*

Among the semiconductor devices suitable for high speed all optical demultiplexing are (i) Mach-Zehnder interferometer, and, (ii) Michelson interferometer [10–12]. These devices operate on the principle of a phase change caused by an incident optical clock signal (cross-phase modulation). This phase change can be adjusted so that the interferometer only yields output when a data signal overlaps a clock signal for demultiplexing applications. The schematic of a MZI device operating as a demultiplexer is shown in Fig. 8.6.2. The input signal beam is split into two beams by an input y-junction, which propagates through semiconductor amplifiers positioned in the upper and lower arms of the interferometer. These beams then merge and interfere at an output y-junction. One of the amplifiers has the clock pulse incident on it. The clock frequency is $1/N$ time the signal bit rate. The clock pulse is absorbed by the amplifier changing its carrier density, which induces an additional phase shift for the signal traveling through that amplifier arm. This changes the output of the device for every N^{th} signal bit. The demultiplxed signal appears at the output at the clock frequency.

The arms of the MZI can be configured with built in phase shifters (or SOA current can be used as a phase shifter) so that the phase difference for the high data rate signal propagating through the two arms is π (before the arrival of the clock pulse). Under this condition, the signals propagating through the two arms interfere destructively, resulting in no output. In the presence of the clock pulse, an additional π phase shift is introduced in one arm of the interferometer, which results in a nonzero output for every N^{th} bit.

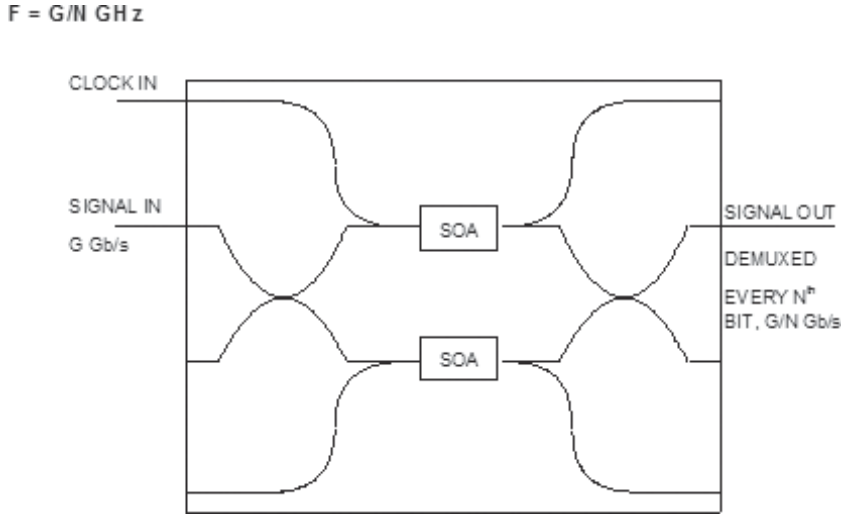

Fig. 8.6.2. Schematic of a optical amplifier based MZI. The clock pulse introduces an additional phase shift in one of the arms of the interferometer which changes the balance and results in an output.

Similar to case of FWM, a complete system would need N MZI elements in order to extract N data bits simultaneously. The response speed i.e. the signal speed which the MZI can demultiplex is determined by the phase response time in the SOA.

The device can be made to operate considerably faster using a differential phase shift scheme which involves introducing a second delayed clock signal in the other arm of the interferometer. The principle of this operation is illustrated in Fig. 8.6.3. In the delayed pulse approach, the differential phase shift between the two arms is maintained over a short duration (1 bit period). As a result, a small gate is established for demultiplexing the high-speed optical time division multiplexed (OTDM) signal. These devices have been used to demultiplex 80 and 160 Gb/s optical signals to 20 Gb/s signals.

Figure 8.6.4 shows the experimental results of demultiplexing a 80 Gb/s signal into 8 channels at 10 Gb/s each [47]. This experiment utilized a MI which operates on the same principle as MZI.

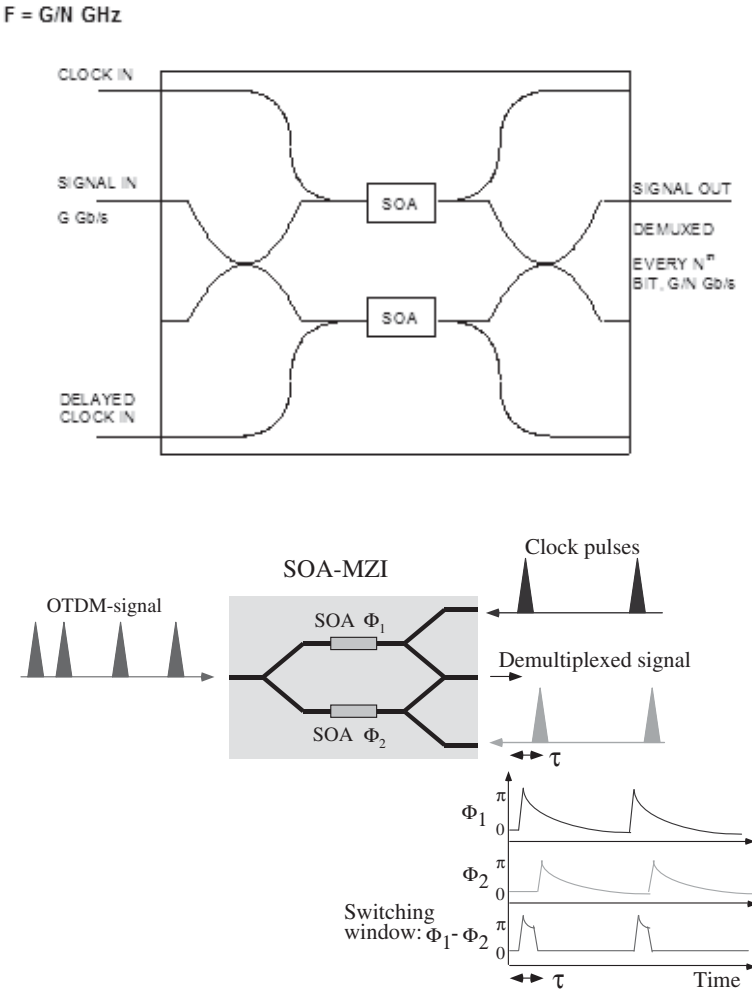

Fig. 8.6.3. Schematic of an optical amplifier based Mach-Zehnder demultiplexer which uses a differential phase shift scheme. The lower figure shows the principle of operation. ϕ_1 and ϕ_2 represent the phases produced by the two clock pulse sets one of which is delayed with respect to the other in the two arms. The phase difference $(\phi_1 - \phi_2)$ between the two arms occurs for a time of duration τ. This increases the speed capability of the demultiplexer.

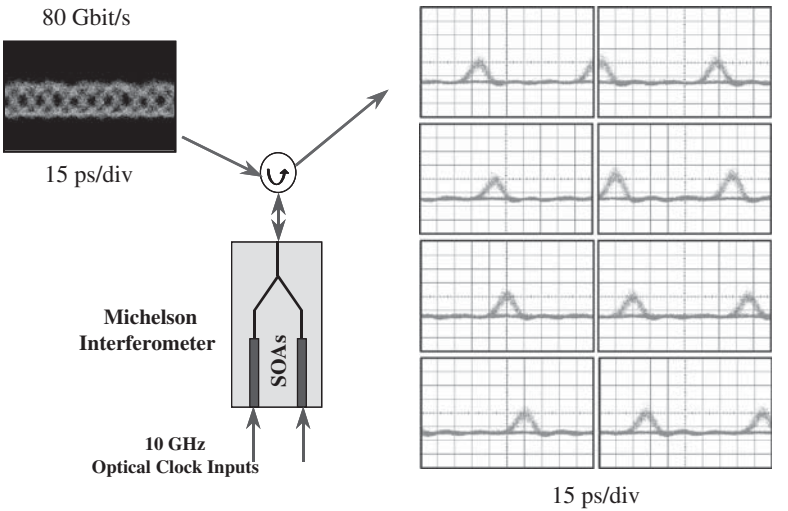

Fig. 8.6.4. The figure shows the demultiplexing of a 80 Gb/s signal to eight 10 Gb/s channels using a Michelson demultiplexer. Scale = 15 ps/div in all traces [47].

8.7. OTDM System Applications

In an optical time division multiplexing (OTDM) system, the data rates are high enough that the process of multiplexing (generation of high data rate signals from several low data rate signals) and demultiplexing (process of conversion of high data rate signals to several low data rate signals) are carried out optically. Several papers on various aspects of OTDM systems and all optical processing using optical amplifiers has been published [65–78]. For the demultiplexing process an optical clock (a timing signal) needs to be extracted from the incoming high speed (>100 Gb/s optical data). This clock recovery process has been carried out using cross gain modulation, cross phase modulation and four wave mixing [65, 77].

8.7.1. *Clock recovery*

The schematic of an experimental set up used for clock recovery from high speed data signals is shown in Fig. 8.7.1. The input optical signal and the local oscillator optical signal produce a FWM signal at the output of the SOA.

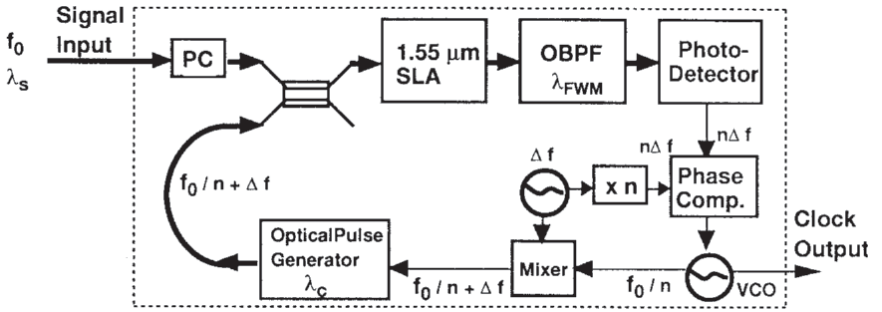

Fig. 8.7.1. Schematic of a clock recovery diagram used for recovering the clock from a high speed optical signal using FWM in SOA. The high speed optical input (at >100 Gb/s) is down converted to a low frequency (at ∼1 MHz) electrical signal using optical to electrical nonlinear down converter. This low frequency signal is phase locked using a conventional electrical phase locked loop [77].

In a transmission system, the timing signal (clock) extracted from the input optical data is used to demultiplex the data to lower data rate channels the error rate of which are then measured using traditional electronic circuits. The clock recovery process could be carried out using an optical phase locked loop in conjunction with an electrical low frequency phase locked loop. This is shown schematically in Fig. 8.7.1. In this process, the high data rate optical signals are converted to a low data rate electrical signal using a four wave mixing process followed by a photodetector. The phase and frequency of this electrical signal is locked to that of a voltage controlled local oscillator using conventional electrical phase locked loop techniques.

The key to the operation of this optical phase locked loop is the FWM optical to electrical converter. It is a semiconductor optical amplifier which has two optical signal inputs at wavelengths λ_1 and λ_2. The wavelength λ_1 is the input wavelength carrying data and the wavelength λ_2 is the optical clock generated by a laser at the demultiplexer. The wavelength λ_1 carries the data at B Gb/s and the wavelength λ_2 is the optical clock at a frequency $F \sim B/N$ GHz $+ f$ kHz. The four wave mixing process produces an optical signal at a wavelength of $2\lambda_1$-λ_2. This optical signal has several electrical components including a low frequency component close to Nf kHz produced by mixing of the electrical N_{th} harmonic of the clock ($NF \sim B + Nf$)

and the incoming signal at B Gb/s. This low frequency component in the optical signal is converted to an electrical signal using an avalanche photodiode, filtered and amplified. This low frequency electrical signal and the Nf kHz signal from a signal generator is used in a conventional phase locked loop configuration to lock the frequency F to B/N. The conventional phase locked loop has a phase detector (electrical mixer) and a voltage controlled oscillator. A stable optical clock is generated using a low frequency electrical phase locked loop which would provide the needed stability, and an optical front end (SOA) which would convert the high data rate signal to a low frequency optical signal.

Although this conversion from a high data rate optical signal to a low frequency optical signal is described above using a four wave mixing process it can also be carried out using the gain saturation process in a semiconductor amplifier. In the latter process the clock signal will be an input and the data signal will be the second input to the amplifier. The gain of the data signal is influenced by the high power clock signal and this gain modulation has a component at the N_{th} harmonic (Nf) of the difference frequency. The phase variance of a phase locked loop (PLL) fabricated using the FWM and the gain modulation schemes have been analyzed [65, 77]. The performance of the gain/phase modulation scheme is limited by the gain recovery time of the amplifier to ∼100 Gb/s using a differential scheme. The FWM scheme can in principle operate at data rates of ∼1 Tb/s.

8.7.2. *OTDM transmission*

The schematic of a optical time division multiplexed (OTDM) transmission set up is shown in Fig. 8.7.2.

A stabilized mode locked fiber laser generates short pulses at 10 GHz repetition rate. The 3.5 ps wide pulses are compressed to 0.98 ps pulses and are coded with data by transmission through a $LiNbO_3$ modulator. It then goes though a time division multiplexer (TDM) which coverts the data stream to a 400 Gb/s data. The TDM consists of a suitable designed sequence of optical delay lines. The

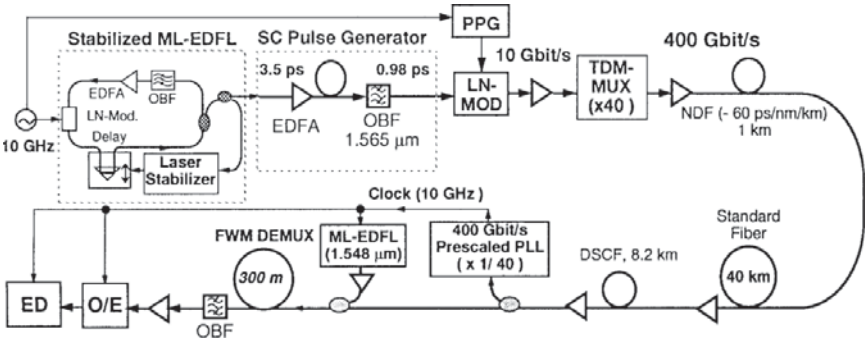

Fig. 8.7.2. Schematic of a 400 Gb/s optical transmission experiment set up [77].

400 Gb/s data is transmitted through various lengths of fiber. The clock is extract from the transmitted data using a FWM in a SOA based clock recovery process. A mode locked fiber laser operating at 10 GHz, the exact frequency of which is recovered by phase locking to the received 400 Gb/s data, provides the optical clock. The demultiplexing in this experiment is carried out using also a FWM process.

The error rate performance of the demultiplexed lower data rate channels are shown in Fig. 8.7.3. Bit-error-rate of $<10^{-9}$ is obtained suggesting good performance.

Very high speed OTDM transmission systems are now being developed in several research laboratories for future installment in commercial traffic. Semiconductor optical amplifiers play a key role in the development of these systems. They can be used for both optical demultiplexing and optical clock recovery using either the FWM process or Mach-Zehnder type devices. A detailed review is given in Ref. [78].

8.7.3. *Gain-transparent SOA-Switch*

The phase change of an input optical signal propagating in a SOA takes place in the presence of another optical signal within the gain or absorption spectrum. The phase change is due to carrier density induced change in index. Thus the signal on which the phase change is induced does not need to be within the gain spectrum of the amplifier.

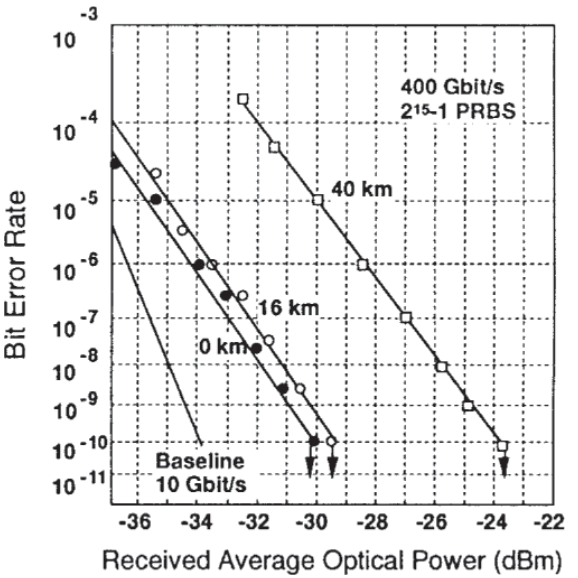

Fig. 8.7.3. Measured Bit-error-rate (BER) results at 10 Gb/s after demultiplexing of the 400 Gb/s data into forty 10 Gb/s data channels. The baseline is the BER data after the modulator. The three other lines are the data after transmission through ∼10 m (labeled 0 km in the figure), 16 km and 40 km of fiber [77].

This is basis of a gain transparent SOA-switch where the switching is induced by control pulses within the SOA gain spectrum on pulses at longer wavelengths which are neither absorbed nor experience gain in SOA.

Figure 8.7.4 shows schematically the gain-transparent (GT) SOA-switch in a hybrid Sagnac-Interferometer configuration A data signal at 1.55 μm and a control signal at 1.3 μm are coupled into the switch. The key element in the switch is a polarization insensitive 1.3 μm MQW-SOA The fiber to fiber gain of SOA is 30 dB (at 1310 nm and 400-mA injection current). The figure also shows a schematic spectrum of the amplified spontaneous emission (ASE) or the gain of the SOA with spectra of the control and the data signals. To achieve the desired switching function, the SOA is placed slightly asymmetrically (about 5 ps off the center) in the fiber loop. Thus the data pulses, which are split by the 3-dB coupler at the interferometer input, propagate through the SOA with a temporal delay. Whenever

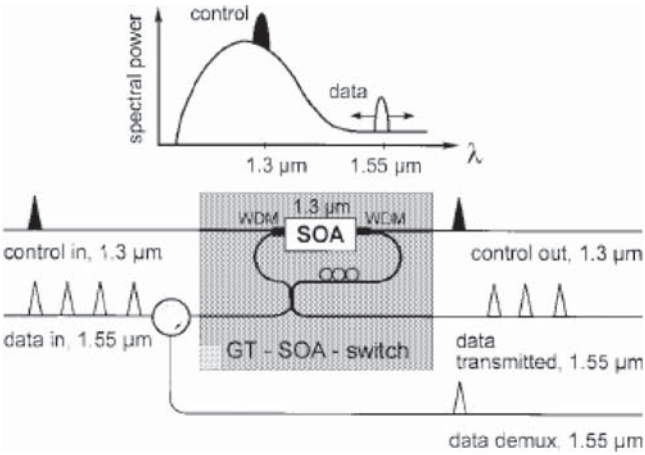

Fig. 8.7.4. GT SOA-switch in Sagnac-interferometer configuration [79].

a control pulse changes the refractive index of the SOA in the time slot between the data pulses, the data pulses are switched to a particular output port (for example the demux port in Fig. 8.7.4). In contrast to a conventional nonlinear interferometric switch, the data signal is far off the gain- and ASE maximum of the SOA. Thus, the data experiences a negligible amplitude change and only extremely low noise is added. This is due to the fact, that the data pulses wavelength is significantly lower than the band gap of the semiconductor material. However, a significant phase change of the data signal (around 1.55 µm) is observed induced by the control signal at 1.3 µm. This is in agreement with results reported in [9] where a 1.3-µm SOA in one branch of a Mach–Zehnder interferometer was used for all-optical 1.3 µm to 1.55 µm wavelength conversion. The, advantages of this switch are: (i) high linearity with respect to the data signal input power and therefore low crosstalk, since the influence of the data signal on the SOA gain and refractive index is negligible; (ii) low noise figure, since there is negligible ASE at the signal wavelength; (iii) wide signal wavelength range, since gain and phase dispersion are low in the signal band; and (iv) negligible intensity modulation of the transmitted data signal, since the gain change in the signal band negligible. GT-SOA switch has high linearly and large bandwidth.

In addition, the nonswitched data pulses are transmitted without distortion by the switching process.

References

[1] M. J. Coupland, K. G. Mambleton and C. Hilsum, *Phys. Lett.* **7**, 231 (1963).
[2] J. W. Crowe and R. M. Graig, Jr., *Appl. Phys. Lett.* **4**, 57 (1964).
[3] W. F. Kosnocky and R. H. Cornely, *IEEE J. Quantum Electron.* **QE-4**, 225 (1968).
[4] T. Saitoh and T. Mukai in Coherence, *Amplification and Quantum Effects in Semiconductor Lasers*, ed. by Y. Yamamoto, Chap. 7 (Wiley, New York, 1991).
[5] M. Nakamura and S. Tsuji, *IEEE J. Quantum Electron.* **QE-17**, 994 (1981).
[6] T. Saitoh and T. Mukai, *J. Lightwave Tech.* **6**, 1656 (1988).
[7] M. O'Mahony, *J. Lightwave Tech.* **5**, 531 (1988).
[8] N. K. Dutta, M. S. Lin, A. B. Piccirilli and R. L. Brown, *J. Appl. Phys.* **67**, 3943 (1990).
[9] C. E. Zah, J. S. Osinski, C. Caneau, S. G. Menocal, L. A. Reith, J. Salzman, F. K. Shokoohi and T. P. Lee, *Electron. Lett.* **23**, 1990 (1987).
[10] B. Mikklesen, S. L. Danielson, C. Joregensen and K. E. Stubkjaer, *Proc. ECOC*, **97**, Oslo, Norway, 245 (1997).
[11] S. L. Danielsen, P. Hansen and K. E. Stubkjaer, *IEEE, J. Quantum Electron.* **16**, 2095 (1998).
[12] T. Durhuus, B. Mikkelsen, C. Joergensen, S. L. Danielsen and K. E. Stubkjaer, *J. Lightwave Technol.* **14**, 942 (1996).
[13] S. Kawanishi, *Proceeding Optical Fiber Communication*, PD-5, Sanfrancisco, CA (2000)
[14] W. Shieh, E. Park and A. E. Willner, *IEEE. Photon. Technol. Lett.* **8**, 524 (1996).
[15] G. P. Agrawal, *J. Opt. Soc. Am. B*, **5**, 147 (1988).
[16] K. Kikuchi, M. Kakui, C. E. Zah and T. P. Lee, *IEEE J. Quantum Electron.* **28**, 151 (1992).
[17] O. Kamatani, S. Kawanishi and M. Saruwatari, *Electron. Lett.* **30**, 807 (1994).
[18] S. Kawanishi, T. Morioka, O. Kamatani, H. Takara, J. M. Jacob and M. Saruwatari, *Electron. Lett.* **30**, 981 (1994).
[19] G. P. Agrawal and N. A. Olsson. *IEEE J. Quantum. Electron.* **25**, 11 (1989); **25**, 2297 (1989).
[20] M. Shtaif and G. Eisenstein, *Appl. Phys. Lett.* **66**, 1458 (1995).
[21] J. Zhou, N. Park, J. W. Dawson, K. J. Vahala, M. A. Newkirk and B. I. Miller, *Appl. Phys. Lett.* **63**, 1179 (1993).
[22] J. Mork and A. Mecozzi, *IEEE J. Quantum Electron.* **QE-33**, 545 (1997).
[23] A. Mecozzi and J. Mork, *IEEE J. Select. Topics Quantum Electron.* **3**, 1190 (1997).
[24] C. Wu and N. K. Dutta, *J. Appl. Phys.* **87**, 2076 (2000).

[25] S. Kawanishi and M. Saruwatari, *J. Lightwave Technol.* **11**, 2123 (1993).
[26] G. P. Agrawal and N. A. Olsson, *IEEE J. Quantum Electron.* **25**, 2297 (1989).
[27] G. P. Agrawal, *J. Appl. Phys.* **63**, 1232 (1988).
[28] J. Zhou, N. Park, K. J. Vahala, M. A. Newkirk and B. I. Miler, *Electron. Lett.* **30**, 859 (1994).
[29] C. Joergensen, T. Durhuus, C. Braagaard, A. B. Mikkelsen and K. E. Subkjaer, *IEEE Photon. Technol. Lett.* **5**, 657 (1993).
[30] D. A. O. Davies, *IEEE Photon. Technol. Lett.* **7**, 617 (1995).
[31] A. Mecozzi, *IEEE Photon. Technol. Lett.* **8**, 1471 (1996).
[32] K. E. Stubkjaer *et al.*, in Proc. 22nd European Conference on Optical Communication (ECOC '96), Oslo, 433 (1996).
[33] C. Joergensen, S. L. Danielsen, T. Durhuus, B. Mikkelsen, K. E. Stubkjaer, N. Vodjdani, F. Ratovelomanana, A. Enard, G. Glastre, D. Rondi and R. Blondeau, *IEEE Photon. Technol. Lett.* **8**, 521 (1996).
[34] N. K. Dutta, C. Wu and H. Fan, *SPIE Proceedings*, **3945**, 204 (2000).
[35] P. N. Freeman, N. K. Dutta and J. Lopata, *IEEE Photon. Technol. Lett.* **9**, 46 (1997).
[36] D. A. O. Davies, *IEEE Photon. Technol. Lett.* **7**, 617 (1995).
[37] S. J. B. Yoo, *J. Lightwave Technol.* **14**, 955 (1996).
[38] C. Joergensen, S. L. Danielsen, M. Vaee, B. Mikkelsen, K. E. Stubkjaer, P. Doussiere, F. Pommerau, L. Goldstein and M. Goix, *Electron. Lett.* **32**, 367 (1996).
[39] S. L. Danielsen, C. Joergensen, M. Vaa, B. Mikkelsen, K. E. Stubkjaer, P. Doussiere, G. Garabedian, F. Pommerau, L. Goldstein, R. Ngo and M. Goix, in Tech. Dig. 1st Optoelectronics and Communications Conf. 346 (1996).
[40] D. Marcenac and A. Mecozzi, *IEEE Photonics Technology Lett.* **9**(6), pp. 749–751, 1997.
[41] T. Durhuus, B. Mikkelsen, C. Joergensen, S. L. Danielsen and K. E. Stubkjaer, *J. Lightwave Technol.* **14**, 942 (1996).
[42] K. Obermann, S. Kindt, D. Breuer, K. petermann, C. Schmidt, S. Diez and H. G. Weber, *IEEE Photon. Technol. Lett.* **9**, 312 (1997).
[43] S. Kawanishi and M. Saruwatari, *Electron. Lett.* **24**, 1452 (1998).
[44] S. Nakamura, Y. Ueno and K. Tajima, *IEEE Photon. Technol. Lett.* **13**, 1091 (2001).
[45] J. Leuthold, C. H. Joyner, B. Mikkelsen, G. Raybon, J. L. Pleumeekers, B. I. Miller, K. Dreyer and C. A. Burrus, *Electron. Lett.* **36**, 1129 (2000).
[46] Y. Ueno, S. Nakamura, K. Tajima and S. Kitamura, *IEEE Photon. Technol. Lett.* **10**, 346 (1998).
[47] I. Kang, C. Dorrer, L. Zhang, M. Dinu, M. Rasras, L. L. Buhl, S. Cabot, A. Bhardwaj, X. Liu, M. A. Cappuzzo, L. Gomez, A. Wong-Foy, Y. F. Chen, N. K. Dutta, S. S. Patel, D. T. Neilson, C. R. Giles, A. Piccirilli and J. Jaques, *IEEE J. of Setected Area of Quantum Electron.* **14**, 258 (2008).
[48] G. P. Agrawal, *Opt. Lett.* **12**, 260 (1987).
[49] F. Favre and D. L. Guen, *IEEE J. Quantum Electron.* **26**, 858 (1990).

[50] G. P. Agrawal, *J. Opt. Soc. Am. B*, **5**, 147 (1988).
[51] J. Zhou, N. Park, J. W. Dawson and K. J. Vahala, *Appl. Phys. Lett.* **63**, 1179 (1993).
[52] J. Zhou, N. Park, J. W. Dawson, K. J. Vahala, M. A. Newkirk and B. I. Miller, *IEEE Photon. Technol. Lett.* **6**, 50 (1994).
[53] A. D'ottavi, P. Spano, G. Hunziker, R. Paiella, R. Dall'Ara, G. Guekos and K. J. Vahala, *IEEE Photon. Technol. Lett.* **10**, 952 (1998).
[54] A. Mecozzi, S. Scotti and A. D'ottavi, *IEEE. J. Quantum Electron.* **31**, 689 (1995).
[55] S. Diez, C. Schmidt, R. Ludwig, H. G. Weber, P. Doussiere and T. Ducellier, *IEEE Photon. Technol. Lett.* **10**, 212 (1998).
[56] L. F. Tiemeijer, *Appl. Phys. Lett.* **59**, 499 (1991).
[57] J. Zhou, N. Park, J. W. Dawson, K. J. Vahala, M. A. Newkirk, U. Koren and B. I. Miller, *Appl. Phys. Lett.* **62**, 2301 (1993).
[58] I. Zacharopoulos, I. Tomkos, D. Syvridis, T. Sphicopoulos, C. Caroubalos and E. Roditi, *IEEE Photon. Technol. Lett.* **10**, 352 (1998).
[59] R. Paiella, G. Hunziker, J. Zhou, K. J. Vahala, U. Koren and B. I. Millers, *IEEE Photon. Technol. Lett.* **8**, 773 (1996).
[60] F. Martelli, A. Mecozzi, A. D'ottavi, S. Scotti, P. Spano, R. Dall'Ara, J. Eckner and G. Guekos, *Appl. Phys. Lett.* **70**, 306 (1997).
[61] T. J. Morgan, R. S. Tucker and G. Yoffe, *IEEE Photon. Technol. Lett.* **10**, 522 (1998).
[62] M. Shtaif, R. Nagar and G. Eisenstein, *IEEE Photon. Technol. Lett.* **7**, 1001 (1995).
[63] H. Sotobayashi and K. Kitayama, *IEEE Photon. Technol. Lett.* **11**, 45 (1999).
[64] J. Inoue and H. Kawaguchi, *IEEE Photon. Technol. Lett.* **10**, 349 (1998).
[65] S. Kawanishi and M. Saruwatari, *IEEE J. Lightwave Technol.* **11**, 2123 (1993).
[66] R. S. Tucker, G. Eisenstein and S. K. Korotky, *J. Lightwave Technol.* **6**, 1737 (1988).
[67] S. Nakamura, Y. Ueno and K. Tajima, *IEEE Photon. Technol. Lett.* **10**, 1575 (1998).
[68] K. L. Hall and K. A. Rauschenbach, *Opt. Lett.* **23**, 1271 (1996).
[69] S. Kawanishi, 2nd Optoelectronics & Communication Conference (OECC '97) Technical Digest, 12, Seoul, Korea (1997).
[70] K. E. Stubkjaer, S. L. Danielsen, M. Vaa, B. Mikkelsen, C. Joergensen, H. N. Poulsen, K. S. Jepsen, A. Kloch and P. B. Hansen, 2nd Optoelectronics & Communication Conference (OECC '97) Tech. Dig. 178, Seoul, Korea (1997).
[71] K. L. Hall and K. A. Rauschenbach, *Electron. Lett.* **32**, 1214 (1996).
[72] N. S. Patel, K. L. Hall and K. A. Rauschenbach, *Appl. Opt.* **37**, 2831 (1998).
[73] O. Kamatani and S. Kawanishi, *J. Lightwave Technol.* **14**, 1757 (1996).
[74] S. Kawanishi, T. Morioka, O. Kamatani, H. Takara, J. M. Jacob and M. Saruwatari, *Electron. Lett.* **30**, 981 (1994).
[75] O. Kamatani, S. Kawanishi and M. Saruwatari, *Electron. Lett.*, **30**, pp. 807–809 (1994).

[76] C. Bintjas, M. Kalyvas, G. Theophilopoulos, T. Stathopoulos, H. Avramopoulos, L. Occhi, L. Schares, G. Guekos, S. Hansmann and R. Dall'Ara, *IEEE Photon. Technol. Lett.* **12**, 834 (2000).
[77] S. Kawanishi, *IEEE J. Quantum Electron.* **QE-34**, 2064 (1998).
[78] H. Sotobayashi and T. Ozeki, in Chapter 2 "*WDM Technologies-Optical Networks*" ed. by A. K. Dutta, N. K. Dutta and M. Fujiwara (Elsevier Science, 2004).
[79] S. Diez, R. Ludwig and H. G. Weber, *IEEE Photon. Technol. Lett.* **11**, 60 (1999).

Chapter 9

Optical Logic Operations

9.1. Introduction

All-optical signal processing is expected to become increasingly important in future ultrahigh capacity telecommunication networks. Optical communications systems with per channel capacity of ∼40 Gb/s are commercially available today, and the capacity has been pushed to several 100 Gb/s in research laboratories [1]. The development of all optical logic technology is important for a wide range of applications in all optical networks, including high speed all optical packet routing, and optical encryption. An important step in the development of this technology is a demonstration of optical logic elements and circuits, which can also operate at high speeds. These logic elements include the traditional Boolean logic functions such as XOR, OR, AND, INVERT etc, and circuits such as parity checker, all-optical adder and shift register. Several articles on principles of all-optical logic have been published [2–29]. All-optical logic schemes were recognized as a possibility in early nonlinear optics studies. This was followed by initial work using nonlinear waveguides. Semiconductor optical amplifiers (SOAs) exhibit nonlinearity in its gain and phase response to input optical signals as described in Chs. 6 and 8. This property is used to construct optical logic gates using SOAs. The all-optical Boolean operations using semiconductor optical amplifier based devices are described in this chapter.

Table 9.2.1. The truth table of XOR.

Data B	Data A	Output XOR
0	0	0
1	0	1
0	1	1
1	1	0

9.2. Optical Logic XOR

It is believed that an ultrafast all-optical exclusive OR (XOR) logic gate is an important component in OTDM communication networks. Its truth table is shown in Table 9.2.1. It can be used in all-optical signal processing such as bit pattern matching [30], pseudo random number generation [31] and label swapping [32].

As is the case for electronic logic gates, all-optical logic gates fundamentally rely on nonlinearities [33]. So far, methods utilizing the nonlinearities of optical fiber [30, 34] and SOA [35–37] have been used to demonstrate all optical XOR functionality. The all-optical logic gate based on the nonlinearities of optical fiber has the potential of operating at terabits per second due to very short relaxation times ($<$100 fs) of its nonlinearity. The disadvantages of optical fiber are its nonlinearity is weak, and, long interaction lengths or high control energy is required to achieve reasonable switching efficiency.

SOA has the advantages of high nonlinearity and ease of integration. All-optical logic XOR has been demonstrated using several methods [35–48]. They are, SOA based Mach-Zehnder interferometer (SOA-MZI) [37, 49−51], semiconductor optical amplifier (SOA) loop mirror (SLALOM) [35], ultrafast nonlinear interferometer (UNI) [36, 47, 48], Sagnac interferometer [42], and other configurations including Terahertz Optical Asymmetric Demultiplexer (TOAD) [38, 43−46]. Also XOR by FWM in SOA with RZ-DPSK modulated inputs [39, 40]. and XOR optical gate based on Cross-Polarization Modulation in SOA have been studied [41]. SOA based

Mach-Zehnder interferometer has been discussed in previous chapters for wavelength conversion and optical demultiplexing.

9.2.1. *XOR using SOA-MZI*

Among the schemes stated above, the SOA-based Mach-Zehnder Inter-ferometer is the most promising candidate due to its attractive features of low energy requirement, low latency, high stability and compactness This makes SOA-MZI suitable for producing complex photonic logic circuits such as shift registers.

The optical XOR gate with SOA-MZI consist of a symmetrical MZI with two SOAs placed in upper and lower arms of the interferometer as shown in Fig. 9.2.1. To perform the XOR function as shown in the truth table, two optical control beams A and B are injected into the two arms separately. The signal, a clock stream of continuous series of "1"'s or a CW beam is split into two equal parts and injected into the two SOAs. Initially the MZI is unbalanced i.e. when $A = 0$ and $B = 0$, the signal at port 2 traveling through the two arms of the SOA acquires a phase difference of π when it recombines at the output port, thus the output is "0". When $A = 1$, $B = 0$, the signal traveling through the arm with signal A acquires a phase change due to the cross phase modulation (XPM) between the pulse train A and signal, and the signal traveling through the lower arm does not have this additional phase change. This results in an output "1". The same phenomenon happens if $A = 0$ and $B = 1$. However, when $A = 1$ and $B = 1$ the phase change for the signal traveling both arms are equal, hence the output is "0". When the phase shift

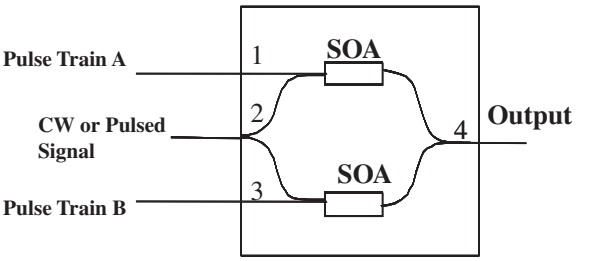

Fig. 9.2.1. Schematic set up of the XOR gate.

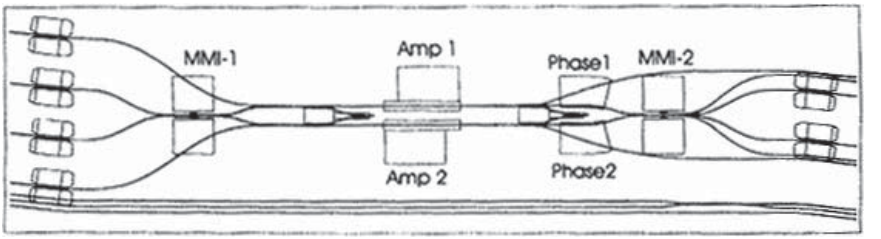

Fig. 9.2.2. Schematic of a Mach-Zehnder interferometer (MZI) with SOA in each arm. The MMI (multimode interference) couplers are used to couple the light into two waveguides. The phase shifters are needed to balance the phase difference between the two arms. The waveguides are angled at the facet to reduce the effect of reflections from the facet.

is optimum, the best contrast ratio is achieved at the output port. Figure 9.2.2 shows the schematic of a SOA based MZI.

Figure 9.2.3 shows the results of the all-optical XOR logical gate operation. The top figure shows the results of a 20 Gb/s pattern and the bottom figure shows the results of a 40 Gb/s pattern. Figure 2(a) and 2(b) show the control signal A, "11001100 . . . " and its 1 bit period delayed control signal B "10011001". The final XOR result is clearly seen in Fig. 2(c). However, the XOR output pulse is broad and pattern dependent, which is due to the long carrier recovery time of SOA in the SOA-MZI, and it is measured to be $\sim$150 ps in this experiment for the 40 Gb/s case when the SOA's are operated at high current.

For laboratory experiments, the pulse trains are created using typical pulsed sources such as gain switched distributed feedback lasers or mode locked semiconductor or fiber lasers followed by optical multiplexing.

An efficient method to over come the limitation imposed by long carrier lifetime is using differential phase modulation scheme [50, 51]. With differential phase modulation scheme, ultrahigh speed (>100 Gb/s) all optical processing, such as wavelength conversion, and all optical demultiplexing [See Ch. 8] has been demonstrated with SOA based interferometer.

A schematic diagram of the SOA-MZI and an illustration detailing the principle of operation as an XOR gate with differential phase

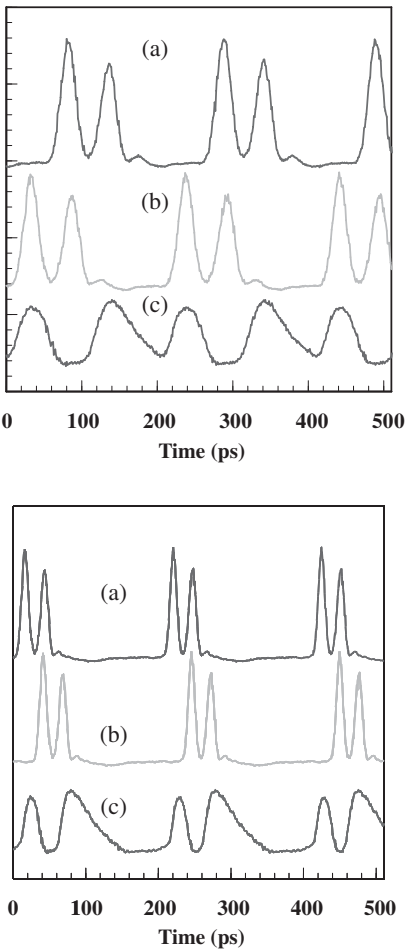

Fig. 9.2.3. Top figure is for 20 Gb/s pattern and the lower figure is for 40 Gb/s pattern. (a) Input data A, (b) Input data B, (c) XOR output [51].

modulation scheme are shown in Fig. 9.2.4. As in Fig. 9.2.4(a), the two input data streams, at wavelength λ_1 and λ_2 respectively, are combined as follows before coupled into ports 1 and 2 of the MZI: in port 1, data A is τ-ps ahead of data B, while in port 2, data B is τ-ps ahead of data A. The continuous wave (CW) light at λ_{XOR} is coupled into port 3. In the MZI, the combined data signals are launched into the two SOAs where they modulate the gain of the SOAs and thereby

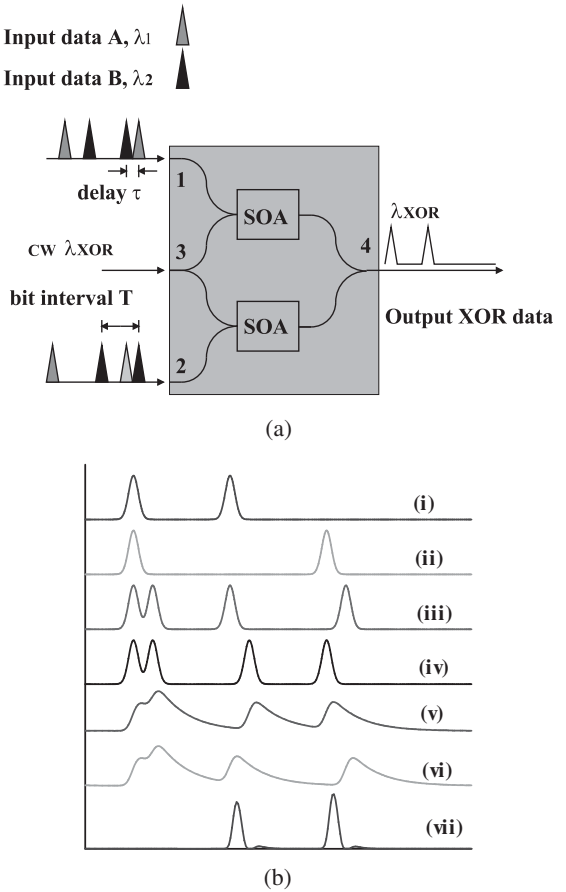

Fig. 9.2.4. Schematic diagram of SOA-MZI, illustration of XOR operation with differential phase scheme and truth table (a) Schematic diagram of SOA-MZI as XOR gate (b) Illustration detailing principle of XOR operation with differential phase scheme: (i) Data A (ii) Data B (iii) Combined signal at port 1 (iv) Combined signal at port 2 (v) Phase change of CW light in SOA1 (vi) Phase change of CW light in SOA2 (vii) Wavelength converted XOR output.

the phase of the co-propagating CW signals. At the output of the MZI, the CW light from the two SOAs interferes. When data A and data B are different, for example, data A is "1", and data B is "0"; the phase change of CW light on the lower branch is induced at first and opens the switching window, a time τ-ps later, when the phase change of CW light on the upper branch is also induced, the phase difference

is reset and the switching window closes, a pulse at wavelength λ_{XOR} is generated, therefore, the output of the MZI becomes "1". When data A and data B are same, for example, both are "1" or "0", the phase change of CW light on the lower branch is same to that on the upper branch, there is no light at wavelength λ_{XOR} generated, therefore, the output of the MZI becomes "0". The duration of the phase difference is determined by the delay τ and not by the gain recovery time of the SOA. This results in higher speed for differential operation. Other methods of effectively decreasing the gain recovery time such as external injection have been published [52–54]. It is discussed in detail in Ch. 6.

Figure 9.2.5 shows the experimental set up for differential XOR operation. Two full duty cycle data signals are produced from two gain switched DFB lasers, DFB1 and DFB2, which were driven from a synthesized signal generator with a microwave variable phase shifter inserted to delay their signals. The wavelength of DFB1 is 1545 nm and the wavelength of DFB2 is 1550 nm, the wavelengths of DFB1 and DFB2 are different in order to avoid interferometric cross talk that could degrade the performance. At 10 GHz, the pulse widths are both 35 ps. The pulses from the DFB lasers are compressed to ∼7 ps using a high dispersion fiber The two signals are combined with a passive multiplexer as shown in Fig. 9.2.5. The timing of all the signals were appropriately adjusted and optimized to enable differential operation. Figure 9.2.6 shows the result for 20 Gb/s (all 1's)

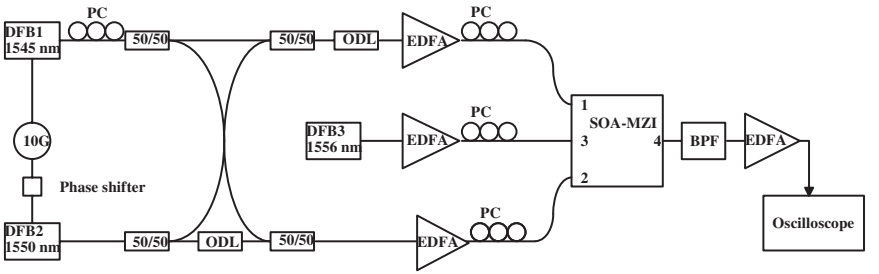

Fig. 9.2.5. Experimental setup of the differential phase modulation scheme PC — polarization controller, ODL — optical delay line, EDFA — Erbium doped fiber amplifier, 50/50 — 3 dB coupler, BPF — band pass filter [51].

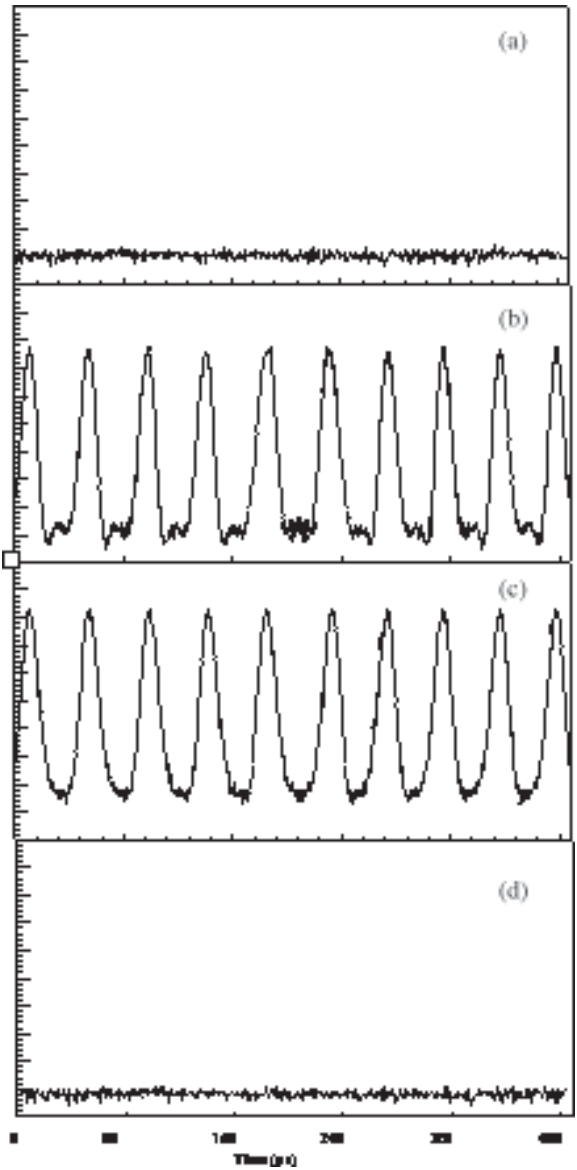

Fig. 9.2.6. Output XOR experimental results all (1's) (a) $A = 0$, $B = 0$; (b) $A = 1$, $B = 0$; (c) $A = 0$, $B = 1$; (d) $A = 1$, $B = 1$. Rate = 20 Gb/s [51].

operation. All the delays were optimized to obtain the data shown in Fig. 9.2.6.

9.2.1.1. *Simulation*

As shown in Figs. 9.2.1 and 9.2.4, the CW light P_{in} is divided and introduced via a 50:50 coupler into the two arms of the MZI.

In the MZI, the control signals are launched into the two SOAs where they modulate the gain of the SOAs and thereby the phase of the co-propagating CW signals. At the output of the MZI, the CW light from the two SOAs interfere and the XOR output intensity can be described by the following basic interferometric equations [51]:

$$P_{\text{XOR}}(t) = \frac{P_{\text{in}}}{4}\{G_1(t) + G_2(t) - 2\sqrt{G_1(t)G_2(t)}\cos[\phi_1(t) - \phi_2(t)]\}. \tag{9.2.1}$$

In which, $G_{1,2}(t)$ is time dependent gain and $\phi_{1,2}(t)$ is phase shift in the two arms of SOA-MZI. The phase shift $\phi_{1,2}(t)$ is related to the gain $G_{1,2}(t)$ by the linewidth enhancement factor α and is given by [55]:

$$\phi_1(t) - \phi_2(t) = -\frac{\alpha}{2}\ln\left(\frac{G_1(t)}{G_2(t)}\right). \tag{9.2.2}$$

The time dependent gain of the SOA satisfies the dynamical equation [51, See also Ch. 8, $\exp(h)$ is the total gain G]:

$$\frac{d\ln(G_{1,2}(t))}{dt} = \frac{\ln G_0 - \ln G_{1,2}(t)}{\tau_c} - \frac{P_{1,2}(t)}{E_{\text{sat}}}(G_{1,2}(t) - 1), \tag{9.2.3}$$

where τ_c is the spontaneous carrier lifetime, G_0 is the unsaturated power gain and E_{sat} is the saturation energy of the SOA. $P_{1,2}$(t) is the instantaneous optical power inside the SOA1 and SOA2. Scheme 1 (non-differential) is considered first. In the scheme 1, data A is coupled into SOA1 and data B is coupled into SOA2, so $P_{1,2}$(t) can

be expressed as follows:

$$P_{1,2}(t) = P_{A,B}(t) + P_{\mathrm{CW}}/2. \tag{9.2.4}$$

In simulation, the data stream pulse is assumed to be a Gaussian pulse with a FWHM (full width at half maximum) pulse width of 1/8 bit period, e.g. $\tau_{\mathrm{FWHM}} = T/8$. The pulse train can then be written as

$$P_{A,B}(t) = \sum_{n=-\infty}^{+\infty} a_{nA,B} \frac{2\sqrt{\ln 2} P_0}{\sqrt{\pi}\tau_{\mathrm{FWHM}}} \exp\left(-\frac{4\ln 2(t-nT)^2}{\tau_{\mathrm{FWHM}}^2}\right), \tag{9.2.5}$$

where P_0 is the single pulse energy, $a_{nA,B}$ represents n_{th} data in data stream A and B, $a_{nA,B} = 1$ or 0.

Figure 9.2.7 shows the calculated phase shift induced on a CW beam by a series of pulses. For a SOA based interferometric device, output pulse amplitude is decided by the maximum phase shift ϕ (as shown in Fig. 9.2.7(a)) induced by the control pulse. Figure 9.2.7(b) shows the relation between phase shift in one arm of the SOA-MZI and single pulse energy P_0 for different repetition rate, the parameters of the SOA are chosen as following, $G_0 = 1000$ and $\alpha = 7$. From Fig. 9.2.7 we can see, the phase shift increases with increasing the single pulse energy, and it decreases with increasing control pulse rate. Phase shift of π can be easily achieved when bit rate is low, e.g. single pulse energy $P_0 = 0.0025E_{\mathrm{sat}}$ can induce a phase shift of π when bit period is same as carrier recovery time ($T = \tau_c$).

In the high bit rate case, however, the phase shift becomes saturated with increasing P_0, e.g. when $T = 0.1\,\tau_c$, the phase shift becomes saturated when P_0 is larger than 0.01 E_{sat}, and the phase shift is only $\pi/3$. For an interferometric device, such as the MZI, the larger phase shift produces larger output signal.

Figure 9.2.8 shows the output XOR of the SOA-MZI when a bit sequence is used in data stream A and data stream B at bit rate of $1/\tau_c$, $P_0 = 0.0025E_{\mathrm{sat}}$ and $P_{\mathrm{CW}} = 0.01P_{\mathrm{sat}}$ ($P_{\mathrm{sat}} = E_{\mathrm{sat}}/\tau_c$). It is clearly seen that the output XOR pulse is broader than the input signal pulse, and there is pattern effects. A deeper insight in the performance of the XOR logic can be gained by displaying the XOR

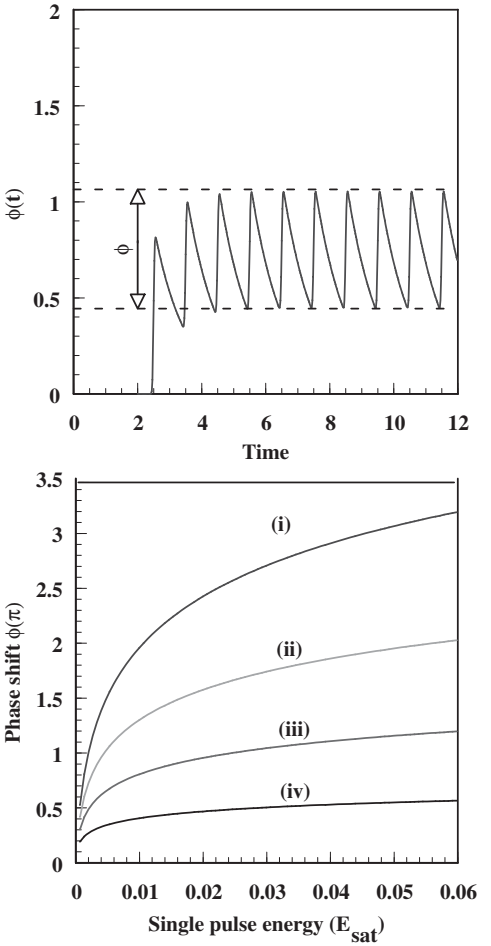

Fig. 9.2.7. Phase shift in one arm of the SOA-MZI induced by control signal (all "1"s) pulses (Top) Evolution of the optical phase of the CW light (Bottom) Relationship between maximum phase shift ϕ and single control pulse energy P_0 for different repetition rate (i) $T = \tau_c$, (ii) $T = \tau_c/2$, (iii) $T = \tau_c/4$, (iv) $T = \tau_c/10$.

generated by a long sequence of different patterns of A and B signals. These diagrams resemble the "classical" eye diagrams, but they are not as informative in the sense that degrading effects, normally observed in point-to-point communication links, such as noise sources added by the detector, optical fiber, etc. are absent. Nevertheless,

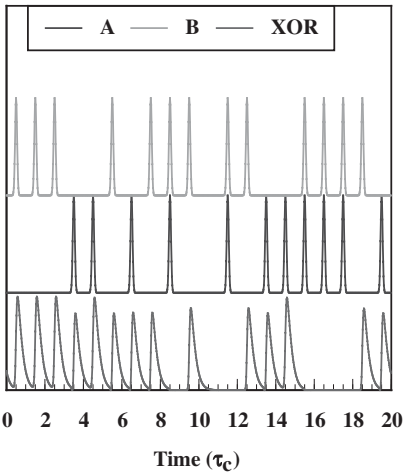

Fig. 9.2.8. Sequence of XOR logic pattern produced at the output of SOA-MZI as a response to PRBS input at bit period $T = 1/\tau_c$. CW input power is $0.02\,P_{\rm sat}$, and the single pulse energy is $0.0025\ E_{\rm sat}$.

theses diagrams, which will be called "pseudo-eye-diagrams" (PEDS) [56], are useful because major features of the operational principle of the MZI device become evident. Following [56, 57], quality factor

$$Q = \frac{P_1 - P_0}{\sigma_1 + \sigma_0}, \tag{9.2.6}$$

has been calculated in the diagrams to simplify the interpretation of the results where $P_1(P_0)$ and $\sigma_1(\sigma_0)$ are respectively, the average power and standard deviation of the XOR output 1 s (0 s).

Figure 9.2.9 presents the simulated PEDs of a "1" in the XOR output for 127 bit $(2^7 - 1)$ pseudorandom sequence of input pulses. The XOR output at bit rates of $1/\tau_{\rm c}$, $2/\tau_{\rm c}$, and $4/\tau_{\rm c}$ are shown where τ_c is the gain recovery time. Q value decreases with increasing data bit rate, and the eye is closed at a bit rate of $4/\tau_{\rm c}$. In the simulation, the single pulse energy is chosen as $0.01E_{\rm sat}$ for the bit rate of $2/\tau_{\rm c}$ and $4/\tau_{\rm c}$ because the phase shift becomes saturated when $P_0 > 0.01E_{\rm sat}$. For better performance of XOR in SOA-MZI, one method is to increase the power of the CW beam, so as to reduce carrier recovery time [52–54]. The relation between Q value and CW

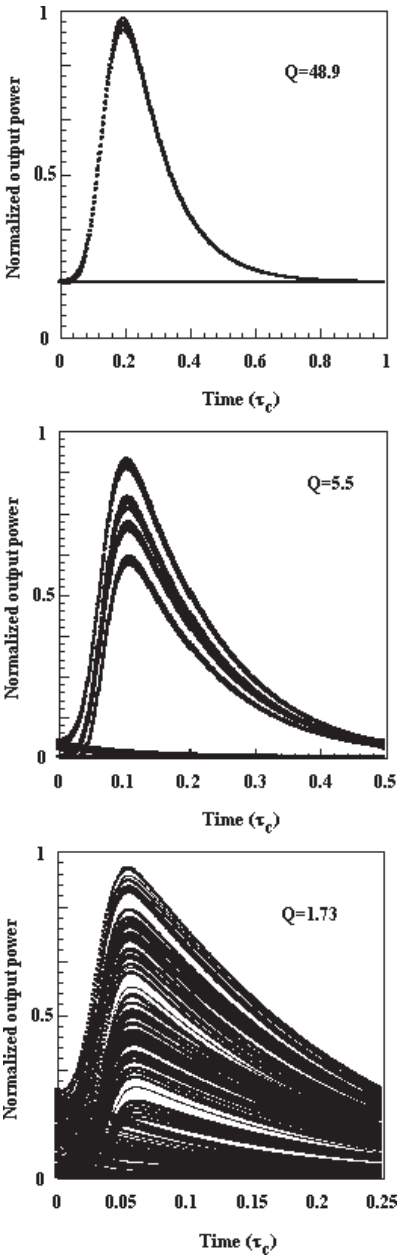

Fig. 9.2.9. Simulated XOR output for different bit rates for non-differential scheme. $P_0 = 0.01E_{\rm sat}$, and $P_{\rm CW} = 0.2P_{\rm sat}$. (Top) $T = \tau_c$, (Middle) $T = 0.5\tau_c$ (Bottom) $T = 0.25\tau_c$.

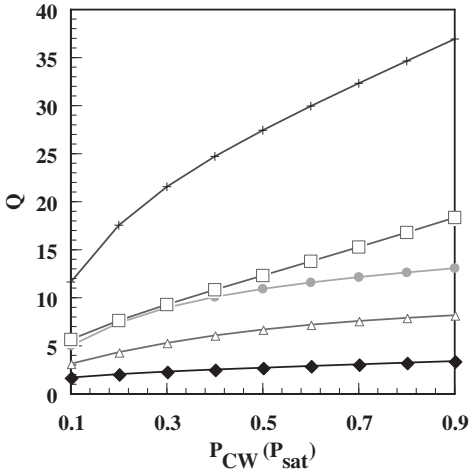

Fig. 9.2.10. The relation between Q value and CW beam intensity P_{CW}. $P_0 = 0.01\,E_{\mathrm{sat}}$ □ and ♦ are with non-differential scheme, $\square - T = 0.5\tau_{\mathrm{c}}$, $\blacklozenge - T = 0.25\tau_{\mathrm{c}}$. +, • and Δ are with differential scheme, $+ - T = 0.5\tau_{\mathrm{c}}$, $\bullet - T = 0.25\tau_{\mathrm{c}}$, $\Delta - T = 0.1\tau_{\mathrm{c}}$ [51].

beam power P_{CW} is shown in Fig. 9.2.10. It shows, Q value increases with increasing P_{CW}. Increasing α values increases the Q factor since it increases the phase change and hence the output power.

For the differential scheme, the two input data streams at wavelength λ_1 and λ_2 respectively, are combined as follows before being coupled into ports 1 and 2 of the MZI. In port 1, data A is τ-ps ahead of data B, while in port 2, data B is τ-ps ahead of data A. $P_{1,2}(t)$ can be expressed as:

$$P_1(t) = \frac{P_A(t) + P_B(t-\tau) + P_{\mathrm{CW}}}{2}, \tag{9.2.7a}$$

$$P_2(t) = \frac{P_A(t-\tau) + P_B(t) + P_{\mathrm{CW}}}{2}. \tag{9.2.7b}$$

In the simulation delay τ is chosen so that maximum phase shift can be achieved when data $A = 1$ and data $B = 0$. Figure 9.2.11 presents the simulated PEDs of the XOR output at bit rates of $2/\tau_c$, $4/\tau_{\mathrm{c}}$, and $10/\tau_{\mathrm{c}}$. Unlike the output pulse in non-differential scheme which has a long tail, the output in the differential scheme is like

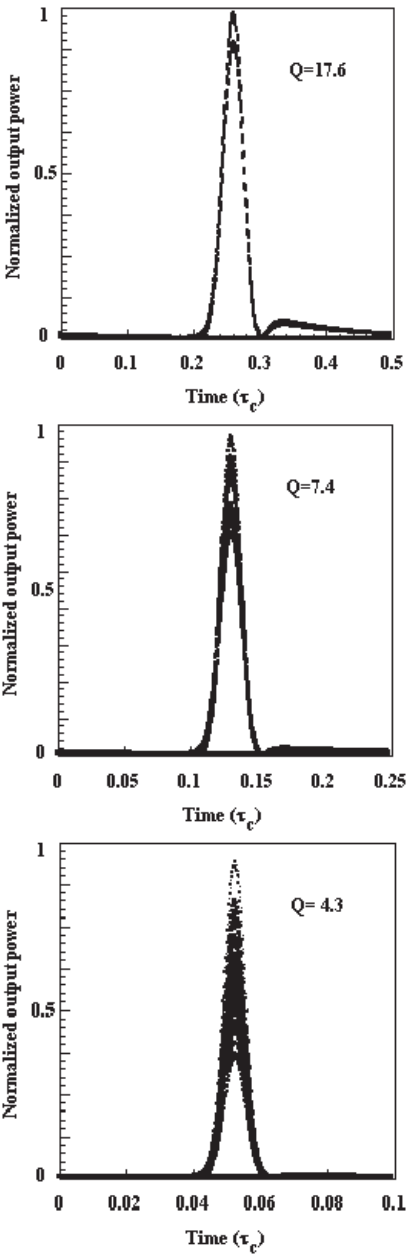

Fig. 9.2.11. Simulated XOR output for different bit rates for differential scheme. $P_0 = 0.01E_{\text{sat}}$, and $P_{\text{CW}} = 0.2P_{\text{sat}}$. (Top) $T = 0.5\tau_{\text{c}}$, (Middle) $T = 0.25\tau_{\text{c}}$ and (Bottom) $T = 0.1\tau_{\text{c}}$ [51].

a Gaussian pulse, and the pulse width is only a fraction of the bit period. Also, the eye is clearly open even at bit rate of $10/\tau_c$.

A comparison of Figs. 9.2.9 and 9.2.11 shows that for the non-differential scheme, all-optical logic XOR in a symmetric SOA-MZI can not be operated at the bit rate larger than $4/\tau_c$, while it can be operated up to $10/\tau_c$ in the differential phase modulation scheme. If the carrier recovery time τ_c is less than 100-ps, one can conclude that all-optical logic XOR in a symmetric SOA-MZI can be operated up to 100 Gb/s with the differential phase modulation scheme. The primary reason for higher speed in differential operation is that the duration of the phase difference is determined by the delay τ (between the input signals) and not by the gain recovery time of the SOA. This results in higher speed for differential operation. As has been identified through simulation that differential scheme allows higher speed compared to non-differential scheme for the same gain recovery time. However, the differential schemes may be more difficult to implement in larger circuits such as parity checkers and shift registers and thus methods of reducing gain recovery times in SOA are important.

9.2.2. *XOR using semiconductor optical amplifier-assisted fiber Sagnac gate*

A fiber Sagnac gate consists of a SOA placed in a fiber loop. The pulse injected in the loop travels in both clockwise and counterclockwise direction. The SOA is located asymmetrically in the loop i.e. the clockwise and counterclockwise pulses arrive at the SOA at slightly different times. The gate utilizes the differential phase change between the two counter propagating signal pulses [42]. This phase change is imposed on them by their nonlinear interaction with the temporally synchronized control pulses A, B in the SOA and is due to the rapid carrier depletion in the presence of one or two control pulses. Crucial to the operation of the device is the position of the SOA with respect to the center of the loop. This has to be asymmetrically placed, so that the two counter-propagating pulses can experience a differential phase change as only one of them interacts with the control pulse in the SOA. In the absence of any control pulses

the gate is reflective and the input signal exit through the same port that they enter (port R). When pulse A is present, a phase shift is observed by the signal pulse at the SOA. This phase shift is due to the carrier density change caused by input pulse A in the SOA. This phase shift results in a transmission of the signal at port T i.e. the gate becomes transmissive. Thus when either pulse A or B is present, the gate becomes transmissive (port T) and if both A and B are present it becomes reflective again (port R). Figure 9.2.12 shows the experimental configuration. The Sagnac interferometer gate with SOA has a 3-dB polarization preserving coupler. This coupler is used

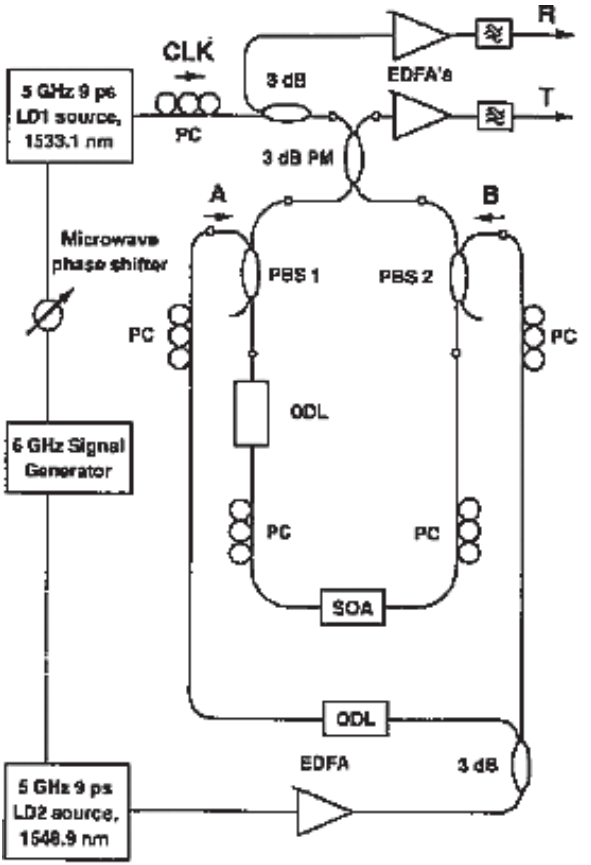

Fig. 9.2.12. Experimental setup for fiber Sagnac gate [42].

for injecting the clock signal. The optical logical inputs A and B are inserted in the loop also using two optical fiber based polarization beam splitters/combiners PBS1 and PBS2. Since the SOA gain is polarization dependent, polarization controllers are used at its input and output for optimum control. A variable optical delay line was introduced in the loop to adjust the temporal position of the SOA with respect to the center of the loop. The scheme can be implemented using either a CW signal (on which the phase change due to the pulsed inputs A and B are imposed) or using a pulsed signal.

9.2.3. *XOR using terahertz optical asymmetric demultiplexer (TOAD)*

The Terahertz Optical Asymmetric Demultiplexer (TOAD) is an interferometric device which consists of an optical loop mirror, with an internal optical nonlinear element (NLE) such as a SOA [43]. The operating principle of TOAD is similar to that of a fiber sagnac gate. A signal pulse enters the loop through the main coupler and produces two pulses in the loop, a clockwise (CW) propagating pulse and a counterclockwise (CCW) propagating pulse. As they transverse the loop, the pulses passes through the NLE once, then they return to the main coupler at the same time (Fig. 9.2.13).

A control pulse is injected into the loop via the intra-loop coupler. It passes once through the NLE, then exits the loop.

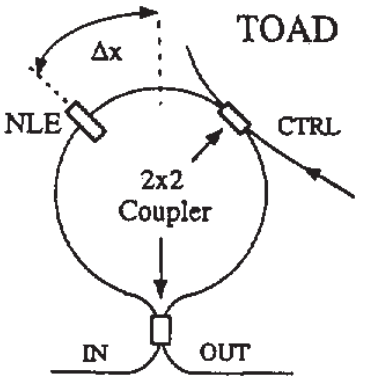

Fig. 9.2.13. Simplified schematic of the TOAD [43].

The control pulse has sufficient energy to significantly modify the optical properties in the NLE. When the control pulse is temporally separated (i.e. far ahead or behind both CW and CCW pulses) the CW and CCW pulses will interfere destructively at the main coupler, and the output is zero. If the CW pulse passes through the NLE when the appropriate transition (of a certain property such as phase change) due to the control pulse occurs and the CCW pulse does not experience this phase change, the pulses interfere due to the phase difference, thus the output of TOAD becomes one. Thus the control pulse injected into the loop produces a switching gate. If there are two sets of control pulses which follow each other, two sets of gates which appear sequentially may be produced. The nature of the output depends on the relative temporal position of the switching pulses and the CW and CCW pulses in the loop. This is shown in Fig. 9.2.14.

A good XOR gate can be created by using two switching pulses A and B (which would form two switching gates) to logically form the output in a single gate by exploiting the fast gain recovery time of the SOA (∼80 ps) in the TOAD [47] and by using a relatively wide switching window (∼130 ps). If the switching window is larger than the gain recovery of the SOA then it is possible to create two temporal conditions to achieve switching as shown in Fig. 9.2.14. One condition Fig. 9.2.14(b) is the normal TOAD operation where the switching pulse is timed to arrive in between the signal pulses in the loop. However, due to the fast gain recovery of the SOA there is also a switching condition Fig. 9.2.14(a) where the switching pulse arrives before either of the counter-propagating loop signal pulses. These two pulses then experience a differential phase shift as the gain of the SOA recovers, as used in the SLALOM [35]. If the switching pulses (A and B) arrives in the switching conditions, shown in Fig. 9.2.14(c), then there is almost no differential phase shift between the loop signal pulses and hence the output is "0". If either A or B control pulse is imposed, the condition shown in Figs. 9.2.14(a) or 9.2.14(b) takes place and the output is "1" as for a demultiplexer.

This XOR technique is limited in speed due to the requirement of the SOA gain recovering between switching events. The modeling suggests that switching speeds of 40 Gb/s is feasible. Higher speed

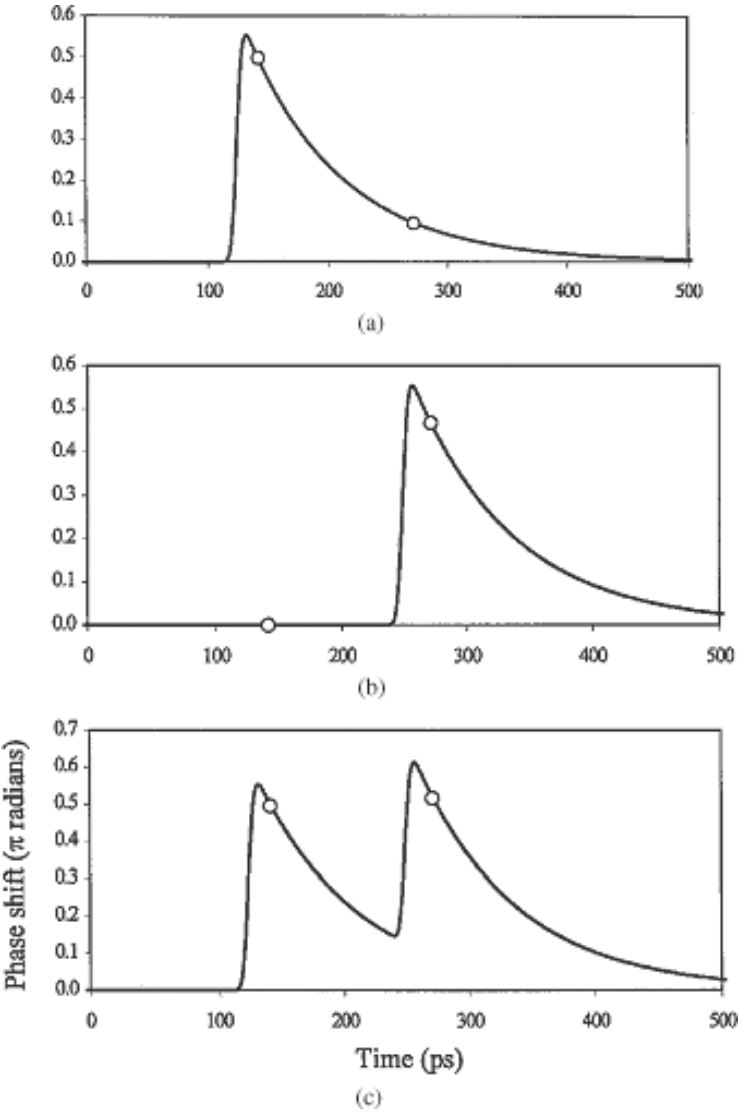

Fig. 9.2.14. Schematic of phase variation produced in a TOAD with the possible switching conditions: (a) switching pulse arrives before both loop signal pulses; (b) switching pulse arrives in between loop signal pulses; (c) switching pulses arrive both before and in between loop signal pulses. The temporal positions of the loop signal pulses are shown as two circles on the phase evolution graphs and the output of the TOAD depends on the phase difference between these loop pulses. SOA offset from loop center = 65 ps, 1/e gain recovery = 80 ps, switching energy = 100 fJ [44].

XOR functionality can also be achieved by using all-fibre NOLMs [45, 46] at the expense of additional latency or by using the logical combination of two SOA based gates as mentioned above.

9.2.4. *XOR using UNI gate*

The operation of the UNI gate relies on rotation of polarization of the incoming signal to be switched in the presence of a switching pulse in a SOA [47, 48]. Figure 9.2.15 shows the schematic.

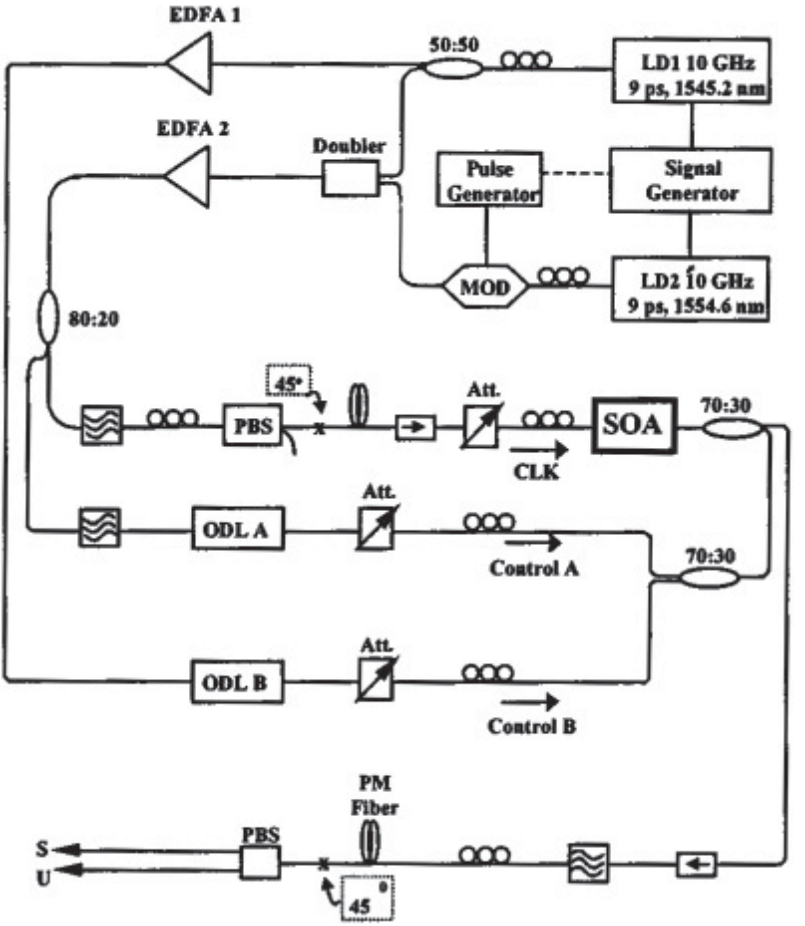

Fig. 9.2.15. Experimental set up of the XOR with UNI gate [48].

The incoming signal pulse is split into two orthogonal polarization components, which are delayed relative to each other in a certain length of birefringent fiber before entry into the SOA. For single logic rail operations, one of these two orthogonal polarizations of the incoming pulse is temporally synchronized with the switching pulse. This causes a local, time-dependent refractive index change in the SOA, which in turn imparts a phase change only on the synchronized polarization component (i.e. the component which is temporally coincident with the time dependent phase change in the SOA) of the signal pulse. At the output of the SOA, the relative delay between the two polarization components is removed with a fiber of equal birefringence and length and the pulses are allowed to interfere on a polarizer that determines blocking or transmission through the switch. Long-lived nonlinearities in amplitude and phase are balanced out to first order in the UNI, as they affect equally the two orthogonal polarization components of the signal.

For the implementation of the XOR operation, both polarization states of the incoming pulse must be accessed in the SOA with the two control data pulses A and B. Each control pulse imparts a phase and amplitude modulation on the signal polarization component to which it is synchronized. If either control pulse is present, the differential phase variation between the orthogonal polarization components results in polarization rotation on the polarizer and the UNI operates as a single rail AND gate. If both control pulses are present, the phase change in the orthogonal polarization components may be adjusted to be equal so that no polarization rotation results. In the experiment three optical signals were used as inputs into the gate. Controls A and B are the logical inputs to the switch and they control its state and CLK (a series of 1's) is the clock input. The outcome of the logic XOR of A, B is imprinted on CLK, which is held continuously to a logical 1 on input to the gate.

9.2.5. *XOR optical gate based on cross-polarization modulation in SOA*

The schematic of the method is shown in Fig. 9.2.16. Optical beams from two laser sources are coupled into the SOA. The polarization

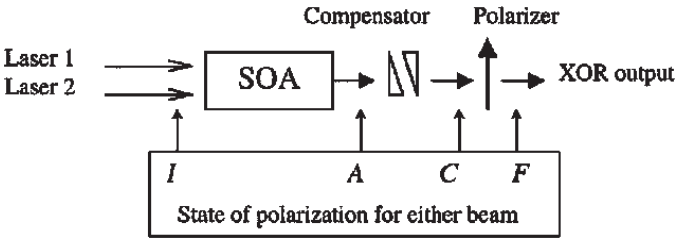

Fig. 9.2.16. Simplified schematic of the XOR gate with cross-polarization modulation [41].

state of input beam 1 is altered by the presence of beam 2 as it exits the SOA. The phenomenon is known as cross-polarization modulation.

In the experiment two optical beams of equal power and same linear polarization are launched in a co-propagation mode into the SOA [13]. The wavelengths of the input beams are separated by few nm. A compensating element and a polarizer are placed after the SOA and tuned in order to stop all light going through i.e. when both input light beams are ON the output of the setup is zero. When both input are OFF, the output is also zero. On the other hand, when a single beam is launched into the system, its polarization just before the polarizer is different from what it was when both beams were ON. Thus, the polarizer does not extinguish this beam entirely and the output is ON. This behavior is characteristic of XOR function. The efficiency of the operation is governed by the magnitude of change in polarization experienced by one of the beams when the other one is turned ON or OFF. A proper setting of the input wavelength and power is needed. The input polarizations are controlled using manual tuning. In practice, strict equality of the input beam power, wavelength and polarization is not really required.

9.2.6. *XOR using FWM in semiconductor optical amplifier with return-to-zero phase-shift-keying (RZ-DPSK) modulated input*

Consider signals at three frequencies injected into a nonlinear medium such as a SOA. The electric fields $E_1(\omega_1)$, $E_2(\omega_2)$, and

$E_3(\omega_3)$ can generate mixing terms at various optical frequencies via FWM in a medium with third-order optical nonlinearity [39, 40]. The signal strength at a frequency of $\omega_1 + \omega_2 - \omega_3$ is given by

$$E_{\mathrm{FWM}}(\omega_1 + \omega_2 - \omega_3) \sim \chi^{(3)} E_1(\omega_1) E_2(\omega_2) E_3^*(\omega_3),$$

where $\omega_1 \neq \omega_2 \neq \omega_3$ and $\chi^{(3)}$ is the third-order nonlinear susceptibility. With phase shift keyed (PSK) input light at frequencies ω_1, ω_2, such that $E_1 \sim \exp(i\pi A_n)$ and $E_2 \sim \exp(i\pi B_n)$, and a CW input light at frequency ω_3, the electric field of the FWM generated signal is given by

$$E_{\mathrm{FWM}}(\omega_1 + \omega_2 - \omega_3) \sim \exp[i\pi(A_n \oplus B_n)],$$

where $\oplus = XOR$. One disadvantage of this approach is that the signal produced is small. However, in principle it has several advantages. For this scheme, the identical intensity pattern of all pulses in PSK data should also mitigate the pattern dependence normally observed in signal processing of on-off-keyed (OOK) data. In addition, the output frequency can be specified using the CW source of frequency ω_3, if the component, $\omega_1 + \omega_2 - \omega_3$, is not resonant with other FWM frequencies such as $2\omega_1 - \omega_2$.

9.3. Optical Logic OR

As an important function in all-optical logic systems, it is desirable to have an OR gate which is stable and compact. All optical OR gate operation has been demonstrated at high speeds (>40 Gb/s). When a SOA is used the speed is limited by the carrier recovery time of the SOA. The following is truth table of OR operation.

9.3.1. *OR gate using gain saturation in an SOA*

The principle of operation of OR gate relies on gain saturation in the SOA. A schematic diagram of the SOA-based all-optical OR gate configuration is depicted in Fig. 9.3.1(a). Two input data streams at wavelengths within the gain spectrum of the SOA are combined and

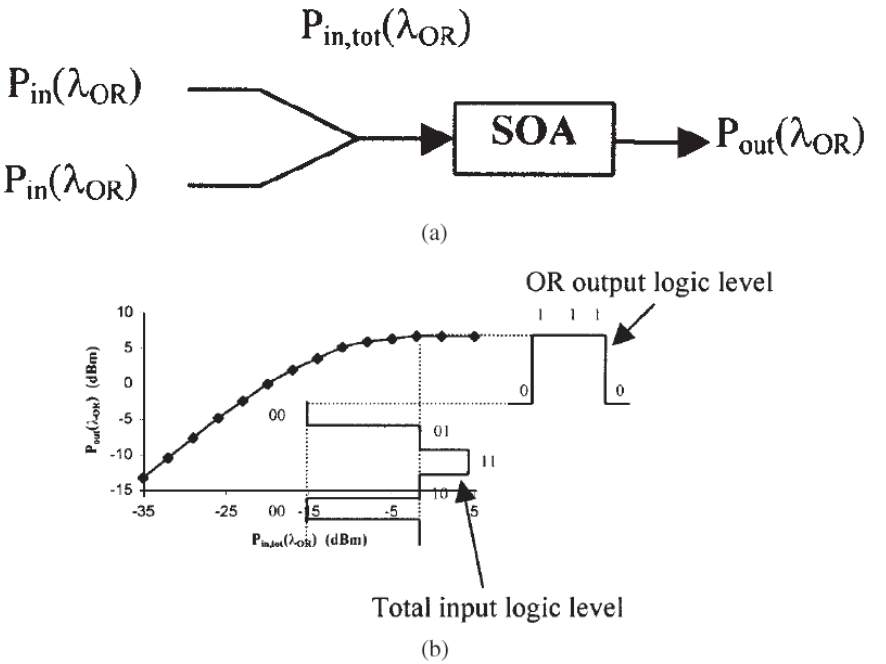

Fig. 9.3.1. (a) Schematic diagram of the all-optical OR logic gate configuration; (b) experimental static curve of the gain saturation and illustration detailing the OR gate's principle of operation [58].

Table 9.3.1. Truth table of the OR gate.

Data B	Data A	Output OR
0	0	0
1	0	1
0	1	1
1	1	1

coupled into the SOA, and the OR logic gate output signal P_{out} is obtained at the SOA output.

Figure 9.3.1(b), shows the output power P_{out} versus the total input power P_{in}. The output power P_{out} saturates for input powers larger than a certain value i.e. when both signals are present the output is also "1". Thus the output signal at OR will correspond to the logical OR (Table 9.3.1) of the two input signals. However, it is

important to note that the pulsed powers must be carefully adjusted with respect to saturation point of the SOA and the wavelength must be within the gain spectrum of SOA.

9.3.2. *OR gate using a SOA and delayed interferometer (DI)*

The OR gate operation is based on the gain saturation and phase modulation of optical signals in the SOA [58–64]. The schematic diagram of the principle is shown in Fig. 9.3.1 and the experimental set up in Fig. 9.3.2. The signals A and B and a CW control signal (which would carry the information of OR output) are injected into the SOA, the data signals A and B will induce a phase shift in the CW signal via cross-phase modulation in the SOA. Then by using a polarization maintaining loop (PML) mirror, the phase-shifted CW signal is split into a clockwise component and a counter clockwise

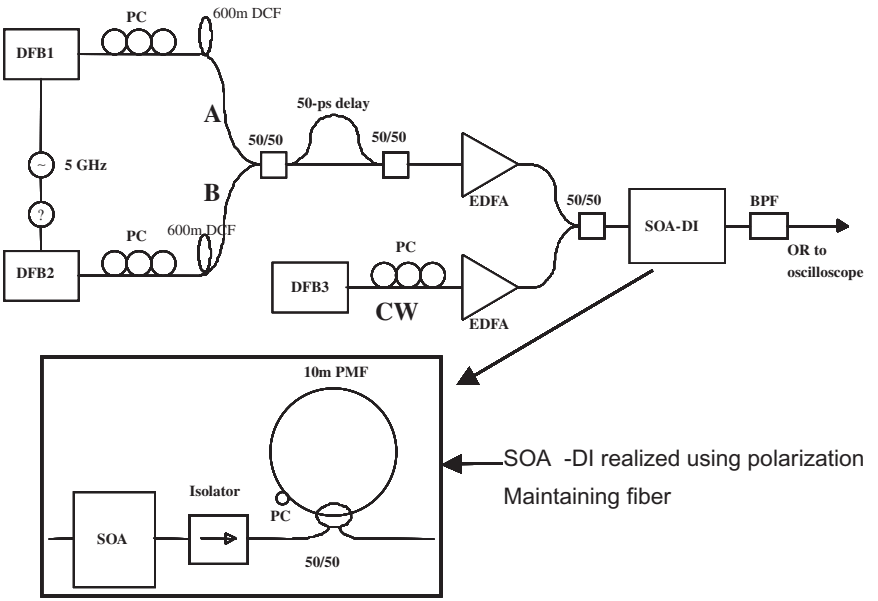

Fig. 9.3.2. Experimental setup for the OR function demonstration, PC: Polarization Controller, DFB: Distributed-Feedback Laser, BPF: Bandpass Filter, DCF: Dispersion Compressing Fiber, PMF: Polarization Maintaining Fiber. DFB1 and DFB2 provide the pulsed sources A and B and DFB3 provide the CW source [61].

component. The polarization maintaining fiber has birefringence i.e. light polarized along two directions in the fiber (fast and slow axis) travel at slightly different speeds. The measured effective index difference for light polarized along the fast and slow axis is 8.3×10^{-4}. The input CW signal is polarized along either the fast or the slow axis of the polarization maintaining fiber in the loop. The in-loop polarization controller (which is near the coupler) is adjusted so that it rotates the polarization by 90°. Thus the clockwise component and the counter clockwise component of the light in the PML are polarized along the two optical axis of the polarization preserving fiber.

Since the optical path is birefringent, the phase difference between the pulses with polarization along the fast and slow axis will accumulate and will result in a differential phase delay of $k_0 \cdot \Delta n \cdot L$, where k_0 is the wave vector in the vacuum, Δn is the difference in index seen by the light propagating along the fast and slow axis, and, L is the fiber length in the PML. Each of the clockwise and counter clockwise components traverses the in-loop polarization controller once and arrive at the coupler with the same polarization where they interfere. Figure 9.3.3(a) shows the output of the PML. The transmission meets the minimum at wavelengths where the phase change is π. The wavelength of the CW source (obtained from a tunable single wavelength laser) is tuned to the minimum of the DI output (Fig. 9.3.3(a)) using a procedure which involves adjusting the wavelength and the polarization controllers iteratively. In the absence of a control pulse, there is no pulse emitted out of DI. If there is a control pulse injected into SOA, it saturates the gain of the SOA which modifies both the gain and phase of the CW signal propagating through the SOA. Thus the pulsed input introduces a time dependent phase shift to the CW signal (Fig. 9.3.3(b)). This signal enters the PML, splits into two signals, and travels in the clockwise and counterclockwise direction. The polarization controller (labeled PC in Fig. 9.3.2), is adjusted so that the clockwise signal travels along the fast axis and the counter clockwise signal travels along the slow axis. Thus the two signals arrive at the coupler at slightly different times due to the birefringence of the polarization maintaining

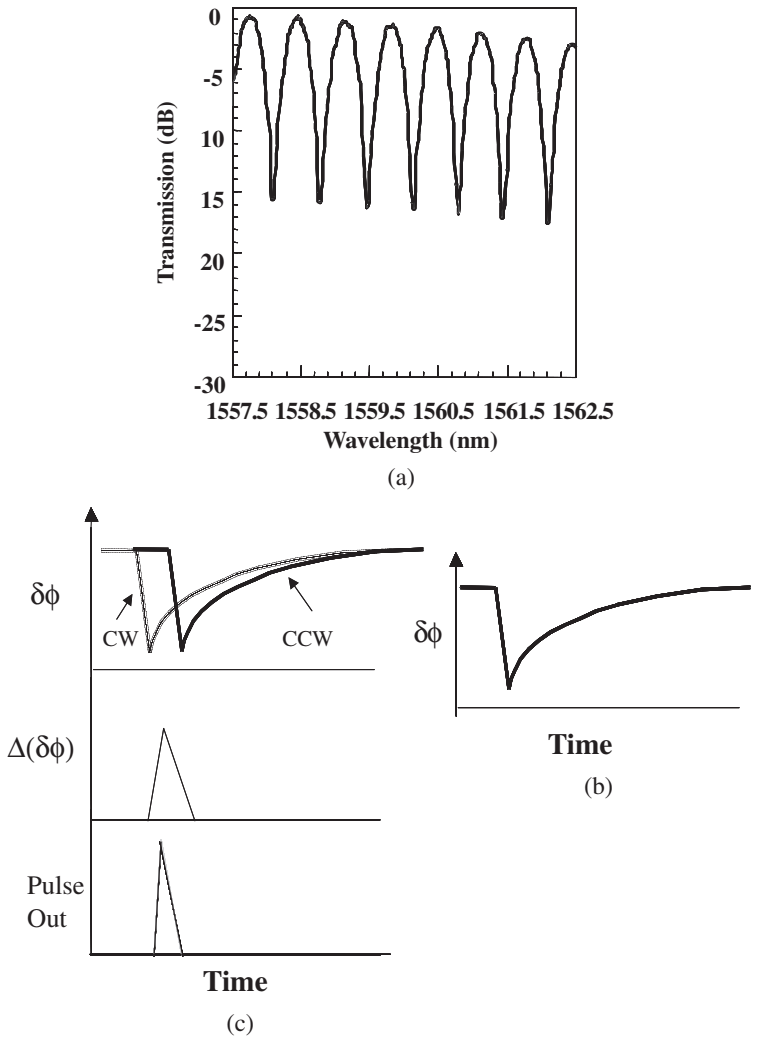

Fig. 9.3.3. (a) Transmission of DI as a function of wavelength. Illustration of the principle of operation: (b) $\delta\phi$ represents the time dependent change in phase of the CW light caused by the input pulse (A or B) in the SOA (c) Time dependent phases of the clockwise (CW-dashed) and counterclockwise (CCW-solid) signal as it arrives at the coupler after traveling through the loop (top Fig. 2(c)), a representation of the phase difference of the clockwise and counterclockwise signal ($\Delta(\delta\phi)$) as a function of time (middle Fig. 2(c)), representation of the pulse output (bottom Fig. 2(c)) [61].

fiber. Hence the two interfering signals at the coupler have slightly displaced time dependent phases (which were originally introduced by the input pulse at SOA). This is shown in top Fig. 9.3.3(c). The phase difference introduces a phase gate, $\Delta(\delta\phi)$ shown as a function of time in middle Fig. 9.3.3(c). The output power of the DI P is given by

$$P = 2\,I \sin^2(\Delta(\delta\phi)/2), \tag{9.3.1}$$

where I is the intensity of the clockwise or counterclockwise propagating signal which are assumed to the equal here.

The phase changes (on the CW signal) can be introduced by either pulsed input signals A or B. Hence there is an output when either A or B is present. The fiber loop acts as a phase gate. When both A and B are present, due to gain saturation, same phase shift is introduced as when either A or B is present, and hence an output of almost equal magnitude is expected.

9.3.2.1. *Experiment*

Figure 9.3.2 illustrates a typical experimental setup, pulse trains at 5 GHz repetition rate are obtained by gain switching two distributed feedback (DFB) lasers using a sinewave signal generator. The signal pulses are compressed to 7 ps by transmission through a 600 m dispersion compensating fiber (DCF). These pulsed sources could be mode locked lasers for higher speed operation. These pulses are multiplexed using traditional methods (delay and combine) to generate data patterns of 10001000 and 10101010 respectively.

Figure 9.3.4 presents the result obtained after DI output. Signal A is a data stream of 10001000, and signal B is a data stream of 10101010, the bottom trace shows the OR output.

9.3.2.2. *Simulation*

OR gate operation has been analyzed by a numerical solution of the SOA rate equations. As is shown in Fig. 9.3.2, the CW signal P_{in} is injected into the SOA-DI as the probe signal. The input signals A and signal B modulate the gain of the SOA and thereby the phase

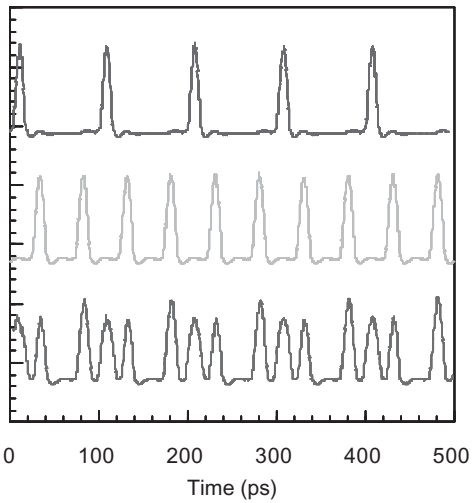

Fig. 9.3.4. Experimental result of SOA DI OR operation of 10001000 and 10101010. Date rate is 40 Gb/s. The observed pulse width is limited by the bandwidth of the signal analyzer [61].

of the probe signals. At the output end of the DI, the CW signals P_{in} traveling along the two axis of PML interfere.

The DI output intensity is described as:

$$P_{OR}(t) = \frac{1}{4}\{P_1(t) + P_2(t) - 2\sqrt{P_1(t)P_2(t)}\cos[\phi_1(t) - \phi_2(t) + \Delta\phi]\}, \tag{9.3.2}$$

where $P_{1,2}(t)$ are the power of clockwise component and counter clockwise component in DI, $\Delta\phi$ is the phase shift due to PML mirror, and $\phi_{1,2}(t)$ are time delayed phase shift in the two arms. The phase shift $\phi(t)$ is related to the gain $G(t)$ in SOA by the linewidth enhancement factor α. It is given by

$$\phi(t) = -\frac{\alpha}{2}\ln(G(t)). \tag{9.3.3}$$

The time dependent gain of the SOA satisfies the equation [61], see also in Ch. 8:

$$\frac{d\ln(G(t))}{dt} = \frac{\ln G_0 - \ln G(t)}{\tau_c} - \frac{P(t)}{E_{\text{sat}}}(G(t) - 1), \tag{9.3.4}$$

where τ_c is the carrier lifetime, G_0 is the unsaturated power gain and E_{sat} is the saturation energy of the SOA. $P(t)$ is the instantaneous input optical power inside the SOA and is given by

$$P(t) = P_A(t) + P_B(t) + P_{\text{CW}}. \tag{9.3.5}$$

The data stream pulses are assumed to be Gaussian pulses with FWHM pulse width of 1/8 bit period, e.g. $\tau_{\text{FWHM}} = T/8$. So,

$$P_{A,B}(t) = \sum_{n=-\infty}^{+\infty} a_{nA,B} \frac{2\sqrt{\ln 2} P_0}{\sqrt{\pi}\tau_{\text{FWHM}}} \exp\left(-\frac{4\ln 2(t-nT)^2}{\tau_{\text{FWHM}}^2}\right), \tag{9.3.6}$$

where P_0 is the energy of a single pulse, $a_{nA,B}$ represents n_{th} data in data stream A and B, $a_{nA,B} = 1$ or 0. To simulate the OR gate performance, we assume both input signals are of RZ pseudorandom bit sequence, and the SOA parameters are as follows: $E_{\text{sat},} = 30\,\text{mW}$, $G_0 = 30\,\text{dB}$. Figure 9.3.5 illustrates the OR operation using the above equations, signal A has (01100110) pattern, and signal B has (11001100) pattern, the bottom trace shows the result of OR operation at the output of DI. In the simulation, the input powers of the two signals are equal, and, the saturated gains

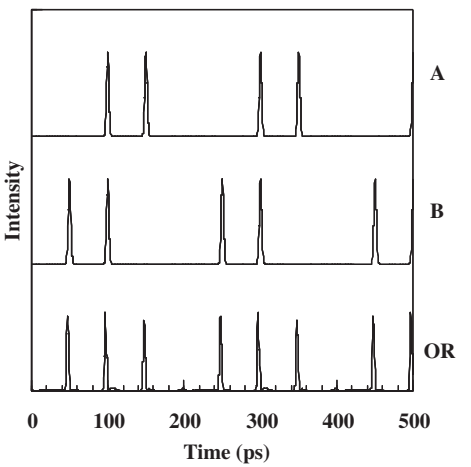

Fig. 9.3.5. Simulation of OR operation using SOA DI.

for the two wavelengths are assumed to be equal. In the experimental case, appropriate loss compensation can be used at the input so that the "1's" at the OR output are of equal magnitude. This is important for true OR operation.

To investigate the "quality" of OR operation by simulation, Q factor of the output signal has been calculated. Q factor gives the information of the optical signal to noise ratio in digital transmission. As before, Q is defined by,

$$Q = \frac{P_1 - P_0}{\sigma_1 + \sigma_0}, \tag{9.3.7}$$

where P_1 and P_0 are the average power of "1" and "0" signal respectively in the output OR data stream, while σ_1 and σ_0 are the standard deviation of 1's and 0's. Figure 9.3.6 represents the simulated eye diagram of OR output for random input data streams A and B.

Figure 9.3.6 shows with increasing carrier lifetime of SOA, the Q factor decreases. Under pseudorandom 20 Gb/s input signals, the simulated eye diagram of output data at a carrier lifetime of 100 ps is not as clean as that for 25 ps. Generally, for long carrier lifetimes, the pattern effect due to the carrier depletion of SOA can lead to pulse distortion, this would limit the pulse repetition rate in high speed logic operation. As discussed earlier, a holding pump beam (see Ch. 6) can be used to reduce the gain recovery time in the SOA and hence improve the high speed performance. Typical holding beam powers are in the 50 to 100 mW range and can be obtained using a semiconductor laser.

To get further information on OR gate performance, the Q-factor for different injected pulse energies has been calculated. With an increase in pulse energy, it's easier for SOA to get saturated, which results in a decrease in Q factor with increasing pulse energy. The linewidth enhancement factor (α-factor) depends on the relative position of the amplifier gain peak and the signal wavelengths and thus can vary depending on the wavelength used. The Q value is found to be larger for larger α because the phase changes are larger for large α and hence the OR signal ("1" values) is larger. This increases the signal to noise ratio and hence the Q-value.

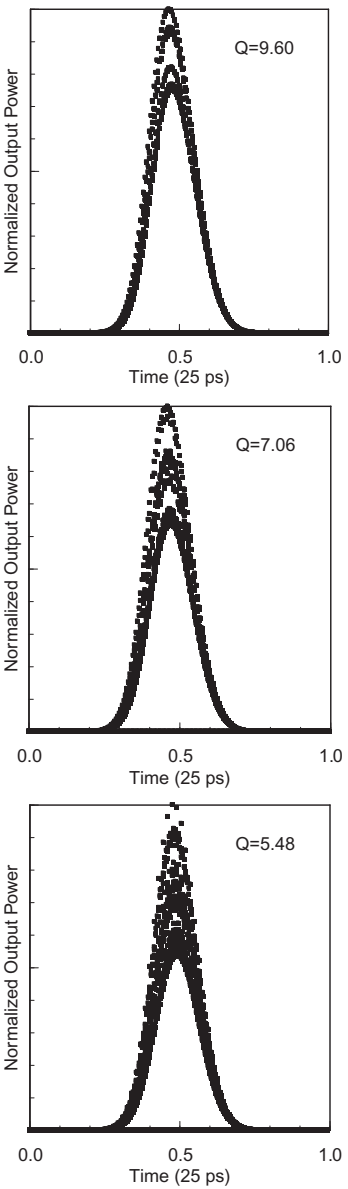

Fig. 9.3.6. The eye-diagrams of OR results for different carrier lifetimes. (Top) $\tau_c = 25\,\text{ps}$ (Middle) $\tau_c = 50\,\text{ps}$, (Bottom) $\tau_c = 100\,\text{ps}$. Note Q value decreases with increasing gain recovery time.

9.4. Optical Logic AND

All optical signal processing is important for future high-speed optical communication network to overcome the speed limitation set by electro-optic processing. All-optical AND gate employing four wave mixing inside SOA [65], and SOA-MZI has been demonstrated [66–68]. It is important that the gates should be stable, and compact. The truth table for AND operation is shown in Table 9.4.1.

9.4.1. *Optical logic AND gate using a SOA based Mach-Zehnder interferometer*

The AND gate is obtained using cross phase modulation of two input signals in the SOAs located in the two arms of a Mach-Zehnder interferometer (SOA-MZI) built using SOA's. The experimental set up is shown in Fig. 1. The signal A which participate in AND operation is injected at port 1 and a delayed version of A is injected at port 2. MZI is initially set so that there is no output if there is no differential phase change in the two arms for an input signal propagating through both arms.

Signal B (which also carry the result of the AND operation) is injected at port 3 of the SOA-MZI. When there is a signal A input "1", in one of the arms there is a phase shift induced on to the control signal and a delayed phase shift appears at the other arm. Thus signal A (if it is 1) produces a phase gate for signal B which travels through both arms and interfere at the output. Thus if B = 1 and A = 1, the output is "1". If A = 0 there is no phase gate and hence the output is "0" for both B = 0 and B = 1, and if A = 1 B = 0, the output is "0". This is the logic function AND.

Table 9.4.1. The truth table of AND.

Data B	Data A	Output AND
0	0	0
1	0	0
0	1	0
1	1	1

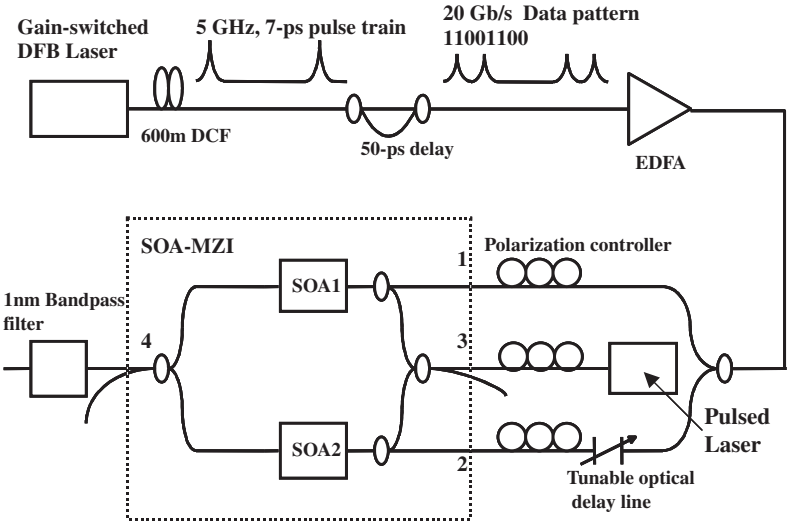

Fig. 9.4.1. Experimental setup for demonstration all-optical AND logic in SOA-MZI.

9.4.1.1. *Experiment*

Pulses at 20 GHz repetition rate and of 7 ps duration are generated by gain switching a distributed feedback (DFB) laser followed by pulse compression using a high dispersion fiber. They could also be generated by mode locked lasers. The 40 Gb/s data pattern of "1100" is generated by demultiplexing the gain switched pulses using a 50:50 coupler and a delay of 25-ps for one pulse train followed by multiplexing. The laser wavelength is 1559 nm. As shown in Fig. 9.4.1, 40 Gb/s data pattern of "1100" is split into two data streams, and one (data stream A) was injected into the control input 1 of the SOA-MZI, and the other (data A delayed by 25 ps) was injected into the control input 2 of the SOA-MZI. The average powers of both data streams are amplified to 10 dBm with erbium doped fiber amplifiers (EDFA). Another set of pulses at 20 GHz repetition rate and of 7 ps duration are generated by gain switching a DFB laser (operating at 1554 nm) followed by pulse compression using a high dispersion fiber. The 40 Gb/s data pattern of "1010" is generated by demultiplexing the gain switched pulses using a 50:50 coupler and a delay of 50-ps for

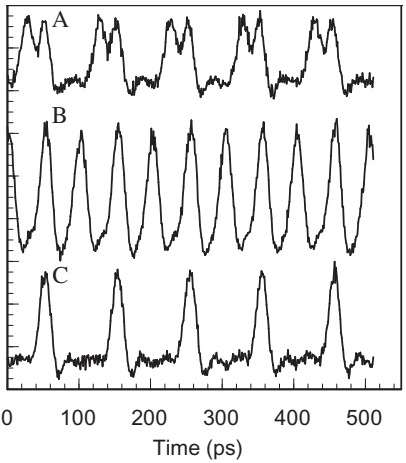

Fig. 9.4.2. This figure shows the results of the all-optical AND logical gate operation. A indicates the control pulse "11001100 . . . ", B is the input pulse "01010101 . . . ". The final AND "01000100 . . . ." result is clearly seen in C.

one pulse train followed by multiplexing. This series of pulses are also amplified to 10 dBm (average power) before being sent into the SOA-MZI port 3. After cross-phase modulation in the SOA, the output signal at 1554 nm is coupled out of SOA-MZI, where a filter selects the 1554 nm signal before it is measured using a 30 GHz sampling oscilloscope. Results are shown in Fig. 9.4.2.

9.4.1.2. *Simulation*

As shown in Fig. 9.4.1, the input pulse "10101010 . . . " P_{in} is introduced into the SOA-MZI and it propagates through both arms and interferes at the output. Signals A and B are injected as discussed earlier and propagate through the SOA's in the two arms of the MZI. In the SOA, the A and delayed A signals modulate the gain of the SOAs, creating a phase gate, and thereby varying the phase of the co-propagating P_{in} signal B. At the output of the SOA-MZI, the P_{in} signal from the two arms of the SOA-MZI interferes. The AND output intensity is calculated using the procedure for SOA operation described earlier.

As shown in Fig. 1, the light P_{in} is divided and introduced via a 50:50 coupler into the two arms of the MZI. In the MZI, the control

signals are launched into the two SOAs where they modulate the gain of the SOAs and thereby the phase of the co-propagating CW signals. At the output of the MZI, the P_{in} light from the two arms interferes. The output intensity is given by the interferometer equations described earlier (Eq. (9.2.1)).

For a SOA based interferometer device, output pulse amplitude is decided by the maximum phase shift ϕ induced by the control pulse. Figure 9.2.7(b) shows the relations between phase shift in one arm of the SOA-MZI and single pulse energy P_0 for different repetition rate. From Fig. 9.2.7 it follows, the phase shift increases with increase in single pulse energy, and it decreases with increasing control pulse rate. Phase shift of π can be easily achieved when bit rate is low, e.g. single pulse energy $P_0 = 0.0025\, E_{\text{sat}}$ can induce a phase shift of π when bit period is same as carrier recovery time ($T = \tau_c$). In the high bit rate case, however, the phase shift becomes saturated with increasing P_0, e.g., when $T = 0.1\tau_c$, the phase shift becomes saturated when P_0 is larger than $0.01\, E_{\text{sat}}$.

A model calculation of AND operation using the above equation is shown in Fig. 9.4.3. The gain recovery time used in the calculation is 25 ps. An insight to the performance of the AND logic can be gained by displaying the superposition of 1's obtained in the AND

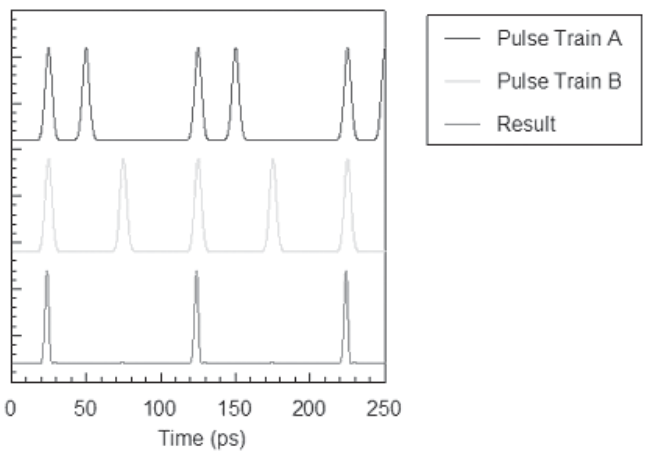

Fig. 9.4.3. Model calculation of AND operation for 40 Gb/s pulse train. The gain recovery time is 25 ps.

operation. These diagrams resemble the "classical" eye diagrams, but they are not as informative in the sense that degrading effects, normally observed in point-to-point communication links, such as noise sources added by the detector, optical fiber, etc. are absent. Nevertheless, these diagrams, which will be called "pseudo-eye-diagrams" (PEDS), are useful because, through isolation of the system effects, features of the operational principle of the analyzed device become evident. The quality factor Q has been calculated in the diagrams to simplify the interpretation of the results.

Figure 9.4.4 represents the simulated PEDS of the AND output for different carrier recovery times for 40 Gb/s for $2^7 - 1$ (127 bit) pseudo-random data. The parameters of the SOA are chosen as follows: $G_0 = 1000$ and $\alpha = 7$. From Fig. 9.4.4, it follows that when carrier recovery time increases from 25 ps to 100 ps, the Q-value of the pulse train decreases from 60 to 6.6. So the carrier recovery time of SOA will restrict the pulse repetition rate in the high speed optical logic systems.

9.5. Optical Logic INVERT

All-optical Inversion operation (Table 9.5.1 i.e. 1 to 0 and 0 to 1) is readily accomplished using a gain saturation scheme in a semiconductor optical amplifier.

Consider two signals injected into the amplifier, one is the signal carrying data at wavelength λ_1 and the second a CW probe signal at wavelength λ_2. When the data is in high state (1), the gain of the amplifier is saturated which reduces the gain on the probe at wavelength λ_2 and hence the output at λ_2 is reduced. When the data signal is low (0), the gain of the amplifier is not reduced and hence the gain on the probe at wavelength λ_2 is high and hence the output at λ_2 is high.

Thus the gain saturation phenomenon (also known as cross gain modulation (XGM)) leads naturally to an Invert operation. The process is also accompanied by cross phase modulation (XPM) i.e. the signal carrying data also modulates the phase of the co-propagating CW probe signal. The process is important in optical networks for conversion of data at one wavelength λ_1 to a second wavelength λ_2.

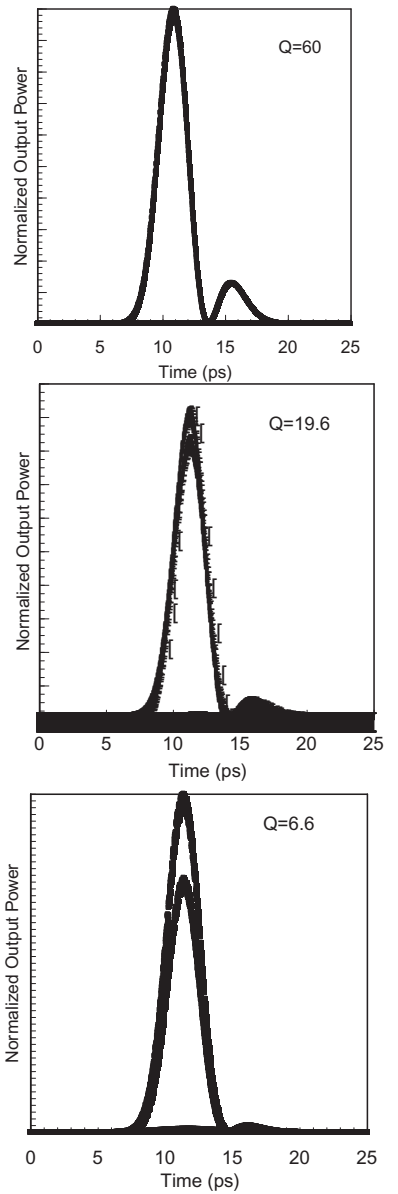

Fig. 9.4.4. The eye-diagrams of AND results for different carrier lifetimes. (Top) $\tau_c = 25\,\text{ps}$ (Middle) $\tau_c = 50\,\text{ps}$, (Bottom) $\tau_c = 100\,\text{ps}$. The data rate is $40\,\text{Gb/s}$.

Table 9.5.1. The truth table for invert operation.

A	Invert
1	0
0	1

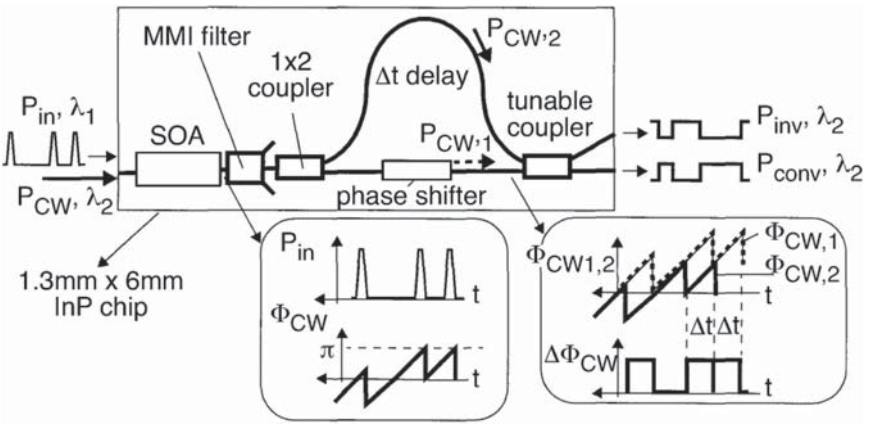

Fig. 9.5.1. Wavelength conversion (invert) operation using a SOA and delayed interferometer (DI) [71].

The speed of Invert operation based on gain saturation is limited by the gain recovery time of the SOA. Wavelength conversion with good signal quality at 40 Gb/s has been reported [69, 70]. Invert operation (or wavelength conversion) at 100 Gb/s has been reported using a SOA in conjunction with a delayed interferometer (DI) [71]. The schematic of the device along with the operating principle is shown in Fig. 9.5.1. The DI is a waveguide based device fabricated using Si/SiO_2 technology. The signal carrying the data along with the CW probe signal is injected into the SOA. The XPM phenomenon produces a time varying phase change on the probe signal, i.e. each optical pulse (1) from the data produces a phase change but the decay of this phase change takes place in a time generally larger than the bit period in the incoming data stream. This is shown in the insert of Fig. 9.5.1. The CW signal enters the DI , it is split into two signals of

equal intensity and propagates through the two arms of the DI before interfering at the output. One of the arms has an additional built in delay (Δt) relative to the other arm. Thus at the output there exists a relative phase difference between the two signals for a duration Δt during which time the signals interfere and produce an output. Thus the DI creates a "phase gate" which allows wavelength conversion at much higher speed. The speed here is determined by the magnitude of Δt and the signal to noise ratio needed for good signal quality. A low Δt would eventually lead to a very low signal to noise ratio.

For the experimental results shown in Fig. 9.5.2, the differential delay in the DI was 10 ps. Optical multiplexing was used to create to

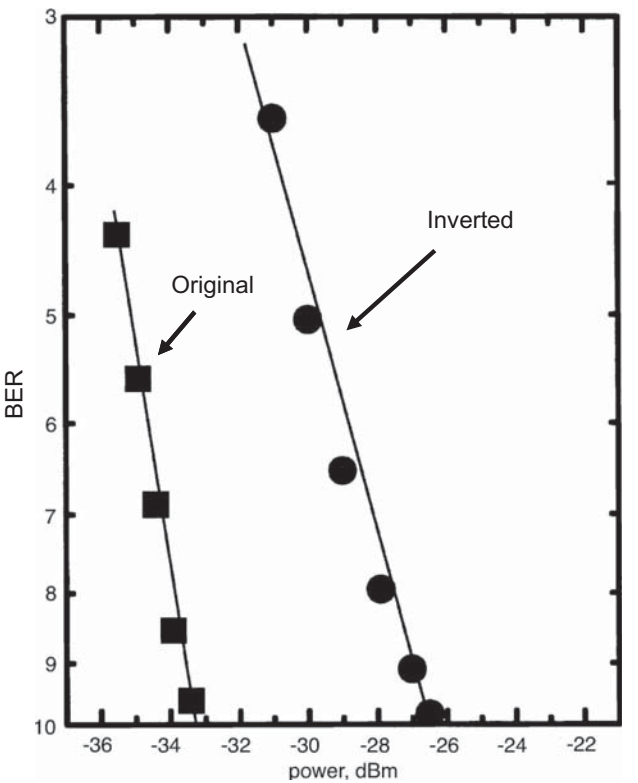

Fig. 9.5.2. Measured bit error rate for 100 Gb/s data for the wavelength converted (Invert) signal (solid circles) and that of the input signal (solid squares) [71].

100 Gb/s data. The data pulses were ∼3 ps wide. After wavelength conversion, the 100 Gb/s data at wavelength was demultiplexed to ten 10 Gb/s channels. The bit error rate measurement on these 10 Gb/s signal is shown in Fig. 9.5.2.

The Invert operation (or wavelength conversion) is important for a wide range of systems including parity generator, scrambling of bits and header generation and processing. The OR and Invert operation can be combined to obtain NOR gates from which a complete set of logic operations could be built. Logic circuits have been demonstrated using SOA based devices. The operating principle and performance of these circuits are described in Ch. 10.

9.6. Effect of Amplifier Noise

The analysis so far has not taken into account the effect of amplified spontaneous emission (ASE). In this section, the effect of high spontaneous emission factor N_{sp} on the quality factor (which determines error rate) of the output logic is examined [72]. As discussed, the device used for all-optical XOR, AND, NOR and NAND is a MZI each arm of which has a SOA. The primary noise in this calculation (which lowers the quality factor) in the absence of ASE noise is pattern effects resulting from long recovery times of gain and carrier induced phase change. The ASE causes additional output noise through spontaneous–spontaneous beat noise and signal-spontaneous beat noise. In addition if one were to measure the error rate of the logic output, the dark current of the photodiode, shot noise and thermal noise need to be considered. An analysis of all these noise terms is given in Ch. 6 when the SOA is used as a pre-amplifier. The ASE related noise depends on spontaneous emission factor N_{sp} of the amplifier.

As before, the operation of SOA-MZI can be studied using a rate equation model. The carrier heating results from a thermalization of carriers in the entire energy band following the pulse. This is a fast process occurring in time scale of ∼0.1 ps to 0.7 ps. The injected pulse reduces the gain at the photon energy of this pulse, i.e. in the gain spectrum it burns a hole. The process is known as spectral

hole burning. By taking into consideration both carrier heating and spectral hole-burning effects, the time-dependent gain for each SOA is given by [Ch. 6]:

$$\frac{dh(t)}{dt} = \frac{h_0 - h(t)}{\tau_C} - (\exp[h(t) + h_{\mathrm{CH}}(t) + h_{\mathrm{SHB}}(t)] - 1)S(t,0), \tag{9.6.1}$$

$$\frac{dh_{\mathrm{CH}}(t)}{dt} = -\frac{h_{\mathrm{CH}}(t)}{\tau_{\mathrm{CH}}} - \frac{\varepsilon_{\mathrm{CH}}}{\tau_{\mathrm{CH}}}(\exp[h(t) + h_{\mathrm{CH}}(t) + h_{\mathrm{SHB}}(t)] - 1)S(t,0), \tag{9.6.2}$$

$$\frac{dh_{\mathrm{SHB}}(t)}{dt} = -\frac{h_{\mathrm{SHB}}(t)}{\tau_{\mathrm{SHB}}} - \frac{\varepsilon_{\mathrm{SHB}}}{\tau_{\mathrm{SHB}}}(\exp[h(t) + h_{\mathrm{CH}}(t) + h_{\mathrm{SHB}}(t)] - 1)S(t,0) - \frac{dh(t)}{dt} - \frac{dh_{\mathrm{CH}}(t)}{dt}. \tag{9.6.3}$$

The gain G(t) is given by:

$$G(t,z) = \exp[h(t) + h_{\mathrm{CH}}(t) + h_{\mathrm{SHB}}(t)], \tag{9.6.4}$$

where $h(t)$ is a integral of optical gain per unit length over the length of the SOA and h_{total} equals the sum of h, h_{CH} and h_{SHB}. τ_c is the carrier lifetime and $G_0 = \exp[h_0]$ is the unsaturated power gain. $S(t,0)$ is the instantaneous input optical intensity inside the SOA and h, h_{CH}, h_{SHB} are the integrated gain (h-factor) values for carrier recombination, carrier heating and spectral hole burning related gain, respectively. τ_{CH} and τ_{SHB} are the carrier heating relaxation rate and the carrier-carrier scattering (spectral hole burning) rate, respectively. $\varepsilon_{\mathrm{CH}}$ and $\varepsilon_{\mathrm{SHB}}$ are the nonlinear gain suppression factors due to carrier heating and spectral hole burning, respectively. The carrier density induced phase change is given by:

$$\Phi(t) = -\frac{1}{2}[\alpha h(t) + \alpha_{\mathrm{CH}} h_{\mathrm{CH}}(t)], \tag{9.6.5}$$

where α is the traditional linewidth enhancement factor, α_{CH} is the carrier heating alpha factor and α_{SHB} is the spectral hole-burning alpha factor.

The data stream pulses are assumed to be Gaussian pulses, i.e.

$$P_{A,B}(t) = \sum_{n=-\infty}^{n=+\infty} a_{nA,B} \frac{2\sqrt{\ln(2)}P_0}{\sqrt{\pi}\tau_{\mathrm{FWHM}}} \exp\left(-\frac{4\ln(2)(t-nT)^2}{\tau_{\mathrm{FWHM}}^2}\right), \tag{9.6.6}$$

where $a_{nA,B}$ represents the nth data in data streams A and B which equals 1 or 0. P_0 is the input pulse energy and T is the bit period. τ_{FWHM} is the pulse width (full width at half maximum). The various Boolean logic operations are now examined using the ASE.

9.6.1. *XOR operation*

The modulated clock signal (probe) from the two arms of MZI interferes obeying the following formula:

$$P_{\mathrm{XOR}}(t) = \frac{P_C}{4}\{G_1(t) + G_2(t) - 2\sqrt{G_1(t)G_2(t)}\cos[\Phi_1(t) - \Phi_2(t)]\}. \tag{9.6.7}$$

P_{c} is the input probe power. For fast all-optical logic operations, the carrier lifetime τ_c must be small. Parameters used in this simulation are: $P_0 = 0.07\,\mathrm{pJ}$, $\tau_{\mathrm{FWHM}} = 2\,\mathrm{ps}$, $\tau_{\mathrm{c}} = 12\,\mathrm{ps}$, $\tau_{\mathrm{CH}} = 0.3\,\mathrm{ps}$, $\tau_{\mathrm{SHB}} = 0.1\,\mathrm{ps}$, $\varepsilon_{\mathrm{CH}} = \varepsilon_{\mathrm{SHB}} = 0.08\,\mathrm{ps}$, $\alpha = 4$, $\alpha_{\mathrm{CH}} = 1$, $\alpha_{\mathrm{SHB}} = 0$ and $P_{\mathrm{sat}} = 30\,\mathrm{mW}$. The instantaneous optical intensity inside each SOA for XOR gate is defined as:

$$P_1(t) = P_A(t) + P_C, \tag{9.6.8}$$

$$P_2(t) = P_C + P_B(t). \tag{9.6.9}$$

Figure 9.6.1(a) illustrates the simulation results of XOR gate operation with a pattern of signal A and a pattern of signal B. The bottom trace shows the XOR output after SOA-MZI. The eye diagram of a XOR bit for pseudo-random streams of A and B bits are shown in Fig. 9.6.2(b). The primary reason for noise in this calculation (which lowers the quality factor) in the absence of ASE noise are pattern

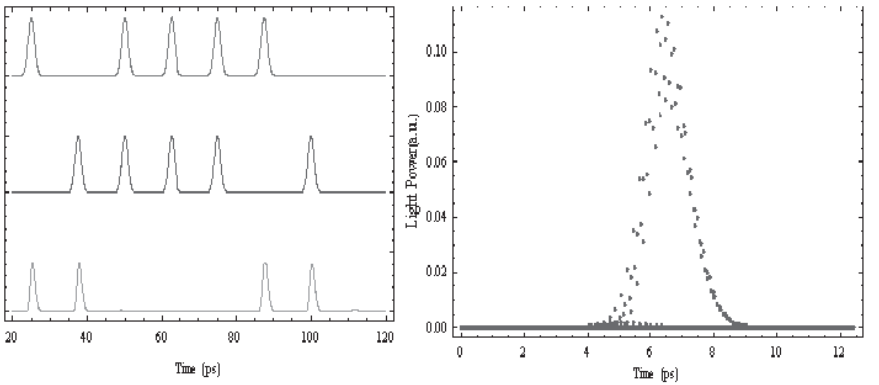

Fig. 9.6.1. (a) The simulated results of SOA-MZI for XOR output. Top two traces are the signals A and B, bottom trace is XOR and (b) The eye diagram for XOR [72].

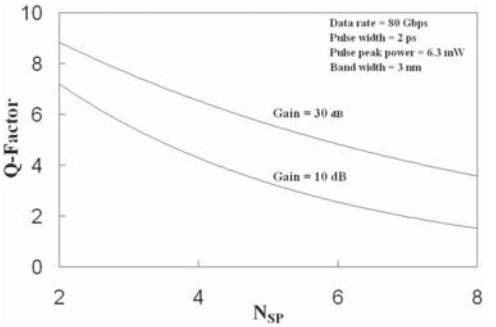

Fig. 9.6.2. Shows Q-factor versus N_{SP} for XOR operation [72].

effects resulting from long recovery times of gain and gain induced phase change. The ASE noise in this calculation is an average noise.

To investigate the "quality" of XOR operation by simulation, quality factor (Q-factor) of the XOR output signal has been calculated. Q-factor gives the information of the optical signal to noise ratio in digital transmission. Q-factor is given by $Q = (S_1 - S_0)/(\sigma_1 + \sigma_2)$, where S_1, S_0 are the average intensities of the expected "1"s and "0"s and σ_1, σ_2 are standard deviations of those intensities. Q-factor increases with decreasing the carrier life time and drops with

increasing the input pulse energy. We have investigated the effect of ASE power. The ASE power is related to N_{SP} by the relation:

$$P_{ASE} = N_{\mathrm{SP}}(G-1)h\upsilon B_0, \tag{9.6.10}$$

where G is the maximum gain, h is Plank's constant, υ is the frequency and B_0 is the band width. The ASE noise is added numerically using Eq. (9.6.10) on the pattern effect noise to obtain the Q-factor. The Q-factor versus N_{SP} for 80 Gb/s data using 10 dB and 30 dB gain for SOAs used for XOR operation is shown in Fig. 9.6.2. The data rate used in the modeling of all the logic functions in this section is 80 Gb/s.

9.6.2. *AND operation*

The AND gate operation has been analyzed by a numerical solution of the SOA rate equations stated earlier. The SOA parameters used in this simulation are the same as in XOR case. The effect of ASE on AND operation has been calculated in a same way as described in Sec. 9.6.1 for XOR. Figure 9.6.3(a) shows Q-factor versus N_{SP} at 10 dB and 30 dB gain of SOAs and 80 Gb/s data rate for AND operation. The time delay between A and its delayed version affects the performance of the AND gate. The calculated Q-factor as a function

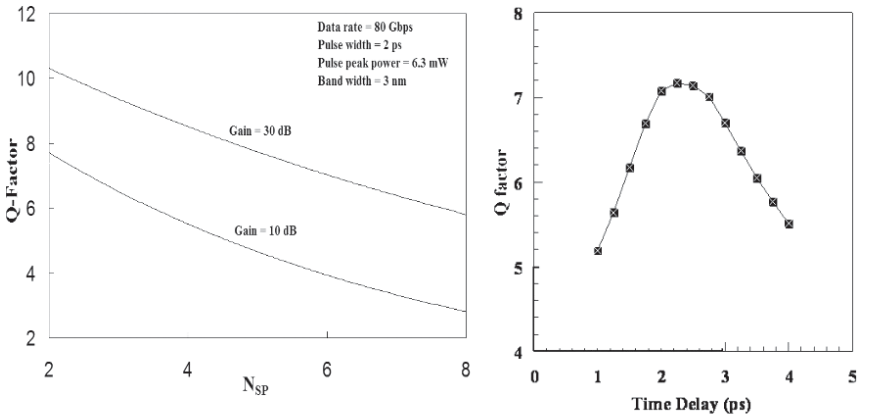

(a) (b)

Fig. 9.6.3. (a) Shows Q-factor versus N_{SP} for AND operation and (b) Calculated Q-factor as a function of time delay [72].

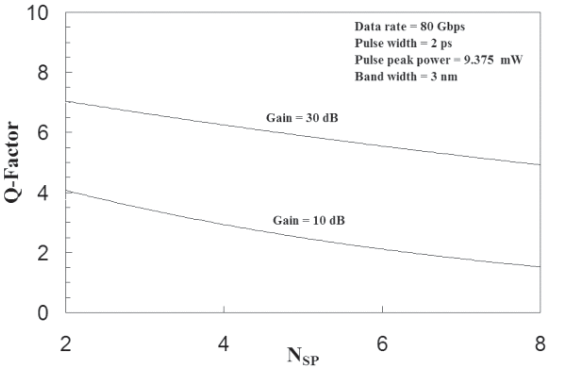

Fig. 9.6.4. Shows Q-factor versus N_{SP} for OR operation [72].

of delay is shown in Fig. 9.6.3(b). The optimum performance (high Q-factor) is achieved for a small range of delays.

9.6.3. *OR operation*

To simulate the OR gate performance with ASE, both input signals are assumed to be equal. The data stream pulses are assumed to be Gaussian pulses with FWHM pulse width as in Eq. (9.6.6). The Q-factor versus N_{SP} at 10 dB and 30 dB gain of SOAs and 80 Gb/s data rate for OR output is shown in Fig. 9.6.4.

9.6.4. *NAND operation*

NAND gate is important for logic operations because logic operations can be built using a combination of NAND gates. In this study, NAND is demonstrated by a series combination of AND and INVERT operations. AND operation has been described previously in Sec. 9.4. The INVERT operation is similar to XOR if one of the inputs is a clock signal. Thus the effect of ASE on NAND is both due to AND and INVERT operations. The Q-factor versus N_{SP} at 10 dB and 30 dB gain of SOAs and 80 Gb/s data rate for NAND output is shown in Fig. 9.6.5.

In this section modeling of all-optical logic gates, XOR, AND, OR, and NAND operations at 80 Gb/s using semiconductor optical

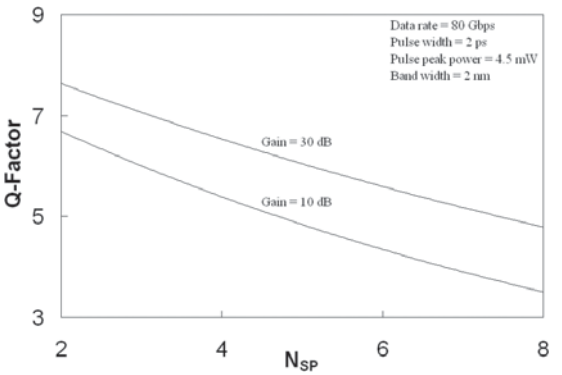

Fig. 9.6.5. Shows Q-factor versus N_{SP} for NAND operation [72].

amplifiers (SOA) has been described. The model takes into account the effect of amplified spontaneous emission (ASE). ASE is calculated as a function of the spontaneous emission factor N_{sp}. A decrease in quality factor is predicted for high N_{sp}. The effect of amplified spontaneous emission (ASE) can be experimentally verified by adding wideband (few nm wide) optical unmodulated signal to the data and measuring the Q-factor as a function of the intensity and bandwidth of this signal. ASE effects are important for cascaded logic operations.

9.7. Optical Logic Using PSK Signals

So far, optical logic using OOK (on-off-keying) signal is has been described. As discussed, the speed of SOA-based optical signal processing is limited by the penalties arising from the nonlinear patterning effects due to the non-instantaneous recovery dynamics of the cross-phase and cross-gain modulation. This results in a pattern effect i.e. the response to a bit depends on the prior sequence of bits. Kang *et al.* [73] has reported XOR using 80 Gb/s patterned OOK signals. The device used is a SOA based MZI as described in Sec. 9.2. The oscilloscope trace of data A and B and the XOR result is shown in Fig. 9.7.1.

An alternate method using a PSK (phase-shift-keying) based scheme has been demonstrated to reduce the pattern effect. The scheme utilizes a photonic-integrated SOA-MZI pair each

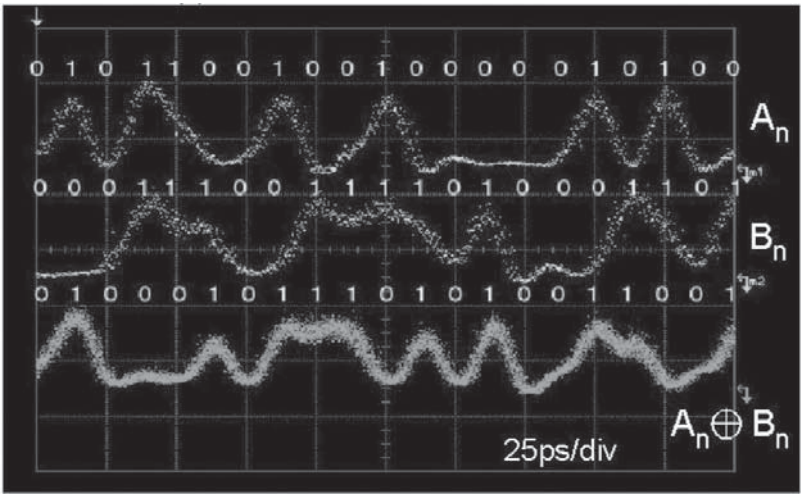

Fig. 9.7.1. Scope traces of data A and B and The XOR product [73].

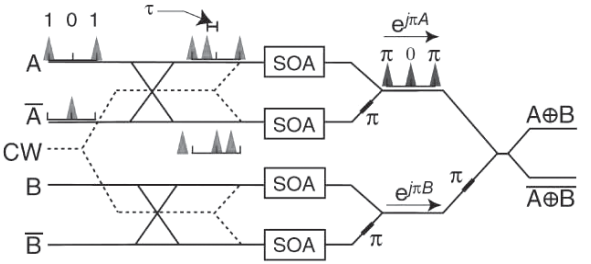

Fig. 9.7.2. Schematic of a all-optical XOR circuit. CW: continuous wave laser, t is the differential time delay [74].

differentially driven by a data input and its complement. The proposed circuit is shown in Fig. 9.7.2. It consists of a pair of semiconductor optical amplifier based Mach-Zhender interferometers (SOA-MZIs). Each SOA-MZI is differentially driven by data and its complement. Note that a single SOA-MZI can be used for all-optical XOR as described in Sec. 9.2. However, for the arrangement in Fig. 9.7.2 each SOA receives a nearly constant-power stream of input pulse train (relative to that for a single SOA-MZI XOR set up). Hence the pattern effect, that arise from the fluctuation in the optical signal

powers when SOAs are directly modulated by OOK signals without the differential set up, is reduced. The pattern effect is largest (in a OOK set up) for a single SOA-MZI, where the SOAs receive a long sequence of 1's followed by a long sequence of 0's, or vice versa.

The principle XOR operation as shown in Fig. 9.7.2 is as follows: the top SOA-MZI converts the input OOK data streams A and its complement A into a binary phase shift keyed (BPSK) signal, $\exp(j\pi \mathrm{A})$. The bottom SOA-MZI similarly outputs a BSPK signal $\exp(j\pi B)$. The conversion of OOK into BPSK was first used for all-optical wavelength conversion of DPSK signals [9, 15]. The next step in XOR operation is the linear optical interference between these two BPSK signals. The intensity envelopes of the output signals emerging from the constructive and destructive ports of the 2×2 coupler are calculated using:

$$\begin{aligned} &|\exp(j\pi A) + \exp(j\pi B)|^2 \sim \text{A NXOR B}, \\ &|\exp(j\pi A) - \exp(j\pi B)|^2 \sim \text{A XOR B}. \end{aligned} \tag{9.7.1}$$

Both AXORB and ANXORB are OOK signal outputs of the 2×2 couplers.

The circuit shown in Fig. 9.7.2 was implemented using hybrid photonic integrated circuit. The waveguides, attenuators, couplers, phase shifters, and, delay lines, were fabricated using Si/SiO_2 planar optical circuit technology. The SOAs are fabricated using InGaAsP/InP material system and are flip-chip bonded onto the Si based circuit. The various optical components are fabricated using 4% silica (index difference between the waveguide core and cladding layer is 4%) on Si planar lightguide circuit (PLC) technology. The photograph of a packaged device is shown in Fig. 9.7.3. The data signals are generated using a mode locked laser and an electro-absorption modulator (EAM). The complementary optical data is generated by a modulating a second EAM with complementary electronic data.

The input data A and B and traces of XOR and XNOR outputs is shown in Fig. 9.7.4. The data is at 86.4 Gb/s. Good eye diagrams for both XOR and XNOR are obtained [74].

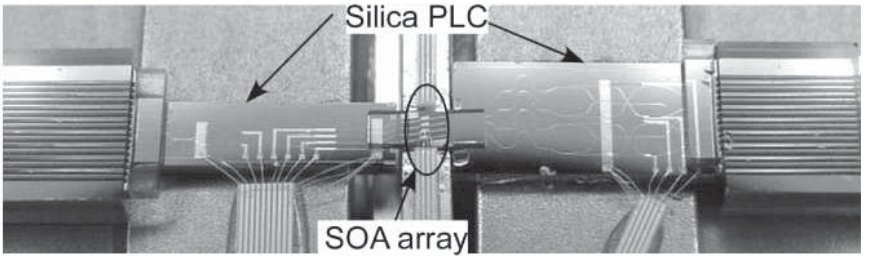

Fig. 9.7.3. Schematic of a packaged chip.

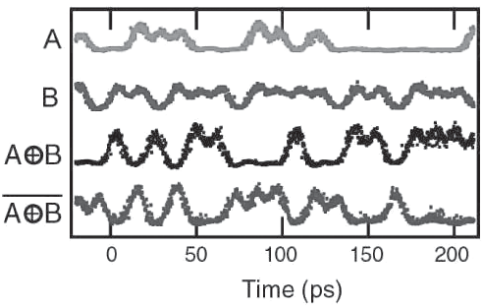

Fig. 9.7.4. Data A, data B and XOR and XNOR outputs [74].

As mentioned earlier, the performance of the high speed Boolean logic operations is limited by the gain and phase response speed of the SOA. SOA fabricated using quantum dot active region can have high speed response (Ch. 6). Thus Mach-Zehnder devices using quantum dot SOAs are likely to provide a higher speed operation compared to that for similar devices using regular SOAs.

References

[1] H. Sotobayashi and T. Ozeki, Ch. 2, in *WDM Technologies-Optical Networks*, eds. A. K. Dutta, N. K. Dutta and M. Fujiwara, Elsevier Science, 2004

[2] H. J. S. Dorren, X. Yang, A. K. Mishra, Z. Li, H. Ju, H. de-Waardt, G. D. Khoe, T. Simoyama, H. Ishikawa, H. Kawashima and T. Hasama, *IEEE J. Select. Topics Quantum Electron.* **10**, 1079 (2004).

[3] N. Elfaramawy and A. Awad, *Proc. ISCC 2004. Ninth International Symposium on Computers and Communications*, **1**, 270 (2004).

[4] K. Tajima, S. Nakamura, A. Furukawa and T. Sasaki, *IEICE Transactions on Electronics* **E87-C**, 1119 (2004).

[5] S. A. Hamilton and B. S. Robinson, *Proc. SPIE* **4871**, 27 (2002).
[6] A. D. McAulay, *Proc. SPIE* **4788**, 83 (2002).
[7] S. Lee, J. H. Kim, Y. I. Kim, Y. T. Byun, Y. M. Jhon, D. H. Woo and S. H. Kim, *J. Opt. Society Korea* **6**, 165 (2002).
[8] T. Fjelde, D. Wolfson, A. Kloch, M. L. Nielsen and H. Wessing, *Proc. SPIE* **4532**, 114 (2001).
[9] T. Yabu, M. Geshiro, T. Kitamura, K. Nishida and S. Sawa, *IEEE J. Quantum Electron.* **38**, 37 (2002).
[10] A. Bhardwaj, P. O. Hedekvist and K. Vahala, *J. Opt. Society America B* **18**, 657 (2001).
[11] K. E. Stubkjaer, *IEEE J. Select. Topics Quantum Electron.* **6**, 1428 (2000).
[12] L. A. Wang, S. H. Chang and Y. F. Lin, *Opt. Eng.* **37**, 1011 (1998).
[13] N. S. Patel, K. L. Hall and K. A. Rauschenbach, *Opt. Lett.* **21**, 1466 (1996).
[14] M. N. Islam, *AIP Conf. Proc.* **342**, 605 (1995).
[15] N. S. Patel, K. A. Rauschenbach and K. L. Hall, *OFC Technical Digest Series Post Conf.* **2**, 384 (1996).
[16] G. R. Williams, M. Vaziri, K. H. Ahn, B. C. Barnett, M. N. Islam, K. O. Hill and B. Malo, *Opt. Lett.* 20, 1671 (1995).
[17] S. M. Zakharov and V. A. Goryachev, *Laser Phys.* **4**, 1 (1994).
[18] O. G. Ivanov, V. Y. Rakovsky and A. S. Shcherbakov, *Proc. SPIE* **1807**, 224 (1993).
[19] S. M. Zakharov, *Laser Phys.* **2**, 872 (1992).
[20] M. Saruwatari, K. Mori and T. Morioka, *IOOC ECOC 17th European Conf. Opt. Commun.* **1**, 177 (1991).
[21] J. M. Jeong and M. E. Marhic, *Opt. Commun.* **85**, 430 (1991).
[22] D. Richardson, H. M. Gibbs and S. W. Koch, *IEEE J. Quantum Electron.* **27**, 804 (1991).
[23] T. Morioka, M. Saruwatari and K. Nakagawa, *GLOBECOM 90 IEEE Global Telecommunications Conf.* **2**, 1311 (1990).
[24] M. Jinno and T. Matsumoto, *Opt. Lett.* **16**, 220 (1991).
[25] C. N. Ironside, M. O'Neill, N. Finlayson, E. M. Wright, W. Banyai, C. T. Seaton and G. T. Stegeman, *IEE Colloquium on 'Non-Linear-Optical-Waveguides' Digest No. 88*, **15**, 1 (1988).
[26] R. Normandin, *Canadian J. Phys.* **65**, 913 (1987).
[27] R. Normandin, *Opt. Lett.* **11**, 751 (1986).
[28] H. A. Haus and N. A. Jr. Whitaker, *Proc. SPIE* **517**, 226 (1985).
[29] A. Lattes, H. A. Haus, F. J. Leonberger and E. P. Ippen, *IEEE J. Quantum Electron.* **QE-19**, 1718 (1983).
[30] K. L. Hall and K. A. Rauschenbach, *Electron. Lett.* **32**, 1214 (1996).
[31] A. J. Poustie, K. J. Blow, R. J. Manning and A. E. Kelly, *Opt. Commun.* **159**, 208 (1999).
[32] T. Fjelde, A. Kloch, D. Wolfson, B. Dagens, A. Coquelin, I. Guillemot, F. Gaborit, F. Poingt and M. Renaud, *IEEE Photon. Technol. Lett.* **13**, 750 (2001).
[33] N. S. Patel, K. L. Hall and K. A. Rauschenbach, *Appl. Opt.* **37**, 2831 (1998).
[34] M. Jinno and T. Matsumoto, *Opt. Lett.* **16**, 220 (1991).

[35] T. Houbavlis, K. Zoiros, A. Hatziefremidis, H. Avramopoulos, L. Occhi, G. Guekos, S. Hansmann, H. Burkhard and R. Dall'Ara, *Electron. Lett.* **35**, 1650 (1999).
[36] C. Bintjas, M. Kalyvas, G. Theophilopoulos, T. Stathopoulos, H. Avramopoulos, L. Occhi, L. Schares, G. Guekos, S. Hansmann and R. Dall'Ara, *IEEE Photon. Technol. Lett.* **12**, 834 (2000).
[37] T. Fjelde, D. Wolfson, A. Kloch, B. Dagens, A. Coquelin, I. Guillemot, F. Gaborit, F. Poingt and M. Renaud, *Electron. Lett.* **36**, 1863 (2000).
[38] H. J. S. Dorren, G. D. Khoe and D. Lenstra, *Opt. Commun.* **205**, 247 (2002).
[39] I. Kang, C. Dorrer and J. Leuthold, *Electron. Lett.* **40**, 496 (2004).
[40] K. Chan, C. K. Chan, L. K. Chen and F. Tong, *IEEE Photon. Technol. Lett.* **16**, 897 (2004).
[41] H. Soto, D. Erasme and G. Guekos, *IEEE Photon. Technol. Lett.* **13**, 335 (2001).
[42] T. Houbavlis, K. Zoiros, K. Vlachos, T. Papakyriakopoulos, H. Avramopoulos, F. Girardin, G. Guekos, R. Dall'Ara, S. Hansmann and H. Burkhard, *IEEE Photon. Technol. Lett.* **11**, 334 (1999).
[43] J. P. Sokoloff, I. Glesk, P. R. Prucnal and R. K. Boncek, *IEEE Photon. Technol. Lett.* **6**, 98 (1994).
[44] A. J. Poustie, K. J. Blow, R. J. Manning and A. E. Kelly, *Opt. Commun.* **159**, 208 (1999).
[45] M. Jinno and T. Matsumoto, *Opt. Lett.* **16**, 220 (1991).
[46] K. L. Hall and K. A. Rauschenbach, *Electron. Lett.* **32**, 114 (1996).
[47] K. L. Hall and K. A. Rauschenbach, *Opt. Lett.* **23**, 1271 (1996).
[48] C. Bintjas, M. Kalyvas, G. Theophilopoulos, T. Stathopoulos, H. Avramopoulos, L. Occhi, L. Schares, G. Guekos, S. Hansmann and R. Dall'Ara, *IEEE Photon. Technol. Lett.* **12**, 834 (2000).
[49] K. Tajima, S. Nakamura and Y. Ueno, *Opt. Quantum Electron.* **33**, 875 (2001).
[50] H. Chen, G. Zhu, Q. Wang, J. Jaques, J. Leuthold, A. B. Piccirilli and N. K. Dutta, *Electron. Lett.* **38**, 1271 (2002).
[51] Q. Wang, G. Zhu, H. Dong, J. Jaques, J. Leuthold, A. B. Piccirilli and N. K. Dutta, *IEEE J. Quantum Electron.* **40**, 703 (2004).
[52] R. J. Manning and G. Sherlock, *Electron. Lett.* **31**, 307 (1995).
[53] R. J. Manning, D. A. O. Davies, D. Cotter and J. K. Lucek, *Electron. Lett.* **30**, 787 (1994).
[54] J. Pleumeekers, M. Kauer, K. Dreyer, C. Burrus, A. G. Dentai, S. Shunk, J. Leuthold and C. H. Joyner, *IEEE Photon. Technol. Lett.* **14**, 12 (2002).
[55] G. P. Agrawal and N. A. Olsson, *IEEE J. Quantum Electron.* **25**, 2297 (1989).
[56] R. Gutierrez-Castrejon, L. Occhi, L. Schares and G. Guekos, *Opt. Commun.* **195**, 167 (2001).
[57] G. P. Agrawal, *Fiber Optic Communication Systems*, Chapter 4 (John Wiley, 1997).
[58] A. Hamie, A. Sharaiha and M. I. Guegan, *Microwave and Optical Tech. Lett.* **39**, 1 (2003).
[59] A. D. McAulay, *Proc. SPIE* **4788**, 83 (2002).

[60] A. Sharaiha, H. W. Li, F. Marchese and J. LeBihan, *Electron. Lett.* **33**, 323 (1997).
[61] H. Dong, Q. Wang, G. Zhu, J. Jaques, A. B. Piccirilli and N. K. Dutta, *Opt. Commun.* **242**, 479 (2004).
[62] T. Fjelde, D. Wolfson, A. Kloch, C. Janz, A. Coquelin, I. Guillemot, F. Gaborit, F. Poingt, B. Dagens and M. Renaud, *Electron. Lett.* **36**, 813 (2000).
[63] L. Y. Chan, K. K. Qureshi, P. K. A. Wai, B. Moses, L. F. K. Lui, H. Y. Tam and M. S. Demokan, *IEEE Photon. Technol. Lett.* **15**, 593 (2003).
[64] A. Hamie, A. Sharaiha, M. Guegan and B. Pucel, *IEEE Photon. Technol. Lett.* **14**, 1439 (2002); A. Hamie, A. Sharaiha, M. Guegan, B. Pucel and J. Le-Bihan, *Proc. SPIE* **4989**, 123 (2003).
[65] D. Nesset, M. C. Tatham and D. Cotter, *Electron. Lett.* **31**, 896 (1996).
[66] B. K. Kang, J. H. Kim, Y. H. Park, S. Lee, Y. M. Jhon, D. H. Woo, S. H. Kim and S. H. Park, *LEOS Proc. 13th Ann. Meeting* **1**, 117 (2000).
[67] E. S. Awad, P. Cho and J. Goldhar, *IEEE Phonton. Tech. Lett.* **13**, 472 (2001).
[68] B. E. Olsson and P. A. Andrekson, *OFC Tech. Digest* **2**, 375 (1998).
[69] B. Mikkelsen, K. S. Jepsen, M. Vaa, H. N. Poulsen, K. E. Stubkjaer, R. Hess, M. Duelk, W. Vogt, E. Gamper, E. Gini, P. A. Besse, H. Melchior, S. Bouchoule and F. Devaux, *Electron. Lett.* **33**, 2137 (1997).
[70] J. Leuthold, C. H. Joyner, B. Mikkelsen, G. Raybon, J. L. Pleumeekers, B. I. Miller K. Dreyer and C. A. Burrus, *Proc. Opt. Fiber Comm. Conf. (OFC), Washington DC*, **4**, 218 (2000).
[71] J. Leuthold, C. H. Joyner, B. Mikkelsen, G. Raybon, J. L. Pleumeekers, B. I. Miller, K. Dreyer and C. A. Burrus, *Electron. Lett.* **36**, 1129 (2000).
[72] A. Kotb, S. Ma, Z. Chen. N. K. Dutta and G. Said, *Optics Communication* **284**, 5798 (2011).
[73] I. Kang, C. Dorrer, L. Zhang, M. Dinu, M. Rasras, L. L. Buhl, S. Cabot, A. Bharadwaj, X. Liu, M. A. Cappuzzo, L. Gomez, A. Wong-Foy, Y. F. Chen, N. K. Dutta, S. Patel, D. Neilson, C. R. Jiles, A. Piccirilli and J. Jaques, *IEEE J. Select. Topic in Quantum Electronics* **14**, 758 (2008).
[74] I. Kang, M. Rasras, L. Buhl, M. Dinu, S. Cabot, M. Cappuzzo, L. T. Gomez, Y. F. Chen, S. S. Patel, N. Dutta, A. Piccirilli and J. Jaques, *C. R. Giles Optics Express* **17**, 19062 (2009).

Chapter 10

Optical Logic Circuits

10.1. Introduction

All-optical Boolean logic operations such as XOR, OR, AND and INVERT are important for various high speed all-optical signal processing applications. In particular all-optical XOR and all-optical AND gates are fundamental in the implementation of various all-optical systems such as packet switches, binary adders, binary counters, decision circuits, optical processor, data encoder and bit-pattern recognition circuits. These circuits are important for optical communication networks. In this chapter the demonstration and higher speed implementation of several of these operations are described.

10.2. Adder

Binary addition is an important function in all-optical logic circuits. The ADDER function can in general be separated into half-adder [1–5] and full-adder [6] operations. The half-adder operation is easier to carry out and in general involves a demonstration of a "CARRY" bit and a " SUM" bit function. These bits are then routed through a similar operation with suitable delay to carry out a full-adder function.

The half adder is a combinational logic function of simple addition of two binary digits. The truth table is shown in Table 10.1.1. Logic CARRY is logic "1" when both inputs are "1". Otherwise, it is logic "0". Logic SUM represents the least significant bit of the two

Table 10.1.1. Truth table of half adder.

A	B	SUM	CARRY
0	0	0	0
0	1	1	0
1	0	1	0
1	1	0	1

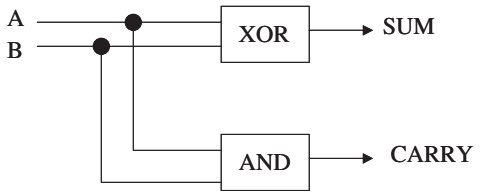

Fig. 10.2.1. Basic structure of half adder [4].

bit binary summation. The binary functions of SUM and CARRY are similar to that carried out by XOR and AND operations.

The all-optical half adder experimental results are demonstrated in Fig. 10.2.2. The circuit used in the demonstration is similar to that shown in Fig. 10.2.1. The all-optical half adder function has been shown to operate at speeds of 10 Gb/s [4,5]. Half adder can be constructed using SOA-MZI. As shown in Ch. 9 the SOA-MZI can perform the XOR and AND functions and hence they can perform the SUM and CARRY operation.

A full adder requires three inputs: the two bits to be currently added and the CARRY bit from the previous bit ADDITION. This is achieved as follows [3]: First an all-optical XOR gate is used to generate the ADDITION (SUM) and all-optical AND gate is used to generate the CARRY bits. The CARRY memory is coupled to the ADDITION memory and the capacities of the two memories are delayed by a single bit. In this way, the CARRY bits are cycled back into the ADDITION with an appropriate shift in significant position on each circulation around the memory. A carry-ripple process takes place on each memory circulation until the correct binary ADDITION of the two input words is achieved. When this is completed,

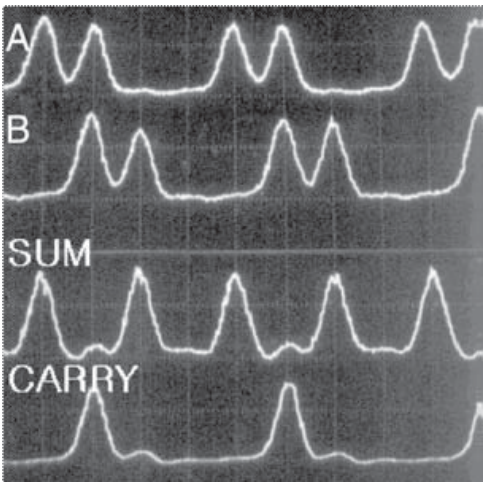

Fig. 10.2.2. Experimental results of all-optical half adder: Input signal A, input signal B, output signal: logic SUM, output signal: logic CARRY at 10 Gb/s [4].

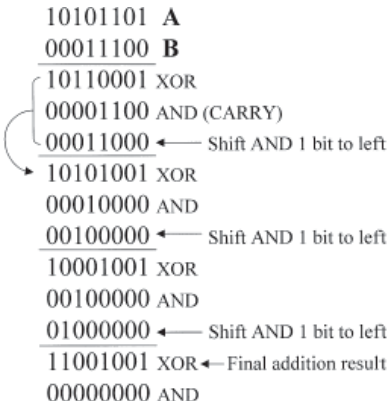

Fig. 10.2.3. Theoretical bit-differential addition of the two 8-bit binary words A: 10101101 and B: 00011100 [6].

the CARRY memory resets to all ZEROS and a further word addition can be initiated. This bit differential delay technique allows the full adder function to be performed entirely optically. Figure 10.2.3 shows the addition of two bit binary words using bit differential delay.

The schematic of a full-adder operation with bit shifting circuit with a bit delay is shown in Fig. 10.2.4.

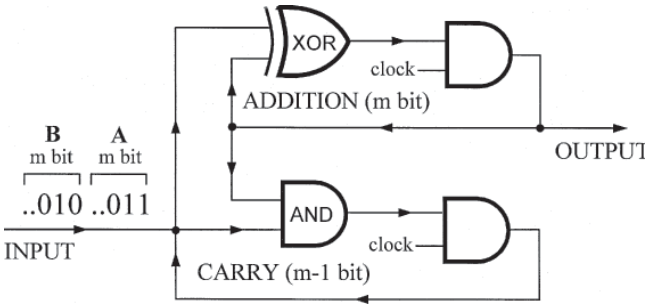

Fig. 10.2.4. Schematic circuit of a full-adder [6].

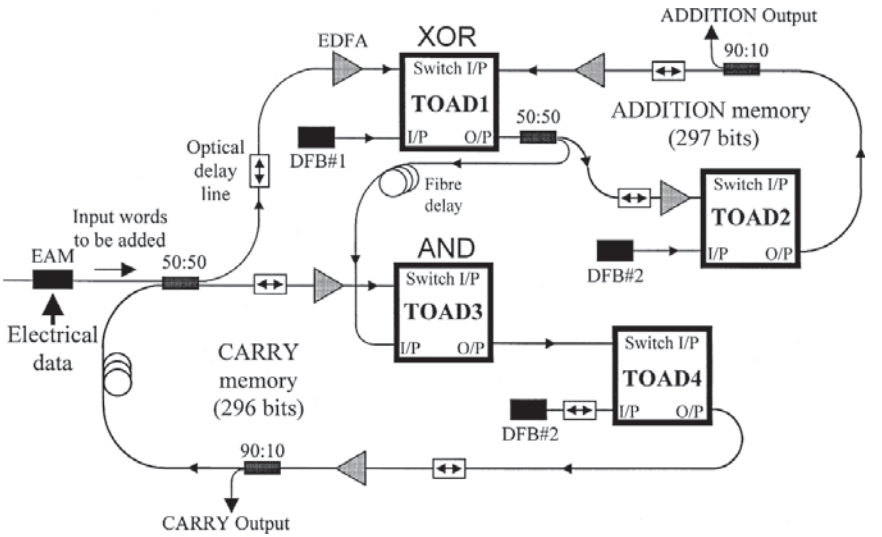

Fig. 10.2.5. Experimental set up used to demonstrate all-optical adder [6].

The above circuit was built using TOAD type devices (see Ch. 9). The TOAD was used in a form so as to perform the XOR and AND function. A fiber delay line is used for the bit-delay (Fig. 10.2.5).

The experimental results are demonstrated in Fig. 10.2.6. For higher speed operation, it is desirable to have integrated versions of the SOA based switching gates. This will allow incorporation of specific delays in the circuit. Such temporal delays would be

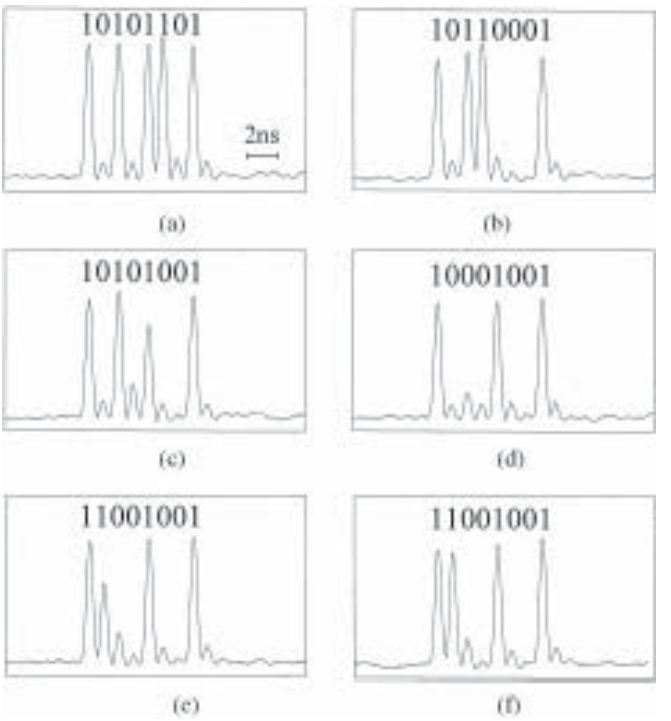

Fig. 10.2.6. (a)–(f) Experimentally measured output from the ADDITION memory after 1->6 memory circulations, respectively. The expected binary sequence is shown at the top of each figure [6].

stable. Using SOA-MZI and using InP materials many laboratories are pursuing higher speed optical adder operation.

10.3. Parity Checker

During the transmission of optical pulse trains from one point to another, noise or other disturbances can cause distortions in the digital signal. Thus it is important to have a scheme which can identify the presence of possible errors.

Parity checker is a method that adds a parity bit to the end of each word or byte. At the receiving end, the system will check if the received parity bit agrees with the parity of the received word. For example, if the input signals are "1011", there are three "1"s and

it is an odd number. The parity of this word is odd. A parity bit is added to the end of this 4-bit word during transmission. A parity bit is generated from the received word at the receiver and compared with the received parity bit. If the received parity bit is "1" or odd, then the transmitted signal "1011" is assumed to have no error, if the parity is "0" or even, then there must be error in the transmission. This method is widely used in signal transmission system.

In all-optical communication system, the parity generator is an optical circuit that produces the parity bit. It can be constructed using optical XOR gates. The XOR operation is very similar to a "parity generation" operation of two bits. Thus a sequence of XOR gates which produces XOR outputs successively can be used to generate the parity of a word. The schematic set up of 4-bit even and odd parity generators are shown in Fig. 10.3.1. The successive four bits of a 4-bit word undergoes XOR operation, the output of these two XOR gates undergoes further XOR operation to generate the even parity bit. Since the XOR operation occurs simultaneously on all bits of the 4-bit word, the process is often called a parallel scheme. For odd parity generator, a NOT gate "Invert operation" is needed before the output. A similar scheme works for parity generation from a 8-bit word. In this case, the successive 8 bits undergo XOR operation using four XOR gates. The outputs go to two XOR gates followed by a final XOR. This is shown in Fig. 10.3.2

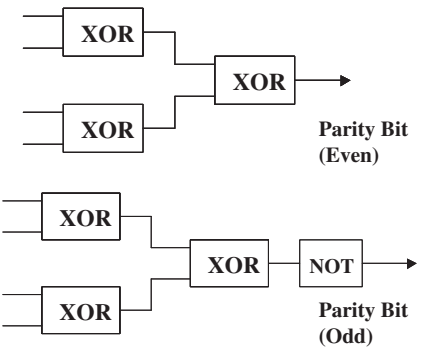

Fig. 10.3.1. Schematic of a even parity generator for a 4-bit word (Top). The odd parity generator has a NOT (INVET) function to the output.

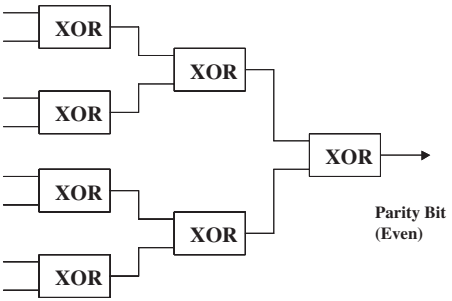

Fig. 10.3.2. Schematic of 8-bit even parity generator.

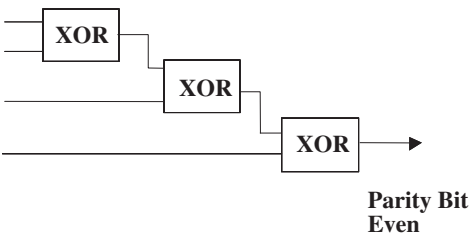

Fig. 10.3.3. Serial scheme for even parity generation from a 4-bit word.

Although the parallel scheme for parity checker is important for actual systems, for demonstration purposes a serial scheme whereby the XOR operation is carrier out serially is useful. A serial scheme for parity generator is shown in Fig. 10.3.3.

In this scheme the XOR of the first two bits undergoes an XOR operation with the next and so on. In principle, the same XOR gate can be used to generate the parity bit by cycling the word through the same XOR gate delayed by one bit each time it cycles through. This scheme is often used in laboratory experiments.

At the receiving end, the parity checker determines if the parity of the signal agrees with the parity bit. Parity checkers are constructed using several XOR operations. The parity checker has two elements (i) generation of a parity bit from the received word and (ii) comparison of the generated parity bit with the received parity bit. The parity checker for a 8-bit word is shown in Fig. 10.3.4(a). The parity generator is similar to that of Fig. 10.3.2. The output of

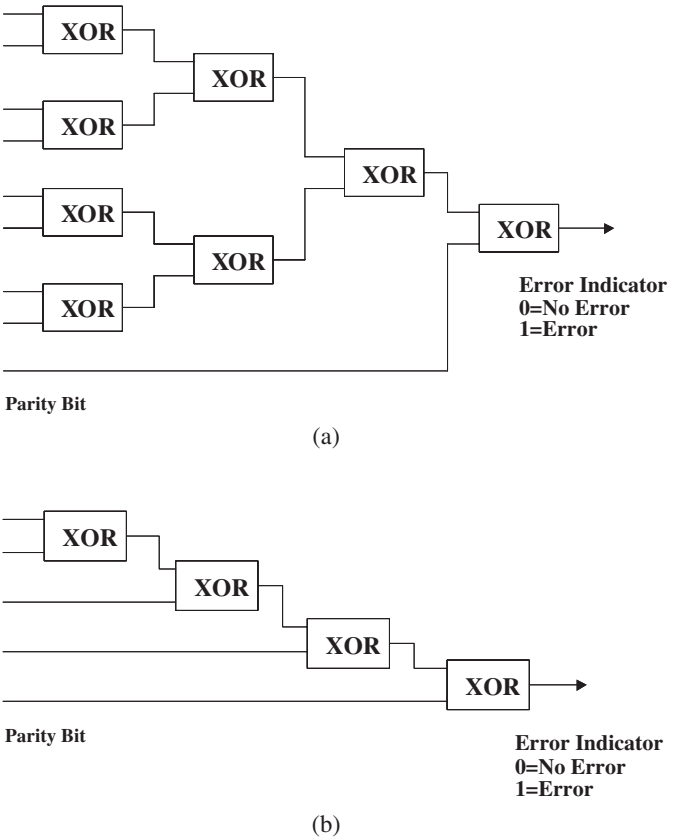

Fig. 10.3.4. Schematic of (a) 8-bit even parity checker (b) 4-bit parity checker.

the parity generator and the received parity bit is compared with a XOR gate. If the parity of the word or byte is the same as the parity bit, the result is "0", no error (assuming the possibility of two or more errors occurring at the same time is very small). The result "1" indicates that there must be error during the transmission. A parity checker using a series parity generator is shown in Fig. 10.3.4(b).

A parity checking operation with bit-differential delay is shown in Fig. 10.3.5 [4]. The operating principle and experimental results are shown in Figs. 10.3.6 and 10.3.7 respectively. The principle of parity generation using XOR in serial scheme (a one bit delayed

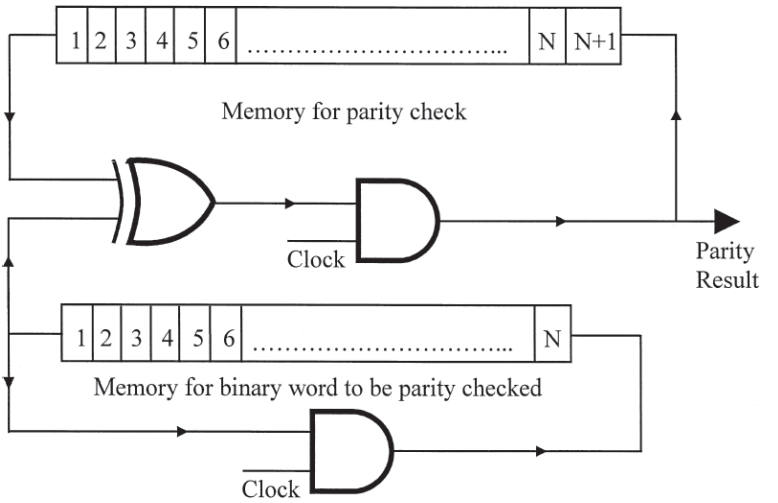

Fig. 10.3.5. Logic diagram of the parity counter with bit-differential delay [7].

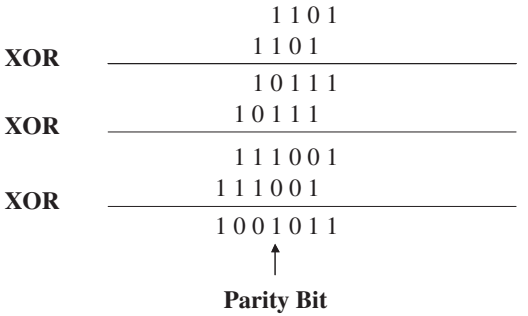

Fig. 10.3.6. The operating principle of parity checker with differential delay. A 4-bit word is used for illustration.

XOR operation in sequence) is shown for a 4-bit word in Fig. 10.3.6. TOAD is used to perform XOR and AND function in the experiment. The parity bits are generated in the middle of the pulse train. It is the 4^{th} bit after three XOR operations with successive one-bit delays.

In order to perform all-optical parity checking at higher data rates, an integrated SOA-MZI based XOR operation scheme in a series configuration can be implemented as shown in Fig. 10.3.8 [8],

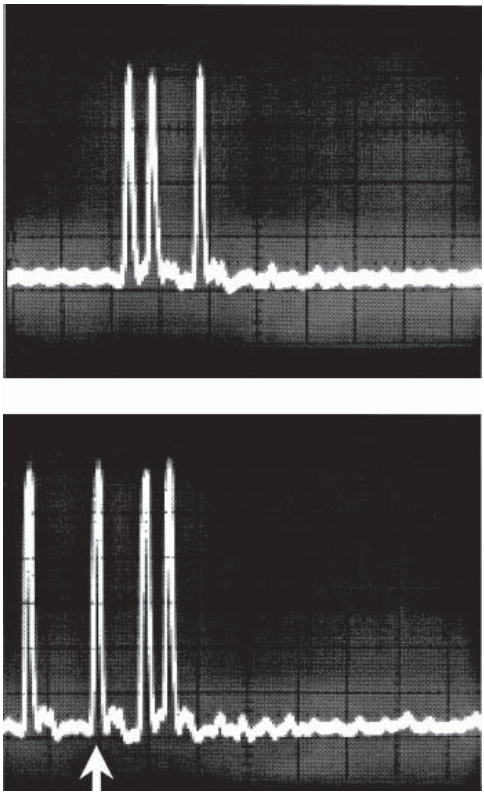

Fig. 10.3.7. Experimental result (2ns /div) (Top), and the input word (1101) (Bottom), results after 3 rounds of XOR operation (1001) as shown in Fig. 10.3.6. The parity bit is a "1" in the middle of the pulse train (marked with an arrow) [7].

the simulation results are shown in Figs. 10.3.9 and 10.3.10. The XOR is used with input pulses at two different wavelengths, as shown in Fig. 10.3.9. The input pulse train has every N set of bits ($N = 8$ for 8-bit WORD) at one wavelength and the $(N + 1)$th bit is at a different wavelength. Therefore the $(N+1)$th bit can be coupled out using a wavelength selective coupler, which can be the parity bit or the result of the parity checker operation.

An AND operation is also needed in the circuit. It converts the wavelength to the desired wavelength for the SOA-MZI and reshapes

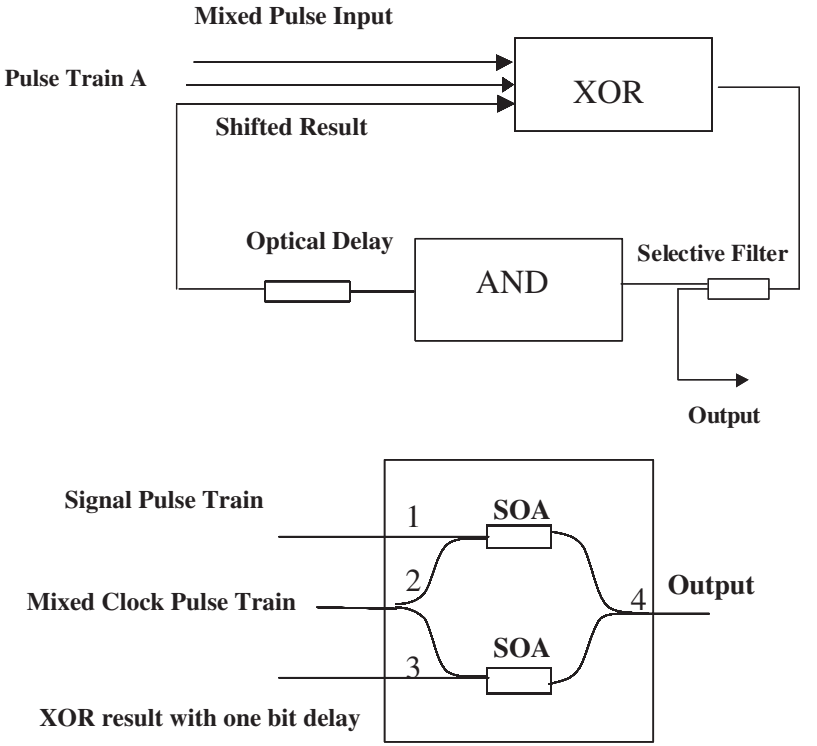

Fig. 10.3.8. (Top) Schematic of parity checker in series configuration. (Bottom) Set up of SOA-MZI in series configuration.

the pulse, minimizing the distortion caused by noise and pattern effect during all-optical XOR operation. The mixed input pulse in Fig. 10.3.8 is made such that every N bits are of one wavelength and the following $(N + 1)$th bit is of different wavelength. Therefore this $(N + 1)$th bit can be coupled out through the wavelength selective coupler, which can be the parity bit or the parity checker result bit.

The numerical results of parity generator and parity checker are obtained with optimized reshaping and wavelength conversion element. To achieve such optimized condition, precise timing between the gates and amplitude control must be maintained.

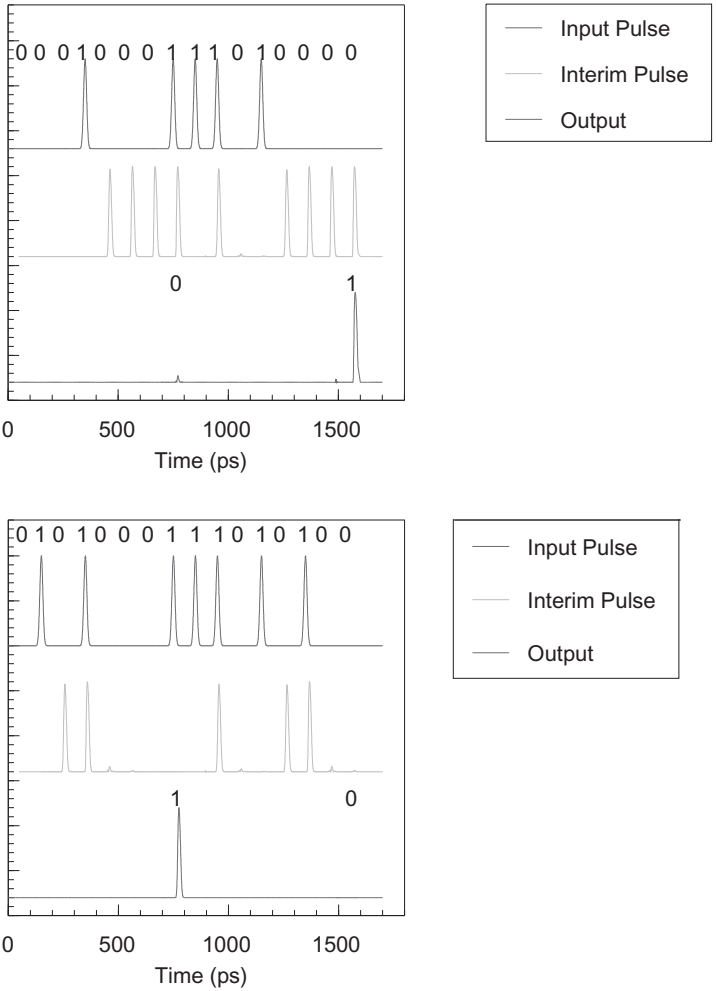

Fig. 10.3.9. Simulation results of 8-bit parity generator. For the top trace after the 8-bit word (00010001), which as even parity, an even parity bit (0) is generated at the 8th bit and for the (11010000) 8-bit word, which has odd parity, an odd parity bit (1) is generated at the location of 8th bit. The bottom trace shows similar results for a different set of 8-bit words. Note that at the end of every 8^{th} bit of a 8-bit WORD a parity bit is generated which represents the parity of the previous 8-bits. The interim pulses are the shifted results of XOR used as the input of next XOR operation.

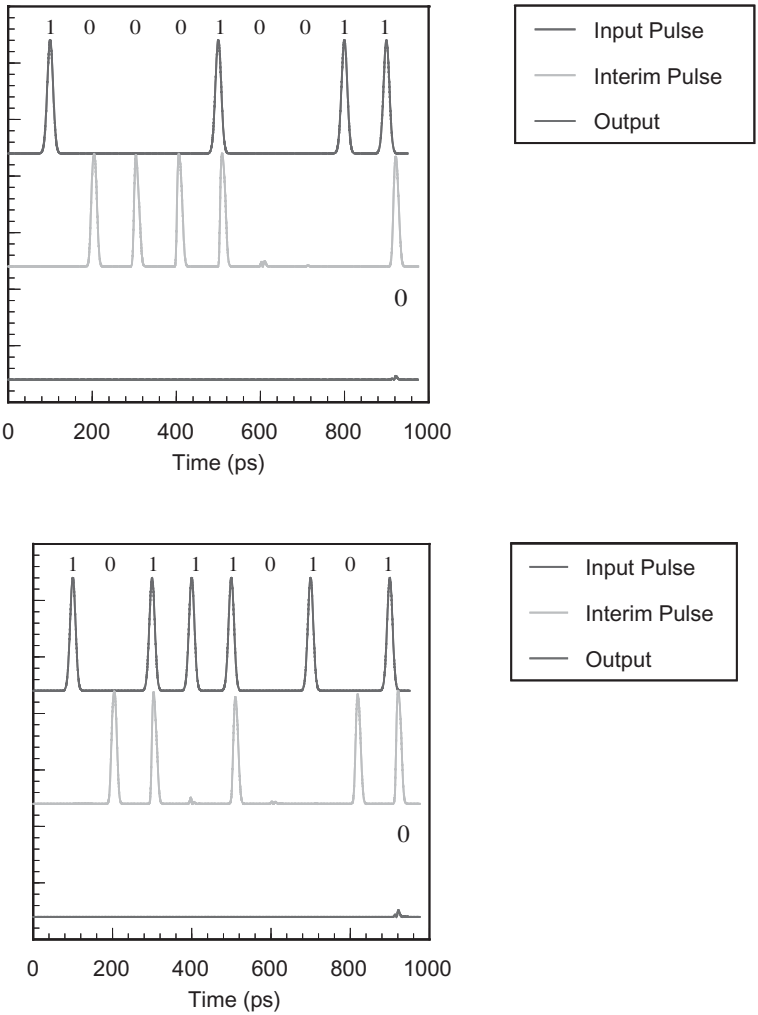

Fig. 10.3.10. Simulation results of 8-bit parity checker. Note the 8-bitWORD (10001001) for (a) which has odd parity has a odd parity bit "1" added to the end. At this temporal position (end of the WORD) the parity checker produces a "0" bit indicating the operation was carried out successfully. The same successful result is obtained in (b) for a different WORD (10111010). The interim pulses are the shifted results of XOR used as the input of next XOR operation.

10.4. All-optical Pseudo-Random Binary Sequence (PRBS) Generator

Pseudo-random binary sequence (PRBS) generators are important for a range of applications in a communication system which including testing, bit scrambling, bit de-scrambling (Fig. 10.4.1). In all-optical communication network, one fundamental measurement is how accurately the receiver can determine the logic state of each received bit. In case that the system cannot carry live traffic during the test, so it is suitable to inject a known bit stream pattern to the under test device. The most common input test pattern is the pseudo-random binary sequence. This bit sequence is designed to approximate the truly random data [9].

In an electronic system, a pseudo-random binary sequence generator with N shift register stages is able to generate all the combination of m bits $(2^n - 1)$ and 0s [11].

All-optical pseudorandom bit stream generator can be made with optical delay line and XOR gates (Fig. 10.4.2). The optical delay lines play the role of shift register. The two inputs of XOR need to be carefully chosen. If the right combination is not chosen, the maximum length $(2^n - 1)$ cannot be obtained. Some of the combinations are shown in Table 10.4.1 [10].

One way to examine the output of a PRBS generator is by measuring the frequency spectrum. The PRBS frequency spectrum consists of many discrete lines under the envelope of $\sin(x)/x$ shape as shown in Fig. 10.4.3. The frequency space between two neighboring

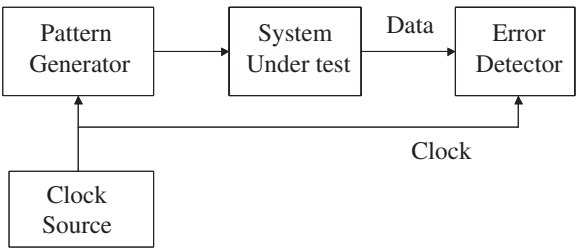

Fig. 10.4.1. Basic bit-error-ratio tester [10].

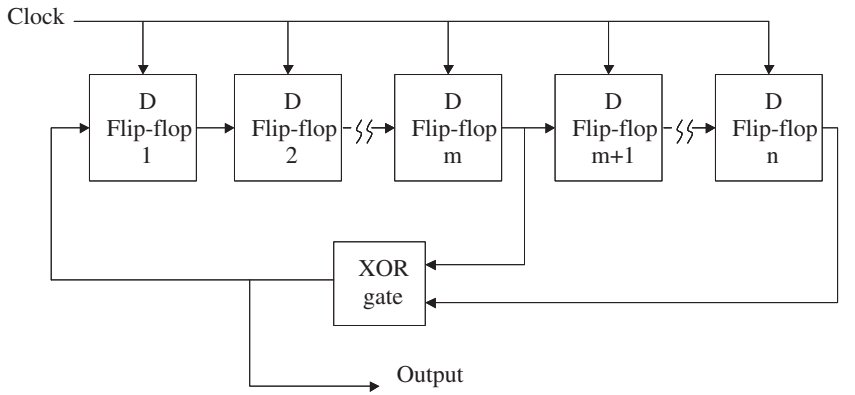

Fig. 10.4.2. PRBS generator using shift registers with feedback [10].

Table 10.4.1. The combinations of PRBS shift register [10].

Sequence Length	Shift-Register Configuration
$2^7 - 1$	$D^6+D^7+1=0$, inverted
$2^{10} - 1$	$D^{10}+D^7+1=0$, inverted
$2^{15} - 1$	$D^{15}+D^{14}+1=0$, inverted
$2^{20} - 1$	$D^{20}+D^{17}+1=0$, inverted
$2^{23} - 1$	$D^{23}+D^{18}+1=0$, inverted
$2^{31} - 1$	$D^{31}+D^{28}+1=0$, inverted

lines is given by [10]

$$\Delta f = \frac{f_b}{2^n - 1}, \tag{10.4.1}$$

where Δf is the frequency spacing and f_b is the bit rate. Figure 10.4.4 shows the measured RF spectrum for the PRBS generator of Ref. [12]. Temporal positions of the bits were also measured. Both the temporal position and spectrum aggress with the expected PRBS performance.

For higher speed PRBS generator where the bit periods are short, a device with all functionalities integrated on the same chip is needed. The schematic configuration of an integrated device which uses SOA-MZI for XOR operation and an AND gate is shown in Fig. 10.4.5.

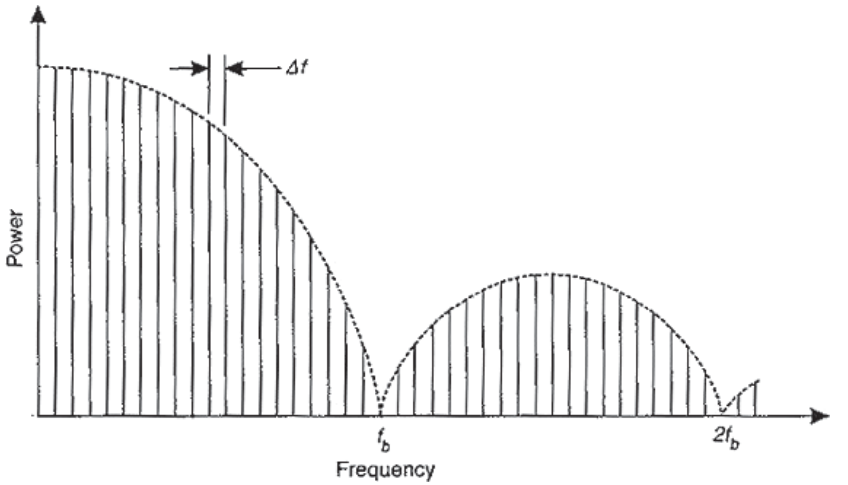

Fig. 10.4.3. PRBS frequency spectrum [10].

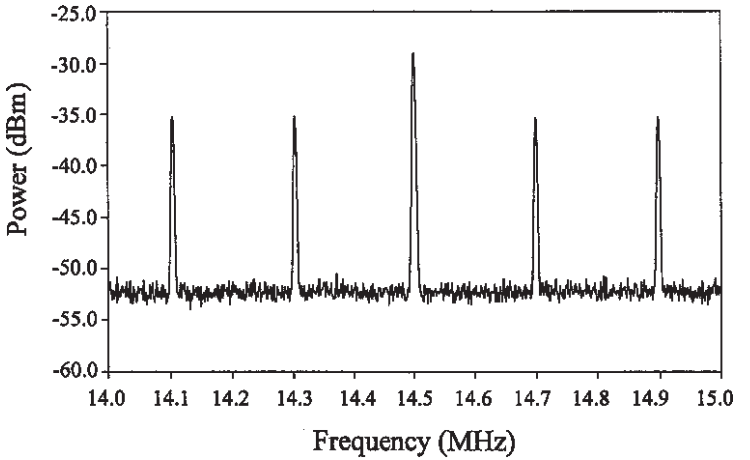

Fig. 10.4.4. Experimentally measured RF spectrum [12].

The delays (m bits, n bits) must be suitably chosen to produce a maximal sequence in the pseudo random pattern. The AND gate is needed for pulse reshaping and wavelength conversion. The initial pulse is used to start the cycle. The simulated result of 6 stage PRBS $(2^6 - 1)$ is shown in Fig. 10.4.6.

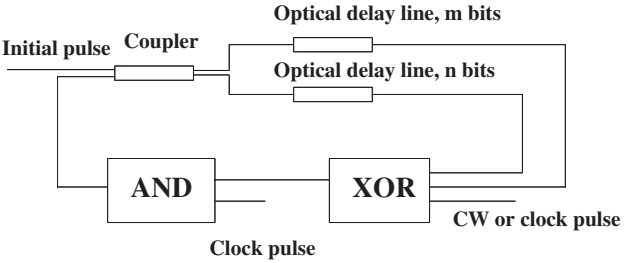

Fig. 10.4.5. The schematic setup of $2^n - 1$ PRBS generator.

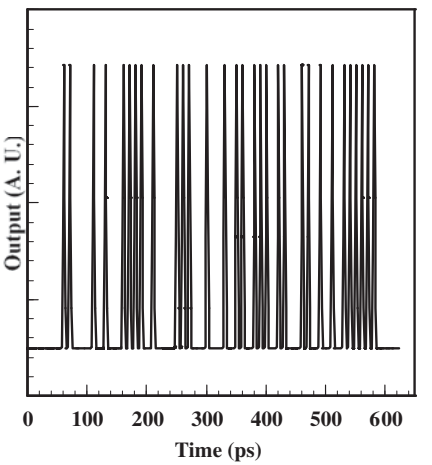

Fig. 10.4.6. Simulated bit stream from 6-stage PRBS.

10.5. All-Optical Header Processor

A set of bits known as "header bits" are included along with the data bits in a communication system. The header bits carry the information related to the processing of data bits. All-optical header processing plays an important role in high-speed all-optical network. The header bits must be processed quickly to make the switching or routing decision for the data. Different schemes for header processing based on semiconductor optical amplifier have been reported [13–29]. We describe the multi-output header processing based on two-pulse correlation in Sec. 10.5.1, cascaded SOA-MZI

header processor in Sec. 10.5.2 and asynchronous multi-output all-Optical header processor in Sec. 10.5.3.

10.5.1. *Multi-output based on two pulse correlation principle*

All optical header processing has been demonstrated using the schematic configuration shown in Fig. 10.5.1. The operation is based on a semiconductor optical amplifier positioned appropriately in a fiber loop mirror. A two-pulse correlation scheme in the semiconductor optical amplifier in the loop mirror is used to retrieve the header from the packet [15,22]. There are three time scales in the SOA configuration in a fiber loop, the time between two pulses T, the time related to the displacement of the semiconductor optical amplifier to the center of the loop mirror, t and the recovery time of the SOA, t_c.

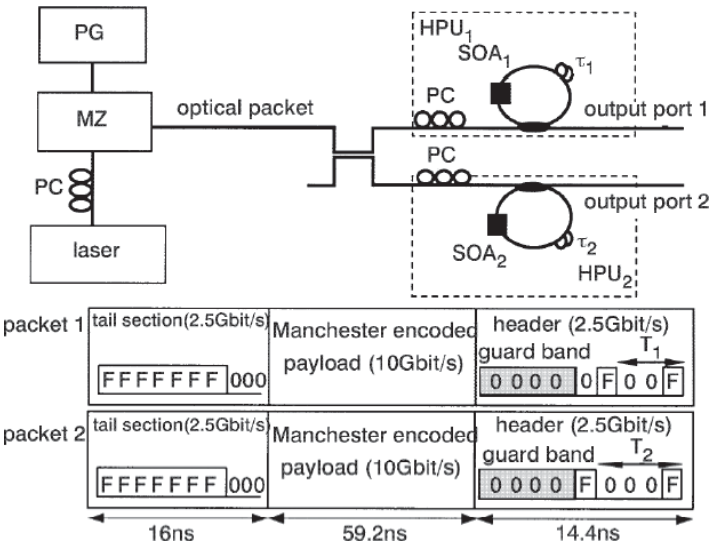

Fig. 10.5.1. Experimental setup of a all-optical header processor and packet structure. The basic device used is a semiconductor optical amplifier in a loop mirror configuration. The optical packet is split and it propagates through the loop mirrors with SOA. Typical packets are also shown [15].

In the case of $T - 2t > t_c$, the first pulse propagating in the counter-clockwise direction arrives at the SOA before the two clockwise propagating pulses. No phase difference appears between the two counter propagating pulses because the gain is unsaturated. Hence no pulse output occurs from the fiber loop. If $|T - 2t| < t_c$, gain saturation in SOA causes phase difference between the counter-clockwise and clockwise pulses. A pulse output then takes place from the fiber loop. For the case when, $2t - T > t_c$ the counter-clockwise pulse arrives at the SOA after the two clockwise pulses have left the loop. Hence there is no pulse output from the loop mirror.

As shown in Fig. 10.5.1, the input header is split into two equal parts. The difference between the upper branch and the lower branch is the position of the SOA insider the loop. By carefully choosing the position of the SOA in the fiber loop, in accordance with the principle described above, the header will be switched to different output ports according to its pattern. The experimental results are shown in Fig. 10.5.2.

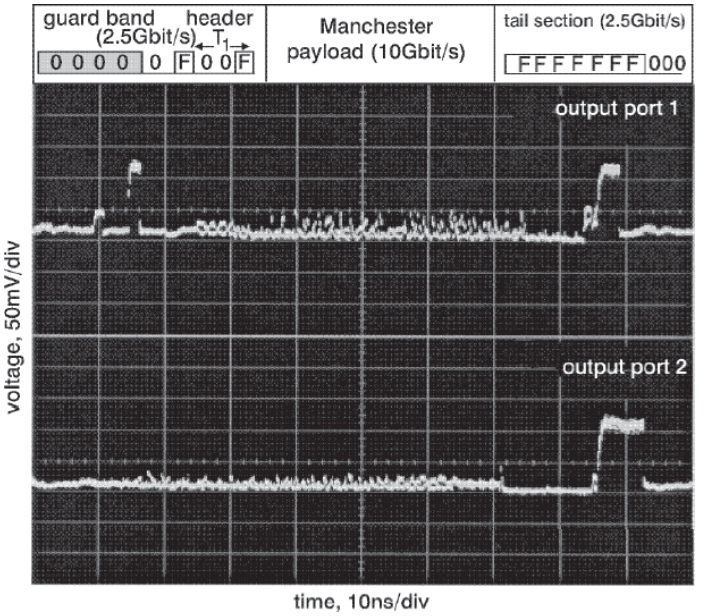

Fig. 10.5.2. Output at ports 1 and 2 when packet 1 is processed [15].

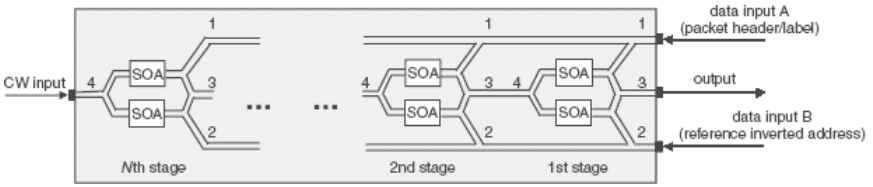

Fig. 10.5.3. Proposed architecture for all-optical packet header processor or optical correlator [23].

10.5.2. *All-optical packet header processor based on cascaded SOA-MZIs*

A semiconductor optical amplifier based Mach-Zehnder interferometer (SOA-MZI) in a cascaded configuration has been proposed for header processing [23,24]. The proposed structure of all-optical header processor using N XOR gates is shown in Fig. 10.5.3 [23,24]. Each SOA-MZI performs XOR operation. They are in counter-propagating configuration so that no filter is needed. As the result of the cascaded XOR functions, the output is logic "1", if the input A is the inverse of input B. Otherwise the output is "0". The simulation results are shown in Fig. 10.5.4.

10.5.3. *Ultrafast asynchronous multi-output all-optical header processor*

The experimental setup (Fig. 10.5.5) consists of two parts [25]. The header preprocessor (HPP) [26] and the header correlator, TOAD [27]. The header preprocessor separates the header from the payload and also provides the control pulses to the TOAD. The configuration of the header preprocessor is shown in the dashed box in Fig. 10.5.5. The format of the packet is such that there are several "0"s before the header and its time duration is longer than the recovery time of the SOA. The payload behind the header is Manchester encoded and the transition between "1" and "0" is faster than the recovery time. Thus when the header arrives at the SOA, the gain is unsaturated. Due to the self -induced polarization modulation, the header is switched to one port. Since the gain is saturated when payload is transmitted inside the SOA, it is switched to the other output port.

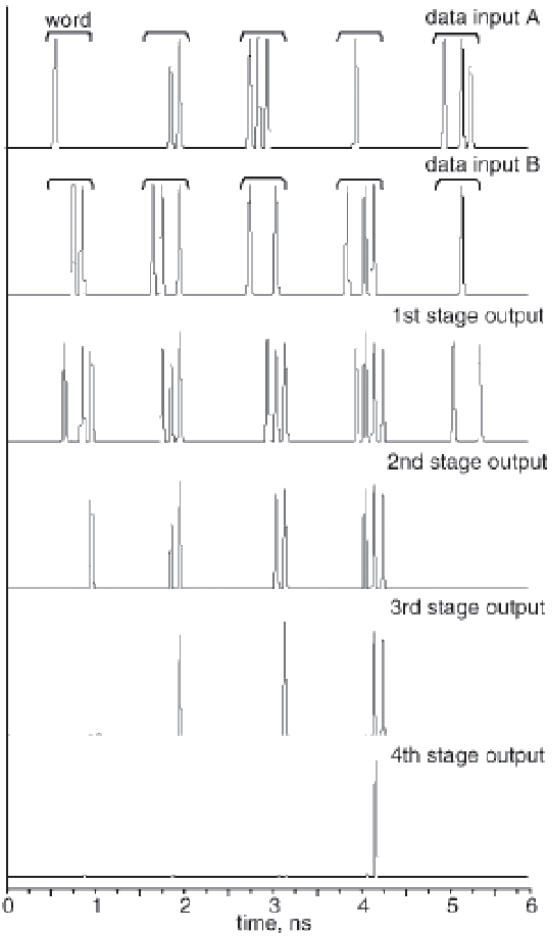

Fig. 10.5.4. Simulation results of bit-pattern matching (header = address recognition) [23].

The operation of TOAD is as follows: the output of HPP is split into two parts, the low power signal and the higher power control pulse. There are three possible cases depending on the arrival time of the control pulse at the SOA. As illustrated in Fig. 10.5.6(a), when the control pulse arrives after the second pulses in both directions, no phase change is induced. Thus the output is "0". For case (c), the control is between the second pulses of the counter-clockwise and clockwise signal, the output is also "0" since the induced phase

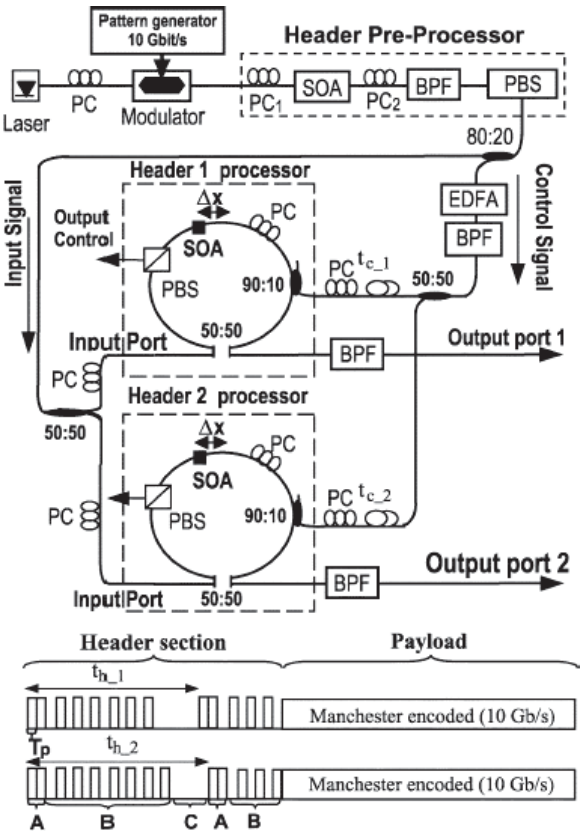

Fig. 10.5.5. Experimental setup to demonstrate the header processing system and packet structure are presented. PC: Polarization controller. EDFA: Erbium-doped fiber amplifier. BPF: Bandpass filter. For the pulse sequence shown at the bottom, (A) Header pulses. (B) Alternating "1" and "0" bits. (C) Sequence of "0s" [25].

changes are almost equal. In case (b), the control pulse arrives at the SOA before the second counter-clockwise pulse and after the second clockwise pulse, the output is "1", due to the phase difference between the counter propagating pulses. This process allows the implementation of header recognition.

Unlike the two pulse correlation case in Sec. 10.5.1, the header processing does not depend on the recovery time of the SOA The experimental results are shown in Fig. 10.5.7.

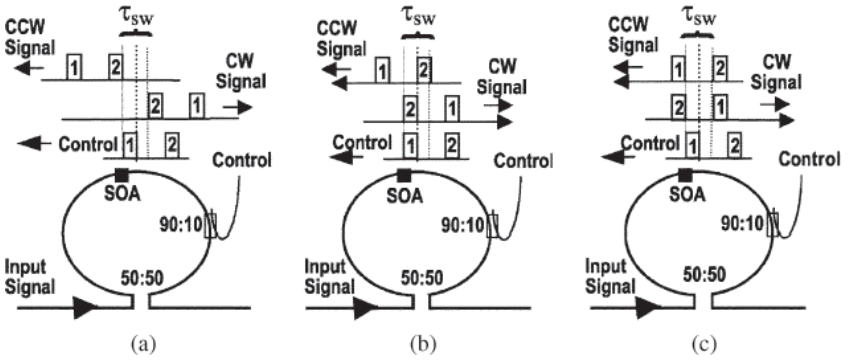

Fig. 10.5.6. Timing of the control pulses for the three relevant cases for the operation of the header processor. (a) The control arrives at the SOA after all the pulses have passed the SOA. (b) The control arrives at the SOA after the second CW pulse has passed the SOA but before that the second CCW arrives at the SOA. (c) The control arrives at the SOA before both the CW and CCW second pulses arrive at the SOA [25].

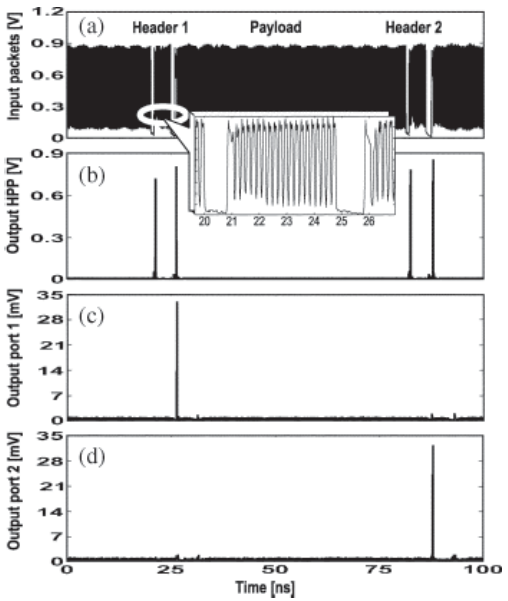

Fig. 10.5.7. Measured oscilloscope traces. (a) The optical data packets that input the header processor. Packets with two different headers are shown. The inset shows details of the packet header. (b) The output of the HPP. It is clearly visible that only pulses synchronized with the leading edge of the header bits output the HPP. (c) Output at Port 1. It is visible that only Packet 1 is recognized. (d) Similar to (c), but now for Packet 2 [25].

Optical logic circuits are being investigated by several research groups. As mentioned before, for higher speed operation quantum dot based SOA is important. Many optical logic circuits require several devices to be integrated on the same chip. Thus much of the advances in the optical logic circuit development would not have been possible without the advances in materials and processing technology. An avenue that is being pursued by several researchers involve hybrid integration where the optical waveguides are fabricated using silica based technologies and the semiconductor amplifier use InGaAsP/InP materials technology. Both sets of chips are fabricated in the form of arrays and then they are optically aligned. The challenges of much of the current optical logic circuit research is intimately linked with the challenges in materials growth which include not only the investigation of new material systems but also improvements in existing technologies, such as quantum dots, to make them more reproducible.

References

[1] S. Kumar, D. Gurkan and A. E. Willner, OFC Conf. Cat. No. 04CH37532 (2004).
[2] D. Tsiokos, E. Kehayas, K. Vyrsokinos, T. Houbavlis, L. Stampoulidis, G. T. Kanellos, N. Pleros, G. Guekos and H. Avramopoulos, *IEEE Photon. Technol. Lett.* **16**, 284 (2004).
[3] S. Kim, S. Lee, B. Kang, S. Lee and J. Park, *Technical Digest. CLEO* 4$^{\text{th}}$ *Pacific Rim Conf.* **2**, 254 (2001).
[4] J. H. Kim, Y. T. Byun, Y. M. Jhon, S. Lee, D. H. Woo and S. H. Kim, *Opt. Commun.* **218**, 345 (2003).
[5] A. J. Poustie, K. I. Blow, A. E. Kelly and R. J. Manning, *Opt. Commun.* **156**, 22 (1998).
[6] A. J. Poustie, K. I. Blow, A. E. Kelly and R. J. Manning, *Opt. Commun.* **168**, 89 (1999).
[7] A. J. Poustie, K. J. Blow, A. E. Kelly and R. J. Manning, *Opt. Commun.* **162**, 37 (1999).
[8] T. Houbavlis, K. E. Zoiros, M. Kalyvas, G. Theophilopoulos, C. Bintjas, K. Yiannopoulos, N. Pleros, K. Vlachos, H. Avramopoulos, L. Schares, L. Occhi, G. Guekos, J. R. Taylor, S. Hansmann and W. Miller, *J. Lightwave Technol.* **23**, 781 (2005).
[9] J. M. Senior, *Optical Fibre Communications Principles and Practice* (Prentice-Hall, London, 1985).
[10] D. Derickson, *Fiber Optic Test and Measurement* (Prentice Hall PTR, 1998).

[11] P. Horowitz, W. Hill, *The Art of Electronics*, 2nd edn., Vol. 655 (Cambridge Univ. Press, Cambridge, 1989).
[12] A. J. Poustie, K. J. Blow, R. J. Manning and A. E. Kelly, *Opt. Commun.* **159**, 208 (1999).
[13] A. E. Willner, D. Gurkan, A. B. Sahin, J. E. McGeehan and M. C. Hauer, *IEEE Commun. Mag.* **41**, S38 (2003).
[14] I. Glesk, K. I. Kang and P. R. Prucnal, *Electron. Lett.* **30**, 1322 (1994).
[15] N. Calabretta, Y. Liu, H. de Waardt, M. T. Hill, G. D. Khoe and H. J. S. Dorren, *Electron. Lett.* **37**, 1238 (2001).
[16] M. T. Hill, A. Srivatsa, N. Calabretta, Y. Liu, H. deWaardt, G. D. Khoe and H. J. S. Dorren, *Electron. Lett.* **37**, 774 (2001).
[17] D. J. Blumenthal, B. Olsson, G. Rossi, T. E. Dimmick, L. Rau, M. Masanovic, O. Lavrova, R. Doshi, O. Jerphagnon, J. E. Bowers, V. Kaman, L. A. Coldren and J. Barton, *J. Lightwave Technol.* **18**, 2058 (2000).
[18] Y. M. Lin, W. I. Way and G. K. Chang, *IEEE Photon. Technol. Lett.* **12**, 1088 (2000).
[19] D. J. Blumenthal, A. Carena, L. Rau, V. Curri and S. Humphries, *IEEE Photon. Technol. Lett.* **11**, 1497 (1999).
[20] T. Fjelde, A. Kloch, D. Wolfson, B. Dagens, A. Coquelin, I. Guillemot, F. Gaborit, F. Poingt and M. Renaud, *Proc. ECOC'2000* **4**, 63 (2000).
[21] M. C. Hauer, J. McGeehan, J. Touch, P. Kamath, J. Bannister, E. R. Lyons, C. H. Lin, A. A. Au, H. P. Lee, D. S. Starodubov and A. E. Willner, *Proceedings OFC'02* **WM7**, 268 (2002).
[22] A. Srivastava, H. d. Waardt, M. T. Hill, G. D. Khoe and H. J. S. Dorren, *Electron. Lett.* **37**, 234 (2001).
[23] J. M. Martinez, F. Ramos and J. Marti, *Electron. Lett.* **40**, 894 (2004).
[24] F. Ramos, J. M. Martinez, K. Schulze, J. Marti, R. Llorente and R. Clavero, *Proc. SPIE* **5247**, 142 (2003).
[25] N. Calabretta, H. de Waardt, G. D. Khoe and H. J. S. Dorren, *IEEE Photon. Technol. Lett.* **16**, 1182 (2004).
[26] N. Calabretta, Y. Liu, H. deWaardt, M. T. Hill, G. D. Khoe and H. J. S. Dorren, *J. Lightwave Technol.* **22**, 372 (2004).
[27] J. P. Sokoloff, P. R. Prucnal, I. Glesk and M. Kane, *IEEE Photon. Technol. Lett.* **5**, 787 (1993).
[28] X. D. Cao, M. Jiang, K. H. Ahn, Y, Liang, B. C. Barnett and M. N. Islam, *Digest IEEE/LEOS* **18**, (1996).
[29] K. H. Ahn, J. W. Lou, Y. Liang, O. Boyraz, T. J. Xia, Y. H. Kao and M. N. Islam, *IEEE Photon. Technol. Lett.* **11**, 140 (1999).

Chapter 11

Quantum Dot Amplifiers

11.1. Introduction

Extensive research has been carried out on semiconductor optical amplifiers (SOA) with quantum dot (QD) active region over the last ten years. Like SOAs with multi quantum well (MQW) active region, the peak of the gain spectrum in QD amplifiers depend on the size of the dots in addition to the material composition of the dots, and, the material composition of the region in which the dots are embedded. In order to have sufficient optical gain, multiple layers of quantum dots are often used in the active (gain) region. The quantum dot semiconductor optical amplifiers (QD-SOA) have some advantages over conventional bulk or quantum well devices because of higher saturation power, faster gain recovery and large amplification bandwidth [1–10]. All of these features make QD-SOA device a promising component in high data rate all-optical switching and data processing applications. The active region of QD amplifiers consists of quantum dots (typically about 10 to 20 nm in size in all dimensions) embedded in a higher band gap material. The higher band gap material provides the carrier confinement in QDs. Due to its small size, the energy level of the electrons and holes in a QD material is quantized. For A MQW active region, only the kinetic energy along the small dimension (width of the well) is quantized. For QD active region, the kinetic energy in all three dimensions are quantized. In the first approximation, the energy levels in a quantum dot is obtained by solving the Schrodinger equation in a three dimensional potential well. The energy levels in this case, not only depends on the dimensions of the well (dots) but also on the depth of the well (band

gap difference between the QD material and the embedding layer material).

11.2. Quantum Dot Materials Growth

The quantum dot material, as the name implies, consists of dots (sometime irregular) of a semiconductor (e.g. InAs) embedded in another semiconductor (e.g. InGaAs). The growth process utilized for dot formation is generally the Stranski–Krastanov growth (S-K growth) process. In S-K growth process, a 'layer-plus-island growth' process occurs. The S-K growth is a two step process: initially, complete films of InAs (adsorbate), up to several monolayers thick, are grown in a layer-by-layer fashion on a lattice matched (or nearly lattice matched) crystal substrate.

Beyond a critical layer thickness, which depends on strain and the chemical potential of the deposited film, growth continues through the nucleation and coalescence of InAs (adsorbate) 'islands'. This growth mechanism was first noted by Ivan Stranski and Lyubomir Krastanov in 1938 and is known as the Stranski–Krastanov growth. In recent years, molecular beam epitaxy technique has been used to grow quantum dot material.

The quantum dot active region (i.e. quantum dots and the embedding layers), are often surrounded by a set of separate confinement layers which have n-type and p-type cladding layers on either side similar to that for a regular SOA (Ch. 2). The lateral confinement in this heterostructure could be either strongly index guided (buried heterostructure) or weakly index guided (e.g. ridge waveguide type) i.e. the lateral index and current confinement follows the same methods as described earlier (Chs. 2, 4). The creation of low reflectivity facets also follow the procedures described in Ch. 5.

The structure of a quantum-dot SOAs along with the scanning electron photomicrographs of the QD active region is shown in Fig. 11.2.1 [7]. The quantum-dot layers consist of InAs QDs (grown using S-K method by molecular beam epitaxy) embedded in $In_{0.17}Ga_{0.83}As$. The QD material in this case has a ground state emission peak of $\sim 1.3\,\mu m$. The embedding layer affects the emission

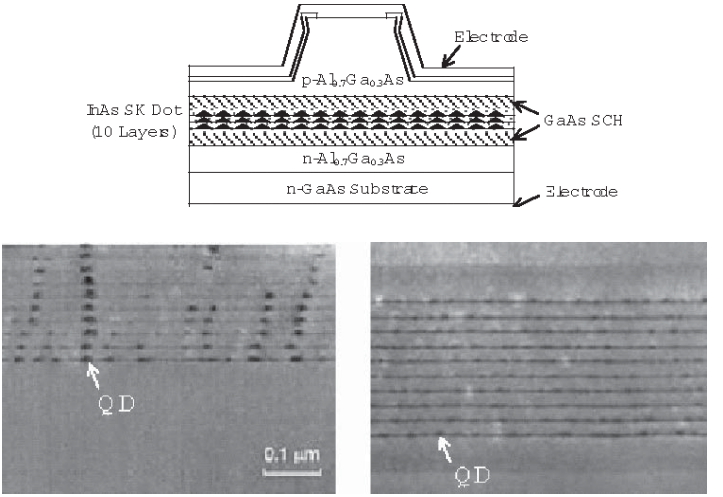

Fig. 11.2.1. Structure of ridge waveguide type quantum dot (QD) SOA. GaAs separate confinement heterostructure (SCH) is also shown (a) aligned quantum dots (b) nonaligned QDs [7].

wavelength [8]. In order to obtain sufficient gain from the quantum dots, the quantum-dot layers are generally repeated a few times (10 in Fig. 11.2.1). Generally, close stacking of quantum-dot layers causes vertical lining of dots (Fig. 11.2.1(a)), which leads to strain accumulation. The researchers in [7–9] developed a technique to eliminate lining up (Fig. 11.2.1(b)) and hence strain accumulation. This leads to improved crystal quality. This material (Fig. 11.2.1) was processed into a ridge waveguide structure 10 μm wide and 2.5 mm long. The facet reflectivity was reduced by applying antireflection (AR) coating. The entire structure is grown on a *n*-GaAs substrate.

The structure of an index guided QD amplifier is shown in Fig. 11.2.2. In this structure the InAs QDs are buried in InGaAsP. The final cladding layers are *p*-InP. The structure is laterally buried in a current confining (InP based) structure and the entire set of layers are grown on a *n*-InP substrate. The QD waveguide is tilted with respect to the facet to reduce facet reflection, and, the facets are further coated with antireflection films.

A modification of the QD-SOA is a columnar QD SOA (CQD SOA) [12]. A tensile strained barrier layer is used to control the

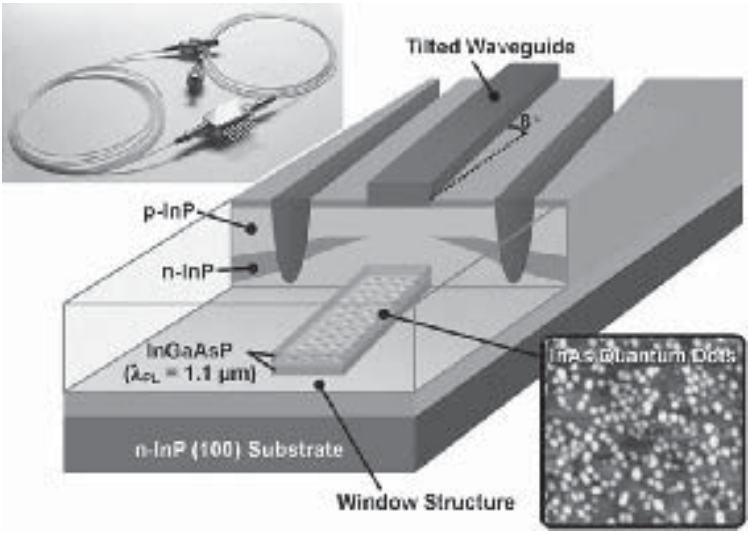

Fig. 11.2.2. Structure of an InAs/InGaAsP/InP semiconductor optical amplifier fabricated on an InP substrate [11]. The inset is a picture of fiber-pigtailed butterfly module (which has a QD-SOA) with temperature controller.

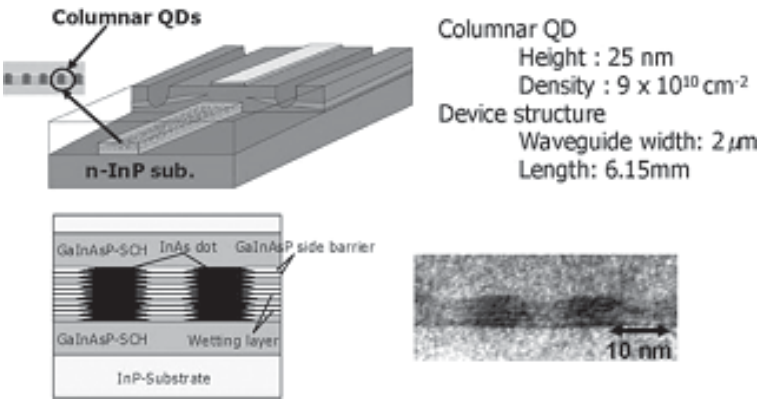

Fig. 11.2.3. Structure of columnar quantum dot (CQD) with a number of layers, SCH: separate confinement heterostructure [12].

position of the QDs in this case. The structure has 22 stacks of QD layers, each sandwiched between 160 nm thick tensile strained InGaAsP separate confinement heterostructure layers, as shown in Fig. 11.2.3. This type of dot configuration can significantly increase

the modal gain of the SOA and has polarization-independent gain [12]. The planar density of the dots is $9 \times 10^{10}\,\mathrm{cm}^{-2}$, the height of the dots is 25 nm, and the total active region thickness is about 350 nm. This QD amplifier operates near 1500 nm. The CQD-SOA, shown in Fig. 11.2.3 is a 6.15-mm-long device with an 8 degree tilted waveguide (to reduce facet reflection) and is antireflection-coated. The device has larger transverse-magnetic (TM) mode gain than transverse electric (TE) mode gain [5].

11.3. Quantum Dot Amplifier Performance

The quantum dots have a discrete set of energy levels in the conduction band and valence band. Depending on the size of the dots and the bandgap of the wetting layer (the layer in which the dots are embedded), one or two of these discrete energy levels are distinct i.e. separated from the wetting layer. The higher energy levels merge with the wetting layer. These differences are evident in the amplified spontaneous emission (ASE) spectrum of the QD SOA.

Sometimes a distinct emission is observed only from the electron transition from the ground state (GS) and in other cases two separate distinct emissions i.e. electron transition from both ground state (GS) and excited state (ES) are observed. Thus both one state and two-state model for QD SOA have been developed. Example of a ground state amplified spontaneous emission is shown in Fig. 11.3.1.

The amplified spontaneous emission (ASE) from an InAs/InGa As/InP QD SOA is shown in Fig. 11.3.2 [12]. At low currents, the conduction band ground state of the QD is populated, and the spectrum peak is near 1540 nm.

The broadening of the spectrum is believed to be due to distribution in the dimension of the dots i.e. not all dots are of the same size. At high currents a second peak in the spectrum (near 1470 nm) emerges due to transitions from the excited state in the conduction band to the valence band. In Fig. 11.3.2, the extrapolated QD excited state (ES) and ground state (GS) ASE profile is also shown. The ∼70 nm difference between the peaks of the spectrum (ES and GS transitions) corresponds to an energy spacing

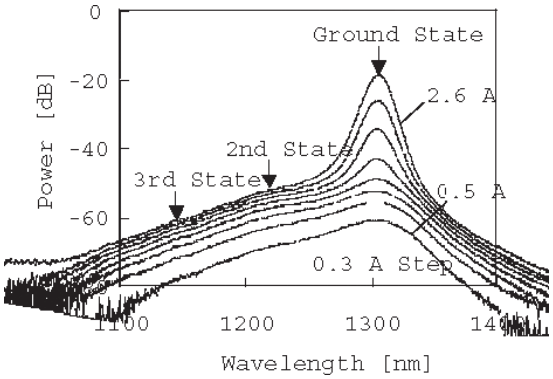

Fig. 11.3.1. The amplified spontaneous emission (ASE) spectra of a quantum dot (QD) amplifier at different bias current [11]. Also shown in the figure are the extrapolated QD excited state locations. This spectrum is for the device shown in Fig. 11.2.1.

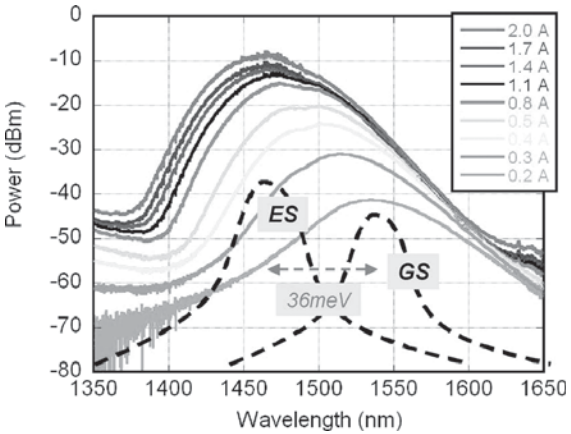

Fig. 11.3.2. The amplified spontaneous emission (ASE) spectra of a quantum dot (QD) amplifier at different bias current [12]. Also shown in the figure are the extrapolated QD ground and excited state emission profiles. This spectrum is for the device shown in Fig. 11.2.3 [12].

of ∼36 meV, which agrees well with the calculation using the dot dimensions.

The measured gain as a function of wavelength of the QD-SOA in Fig. 11.2.3 is shown in Fig. 11.3.3. Note that a fiber-to-fiber gain of >30 dB is feasible. The 3-dB gain saturation power is ∼17 dB.

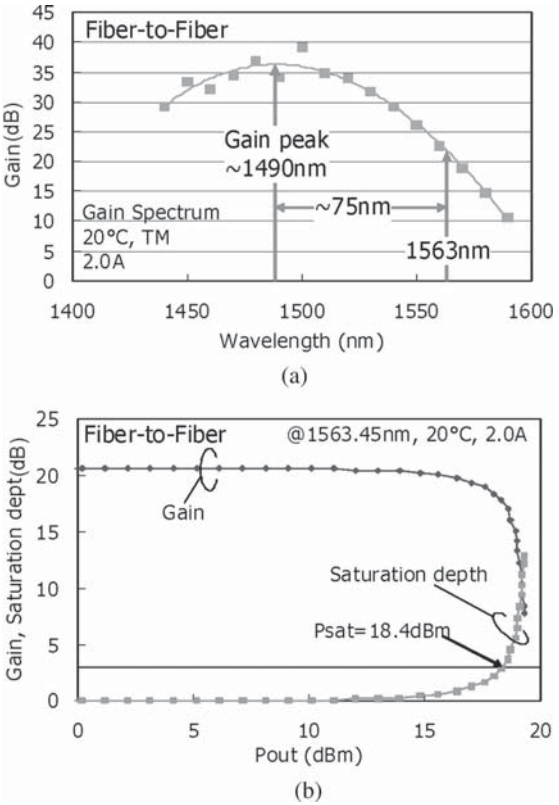

Fig. 11.3.3. (a) The measured gain spectra of a quantum dot (QD) amplifier at 20C. The device was put in a packaged module. (b) The measured gain as a function of output power. This data is for the device shown in Fig. 11.2.3 [12].

The QD-SOA structure shown in Fig. 11.2.2 has been characterized. The performance shown (Fig. 11.3.4) was measured with a device having a tilted waveguide (8-degree off angle) and window structure to suppress lasing action. The waveguide length, stripe width, number of QD layers, and density of QDs of the QD-SOA are 6.15 mm, 2.2 μm, 5, and $4 \times 10^{10}\,\mathrm{cm}^{-2}$, respectively [11].

11.4. Gain Dynamics

The model of gain dynamics in QD-SOA using both one state (ground state of conduction band transition only) and two-state (both excited

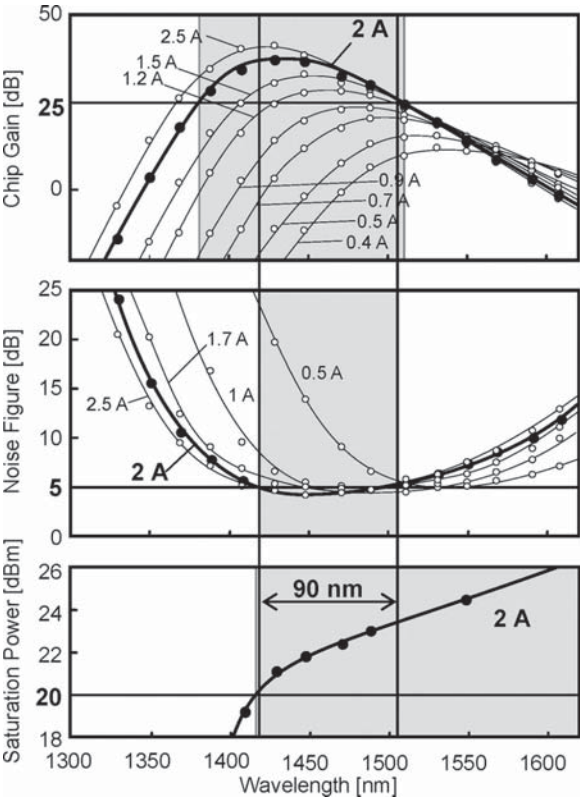

Fig. 11.3.4. Wavelength dependence gain, noise figure and saturation output power is shown for the QD-SOA structure of Fig. 11.2.2 [11].

state and ground state transitions) have been developed. They are described in this section.

11.4.1. *Gain dynamics — one state model*

Theory of the signal amplification using only ground state transition in a quantum-dot SOA has been developed [6–8, 19–27]. Current injection in a quantum dot is schematically shown in Fig. 11.4.1. For self-assembled QDs the dots are immersed in a wetting layer. The carriers are injected into the wetting layers where it makes a fast transfer to the quantum dot. Figure 11.4.1 assumes that all carriers make a transition to a single quantum dot level (conduction band state).

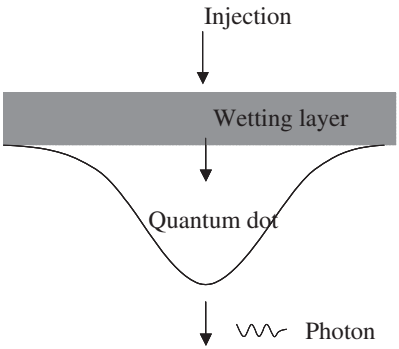

Fig. 11.4.1. Carrier injection model in the conduction band of a Quantum dot.

However, in some cases, there are two quantum dot levels involved i.e. there is a confined excited state in the conduction band in addition to the ground state. The carriers from the wetting layer populate both of these states in these cases as discussed before.

The model assumes that all the quantum dots in SOA are identical and uniform. Also there is only one confined energy level in the conduction and valance band of each dot. The carrier density is N_w in the wetting layer, N_{id} in the ith quantum dot, and $N_{i\max}$ as the maximum carrier density that ith quantum-dot can sustain. The rate equations for carrier density are as follows [8,9]:

$$\frac{dN_w}{dt} = \frac{J}{ed} - \frac{N_w}{\tau_{w\to d}}\left(1 - \frac{N_{id}}{N_{i\max}}\right) - \frac{N_w}{\tau_{wr}} + \sum_i \frac{N_{id}}{\tau_{d\to w}}, \qquad (11.4.1)$$

$$\frac{dN_{id}}{dt} = \frac{N_w}{\tau_{w\to d}}\left(1 - \frac{N_{id}}{N_{i\max}}\right) - \frac{N_{id}}{\tau_{dr}} - \sum_i \frac{N_{id}}{\tau_{d\to w}} - \Gamma g S, \qquad (11.4.2)$$

where J is the injection current density, d is the total wetting layer thickness, $\tau_{w\to d}^{-1}$ is the transition rate between the wetting layer and the ground state in quantum dot, τ_{wr}^{-1} is the carrier recombination rate in wetting layer, $\tau_{d\to w}^{-1}$ is the excitation rate from ground state to wetting layer, τ_{dr}^{-1} is the recombination rate in semiconductor dot, and $S(t,z)$ is the optical intensity. Two additional gain dynamic equations induced by carrier heating and spectral hole

burning effects are:

$$\frac{\partial g_{\mathrm{SHB}}}{\partial t} = -\frac{g_{\mathrm{SHB}}}{\tau_{\mathrm{SHB}}} - \frac{\varepsilon_{\mathrm{SHB}}}{\tau_{\mathrm{SHB}}} g_{\mathrm{total}} S(t,z) - \left(\frac{\partial g_{\mathrm{CH}}}{\partial t} + \frac{\partial g_{l}}{\partial t}\right), \quad (11.4.3)$$

$$\frac{\partial g_{\mathrm{CH}}}{\partial t} = -\frac{g_{\mathrm{CH}}}{\tau_{\mathrm{CH}}} - \frac{\varepsilon_{\mathrm{CH}}}{\tau_{\mathrm{CH}}} g_{\mathrm{total}} S(t,z), \quad (11.4.4)$$

where τ_{SHB}^{-1} is the carrier-carrier scattering rate associated with spectral hole burning (SHB) while τ_{CH}^{-1} is the carrier temperature relaxation rate. $\varepsilon_{\mathrm{SHB}}$ and $\varepsilon_{\mathrm{CH}}$ are the nonlinear gain suppression factors due to carrier heating and spectral hole burning [26,27], and g_d is the gain for the quantum dot transition. The total gain is given by:

$$g_{\mathrm{total}} = g_d + g_{\mathrm{SHB}} + g_{\mathrm{CH}}. \quad (11.4.5)$$

The equation for the intensity S(t, z) of the CW signal is given by,

$$\frac{\partial S(t,z)}{\partial z} = \Gamma g S(t,z). \quad (11.4.6)$$

Solution of (11.4.6) is

$$S(t,z) = S(t,0)G(t,z), \quad (11.4.7)$$

where $G(t,z) = \exp[h(t)]$ and $h(t) = \int_0^z g(t,z)dz$.

Integration of (11.4.7) over z leads to

$$\int_0^z \Gamma g S(t,z')dz' = S(t,z) - S(t,0) = [G(t,z) - 1]S(t,0). \quad (11.4.8)$$

The previous set of equations is now transformed into the following temporal gain equations:

$$\frac{dh_d}{dt} = \frac{h_w}{\tau_{w\to d}}\left(1 - \frac{h_d}{h_{\max}}\right) - \frac{h_d}{\tau_{dr}} - [\exp(h_d + h_{\mathrm{SHB}} + h_{\mathrm{CH}}) - 1]S(t,0), \quad (11.4.9)$$

$$\frac{dh_w}{dt} = \frac{(h_{in} - h_w)}{\tau_{wr}} - \frac{h_w}{\tau_{w\to d}}\left(1 - \frac{h_d}{h_{\max}}\right), \tag{11.4.10}$$

$$\frac{dh_{\mathrm{SHB}}}{dt} = -\frac{h_{\mathrm{SHB}}}{\tau_{\mathrm{SHB}}} - \frac{\varepsilon_{\mathrm{SHB}}}{\tau_{\mathrm{SHB}}}[\exp(h_d + h_{\mathrm{SHB}} + h_{\mathrm{CH}}) - 1]S(t,0) - \frac{dh_d}{dt} - \frac{dh_{\mathrm{CH}}}{dt}, \tag{11.4.11}$$

$$\frac{dh_{\mathrm{CH}}}{dt} = -\frac{h_{\mathrm{CH}}}{\tau_{\mathrm{CH}}} - \frac{\varepsilon_{\mathrm{CH}}}{\tau_{\mathrm{CH}}}[\exp(h_d + h_{\mathrm{SHB}} + h_{\mathrm{CH}}) - 1]S(t,0), \tag{11.4.12}$$

where $h_{\max}$ is the maximum value of integrated gain.

$$h_{\max} = \int_0^z a(N_{\max} - N_{tr})dz',$$

N_{tr} is the carrier density at transparency, a is the differential gain of SOA, $h_{\mathrm{in}} = \int_0^z \frac{\alpha J \tau_{wr}}{ed}dz'$, $\varepsilon_{\mathrm{SHB}}$ and $\varepsilon_{\mathrm{CH}}$ are the gain suppression factors due to spectral hole burning and carrier heating effect respectively. The phase change equation is given by:

$$\phi(t) = -\frac{1}{2}\alpha h_d(t) - \frac{1}{2}\alpha_{\mathrm{CH}} h_{\mathrm{CH}}(t), \tag{11.4.13}$$

where α is the linewidth enhancement factor, $\alpha \sim 5$ and $\alpha_{\mathrm{CH}} \sim 1$. In the QD model used here, the majority of the carriers are injected into the wetting layer from which they transfer to the QD energy levels. The carrier relaxation time from the wetting layer to the QD is ∼0.5 to 10 ps [9]. The wetting layer is populated by the injected current and it serves as a reservoir of carriers for the QD. Thus with increasing current more carriers are present for transitions to the QD. This results in increasing saturation power and faster gain recovery for QD amplifiers with increasing current.

The calculated result for optical gain as a function of output power for different injected current densities is shown in Fig. 11.4.2. With increasing current density, the saturation power increases. In the calculation, the parameters are set as follows [9]: $\tau_{w\to d} = 6$ ps, $\tau_{wr} = 0.2$ ns, $\tau_{dr} = 0.4$ ns, $\tau_{d\to w} = 10$ ns, $\tau_{\mathrm{SHB}} = 100$ fs, $\tau_{\mathrm{CH}} = 300$ fs, $\varepsilon_{\mathrm{SHB}} = \varepsilon_{\mathrm{CH}} = 0.2$/Watt, and, $\Gamma = 0.15$.

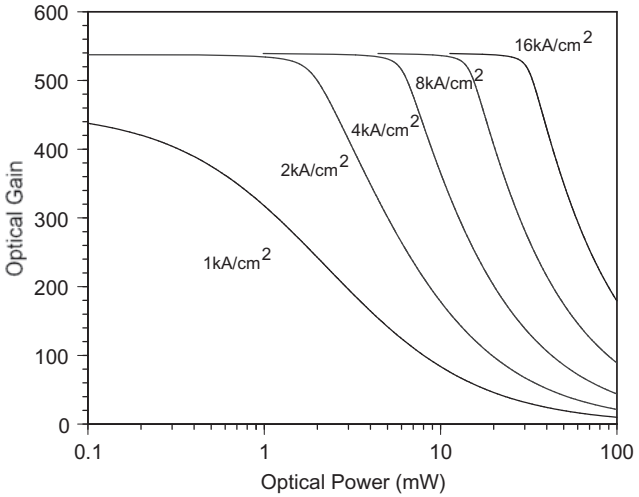

Fig. 11.4.2. Calculated optical gain as a function of output optical power for various injected current densities. The gain decreases at a higher power at higher current density [19].

The calculated gain and phase recovery curves following a 1.5 ps wide pulse with 2 pJ pulse energy for two injected current densities is shown in Fig. 11.4.3. The gain recovers faster at high current density.

11.4.2. *Gain dynamics — two state model*

A model of gain in quantum dot amplifiers using a two state model in the conduction band (excited state and ground state) has been developed [7]. It is interesting to show a comparison between the bulk and QD-SOA gain at various currents (Fig. 11.4.4).

In this model, the conduction band states (electrons) have essentially two confined states (ground state and excited state). The transition resulting in photon emission takes place from these states to the valence band. The wetting layer which is the buried InGaAsP layer has carriers injected into it by the injection current. These carriers make transition to the excited state followed by transition to the ground state (sequentially) in the conduction band as shown in Fig. 11.4.5.

Based on the model shown in Fig. 11.4.5, the pump current is injected solely onto the wetting layer of the device. If the direct

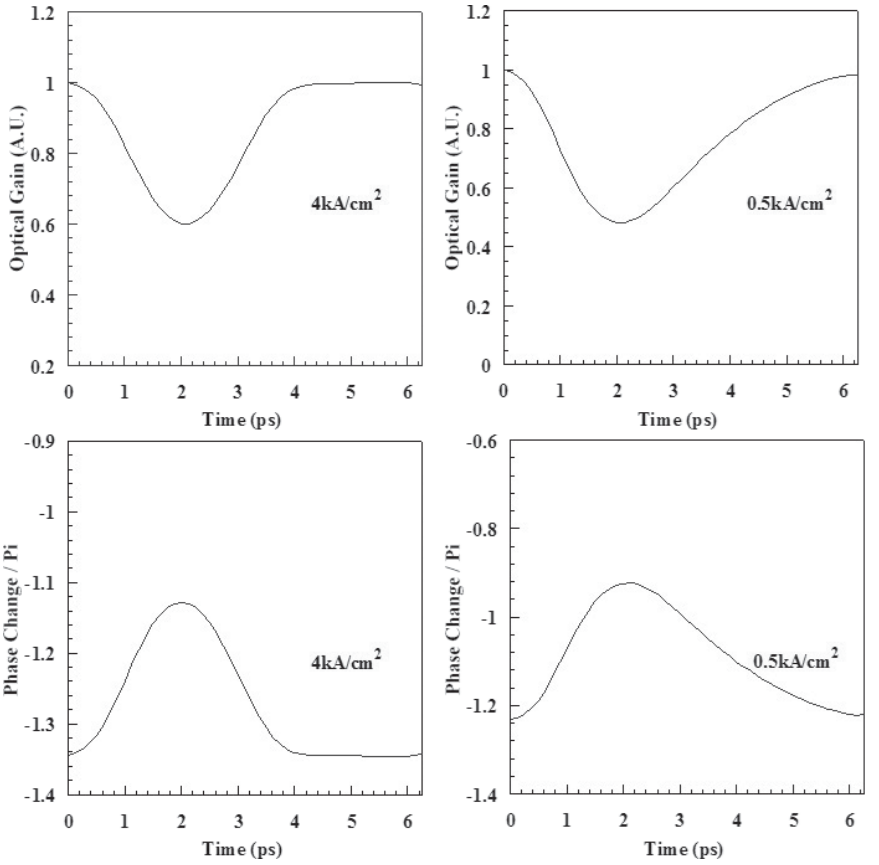

Fig. 11.4.3. Calculated gain and phase change following a 1.5 ps wide, 2 pJ pulse for two different current densities [19].

transition of carriers from the wetting layer to the QD ground state is neglected, the carrier dynamics between quantum dot states are described by the following rate equations:

$$\frac{dN_w}{dt} = \frac{I}{eV} - \frac{N_w}{\tau_{wr}} - \frac{N_w}{\tau_{w-e}}\left(1 - \frac{N_{es}}{N_{esm}}\right) + \frac{N_{es}}{\tau_{e-w}}\left(1 - \frac{N_w}{N_{wm}}\right), \tag{11.4.14}$$

$$\frac{dN_{es}}{dt} = -\frac{N_{es}}{\tau_{esr}} + \frac{N_w}{\tau_{w-e}}\left(1 - \frac{N_{es}}{N_{esm}}\right) - \frac{N_{es}}{\tau_{e-w}}\left(1 - \frac{N_w}{N_{wm}}\right)$$

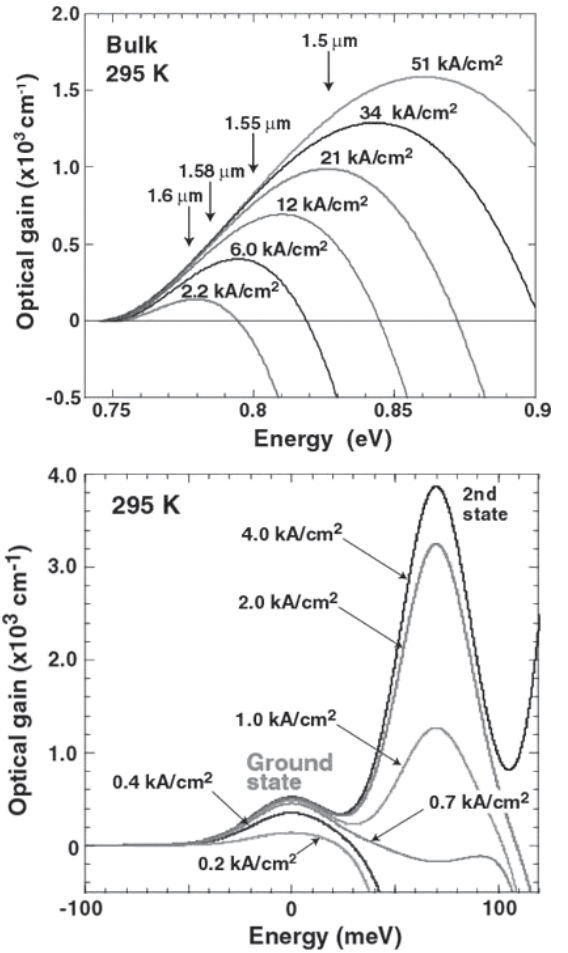

Fig. 11.4.4. The calculated gain at various currents for regular bulk active region (top) and quantum dot SOA (bottom) [7]. At low currents the ground state (GS) of QD is occupied, and GS transition high gain. At higher currents, the higher gain is from the excited state.

$$+\frac{N_{gs}}{\tau_{g-e}}\left(1-\frac{N_{es}}{N_{esm}}\right)-\frac{N_{es}}{\tau_{e-g}}\left(1-\frac{N_{gs}}{N_{gsm}}\right), \tag{11.4.15}$$

$$\frac{dN_{gs}}{dt}=-\frac{N_{gs}}{\tau_{gsr}}-\frac{N_{gs}}{\tau_{g-e}}\left(1-\frac{N_{es}}{N_{esm}}\right)+\frac{N_{es}}{\tau_{e-g}}\left(1-\frac{N_{gs}}{N_{gsm}}\right)$$
$$-\frac{\Gamma_d}{A_d}a\left(2\frac{N_{gs}}{N_{gsm}}-1\right)\frac{S(t)}{\hbar\omega}, \tag{11.4.16}$$

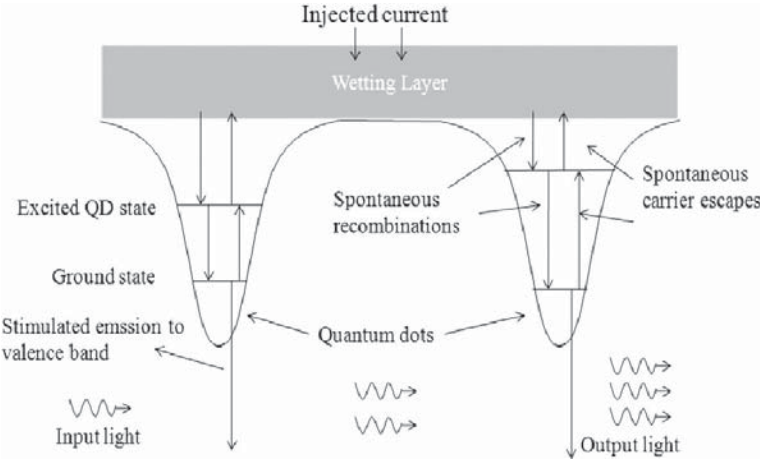

Fig. 11.4.5. The energy levels and carrier transition diagram of InAs/InGa AsP/InP QD-SOA. This two QD level model is used here in the gain dynamics model.

where N_w, N_{es} and N_{gs} are the carrier density of the wetting layer, QD excited state and QD ground state, respectively. Γ_d is the confinement factor of the active layer. A_d is the effective cross-section area of the quantum dot layer, I is the injected current, V is the volume of the active layer, a is differential gain, $S(t)$ is photon density in the active region. τ_{wr}, τ_{esr} and τ_{gsr} are the carrier lifetimes of the energy levels, respectively as follows; τ_{a-b} is the carrier relaxation time from QD energy level a to level b (a, b being "w", "e" or "g" for wetting layer, excited state and ground state, respectively).

The Eqs. (11.4.14) to (11.4.16) are simplified by normalizing all the terms using the maximum density of carriers in each state N_{wm}, N_{esm} and N_{gsm}, i.e.,

$$w = \frac{N_w}{N_{wm}}, \tag{11.4.17}$$

$$h = \frac{N_{es}}{N_{esm}}, \tag{11.4.18}$$

$$f = \frac{N_{gs}}{N_{gsm}}. \tag{11.4.19}$$

Using (11.4.14) to (11.4.16), the rate equations in the above quantities are:

$$\frac{dw}{dt} = \frac{I}{eVN_{wm}} - \frac{w}{\tau_{wr}} - \frac{w}{\tau_{w-e}}(1-h) + \frac{N_{esm}}{N_{wm}}\frac{h}{\tau_{e-w}}(1-w), \tag{11.4.20}$$

$$\frac{dh}{dt} = -\frac{h}{\tau_{esr}} + \frac{N_{wm}}{N_{esm}}\frac{w}{\tau_{w-e}}(1-h) - \frac{h}{\tau_{e-w}}(1-w) + \frac{N_{gsm}}{N_{esm}}\frac{f}{\tau_{g-e}}(1-h) - \frac{h}{\tau_{e-g}}(1-f), \tag{11.4.21}$$

$$\frac{df}{dt} = -\frac{f}{\tau_{gsr}} - \frac{f}{\tau_{g-e}}(1-h) + \frac{N_{esm}}{N_{gsm}}\frac{h}{\tau_{e-g}}(1-f) - \frac{\Gamma_d}{A_d}a(2f-1)\frac{1}{N_{gsm}}\frac{S(t)}{\hbar\omega}, \tag{11.4.22}$$

where w, h and f are the occupation probabilities of the wetting layer, the QD excited state and ground state, respectively;

11.4.3. *Gain recovery results*

Using the above rate equations, the temporal gain of the device has been studied under single pulse injection. The input light field intensity $S(t)$ is centered at $t = 0$ with a pulse width of 2 ps. The result for different pulse energies are shown in Fig. 11.4.6.

Figure 11.4.6(a) shows that the wetting layer occupation probability is not significantly changed by single pulse input. The QD excited state takes a longer time (FWHM ∼3.1 ps) to recover than the QD ground state (FWHM ∼2.2 ps). The short excited state to ground state (ES-GS) transition time constant ($\tau_{e-g} \sim 1$ ps) of the quantum dots suggests that the carrier density of the ground state recovers (mostly within the pulse duration) for pulses wider than 1 ps, resulting in a population response and gain response with little pattern effect. Figure 11.4.6(b) shows the gain response and gain recovery of the device (active layer length = 1 mm) under single pulse input for 3 different pulse energies. In the figure, the linear gain of

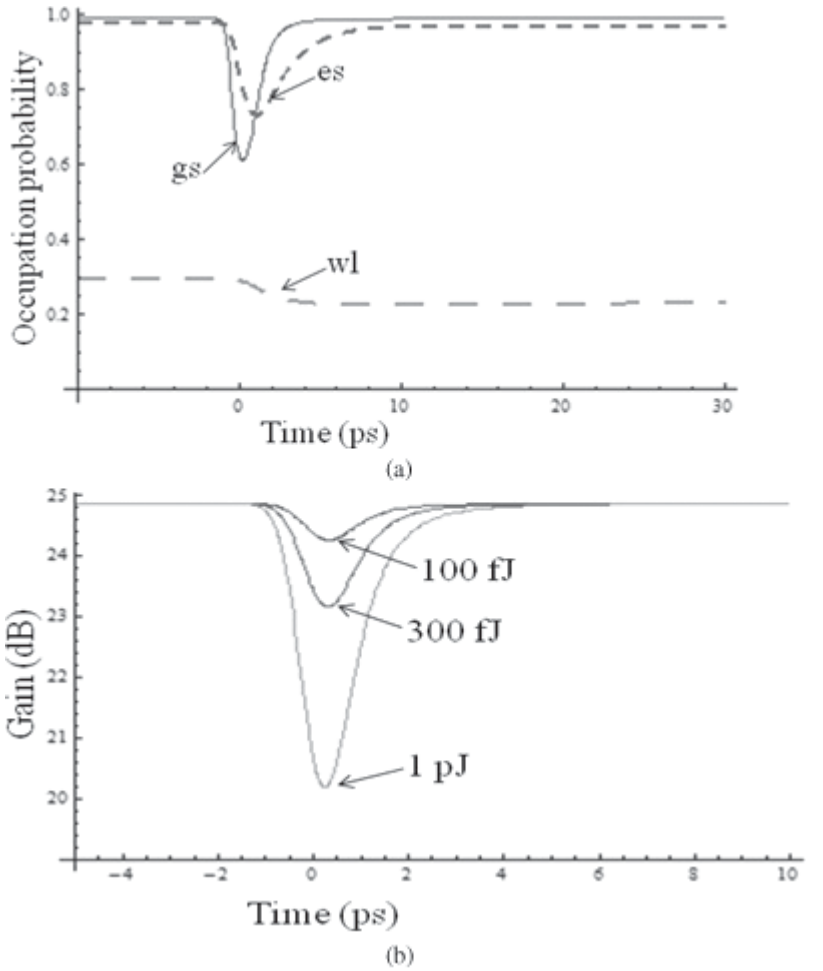

Fig. 11.4.6. (a) Calculated occupation probability dynamics for wetting layer, QD excited state and ground state; (b) Temporal gain for three pulse energies.

the device is determined by:

$$g_l = \Gamma_d a(N_g - N_t), \tag{11.4.23}$$

where a is the gain coefficient of the device, and N_t is the transparency carrier density of QD ground state, and N_g is the density of ground state population.

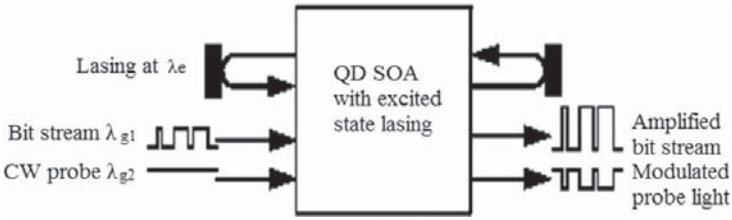

Fig. 11.4.7. Schematic of the cross gain modulation with ground state gain. The figure also shows excited state lasing with mirrors [13].

The gain recovery time is important for cross-gain modulation (XGM) which is essential for functional applications (described in Sec. 11.5) such as wavelength conversion. The gain recovery time is limited by carrier relaxation times from wetting layer to excited state and from excited state to the ground state. It has been suggested that since the relaxation time from excited state to ground state is short (∼0.1 ps), the gain recovery can be faster by simultaneous excited state lasing along with ground state based XGM [13]. Lasing can be induced at the excited state wavelength by adding appropriate wavelength selective mirrors to the QD-SOA. The schematic of this process is illustrated in Fig. 11.4.7. The excited state lasing provides energy storage for the QD excited state, and, maintains the excited state inversion which reduces low frequency pattern effects.

The above process has been examined using the rate equation model. The small signal response of XGM has been derived [13]. The QD-SOA without excited state lasing shows kinks in the response at lifetimes corresponding to the wetting layer and carrier capture (Fig. 11.4.8). The QD-SOA with excited state lasing shows a flat response from DC to ∼1 THz. The flat response is important for XGM at THz frequencies.

11.5. Functional Performance

Among the functional performance of SOAs are amplification in digital transmission systems, wavelength conversion and optical demultiplexing. These functions have been demonstrated using QD-SOAs

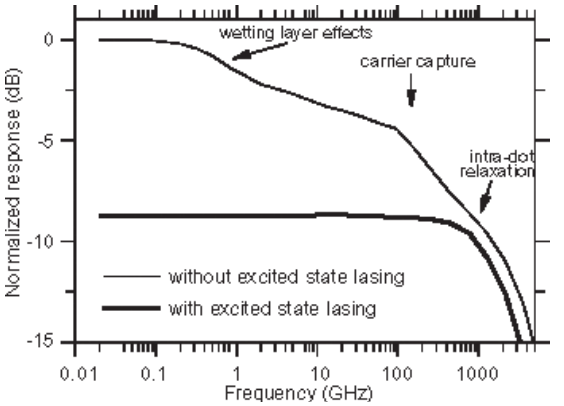

Fig. 11.4.8. Calculated frequency response of cross gain modulation (XGM) in QD-SOA. The time constants used for the excited to ground state relaxation and carrier capture into the excited state were 100 fs and 2 ps in the model [13].

[11–21, 28–42] and discussed in previous chapters using regular SOAs. QD-SOAs due to their faster gain recovery are capable of higher speed performance.

11.5.1. *Amplification*

QD-SOAs have a faster response to changes in gain i.e. the gain recovers faster compared to a SOA with quantum well active region (QW-SOA) or SOA with bulk active region. As mentioned earlier, this is due to the fast transfer of carriers from the wetting layer. This results in high-quality waveform for QD SOAs operating as an amplifier in the gain saturated regime. Eye diagrams after amplification of 40 Gb/s signals are shown in Fig. 11.5.1. The eye-diagrams from left to right are for input signal, amplified signal using QD-SOA and amplified signal using QW-SOA respectively. The amplified signals in QD and QW SOAs are both for 2.5-dB gain saturation. The QD-SOA emits near 1550 nm. Results of a bit-error-rate (BER) measurement at 10 Gb/s for an amplification experiment using QD-SOA and QW-SOA operating as an amplifier is shown in Fig. 11.5.1. The QW-SOA shows pattern effect.

A comparison of BER measurements of QD-SOA and MQW-SOA has been reported. Both of these devices emit near 1550 nm. The data

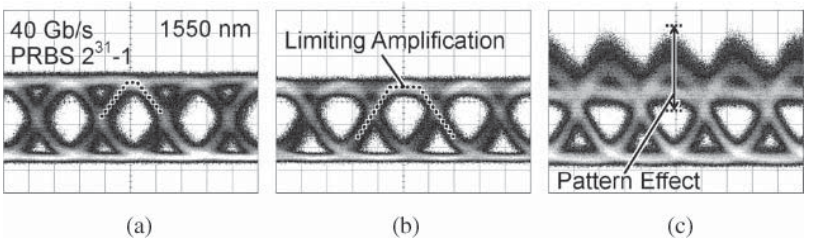

Fig. 11.5.1. Eye diagrams for 40-Gb/s input signal and signals amplified in QD and QW SOAs. (a) Input. (b) Quantum dot. (c) Quantum well [11].

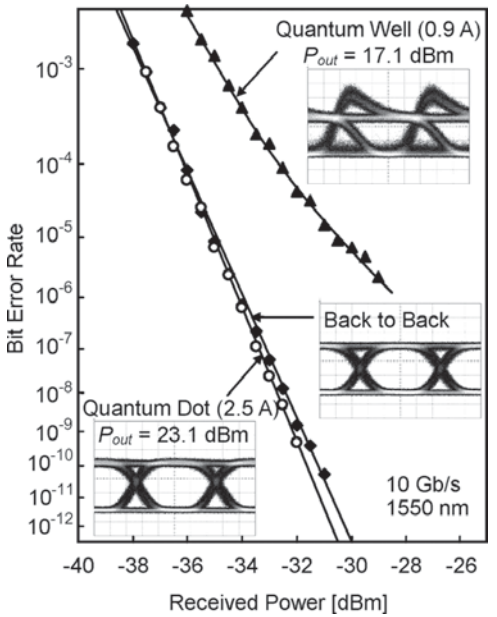

Fig. 11.5.2. Bit-error-rate measurements after amplification for QD-SOA and QW-SOA operating in the gain saturated regime. The QD-SOA operates error free at a relatively high output power of ∼23 dBm [11].

for a 10 Gb/s transmission experiment is shown in Fig. 11.5.2. The experiments were carried out in the gain saturated regime when the amplifier output power is high. This is relevant point of comparison because this illustrates use in multichannel WDM transmission system. The QD-SOA shows good performance to powers of ∼23 dBm where as for the MQW-SOA a performance reduction (as illustrated

by higher BER and bending of BER curve) is observed at ∼17 dBm. For The QD-SOA the back-to-back (without amplification) result is similar to that for after amplification. Also, clear eye diagrams are observed before and after amplification.

QD-SOA emitting near 1300 nm has been used in transmission experiments as amplifiers [14]. The BER measurement of a QD-SOA used as an amplifier is shown in Fig. 11.5.3. The experiment is for a 42.7 Gb/s Non-return-to-zero (NRZ) on-of-keying (OOK) modulation. The BER data after transmission through 45 km, 75 km single

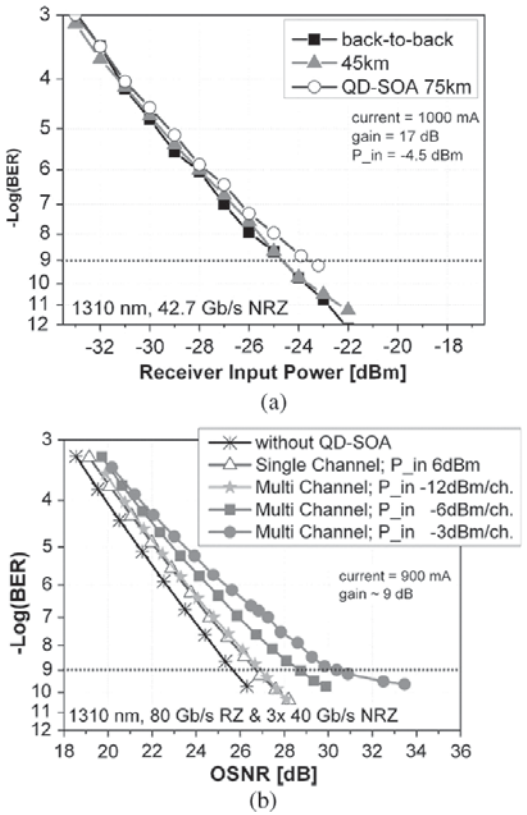

Fig. 11.5.3. (a) Measured BER for an amplification experiment using QD-SOA with gain near 1300 nm. The SOA gain was 17 dB and the data rate is 42.7 Gb/s. (b) Measured BER for a multichannel amplification experiment (at 40 Gb/s) and for single channel 80 Gb/s amplification experiment [14].

mode fiber is shown in Fig. 11.5.3(a). Also shown is the back to back data. Error free amplification is observed. The QD-SOA was also used as a booster amplifier at a higher data rate (80 Gb/s) and for multichannel amplification. The 80 Gb/s data was generated by time division multiplexing of two 40 Gb/s data streams. For the multichannel WDM transmission, the 3 data wavelengths used were 1300, 1305 and 1310 nm respectively. The BER measurements are demonstrated in Fig. 11.5.3(b).

11.5.2. *Cross gain modulation and wavelength conversion*

Wavelength conversion using cross gain modulation (XGM) in QD-SOA has been studied. In this process, a higher power signal (carrying data is injected into SOA) saturates the gain of the amplifier at "1's" compared to that at "0's". This saturation reduces the gain of a probe signal (injected into the amplifier at a different wavelength) at "1's" compared to that at "0's". This leads to a data transfer from the pump wavelength to the probe wavelength in an inverted form i.e. 1's become 0's and vice versa. For error-free data transfer, the XGM process needs to be fast.

The small signal response of a QD-SOA has been reported [15]. The data is shown in Fig. 11.5.4. A sine wave modulated pump signal and a CW probe signal is injected into the QD-SOA in this case

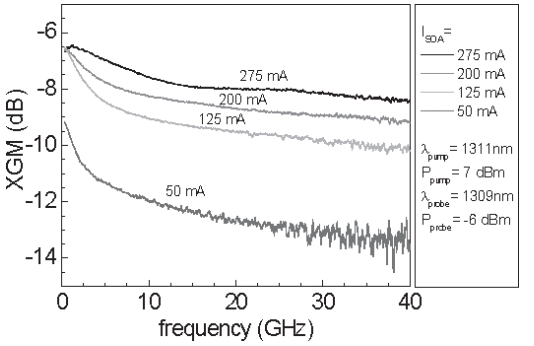

Fig. 11.5.4. Small signal response of cross gain modulation of a QD-SOA for various injection currents [15].

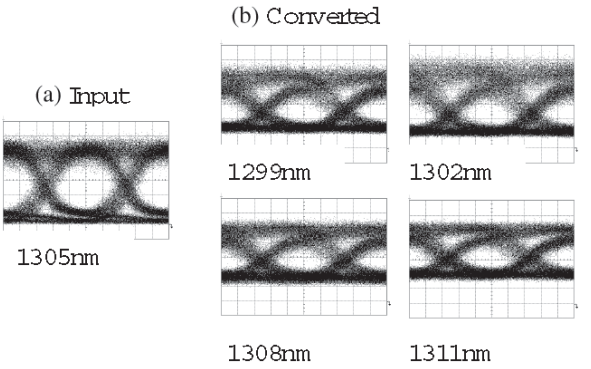

Fig. 11.5.5. Eye diagram of wavelength conversion results at 40 Gb/s. The input signal is at 1305 nm, the converted data are at different wavelengths [11].

and the transferred modulation to the probe signal as a function of modulation frequency is measured.

Figure 11.5.5 shows the eye patterns for wavelength conversion based on the cross-gain modulation at 40 Gb/s. The eye patterns of the wavelength converted lights for various wavelengths were measured [11]. The converted patterns have clear eye-openings, which is not achievable by SOAs using bulk or QW active regions at the bit-rate of 10–40 Gb/s. The slow decay at the offset can be suppressed at higher injection currents [11].

Simultaneous wavelength conversion from data at one wavelength to multiple wavelengths using QD SOA has been demonstrated [16]. The system operates near 1550 nm i.e. QD SOA has a broad gain spectrum centered near 1550 nm. The quantum dot active region was grown on a n-type InP (100 oriented) substrate by metal-organic vapour-phase epitaxy [16]. In the active region, five-fold stacked InAs QD layers separated by a 40 nm-thick of InGaAsP ($\lambda = 1.25\,\mu$m) were placed in the centre of a 500 nm-thick lattice-matched InGaAsP ($\lambda = 1.25\,\mu$m) waveguide core. The SOA length was 2.2 mm. The active region optical waveguide was tilted by 7° and the chip facets were antireflection coated. The tilted waveguide is needed for reducing the effective facet reflectivity. The QD-SOA chip was bonded and mounted to a thermoelectric controlled mount.

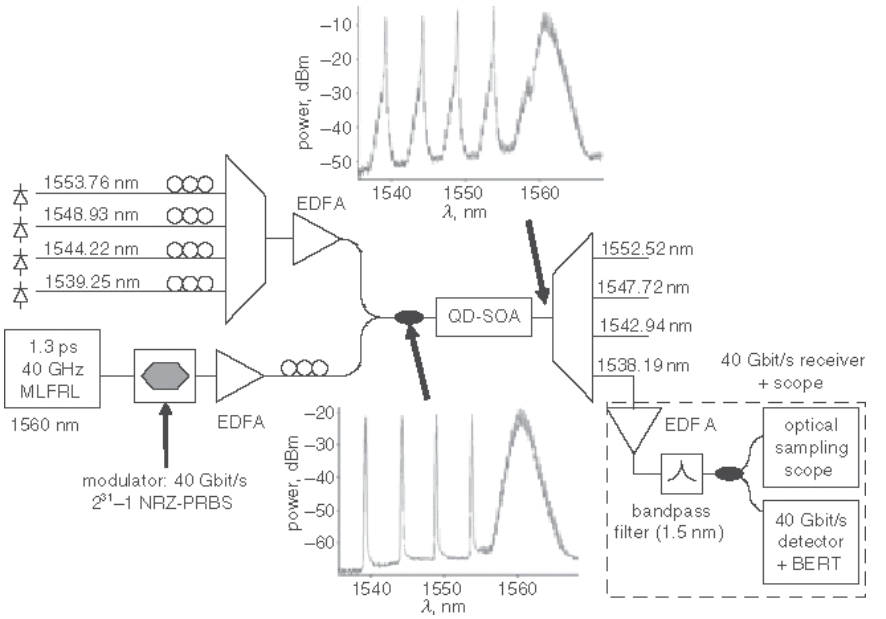

Fig. 11.5.6. Schematic of a wavelength conversion experiment [16].

The schematic of the experiment is shown in Fig. 11.5.6 [16]. The schematic shows data transfer at 40 Gb/s from 1560 nm wavelength simultaneously to four separate wavelength. The latter are obtained from four diode lasers, the output of these lasers are combined using a 4×1 multiplexer and then amplified using an erbium doped fiber amplifier (EDFA) prior to injection into a QD-SOA along with the data carrying signal at 1560 nm. The 40 Gb/s data is generated using a mode locked laser operating at 40 GHz and a modulator. The spectrum of the signals both at the input and output of QD-SOA is also shown. The output signal is separated into separate wavelengths using an optical demultiplexer and is analyzed for error rate performance after going through a tunable bandpass filter.

Figure 11.5.7 shows the results of the BER measurement of all four wavelength converted signals.

Cross gain modulation in QD-SOA has been used to demonstrate wavelength conversion at 160 Gb/s. The QD-SOA in this case has a gain spectrum near 1550 nm. The experimental schematic

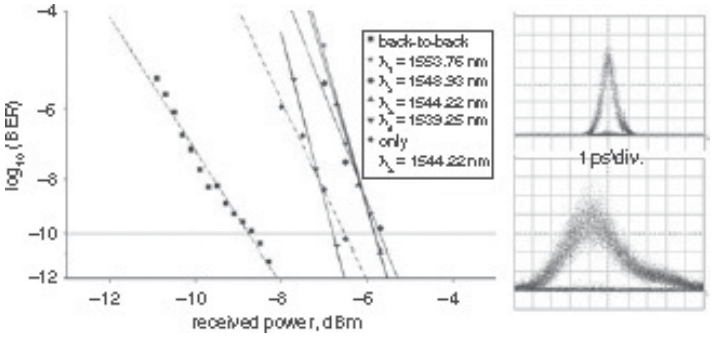

Fig. 11.5.7. BER data for all four channels and back–to–back results [16].

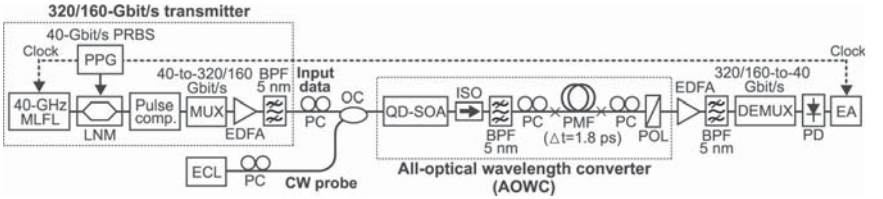

Fig. 11.5.8. Schematic of experimental setup. The 160 Gb/s data is used to show wavelength conversion by XGM and the 320 Gb/s data is used to show wavelength conversion using four wave mixing (FWM discussed in the next section) [17].

is shown in Fig. 11.5.8. The various elements in the set up are: Mode-locked fiber laser (MLFL), Pulse pattern generator (PPG), $LiNbO_3$ modulator (LNM), Multiplexer MUX), External-cavity laser-diode (ECL), Erbium-doped fiber amplifier (EDFA), Bandpass filter (BPF), Polarization controller (PC), Optical coupler (OC), Isolator (ISO), Polarization-maintaining fiber (PMF), Polarizer (POL), Demultiplexer (DEMUX), Photo-diode (PD), Error analyzer (EA). The wavelength of the input data and CW probe (converted) signals was 1545 nm and 1560 nm, respectively. The injected power into the QD-SOA of the pump and probe signals was 3.7 dBm and 6.9 dBm, respectively.

The BER at 160 Gb/s is measured by demultiplexing the data to four 40 Gb/s tributaries. The label best and worst (Fig. 11.5.8(a)) indicates best and worst BER performance among these tributaries. Figure 11.5.9 shows the BER characteristics of the 40-Gbit/s

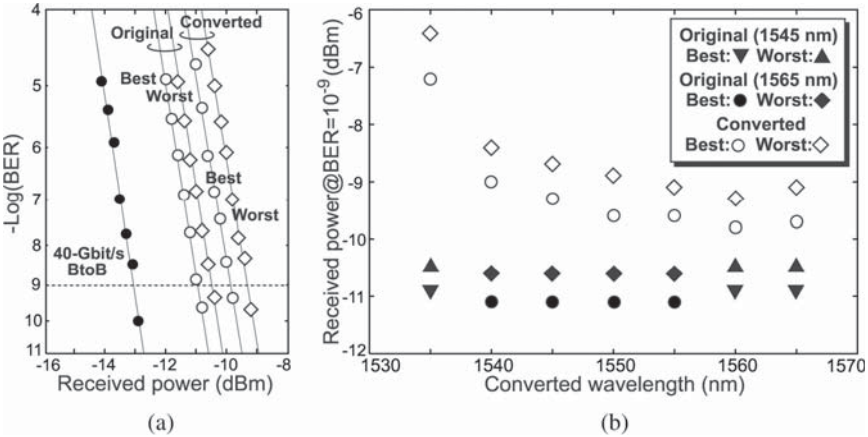

Fig. 11.5.9. (a) BER measurements of the 40 Gb/s wavelength converted signals, (b) Received power at BER $= 10^{-9}$ for wavelength conversion across the entire C-band [17].

back-to-back (B-to-B), 160-Gbit/s input data (original), and converted signals. In all the 40-Gbit/s tributaries, the power penalties for the error-free (BER $= 10^{-9}$) operation, between the original and converted signals were less than 1.6 dB. Figure 11.5.8(b) shows the error-free received powers of the original and converted signals over the entire C-band.

11.5.3. *Four-wave mixing*

As discussed in Ch. 8, four wave mixing (FWM) is an important process in semiconductor optical amplifiers (SOAs). It has been used in several optical network studies such as optical demultiplexing and wavelength conversion. These processes use high speed (∼40 to 400 Gb/s or higher) optical data streams as input to the SOA. The FWM efficiency decreases rapidly with increasing detuning i.e. increasing separation between the pump and signal wavelengths. The measured FWM intensity as a function of detuning Δf for QD-SOA and QW-SOA is shown in Fig. 11.5.10.

FWM has been used in wavelength conversion near 1300 nm. The QD-SOA used has optical gain near 1300 nm. Small signal modulation bandwidth of FWM signal has been measured [14] for 1300 nm

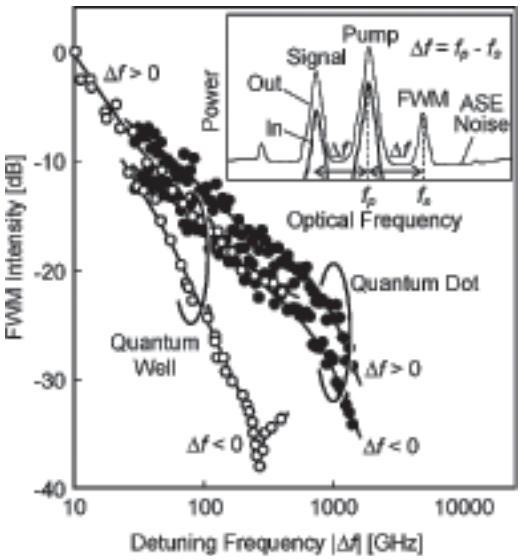

Fig. 11.5.10. Measured four wave mixing (FWM) efficiency for QD-SOA and QW-SOA as a function of detuning (separation between pump and signal wavelengths). The inset shows the spectrum of the output which includes the input pump, input signal and two FWM generated intensities [11].

QD-SOA. The data as a function of modulation frequency for various SOA currents is shown in Fig. 11.5.11 [14]. The data shows the FWM power increases with increasing SOA current as expected. Flat frequency response to 40 GHz is shown. The BER measurements for FWM based wavelength conversion from 1314 nm data at 40 Gb/s (OOK data) to 1309 nm is shown in Fig. 11.5.12 [14]. The pump input power (to QD-SOA) was 12 dBm and data signal input power was 6 dBm. The results appear to be better for down conversion.

Wavelength conversion at 320 Gb/s has been demonstrated using FWM in a QD-SOA. The experimental set up is shown in Fig. 11.5.8. In the 320-Gbit/s experiment, the wavelength of the input data and CW probe signals was 1545 nm and 1559 nm, respectively. The power of the input data and probe signals injected into the QD-SOA was 6.7 dBm and 6.9 dBm, respectively. The calculated conversion efficiency, which is defined as the power ratio between the input data

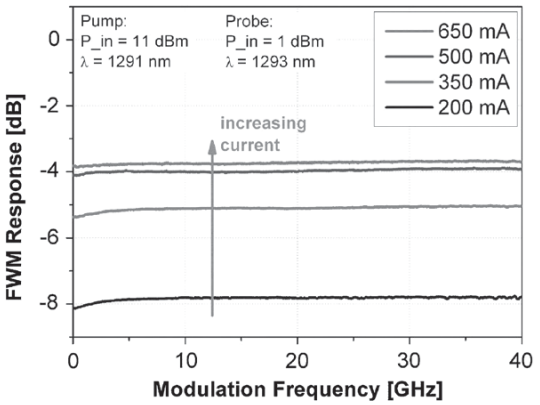

Fig. 11.5.11. FWM modulation response for various SOA currents [14].

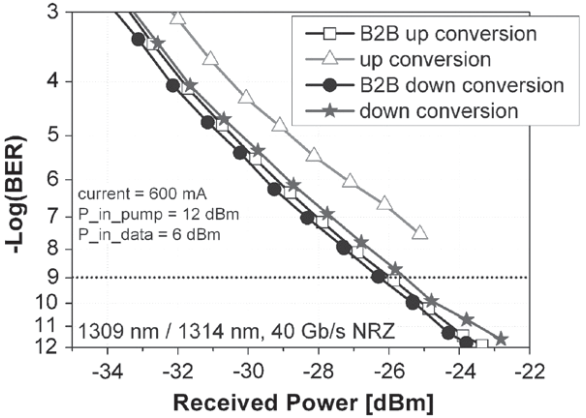

Fig. 11.5.12. BER vs. received power for wavelength conversion using FWM and a 1300 nm QD-SOA [14].

and converted signals, was −13 dB. The BER characteristics of the demultiplexed 40-Gbit/s input data (original) and converted signals were measured. For all the eight 40-Gbit/s tributaries, no error floors were observed. The average power penalty for BER $= 10^{-9}$ between the original and converted signals was approximately 4.2 dB. The result of the BER measurements is shown in Fig. 11.5.13.

Carrier density modulation and nonlinear gain effects (including dynamic carrier heating and spectral hole burning) in the SOA contribute to the generation of the FWM signal. When the wavelength

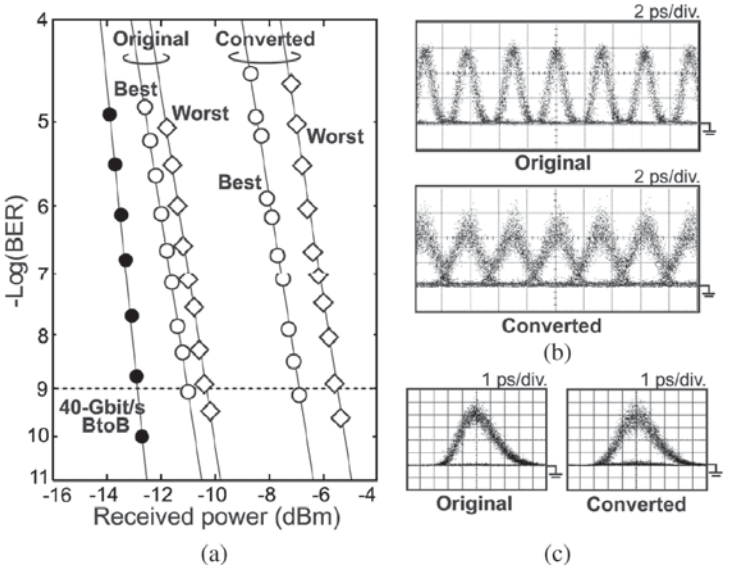

Fig. 11.5.13. (a) BER results of original and 40 Gb/s tributaries. (b) and (c) show the 320-Gbit/s pulse train and demultiplexed 40-Gbit/s eye patterns of the original and converted signals, respectively [17].

separation λ_d between the pump and the probe beams is larger than 1 nm, nonlinear gain effects dominate in the generation of FWM [21]. Since the effective time constant of the nonlinear gain effects is $\sim$0.6 ps [18], is significantly smaller than the time constant for carrier density modulation, it has been shown that the bandwidth of the FWM could reach as high as $\sim$1 THz [12,23]. The FWM bandwidth for QD-SOA has been calculated using the method described in Sec. 8.2.3.

A small signal modulated probe wave is injected into SOA to generate a modulated FWM wave. By comparing the modulation depth of the two waves, the bandwidth of the FWM process is determined. The wave form of continuous wave (CW) pump (ω_0), modulated probe (ω_1) and conjugate signal (ω_4) can be expressed by:

$$E_0(z,t) = E_0(z)\exp(-i\omega_0 t), \tag{11.5.1}$$

$$E_1(z,t) = [E_1(z) + q_1\exp(-i\omega_m t)]\exp(-i\omega_1 t), \tag{11.5.2}$$

$$E_4(z,t) = [E_4(z) + q_4\exp(-i\omega_m t)]\exp(-i\omega_4 t), \tag{11.5.3}$$

where the detuning between pump and probe is given by

$$\omega_d = \omega_0 - \omega_1 = \omega_4 - \omega_0. \tag{11.5.4}$$

It is assumed as in Ch. 8, $E_0 \gg E_1 \gg E_4$ and $E_1 \gg q_1$. By neglecting higher order small terms, the approximate total input optical intensity is:

$$S(t) = |E_0(z)|^2 + 2E_0^* E_1 \exp(-i\omega_d t) + 2E_0^* q_1 \exp[-i(\omega_d + \omega_m)t]. \tag{11.5.5}$$

Using this input wave form to rate equations (11.4.14-11.4.16), the response of the carrier density to the input pump and the modulated probe is studied. The solution of the equations has the same form as that of the input wave i.e.,

$$N_{es}(t) = \bar{N} + N_1 \exp(-i\omega_d t) + N_2 \exp[-i(\omega_d + \omega_m)t], \tag{11.5.6}$$

where the second term (N_1) produced by the interaction between the pump and the CW component of the probe is mostly responsible for the generation of CW four-wave mixing signal E_4, The third term (N_2) is due to the interaction between the pump and the modulated component of the probe, it is responsible for the small intensity modulation of the FWM signal q_4.

The wave equations describing the three wavelength component of the optical field in the QD-SOA are obtained by the procedures in [20–22] and that of Ch. 8. They are as follows:

$$\frac{dE_0}{dz} = \frac{1}{2} g(1 - i\alpha) E_0, \tag{11.5.7}$$

$$\frac{dE_1}{dz} = \frac{1}{2} g(1 - i\alpha) E_1, \tag{11.5.8}$$

$$\frac{dE_4}{dz} = \frac{1}{2} g(1 - i\alpha) E_4 - \frac{1}{2} g(1 - i\alpha) \frac{N_1}{\bar{N} - N_t} E_0, \tag{11.5.9}$$

$$\frac{dq_1}{dz} = \frac{1}{2} g(1 - i\alpha) q_1 - \frac{1}{2} a N_2 (1 - i\alpha) E_1, \tag{11.5.10}$$

$$\frac{dq_4}{dz} = \frac{1}{2}(1 - i\alpha)\left(gq_4 + aN_2E_4 - g\frac{N_1}{\bar{N} - N_t}\frac{q_1^* E_0}{E_1} - a\frac{N_1 N_2}{\bar{N} - N_t}E_0\right). \tag{11.5.11}$$

The ground state occupation probability at zero net gain (transparency) is $N_t = \frac{1}{2}N_{gsm}$, and a is the gain coefficient. The above set of equations along with the population rate equations are solved numerically. The results are shown in Fig. 11.5.14. QD-SOA parameters used are those generally reported experimental results for typical columnar InAs/InGaAsP/InP QD-SOA: relaxation lifetimes $\tau_{wr} = \tau_{esr} = 200\,\text{ps}$, $\tau_{gsr} = 50\,\text{ps}$, $\tau_{w-e} = 3\,\text{ps}$, $\tau_{e-w} = 0.3\,\text{ns}$, $\tau_{e-g} = 1.0\,\text{ps}$, $\tau_{g-e} = 10\,\text{ps}$, confinement factor $\Gamma = 10\%$, gain suppression factors $\varepsilon_{\text{CH}} = 0.5 \times 10^{-23}\,m^3$, $\varepsilon_{\text{SHB}} = 7.5 \times 10^{-23}\,m^3$, operating center wavelength $\lambda \sim 1550\,\text{nm}$, density of states $n_w = 5.4 \times 10^{17}\,\text{cm}^{-3}$, $n_w : n_e : n_g \cong 15 : 2 : 1$, differential gain $a = 8.6 \times 10^{-15}\,\text{cm}^2$ and effective active length $l = 1.0\,\text{mm}$ [23–24]. Results in Fig. 11.5.14 show that improvement in both FWM efficiency and FWM bandwidth is obtained by using QD-SOA compared to that for a typical bulk active SOA.

11.6. Optical Logic Performance

Optical logic circuits are being investigated by several research groups. Boolean optical logic operations and some simple logic circuits have been discussed previously in Chs. 9 and 10. In this section, results using QD based SOAs which have faster gain and phase recovery times are discussed.

In general, QD SOAs have low pattern effect at high data rates [24, 25], high saturated output power, low noise figure [25–27], fast relaxation speed between active region carrier states [28, 29] and a small carrier heating (CH) impact on gain and phase recovery times [30–33]. These features suggest that QD-SOA have good potential for application in high speed logic circuits. In this section, the previously described model of QD-SOA, which simulates two QD energy level carrier dynamics and nonlinear effects affecting the gain spectrum of the device [34–37], is used for the discussion of optical logic circuits. A simulation of fast all-optical logic gates including AND, XOR

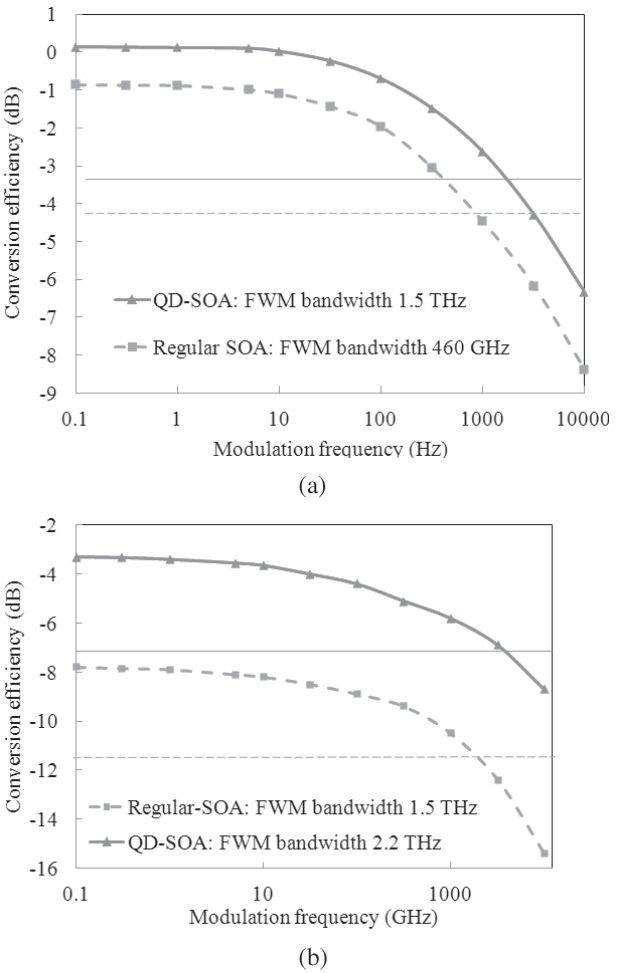

Fig. 11.5.14. Calculated small signal FWM conversion efficiency of QD-SOA, and regular bulk active SOA at: (a) Small pump-probe detuning ∼62.5 GHz (b) Large pump-probe detuning ∼1.25 THz [23].

and NOT has been carried out. These results show that QD-SOA is capable of supporting high speed operations up to 250 Gb/s with no pattern effects. The effect of device induced ASE noise is also discussed.

As discussed in Sec. 11.4 (in the two-state QD-SOA model), the carrier transitions between states is described by the following rate

equations:

$$\frac{dN_w}{dt} = \frac{I}{eV} - \frac{N_w}{\tau_{wr}} - \frac{N_w}{\tau_{w-e}}\left(1 - \frac{N_{es}}{N_{esm}}\right) + \frac{N_{es}}{\tau_{e-w}}\left(1 - \frac{N_w}{N_{wm}}\right), \tag{11.6.1}$$

$$\begin{aligned}\frac{dN_{es}}{dt} = &-\frac{N_{es}}{\tau_{esr}} + \frac{N_w}{\tau_{w-e}}\left(1 - \frac{N_{es}}{N_{esm}}\right) - \frac{N_{es}}{\tau_{e-w}}\left(1 - \frac{N_w}{N_{wm}}\right) \\ &+\frac{N_{gs}}{\tau_{g-e}}\left(1 - \frac{N_{es}}{N_{esm}}\right) - \frac{N_{es}}{\tau_{e-g}}\left(1 - \frac{N_{gs}}{N_{gsm}}\right),\end{aligned} \tag{11.6.2}$$

$$\begin{aligned}\frac{dN_{gs}}{dt} = &-\frac{N_{gs}}{\tau_{gsr}} - \frac{N_{gs}}{\tau_{g-e}}\left(1 - \frac{N_{es}}{N_{esm}}\right) + \frac{N_{es}}{\tau_{e-g}}\left(1 - \frac{N_{gs}}{N_{gsm}}\right) \\ &-\frac{\Gamma_d}{A_d}a\left(2\frac{N_{gs}}{N_{gsm}} - 1\right)\frac{S(t)}{\hbar\omega},\end{aligned} \tag{11.6.3}$$

where N_w, N_{es} and N_{gs} are the carrier density of the wetting layer, QD excited state and QD ground state, respectively. Γ_d is the confinement factor and a is the differential gain. The equations are simplified by normalizing all the carrier density terms using the maximum density of carriers in each of the states N_{wm}, N_{esm} and N_{gsm} as follows:

$$w = \frac{N_w}{N_{wm}}, \tag{11.6.4}$$

$$h = \frac{N_{es}}{N_{esm}}, \tag{11.6.5}$$

$$f = \frac{N_{gs}}{N_{gsm}}. \tag{11.6.6}$$

Substituting into (11.6.4 to 11.6.6), the rate equations are rewritten as:

$$\frac{dw}{dt} = \frac{I}{eVN_{wm}} - \frac{w}{\tau_{wr}} - \frac{w}{\tau_{w-e}}(1-h) + \frac{N_{esm}}{N_{wm}}\frac{h}{\tau_{e-w}}(1-w), \tag{11.6.7}$$

$$\frac{dh}{dt} = -\frac{h}{\tau_{esr}} + \frac{N_{wm}}{N_{esm}}\frac{w}{\tau_{w-e}}(1-h) - \frac{h}{\tau_{e-w}}(1-w)$$
$$+\frac{N_{gsm}}{N_{esm}}\frac{f}{\tau_{g-e}}(1-h) - \frac{h}{\tau_{e-g}}(1-f), \tag{11.6.8}$$

$$\frac{df}{dt} = -\frac{f}{\tau_{gsr}} - \frac{f}{\tau_{g-e}}(1-h) + \frac{N_{esm}}{N_{gsm}}\frac{h}{\tau_{e-g}}(1-f)$$
$$-\frac{\Gamma_d}{A_d}a(2f-1)\frac{1}{N_{gsm}}\frac{S(t)}{\hbar\omega}. \tag{11.6.9}$$

The gain dynamics in the QD-SOA include the contribution from the carrier density pulsation dynamics and nonlinear processes including carrier heating (CH) and spectral hole-burning (SHB) effect. The gain in QD-SOA is given by,

$$g_l = \Gamma_d a(N_g - N_t), \tag{11.6.10}$$

where N_t is the transparency carrier density (zero gain) of the QD ground state. The time dependent gain including nonlinear carrier heating (CH) and spectral hole burning (SHB) effects is expressed as:

$$g(t) = g_l + \Delta g_{\mathrm{CH}} + \Delta g_{\mathrm{SHB}}. \tag{11.6.11}$$

To a first approximation, Δg_{CH} and Δg_{SHB} are proportional to instantaneous light intensity $S(t)$.

$$\Delta g_{\mathrm{CH}} = -\varepsilon_{\mathrm{CH}} g S(t), \tag{11.6.12}$$
$$\Delta g_{\mathrm{SHB}} = -\varepsilon_{\mathrm{SHB}} g S(t), \tag{11.6.13}$$

where ε_{CH} and ε_{SHB} are the gain suppression factors of carrier heating and spectral hole burning effect, respectively. Using (11.6.11–11.6.13), [9, 10, 23]:

$$g(t) = \frac{a(N - N_t)}{1 + (\varepsilon_{\mathrm{CH}} + \varepsilon_{\mathrm{SHB}})S(t)}. \tag{11.6.14}$$

The carrier heating also changes the refractive index of the active region, and thus it induces a phase change to an injected probe wave.

$$\phi(t) = -\frac{1}{2}(\alpha G_l(t) + \alpha_{\mathrm{CH}}\Delta G_{\mathrm{CH}}(t)), \tag{11.6.15}$$

where $G_l(t) = e^{g(t)l}$ is the integrated gain of the device with l being the effective length of the active layer, α and α_{CH} are the regular linewidth enhancement factor, and, the carrier heating linewidth enhancement factor, respectively [24–27]. The quantity α is given by

$$\alpha = -\frac{4\pi}{\lambda}\frac{d\eta/dn}{dg/dn}, \tag{11.6.16}$$

where η is the refractive index of the wavelength. For QD-SOAs, $\alpha_{\mathrm{CH}} \leq 1$.

11.6.1. *XOR, OR, AND optical logic operations*

Boolean logic operations XOR, OR, AND etc. have been previously defined and studied in Ch. 9 using SOA based Mach-Zhender interferometers (MZI).

The results using QD-SOA are now presented. The simulated results are obtained by solving rate equations described above using input light beam powers within the non-saturated regime of the SOA. QD-SOA parameters used here include reported experimental results on self-assembled columnar InAs/InGaAsP/InP QD-SOA: relaxation lifetimes $\tau_{wr} = \tau_{esr} = 200\,\mathrm{ps}$, $\tau_{gsr} = 50\,\mathrm{ps}$, $\tau_{w-e} = 3\,\mathrm{ps}$, $\tau_{e-w} = 300\,\mathrm{ps}$ [38], τ_{e-g} is initially set to 1.0 ps and will vary between 0.4 ps–5.0 ps for later studies, $\tau_{g-e} = 10\,\mathrm{ps}$, confinement factor $\Gamma = 10\%$, gain suppression factors $\varepsilon_{\mathrm{CH}} = 0.5\times10^{-23}\,\mathrm{m}^3$, $\varepsilon_{\mathrm{SHB}} = 7.5\times10^{-23}\,\mathrm{m}^3$ [39,40], linewidth enhancement factors $\alpha = 4$, $\alpha_{\mathrm{CH}} = 0.2$ [29,30], QD energy levels' densities of states $n_w = 5.4 \times 10^{17}\,\mathrm{cm}^{-3}$, $n_w : n_e : n_g \cong 15 : 2 : 1$ [41], stacked QD areal density is $7.5 \times 10^{10}\,\mathrm{cm}^{-2}$, CW saturated output power is 18 dBm around central wavelength of 1.55 μm, device differential gain $a = 8.6 \times 10^{-15}\,\mathrm{cm}^2$ [34–36] and effective length $l = 1.0\,\mathrm{mm}$, noise figure F = 7 dB [25].

Results of XOR, AND, OR logic operations are shown in Figs. 11.6.1, 11.6.2 and 11.6.3, respectively, 2^7-1 PRBS data signals are used as input, initial data SNR is set at 20 dB. The output eye-diagram is also plotted as inset in each figure to show qualitatively the output quality. Quantitative quality evaluation can be done using quality factor method, as described below.

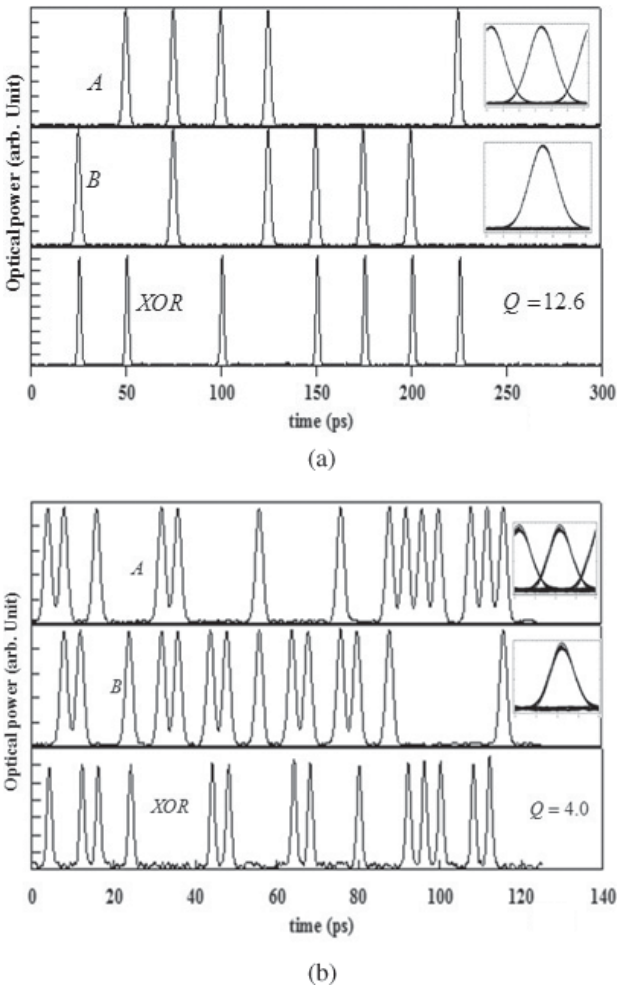

Fig. 11.6.1. A comparison of XOR result for (a) 40 Gb/s and (b) 250 Gb/s XOR operation. Insets are the simulated eye-diagram of the output XOR. The results show that the performance at 250 Gb/s is similar to that at 40 Gb/s [42].

The quality factor for the output data waveform can be expressed as $Q = \frac{S_1 - S_0}{\sigma_1 + \sigma_0}$, where S_0 and S_1 are the average value for all the "1's" and "0's" in the output, respectively; and σ_0 and σ_1 are their standard deviations. The quality factor is related to the BER of the logic operation as, $BER \approx \exp(-Q^2/2)/Q\sqrt{2\pi}$. Since the mechanism for

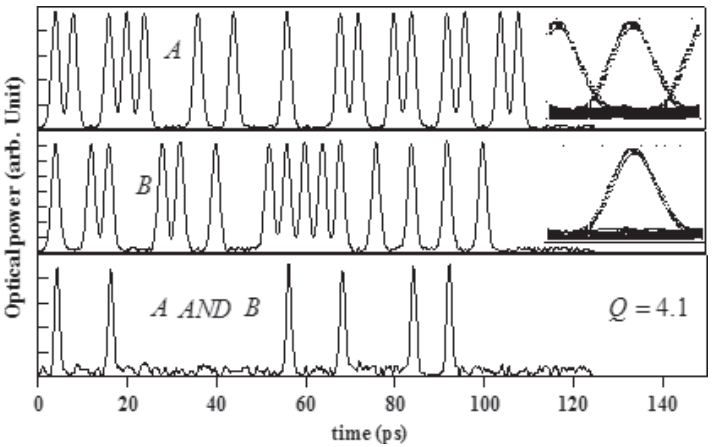

Fig. 11.6.2. Simulated result for all-optical AND gate operating at 250 Gb/s. Insets are eye diagrams and corresponding quality factor Q for the output AND [42].

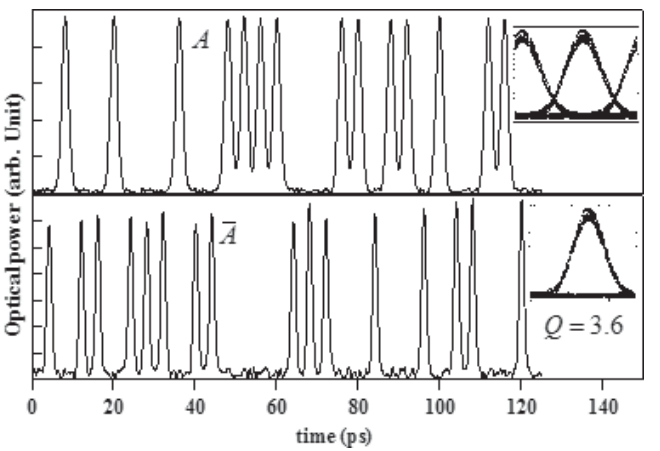

Fig. 11.6.3. Simulated results for all-optical NOT gate operating at 250 Gb/s. Up: data stream$A$, down: inverted data $\bar{A}$. Insets are eye diagrams and corresponding quality factor Q for output wave [42.43].

the three different types of logic gates are similar, similar dependence of Q on various parameters for different gates are expected. Thus the parametric dependence of Q is shown (in Fig. 11.6.4 and 11.6.5) for XOR operation only.

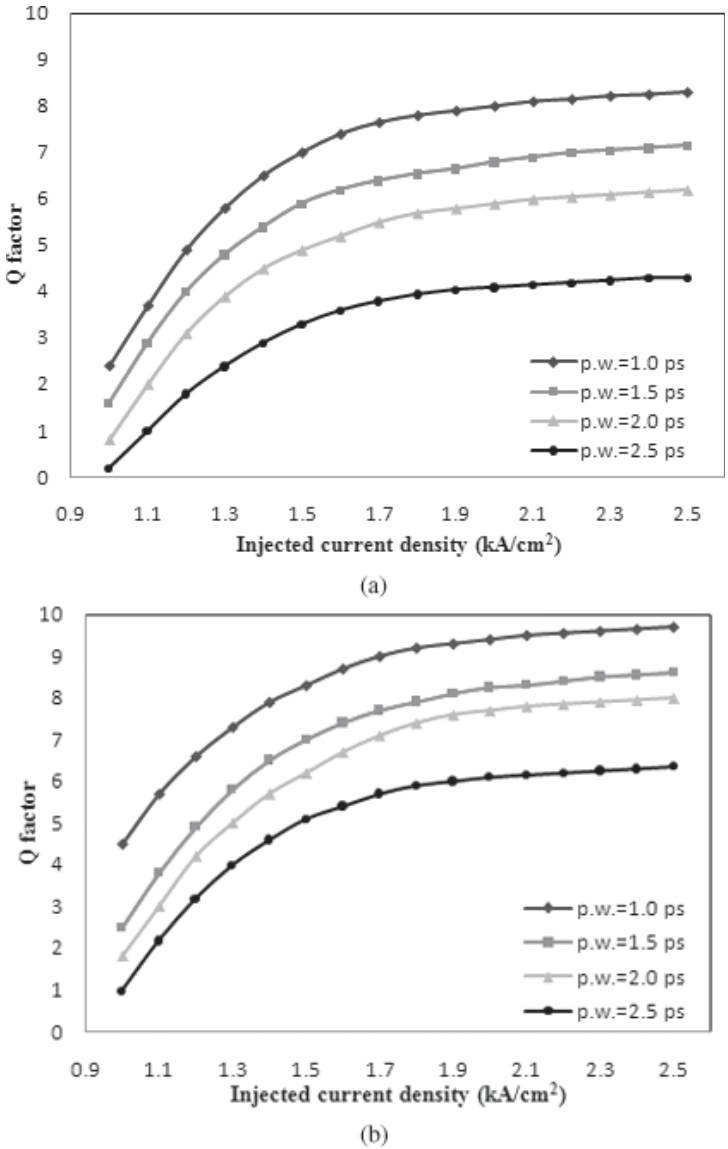

Fig. 11.6.4. Calculated quality factor Q for different pulse widths as a function of injected current density, single pulse energy is set to 0.5 pJ. (a) 250 Gb/s XOR operation (b) 160 Gb/s operation [42,43].

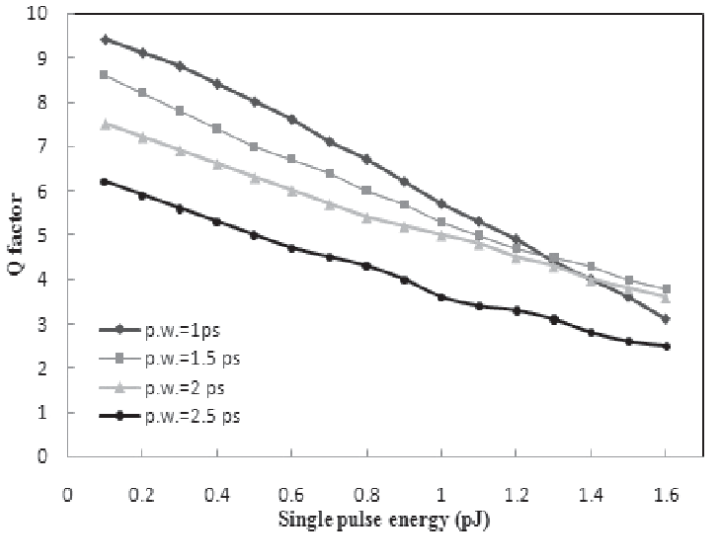

(a)

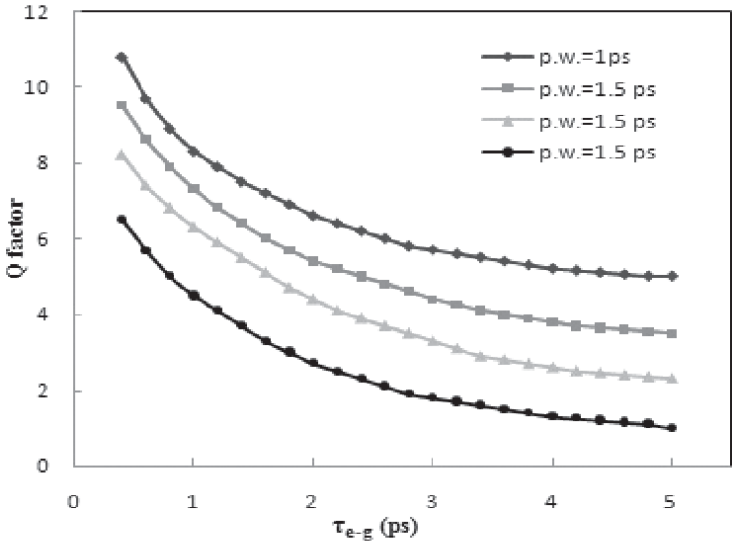

(b)

Fig. 11.6.5. Calculated quality factor, Q, (at 250 Gb/s) for different single pulse energies and transition lifetime from QD excited state to ground state. Injected current density is 1.8 kA/cm^2. (a): Q factor dependence on single pulse energy (b): Q factor dependence on excited state to ground state (ES to GS) transition lifetime [43].

The calculated quality factor shows significant dependence on injected current density, pulse width, single pulse energy, and, transition lifetime from QD excited state to ground state. Figure 11.6.4 shows the dependence of Q on injected current and pulse width, at high data rate. The input single pulse energy is set to 0.5 pJ so that the XOR operation takes place in the non-saturated regime of the QD-SOA. The results show that at low injected current density level ($J < 1.8\,\mathrm{kA/cm^2}$), the Q-factor is low and increases with increased current density.

This can be explained as follows: with increasing current density, more carriers are injected into the wetting layer, and hence each energy level in the quantum dot can recover faster to initial carrier density level after carrier depletion following optical pulse injection and amplification. This reduces the pattern effect considerably. For very high current density Q-values saturate. The smaller pulse width (less energy and hence less carrier depletion) also results in better performance (higher Q-value).

Figure 11.6.5 shows the calculated Q-factor as a function of single pulse energy and carrier transition lifetime between QD excited state and ground state. The calculation is done with an injected current density of $1.8\,\mathrm{kA/cm^2}$. The results show a decrease in output quality (Q-factor) with the increase in single pulse energy of the input data and τ_{e-g}. As single pulse energy increases, the carrier density of the active region of the device undergoes larger depletion, thus it takes longer to recover to initial level. The transition lifetime determines the speed of gain and phase recovery in the active region, thus Q-factor is higher for shorter transition times for high speed operation.

The above results show that QD-SOA based Mach-Zehnder Interferometer can perform logic operations such as AND, XOR and NOT at high speeds ($\sim$250 Gb/s).

11.6.2. *PRBS generator*

Pseudo-random binary sequence (PRBS) generators are important for a range of applications in a communication system which

includes testing, bit scrambling, bit de-scrambling. In all-optical communication network, one fundamental measurement is how accurately the receiver can determine the logic state of each received bit. In case the system cannot carry live traffic during the test, it is important to inject a known bit stream pattern to the device under test. The most common input test pattern is the pseudo-random binary sequence which is designed to approximate the truly random data [43].

A PRBS can be generated using a linear feedback shift register (LFSR). The PRBS sequence generated with a shift register of length m has a period of 2^{m}-1. To generate a stable optical PRBS sequence using LFSR, an optical XOR logic gate is needed. As discussed earlier (Sec. 11.6.1), the QD SOA-MZI based XOR gate is a suitable design for high data rate operation, ∼250 Gb/s [43].

For the scheme analyzed here, the PRBS signals are generated using a LFSR shown in Fig. 11.6.6. An LFSR has m data storing units (optical delay line in all-optical system), each unit is capable of storing one binary data bit for one clock period. The whole system is synchronized with a clock. At each period, the n_{th} and m_{th} bit go through an XOR process. Their XOR output pulses gets reshaped and its wavelength is converted back to system's operation wavelength using an AND gate, and then goes back to the front of LFSR. The output PRBS signals can be tapped as shown. Figure 11.6.6(b) shows the design of the logic functional unit. The main parts of this unit are two MZIs, each arm of which has a SOA with a QD active region. The first MZI serves as an all-optical logic XOR gate for the two bits (m, n), while the other MZI serves as logic AND gate. The band-pass-filter (BPF) reduces ASE noise from the XOR unit.

The principle of the logic XOR operation based on SOA-MZI has been discussed and analyzed earlier in Sec. 11.6.1. After a band-pass filter centered at λ_2, the XOR result of data 1 and 2 enters the input port "e" of a logic AND gate. The LSFR operation begins by using a trigger as input to one arm of the MZI (AND function). The clock signal (at wavelength λ_1 is injected into the center port. In the design shown, the XOR result is reshaped using an AND operation between

XOR result "1" bits. This bit "1" is from a clock pulse train centered at λ_1, injected to port "f." After another band-pass filter centered at λ_1, the AND result represents a reshaped replica of the XOR result, and its wavelength is converted back to that circulating in the LFSR. A simulated PRBS output operating at 250 Gb/s is shown in Fig. 11.6.7(a), its eye-diagram is also plotted in Fig. 11.6.7(b). The eye-diagram shows a clear open eye illustrating the stability of the scheme.

The PRBS sequence generated using this scheme has a repetition bit number of $T = 2^m - 1$. The PRBS sequences are different from truly random bit sequences in that the latter has a continuous spectrum while the former has a discrete spectrum with harmonics.

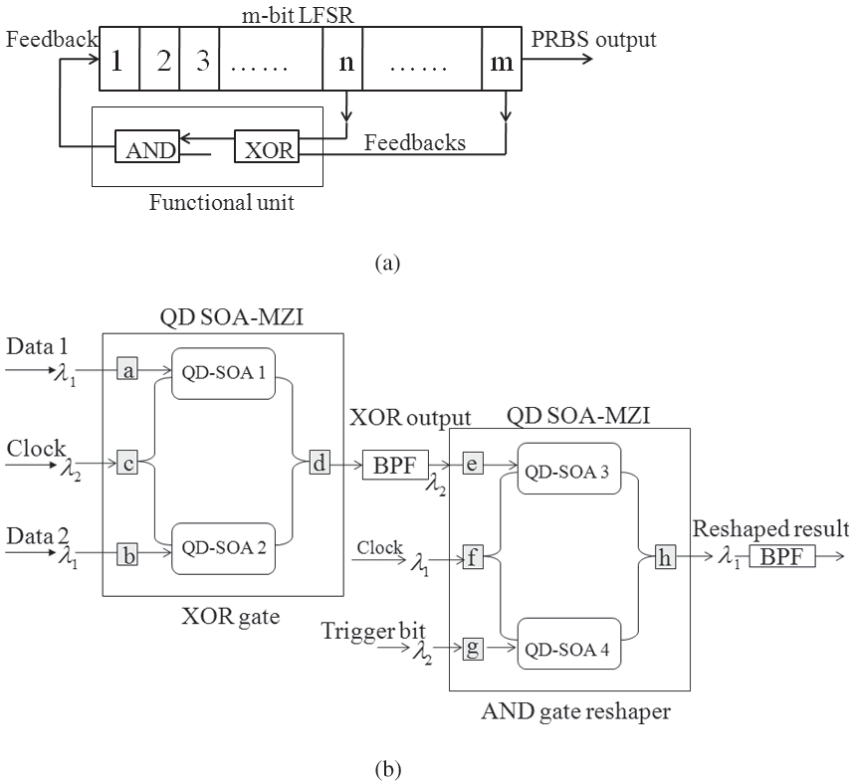

Fig. 11.6.6. Design of PRBS generator. (a): Block diagram of a LFSR (b): functional unit, including two QD-SOA MZIs operating as XOR and AND gate [43].

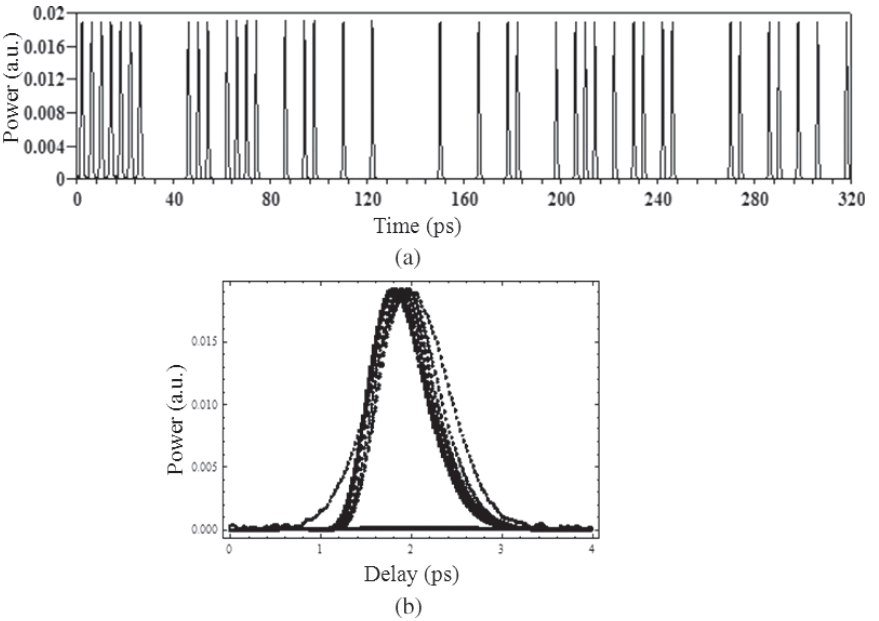

Fig. 11.6.7. (a) Simulation result of PRBS sequences generated using 7-bit LFSR, operating at 250 Gb/s; (b) The eye-diagram of this result. FWHM pulse width is 1.0 ps, injected current density is 1.8 kA/cm^2 [43].

As m increases the generated PRBS spectrum becomes more and more continuous and the output can better represent a truly random signal.

The QD-SOA i.e. semiconductor optical amplifier with a quantum dot region is an important device for high speed optical signal processing. Due to its high saturation power and fast gain and phase recovery times, several experimental results have shown better high speed performance of QD-SOAs compared to SOAs with bulk active or multiquantum well active region. Further studies and commercial applications of these devices are envisioned in the future.

References

[1] T. Akiyama, H. Kuwatsuka, T. Simoyama, Y. Nakata, K. Mukai, M. Sugawara, O. Wada and H. Ishikawa, *J. Quantum. Electron.* **37**, 1059 (2001).

[2] P. Borri, W. Langbein, J. Hvam, F. Heinrichsdorff, M-. Mao and D. Bimberg, *Phys. Stat. Sol.* **224**, 419 (2001).
[3] P. Borri, W. Langbein, J. M. Hvam, F. Heinrichsdorff, M-H. Mao and D. Bimberg, *IEEE Photon. Technol. Lett.* **12**, 594 (2000).
[4] M. Sugawara, N. Hatori, T. Akiyama, Y. Nakata and H. Ishikawa, *Jpn. J. Appl. Phys.* **40** L488 (2001).
[5] M. Sugawara, N. Hatori, T. Akiyama and Y. Nakata, *Proceedings of Indium Phosphide and Related Materials* **01**, 358 (2001).
[6] A. Sakamoto and M. Sugawara, *Photon. Tech. Lett.* **12**, 107 (2000).
[7] M. Sugawara, T. Akiyama, N. Hatori, Y. Nakata, Y. Otsubo and H. Ebe, *Proceedings of SPIE* **4905**, (2002).
[8] M. Sugawara, H. Ebe, N. Hatori, M. Ishida, Y. Arakawa, T. Akiyama, K. Otsubo and Y. Nakata, *Phys. Rev. B* **69**, Art. No. 235332 (2004).
[9] M. Sugawara, T. Akiyama, N. Hatori, Y. Nakata, H. Ebe and H. Ishikawa, *Meas. Sci. Technol.* **13**, 1683 (2002).
[10] A. Sakamoto and M. Sugawara, *IEEE Photon. Technol. Lett.* **12**, 107 (2000).
[11] T. Akiyama, M. Sugawara and Y. Arakawa, *Proceedings of IEEE* **95**, 1757 (2007).
[12] G. Contestabile, A. Maruta and K. Kitayama, *IEEE Photonic Tech. Lett.* **22**, 987 (2010).
[13] M. T. Gill, G. D. Khoe, P. Van Daele and H. J. S. Dorren, *Proc. Optical Fiber Comm.* (2004).
[14] H. Schmeckebier, C. Meuer, D. Bimberg, C. Schmidt-Langhorst, A. Galperin and C. Schubert, *Semicond. Sci. Technol.* **26**, 014009 (2011).
[15] D. Bimberg, C. Meuer, M. Laemmlin, S. Liebich, J. Kim, G. Eisenstein and A. R. Kovsh, *ICTON We. B* 2.3 (2008).
[16] O. Raz, J. Herrera, N. Calabretta, E. Tangdiongga, S. Anantathanasarn, R. Notzel and H. J. S. Dorren, *Electronic Letts.* **44**, 16 (2008).
[17] M. Matsuura, O. Raz, F. Gomez-Agis, N. Calabretta and H. J. S. Dorren, *Optics Express* **19**, B551 (2011).
[18] J. Kim and S. Chuang, *IEEE J. Quantum Electron.* **18**, 2538, (2006).
[19] H. Sun, Q. Wang, H. Dong and N. K. Dutta, *Optics Express* **13**, 1892 (2005).
[20] C. Wu, H. Fan and N. K. Dutta, *J. Appl. Phys.* **87**, 2076 (2000).
[21] K. Kikuchi, M. Kakui, C. E. Zah and T. P. Lee, *IEEE J. Quantum Electron.* **28**, 151 (1992).
[22] G. P. Agrawal, *J. Opt. Soc. Am. B* **5**, 147 (1988).
[23] S. Ma, Z. Chen and N. K. Dutta, *Proc. SPIE* **721**, 10 (2009).
[24] A. Uskov, T. Berg and J. Mork, *IEEE J. Quantum Electron.* **40**, 306 (2004).
[25] T. Akiyama and M. Sugawara, *Proceedings of the IEEE* **95**, 1757 (2007).
[26] A. Meccozi and J. Mork, *IEEE J. Sel. Top. Quant. Electron.* **3**, 1190 (1997).
[27] T. Berg and J. Mork, **40**, 1527 (2004).
[28] P. Reithmaier and G. Eisenstein, Frontier in Optics, OSA 92nd Annual meeting, Rochester, NY, (2008).
[29] P. Borri, W. Langbein. J. M. Hvam, F. Heinrichsdorff, M. H. Mao and D. Bimberg, *IEEE J. Quantum Electron.* **12**, 594 (2000).

[30] P. Borri, W. Langbein. J. M. Hvam, F. Heinrichsdorff, M. H. Mao and D. Bimberg, *IEEE J. Quantum Electron.* **6**, 544 (2000).
[31] P. Borri, W. Langbein, J. M. Hvam, F. Heirichsdorff, M. Mao and D. Bimberg, *Phys. Stat. Sol.* (b), **224**, 419 (2001).
[32] H. Sun, Q. Wang, H. Dong and N. K. Dutta, *Opt. Express* **13**, 1892 (2005).
[33] Y. B. Ezra, B. I. Lembrikov and M. Haridim, *IEEE J. Quantum Electron.* **45**, 34 (2009).
[34] T. Berg, S. Bischoff, I. Magnusdottir and J. Mork, *IEEE Photon. Tech. Lett.* **13**, 541 (2001).
[35] J. Kim and S. Chuang, *IEEE J. Quantum Electron.* **18** 2538, (2006).
[36] O. Quasaimeh, *IEEE J. Quantum Electron.* **16**, 993 (2004).
[37] M. Sugawara, T. Akiyama, N. Hatori, H. Ebe and H. Ishikawa, *Meas. Sci. Technol.* **13**, 1683 (2002).
[38] J. M. Vazquez, H. H. Nilsson, J. Zhang and I. Galbraith, *IEEE J. Quantum Electron.* **42**, 986 (2006).
[39] A. Uskov, E. O'Reilly, M. Laemmlin, N. Ledentsov and D. Bimberg, *Opt. Commun.* **248**, 211 (2005).
[40] X. Jia, Z. Wu and G. Xia, *IEEE J. Quantum Electron.* **43**, 1068 (2007).
[41] J. Kim and S. Chuang, *IEEE J. Quantum Electron.* **18**, 2538 (2006).
[42] S. Ma, Z. Chen, H. Sun and N. K. Dutta, *Proc. SPIE* **7211** OP (2009).
[43] S. Ma, H. Sun, Z. Chen and N. K. Dutta, *Optics Express* **17**, No. 21, 18469 (2009).

Chapter 12

Reflective Semiconductor Optical Amplifiers (RSOA)

12.1. Introduction

So far we have discussed primarily travelling wave semiconductor optical amplifiers and their applications. These devices have very low reflectivity coatings on both facets. Reflective semiconductor optical amplifiers (RSOAs) utilize a high reflectivity coating on one facet and an anti-reflective coating on the other facet to produce a gain medium. Its waveguide structure is similar to that of conventional SOA. RSOAs have high optical gain at low drive currents. RSOAs have shown promise for applications in wavelength division multiplexed passive optical networks (PONs) and in fiber ring mode-locked lasers [1–7].

Figure 12.1.1 shows a schematic diagram of a reflective semiconductor optical amplifier RSOA [1]. One facet of the SOA is antireflection (AR) coated to be used as both the input and output ports, and the other facet is high-reflection (HR) coated to produce high reflectivity. The injected input light is amplified and reflected back

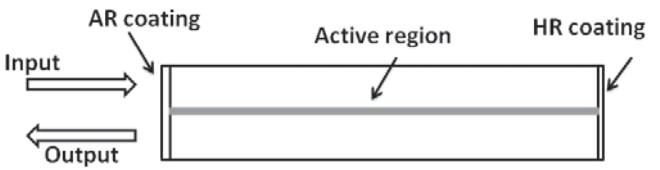

Fig. 12.1.1. Schematic of a reflective semiconductor optical amplifier (RSOA). One facet of the device is antireflection coated (AR) and the other facet is high reflection (HR) coated.

to the same port. A typical value of the fiber-to-fiber gain is ∼10 to 20 dB.

12.2. RSOA Performance

RSOAs have been fabricated both for the 1550 nm and 1300 nm wavelength region although most of the application related work has been reported in the 1550 nm region. Figure 12.2.1 shows the measured gain spectrum of a RSOA at various temperatures at an operating current of 40 mA. The peak gain increases and shifts to shorter wavelength with decreasing temperature as expected. The device has a buried heterostructure active region fabricated using the InP/InGaAsP material system. It has an input facet reflectivity of <0.01%. This low reflectivity results in a low gain ripple (<0.7 dB). The measurements reported in Fig. 12.2 were performed on an uncooled fiber coupled package (TO Can type).

The low input reflectivity in many designs utilize an angled active region waveguide for the input/output facet and a regular (normal to the facet) active region waveguide for the high reflectivity facet. The measured gain spectrum, noise figure and gain ripple of an angled

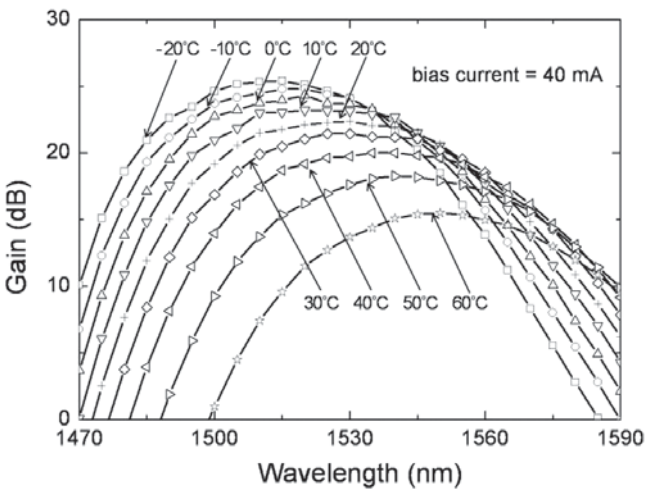

Fig. 12.2.1. Gain spectrum of a RSOA at various temperatures [8].

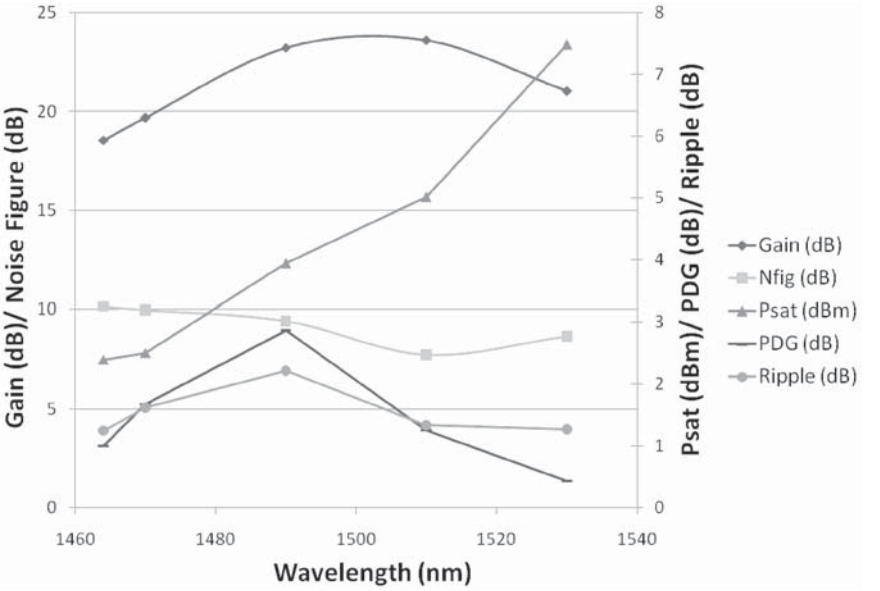

Fig. 12.2.2. The gain, noise figure, saturation power (P_{sat}), polarization dependent gain (PDG) and gain ripple [9].

waveguide device at 25°C is shown in Fig. 12.2.2. The device is 600 µm long and the operating current is 80 mA. The device shows high gain (>20 dB) from 1470 nm to beyond 1535 nm. The saturation power P_{sat}, which represents the maximum output power of the device is also shown, it is >7 dBm at 1530 nm. The noise figure, NF is ∼10 dB. The small signal polarization dependent gain (PDG) and gain ripple is likely to be smaller than that shown in Fig. 12.2.2 when the device is operated near saturation power.

RSOAs have been fabricated in the 1300 nm wavelength region using the InP/InGaAsP material system. A fiber to fiber gain of ∼30 dB has been demonstrated at ∼200 mA of operating current. The device is 400 µm long and has an active region with seven quantum wells [10].

RSOAs are typically packaged in a TO-can type package. This type of package is simple and is important for uncooled operation. The schematic of this fiber coupled package is shown in Fig. 12.2.3.

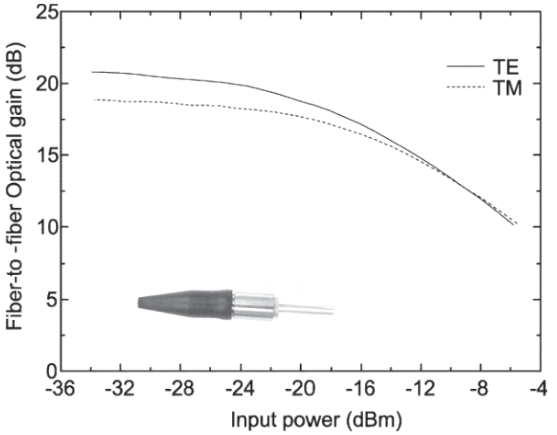

Fig. 12.2.3. Fiber-to-fiber optical gain of a RSOA. The inset shows a TO package [11].

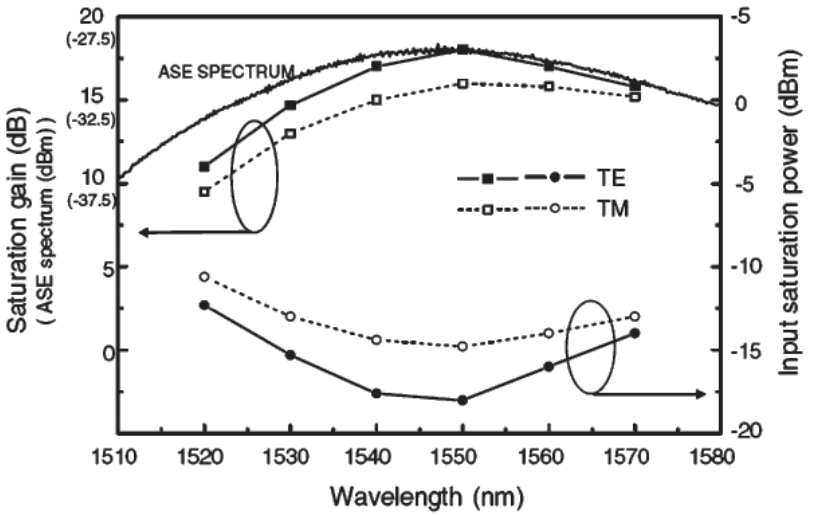

Fig. 12.2.4. Measured wavelength dependence of saturated gain and input saturation power levels for two orthogonal polarization (TE and TM) states of a RSOA in a TO package [11].

The figure shows the gain of a 400 μm long RSOA with 80 mA of current injection.

The measured saturation power and saturated gain as a function of wavelength of a packaged RSOA is shown in Fig. 12.2.4.

12.3. Pulse Propagation Model and Gain Dynamics

In Ch. 6, the rate equation and pulse amplification model in traveling wave semiconductor optical amplifier is described. The amplifier in that model is considered as a lumped element, i.e. the temporal evolution of the pulse as it propagates through the amplifier is averaged and an integrated gain along the length of the amplifier is the only gain parameter required in that model. For a RSOA, a pulse propagation model is important because light propagating though the amplifier is reflected back. The RSOA amplifier length, gain and back facet reflectivity can be used as parameters for performance optimization of RSOA. In this section, the pulse propagation model developed by Connelly in Ref. [12] is described.

Consider a RSOA of length L, the input/output facet is located at $z = 0$ and the reflective facet at $z = L$. The electric field of the light propagating in the amplifier in the positive $+z$ direction can be written as

$$E^{+} = A^{+} \exp(i\omega \mathrm{t} - \mathrm{kz}), \tag{12.3.1}$$

where $A^{+}(z,t)$ is the amplitude of the electric field. A similar expression is written for light propagating in the negative $-z$ direction. In the slowly varying amplitude approximation the forward and backward traveling waves in the RSOA obey the following equations ($A^{\pm}$ are the amplitudes of the optical field, and $|A|^2$ is equal to the optical power) [12]

$$\frac{\partial A^{\pm}}{\partial z} \pm v_g^{-1} \frac{\partial A^{\pm}}{\partial t} = \pm \frac{g}{2[1 + \varepsilon(|A^{+}|^2 + |A^{-}|^2)]} \times (1 - j\alpha) A^{\pm}, \tag{12.3.2}$$

where v_g is the group velocity and α the linewidth enhancement factor. The single-pass transit time L/v_g is 5.1 ps. The rate equation for the gain coefficient g is

$$\frac{\partial g}{\partial t} = \frac{(g_0 - g)}{\tau} - \frac{1}{E_{\mathrm{sat}}} \frac{g(|A^{+}|^2 + |A^{-}|^2)}{2[1 + \varepsilon(|A^{+}|^2 + |A^{-}|^2)]} \tag{12.3.3}$$

g_0 is the unsaturated gain coefficient, τ is the effective carrier lifetime, E_{sat} is the saturation energy and ε is a spectral hole burning parameter. Assuming the RSOA has reflectivities of 0 and 1 at the input and reflective ends respectively the boundary conditions are $A^+(0,t) = \sqrt{P_{\text{in}}}\exp[j\phi(t)]$ and $A^-(L,t) = A^+(L,t)$. P_{in} is the input pulse power and ϕ(t) is the pulse phase, which is equal to $2\pi\int_0^t \Delta v(t)dt$, where $\Delta v(t)$ is the pulse dynamic chirp and $t = 0$ is the simulation start time. To obtain a stable numerical solution for (12.3.2), (12.3.3), a new set of independent space-time intervals are introduced. They are defined by

$$u = (T + z)/2 \quad v = (T - z)/2, \tag{12.3.4}$$

with reduced time $T = v_g t$ (units of distance). Equation (12.3.4) is used to transform (12.3.1) to

$$\frac{\partial A^+}{\partial u} = \frac{g(z,t)}{2[1 + \varepsilon(|A^+|^2 + |A^-|^2)]}(1 - j\alpha)A^+, \tag{12.3.5}$$

$$\frac{\partial A^-}{\partial v} = \frac{g(z,t)}{2[1 + \varepsilon(|A^+|^2 + |A^-|^2)]}(1 - j\alpha)A^-, \tag{12.3.6}$$

The pulse power in the amplifier is given by,

$$P(z,t) = |A^+(z,t) + A^-(z,t)|^2. \tag{12.3.7}$$

The above equations are solved numerically for a pulsed input. The simulation begins at $t = 0$ and $z = 0$.

The above set of equations has been solved [12] using a stream of input pulses at 10 GHz with a pulse width of ∼40 ps. The parameters used in the model are amplifier length, $L = 400\,\mu$m, $R = 1$, and the unsaturated gain $g_0 = 4300\,\text{m}^{-1}$ (corresponds to a round trip internal gain of 15 dB).

The parameters τ, E_{sat} and ε used in the model are 132 ps, 0.45 pJ and $0.92\,\text{W}^{-1}$ respectively. The input and output pulses for both chirped and unchirped pulses are shown in Figs. 12.3.1 and 12.3.2 respectively. The input chirp parameters are typical for a 1550 laser driven by an electro-absorption modulator.

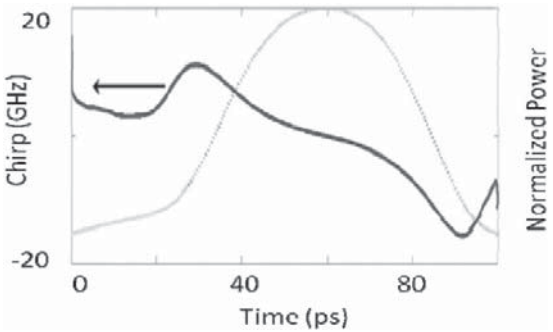

Fig. 12.3.1. The input pulse used in the model is shown. The normalized power is in arbitrary units [12].

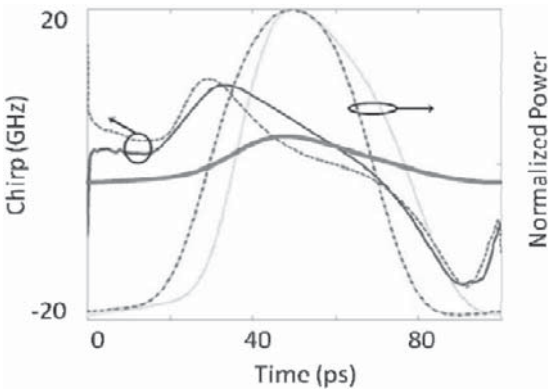

Fig. 12.3.2. The figure shows the modeling results. The solid line is the output chirp and the dashed line is the input chirp (same as Fig. 12.3.1). The solid line is the output pulse with the above chirped input pulse (dashed). Also shown are output chirp for an unchirped input pulse (thick solid line) and output pulse with unchirped input pulse (dash-dotted line). The normalized power is in arbitrary units [12].

Another output of the model is shown in Fig. 12.3.3. The figure shows the gain coefficient as a function of time at 200 μm i.e. at the middle of the 400 μm long amplifier. Also shown are the total power and the forward and backward traveling powers. The temporal variation of gain is due to the time varying forward and backward propagating pulses.

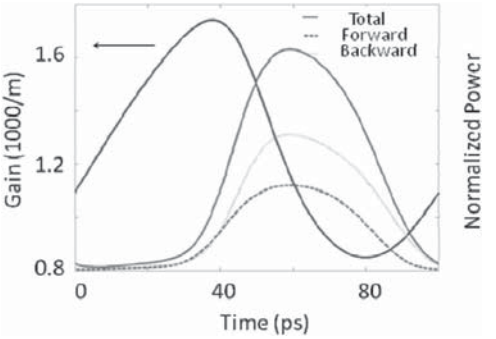

Fig. 12.3.3. The figure shows temporal variation of gain at 200 μm. The RSOA amplifier length is 400 μm. The total power and forward and backward propagating powers are also shown [12].

12.4. RSOA Based Transmitter — Concept

The wavelength-division-multiplexed passive optical network (WDM-PON) is important for Fiber to the home or local area network applications [13, 14]. A wavelength independent (i.e. the capability to receive and transmit data at any wavelength) optical network terminal (ONT) at the subscriber premises is important for WDM-PON. The upstream transmission from the ONT is carried out using a re-modulation scheme, where the downstream optical signal is reused for upstream transmission. The device used in the ONT must have a broadband optical gain medium. Among the devices studied are Fabry–Perot laser diode, and semiconductor optical amplifier (SOA) [1–5]. Among these devices, RSOAs are most promising due to a polarization independent broadband gain medium with high gain. The RSOAs used for these systems need to have low input saturation power and high gain.

Figure 12.4.1 shows the schematic of a WDM-PON architecture. The quantities labeled SML1, SML2 etc. are single mode lasers located at the central office (CO). The output of these lasers are combined using a arrayed waveguide router (AWG) and transmitted using a optical fiber link to remote node (RN) through a circulator to another AWG. The signal from the RN goes to the optical network units (ONU). The signal from the AWG at a given wavelength goes

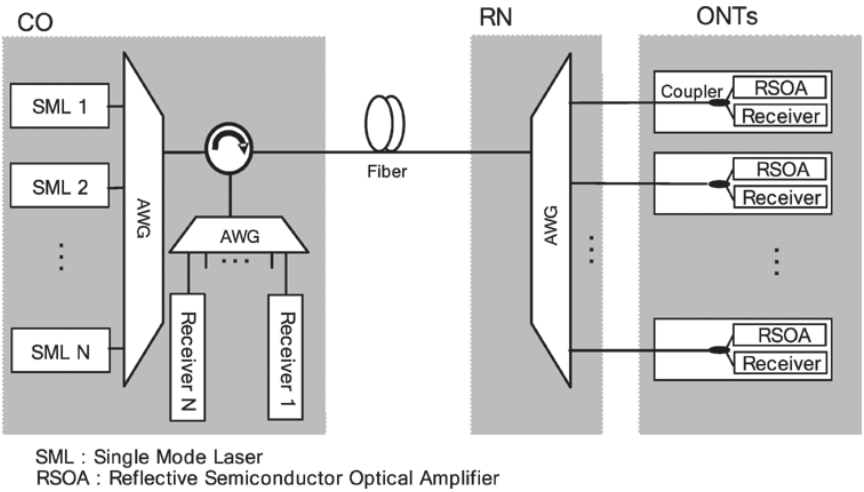

Fig. 12.4.1. Schematic of a WDM-PON architecture [11].

to a coupler (circulator) which transmits some of the signal to a receiver and the rest to a RSOA. The RSOA remodulates the light from the upstream signal with downstream data and sends it back to the central office using the same circulator and the remote node.

The RSOA is designed to have a low input saturation power so that the downstream signal extinction ratio is minimized as the signal travels through the RSOA. The input saturation power $P_{\text{in,sat}}$ equals saturated output power P_{sat} divided by the saturated gain G_s of the amplifier, i.e. $P_{\text{in,sat}} = P_{\text{sat}}/G_s$. The measured data on a RSOA used for a WDM-PON experiment is shown in Fig. 12.4.2.

For Fig. 12.4.2, the downstream signal was generated by modulating a 1550 nm single wavelength laser (distributed feedback laser) at 2.5 Gb/s and the upstream signal is obtained by modulating the RSOA at 1.25 Gb/s.

Higher extinction ratio (ER) of the downstream signal at the RSOA leads to lower performance of the upstream signal (Fig. 12.4.2). Note that error-free upstream transmission with the downstream ER of up to 5 dB was achieved. As expected, a deterioration of the upstream performance as the downstream ER increases is observed. When the optical power injected into the RSOA is

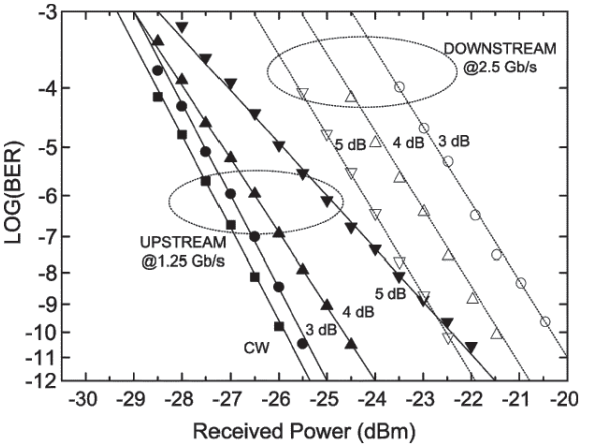

Fig. 12.4.2. Measured BER performance of upstream and downstream transmission over 20 km of single mode fiber for several values of downstream extinction ratio (ER). The power injected to RSOA is −15 dBm [11].

−15 dBm with its ER of 5 dB, the suppressed ER in the upstream was measured to be 3.0 dB, inducing the power penalty of around 3.5 dB. This power penalty can be lowered by increasing the optical power injected to the RSOA. But the maximum injection power is limited by the overall link power budget and the transmitted power per channel from the central office (CO).

A 10 Gb/s modulation experiment using RSOAs has been reported. It uses duobinary modulation and electronic equalization. The schematic of the experiment is shown in Fig. 12.4.3. An avalanche photodiode module is used as a photodetector and a CW tunable laser is used as a self seed for the RSOA. The gain spectrum of the RSOA is shown in the inset.

The BER measurements at various data rates (1.25 Gb/s, 2.5 Gb/s and 10 Gb/s) are shown in Fig. 12.4.4. Both back to back (b to b) BER data and after 10 km transmission are presented with equalization (EQ). The 10 Gb/s result is for duo-binary modulation after equalization (D + EQ).

The bandwidth limitation of the RSOA in transmission has been examined by using electronic equalizers [8, 16] (for a RSOA whose modulation bandwidth is ∼2 GHz). A CW seed light at 1550 nm is

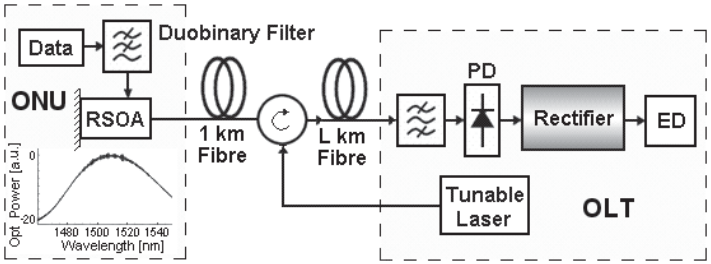

Fig. 12.4.3. Experimental set up demonstrating RSOA performance at 10 Gb/s. OLT: Optical line terminal. PD: photodetector. A CW tunable laser is used to seed the RSOA. L is the length of fiber used prior to detection and measurement. The inset shows the gain spectrum of RSOA [15].

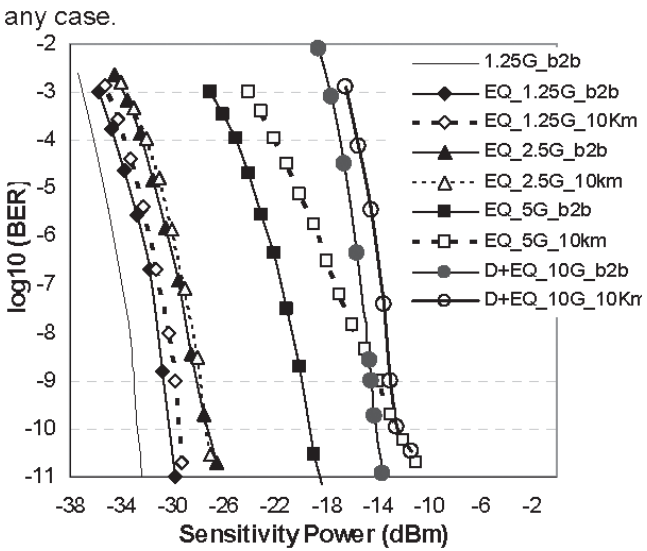

Fig. 12.4.4. The data on bit-error-rate measurements under various conditions. The data rates are 1.25 Gb/s, 2.5 Gb/s and 10 Gb/s. The APD receiver sensitivity was −27 dBm. Both back to back (b to b) BER data and after 10 km transmission are presented with equalization (EQ). The 10 Gb/s is for duo-binary modulation after equalization (D + EQ) [15].

injected into the RSOA and the SOA current was modulated with a 9.95-Gb/s NRZ (OOK) signal. After detecting the modulated output from RSOA by using a PIN photodiode, the received electrical signal error rate was measured. When the electronic equalizer was not used,

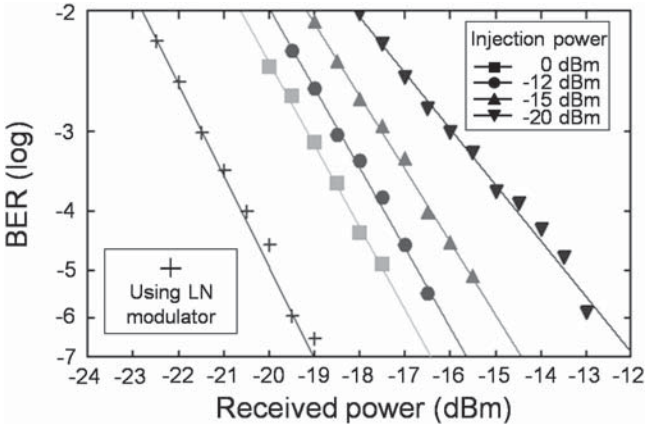

Fig. 12.4.5. BER as a function of received power obtained for various input powers of RSOA. Note that power penalty increases (i.e. more optical power is required for same BER) at high RSOA input powers [8].

there was no eye opening at the decision point due to the severe bandwidth limitation. On the contrary, when the electronic equalizer was applied a clear eye opening was observed. Figure 12.4.5 shows the BER curves obtained by using the electronic equalizer. In this figure, the BER curve of the 10-Gb/s signal generated by using a $LiNbO_3$ modulator (bandwidth: 20 GHz) is shown as a reference. When the optical power of the seed light incident on the RSOA is set to 0 dBm, the receiver sensitivity (@BER $= 10^{-5}$) was measured to be -17.5 dBm.

Frequency response of RSOAs as function of input power and input modulation frequency has been measured for various package designs [16]. The results show although a TO can package is more compact and perhaps more suitable for PON applications, it has a lower bandwidth than a butterfly package.

Higher speed performance of RSOA using direct modulation has been demonstrated using electronic equalization. The RSOA used in this work had a planar buried heterostructure (index guided device) with a bulk active layer. The length of the active region was 400 μm. The rear facet was coated with high-reflection coating with a reflectivity of 85%, while the front facet was anti-reflection coated to have

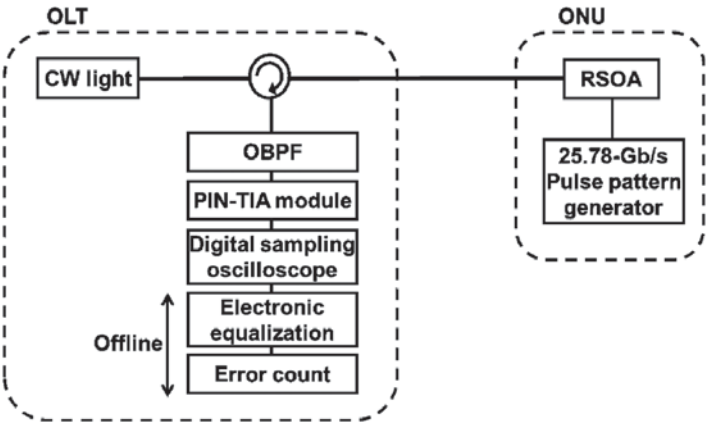

Fig. 12.4.6. Experimental set up for 25 Gb/s RSOA performance evaluation. OBPF is optical bandpass filter. PIN is the photodiode [16].

the reflectivity of 10^{-4}. The schematic of the experiment is shown in Fig. 12.4.6. The RSOA is seeded with CW light from a single wavelength laser and is modulated with a signal at 25.78 Gb/s. The butterfly packaged RSOA had a modulation bandwidth of 3.2 GHz which decreased at 20 dB/decade.

The eye diagram of the modulated light without (left) and with (right) electronic equalization is shown in Fig. 12.4.7. Also, the bit-error-rate measurement after electronic equalization is shown in the same figure. The results illustrate high speed operation using RSOA based transmitter and electronic equalization is feasible.

12.5. Optical Transmission Applications

As mentioned in the previous section, self-seeding RSOAs are important as colorless upstream transmitters for optical network units (ONU) in a wavelength division multiplexed passive optical network (WDM-PON). The WDM-PON is important for broadband fiber based access to the home/subscribers. In the RSOA based transmitter shown in Fig. 12.5.1, the ASE light emitted from a RSOA is spectrally sliced by an AWG in the return node (RN) and fed back via a passive reflective path to seed itself without requiring centralized broadband sources. A bandpass filter (BPF) is used in front of

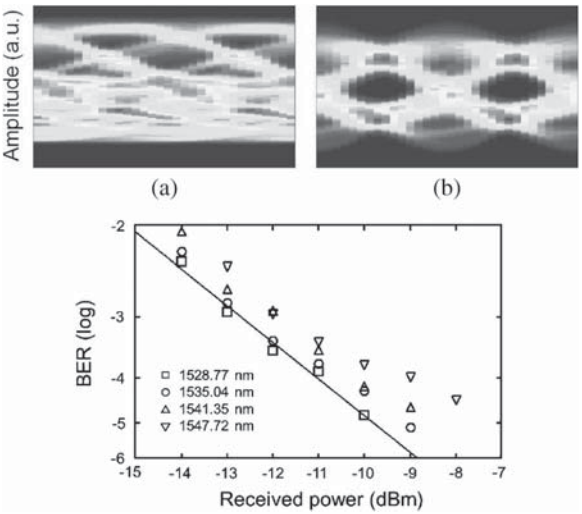

Fig. 12.4.7. Eye diagram of modulated RSOA output (a) without electronic equalization, (b) with electronic equalization. The lower figure shows the bit-error-rate (data) with equalization. Data for different input wavelengths are shown [16].

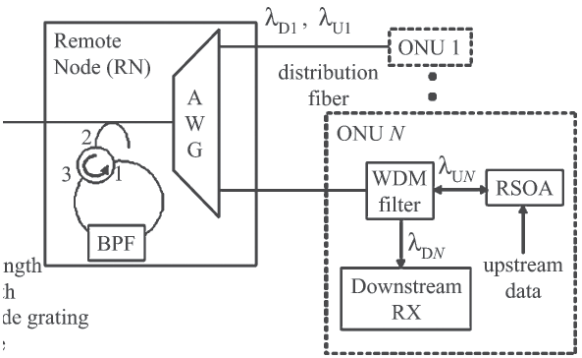

Fig. 12.5.1. Schematic of a RSOA based transmitter at a optical network unit [5]. The RSOA is modulated with data to be transmitted (upstream data). The WDM filter is set to one of the arrayed waveguide router (AWG) transmission wavelength [5].

RSOA to select a particular wavelength. The bandwidth of this filter is comparable to the free spectral range (FSR) of the AWG so that only one spectrally sliced light per output port of AWG is coupled to the RSOA.

Use of RSOAs in this form makes active temperature tracking unnecessary. The RSOAs are directly modulated with upstream data for transmission to the remote node (RN). Also identical RSOAs can be placed at all ONUs since the wavelength of the input (seeding) light, and hence, the transmitting wavelength from each RSOA is determined by the spectral characteristics of the AWG and the wavelength filter (BPF).

The schematic of a complete WDM-PON transmission system is shown in Fig. 12.5.2 [5]. The diagram has N ONUs, each with a directly modulated RSOA as an upstream transmitter. Two AWGs are used at the optical line terminal (OLT) and RN to wavelength combine and separate upstream wavelength channels that carry signals from the ONUs to the OLT, and downstream wavelength channels that carry signals from the OLT to the ONUs. The two AWGs are identical. The inset of Fig. 12.5.2 shows the upstream and downstream group of wavelengths. This type of wavelength separation, between the downstream and upstream channels reduces crosstalk. The wavelengths are spaced at a multiple of the AWG's free spectral range (FSR). Each ONU is assigned with unique downstream and upstream wavelengths that exit and enter through the same AWG

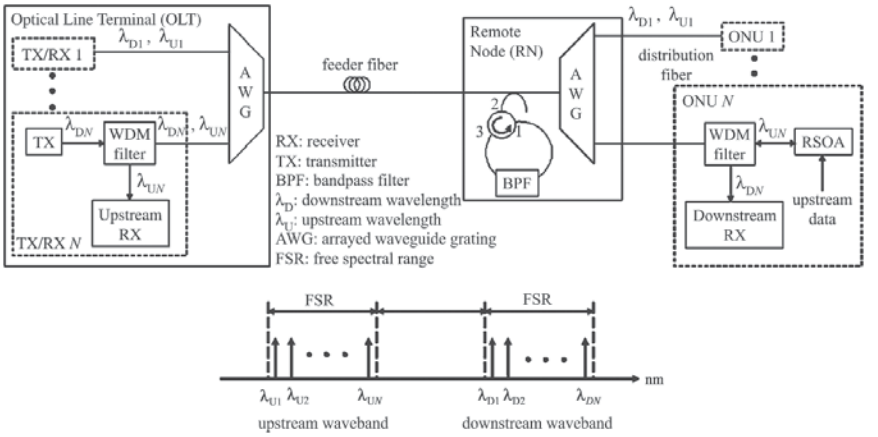

Fig. 12.5.2. Schematic of a WDM-PON architecture using RSOA for upstream data transmission [5].

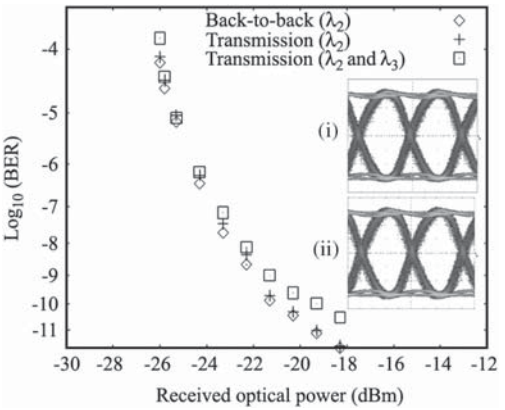

Fig. 12.5.3. Measured BER curves of 1.25-Gb/s self-seeded upstream signals on λ_2. The inset shows electrical eye diagrams of signals on λ_2 at BER = 10−9 after a 21-km transmission: (i) Single-channel transmission (λ_2) and (ii) dual-channel transmission (λ_2 and λ_3) [5].

port. At the OLT and ONU, these wavelengths are further combined and separated using WDM filters.

Experiments have been carried out [5] using a 1.25 Gb/s upstream data which is used to directly modulate the RSOA. Figure 12.5.3 shows the results with wavelength λ_2 as the self-seeded wavelength of RSOA (of a ONU) with and without a second wavelength λ_3 at the OLT. The data shown is the BER after 21 km transmission to OLT. These results show that RSOAs can be used as directly modulated light sources, removing the need for external modulators.

Reflective semiconductor optical amplifiers are being actively studied for passive optical network (PON) application by several key vendors of optical transmission equipment. Laboratory experiments and field trials show that RSOA is important for WDM PON applications.

References

[1] M. D. Feuer, J. M. Wiesenfeld, J. S. Perino, C. A. Burrus, G. Raybon, S. C. Shunk and N. K. Dutta, *IEEE Photon. Technol. Lett.* **8**(9), 1175 (1996).
[2] W. R. Lee, S. H. Cho, J. Park, B. K. Kim and B. Kim, *ETRI J.* **27**, 334 (2005).

[3] W. Hung, C. Chan, L. Chen and F. Tong, *IEEE Photon. Technol. Lett.* **15**(10), 1476 (2003).
[4] H. Takesue and T. Sugie, *J. Lightw. Technol.* **21**(11), 2546 (2003).
[5] E. Wong, K. L. Lee and T. B. Anderson, *J. Lightw. Technol.* **25**, 67 (2007).
[6] W. Zhang, J. Sun, J. Wang and L. Liu, *IEEE Photon. Technol. Lett.* **19**(19), 1418 (2007).
[7] L. Q. Guo and M. J. Connelly, *Opt. Commun.* **281**(17), 4470 (2008).
[8] Y. Takushima, K. Y. Cho and Y. C. Chung, *Proc. IEEE* **C-34** (2008).
[9] A. E. Kelly, C. Michie, Wende Zhong, S. Karagianopoulos, W. I. Madden, C. Tombling and I. Andonovic, *IEEE J. Sel. Area of Comm.* **28**, 943 (2010).
[10] L. F. Tiemeijer, G. N. van den Hoven, P. J. A. Thijs, T. van Dongen, J. J. M. Binsma, E. J. Jansen and A. J. M. Verboven, *IEEE Photonic Tech. Lett.* **9**, 37 (1997).
[11] W. Lee, M. Y. Park, S. H. Cho, J. Lee, C. Kim, G. Jeong and B. W. Kim, *IEEE Photonic Tech. Lett.* **17**, 2460 (2005).
[12] M. J. Connelly, *IEEE Photonic Tech. Lett.* **24**, 95 (2012).
[13] H. Takesue and T. Sugie, *J. Lightw. Technol.* **21**, 2546 (2003).
[14] J. M. Kang and S. K. Han, *IEEE Photon. Technol. Lett.* **18**, 502 (2006).
[15] M. Omella, V. Polo, J. Lazaro, B. Schrenk and J. Prat, *European Conf. on Optical Comm. ECOC*, **Tu.3.E.4** (2008).
[16] K. Y. Cho, B. S. Choi, Y. Takushima and Y. C. Chung, *IEEE Photonic Tech. Lett.* **23**, 495 (2011).

Chapter 13

Two-Photon Absorption in Amplifiers

13.1. Introduction

Two-photon absorption (TPA) is a nonlinear absorption process in semiconductors. As the name implies, it involves the absorption of two photons and during the process the electron makes a transition from the valence band to a high energy state in the conduction band. The two-photon absorption probability is large when the incident photon energy is close to the band gap energy in the semiconductor. When the semiconductor is fabricated as SOA, the single photon absorption near the band edge becomes gain at sufficiently high injection current and the two-photon absorption process becomes important for sufficiently high incident light intensities. The two-photon absorption of a high intensity beam (pump) changes the amount of carriers in the active region of SOA which results in a phase change for a second low intensity beam (probe) propagating through the SOA. Since, the carriers (electrons) created by TPA have high energy, they escape the active region well and drift through the p-cladding region to the contacts. Thus the phase change created by TPA is a fast process. This fast change has been studied for wavelength conversion, and optical logic at very high speeds.

13.2. Two-Photon Absorption in Semiconductors

Two-Photon Absorption in semiconductors has been extensively studied [1–8]. There are two distinct frequency regimes for TPA

in semiconductors defined by (i) when the incident photon energy is close to the bandgap or (ii) when the incident photon energy is considerably less than the bandgap. These cases correspond to real and virtual excitation. The bandgap resonant effects result in real excitation and large nonlinear effects in degenerate and non-degenerate TPA and other nonlinear phenomenon are observed. However, if the incident photon energy is much less than the bandgap, a considerably smaller but faster nonlinear refractive index due to bound electronic effects are observed. In this chapter, a TPA process where the incident photon energy is close to the bandgap is considered.

The TPA ($\beta(\omega)$) as a function of the frequency of light (ω) has been calculated using second order perturbation theory for direct gap semiconductors. The expression is given by [8]

$$\beta(\omega) = \mathrm{K}\frac{\sqrt{E_p}}{n_0^2 E_g^3} F_2\left(\frac{\hbar\omega}{E_g}\right), \tag{13.2.1}$$

where $E_p = E_g(m_c/m_0)$ and

$$F_2(x) = \frac{(2x-1)^{3/2}}{(2x)^5},$$

$$K = \frac{2^9\pi}{5}\frac{e^4}{\sqrt{m_0}c^2},$$

where $\mathrm{m_c}$ is the conduction band mass, $\mathrm{m_0}$ is the free electron mass, c is the velocity of light, e is the charge of an electron, and, E_g is the bandgap. A considerable amount of data exists on TPA in semiconductors. A scaled version of the result as a function of bandgap and its comparison with Eq. (13.2.1) is shown in Fig. 13.2.1. The value of K is 1940 in units such as β is in $\mathrm{cm^{-1}/GW}$ and E_g and E_p are in eV [8].

The real part n_R and imaginary part n_I of two-photon induced index change for semiconductors for incident wavelengths near the band gap has been previously calculated [1]. The linewidth enhancement α_2 can be derived using this calculation. The imaginary part of the index n_I is related to two-photon absorption. The expression

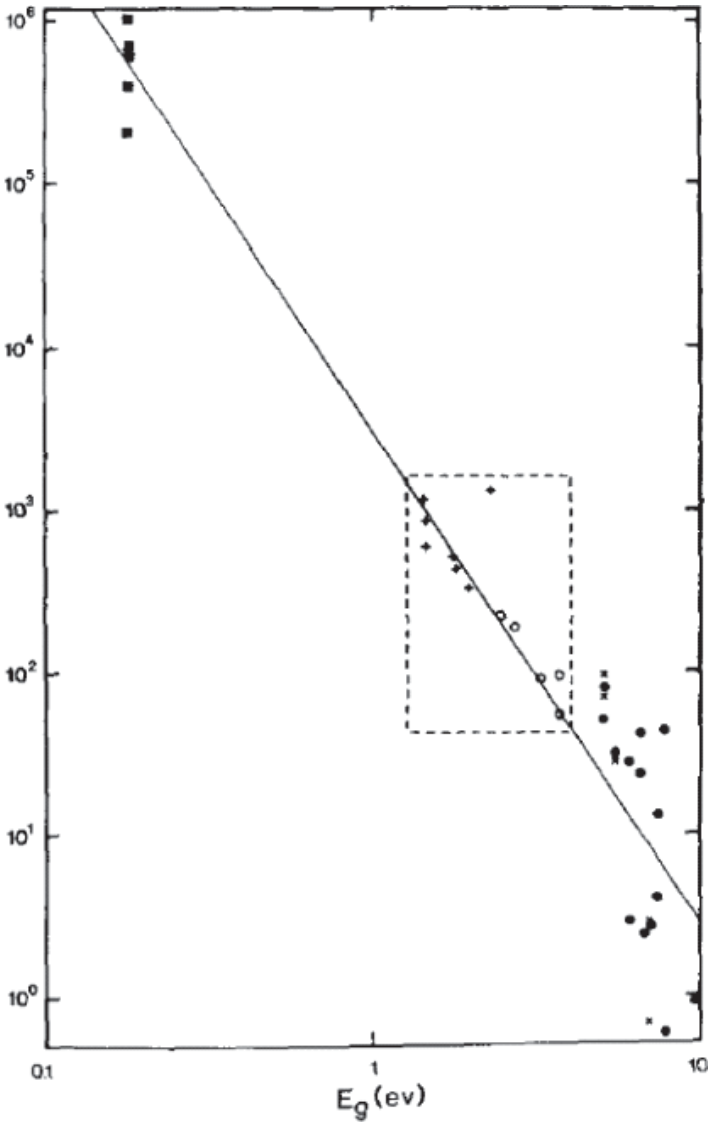

Fig. 13.2.1. A log-log plot of the scaled two-photon absorption coefficient versus energy gap from [8]. The solid line is a least squares fit of the data enclosed by the dashed box to a line of slope −3. The fit also gives a good estimate of TPA in wide-gap optical solids (lower right) [9] and InSb (upper left) [10].

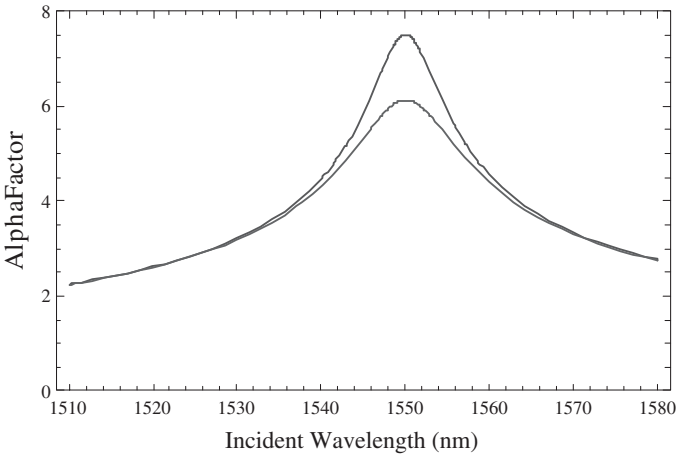

Fig. 13.2.2. Calculated two-photon absorption related alpha-factor as a function of incident wavelength for a semiconductor with a band gap of 1550 nm.

for α_2 is as follows:

$$\alpha_2 = \left(\frac{4\pi}{\lambda}\right)\left(\frac{n_R}{n_I}\right) = \frac{3x^2}{8(2x-1)^{3/2}[(1-x)^2+\gamma_1^2]^{1/4}}, \qquad (13.2.2)$$

where λ is the incident wavelength, $x = \hbar\omega/E_g$ where $\hbar\omega$ is the incident photon energy and E_g is the band gap, $\gamma_1 = \gamma/E_g$ where γ is the linewidth broadening parameter. The lineshape function and the corresponding linewidth broadening parameter are introduced phenomenologically [1]. The calculated α_2 as a function of photon energy is shown in Fig. 13.2.2 for InGaAsP with a band gap of 1550 nm. The two curves are for two values of the broadening parameter (γ) of the absorption line shape. $\gamma = 2, 3$ meV for the two curves respectively. The alpha factor is higher for $\gamma = 2$ meV. The calculated value is consistent with measurements [8].

Two-photon absorption limits the gain for short pulses in SOA. It also limits the output power. The equation for the optical power $E(z)$ in the amplifier is given by [11]

$$\frac{dE(z)}{dz} = \Gamma g_0 E_{\text{sat}}\left[1 - \exp\left(-\frac{E(z)}{E_{\text{sat}}}\right)\right] - lE(z) - \gamma(z)E^2(z), \qquad (13.2.3)$$

where the first term represents gain saturation, the second term is the optical loss due to free carrier absorption and the third term is the optical loss due to TPA. Γ is the mode confinement factor, g_0 is the unsaturated gain, E_{sat} is the saturation power, l is the loss coefficient (typically $\sim 1\,\text{cm}^{-1}$) and the normalized, TPA loss $\gamma(z)$ is given by

$$\gamma(z) = \frac{\beta}{A_{\text{mode}}} \frac{\int |A(z,t)|^4 dt}{(\int |A(z,t)|^2 dt)^2}, \tag{13.2.4}$$

where $A(z,t)$ is the amplitude of the pulse, β is the TPA absorption coefficient with a typical value of 20–40 cm^{-1}/GW for most semiconductors. For Gaussian pulses, $\gamma(z) \sim \beta/(1.5\,\tau A_{\text{mode}})$ where τ is the pulse width. If the input pulse energy is E_{in} i.e. $E(z)$ at $z = 0$ is E_{in}, then the output pulse energy in the absence of TPA and gain saturation is given by $E_{\text{out}}/E_{\text{in}} = \exp[(\Gamma g_o - l)L]$. The results of effective gain g (right hand side of Fig. 13.2.3) in the presence of TPA for two pulse energies (1 ps and 10 ps) with and without TPA are shown in Fig. 13.2.3 [11]. The values of $L, \Gamma, l, E_{\text{sat}}, A_{\text{mode}}$ are 0.8 cm, 0.003, 0.7 cm^{-1}, 100 pJ, and, 14 μm^2 respectively. The value

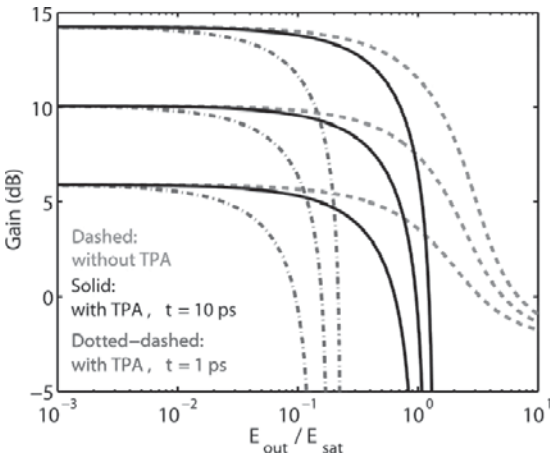

Fig. 13.2.3. Effective gain for three cases (without TPA — dashed, with 10 ps pulse — solid and with 1 ps pulse — dot dashed). The three curves in each cases correspond to unsaturated gain g_0 values of 800 cm^{-1}, 1200 cm^{-1} and 1600 cm^{-1} [11].

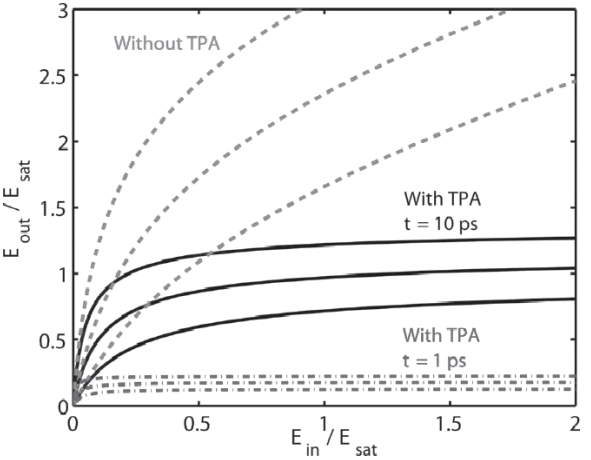

Fig. 13.2.4. The output power plotted as a ratio of E_{sat} as a function of input power for three cases (without TPA — dashed, with 10 ps pulse — solid and with 1 ps pulse — dot dashed). The three curves in each cases correspond to unsaturated gain (g_o) values of 800 cm^{-1}, 1200 cm^{-1} and 1600 cm^{-1} [11].

of TPA absorption coefficient β used is 35 cm^{-1}/GW. These parameters correspond to that of a InGaAsP SOA [11].

The output power as a function of input power is shown in Fig. 13.2.4 for three cases (i) without TPA, (ii) pulse width of 10 ps and (iii) pulse width of 1 ps [11]. In the presence of TPA, the TPA induced dynamic gain saturation energy is obtained from Eq. (13.2.3). It is given by

$$E_{\mathrm{TPA}} = \Gamma g_o / \mathrm{e}\gamma = 1.5\ A_{\mathrm{mode}} \tau \Gamma g_o / e\beta. \tag{13.2.5}$$

The above E_{TPA} decreases linearly with pulse width.

13.3. Phase Dynamics and Other TPA Studies

Nonlinear phase shift induced by short optical pulses in SOA has been measured using a pump-probe experiment [12–14]. The experimental set up used in Ref. [13] is shown in Fig. 13.3.1. The pump (high power) induced refractive index change causes a phase shift on a co-propagating weak probe pulse. The phase shift is measured by interference of the probe pulse with a reference beam. The reference

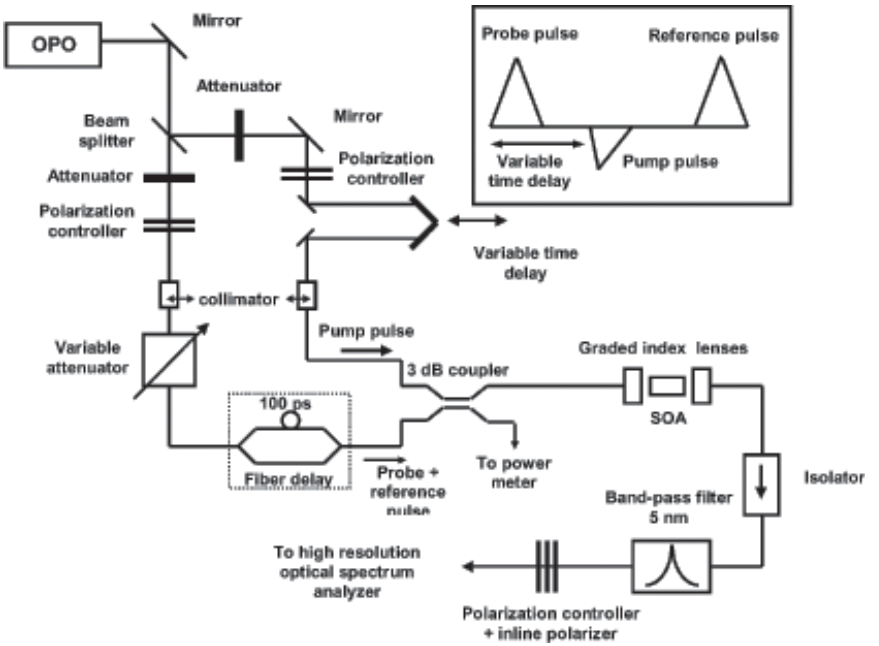

Fig. 13.3.1. Experimental set up for pump-probe experiment for phase dynamics measurement. The temporal positions of the pump, probe and reference pulses are shown in the inset. The pump pulse is orthogonally linearly polarized compared to the probe and reference pulses both of which are also linearly polarized. The pump power measured at the coupler was $\sim$700 μW and the combined power of probe and reference beams were $\sim$60 μW [13].

pulse travels through the amplifier temporally ahead of the pump pulse, as a result it is not affected by the refractive index change induced by the pump. The pump pulse is cross linearly polarized from the probe and reference pulses to allow good discrimination. The delay between the pump and probe pulse is controlled using a variable delay line.

An optical parametric oscillator (OPO) pumped with a mode-locked Ti: Sapphire laser is used to produce optical pulses. The pulses were $\sim$140 fs wide (FWHM) and had a repetition rate of 80 MHz. The wavelength of the pulses was 1550 nm. The reference pulse is $\sim$100 ps ahead of the probe pulse in the amplifier. A variable attenuator is used to adjust the pulse power.

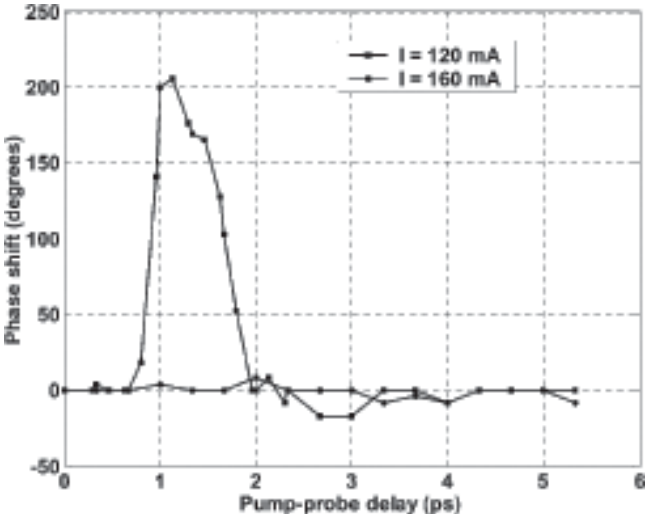

Fig. 13.3.2. Measured phase change of the probe beam as a function of pump-probe delay for two SOA currents [13].

Figure 13.3.2 shows the measured phase change as a function of pump probe delay for two SOA currents. For SOA current of 120 mA, the delay experiment shows that the phase change induced by the pump pulse has a duration of <1 ps. The result show that large phase change ($\sim$180°) is obtained with reasonable pump powers. The phase change $\Delta\phi$ on the probe pulse is given by the equation

$$\Delta\phi = (1/2)\alpha g - (1/2)\beta\alpha_2 S(t), \tag{13.3.1}$$

where the first term is the gain g induced phase change (discussed earlier, Ch. 6), and, α is the linewidth enhancement factor. The second term is the TPA induced phase change, it is proportional to the pump intensity $S(t)$, β is the TPA absorption coefficient, and α_2 is the linewidth enhancement factor associated with the TPA process. The gain induced phase change and the TPA induced phase change oppose each other. As SOA current increases, so does g. This cancel the TPA induced phase change as shown in Fig. 13.3.2 for a SOA current of 160 mA. An analysis of the data shows $\alpha_2 = -4$[13].

13.3.1. *Optical sampling*

TPA has been used in optical sampling studies to measure short pulse widths [15]. In this process, TPA produces a photocurrent. A Fabry-Perot microcavity is used to enhance the optical intensity by increasing the interaction length in the device. The device, which is used for TPA at 1550 nm, consists of a GaAs/AlAs PIN microcavity photodetector grown on a GaAs substrate. The front p-doped mirror consists of nine pairs while the back n-doped mirror consists of 18 pairs of AlAs/GaAs designed for high reflectivity at 1550 nm. The device studied was a 100 μm diameter vertical structure [15]. To use TPA for optical sampling, the duration of the optical sampling pulse $I_s(t - t_1)$ used must be significantly shorter than the optical signal pulses $I_{\text{sig}}(t)$ under test. The signal and the delayed sampling pulses are incident on the microcavity device and the electrical signal $i(t)$ generated by the TPA process in the device is measured as a function of sampling delay t_1. This results in an intensity cross-correlation measurement between I_{s} and I_{sig}. The experimental set up is shown in Fig. 13.3.3(a) and the measured autocorrelation result of a pulse is shown in Fig. 13.3.3(b). The 10 GHz optical pulse train is generated by modulating a mode locked laser. The pulses are amplified using erbium doped fiber amplifier (EDFA) and are transmitted through couplers and delay lines followed by power meters. They further go through a coupler and split for independent pulsewidth measurement using TPA and second harmonic generation (SHG). The two measurements agree as shown in Fig. 13.3.3(b).

13.3.2. *Clock recovery*

TPA has been used in clock recovery studies using a phase locked loop [16]. The phase locked loop is of the conventional type, it uses a voltage control oscillator (VCO). The experimental set up is shown in Fig. 13.3.4. The offset between the data rate and the locally generated clock is fed back to control the output of the VCO and hence that of the locally generated clock so that it matches with the data.

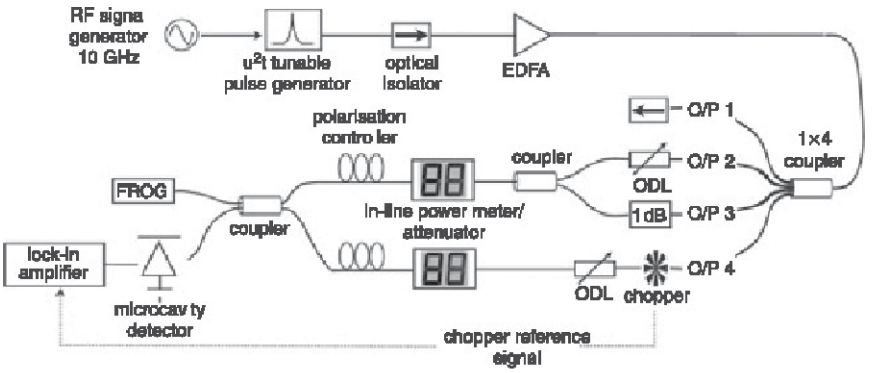

(a)

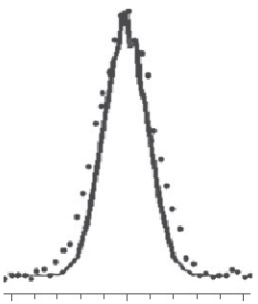

(b)

Fig. 13.3.3. (a) Schematic of the experimental set up. (b) The autocorrelation trace of the pulse measured using TPA. The dots are measured using the conventional second harmonic generation method [15].

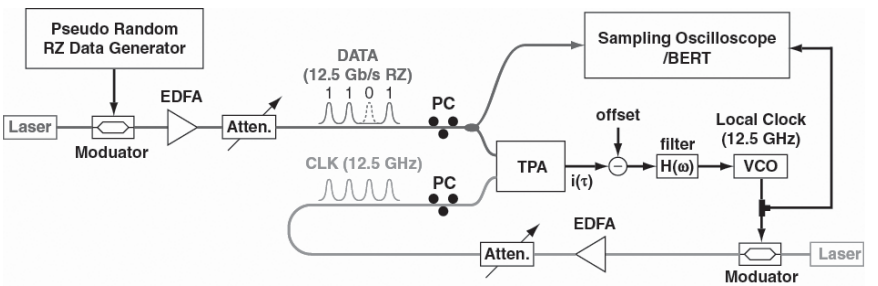

Fig. 13.3.4. Experimental set up for clock recovery using TPA [16].

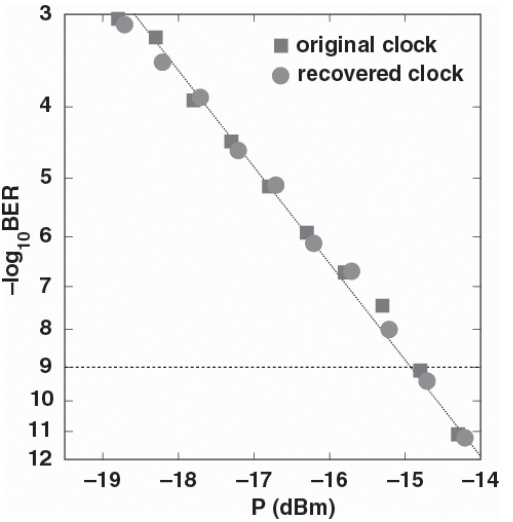

Fig. 13.3.5. BER measurement with the original clock and the recovered clock [16].

The TPA module noted above is the semiconductor device which produces TPA induced photocurrent. The output of a CW laser traverses through a modulator which is modulated with a 12.5 Gb/s RZ data. The modulated data is amplified using an Erbium doped fiber amplifier (EDFA). The BER measurements using the original and the recovered clock are shown in Fig. 13.3.5. The overlapping data shows that the clock recovery system is good.

13.3.3. *Two-photon gain (TPG)*

Two-photon gain (TPG) has also been observed in semiconductor amplifier like structures [17,18]. The structure consists of 0.5 μm thick $Al_{0:11}Ga_{0:89}As$ active layer having a band gap 30 meV smaller than twice the photon energy for 1.56 μm photons. The TPG structure was epitaxially grown on GaAs substrate with cladding layers and a core layer which acts as a highly confining single-mode slab waveguide. Lateral confinement was achieved by a ridge structure. The mode confinement factor for 1.56 μm light is estimated to be 0.6. The facets were antireflection coated to suppress lasing as in SOAs.

The TPG of the structure was measured as a function of amplifier current. The input laser was a mode-locked fiber laser source generating 100 fs pulses at 1560 nm central wavelength. The repetition rate was 37 MHz and the average power was 40 mW. In the presence of TPG the intensity propagation in the amplifier in the simplest form is given by

$$dI/dz = \Gamma\gamma I^2 - \alpha I, \tag{13.3.2}$$

where I is the intensity, Γ is the confinement factor, γ is the two-photon gain (TPG) of the semiconductor and α is the absorption. In order to observe TPG, the nonlinear behavior of the amplification was examined as a function of input power. The SOA lengths were 1.5 and 2.9 mm. The data is shown in Fig. 13.3.6. The plotted data is normalized to the slope at low powers to demonstrate clearly the superlinear behavior at high input powers. The inset shows the

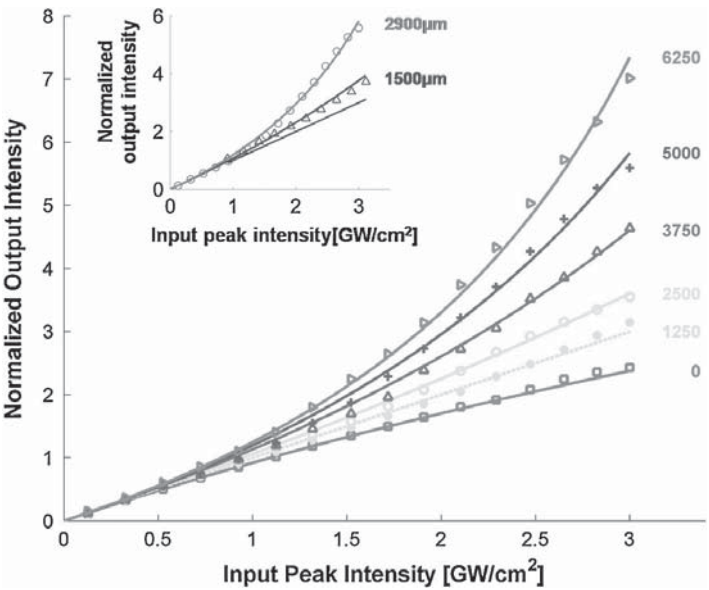

Fig. 13.3.6. Measured output power at 1560 nm as a function of input peak power for various amplifier currents in A/cm^2-μm. The plotted data is normalized to the slope at low powers to demonstrate clearly the superlinear behavior at high input powers. The inset shows the data for both 2.9 mm and 1.5 mm device at ∼5000 A/cm^2-μm [17].

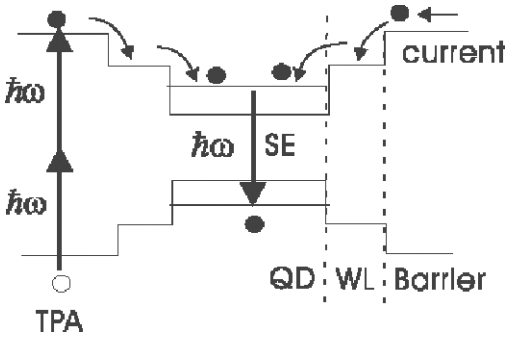

Fig. 13.3.7. Schematic of two-photon absorption (TPA) in the bulk waveguide region in QD-SOA and carrier transfer to quantum dots [19].

data for both 2.9 mm and 1.5 mm device at $\sim$5000 A/cm^2-μm. The solid lines are fit to the data using Eq. (13.3.2) with $\Gamma = 0.6$, $\gamma = 3.5\,\mathrm{cm}^{-1}/\mathrm{GW}$ and $\alpha = 16\,\mathrm{cm}^{-1}$. The figure shows that two-photon gain (TPG) is present at high input powers.

13.3.4. *TPA in QD-SOA*

The effect of TPA on QD-SOA performance has been simulated when the TPA takes place in the waveguide adjacent to the QD active region. Figure 13.3.7 illustrates schematically QD SOA carrier dynamics under TPA occurring in the bulk waveguide region [19]. The amplification process depletes carriers in QDs, while carriers generated by current injection and TPA also refills the carrier-depleted QDs on ultrafast timescales by carrier relaxation from bulk region to QDs via the wetting layer. It follows that the carrier capture rate becomes enhanced by these extra-carriers generated by TPA, compared to the case without TPA. This (presence of TPA) results in much reduced pattern dependence of the gain recovery process [19].

13.4. Optical Logic Performance

In this section, the performance of various all-optical logic gates, such as XOR, AND, NAND and NOT, based on TPA of pump beams is discussed. As in Ch. 9, the proposed device is a MZI each arm of which has a SOA [20–24]. The pump beams are the data signals

which are injected into each arm. The probe beam is a weaker signal injected into the middle arm. The pump and probe beams have single pulse durations ∼0.5 ps. The concept of XOR using SOA based MZI is the same as has been described and demonstrated earlier for XOR [Ch. 9]. The principal new element of the current analysis is that the phase change $\Delta\phi$ due to the pump beam has a fast component, the magnitude of which is given by [12–14]

$$\Delta\phi = -(1/2)\beta\alpha_2 S(t), \tag{13.4.1}$$

where β is the two-photon absorption parameter, α_2 is the linewidth enhancement factor for two-photon absorption and $S(t)$ is the optical pump pulse energy. The negative sign represents the observation that the TPA induced phase change is in opposite direction from that for gain change induced phase change [12–14]. The experimentally derived α_2 is within the range of 4 to 5 [12–14]. The linewidth enhancement factor β value is in the range of 20 to 35 cm/GW [12, 25]. For a SOA with a cross section area 0.5 μm^2 with a 250 Gb/s pulse train input at an average input power of 20 mW and full width at half maximum pulse at 0.5 ps, the peak power density is ∼32 $MWcm^{-2}$. Using $\beta = 20$ and $\alpha_2 = 4$, this results in a peak phase change of $\sim 0.4\pi$ rad. Thus the phase changes are large enough for temporal interference of probe pulses traveling through the two arms of the MZI. The calculation has been carried out with a TPA induced phase change of $\sim 0.4\pi$ to illustrate that good signal to noise ratio (and hence good Q-factor) can be obtained with modest increase in input powers. Higher input power, which would result in a phase change of π, would increase the signal intensity by a factor of ∼3.

The input average power of the SOA used in this paper to obtain significant two-photon absorption is 20 mW which corresponds to a peak power of 160 mW at 250 Gb/s when the input pulse width (used in the simulation here) is 0.5 ps. Although this peak power seems high at first glance, Ref. [12] reports measurements on SOAs with high optical peak power. Figure 8 of Ref. 12 shows data using 400 fJ to 6.4 pJ pulses with a pulse width of ∼200 fs. An optical pulse with an energy of 1 pJ in a 200 fs wide pulse has a peak power of 5 W. Measurements at high peak power (a few W) have been reported in

Ref. [14]. Thus a few hundred mW of peak power in an ultra-short pulse is acceptable for SOAs.

When the two-photon absorption of a high intensity pump beam takes place in a semiconductor optical amplifier there is an associated fast phase change of a weak probe signal. Based on this ultrafast phase response, the cross phase modulation between the pump and probe can be utilized to realize high speed all-optical logic. The principle of logic operations (XOR, AND, NAND etc.) are same as discussed in Ch. 9 using a SOA based MZI.

The MZI output is given by:

$$P_{\text{out}}(t) = \frac{P_{\text{in}}}{4}\{G_1(t) + G_2(t) - 2\sqrt{G_1(t)G_2(t)}\cos[\phi_1(t) - \phi_2(t)]\}, \tag{13.4.2}$$

where P_{in} is the input optical power of the weak probe signal, G_1 and G_2 are the gain in two arms of SOA-MZI, $\varphi_1 - \varphi_2$ is the phase difference of the probe signal in two arms.

The temporal gain and phase change in the SOA has been analyzed by a numerical solution of the SOA rate equations taking into account of TPA. The time dependent gain of the SOA satisfies the temporal gain rate equations [same as discussed earlier in Chs. 9 and 11)]:

$$\frac{dh_l(t)}{dt} = \frac{h_0 - h_l(t)}{\tau_c} - \frac{S(t,0)}{E_{\text{sat}}}[e^{h_{\text{total}}} - 1], \tag{13.4.3}$$

$$\frac{dh_{\text{CH}}}{dt} = -\frac{h_{\text{CH}}}{\tau_{\text{CH}}} - \frac{\varepsilon_{\text{CH}}}{\tau_{\text{CH}}}[e^{h_{\text{total}}} - 1]S(t,0), \tag{13.4.4}$$

$$\frac{dh_{\text{SHB}}}{dt} = -\frac{h_{\text{SHB}}}{\tau_{\text{SHB}}} - \frac{\varepsilon_{\text{SHB}}}{\tau_{\text{SHB}}}[e^{h_{\text{total}}} - 1]S(t,0) - \frac{dh_l}{dt} - \frac{dh_{\text{CH}}}{dt}, \tag{13.4.5}$$

where $h(t)$ is a integral of optical gain over the length of SOA and h_{total} equals the sum of h_l, h_{CH} and h_{SHB}. τ_c is the carrier lifetime, $\exp[h_0] = G_0$ is the unsaturated power gain and E_{sat} is the saturation energy of the SOA. $S(t,0)$ is the instantaneous input optical intensity inside the SOA and $h_l, h_{\text{CH}}, h_{\text{SHB}}$ are the h-factor values for carrier recombination, carrier heating and spectral hole burning respectively.

Equations (13.4.4) and (13.4.5) accounts for the intra-band carrier dynamics (i.e. carrier heating and spectral hole burning effects). For the β value (20 cm/GW) used, the change in intensity due to two photon absorption is low, hence it has been neglected in this model. The carrier density induced phase change is given by:

$$\varphi(t) = -\frac{1}{2}[\alpha h_l(t) + \alpha_{\mathrm{CH}} h_{\mathrm{CH}}(t)] - \frac{1}{2}\beta\alpha_2 S(t), \tag{13.4.6}$$

where α is the traditional linewidth enhancement factor (i.e. $\alpha = 5$), α_{ch} is the carrier heating linewidth enhancement factor (i.e $\alpha_{\mathrm{ch}} = 1$), other SOA parameters are as follows: $E_{\mathrm{sat}} = 30\,\mathrm{mW}$, $G_0 = 10\,\mathrm{dB}$, $\tau_c = 30\,\mathrm{ps}$, $\tau_{FWHM} = 0.5\,\mathrm{ps}$, $\tau_{\mathrm{SHB}} = 100\,\mathrm{fs}$, $\tau_{\mathrm{CH}} = 300\,\mathrm{fs}$, $\varepsilon_{\mathrm{SHB}} = \varepsilon_{\mathrm{CH}} = 0.08\,\mathrm{ps}$ [26, 27]. Note that a low gain of 10 dB reduces the amount of gain induced phase change which is slower than the two photon absorption related phase change. The second term in (13.4.6) is due to two-photon absorption. The TPA related quantities β, α_2 are 20 cm/GW [12, 25], and -4 [11–13] respectively in this model. The calculated change in gain and phase as a function of time when a 250 Gb/s pulse train is injected into the SOA is shown in Fig. 13.4.1. The pulse width (full width at half maximum) is 0.5 ps, the average power is 20 mW and the SOA cross section is $0.5\,\mu\mathrm{m}^2$.

13.4.1. *Boolean logic (XOR, AND, NAND) operations*

To simulate the XOR, AND, NOT and NAND logic performances, all input signals are of return-zero (RZ) type. The random sequence is generated using a random number generator in the software used for modeling.

The data stream pulses (A and B) are Gaussian pulses, i.e.

$$P_{A,B}(t) = \sum_{n=-\infty}^{+\infty} a_{nA,B} \frac{2\sqrt{\ln 2}P_0}{\sqrt{\pi}\tau_{\mathrm{FWHM}}} \exp\left(-\frac{4\ln 2(t-nT)^2}{\tau_{\mathrm{FWHM}}^2}\right), \tag{13.4.7}$$

where P_0 is the energy of a single pulse, $a_{nA,B}$ represents n_{th} data in data stream A and B, $a_{nA,B} = 1$ or 0. Figure 13.4.2 shows the calculated XOR results for 250 Gb/s input data using the above

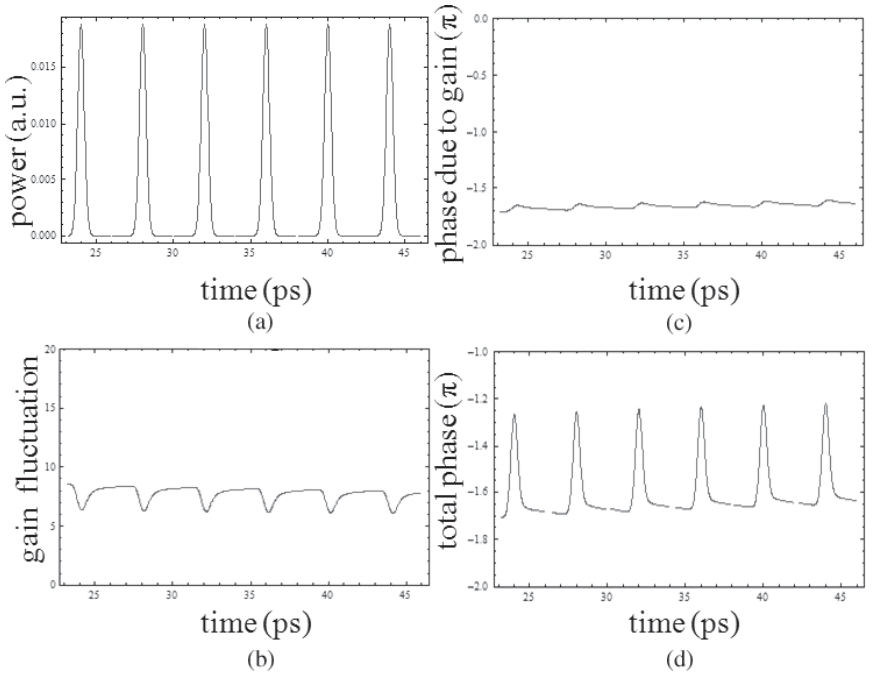

Fig. 13.4.1. Calculated gain and phase response in a SOA to the injection of a pulse train. (a) Input waveform (b) gain modulation as a function of time, (c) phase modulation due to gain modulation as a function of time, (d) total phase modulation including two-photon absorption as a function of time. Note the periodic total phase change is due to two-photon absorption is shown in Fig. 13.4.1(d) [28].

equations, signal A has 00001000011 pattern, and signal B has 10010010001 pattern. Signals A and B are on the left and the XOR output is on the upper right. The bottom right shows the eye diagram for an input of 100 random A and 100 random B bits.

Figure 13.4.3 shows the calculated AND result for 250 Gb/s input data using the above equations. Signals A and B are on the left and the AND output is on the upper right. The bottom right shows the eye diagram for an input of 100 random A and 100 random B bits.

The INVERT operation is similar to a XOR operation with one of the inputs replaced by a clock signal (series of 1's). Figure 13.4.4 shows the calculated INVERT result for 250 Gb/s input data using

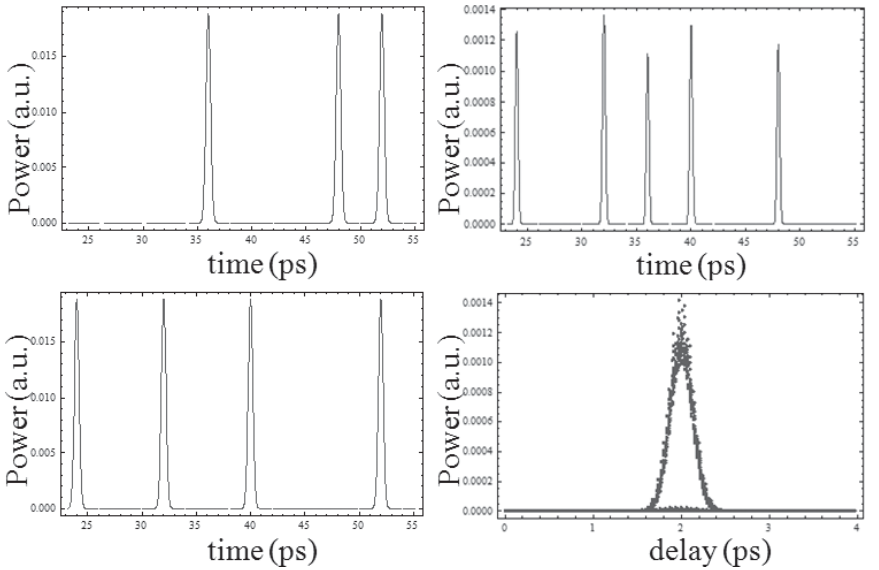

Fig. 13.4.2. Data A and Data B are shown on the left. XOR (of A and B data) and an eye pattern (after 100 pseudo-random A and B bits) are shown on the right [28].

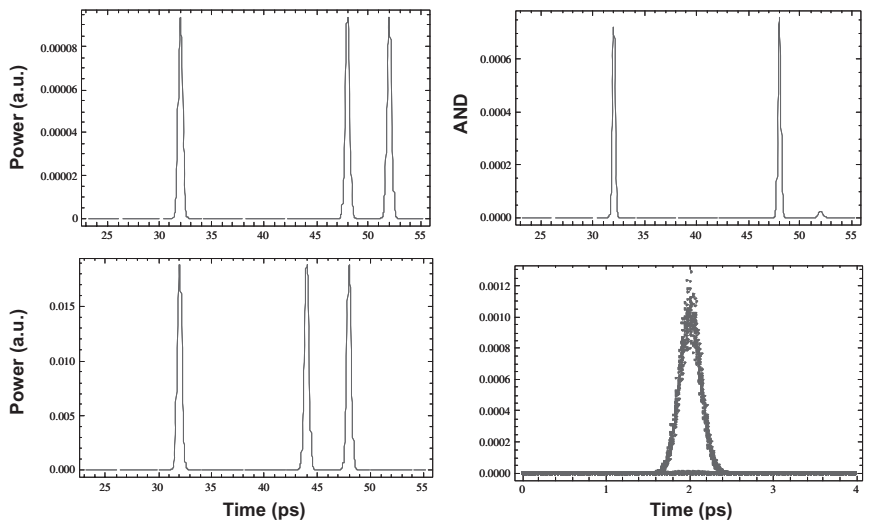

Fig. 13.4.3. Data A and Data B are shown on the left. AND (of A and B data) and an eye pattern (after 100 pseudo-random A and B bits) are shown on the right [28, 29].

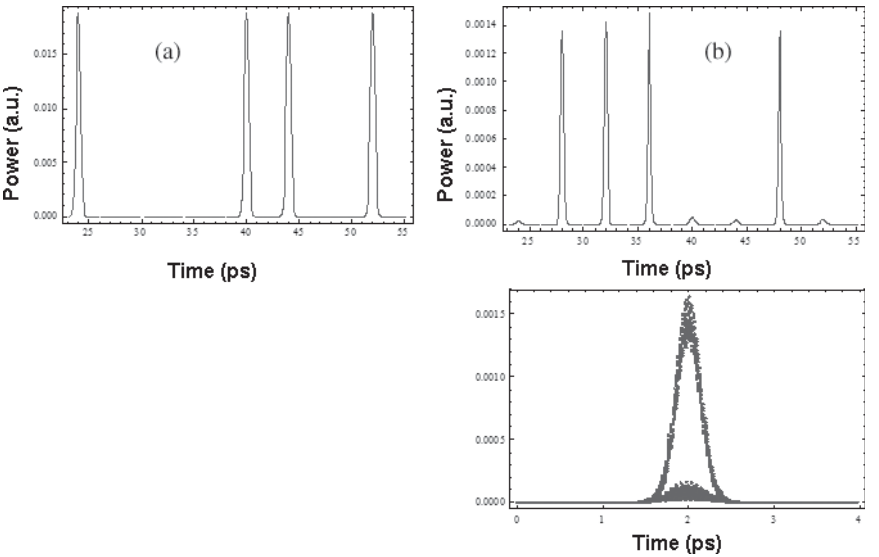

Fig. 13.4.4. Simulation result of the logic INVERT gate: the input data stream A's wave form on the left top (a), the INVERT A result is shown on the right with its eye-diagram.

the above equations. Signals A is on the left and the INVERT output is on the upper right. The bottom right shows the eye diagram.

For all of the logic gates, the quality factor Q (defined in Ch. 9) has been calculated at data rates of 160 Gb/s and 250 Gb/s respectively. The result for XOR as a function of average pump power is shown in Fig. 13.4.5. Similar results are obtained for the other logic operations.

A NAND design, where the logic NAND operation is a serial combination of AND and INVERT gates, has been simulated. NAND gate is important because any logic operation can be built using NAND gates. The calculated eye-diagram of the model of a NAND gate using the same parameter values used in AND and INVERT modeling is good, i.e. an open eye is obtained. The Q-factor dependence on data rate and input power for optical NAND gate has been calculated. The result is shown in Fig. 13.4.6. For sufficiently large input power (average power >18 dBm), the logic gates can generate good quality factor (i.e. $Q > 6$) to high data rates viz. ∼250 Gb/s.

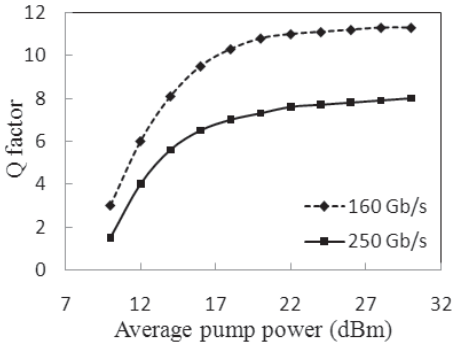

Fig. 13.4.5. Calculated output quality factor Q at different pump power values for XOR logic gate [28].

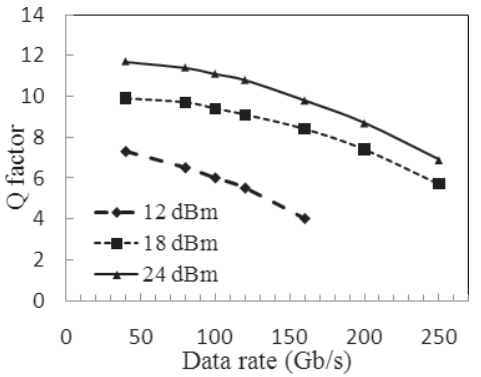

Fig. 13.4.6. NAND gate output quality Q-factor as a function of data rate for three input data stream average powers [29].

This can be explained as follows: at low power levels, the phase change due to TPA is small, and the pattern effect due to slower gain induced phase change is more significant. As the injected power increases, the TPA induced fast phase modulation becomes a major contribution of the total phase shift, and the pattern effect becomes relatively small, resulting in higher Q-factor.

13.4.2. *PRBS generation*

Pseudo-random binary sequence (PRBS) generators are important for a range of applications in a communication system which

including testing, bit scrambling, bit de-scrambling. In a communication network, one important measurement is how accurately the receiver can determine the logic state of each received bit in a nearly random digital data stream. In case the system cannot carry live traffic during the test, it is important to inject a known bit stream pattern to the device under test. The most common input test pattern is the pseudo-random binary sequence. This bit sequence is designed to approximate the truly random data.

As stated in Sec. 11.6, PRBS signal is generated using a linear feedback shift register (LFSR), shown in Fig. 11.6.6a. It has m data storing units (delay line in optics), each unit is capable of storing one bit of binary data temporarily during one clock period (Ch. 10). The all optical PRBS generation by a 7-bit optical LFSR (m = 7) is simulated by modeling the logic XOR and logic AND operations in the presence of fast two-photon absorption induced phase change. The simulated output of this PRBS generator is shown in Fig. 13.4.7. The fast PRBS generation (@250 Gb/s) is feasible because of fast XOR and AND operation.

The logic XOR, AND, NOT and NAND operations using TPA in SOA-MZI has been calculated. The data pulses are short enough and have high enough average power so that the peak powers are large to cause significant two-photon absorption and consequent fast phase change. This fast phase change has the same duration as the data pulses and thus the system allows fast XOR logic operation. The modeling shows operation at ∼250 Gb/s is feasible using TPA induced phase change duration equal to data pulse width both of which are 0.5 ps. The basic mechanism for phase change is carrier induced change in refractive index. The TPA process generates hot carriers in the active region of the SOA. These carriers have energies of ∼0.8 eV (which approximately equals the band gap of the active region) which is considerably larger than the energy barrier (∼0.3 eV) at the cladding layer/active layer interface. Assuming ballistic transport, this allows the hot carriers ($v \sim 2.5 \times 10^6$ m/s) to escape the active region with a time scale of the ∼0.15 ps for a cladding thickness of ∼0.3 μm. Since the TPA induced carriers are present only for a short duration (both generation time — determined by input pulse

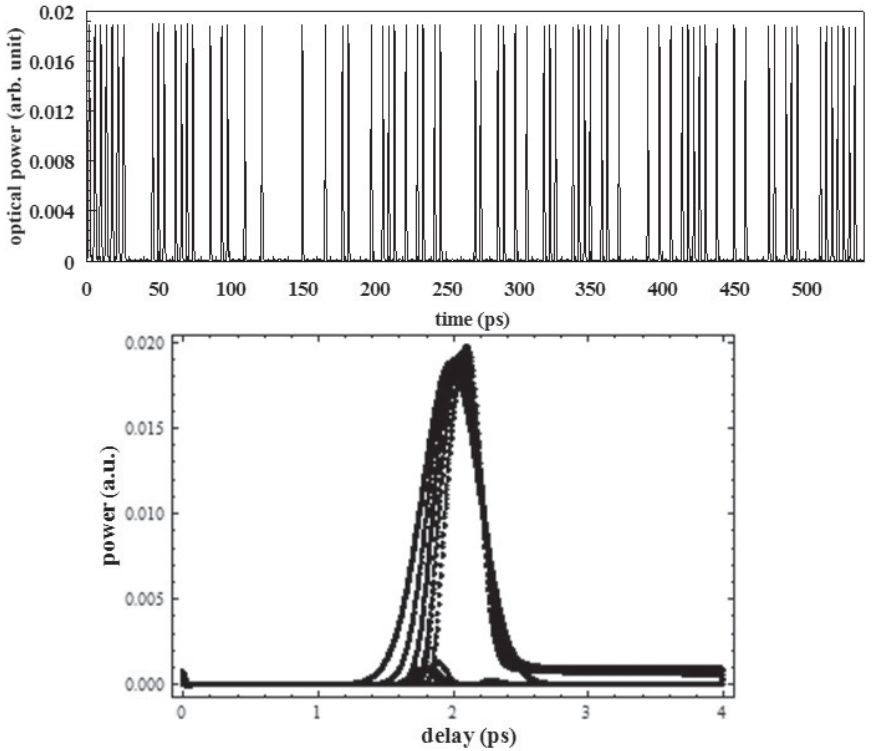

Fig. 13.4.7. The figure shows the simulated output of a PRBS generator (top) and eye diagram (bottom). The first 7 bits in the PRBS output are the input trigger bits, they are followed by $2^7 - 1 - 7 = 120$ bits followed by a new set of 7 trigger bits. The calculated Q factor is 6.8 [28].

length, and escape times are short), the phase change also occurs for a short duration. If the duration of phase change is $\sim$0.15 ps (vs. 0.5 ps used in the model here) faster logic operation is feasible. An important challenge in the demonstration of optical logic at these speeds is the generation of stable synchronized data signals with sub-picosecond level pulse width and precise stable optical delay lines.

References

[1] S. S. Jha and N. Bloembergen, *Phys. Rev.* **171**, 891 (1968).
[2] C. Flytzanis, *Phys. Lett.* **31A**, 273 (1970).
[3] J. A. Van Vechten and D. E. Aspnes, *Phys. Lett.* **30A**, 346 (1969).

[4] C. C. Wang, *Phys. Rev. E.* **2**, 2045 (1970).
[5] N. L. Boling, A. J. Glass and A. Owyoung, *IEEE J. Quantum Electron.* **QE-14**, 601 (1978).
[6] C. C. Lee and H. Y. Fan, *Phys. Rev. B.* **9**, 3502 (1974).
[7] H. M. Nussenzveig, (New York: Academic, 1972).
[8] M. Sheik-Bahae, D. C. Hutchings, D. J. Hagan and E. V. Stryland, *IEEE, JQE* **27**, 1296 (1991).
[9] R. S. Adhav, *Phys. Rev. E.* **17**, 4620 (1978).
[10] A. M. Johnson, C. R. Pidgeon and J. Dempsey, *Phys. Rev. E.* **22**, 825 (1980).
[11] F. R. Ahmed, Y. W. Tseng, M. A. Kats and E. Rana, *Optics Letts.* **33**, 1041 (2008).
[12] H. J. S. Dorren, G. D. Khoe and D. Lenstra, *Optics Communications* **205**, 247 (2002).
[13] H. J. S. Dorren, X. Yang, A. K. Mishra, Z. Li., H. Ju, H. de-Waardt, G. D. Khoe, T. Simoyama, H. Ishikawa, H. Kawashima and T. Hasama, *IEEE, JQE* **10**, 1079 (2004).
[14] H. J. S. Dorren, X. Yang, D. Lenstra, H. de Waart, G. D. Khoe, T. Simoyama, H. Ishikawa, H. Kawashima and T. Hasama, *IEEE, Photonics Tech. Letts.* **15**, 792 (2003).
[15] P. J. Maguire, L. P. Barry, T. Krug, M. Lynch, A. L. Bradley, J. F. Donegan and H. Folliot, *Electronic Lett.* **41** 8 (2005).
[16] R. Salem and T.E. Murphy, *Proc. of Nonlinear Optics*, Paper TuB7 (2004).
[17] A. Nevet, A. Hayat and M. Orenstein, *Phys. Rev. Lett.* **104**, 207404 (2010).
[18] A. Nevet, A. Hayat and M. Orenstein, *Optics. Lett.* **35**, 3877 (2010).
[19] H. Ju, A. V. Uskov, R. Notzel, Z. Li, J. M. Vazquez, D. Lenstra, G. D. Khoe and H. J. S. Dorren, *Appl. Phys. B.* 005-2107-8 (2006).
[20] Q. Wang, G. Zhu, H. Chen, J. Jaques, J. Leuthold, A. B. Piccirilli and N. K. Dutta, *IEEE J. Quantum Electron.* **40**, 703 (2004).
[21] J. Y. Kim, J. M. Kang, T. Y. Kim and S. K. Han, *Electron. Lett.* **42**, 303 (2006).
[22] T. Houbavlis, K. Zoiros, A. Hatziefremidis, H. Avramopoulos, L. Occhi, G. Guekos, S. Hansmann, H. Burkhard and R. Dall'Ara, *Electron. Lett.* **35**, 1650 (1999).
[23] C. Bintjas, M. Kalyvas, G. Theophilopoulos, T. Stathopoulos, H. Avramopoulos, L. Occhi, L. Schares, G. Guekos, S. Hansmann and R. Dall'Ara, *IEEE Photon. Technol. Lett.* **12**, 834 (2000).
[24] K. Chan, C. Chan, L. Chen and F. Tong, *IEEE Photon. Technol. Lett.* **16**, 897 (2004).
[25] H. Folliot, M. Lynch, A. L. Bradley, T. Krug, L. A. Dunbar, J. Hegarty and J. F. Donegan, *J. Opt. Soc. Am. B.* **19**, 2396 (2002).
[26] A. Meccozi and J. Mork, *IEEE J. Sel. Top. Quant. Electron.* **3**, 1190 (1997).
[27] T. Berg and J. Mork, *IEEE J. Quantum Electron.* **40**, 1527 (2004).
[28] S. Ma, Z. Chen and N. K. Dutta, *Optics Communications* **282**, 4508 (2010).
[29] A. Kotb, S. Ma, Z. Chen and N. K. Dutta, *Optics Comm.* **283**, 4707 (2010).

Chapter 14

Semiconductor Optical Amplifiers as Broadband Sources

14.1. Introduction

Semiconductor optical amplifier has a broad emission spectrum. The emission arises from the amplified spontaneous emission (ASE) in the active region of the device. The width of the emission spectrum is typically 40 to 60 nm and can be larger if excited state emission in quantum dot material is considered. This broad emission spectrum can have high power if the device is fabricated as a RSOA type design or a superluminescent diode (SLD) type design. The conventional travelling wave SOA, the reflective SOA and the SLD have essentially the same active region structure, they differ in facet reflectivity (facet coating used) and may differ in transverse mode confinement depending on the application of the device. In this chapter, application and configuration of these SOA type devices as broadband sources are described. Another useful broadband source is the ASE from an optical fiber amplifier. The SOA type sources can be made over a wide range of wavelengths (using different semiconductor gain medium), the fiber ASE sources are somewhat limited in wavelength due to availability of rare doped fibers in a fewer set of spectral regions.

14.2. High Power Broadband SOA Type Source

A high power broadband SOA type source is generally called a SLD [1–10]. The SLD device structure is optimized for high power and broad spectral width and has been fabricated using GaAs/AlGaAs,

GaAs/InGaAs and InP/InGaAsP material system. These systems generally produce SLDs in the wavelength ranges of 800 nm, 1000 nm and 1300–1600 nm respectively. The output power of the SLD (with a zero reflectivity at the output facet) is approximately given by [2]

$$P = R_{\rm sp}[(e^{(g-\alpha)L} - 1)/(g - \alpha)], \qquad (14.2.1)$$

where $R_{\rm sp}$ is the spontaneous emission per unit length into the guided mode, g is the optical gain, α is the optical absorption and L is the length of the device. Equation (14.2.1) is obtained by integrating the net gain ($g-\alpha$) over the length of the device. Since the optical gain increases with increasing current, the output of the SLD increases rapidly with increasing current until it saturates due to heating and other effects such as leakage current in the device (Ch. 4). The schematic of a high power SLD structure fabricated using the GaAs/AlGaAs material system is shown in Fig. 14.2.1.

The SLD device has an inclined stripe with respect to the facet for reducing facet reflectivity. The output power as a function of current and spectrum at room temperature are shown in Fig. 14.2.2. The structure has index guiding and good carrier confinement which

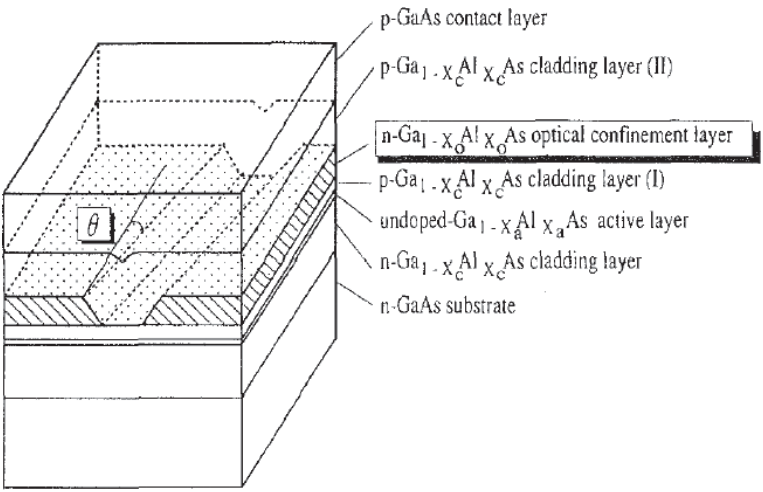

Fig. 14.2.1. Schematic of GaAs/AlGaAs SLD structure [10].

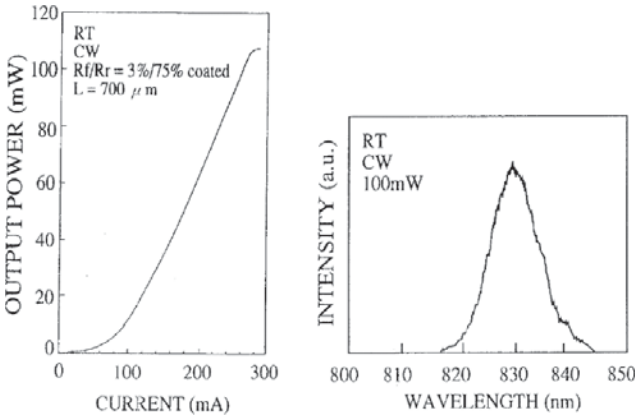

Fig. 14.2.2. Measured output power as a function of current and spectrum at 100 mW output are shown [10].

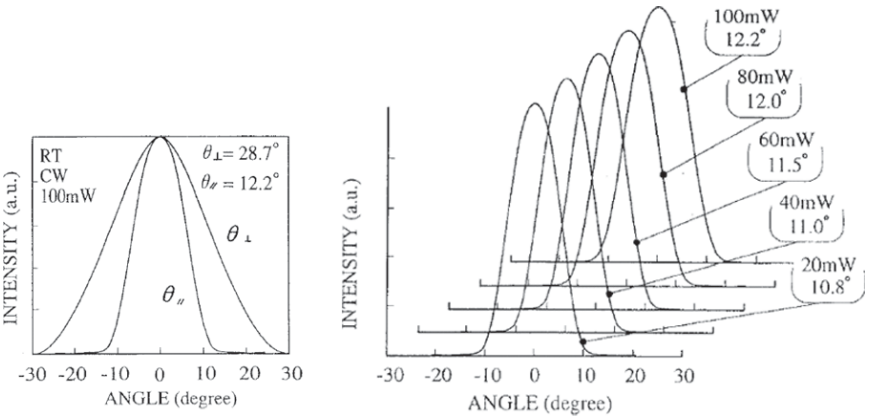

Fig. 14.2.3. Far field beam divergence along and normal to junction are shown on the left and far field along the junction at various currents are shown on the right [10].

results in high output power and good stability of the output beam as a function of current (Fig. 14.2.3).

SLDs have been fabricated with quantum dot (QD) active region. As stated in Ch. 11, the QD-SOA exhibits optical emission both for ground state and excited state transitions. Since the excited state emission is at a shorter wavelength in QD-SLD (or QD-SOA)

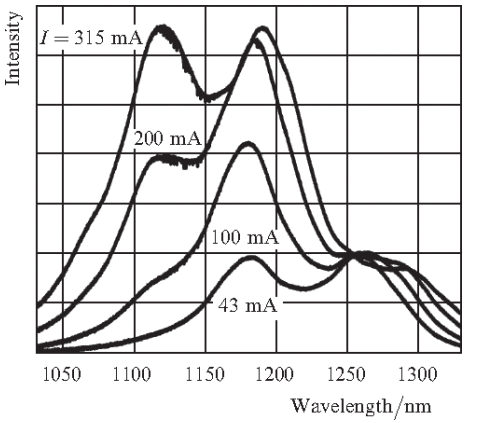

Fig. 14.2.4. Emission spectrum of a QD-SLD with InAs/InGaAs QD active region. The excited state emission becomes more pronounced at high currents [12].

compared to that for the ground state, the combined ground state and excited emission from a QD-SLD is expected to have a broader spectral width. This has been demonstrated in several types of QD-SLD [11–14]. The spectral emission of a self assembled InAs/$In_{0.15}Ga_{0.85}As$ QD-SLD for various currents is shown in Fig. 14.2.4. The device has 10 QD-layers of InAs/InGaAs separated by 33 nm thick GaAs layers. The layers are fabricated in n-GaAs substrate and have p-type and n-type AlGaAs cladding layers. The wafer was fabricated into 4 μm wide ridge waveguide devices and the ridges were angled at 7° to the cleaved facets (to reduce reflection) and they were further antireflection coated.

The light output vs. current characteristics of a QD-SLD of the above type is shown in Fig. 14.2.5(a). Longer devices emit higher power due to lower thermal impedance of longer devices. Also, shown in the Figure is an initial stability test. The output as a function of operating time for SLDs operating at two currents is shown in Fig. 14.2.5(b). It shows fairly stable operation for the duration shown.

InGaAs QD-SLDs with high output power under pulsed operation has been reported [11]. The devices has 6° angled active region stripe relative to the facets and has a length of 1.5 mm. The spectral width of the device at 2500 mA operation is 110 nm (Fig. 14.2.6).

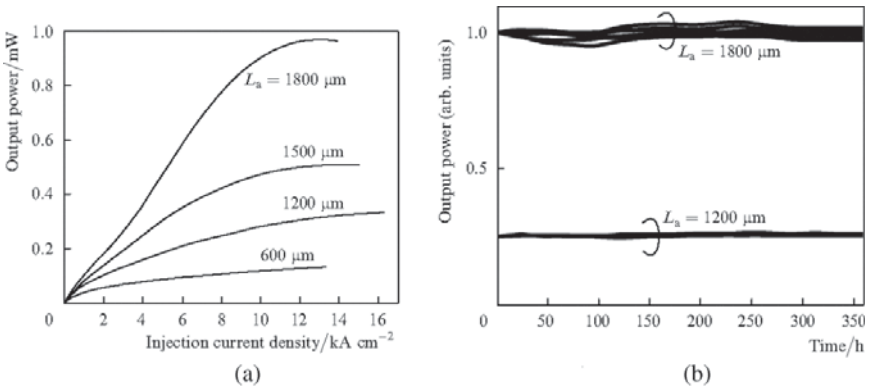

Fig. 14.2.5. (a) Light output as a function of current for SLDs of different lengths. (b) Output power as a function of operating time [12].

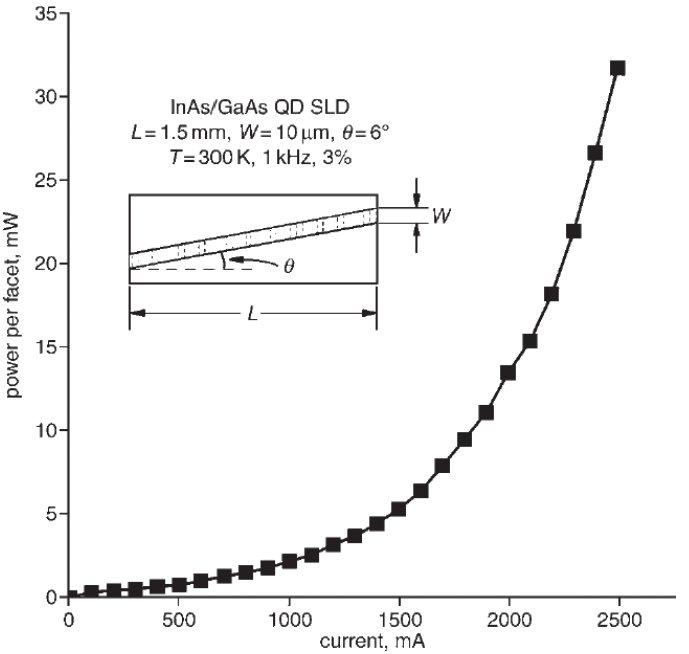

Fig. 14.2.6. Pulsed light vs. current characteristics of a QD-SLD [11].

For high power output and broad emission spectrum a QD-SLD monolithically integrated with a SOA has been reported. The active region consists of ten InAs-QD layers separated from each other by GaAs spacer layers. Each QD layer with the QDs is formed by depositing a monolayer of InAs at 480°C covered by a 2-nm thick $In_{0.15}$ $Ga_{0.85}$ As. Ten such QD layers plus the GaAs waveguide layers form the whole active region which is sandwiched between n-type and p-type $Al_{0.5}Ga_{0.5}As$ cladding layers followed by a p-GaAs contact layer. The entire structure is grown over a n-GaAs substrate. The wafer was processed into 10 μm wide ridge waveguide devices in a form where the SLD is monolithically integrated with the SOA (Fig. 14.2.7, 14.2.8) [14]. The SLD is 1 mm long and the SOA is 3 mm long.

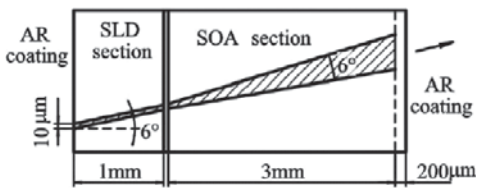

Fig. 14.2.7. Schematic of the integrated SLD and SOA structure [14].

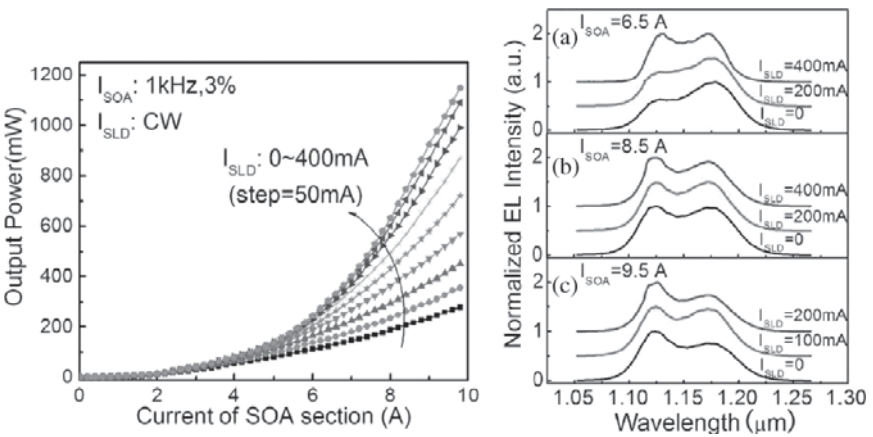

Fig. 14.2.8. Pulsed light as a function of SOA current and spectrum at various currents are shown [14].

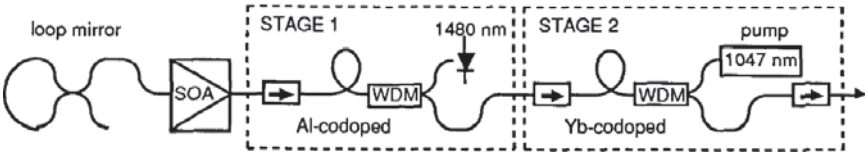

Fig. 14.3.1. Schematic of a SOA spectrally sliced source based on SOA [15].

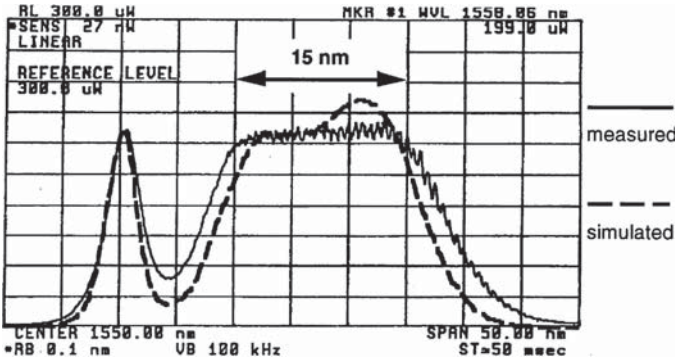

Fig. 14.3.2. The spectrum of the ASE source which includes the ASE from the EDFA. The solid line is measured data and the dashed line shows the model [15].

14.3. Wavelength Division Multiplexing (WDM) Applications

Wavelength division multiplexing (WDM) systems require light sources which emit at different wavelengths. A SOA based source ASE power of the SOA is spectrally sliced (separated) into a set of optical outputs each in a narrow range of wavelengths could be used in WDM transmission [15, 16]. A schematic of a source used in WDM experiments in shown in Fig. 14.3.1. The loop mirror attached to the SOA is for improving the output power. The dashed boxes in Fig. 14.3.1 represent two stages of erbium doped fiber amplifiers (EDFA). The total output power after two-stage amplification is ∼20 dBm. The spectrum of the source is shown in Fig. 14.3.2. It includes the ASE from the EDFAs.

The above ASE source was used in WDM transmission experiments by slicing a portion of the output spectrum. The schematic of the experiment along with the bit-error-rate data is shown

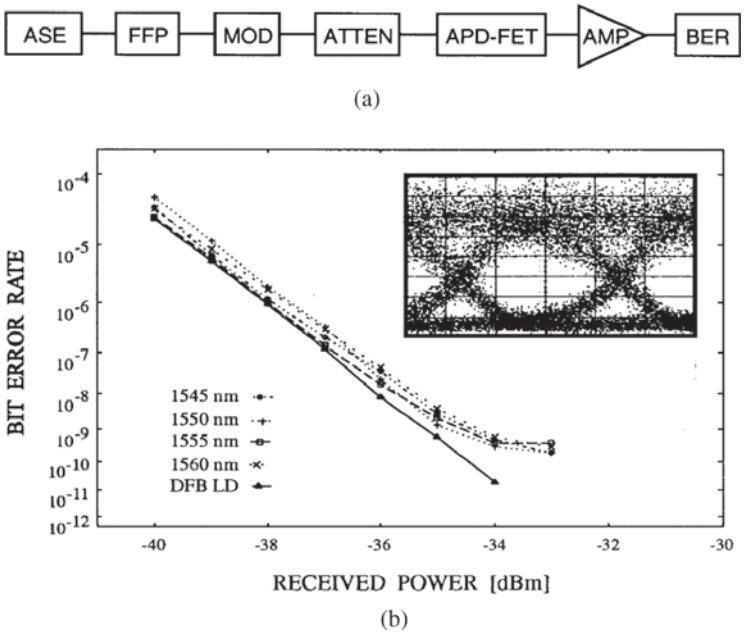

Fig. 14.3.3. (a) Schematic of the transmission experiment set up. The data rate is 622 Mb/s. The BER as a function of received power for four spectrally filtered center wavelengths (1545 nm, 1550 nm, 1555 nm, 1560 nm) and using a distributed feedback laser are shown. All five sources essentially have the same BER up to 10^{-9} BER. The DFB laser performs better for lower BER [15].

in Fig. 14.3.3. A fiber Fabry-Perot (FFP) filter is used to obtain the output power from ASE in a narrow spectral range. The FWHM of the filter is 0.23 nm and the typical output power is $\sim$90 μW. The modulator used is a $LiNbO_3$ modulator, the data rate is 622 Mb/s. The modulator is followed by an attenuator and an APD (avalanche photodiode) based receiver with a preamplifier (FET based). The BER data in Fig. 14.3.3 is good which shows that the ASE source may be an important low cost source for some applications.

SOA based multiwavelength light sources have been reported. In these sources the SOA is used as a gain medium in the optical cavity. The source shown in Fig. 14.3.4 has 99% reflectivity mirrors and a SOA gain medium with gain centered near 1550 nm

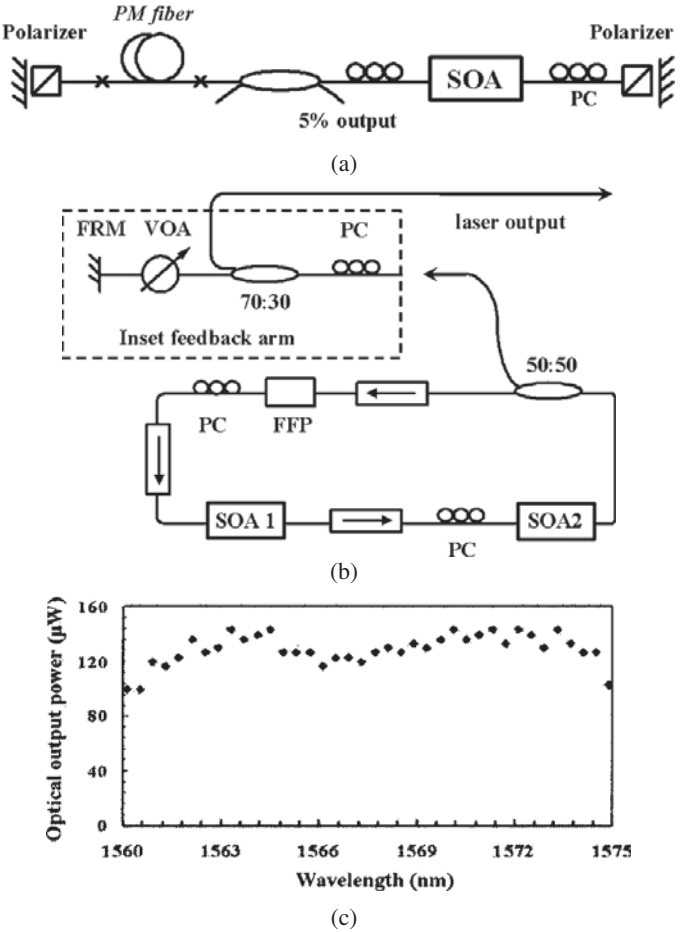

Fig. 14.3.4. Schematic of two types of multiwavelength sources using fiber gain medium. The top figure (a) is for a linear optical cavity and the lower figure (b) is for a ring cavity. The ring cavity also has a feedback structure which can be used to optimize performance. Figure (c) shows the output at various emission wavelengths [17].

fabricated using the InGaAsP/InP material system [17]. A linear cavity shown in Fig. 14.3.4(a) or a ring cavity (built using optical fiber) shown in Fig. 14.3.4(b) has been studied. The ring cavity has been shown to produce a more uniform power output for the emission wavelengths.

14.4. Optical Coherence Tomography Source

For optical coherence tomography (OCT) applications it is important to have a broadband source. Such sources have low coherence length which allows better resolution. The operating wavelength needs to be in the range of 800 nm–1400 nm to avoid multiple scattering in skin tissue [18]. The center wavelengths of 800 nm and 1300 nm are important for ophthalmic and skin diagnosis, respectively. However, at a center wavelength of 1050 nm there is a reduction in scattering due to water which is important for deep tissue imaging. Thus broadband sources in the usual range where semiconductor optical devices can be fabricated are important for OCT. The axial resolution Δz, is the coherence length of the light source. The relationship between spectral width and Δz is given by

$$\Delta z = (2 \ln 2/\pi)(\lambda_0^2/\Delta\lambda). \tag{14.4.1}$$

Thus it is important to have a large source spectral width. The calculated resolution as a function of spectral width is shown in Fig. 14.4.1.

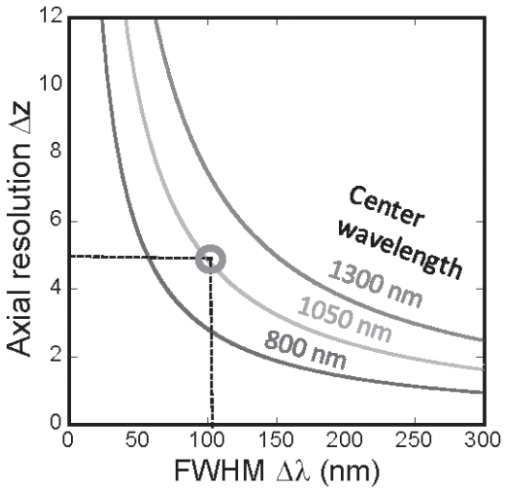

Fig. 14.4.1. Calculated axial resolution (in μm) for SLDs emitting at 800 nm, 1050 nm and 1300 nm respectively. A typical resolution is 5 μm as shown by the dashed line [18].

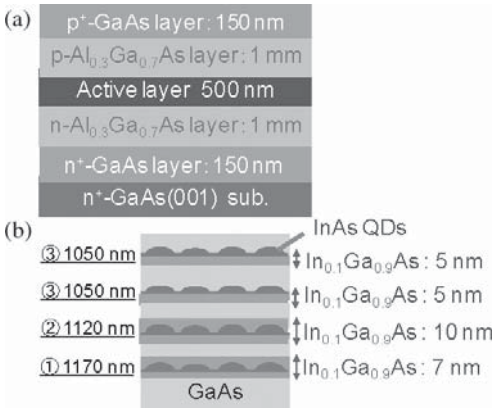

Fig. 14.4.2. The active region of a QD-SLD emitting near 1050 nm [18].

QD-SLD has been fabricated which emits near 1050 nm to reduce water scattering effects as mentioned previously. The schematic of the active region of the device is shown in Fig. 14.4.2. The structure is grown on n-GaAs substrate and has four QD layers. Each QD layer is separated by 50-nm-thick GaAs barriers which are sandwiched between 1-μm-thick p-type and n-type $Al_{0.3}Ga_{0.7}As$ cladding layers. The fabricated SLD device is of the ridge waveguide type with a ridge width of 9 μm. The device length is 300 μm. The spectrum of the device at various currents and FWHM as a function of current is shown Fig. 14.4.3. An axial resolution of 5.4 μm was obtained using this device in an OCT system (measured $\Delta\lambda$ of 122 nm under operating conditions) which is somewhat larger than the calculated value of 4.4 μm.

A source with broader bandwidth can be obtained by combining the output of two SLDs. Such combination has been used to produce a ∼200 nm wide source for OCT experiments. One of the SLDs has center wavelength of 1233 nm and has a spectral width of 80 nm, the second SLD has a center wavelength of 1335 nm and a spectral width of 110 nm. The output of the two SLDs is coupled to a single mode fiber. The output power of the source is 10 mW and the resulting spectral width is ∼200 nm [19]. The spectrum of the source is shown in Fig. 14.4.4.

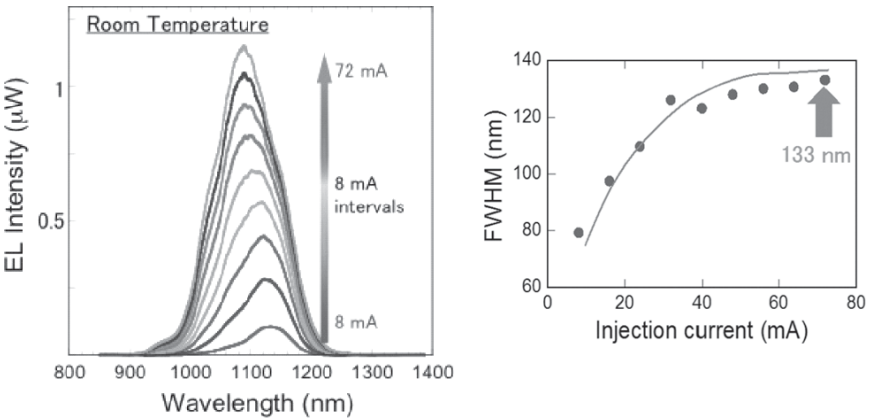

Fig. 14.4.3. The spectrum of the device at various currents and FWHM as a function of current are shown [18].

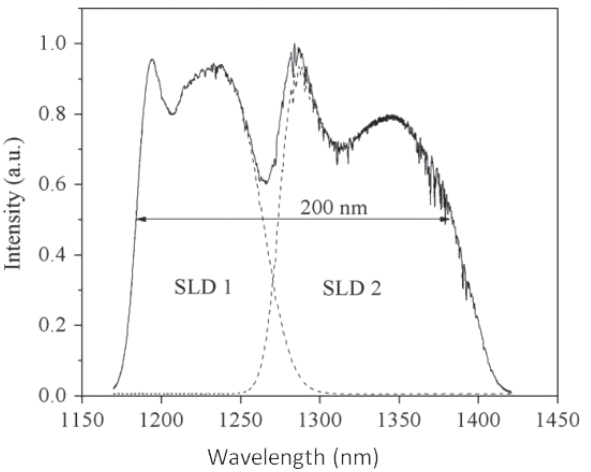

Fig. 14.4.4. Spectral output of a SLD source used in OCT experiment [19].

An OCT system using this source was shown to have an axial resolution of 3.9 μm and lateral resolution of 6.5 μm [19].

14.5. Sensor Applications

Several authors have reported results on fiber optic sensors which utilize a fiber Bragg grating (FBG) and a broadband light source

[20–24]. The light sources in many studies have been the amplified spontaneous emission from a SOA (or SLD) type source and in some cases it has been the ASE from a doped fiber amplifier. The sensing element generally is the FBG whose reflection or transmission property changes (i.e. it reflects or transmits a slightly different wavelength) due to a change in its environment. Such changes could be temperature, pressure, vibration or any mechanical or electromechanical changes that changes the effective periodicity of the grating through a change in grating period or a change in refractive index of the grating medium.

The operating principle of a FBG based sensor system is to monitor the shift in wavelength of the returned reflected signal with the changes in the physical properties of the grating or its environment (e.g. strain, temperature). The Bragg wavelength (the wavelength of the reflected signal, λ_B) is given by [20].

$$\lambda_B = 2n\Lambda, \tag{14.5.1}$$

where Λ is the grating pitch and n is the effective index of the core. When a spectrally broadband source of light is injected into the fiber with a FBG, a narrowband spectral component at the Bragg wavelength is reflected by the grating (Fig. 14.5.1). In the transmitted light, this spectral component is missing. The temperature response of the sensor arises primarily through a change in index

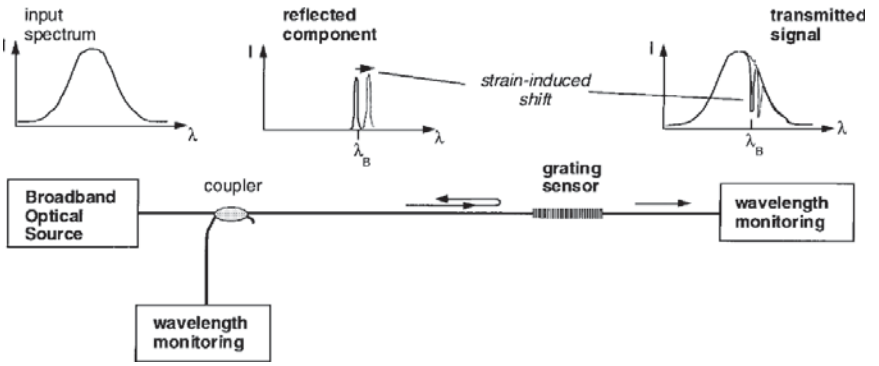

Fig. 14.5.1. Schematic of a FBG based sensor [24].

(n in Equation 14.5.1) and the strain response is due to a physical change in length of sensor (i.e. small change in grating pitch Λ). The shift in Bragg wavelength (λ_B) due to a change in strain or temperature can be expressed by [24]

$$\Delta\lambda_B = 2n\Lambda[\{1 - (n^2/2)(P_{12} - \nu(P_{11} + P_{12}))\}e + \{\alpha + (dn/dT)/n\}\Delta T], \quad (14.5.2)$$

where P_{ij} are the Pockel's (piezo) coefficients of the stress-optic tensor, ν is Poisson's ratio, e is the applied strain, and α is the coefficient of thermal expansion (CTE) of the fiber material (e.g. silica), and ΔT is the temperature change. The quantity $(n^2/2)(P_{12} - \nu(P_{11} + P_{12}))$ has a numerical value of $\sim$0.22.

The strain response of a FBG at constant temperature has been measured. It is found to be [24]

$$(1/\lambda_B)(\delta\lambda_B/\delta\varepsilon) = 0.78 \times 10^{-6}\mu\varepsilon^{-1}. \quad (14.5.3)$$

This response gives a "rule-of-thumb" measure of the grating shift with strain of 1 nm per 1000 $\mu\varepsilon$ at 1.3 μm wavelength. In silica fibers, the thermal response is the dominant effect, which accounts for 95% of the observed shift. The normalized thermal response at constant strain is [24]

$$(1/\lambda_B)(\delta\lambda_B/\delta\mathrm{T}) = 6.7 \times 10^{-6}\,\mathrm{C}^{-1}. \quad (14.5.4)$$

A wavelength resolution of $\sim$1 pm (0.001 nm) is required (at $\sim$1.3 μm) to resolve a temperature change of $\sim$0.1 C, or a strain change of 1 μ strain.

One of the advantages of Bragg gratings is that the sensed information is encoded directly into wavelength, which is an absolute parameter. The output wavelength does not depend directly on the total light levels, losses in the connecting fibers and couplers, or source power. The FBG based sensor system allows wavelength division multiplexing i.e. each sensor is assigned a different wavelength band of the broadband source spectrum. This allows quasi-distributed sensing of strain, temperature, or other areas by associating each spectral band with a particular spatial location.

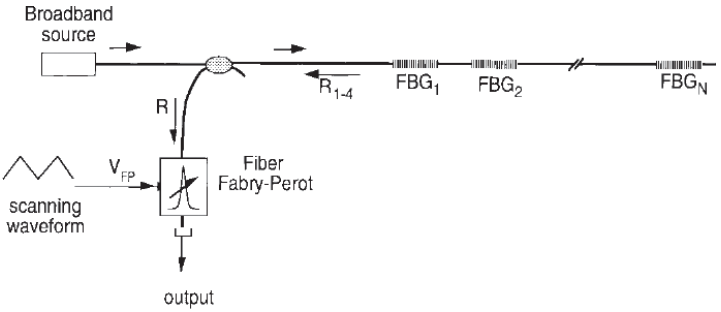

Fig. 14.5.2. Scanning filter for monitoring FBG output [24].

The concept is illustrated in Fig. 14.5.2. A scanning filter (by tuning voltage) is used to examine the reflected output. From the voltages at which the signal is observed the FBGs can be monitored.

Temperature and strain sensors using fiber Bragg grating are used in many applications where remote monitoring is required.

References

[1] G. A. Alphonse, D. B. Gilbert, M. G. Harvey and M. Ettenberg, *IEEE J. Quantum Electron.* **24**, 2454 (1988).
[2] N. K. Dutta and P. P. Deimel, *IEEE J. Quantum Electron.* **QE-19**, 496 (1983).
[3] N. S. K. Kwong, K. Y. Lau and N. Bar-Chaim, *IEEE J. Quantum Electron.* **25**, 696 (1989).
[4] C. S. Wang, W. H. Chen, C. J. Hwang, W. K. Bums and R. P. Moeller, *Appl. Phys. Lett.* **41**, 587 (1982).
[5] K. Tateoka, H. Naito, M. Yuri, M. Kume, K. Hamada, H. Shimizu, M. Kazumura and I. Teramoto, *IEEE J. Quantum Electron.* **27**, 1568 (1991).
[6] L. Goldberg and D. Mehuys, *Electron. Lett.* **30**, 1682 (1994).
[7] O. Imafuji, T. Takayama, H. Sugiura, M. Yuri, H. Naito, M. Kume and K. Itoh, *IEEE J. Quantum Electron.* **29**, 1889 (1993).
[8] T. Takayama, O. Imafuji, H. Sugiura, M. Yuri, H. Naito, M. Kume and K. Itoh, *Jpn. J. Appl. Phys.* **34**, 3533 (1995).
[9] T. Takayama, O. Imafuji, M. Yuri, H. Naito, M. Kume, A. Yoshikawa and K. Itoh, *IEEE J. Select. Topics Quantum Electron.* **1**, 562 (1995).
[10] T. Takayama, O. Imafuji, Y.i Kouchi, M. Yuri, A. Yoshikawa and K. Itoh, *IEEE J. Quant. Elec.* **32**, 1981 (1996).
[11] N. Liu, P. Jin and Z. G. Wang, *Electronic Lett.* **41**, No. 25 (2005).
[12] E. V. Andreeva, A. E. Zhukov, V. V. Prokhorov, V. M. Ustinov and S. D. Yakubovich, *Quantum Electronics* **36**, 527 (2006).

[13] T. K. Ong, M. Yin, Z. Yu, Y. Chuen Chan and Y. L. Lam, *Meas. Sci. Tech.* **15**, 1591 (2004).
[14] X. Li, P. Jin, Q. An, Z. Wang, X. Lv, H. Wei, J. Wu, and Z. Wang, *Nano Res. Letts.* **6**, 625 (2011).
[15] D. D. Simpson and W. T. Holloway, *Optical Amp. and Appl.* OSA meeting, PD2-2, 184 (1994).
[16] A. Ghazisaeidi, F. Vacondio, A. Bononi and L. A. Rusch, *Journal of Lightwave Tech.* **27**, 2667 (2009).
[17] N. Pleros, C. Bintjas, M. Kalyvas, G. Theophilopoulos, K. Yiannopoulos, S. Sygletos and H. Avramopoulos, *IEEE Photonic Tech. Lett.* **14**, 693 (2002).
[18] I. Tsubaki, Y. Harada and T. Kita, *Phys. Status Solidi C*, 1–4 (2012).
[19] M. D. Bayleyegn, H. Makhlouf, C. Crotti, K. Plamann and A. Dubois, *Optics Comm.* (2012).
[20] W. W. Morey, J. R. Dunphy and G. Meltz, in Proc. SPIE Distributed and Multiplexed Fiber Optic Sensors, Boston, MA, Sept. 1991, **1586**, 216 (1991).
[21] S. M. Melle, K. Liu and R. M. Measures, *IEEE Photon. Technol. Lett.* **4**, p. 516 (1992).
[22] M. A. Davis and A. D. Kersey, *Electron. Lett.* **30**, 75 (1994).
[23] M. A. Davis, D. G. Bellemore and A. D. Kersey, in Proc. SPIE 1995 North American Conf. Smart Structures Materials, San Diego, CA, **2446**, 227 (1995).
[24] A. D. Kersey, M. A. Davis, H. J. Patrick, M. LeBlanc, K. P. Koo, C. G. Askins, M. A. Putnam and E. J. Friebele, *J. Lightwave Tech.* **15**, 1442 (1997).

Index